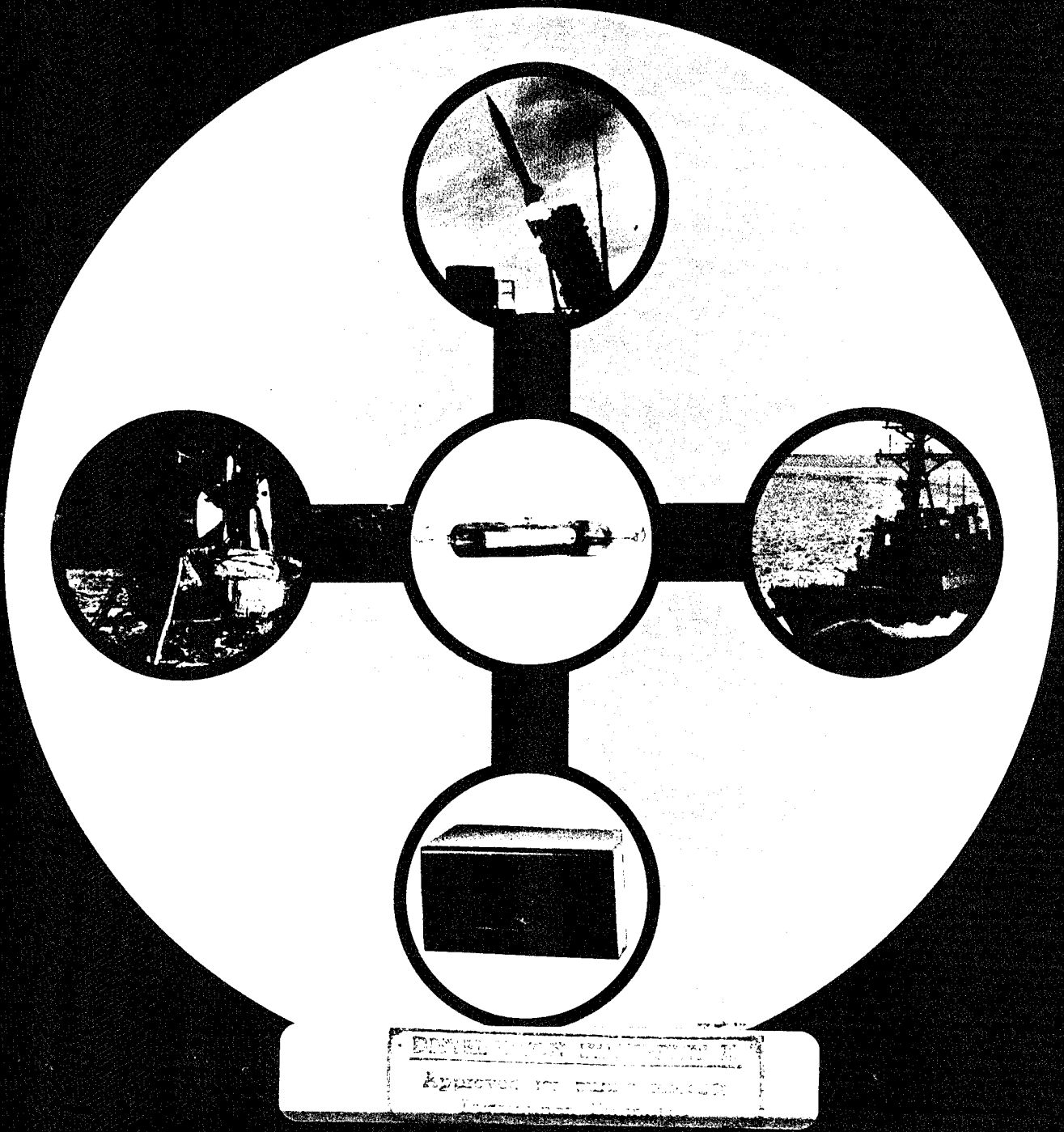
PROCEEDINGS OF THE
FIRST INTERNATIONAL WORKSHOP ON CROSSED-FIELD DEVICES



August 15-16, 1995
Ann Arbor, Michigan

REPORT DOCUMENTATION PAGE

Form Approved
OMB No. 0704-0188

Public reporting burden for this collection of information is estimated to average 1 hour per response, including the time for reviewing instructions, searching existing data sources, gathering and maintaining the data needed, and completing and reviewing the collection of information. Send comments regarding this burden estimate or any other aspect of this collection of information, including suggestions for reducing this burden, to Washington Headquarters Services, Directorate for Information Operations and Reports, 1215 Jefferson Davis Highway, Suite 1204, Arlington, VA 22202-4302, and to the Office of Management and Budget, Paperwork Reduction Project (0704-0188), Washington, DC 20503.

1. AGENCY USE ONLY *(Leave blank)*	2. REPORT DATE	3. REPORT TYPE AND DATES COVERED
	3/96	Proceedings Aug. 15-16, 1995

4. TITLE AND SUBTITLE
Proceedings of the First International Workshop on Crossed-Field Devices

5. FUNDING NUMBERS
N00014-92-C-2265
P.O. #951118

6. AUTHOR(S)
EDITORS: David Chernin and Y.Y. Lau

7. PERFORMING ORGANIZATION NAME(S) AND ADDRESS(ES)
The University of Michigan
Department of Nuclear Engineering and Radiological Sciences
Cooley Bldg., Room 112
Ann Arbor, MI 48109-2104

8. PERFORMING ORGANIZATION REPORT NUMBER

9. SPONSORING/MONITORING AGENCY NAME(S) AND ADDRESS(ES)
Naval Research Laboratory
Washington, D.C. 20375
Naval Surface Warfare Center
Crane Division
Crane, IN 47522

10. SPONSORING/MONITORING AGENCY REPORT NUMBER

11. SUPPLEMENTARY NOTES
Prepared in cooperation with: Science Applications International Corporation
McLean, VA

12a. DISTRIBUTION/AVAILABILITY STATEMENT
Unlimited Distribution

12b. DISTRIBUTION CODE

13. ABSTRACT *(Maximum 200 words)*

These proceedings contain 30 papers presented at The First International Workshop on Crossed-Field Devices in Ann Arbor, MI, on August 15-16, 1995. The papers include historical surveys, defense and commercial applications, supporting technologies and simulation and modeling of crossed-field devices, including magnetron and crossed-field amplifier.

14. SUBJECT TERMS
magnetron, crossed-field amplifiers, microwave sources

15. NUMBER OF PAGES
341

16. PRICE CODE

17. SECURITY CLASSIFICATION OF REPORT	18. SECURITY CLASSIFICATION OF THIS PAGE	19. SECURITY CLASSIFICATION OF ABSTRACT	20. LIMITATION OF ABSTRACT
Unclassified	Unclassified	Unclassified	UL

GENERAL INSTRUCTIONS FOR COMPLETING SF 298

The Report Documentation Page (RDP) is used in announcing and cataloging reports. It is important that this information be consistent with the rest of the report, particularly the cover and title page. Instructions for filling in each block of the form follow. It is important to ***stay within the lines*** to meet ***optical scanning requirements***.

Block 1. Agency Use Only *(Leave blank)*.

Block 2. Report Date. Full publication date including day, month, and year, if available (e.g. 1 Jan 88). Must cite at least the year.

Block 3. Type of Report and Dates Covered. State whether report is interim, final, etc. If applicable, enter inclusive report dates (e.g. 10 Jun 87 - 30 Jun 88).

Block 4. Title and Subtitle. A title is taken from the part of the report that provides the most meaningful and complete information. When a report is prepared in more than one volume, repeat the primary title, add volume number, and include subtitle for the specific volume. On classified documents enter the title classification in parentheses.

Block 5. Funding Numbers. To include contract and grant numbers; may include program element number(s), project number(s), task number(s), and work unit number(s). Use the following labels:

C	- Contract	**PR**	- Project
G	- Grant	**TA**	- Task
PE	- Program Element	**WU**	- Work Unit Accession No.

Block 6. Author(s). Name(s) of person(s) responsible for writing the report, performing the research, or credited with the content of the report. If editor or compiler, this should follow the name(s).

Block 7. Performing Organization Name(s) and Address(es). Self-explanatory.

Block 8. Performing Organization Report Number. Enter the unique alphanumeric report number(s) assigned by the organization performing the report.

Block 9. Sponsoring/Monitoring Agency Name(s) and Address(es). Self-explanatory.

Block 10. Sponsoring/Monitoring Agency Report Number. *(If known)*

Block 11. Supplementary Notes. Enter information not included elsewhere such as: Prepared in cooperation with...; Trans. of...; To be published in.... When a report is revised, include a statement whether the new report supersedes or supplements the older report.

Block 12a. Distribution/Availability Statement. Denotes public availability or limitations. Cite any availability to the public. Enter additional limitations or special markings in all capitals (e.g. NOFORN, REL, ITAR).

DOD - See DoDD 5230.24, "Distribution Statements on Technical Documents."
DOE - See authorities.
NASA - See Handbook NHB 2200.2.
NTIS - Leave blank.

Block 12b. Distribution Code.

DOD - Leave blank.
DOE - Enter DOE distribution categories from the Standard Distribution for Unclassified Scientific and Technical Reports.
NASA - Leave blank.
NTIS - Leave blank.

Block 13. Abstract. Include a brief *(Maximum 200 words)* factual summary of the most significant information contained in the report.

Block 14. Subject Terms. Keywords or phrases identifying major subjects in the report.

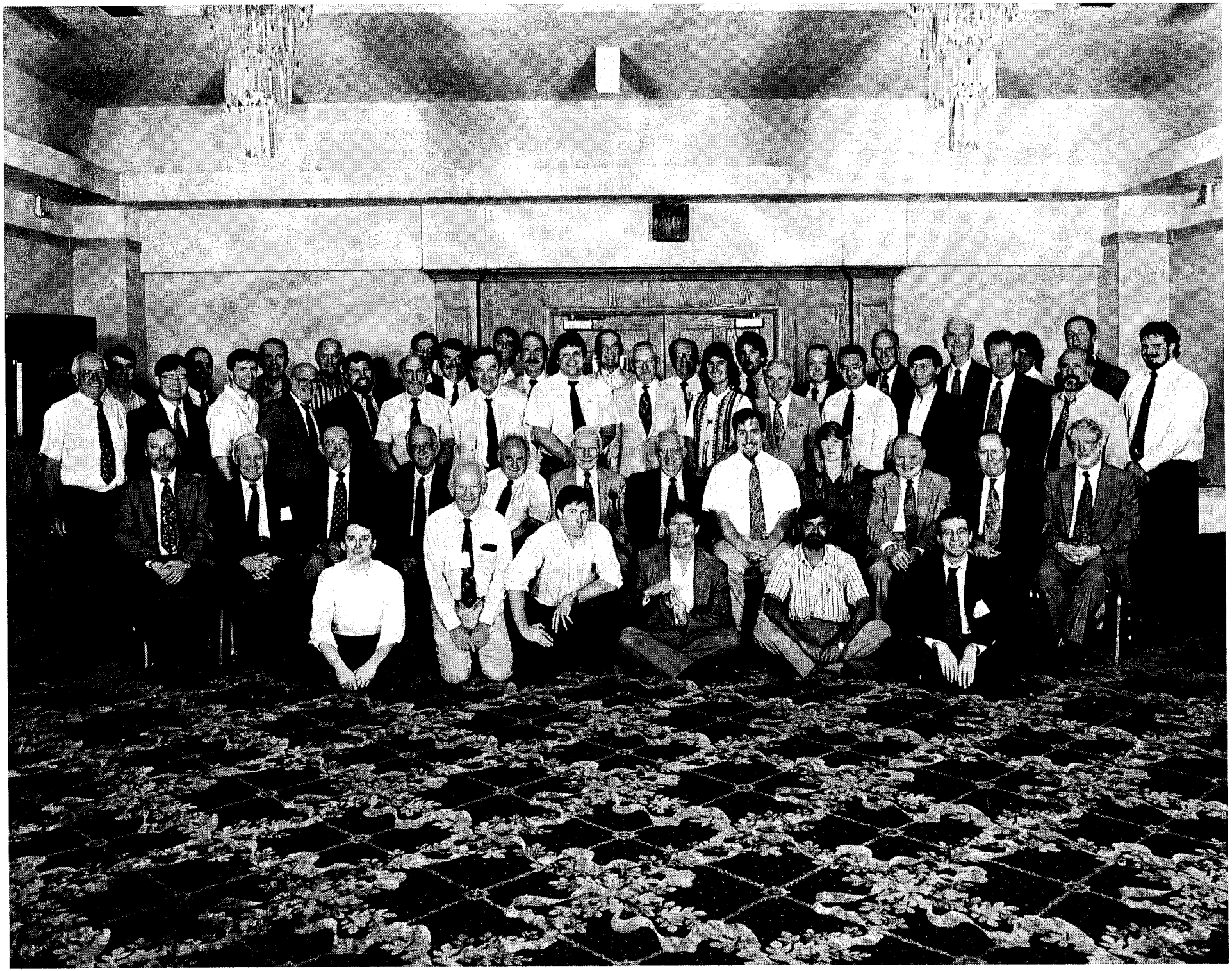
Block 15. Number of Pages. Enter the total number of pages.

Block 16. Price Code. Enter appropriate price code *(NTIS only)*.

Blocks 17. - 19. Security Classifications. Self-explanatory. Enter U.S. Security Classification in accordance with U.S. Security Regulations (i.e., UNCLASSIFIED). If form contains classified information, stamp classification on the top and bottom of the page.

Block 20. Limitation of Abstract. This block must be completed to assign a limitation to the abstract. Enter either UL (unlimited) or SAR (same as report). An entry in this block is necessary if the abstract is to be limited. If blank, the abstract is assumed to be unlimited.

*U.S.GPO:1993-0-358-779



PROCEEDINGS OF THE
FIRST INTERNATIONAL WORKSHOP ON CROSSED-FIELD DEVICES



August 15-16, 1995
Ann Arbor, Michigan

Sponsored by

NAVAL RESEARCH LABORATORY

and

NAVAL SURFACE WARFARE CENTER
CRANE DIVISION

19960327 104

Organized by

THE UNIVERSITY OF MICHIGAN

and

SCIENCE APPLICATIONS
INTERNATIONAL CORPORATION

DTIC QUALITY INSPECTED 1

Foreword

Contained in these Proceedings are thirty (30) full-length papers that were presented at the First International Workshop on Crossed-Field Devices, which was held in Ann Arbor, Michigan, on 15 and 16 August 1995, at the Crowne Plaza Hotel. This Workshop, superbly organized by the University of Michigan and Science Applications International Corporation, was sponsored by the Naval Research Laboratory and the Naval Surface Warfare Center/Crane Division. The Workshop brought together researchers, manufacturers, and end-users of crossed-field devices (primarily magnetrons and crossed-field amplifiers) to discuss problems with, applications of, and opportunities for these versatile and widely used microwave devices. The Workshop, beginning with plenary talks of an historical nature by some of the field's pioneers, progressed through technical sessions on applications, supporting technologies, and modeling, and concluded with a panel discussion of future prospects and technical challenges.

The Workshop was attended by over 80 participants, among them 15 students from six universities. There was significant participation from the commercial and industrial sectors, as well as from U.S. Government laboratories and agencies, including the Air Force (Phillips Lab), Army (Ft. Monmouth, Adelphi), Commerce Department (NTIA), NASA (Lewis), and Navy (NRL, NSWC/Crane). International participation was significant with participants from Japan, Korea, Russia, United Kingdom, and Sweden.

Fourteen papers presented at the Workshop are not included in these Proceedings. These papers were primarily in the defense, commercial, and industrial applications areas. Among them were papers on ultra low-noise crossed-field amplifier design and development, injection-locked magnetron arrays, radiolocation, lighting applications, solid oil melting, microwave CVD diamond deposition, chemical synthesis and waste destruction, as well as general surveys of Russian magnetron work and of industrial applications in the food, rubber, and foundry industries.

These Proceedings will be deposited with the National Technical Information Services so that future citations to the papers contained here will be recognized by archival journals.

It is our hope that the topic will continue to be of comparable and intense interest in the future, and that the Second International Workshop will be, if anything, more successful.

Richard H. Abrams, Jr.
Naval Research Laboratory
Washington, DC

Preface

This volume contains contributed papers from the First International Workshop on Crossed-Field Devices, which was held in Ann Arbor, Michigan, on August 15-16, 1995. The goal of the Workshop, the first of its kind, was to bring together people from industry, government, and academia to review the historical development of magnetrons and crossed-field amplifiers, assess the present state of research, development, and applications, and formulate a working vision for the future. The Workshop was fundamentally technical in nature, with little formal discussion of business or management matters.

A unique and well received feature of the meeting was the Plenary session, at which some of the industry's pioneers presented their personal perspectives on the evolution of crossed-field devices from the early days during and immediately following World War II to the present. Attendees were reminded of the critical roles that crossed-field devices have played and continue to play in the nation's defense as well as in expanding commercial markets. They were also reminded of the pressing need to improve our products' performance, since competition from other sources is strong and growing. The recent partial displacement of CFA's in the Aegis SPY-1 and in Patriot by traveling wave tubes makes this point very vividly. Nonetheless, there remain numerous applications in which crossed-field devices are the clear choice. Many of these were described in the technical sessions that followed.

The four technical sessions, on Defense Applications, Commercial Applications, Supporting Technologies, and Simulation and Modeling, were designed to give the audience a broad exposure to the present state-of-the-art in crossed-field device technology. Highlights included reports on the low noise CFA development work for Aegis, papers on the applications of magnetrons in the materials processing, food and lighting industries, a presentation on noise, interference, and spectrum allocation issues, summaries of international efforts, and advances in basic research.

The final session of the Workshop was a Panel Discussion on the Future of Crossed-Field Devices that focused on formulating challenges for the community to address in the years ahead.

A memorable moment during the Workshop was the appearance of University of Michigan Emeritus Professor William G. Dow, who was a pioneer in crossed-field devices and was to celebrate his 100th birthday in September, 1995. He was warmly greeted by his colleagues, several of whom were former students. Professor Dow's graceful appearance added a special sense of history and continuity to the meeting.

On a more somber note, all attendees were saddened by the passing of Rodney Vaughan in February, 1995 at the age of 73. Rodney will always be remembered not only for his technical prowess and his accomplishments, but also for his charm, his vigor, his eloquence, and his integrity. The crossed-field community is made much poorer by his loss. The session on simulation and modeling was dedicated to his memory.

During the planning for the Workshop a decision was made to publish these Proceedings to serve as a permanent record of the meeting. Contributions would be voluntary, but it was hoped that the speakers' response would be adequate to allow publication of a substantial fraction of the Workshop's content. In fact, our hopes and expectations were greatly exceeded. Nearly 70% of the Workshop presentations are represented in this volume, which has afforded the speakers the opportunity to provide additional details in a permanent form, expanding upon the content of their short talk or poster session. With so few modern books available on crossed-field microwave devices, it is our hope that these Proceedings will be actively used by working engineers and scientists as well as by students now and in the future.

Dr. Richard Abrams, Jr., of the Naval Research Laboratory, was the original force behind the Workshop. It was his idea to expand a small, routine meeting on a specialized topic to an international gathering with a greatly expanded scope. The enthusiasm and encouragement of Dr. Robert Parker of NRL, and of Mr. Joe Dutkowski and Mr. Rex Bond of NSWC/Crane are also gratefully acknowledged. The efforts of Professor Chung Chan and, especially, Mr. Tom Ruden, in soliciting and helping to organize the Technical Sessions have substantially strengthened the program and are greatly appreciated. Of course, the voluntary cooperation of the attendees in contributing their time and effort to the completion of their manuscripts for this volume has made the challenging task of assembling these Proceedings that much easier.

Though relatively small in size, the Workshop itself, as well as the compilation of these Proceedings, required the cooperative efforts of many. A large debt is owed in particular to the efficient and effective behind-the-scenes efforts of the University of Michigan support staff, Diana Corey (Workshop Secretary) and Ann Bell, and graduate students, in particular John Luginsland, L. K. Ang, Peggy Christenson, Rami Kishek, and Agust Valfells.

The responses and comments that we have received have been quite favorable and suggest that the Workshop met its goal of stimulating interaction and cooperation in the crossed-field community. We are encouraged to hope that the Workshop and these Proceedings will be the first of a series.

David Chernin, Science Applications International Corporation, McLean, VA
Y. Y. Lau, University of Michigan, Ann Arbor, MI

Table of Contents

Foreword i

Preface ii

Part I. Plenary Session

Chairman: Richard Abrams, Jr.

Past, Present, and Future of Cossed-Field Devices: A Personal View.
Joseph A. Saloom 1

The History of the Reentrant Beam Crossed-Field Amplifier with Emphasis on Noise Comparison with the Magnetron.
William C. Brown 9

The Development of Crossed-Field Devices in the UK, from the Original 10cm Cavity Magnetron to the Present and Beyond.
Barry Vyse 23

Historical Perspective on Magnetron Development.
Robert E. Edwards 41

Part II. Applications: Defense, Commercial and Industrial

Co-chairmen: Rex Bond, Thomas E. Ruden

Low Noise CFA Measurements, Analysis, and Simulation.
Steve Hillenberg, Dean Thelen, Alexander MacMullen 51

Low-Field Magnetron Study.
Thomas E. Ruden, George E. Dombrowski, David Hobbs, George Boles 66

An Electronically Steerable Phased Array Module (ESPAM) Using the Microwave Oven Magnetron with External Circuitry as a High-Gain Phase-Locked Amplifier.
William C. Brown 78

Analysis of Magnetron Failure Modes Versus Power Level.
George A. Solomon 85

Application of Magnetrons with Medical Linear Accelerators.
G. T. Konrad 89

Part III. Supporting Technologies

Chairman: Chung Chan

Observation and Interpretation of Leakage Current in a Nonrelativistic Smooth Bore Magnetron
Jan E. Eninger and Bo H. Vanderberg 96

Investigation of Secondary Electron Emission from CVD Diamond Films for Crossed-Field Devices.
G. T. Mearini, I. L. Kransky, J. A. Dayton, Jr 115

Secondary Electron Emission Study for Crossed-Field Amplifier Applications.
Arnold Shih, Charles Hor, Richard Abrams 125

Investigations of Noise Mechanisms in a Reentrant Crossed-Field Amplifier.
Robert MacGregor, John Z. Ye, Chung Chan, Thomas E. Ruden 133

Rep-Rate Operation of a Magnetically Insulated Line Oscillator (MILO)
S. E Calico, F. J. Agee, M. C. Clark, R. W. Lemke, M. C. Scott 147

The Cooker Magnetron as a Standard in Crossed-Field Device Research.
John M. Osepchuk 159

The High Signal-to-Noise Ratio of the Microwave Oven Magnetron and Evidence of a Negative Feedback Loop to Control it.
William C. Brown 178

Instabilities, Turbulence and Organized Structures in Magnetized Electron Columns.
K. S. Fine, C. F. Driscoll, A. C. Cass, T. B. Mitchell, X.-P. Huang 188

Probing Space Charge in a Crossed-Field Amplifier.
John Z. Ye, Robert MacGregor, Chung Chan, Thomas E. Ruden 202

Frequency Twinning in Magnetrons.
E. M. Ball, M. Brady, R. G. Carter 212

Part IV. Rodney Vaughan Memorial Session on Modeling and Simulation

Co-Chairmen: David Chernin, Y. Y. Lau

CFA Computer Modeling Using a Moving Wavelength Code.
Hunter L. McDowell 217

Recent Advances in Simulation of Magnetrons and Crossed-Field Amplifiers.
George E. Dombrowski 236

Computer Simulations of Low-Noise States in a High Power Crossed-Field Amplifier.
David P. Chernin 246

Improved Formulas for Magnetron Characteristic Curves.
Spilios Riyopoulos 256

Rapid Current Transition in a Crossed-Field Diode.
J. P. Verboncoeur, C. K. Birdsall 268

Analysis of Multipactor Discharge in an RF Circuit.
R. Kishek, Y. Y. Lau, R. M. Gilgenbach 274

Transverse Asymmetry in a Crossed-Field Diode.
K. L. Cartwright, J. P. Verboncoeur, V. P. Gopinath, C. K. Birdsall 282

Similarity of Stability Characteristic of Planar and Coaxial Crossed-Field Diodes.
V. P. Gopinath, J. P. Verboncoeur, C. K. Birdsall 292

Resonant Diocotron Mode and the Evolution of the Sheath in a CFA.
D. J. Kaup, Gary E. Thomas 300

Effect of Random Secondary Emission Velocities in Electron Multipactors.
Spilios Riyopoulos, David Chernin, Demos Dialetis 314

Electron Sheaths in a Crossed-Field Gap -- Equilibrium Solutions and Transition to Turbulence.
Peggy J. Christenson, Y. Y. Lau 322

Part V. Panel Discussions

Chairman: Lenne Vanzant

The Future Outlook for Crossed-Field Devices.
William C. Brown 332

A Proposed Two-Port, Unidirectional Magnetron Amplifier.
George K. Farney 334

Crossed-Field Research in Universities
Y. Y. Lau 337

Recommendations and Predictions on the Future of Crossed-Field Devices.
John M. Osepchuk 339

List of Authors 341

Past, Present, and Future of Crossed-Field Devices: A Personal View

Joseph A. Saloom
18 Hollow Tree Road
Boxford, MA 01921

Abstract

A brief review will be given of the history of the origin of the coaxial magnetron and the forward wave crossed-field amplifier. Some comments will be made on the founding of S-F-D Laboratories and the status of the technology at that time, with a description of the difficulties in retrofitting the coaxial magnetron and forward wave crossed-field amplifier into operating systems. These comments will be followed by a description of the present market size for coaxial magnetrons and crossed-field amplifiers. The market sizes will be compared to other microwave tube oscillator and amplifier markets. The paper will end with a look to the future of the technology and with the issuance of challenges to the audience, the Government, Universities, and Industry to meet the future needs of the users of crossed-field devices.

I would like to recount some of the history of crossed-field devices. The first part of this paper will deal with some history as I experienced it, then I'll make a few comments on where I think we are now in our history. The final part will present challenges for the future. Every time I give a talk, Lenne Vanzant requests that I include challenges. Maybe his composition or English instructor in high school taught him that. To begin with let me state that I have no drawings, no circuit diagrams, and am assuming that the reader knows what a coaxial magnetron and crossed-field amplifier are, and how they work.

The stories I will tell about crossed-field devices may not be accurate as written somewhere in history books by scholars. My story is that of a soldier giving his narrow view of the grand strategy of the battle. When I was in college in the late forties, I was already married, and my wife helped me along by translating and teaching Spanish. I was making my living as a tube assembler and furnace operator. One day she came home with a book by a soldier in Cortez's army, written in Spanish, and read me much of the book. The book was by Bernal Diaz de Costillo, the soldier. His lament in the book was that scholars in the great Spanish universities were writing the history of the conquest of Mexico, and that none of them had talked to him. So he wrote his own book, from the soldiers point of view, and it was finally translated into English. When Archibald MacLeish, the Poet Laureate of the US, read this account he wrote a poem in blank verse, called "The Conquistador" and won the top prize for poetry that year. The scholars did not agree with Bernal's account, but I did. So forget accurate history; my story is that of a participant, a soldier, not a historian.

Crossed-field devices, especially the magnetron, have a wonderful history starting with World War II. I served in that war and saw a lot of 4J52's made by Litton, Raytheon, and Western Electric, among others. Some people say the magnetron made radar, and that radar won the war. My first encounter with the magnetron came from the story told me by Vic Ronci, my supervisor, at Bell Labs. The story he told was later reported in one of C.P. Snow's books on the history of WW2. The story goes that the British agreed to give us the design of their magnetron, and that it was so secret that the drawings and a sample magnetron were carried over in a briefcase and the carrier stayed until Bell Labs and Western Electric made a copy. The actual magnetron was given to Vic Ronci in a darkened movie theater. Sounds like a spy novel - and I guess that is what it was.

When I finished my PhD at the University of Illinois in the early fifties, I joined Bell Labs, and immediately worked on testing magnetrons and trying to find out why the 4J52's made at that time by five manufacturers, behaved very differently in the system, when all five manufacturers tubes met the spec. and passed the acceptance test procedures. We used Reike diagrams in those days. The result of testing hundreds of magnetrons was that a new specification was needed. It was called the phase of sink (from the Reike Diagram) and was specified as the location of the first minimum in the VSWR from the magnetron flange, and if this parameter were controlled, then all the manufacturers' tubes worked. It was years later, on the AEGIS CFA, that I learned about out of band mismatch, a related and similar problem.

John Pierce was at Bell Labs at the time and showed no interest at all in crossed field devices. He concentrated on the TWT and confessed many times that he did not understand magnetrons. He repeated this theme at the 1994 tube conference in Monterey, when he stated "Crossed-field devices are like the Lord. They are very powerful, but difficult to understand!" I'm sure many others would agree.

At that time, in the early fifties, other people some of you know were at Bell Labs. Grant St. John George Farney, Jerry Drexler, and of course Joe Feinstein. Most of us were working on TWTs for the new transcontinental long haul microwave system - with the goal of transmitting the Rose Bowl game across the country, and to be the first with a national microwave system. Joe Feinstein joined Bell Labs from the Bureau of Standards, when they decided to move his unit, engaged in plasma physics, to Colorado. His office was across the hall from mine, and I would see him there, with his colleague, Bob Collier, working on a new type of magnetron. He may have called the new tube a coaxial magnetron, but I'm not sure. He may have called it a TE01 controlled anode magnetron - I'm not sure.

Let me digress a moment and say a few words about the history of the TE01 mode, which is the foundation of the coaxial magnetron. In the late thirties and forties, the dominant force at Bell Labs in electromagnetic theory was a person named Schelkunoff. The dominant experimentalist in practical waveguides was George Southworth. Both later on wrote books on their work. Well, George was working on various modes of transmission when he came up with the experimental data that there was a mode, whose losses decreased with increasing frequency. All other modes did not, according to his measurements. He went to Schelkunoff and was told that the TE01 mode was a mathematical anomaly, that he had noted it, but felt it to be unreal, because

how could the losses go down with increasing frequency? They finally made peace when George repeated his measurements in a more refined way, and following that everyone believed the mode to be real.

When Joe Feinstein joined Bell he started work on the coaxial magnetron with Bob Collier. After Joe had shown that the magnetron would work, and that the TE01 mode would electromagnetically strap the anode, there appeared to be two systems, both at Ku band, that needed such a tube. One was the Nike Hercules radar and the other was the Hustler program for a radar on the B-58. The famous 7208 magnetron was the result. The tube is still being manufactured by both Litton and Varian.

When these tubes arrived on the scene at Bell Labs there was little support for their continued development, although they did get developed and manufactured and delivered to the Nike Hercules and B-58 people. At that time ATT was having a lot of trouble expanding its telephone business, and in particular, in New York City where there were a lot of problems. The Labs decided in late 1958 to stop developing any new tubes, unless they were needed for the telephone part of their business. So magnetrons were on their way out. By this time I had moved to Reading, PA, to a branch Lab to help get the 7208 into manufacturing and to develop any new tubes needed. When a new tube requirement came up in 1958, the Labs made the decision to use the 7008, a tube manufactured by RCA, and used the principle of locking up the pi- mode with four external cavities. This was a step somewhere between the normal vane and strap magnetron and the coaxial magnetron.

I appealed the decision, and lost. It was clear that if I wanted to stay in crossed-field development, that I had to go somewhere else. So I resigned and was about to start to look around, when Jerry Drexler asked me to form a team with him, and to be recruited as a pair.

We had worked well together and as a team, he thought, we would be more valuable to any company as a pair. Jerry then mentioned to Joe Feinstein this team recruiting proposition we had worked out. Joe responded that if we could get a vacuum pump, and around $250K that we could go off on our own. Jerry called me about Joe's comments, and at that instant the concept of a new company was born.

I was the first to quit, and spent most of my time drawing up a prospectus. A little later Joe and Jerry quit, and we finished the prospectus and started to look for money. Our first thought was to bring tube technology to a company not already in the tube business -- companies like Singer and Schulmberger, who were in other businesses, but had shown some interest in electronics. We met with them in fancy restaurants in New York, and some interest was shown, but not a lot. We met once with venture capitalists, and it was so distasteful to us that we never followed up. They reminded me of bird dogs searching a corn field for quail or pheasants. Not our type.

Through Lou Malter, who was then a VP for research for Varian, we were encouraged to talk to Varian. Little did we know that the previous year, Varian had bought Bomac, of Beverly, MA and that most of the engineers had left to form a company called METCOM, and were seriously underbidding Varian on new orders. Had we been more aware of that we might have asked for

more money. We were three engineers, whose goals in life were not money, not to form a new company, but to find some way to carry on with our work. The final argument we used to join with Varian was that we had a better chance of being understood by them, than by a company not in the tube business.

In May, 1959, SFD was founded in Union, NJ. I was made president. I had no choice. Both Jerry and Joe were convinced that I was the least competent, and therefore the most qualified to be president. We set about renting a building, redoing its insides, and recruiting people. Some say that we took too many people from Bell Labs and we argued that no one in America is indentured. Most of the people we hired were assemblers and all of them were graduate watchmakers. George Farney and Hunter McDowell were early hires. An extremely competent group of "can do" people. We divided each project into two parts - mechanical and electrical. The mechanical engineer was in charge of the design and assembly and the electrical engineer was in charge of electrical design and test. The process worked, but it was expensive. To emphasize the care and skill that went into our tubes let me mention what I heard recently from Neil Wilson of the Army. He said that he had tested some 8 Ka band tubes made more than 30 years before the test and that they all started up and ran well. Jim DeGan of Varian reported to me last month that they had received 5 or 6 C-band megawatt tubes that were over 30 years old and that they all worked. SFD was a collection of very competent and careful people. It was years later that we had to have a quality control department. We were the right size for producing quality tubes. The Government specifications demanded we have a quality department, whether we needed it or not.

The coaxial magnetron had many advantages, but it also had its faults. It was hard to cool at high average powers. The fins for cooling were distant from the anode where the heat was generated. It also had the propensity not to start too easily. The rate of rise of the pulse had to be slowed down as compared to a hole and slot or rising sun magnetron. Our detractors stated that the tube was O.K. if it would start and if it operated at low average power. The real beauty of the tube came forward when one looked at the spectrum. It was a beautiful spectrum, a classical spectrum, with very low side lobs and not a lot of trash displayed on the screen. The cost of the tube was at least five times the cost of a standard magnetron. Its lifetime and tolerance to its environment was at least ten times that of a conventional tube. At that time, the maximum life specified on a magnetron was 200 hours. It was Nate Butler of the Navy who changed that to around 1000 hours and that made our case.

In a conventional hole and slot magnetron the mode separation from the pi mode goes as $1/N^2$ and in a rising sun magnetron the separation is 1/N, where N is the number of resonators. This pretty much limited the number of resonators in the hole and slot magnetron to around 16 and in the rising sun to somewhere around the low twenties. This was a serious limit if one wanted to increase the average power. If one can increase the number of resonators at a given frequency, the cathode diameter would increase, and hence the tube would be able to handle more power. In the coaxial magnetron, with its TE01 mode control, the number of vanes in the anode could be increased with impunity. We built anodes with resonators numbering in the 30's to over 100.

SFD grew to over 200 people and was profitable. Chet Lob, now of Varian, was the last president of the company. During the McNamara recession in the late sixties, the plant was closed and the company moved to Beverly. At that time Chet Lob as the president had the burden of the transfer. Just prior to the move Joe Feinstein was made the vice president for research for Varian, and I had become a Group V.P. for Varian, running a group of divisions and subsidiaries on the east coast. I was the only officer of the company not located in Palo Alto. My children now appreciate that I did not move to California.

Bill Brown has told you about the first crossed-field amplifier - the Amplitron. In the early fifties, when I first heard of the Amplitron, it was considered to be a great advance, but it also had detractors, other than John Pierce. It was called a "locked oscillator" and Bill Brown had to defend it against existing devices. When we started our work on crossed-field amplifiers at SFD Labs, we wanted to build what we called "a true amplifier." We concentrated for the first several years on only "forward wave" amplifiers. The amplitron was a "backward wave" amplifier. They were called that because the phase velocity and group velocity of the waves were in opposite directions. You can believe that we used the words "backward" and "forward" effectively in our early marketing! The efficiency was the dominant advantage. So great was the efficiency that Bill Brown together with others at MIT proposed using the tubes to capture the power of the sun. Bill will no doubt tell you about his gigantic national proposals in this area. Efficiencies of around 85% were reported by him on the Amplitron.

It was George Farney who finally convinced Joe Feinstein to do some work on backward wave circuits. I thought he would lose his job, but he persisted, and SFD did sell some varieties of backward wave tubes, but with a large reentrant section. George would come up with one new circuit every month, and the major advantages of his designs was that one could match to them. It was many years later that Varian became a second source for the Amplitron, and long after Joe Feinstein had gone west.

Crossed-field amplifiers were now on the scene and were rather quickly adopted by systems. By quickly, I mean fifteen years! It was fifteen years after we started the famous AEGIS tube that it was purchased in quantities of more than one.

Well, where are we now? How many systems used coaxial magnetrons? How many systems used the crossed-field amplifier? What was market share when compared to other tubes? Some answers are given in the table.

1994
Selected Markets for Microwave Tubes

Tube Type	Market Size
Magnetrons (all types)	$26.8M
Magnetrons (coaxial only: 211 types/models)	$20.0M
Crossed-field amplifiers (28 types/models)	$13.0M
High power pulsed TWTs	$25.6M
High power pulsed Klystrons	$14.3M
Coupled cavity TWTs	$75.5M
All TWTs	$156.4M
All Klystrons	$50.3M
All Coupled Cavity	$83.8M

In looking to the future of the crossed-field amplifier area we find it to be somewhat clouded. On the one hand there is the decrease in the defense budgets, but perhaps more importantly, we need to do certain things to reinvigorate this area of technology.

When one is in the process of deciding whether to use one type of tube or another for a system application there are many trade-offs. The crossed-field amplifier characteristics that are an advantage include low voltage, compactness, and efficiency. On the other hand, coupled cavity tubes at powers up to the AEGIS level offer the advantages of higher gain, ease of modulation, and lower noise.

In the early days of the crossed-field amplifier work, we had a tremendous advantage in low voltage operation. It made us all believe that if a system were transportable, the CFA had a big advantage due to its low weight. Today the power supplies for the modulators are of a new type-called switcher power supplies with capabilities of around 100 watts per cubic inch. In addition, the development of higher voltage IGBT'S (Insulated Gate Bi-polar Transistors) have led to smaller modulators. When these two new advances are combined with the vastly improved high turns ratio pulsed transformers we find that the advantages we all thought we had over the coupled cavity tubes are beginning to disappear. The coupled cavity tubes are much more of a threat to the CFA now, more than they ever were.

It was a heartbreaker to me when the Army and Hughes Aircraft decided to use a coupled cavity tube in the TPQ-36 and TPQ-37 systems. Crossed-field amplifiers competed toe to toe for over a year and finally lost out to the coupled cavity tube. It wasn't as we all thought - that Hughes wanted to use a Hughes tube. It was more fundamental. The target sizes for these artillery and

mortar locator systems were small and noise was important. Since the systems were transportable, the ease of modulation was also important.

This lesson was further sent to me when the AEGIS system folks decided to replace a driver TWT and a driver CFA with one coupled cavity tube of the same gain. Here the lesson was on the advantages of high gain and low noise.

I don't believe we can do much about the gain, since in my experience, any time we have increased the gain of a CFA, we have paid the price on increased instability. But we can, and we should, do something about the ease of modulation and the noise issues and perhaps bandwidth issues as well.

There was a time, in the early days of SFD when we tried to build a self modulated tube. With DC placed on the tube, we tried to have the rf alone modulate the tube. We built several tubes that worked in this way, but with some sacrifice in efficiency. More importantly, the resultant modulation was unreliable. At about the same time, a device called the DEMATRON, a crossed-field amplifier with no reentrancy, did in fact demonstrate pure rf modulation. The price in efficiency was high however, and the product never made it to the market. At SFD, still in search of ease of modulation, we modified our pure self modulated tube, and inserted a control grid in the drift space. We built a dozen or so of these tubes and sold them to RCA for a system I believe was called the MPS-36. We must as a community look again at self modulation. Compared to other tubes, the CFA is at a disadvantage in ease of modulation and we will be forever at a disadvantage.

On the noise front, the CFA has always been at a disadvantage, and is now more of a disadvantage as targets get smaller, closer together, and operate in a noisy environment. Recent success, or partial success, in this area must be continued and the battle won. In the early days, this was not a serious disadvantage, but it is now and we must pursue reduction of noise in the CFA with vigor.

Lurking in the background as a disadvantage to the CFA over the coupled cavity tube is bandwidth. The linear tube folks have never abandoned their relentless search for high power broad band, high impedance circuits that can be matched. In the CFA area we have all but abandoned our R&D in this area. It is my opinion that some effort must be started here.

All three of these disadvantages must be addressed by a continuation of the excellent modeling and simulation going on now at our Universities and in our Industry. Without such efforts, we cannot afford to do the work.

To attack these three issues, these three disadvantages, I would suggest that the Government Laboratories, in their granting of contracts, to make each contract a joint effort, a joint bid, from one university and one or two industrial firms, with each a part of the contract. In addition, the people from the Government Labs, both Crane and NRL should be a part of the technical team, with their roles well defined. We do not have enough talent in the USA to tackle these three issues with three independent groups. In fact, this closer industrial association with universities

that I suggest may be our only hope for maintaining or improving the very small supply of engineers skilled in this area.

Crossed-field devices have the advantages of low voltage, high efficiency, and compactness, which are of critical importance to mobile or transportable systems. We must now reduce the noise, improve the ease of modulation, and be prepared for the system user as he demands more bandwidth. And we need to make these advances in a way we can afford. For that reason we must continue our work in modeling and simulation. Above all we must preserve and continuously improve our talent base. In this regard, I would encourage Dr. Robert Parker and Dr. Richard Abrams to heed the remarks of Jack Kilby, the head of AGED, who asked us to concentrate on re-inventing the vacuum electronics initiative. We have to add a lot more intellectual effort in our industry on the myriad of opportunities and challenges, and look again at ourselves and the directions we are going, and how we do business.

I would like to thank Professor Y.Y. Lau, Dave Chernin, and everyone else who gave birth to this workshop.

THE HISTORY OF THE REENTRANT BEAM CROSSED FIELD AMPLIFIER WITH EMPHASIS ON NOISE COMPARISON WITH THE MAGNETRON.

William C. Brown
Microwave Power Transmission Systems
6 Perry Lane, Weston MA 02193

ABSTRACT

The history of the reentrant beam crossed field amplifier, generally referred to as the CFA, is first reviewed. The principle was first applied to pulsed, high-power, broadband amplifiers and highly stabilized oscillators for radar use. It was then applied to CW tubes whose applications included the 400 kilowatt super power CFA and the low power CFA used for high data rate communication in the Apollo program. Then the author reviews his experience with noise in both the CFA and the conventional magnetron in the hope that this experience may be of value in obtaining a better understanding of noise generating processes in both of these devices.

1.0 INTRODUCTION

The original purpose of this paper was to give the history of the original crossed field amplifier device, or CFA, and to describe the subsequent developments that produced the Stabilotron, the Super Power Amplitron, and the reflex Amplitron. However, during the course of the conference it became evident that an important problem encountered with the use of the CFA device in certain systems was the noise from the device. Because the author has had some experience with noise in this device and considerably more in a closely related device, the ordinary magnetron, he believes that narrating some of his observations of noise in these two devices might be of help to others who are attempting to understand the complex operation of the crossed field device and thereby perhaps solve the noise problem.

Therefore, in this paper, the general history and description of the CFA will first be presented with greatly reduced scope and then some of the historical observations by the writer on noise in both the CFA and the magnetron will be presented.

2.0 THE GENERAL HISORY AND DESCRIPTION OF THE REENTRANT BEAM CROSSED FIELD AMPLIFIER

I am honored to have been invited to present the history of the reentrant beam crossed field amplifier at this conference. By coincidence, 1995 was the same year that this microwave tube device was recognized for its contribution to microwave technology and the author honored with the "Pioneer Award" from the IEEE Microwave Theory and Techniques Society.

Before proceeding with the abbreviated history and description of this device, it may be useful to remove the confusion with respect to the various names that have been given this device. In the title of this paper, the device has been referred to as the "reentrant beam crossed field amplifier", but in a historical progression it has also been referred to as the "platinotron", the

"Amplitron" and simply as the "CFA" or "crossed field amplifier". When the device was originally introduced and the first paper written the author named it the "platinotron", a word that combined the Greek word "platino", signifying a broad plateau, with the usual "tron" added as a suffix for an electronic device. The Raytheon marketing department, however, thought that "Amplitron" was a better term, as indeed it probably was. However, Raytheon trademarked the term so the growing competition could not use the term "Amplitron" and began to refer to it as the "crossed field amplifier", or simply as the CFA. Currently, this is the generally used term for the device. However, the term CFA also includes the injected beam crossed field amplifier as well as the reentrant beam crossed field amplifier. But the injected beam CFA is not now in general use so the term "CFA" is generally understood to mean the reentrant beam crossed field amplifier.

The emergence of the "CFA" in 1953 came at a most opportune moment when radar technology after World War II demanded a much more sophisticated device than the magnetron oscillator which had been the backbone of all radar during World War II. The need then was for a broadband amplifier that could generate megawatts of microwave power efficiently.

In the more than forty years that have elapsed since its introduction , the CFA has established itself in many major pulsed radar systems, including the FAA's Air Route Surveillance Radar, the Navy's Aegis radar, and the radars used in the Hawk and Patriot Missile Systems. It has been estimated that over this period of time tube sales from Raytheon and other companies have amounted to between one and two billion dollars, and the radar systems in which they were used to many times that.

Figure 1 shows both the original QK 403 tube that successfully demonstrated the platinotron or CFA principle and the highly successful QK 434 that was directly scaled from the QK 403. The QK 434 was thoroughly tested and the results were documented in the first paper published on the CFA as well as in the final report on the work supported by the Army Signal Corps. (1,2). More about the QK 434 will be discussed in the second part of this paper that deals with the subject of noise.

Figure 2 shows many but not all of the CFAs designed by Raytheon engineers for specific radar systems. It should be pointed out that several other companies contributed to the subseqent developoment of the CFA including Varian and Litton. An expanded history of the CFA would ackknowledge their contribtuions in more detail.

One of the outstanding CFA developments that Raytheon produced was the QK 622, an S Band tube with outstanding performance features including 80% efficiency, 3 megawatts of peak power at long pulse duration, and an average power output of 15 kilowatts. (3) This CFA was to play an important part in a subsequent super power CFA development.

The first applications of the CFA's were in radar. All of these tubes were pulsed tubes with duty cycles as high as 3%. There were a number of potential applications for continous operable or CW tubes. However the design of these pulsed tubes was not suitable for continuous or CW operation. They all exhibited too much axial leakage of electrons to the ends of the tube, or to the intruding pole pieces of the magnetic field, at the relatively low ratios

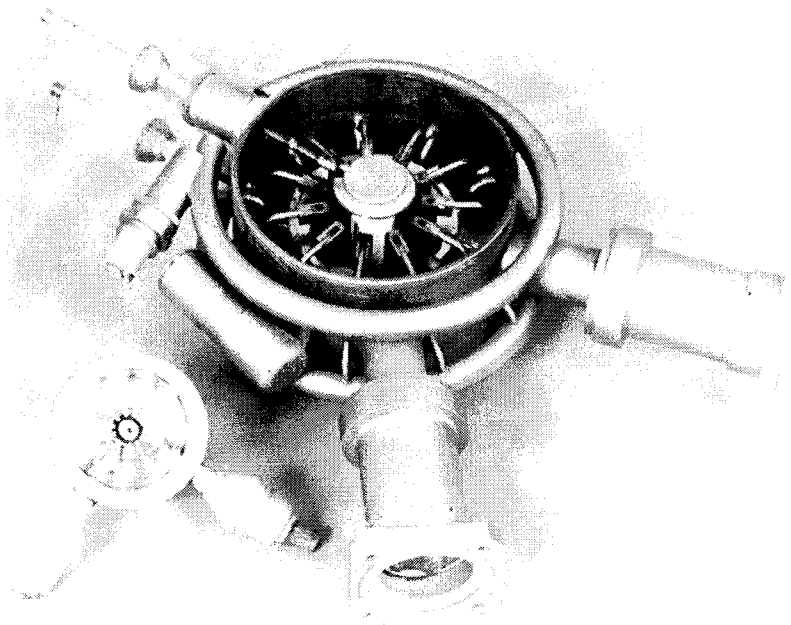


Figure 1. At bottom left is QK 408 that demonstrated CFA principle. At top is the highly successful QK 434 L-Band tube that was scaled from the QK 408.

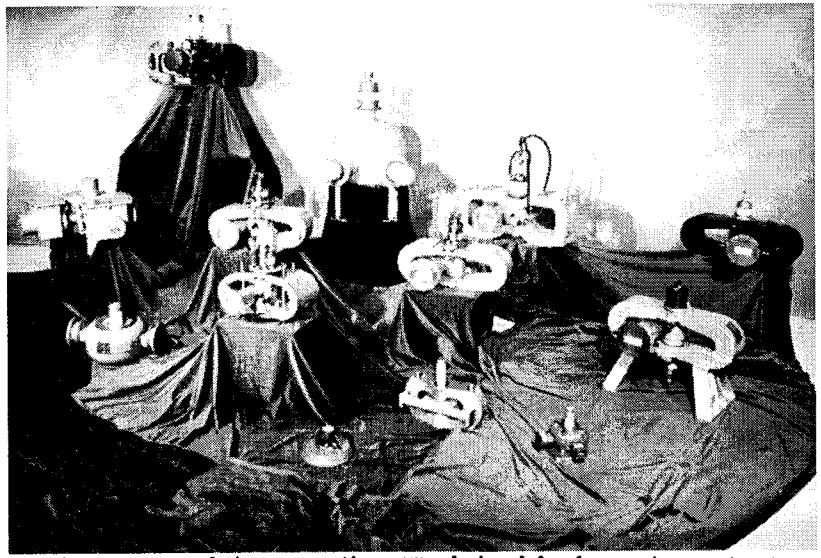


Figure 2. Some of the many Raytheon CFAs designed for frequencies ranging from 500 MHz to 14,000 MHz and peak power levels ranging up to 6 megawatts.

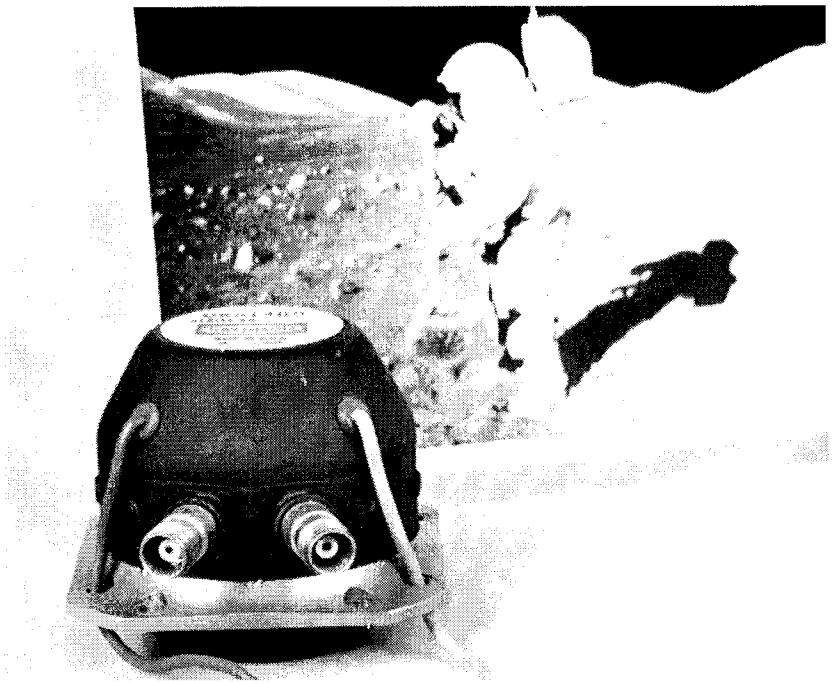


Figure 4. The 25 watt CW used for all high data rate communication between the moon and the Earth during the Apollo program.

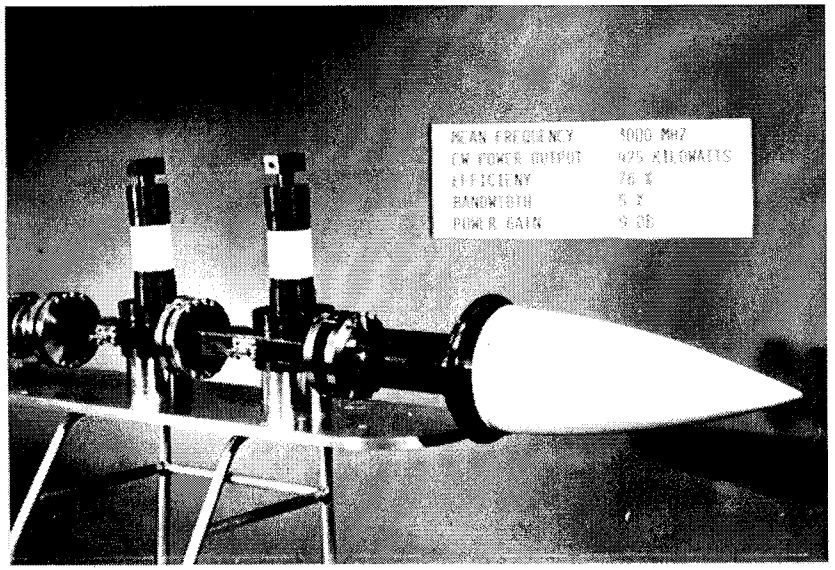


Figure 3. The super power Amplitron produced 425 kilowatts of continuous power and operated with efficiency of 76% over a band of 2.9 to 3.1 MHz.

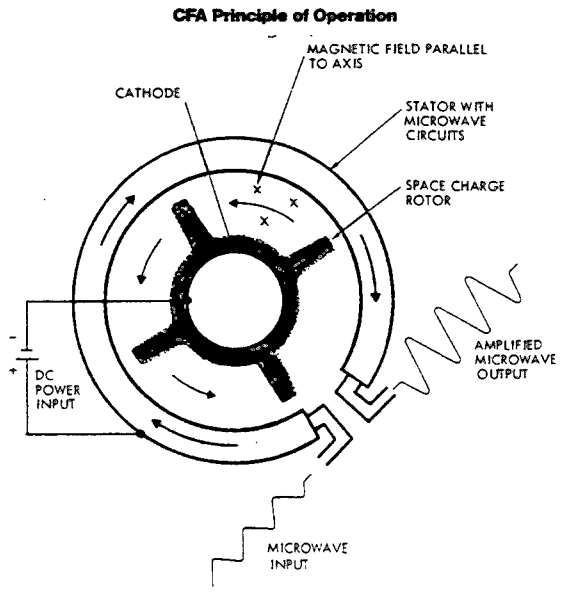


Figure 5. Principle of operation of the reentrant beam CFA

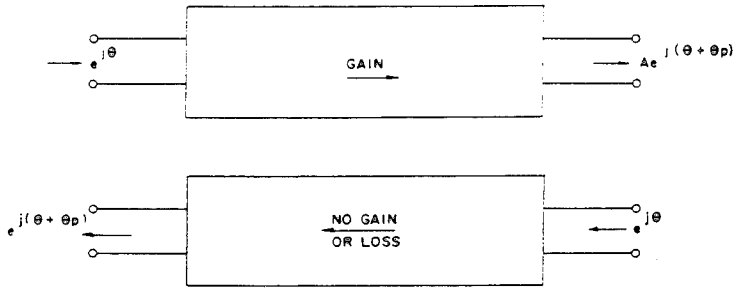


Figure 6. Directional properties of the CFA

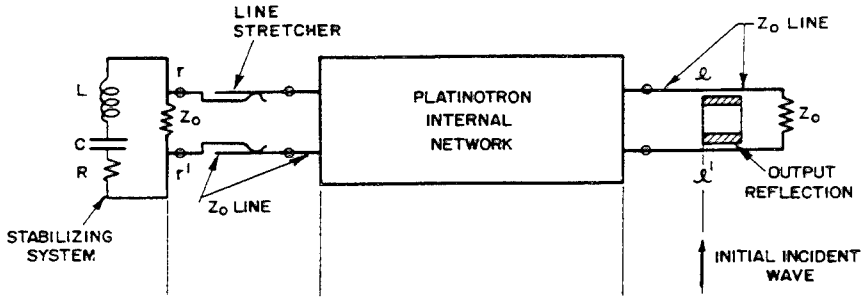


Figure 7. Principle of the Stabilotron: partial reflection in CFA output, reflection from high Q cavity at input

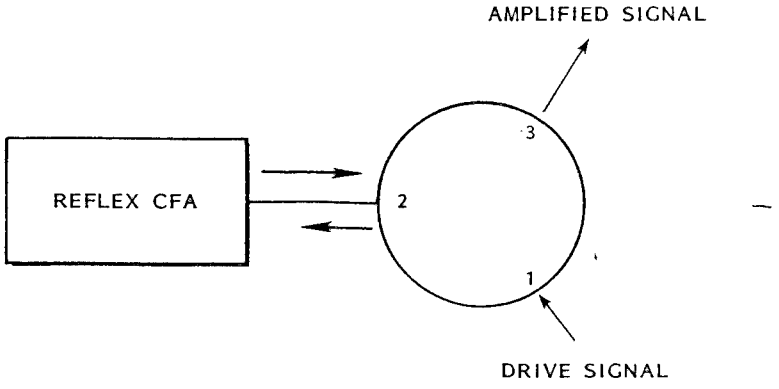


Figure 8. Single terminal reflex CFA combined with three port ferrite circulator to form a two port amplifier

of anode current to anode voltage that would be characteristic of CW operation. This was remedied by placing the magnetic pole pieces at cathode potential which eliminated 90% of the leakage current.

This new design for CW operation made it possible to think in terms of a super power tube by combining the high 80% efficiency of the CFA as exhibited by the QK 622, as noted above, with a method of dissipating very high levels of heat caused by the residual kinetic energy of the electrons when they are collected on the anode of the tube. This advanced method of heat disposal used small cooling channels at the tips of the vanes that comprised the microwave network and forced water at high velocity through these small channels.

The development of such a super power tube was proposed to DARPA, the Defense Advanced Research Projects Agency established by the US Government in response to the national concern after the Russian space program had succeeded in the successful launching of Sputnik, the first artificial satellite to orbit the Earth. The proposal was accepted and the resulting contract between the Dept. of Defense and the Raytheon Company produced a super power tube at 3 GHz that operated with 425 kilowatts of continuous power at 76 % efficiency. The availability of such large amounts of power motivated interest in using microwave beams to transport large blocks of electrical power from one point to another at high overall efficiency. (4,5)This tube is shown in figure 3.

The platinotron principle was also adapted to an important communication application, that of sending information at high data rate from the moon to the Earth during the Apollo program. This tube is shown in figure 4. It produced about 25 watts of continuous power with about 1 watt of drive power. Although this tube was used successfully during the entire Apollo program, the CFA did not find its way into general use for communication because of the short life of the cathode that was caused by electrons bombarding the cathode and breaking up the barium oxide coating. If, at that time, it had been recognized that the use of a carburized thoriated tungsten cathode would have avoided this short life problem, the CFA might have had a broad application to communications.

1.1 The General Principle of Operation of the CFA and Comparison With the magnetron.

The general principle of operation of the CFA is shown in Figure 5. (1,2,6,7). Physically, the CFA is distinguished from the conventional magnetron by the fact that it has a non reentrant circuit which is terminated at its ends with an input and an output port, while the magnetron has a reentrant circuit and only one port. Both devices have a similar internal microwave circuit that is characterized as a band pass filter with a high ratio of upper to lower cutoff frequencies. The characteristic impedance of the circuit varies from infinity at the lower cutoff frequency to nominal values in the 100 ohm range at about the middle of the pass band.

But there is a difference in the way in which this circuit is utilized by the CFA and the magnetron. The magnetron operates at the lower end of the pass band as a resonant structure while the CFA operates up nearer the center of the band where the characteristic impedance of the network can be easily matched at its external input and output ports to coaxial lines or waveguide. Furthermore. In this region the phase shift versus frequency characteristic

has flattened out to a relatively low slope so that the operational CFA device may have a practical bandwidth of 10% or more in which the efficiency remains nearly constant over the band. Furthermore, the slope is nearly constant so that the phase shift is linear over a significant range of frequencies. The ease with which such a bandwidth could be achieved from a fabrication point of view was in sharp contrast to the efforts involved in designing klystrons with similar bandwidth and where the efficiency was down by 3 db at the band edges. The combination of mechanical simplicity, high efficiency over a large bandwidth, and the linear phase shift characteristic, was a major reason for the immediate success of the CFA after it was introduced.

A common necessity for the operation of both the CFA and the magnetron is an axial magnetic field. The function of this field is to cause electrons that are emitted by the cathode to rotate around the cathode in concentric circles. Electrons are emitted in response to a voltage applied between the anode and cathode of the tube. As this voltage is increased, the electrons travel in ever larger concentric circles and increase their angular velocity until it reaches the angular velocity with which the microwaves are being propagated on the microwave circuit at the anode. At this point spokes of space charge are formed which induce microwave power into the circuit on the anode. The magnetron and the CFA obey the same scaling relationships between the operating frequency, the applied magnetic field, the applied voltage, the physical dimensions of the interaction area, and the number of space charge spokes.

2.2 The Stabilotron and Relex Amplitron Derivatives of the Early CFA Activity

The super power CFA and the CFA used for communications in the Apollo program that have already been described are derivatives of the early CFA activity. Two others are the Stabilotron and the reflex Amplitron. The stabilotron development found an early application in the search radar of the Hawk Missile System. The reflex Amplitron was a more recent development aimed at use in the radar aboard an airborne missile.

Both of these derivatives made use of a property of the CFA shown in Figure 6. The CFA exhibits gain in one direction while no gain but little loss is exhibited in the other direction. (1)

The Stabilotron, whose schematic of operation is shown in figure 7, is essentially a highly frequency stabilized oscillator that takes advantage of the CFA property shown in Figure 6. (1,8) To use this property for the stabilotron, part of the normal output power of the CFA is reflected back through the tube to a paralleled matched load and cavity resonator at the input. At the resonant frequency of the cavity almost all of the power is reflected and is then amplified to become the power output of the device. Any power not near the resonant frequency of the cavity is absorbed in the matched load at the input. The resulting oscillations occur at a frequency where the round the loop phase shift of the device is some integral multiple of 360 electrical degrees. With a high Q cavity this occurs very close to the resonance of the cavity because the phase of the reflected wave varies rapidly with frequency around the resonant frequency of the cavity. However, a line stretcher is required if the stabilotron is to be tunable over a sizeable frequency range because phase shift occurs in other portions of the loop between input and

output. The oscillation frequency of the stabilotron is highly insensitive to changes in the reactive component of load and to changes in the current input to the tube and therefore to changes in the power output. (8)

The stabilotron, representing one of the first applications of the CFA in a system, was introduced into the Hawk Missile system in 1954 where it is still used, more than forty years later.

The reflex amplitron principle, shown in Figure 8 also makes use of the CFA property shown in Figure 6. The reflex amplitron is a single port device and requires a ferrite circulator to become the two port device needed for an amplifier. The justification for the device is that it greatly simplifies the construction of the tube if only one port is needed. In operating the device a signal is inserted into the tube through one of the terminals of the ferrite circulator. The signal then travels without gain or appreciable attenuation to the input of the microwave circuit where it is reflected in its entirety. The signal is then amplified and exits the system through the other port of the ferrite circulator. The reflex amplitron principle was motivated by the need for a compact, efficient amplifier at high microwave frequencies for radar aboard an airborne missile.

3.0 A Comparison of Noise in the CFA and the Magnetron.

3.1 Introduction

Despite the impressive application of the CFA, its usefulness in some important applications has been compromised by spurious emissions of noise whose cause has been difficult to discover and to correct. Because the solution of this problem is so important, the purpose and direction of this paper has been revised to stress a historical comparison of noise behavior in the CFA with noise behavior in the closely related device, the conventional magnetron oscillator. Noise in this context is defined to include random noise near the carrier as well as removed from it, discreet noise, and any peculiar signal output of the device that interferes with proper operation of the equipment in which it might be installed.

The material that follows has for the most part been taken from a report whose preparation was supported by the Raytheon Company when the author became a consultant for them after his retirement from Raytheon. The title of this report is "A Reporting of Personal Observations of Noise in Magnetrons and CFAs". (11) It was prepared in 1988. This 150 page report contains important ex-cerpts from final reports and other documents that may be difficult to obtain. The author will make this report available for copying to anyone wishing this source material. There is obviously much more data in this report than can be presented in this paper.

Because of the close physical similarities of the CFA and the magnaetron, it might be concluded that their noise properties would be very similar. However, it has been found that there are some differences. The CFA is free of some of the adverse noise behavior of pulsed magnetrons. On the other hand, there has not been a one on one camparison of a continusously operable or CW CFA with the microwave oven magnetron whose signal to noise ratio has been found to be very high for noise close to the carrier or removed from it.

In addition to the possible help that a recounting of observations of noise in the CFA and magnetron might be to others studying the noise problem in the Aegis application, it may also be of help in finding the internal feedback mechanism in the microwave oven magnetron that keeps it in a quiet mode of operation despite many changes in operating conditions, including power input and power output, and changes in the load into which the tube operates.

To the author's knowledge there is no simulation and associated computer program that describes this built in feedback behavior that regulates the back bombardment power to keep the primary emitting cathode at the minimum temperature that will supply just enough current for the operation of the magnetron. And this is the operating condition of the cathode that is associated with low noise, and, of course, with the maximum life of the cathode.

This feedback mechanism in the microwave oven magnetron is probably associated with the phase relationship between the spokes of space charge and the wave travelling on the microwave circuit, because this phase relationship governs the amount of energy in the electrons returning to the cathode and bombarding it to heat the cathode.

There is also some evidence that when the cathode in a CFA is a pure secondary emitter that the space charge spokes rotate to control the amount of back-bombardment to supply the minimum amount of secondary electrons necessary to supply the anode current of the CFA. (10) Therefore the condition of the secondary emitting surface may be a critical factor in governing the phase relationship between the space charge spokes and the wave on the microwave circuit. So, if there were a proper simulation of the control of backbombardment power, it might apply to secondary emitting cathodes as well as to primary emitting ones.

In any event such a simulation would be very useful for the optimum design of magnetrons for the many wireless power transmission applications in which the ordinary microwave oven magnetron, converted into a high gain, phase locked amplifier with external circuitry, is intended to play an important role. This role is the generator in an "electronically steerable phased array module" now called an ESPAM, that consists of the generator and a section of slotted waveguide array. Thousands of these ESPAMs would be used in electronically steerable phased arrays for beaming power.

For the reader unfamiliar with the conversion of the magnetron into a phase-locked, high gain (30 db) amplifier with external circuitry, it should be noted that this is a recent development. (9) The magnetron is converted into an amplifier with the aid of a three port ferrite circulator so that the assembly becomoes a two port device with input and output. Also in the assembly is a phase comparator that compares the phase of the input with that of the output and any error signal is used to retune the magnetron to match its oscillatory frequency to that of the drive signal. It should be pointed out that from a noise point of view, the noise from the magnetron running by itself as an oscillator and determining its own frequency is the same as when it is run as an amplifier.

We will now turn to some of the comparative observations of noise in CFAs and magnetrons.

3.2 Comparison of the Magnetron as Represented by the 5J26 and the CFA as Represented by the QK 434.

The first opportunity to compare the behavior of the magnetron with the CFA occurred very early in the history of the CFA. Disregarding the very early work in converting the conventional magnetron into a broadband amplifier, the development of the first tube intended for an application was the QK 434. It was designed as a candidate to replace the 5J26 magnetron which had been the backbone of many L Band radars during World War II, but which had run into difficulty in a radar system designed for the "DEW line" radar. Of course it was not known in advance what the behavior of the QK 434 might be and how many variables would be introduced by the new design. To keep these variables to a small number it was decided to use the same cathode in the CFA as in the 5J26 magnetron. This was a fortunate decision as we shall see.

During World War II the 5J26 magnetron had been successfully operated with one and two microsecond pulsed lengths. However, the proposed "DEW Line" application after World War II called for a five microsecond pulse duration. But at this pulse duration the 5J26 exhibited the anomaly of oscillating at one frequency during the first part of the pulse and then suddenly shifting for the remainder of the pulse to another frequency two or three MHz away from the first frequency. This behavior was intolerable to successful operation of the radar.

Such frequency skipping performance indicated two states of operation that were a function of time. But what operating condition could change in such a small interval of time? About the only thing that could change was an increase in the temperature of the electron emitting material of the cathode, caused by back bombarding electrons returning to the cathode. The material was barium oxide whose heat conductivity is very poor so that the surface temperature of the material could heat up rapidly under the kilowatts of backbombardment power. An increase in temperature would greatly increase its capability to emit electrons, The scenario, then, is that during the pulse the temperature and primary emission of the cathode increases to some point where there is a change in the mode of operation of the tube.

It would be anticipated then that the QK 434 CFA might exhibit this same performance because it had the same cathode. The amazing finding in the QK 434 was that there was no frequency skipping when it was run as an oscillator, and no change in the quality of the spectrum of the microwave output when it was run as an amplifier with a five microsecond pulse over an extremely wide range of operating conditions with respect to the frequency and power level of the rf drive, the variation in magnetic field, applied voltage and current, and variations in load. All of this data is recorded in the original paper and final report on the platinotron, or CFA. (1,2)

Although the transient temperature behavior of the cathode of the CFA QK 434 was not monitored during these tests, there must have been a tremendous change in the temperature of the cathode and therefore of its primary emitting capability. But it made no difference, so, in retrospect, it is necessary to look for some other condition in the CFA that eliminates one of the two states of operation observed in the magnetron oscillator.

To the author's knowledge, in all of the CFA's that were ever produced, with

all kinds of cathodes including purely secondary emitting ones, there was no incidence of a change of operating mode during the pulse, however long it might be. For some reason, still to be positively identified, the CFA always operates in one mode or state regardless of the cathode that is being used.

Two differences between the devices that in some way might limit the tube to one mode of operation come to mind. The first difference is a reentrant versus a non reentrant microwave circuit. The second difference is in the rf fields seen by the space charge spokes. For a given output power level, the fields are much higher in the magnetron than in the CFA.

A third difference that might be proposed is that when the CFA is providing significant gain there is a significant circumferential variation in the electric field presented to the space charge spokes as they rotate around the cathode. However, when the CFA is operated at low gain there is only a slight circumferential variation in fields that approximates the situation found in the magnetron., But no change in the mode of operation has been noted at low gain in the CFA.

Unfortunately, because of the lack of suitable instrumentation, no noise measurements were made on either the QK 434 or the 5J26. The interesting observation, if it could have been made, would have been the noise level before and after the mode change in the middle of the five microsecond pulse applied to the 5J26; and then compare those noise levels to that of the QK 434 to see if the QK 434 was in the quiet or noisy mode.

3.3 Two mode and associated noise behavior of a CW X-Band Magnetron

The reason to suspect that there was a difference in the noise level before and after the break in the middle of the pulse applied to the 5J26, arose from the observed performance on an X-Band CW magnetron that had been designed for use in the CW radar of the Raytheon Hawk Missile System. In this application the signal to noise ratio of the transmitter in the CW radar was very important and could be observed on a conventional spectrum analyzer.

It was noted that as the applied voltage to the tube was increased to increase the current and the power output, there would be a value of current reached at which there would be an abrupt shift in frequency by a small amount and a slight but abrupt change in the operating voltage imposed upon the magnetron. Because the voltage-current relationship was dependent upon a value of magnetic field measured in gauss, this slight but abrupt change in the voltage current relationship became known as a "gauss-line discontinuity". At this discontinuity there would also be an abrupt change in the amount of white noise associated with the tube as observed on a spectrum analyzer.

Thus there seemed to be two possible states of operation, one much more noisy than the other. This problem could be remedied to a large extent by long aging of the CW tubes that changed the emission properties of the thoria cathode, but the procedure was never completely satisfactory. At the very end of the use of the magnetron in the missile system, it was found that a cathode made of thorium, a material that had very low secondary emission, eliminated the problem. But this finding came too late to preserve the use of the magnetron in the missile system so that no field experience with the magnetron with the

new cathode was obtained.

3.4 Further observations on quiet and noisy states of operation in the microwave oven magnetron

Much of what will be discussed in the following material is discussed in more detail in the report "A Reporting of Personal Obseervations of Noise in Magnetrons and CFAs," that has been previously referred to. It may also be covered in a separate article in the proceedings of this conference on crossed field devices, depending upon the deadline for submitting material. But a separate and more complete paper that will present more data and how it fits into formal control theory should be written.

It may be possible to regard the microwave oven magnetron as a black box and to characterize its performance in terms of control theory, without understanding what is actual going on in the box. That is where we need an accurate simulation of what is going on in terms of electron flow in the magnetron to explain the externally observed behavior.

The finding of two states of operation in the X-Band CW magnetron also relates to a later finding in the common microwave oven magnetron where it was found that whether or not the cathode was temperature limited in its emission made a big difference in the noise performance of the device. The reader may very well be concerned with how it was known that the cathode was operating in a temperature limited condition, beyond the observation that the temperature seemed to be close to that predicted by the Richardson-Dushman relationship between emission and temperature for the particular cathode material. However, from an experimental observation point of view, this relationship is a very loose one, depending upon accurate reading of the filament temperature and a myriad of other factors.

Fortunately, there is a technique that can tell how close the cathode is operating to a temperature limited emission condition. If the cathode is operating in a temperature limited mode, then when a small step function in anode voltage is applied to the tube, there will be no instantaneous increase in anode current. Rather there will be time required to heat the mass of the filamentary cathode to the temperature required for the increase in current to satisfy the steady state operating condition between the tube and the power supply. If there is some excess emission, then there will be some instantaneous increase in anode current with the remainder requiring a higher temperature of the cathode.

It has been observed that if the filamentary cathode is in an emission limited condition, and if the magnetron is being operated with external circuitry as an amplifier so that the phase shift between the input and output can be measured, there will be a transient phase shift while the magnetron is presumably shifting the position of the space charge spokes to increase the amount of back bombardment to heat the filamentary cathode. On the other hand, if the magnetron is operating as a free running oscillator, then presumably there will be a transient shift in frequency of the tube while it is adjusting itself to the new operating conditions.

In this context of frequency shifting with a change in anode current which is called "frequency pushing" it should be noted that there are two components.

One is caused by the increase in space charge density in the spoke, and the other is caused by the shift of the space charge spoke to produce changes in the amount of back bombardment. It has been noted that these shifts are in the opposite direction and may be responsible for the observation that the pushing figure may flatten out and even change its slope with an increase in current.

Experimentally, it has been observed that the excess emission that is obtained from applying the step function of voltage increases as the anode current of the tube is increased. More specifically, the ratio of excess emission to the steady state value of the current increases with anode current. Conversely, it has been found that when there is no excess emission at lower values of anode current, the tube ceases to run. These observations were made under conditions of no external flow of power into the filament.

Another interesting observation is that if external heater power is introduced into the tube while the tube has been running without heater power, then the filament still operates at nearly the same temperature because the backbombardment power is reduced by nearly the same amount as the external heater power is increased. If this reduction in backbombardment power is visualized as a negative feedback process to compensate for the introduction of an external factor to heat up the cathode, then it compensates by a ratio factor of over twenty.

If now we associate the low noise operation the tube with a negative feedback process to keep the cathode near a temperature limited condition, we see that the microwave oven magnetron prefers to use this feedback process to produce noise free operation over a very wide range of operating condition imposed upon the tube.

e

3.5 Precipitation of the Noisy State of Operation in the Microwave Oven Magnetron

If the microwave oven magnetron is being operated CW with no external filament power, and then external filament power is added, there will be a decrease in backbombardment power to compensate until a value of filament power is reached which suddenly transforms the quiet operation into noisy operation. The anode voltage at this point drops by 150 to 200 volts and the temperature of the filamentary cathode increases. The reduction in backbombardment power no longer compensates for the external heater power.

3.6 The Correlation of Low Frequency Noise With Noise Around the Carrier in the Microwave Oven Magnetron.

When the microwave oven magnetron is in a noisy state triggered by the injection of too much external heater power, there is a broad range of noise below 1000 MHz. When the external heater power is removed, both the low frequency noise and the noise around the 2.45 MHz signal vanishes. It is therefore assumed that the low frequency noise is noise modulating the carrier at 2.45 GHz.

This observation strongly suggests that if there is too much space charge around the cathode that is not getting transported immediately to the space charge spokes, oscillations will occur at low frequencies through some mechanism not now well defined. These low frequency oscillations are closely

coupled to the cathode and the power coupled to the cathode exits to the external world through the cathode support. In the microwave oven this low frequency power would be a source of interference with other uses of the electromagnetic spectrum if it were not prevented from exiting the packaged magnetron by a low frequency filter contained in the package.

3.7 Conclusion and Summary of Observations of Noise in CFAs and Magnetrons

The observations made in the second part of this paper are meant to motivate as well as to help those who are working on the basic theory of CFAs and magnetrons to explain why quiet operation of magnetrons and presumably CFAs is associated with an emission limited condition of the cathode, and how such a condition can be maintained over a wide range of operating conditions by an internal feedback control mechanism.

Following is a summary of the observations:

- It is observed that all CFAs have no discontinuities in the relationship between applied potential to the anode and the resulting current, as do magnetrons. Any exception to this, and correlated with some design change, would be very important, particularly if it resulted in a high level of noise on one side of the discontinuity. Currently there is no explanation for this difference between ordinary magnetrons and CFAs.

- Microwave oven magnetrons with a carburized thoriated tungsten cathode want to operate in a noise free condition unless an excess amount of external heater power is applied. This noise free condition is correlated with a helical carburized tungsten cathode that operates very close to a temperature limited emission condition.

- There is an internal negative feedback mechanism in the microwave oven magnetron that keeps the cathode near the temperature limited emission condition under a broad range of imposed operating conditions.

- A noisy spectrum at 2.45 GHz, when there is enough external heater power applied to trigger it, is correlated with the generation of noise below 1 GHz that is conducted along the cathode support and radiated unless filtering to prevent it is provided. The noise at both frequencies vanishes when the external heater power is removed.

- There is a sudden reduction of the anode voltage by about 150 volts when the microwave oven magnetron goes into the noisy mode of operation.

REFERENCES

1. W. C. Brown, "Description and Operating Characteristics of the Platinotron, a new microwave tube device" , Proceedings of the IRE, Vol. 45, No. 9, PP. 1209-1222, Sept., 1957

2. W. C. Brown, "Design and development of the platinotron, Amplitron and

Stabilotron', Final Report; Signal Corps Contract No. DA-36-039-sc-56644' Signal Corps Project No. 322A, Dept. of the Army Project No. 3-19-03-021, August 1, 1953-December 31, 1955.

3. W. A. Smith and F. A. Zawaada "A 3-megawatt, 15 kilowatt S-Band Amplitron," Microwave Journal, Vol. 3, October 1959,

4. J. F. Skowron, G. H. Macmaster and W. C. Brown, "The Super Power CW Amplitron," Microwave Journal, October 1964.

5. Final Report, "Ultra High Power Amplitron", CW Amplitron Development, RADC-TDR-64, Vol I, Rome Air Development Center, Project No. 5573, Task No. 557302, Prepared under Contract No. AF30(602)2205 by Raytheon Co.

6. G. E. Dombrowaski, "Theory of the Amplitron", IRE Trans. on Electron Devices, Vol. ED-6, pp 419 to 428, October 1959

7. J. F. Skowron, "The continuous cathode (emitting sole) crossed-field amplifier," Proc. IEEE, Vol. 61, pp 330-356, March 1973

8. W. C. Brown, "The platinotron, Amplitron, and Stabilotron," in Okress, Crossed-field Microwave Devices, Academic Press, 1961, Vol. 2, pp 165-209.

9. W. C. Brown, "Development of electronically steerable phased array module (ESPAM) with magnetron directional amplifier (MDA) power source." Final Report, Sept. 1, 1995, Texas A&M Research Foundation, Subgrant No. L300060, Prime Grant No. NAGW-11194, Project RF-2500-95

10. W. C. Brown, Internal Study at Raytheon on the phase shift behavior through a pulsed CFA as a function of operating parameters imposed on the tube.

11. W. C. Brown, "A reporting of personal observations of noise in magnetrons and CFAs," Internal Raytheon report prepared in 1988.

The Development of Crossed-Field Devices in the UK, from the Original 10cm Cavity Magnetron to the Present and Beyond

Barry Vyse PhD

Vyse Ltd, 14 Cranbourne Drive Pinner Middx. HA5 1BZ, UK
Tel: 44-(0)181-866-4428
Fax:44-(0)181-933-0918

THE DEVELOPMENT OF CROSSED-FIELD DEVICES IN THE UK, FROM THE ORIGINAL 10CM CAVITY MAGNETRON TO THE PRESENT AND BEYOND

Abstract

The paper plots the development of Crossed Field Devices in the UK from the invention of the original 10 cm Cavity Magnetron in 1939/40 through to the present time. The major success story concerns the development of the Magnetron in all its forms and applications but contributions have also been made to the development of the Backward Wave Oscillator, Crossed Field Amplifier and other less well known devices.

Key points in the development and understanding of how these devices work are touched on, together with comment on areas still to be understood and explored.

Introduction

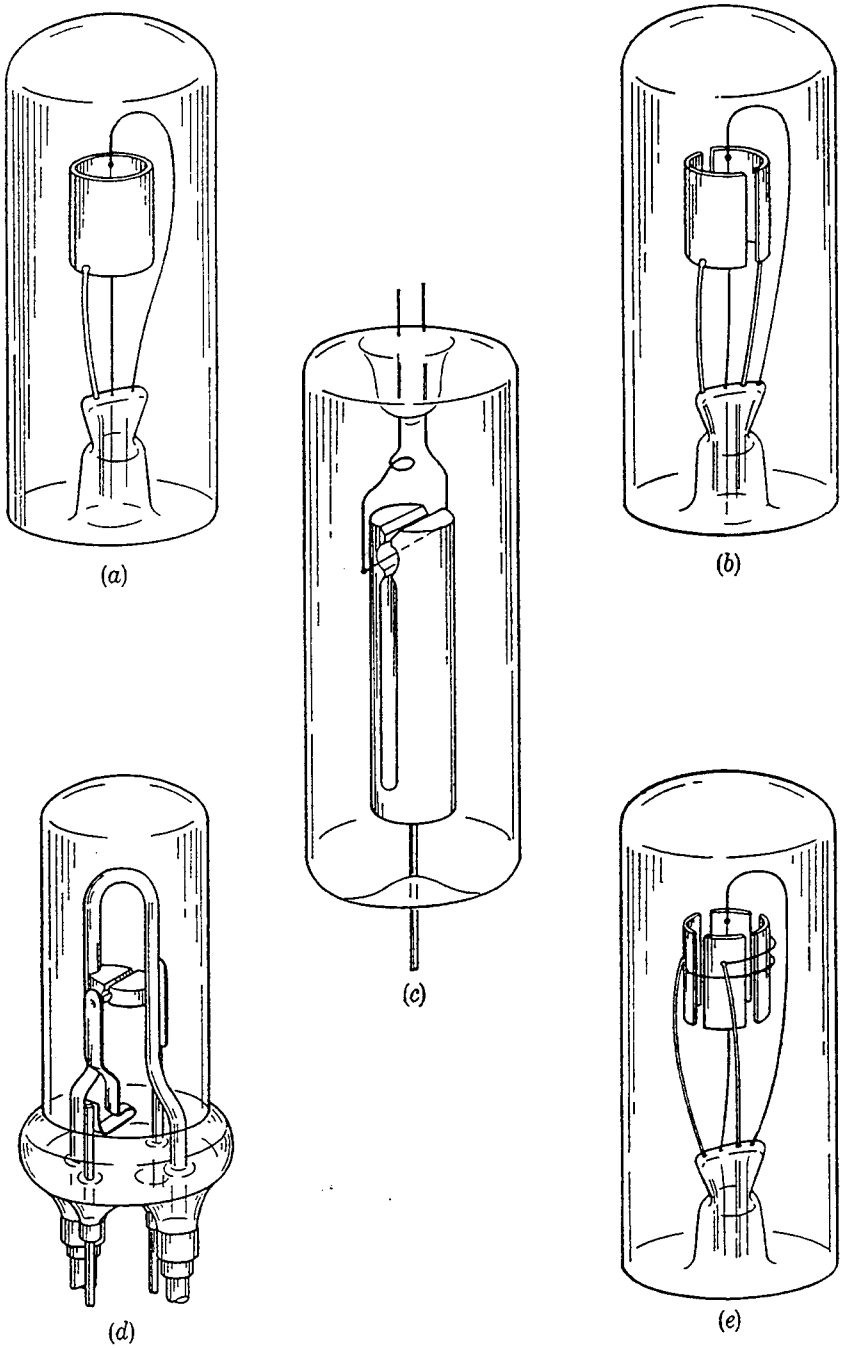
The invention of the Cavity Magnetron was one of the truly great events in history - it was also one of the World's best kept secrets. It took place in England in 1940.

Not only does the Magnetron stand alongside other great inventions like the telephone and the gramophone, making possible a great technological advance, in this case Radar, but it occurred at a time when Hitler's bombers were bearing down on London and his U-boat wolfpacks were sending millions of tons of shipping to the bottom of the ocean. It must have appeared like a gift from heaven. The Magnetron could not stop the bombers coming but it could tell where and when and allow the marshalling of precious defences in the most effective way.

It was an immense achievement which was given special recognition - but only, of course, after the war was over.

Split-Anode Magnetrons

Prior to 1940 the state-of-the-art consisted of High Frequency Valves (Tubes) with performance up to a few hundred Mhz. In an attempt to overcome the limitations of electron transit times between grids in conventional tubes, work at higher frequencies had shifted to modified valves such as shown in Figure 1 - known as Split-Anode Magnetrons. Several groups around the world, particularly France, United States, Russia, Japan as well as England, were working in this area. As shown in Figure 1, Split-anode Magnetrons looked like valves, glass envelopes and filamentary bright-emitter cathodes, but were attempts to exploit observations of strange, high frequency, spurious oscillations. Some of these devices were based on variations of a Cylindrical Diode in which the electrons were turned by an axial magnetic field to move past gaps in the anode - hence Split Anode Magnetron.



—Early types of magnetrons: (*a*) Hull original diode; (*b*) split anode; (*c*) split anode with internal resonator; (*d*) improved split anode; (*e*) four-segment anode.

FIGURE 1: SPLIT-ANODE MAGNETRONS (TAKEN FROM COLLINS, REF 1)

By the beginning of 1940 the state-of-the-art was a few watts at 50cm or so - interesting but not spectacular.

So what happened in 1940 to turn a few watts of almost spurious radiation into 100KW of well defined signal generated by a concise and practical device? In historical perspective, it might appear that the invention occurred in one blinding flash of inspiration. In reality a small group of dedicated and highly motivated collaborators made a series of advances over a short period of time which is foreshortened by hindsight to give the impression of a step change in the sate-of-the-art.

Early 10cm Cavity Magnetrons

Figure 2 shows a picture of the original 10 cm Cavity Magnetron invented by Randall and Boot at Birmingham University in England in 1940. This device operated CW, producing about 400 watts of rf power in S-band. It was continuously pumped and worked with a large Electro-magnet.

Within a year, ECS McGaw working at the Hirst Research Centre of the GEC at Wembley, England had developed the device shown in figure 3.

The GEC Magnetron was a properly engineered, sealed-off device which operated pulsed, generating 100KW of rf power with good efficiency at a well defined frequency around 9.6 cm wavelength.

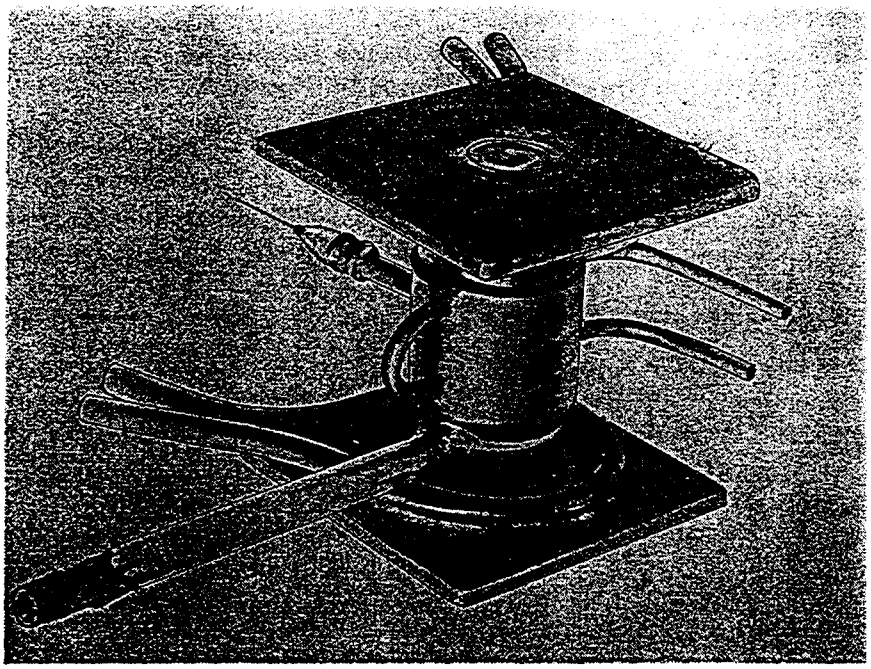
It was a staggering performance, many orders of magnitude greater than had been achieved before and in a convenient engineered package that could be used in real Radar systems in the field.

It was this device that was brought over here to the United States in great secrecy in 1941 by Sir Henry Tizzard. Since then the work carried out by MIT and other Organisations in the US has become legend and the development of Microwave Tubes has gone on in parallel on both sides of the Atlantic ever since.

Major Components of the Original 10cm Magnetron

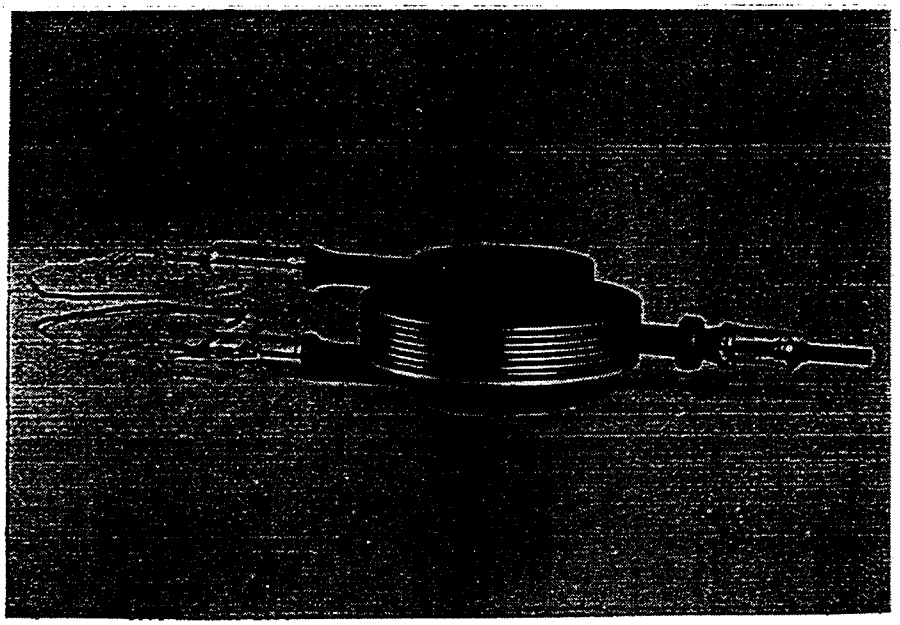
The great achievement of Randall and Boot was the creation of the solid copper, hole and slot rf circuit. I believe they saw it as a series of strongly coupled resonators. The drilling jig for this first Cavity Magnetron block was the cartridge chamber of a colt revolver and so had six segments. Slots were cut into the holes with dimensions chosen such that the resonance frequency could be calculated using the gap as a capacitor and the hole as an inductor.

The Randall and Boot device had a filamentary cathode and the electrons were constrained to rotate past the gaps formed by the slots in the anode block by the combined action of the axial magnetic field and radial electric field and so could interact with the resonant signals on the rf circuit. They coupled the rf power out of the block by means of a coaxial coupling loop.



—First British 10-cm magnetron.

FIGURE 2: ORIGINAL BRITISH 10CM CAVITY MAGNETRON



The E1189, the Wembley development of the magnetron.

FIGURE 3: E1189, 10CM MAGNETRON - EARLY PRODUCTION VERSION (REF 2)

ECS McGaw at the Hirst Research Centre of the GEC (2) immediately recognised the potential of the new circuit both as an rf structure and as a means of forming the vacuum envelope of the device, making it more practical to mount in the magnet. He also possessed the engineering and vacuum technology to make a sealed off device.

McGaw's crucial development was the introduction of the large diameter oxide cathode which had been developed by the French.

Whether ECS McGaw knew that the cathode was an important element in forming the rf Slow-wave Structure as we would call it today, is debatable. What he did know was that much better thermionic electron emission was required to sustain high power generation, but even he could not have foreseen the amazing improvement in emission afforded by the oxide cathode under pulsed conditions of less than about 1 microsecond, aided by what became known as secondary back bombardment of the cathode.

McGaw also increased the number of segments from 6 to 8 and produced the sealed-off device of design adequate for production, then added a permanent magnet.

Randall and Boot were credited with the invention of the Cavity Magnetron. Certainly they made crucial advances but it can fairly be said that McGaw designed an made the Magnetron that really worked.

A few months later, Sayer, also of Birmingham University, made a further advance with the introduction of straps linking alternate segments that greatly improved the frequency stability of the device.

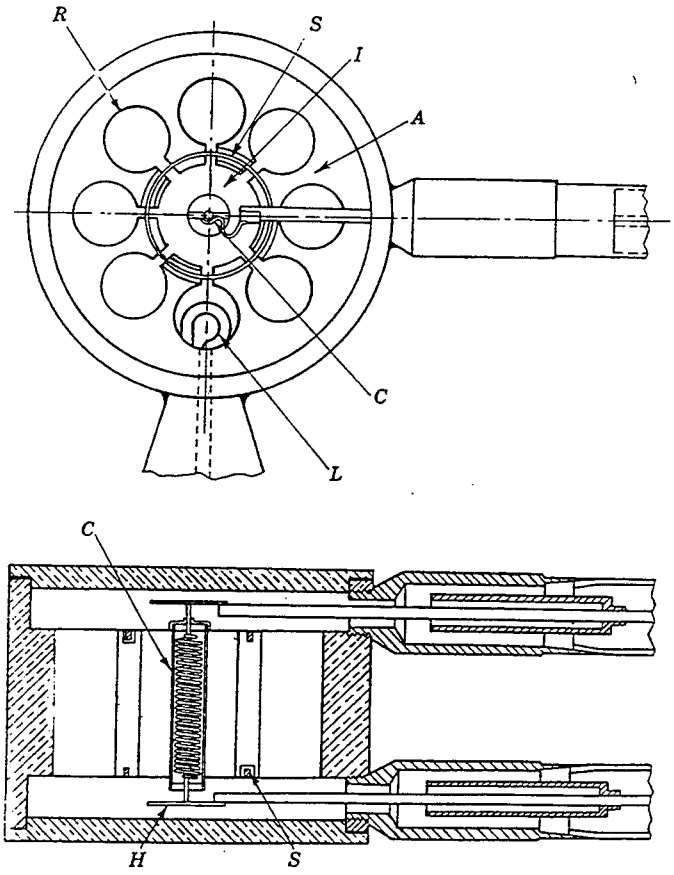
Figure 4 shows the major features of the early production Magnetrons - the cavities, slots, output loop, straps, cathode and support side arm, heater. The magnetic field is axial and provided by an external permanent magnet.

Principles of Operation

The Magnetron was invented not designed. The early workers had, at best, a very limited theoretical understanding of how the device worked. They advanced by experimentation, observation and the development of intuitive understanding rather than theoretical calculation. In fact, one might conclude that, had they known how theoretically complicated the device was, they would never have started.

The following is a list of the main principles of operation of the Magnetron which were to occupy enormous effort over subsequent years up to the present time in the understanding, expansion, clarification, refinement and application to a whole range of devices flowing down from these beginnings.

- Resonance: Coupled Cavities or Slow Wave Structures
- Phase and Group Velocity



—Cross-sectional views of typical magnetron

FIGURE 4: CROSS-SECTION OF HOLE AND SLOT MAGNETRON SHOWING MAJOR COMPONENTS (COLLINS REF 1)

- Mode Separation and Competition
- The Properties of the Rotating Crossed-field Electron Beam
- Synchronism, Cumulative Interaction
- Phase Focusing
- Start-up: Noise, Growth, Saturation

Figure 5 shows an anode block, this time showing the fields generated in the pi-mode resonance with associated charges, currents and magnetic fields.

The circuit is a re-entrant and, therefore, resonant structure but if it were broken and opened out it would form what we now call a Slow-wave Structure - a structure that will propagate an electromagnetic wave at a velocity small compared with that of light and which will present fringing rf fields in a format that can be influenced by an electron beam passing close to the circuit. Much work has been, and continues to be done in this area depending on the application, strapped vane, rising sun, interdigital, modified helix, coaxial cavity, loaded structures, meander lines and ladder lines etc.

Figure 6 shows an omega-beta diagram or Dispersion Curve; a very useful tool for describing a Slow-wave Circuit and electron beam interaction. Basically, this diagram shows frequency on the vertical scale and wave number on the horizontal. A totally non-dispersive structure like a perfect helix would have a straight line through the origin with phase velocity equal to the group velocity equal, in turn, to a fraction that of light.

Real structures have, or are designed to have, non-linear, dispersive characteristics like the one shown in figure 6 for a strapped magnetron block.

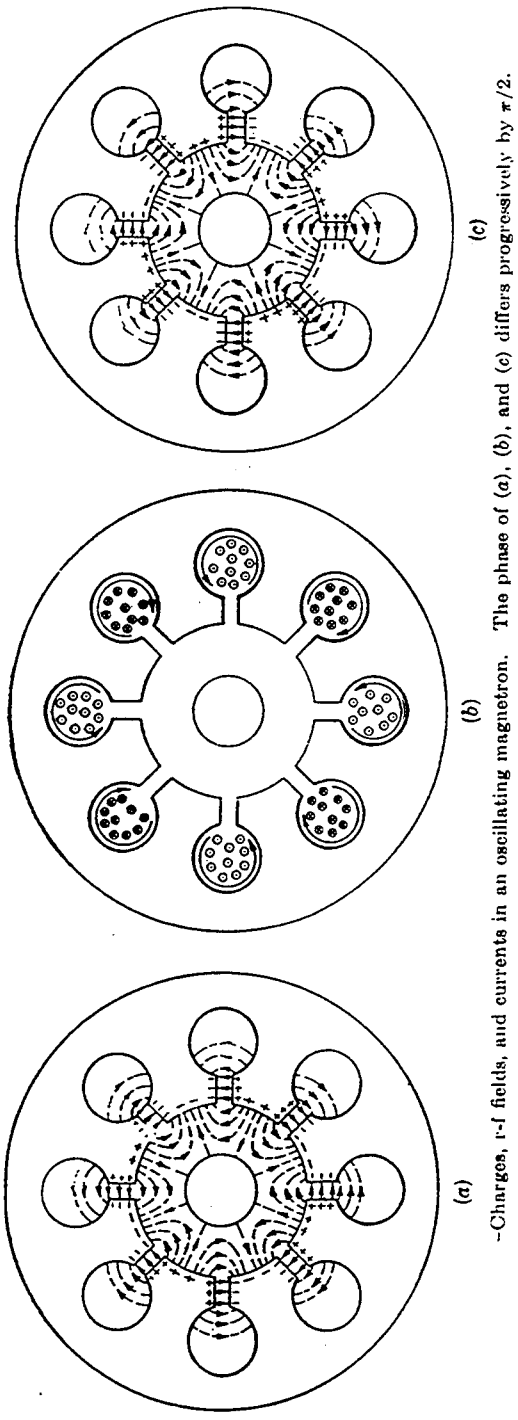
At any given frequency, the wave propagating down the structure is composed of a Fourier Series of Space Harmonics as intercepted by a horizontal line. The phase velocity is represented by the slope of the line through the origin and the Group velocity by the gradient at that point.

A mode is composed of all the space harmonics with the same group velocity. However. for interaction to take place, it is only necessary for the electron beam to travel synchronously with any one of the space harmonics.

It can now be seen that the great advance of strapping, as an example, was the lowering of the frequency of the pi-mode of oscillation to the point that it was the first fundamental space harmonic available for interaction with the beam as it switches on.

In a CFD, electrons drawn off the cathode by the voltage applied between anode and cathode are turned by the axial magnetic field and would, in isolation, describe cycloidal paths back to the cathode according to classical theory. In practice, there are a very large number of electrons available from the cathode and the space charge they represent severely modifies the picture.

One idealised solution evolved by Buneman is described in figure 7 and is particularly helpful in understanding how devices work.



(c) (b) (a)

-Charges, r-f fields, and currents in an oscillating magnetron. The phase of (a), (b), and (c) differs progressively by $\pi/2$.

FIGURE 5: ANODE BLOCK DIAGRAM SHOWING FIELD AND CURRENT PATTERNS (COLLINS REF 1)

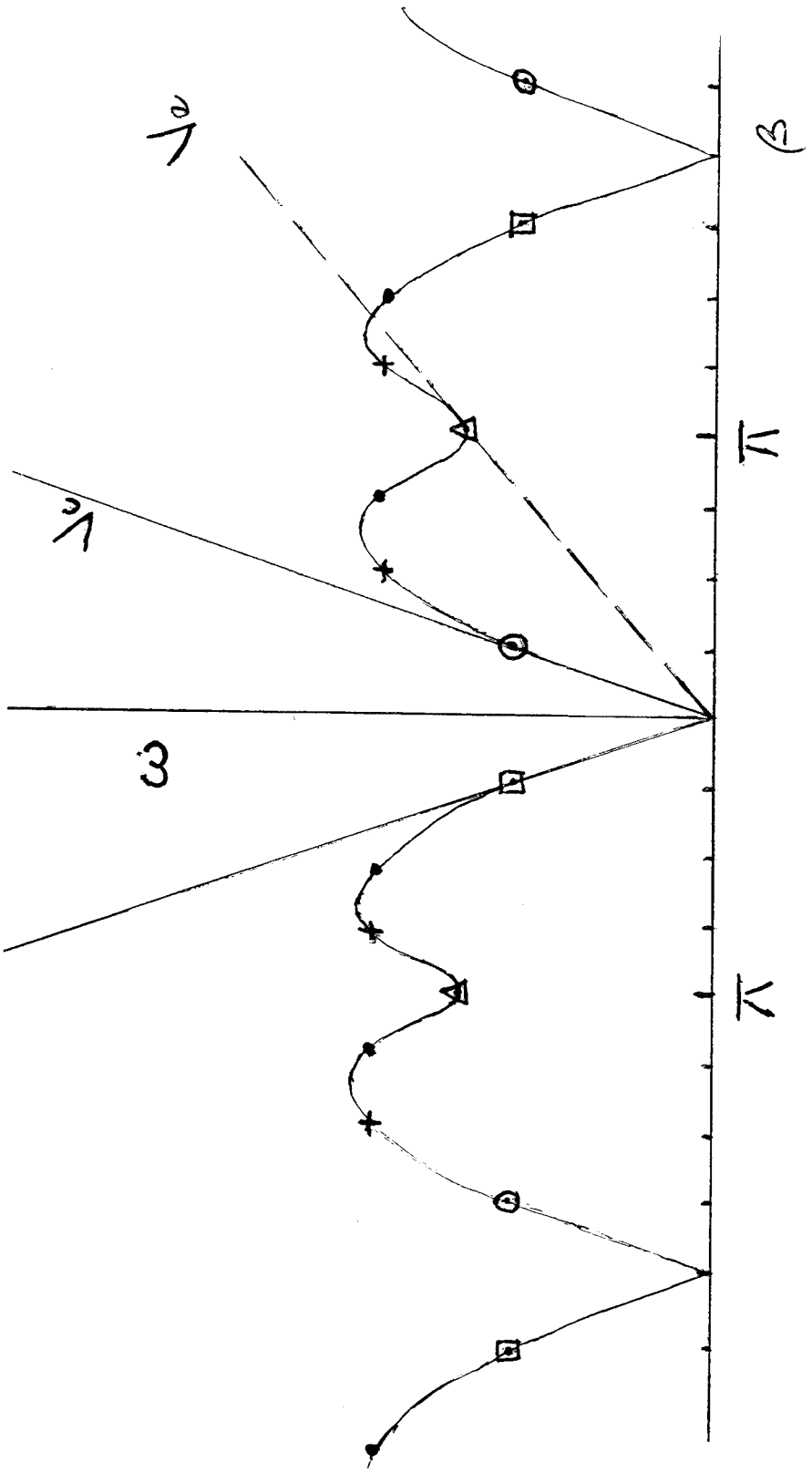
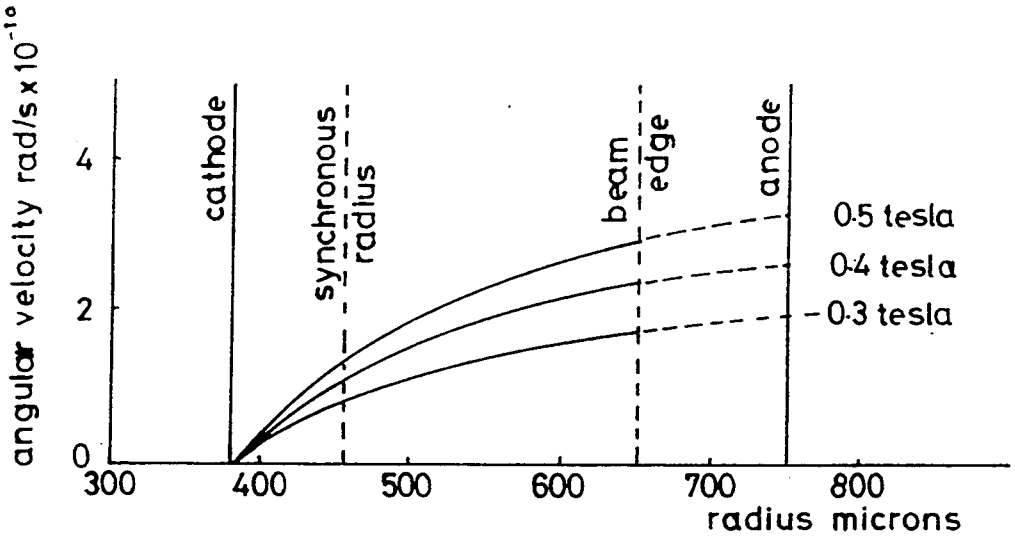


FIGURE 6: TYPICAL MAGNETRON DISPERSION CURVE



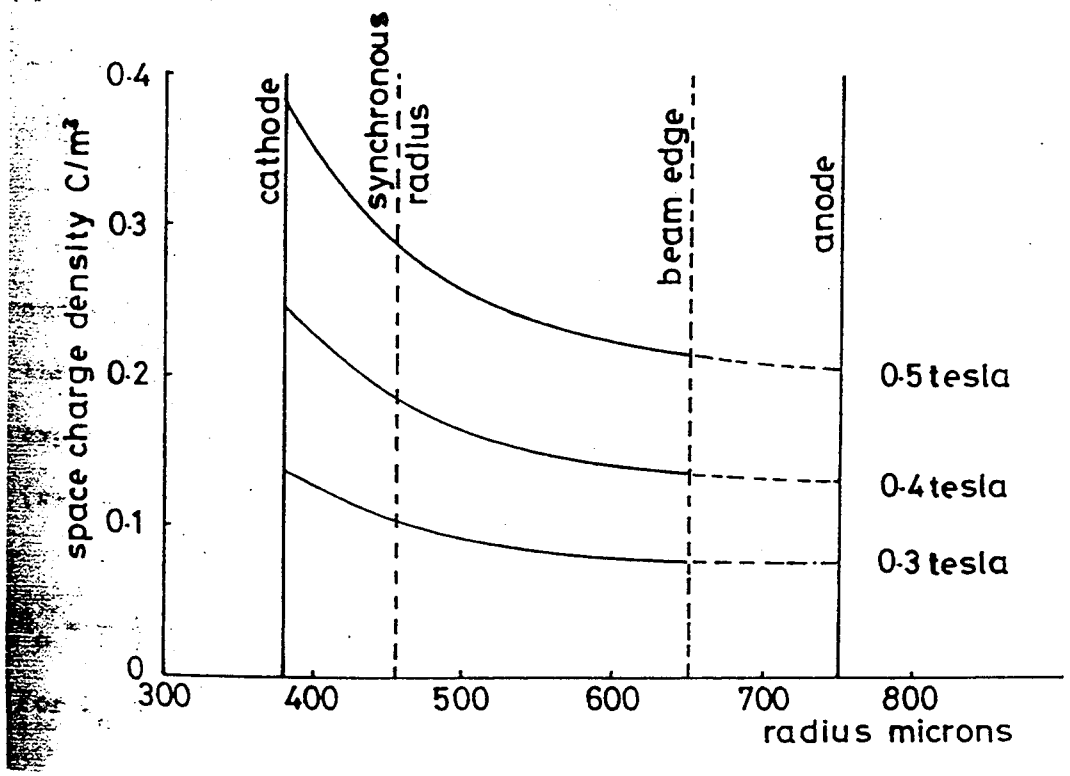


FIGURE 7: ANGULAR VELOCITY AND CHARGE DENSITY IN BUNEMAN ROTATING CROSSED-FIELD BEAM

The Buneman solution, when applied to a re-entrant magnetron shows a rotating beam of electrons with zero angular velocity at the cathode surface, increasing to the outer edge of the beam which is determined by the magnitude of the applied voltage. The appropriate space charge density is also shown - highest at the cathode, slowly dropping off towards the outer edge. In a properly designed magnetron, the angular velocity of the outer edge of the beam is arranged to be equal to the angular rate of rotation of the beam on the circuit - Synchronism - the condition in which Cumulative interaction can take place.

Actually, the crossed-field beam is not well behaved but becomes spontaneously very noisy. This is one of the areas which proved most intractable to analytical solution and is the subject of on-going research.

Note, the Magnetron operates in a Cut-off condition.

Phase Focusing - Spokes: once synchronism has been established in a CFD and interaction has started, other very interesting mechanisms take over - selective removal of unfavourable electrons and Spoke formation. The process is illustrated in Figure 8.

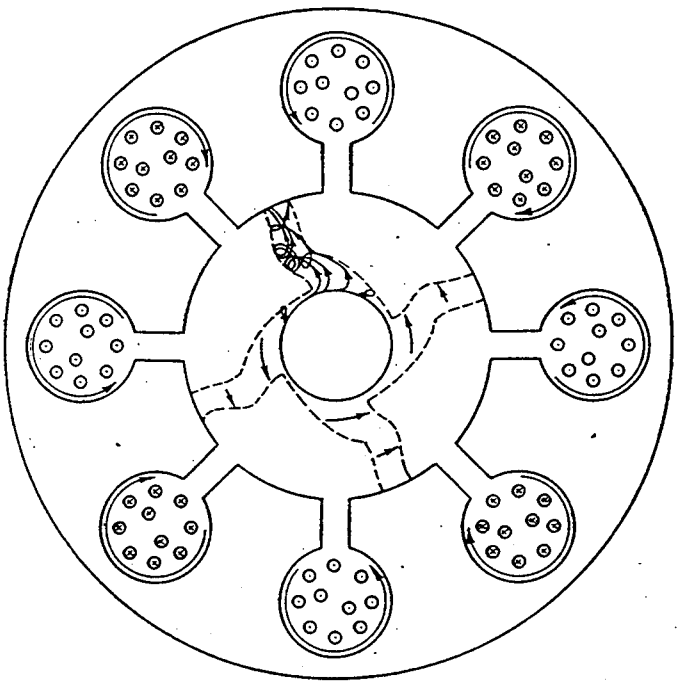
Electrons that happen to be emitted in the wrong phase are accelerated by the wave and immediately removed from the interaction by the action of the magnetic field. Much of this energy is returned to the cathode or sole and lost in the form of heat. Electrons which happen to be in the retarding phase with respect to the circuit wave are slowed down and drift out to the anode down the potential gradient giving up energy to the wave as they go - conversion of potential energy into rf energy. Furthermore, as the electrons slow or accelerate they experience restoring forces that focus the beam into structures like the rotating spokes of a wheel - Phase Focusing.

Spokes are a highly non-linear phenomenon not readily handled analytically and have occupied much effort to understand. The work is on-going as several of the papers in these Proceedings demonstrate..

At switch-on of a CW device and on each pulse of a pulsed device, a CFD starts to work spontaneously. The process is interesting. In the case of the Magnetron the device springs spontaneously and very rapidly into oscillation, indicating the presence of strong gain and feedback mechanisms.

Figure 9 indicates the main elements of the growth process. On the application of a voltage, the crossed field beam drawn out from the cathode becomes instantaneously very high-level noisy due to its inherent instability - a phenomenon worthy of on-going research. The noise generated in the beam excites a noise signal on the rf circuit which can be seen as a narrow band resonant probe - Starting noise.

Once synchronism has been achieved, interaction and linear growth occur as shown by the straight line on the log curve.



—Space charge in oscillating magnetron.

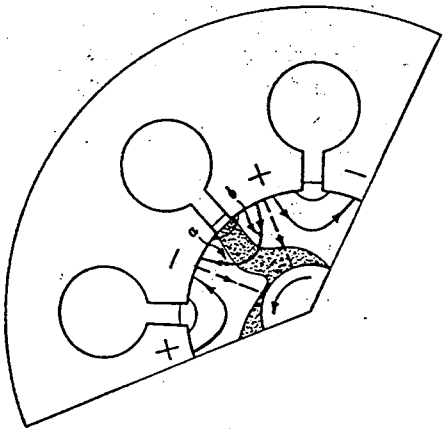


Diagram showing focusing action of r-f fields on space charge.

FIGURE 8: PHASE FOCUSSING - SPOKES (COLLINS REF 1)

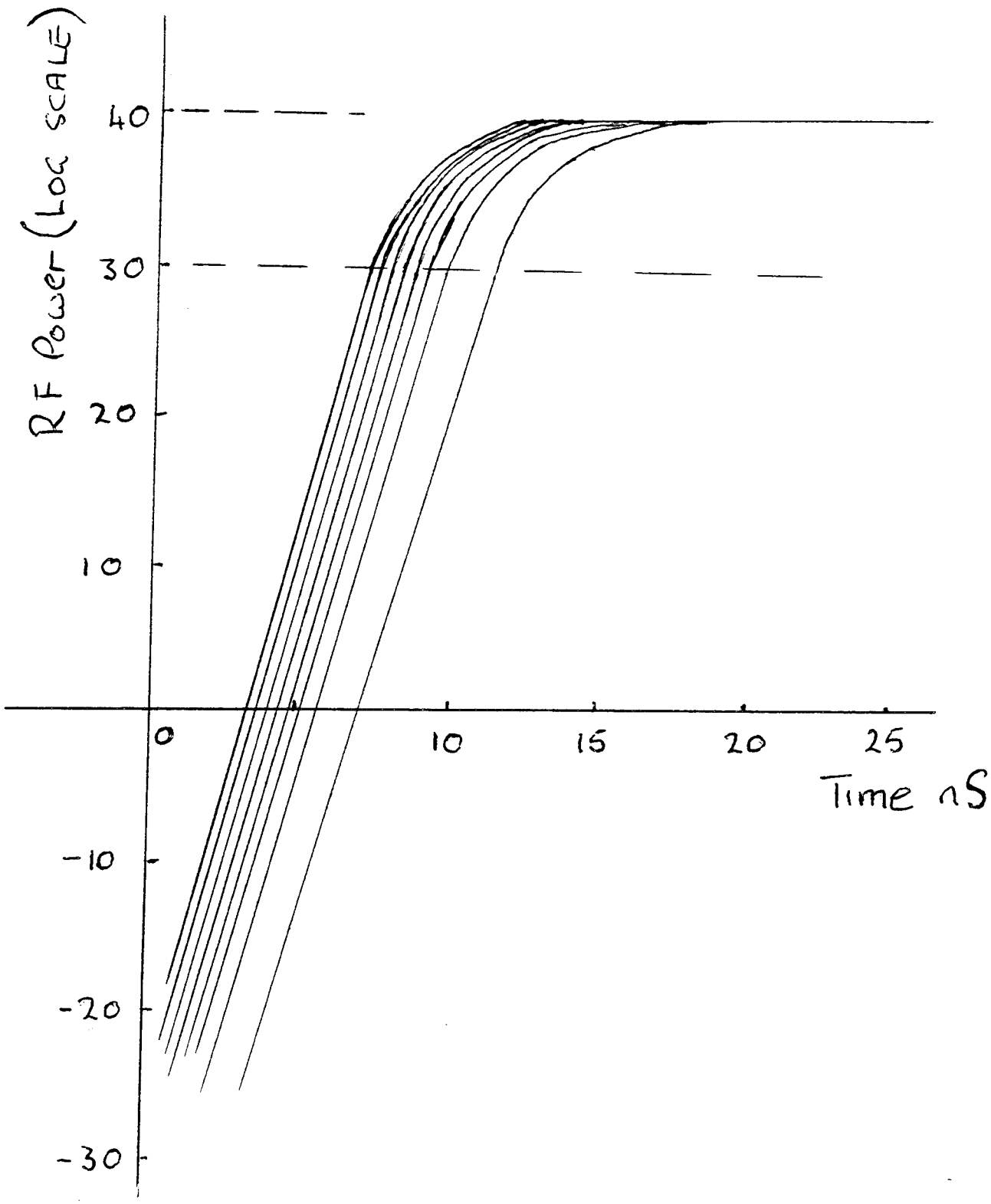


FIGURE 9: START OF OSCILLATION - RF POWER GROWTH IN MAGNETRONS (REF 3)

At high signal level, non-linear effects take over, as they must, and the interaction saturates; saturation occurs over the final 10dB of growth. This region is also a difficult process to describe and has been the subject of long-term and on-going research.

The variation in the amplitude of the noise signal on the circuit from pulse to pulse is the well understood source of pulse to pulse jitter (3).

CFD Evolution Tree

The paper started by describing the Early Magnetrons. It may be enlightening to consider how the development of CFDs has progressed since then - it is a amazing success story.

Figure 10 shows a simple Evolution Tree - we could make it much more detailed but this is nonetheless informative.

Crossed-field Backward Wave Oscillators were developed strongly in the UK, France and US in the 50/60s because of their effectiveness as relatively broadband, high power, electronically tuned Oscillators in he L-S-C- X and Ku-bands, mainly for military EW applications. High Power TWTs have now largely taken over these functions but I understand that very high performance devices are available and still being developed in Russia.

Crossed field Amplifiers have been developed in many forms, FWA, BWA, Amplitrons etc even against competition from truly linear broadband TWTs, because of the relative small size, high efficiency, low voltage and phase linearity that they can produce. However, nearly all this work has occurred in the US, work in UK being limited to a very few specialised devices.

Much work was carried out in the 60/70s in pursuit of circuitless amplifiers based on the Diocotron effect - the instability of crossed-field beams with velocity gradients but to the best of my knowledge they never developed into usable devices. This is possibly an area that should be revisited in the light of modern capability to analyse dense crossed-field beams and the advent of powerful computers.

MILO is interesting as a relativistic generator of super high rf power.

Range of Performance

In Europe, UK in particular, the major success story has been in the development and proliferation of magnetrons and its derivatives. These devices have been the workhorse for the generation of rf power in many applications affecting all our lives.

The concept has proved immensely flexible, Magnetrons having been designed to operate over a huge range of performances as highlighted below,

CFD Evolution Tree

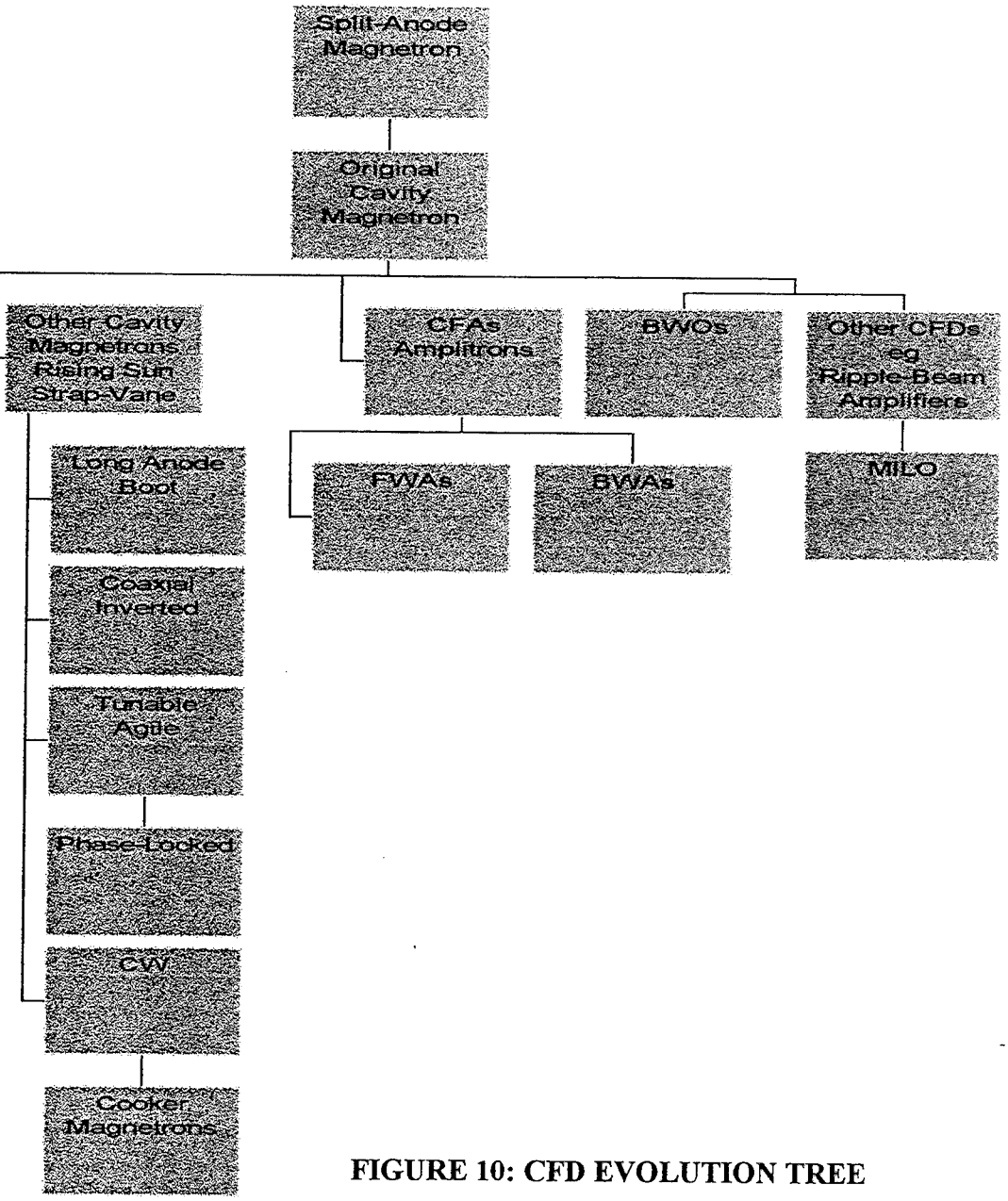


FIGURE 10: CFD EVOLUTION TREE

- Power: 1 watt to 1gigawatt
- Duty: monopulse to CW
- Frequency: 1-100GHz
- Size: few grammes to very large
- Tunability: fixed frequency to 50%
- Speed of tuning: fixed to instantaneous
- Warm-up time: down to sub-second
- Environment: missile rugged
- Stability: highly stabilised
- Life: up to 50,000 hrs

Magnetrons have been made with rf output powers from 1 watt to several Gigawatts. The smallest magnetron I am aware of produced 200 watts peak in X-band and weighed only 50 grms. The device had excellent frequency stability, low inter-line noise and featured a rugged directly heated cathode capable of sub-second switch-on times. By contrast, the largest cavity magnetron being produced in the UK at present is the !0 MW S-band Boot Magnetron used with separate solenoid for medical LINAC applications. However, much larger devices have been made in the past. There were reports from Russia at one time of a 500MW device working on relativistic principles. More recently, MILO devices have been developed generating rf power in excess of 1GW.

Magnetrons are currently made in the UK from 1 GHz to 100 GHz. An example of the former is the EEV long anode radar magnetron producing 2 MW pulses. At the other extreme, devices are made with rising sun circuits at 90GHz for radar modelling applications.

Clearly Magnetrons are extremely effective and efficient generators of short microwave pulses, hence their use in marine, ground, airborne and weather radar applications. At the other extreme, they can be designed as very efficient mean power rf generators. Countless millions of these devices are installed around the world in domestic and industrial microwave cookers and heaters. Powers range from a few hundreds watts mean to many Kilowatts.

High frequency stability and very long life has been achieved through coaxial magnetron designs in which an external, high Q cavity is utilised to tailor the characteristics of the rf circuit and loading.

In recent times there has been important development of the pulsed magnetron as a low voltage, narrow-band, saturated amplifier for missile seeker applications. These devices are used a phase-locked amplifiers with a few percent bandwidth and very quick warm-up. They have the additional advantages of being very small and lightweight and relatively inexpensive.

For completeness here is a list of the applications served by magnetrons. It is certainly not comprehensive but serves to emphasise the great flexibility of the magnetron concept.

Ground Radar	Weather Radar	MTI	Fusion
LINAC	Beacons	Marine Radar	Scientific
IFF	Seekers		

Research and Development

Although clearly mature, CFDs continue to be developed, better, lighter magnets, wider tuning elements, greater frequency agility, better phase-locked performance, higher power and more stable performance and, of course, longer life. Development continues in different sorts of device eg Milo.

At long last computers are starting to unravel some of the mysteries and complexities of dense crossed-field beam. It is likely that further advances will result from the improved understanding derived from the computer modelling of devices which have been beyond our capability for analytical treatment.

So where do CFDs go from here?

•Firstly they will continue to be used widely as the most efficient high power, rf generators.
•They will continue to be developed and modified to meet specific needs and applications.
•Newer devices such as MILO will emerge.
•There remain important areas where more advanced knowledge and research should pay dividends. These include,

a) the understanding of noise generation in the crossed field beam.

b) the use of the crossed-field beam as a signal amplifier in circuitless amplifiers.

c) the understanding and control of the saturation characteristics of the crossed field beam.

d) control of back-bombardment.

With the above come the prospects for lower noise amplifiers, improved second order performance, higher mean power devices through reduction of backbombardment power, longer life and possibly a new class of circuitless amplifiers.

References

1. G B Collins, "Microwave Magnetrons", McGaw-Hill, New York1948
2. Robert Clayton and Joan Algar, "The GEC Research Laboratories 1919-1984", Peter Peregrinus Ltd
3. B Vyse. Post Graduate Thesis, "Jitter and the Growth of RF Oscillations in Pulsed Magnetrons"

HISTORICAL PERSPECTIVE ON MAGNETRON DEVELOPMENT

ROBERT E. EDWARDS
RAYTHEON COMPANY (RETIRED)
96 OUTLOOK DRIVE
LEXINGTON, MA 02173

Abstract

The magnetron tubes that are so widely used in today's microwave ovens and radars evolved from experimental laboratory studies in the 1920's and 1930's. Demand for higher power, higher frequency radars in WW II stimulated development of more practical versions. British, U.S. and Japanese scientists rapidly achieved remarkable performance, having a major impact on the war. Special magnetrons have been created for applications far beyond the original concepts: jamming IFF, navigation, altimetry, weather mapping, air traffic control, frequency agility, industrial heating and food processing. It is interesting to review the circumstances and the innovations which made these amazing results possible.

Uses and Advantages

Magnetron history dates back to at least 1921, when A. V. Hull reported on his investigations of microwave oscillations in a cylindrical diode, which consisted of nothing more than a cylindrical anode with a centrally located cathode wire emitting electrons that passed through a magnetic field on their way to the anode, all within a vacuum enclosure. From this modest beginning has sprung an industry with far-reaching capabilities that influence our lives more than most of us realize (see Table 1):

Table 1. Typical Magnetron Applications

Air Traffic Control and Small Boat Radars	Missile Systems
Search and Navigation Radars; MTI	Jamming
Altimeters; Beacons; IFF	Medical Diathermy
Weather Radar	Industrial Processing
Terrain Following and Fire Control Radars	Microwave Cooking
CW Doppler Radars	

The popularity of magnetrons is largely due to their high efficiency in converting DC or pulsed input power to useful rf output power. Conversion efficiencies of 40 to 60 percent are common, with some tubes even achieving 85 percent. This, combined with compact size, low weight, reasonable operating voltage, relatively low cost, and adaptability to a variety of operating conditions, provides characteristics which have made magnetrons a favored choice as the rf power source for many important microwave systems.

Early Development

Throughout the 1920's and early 1930's magnetron studies progressed from Hull's cylindrical diode through series of split-anode and resonant circuit designs (see Figure 1). Various modes, rf field patterns and types of interaction between the electron flow and the rf fields were also explored. Theoretical analyses of performance were generated and hardware models capable of delivering power output at microwave frequencies were produced in several countries, including England, the U.S., Russia and Japan. However, most devices had low efficiency (1 to 10 percent) and were limited by unwanted spurious modes of oscillation [1] [2] [3].

World War II created the impetus for accelerated development of higher power microwave sources for radar systems. England had already deployed low frequency radars for coastal defense, but needed higher power, higher frequency systems to improve target discrimination. In November 1939, scientists at Birmingham University devised a six-cavity magnetron [4], adapted from the recently reported Varian klystron cavity format. The first tube was tested on February 21, 1940, soon amazing everyone with a power output of 400 watts CW at 9.8 cm wavelength. Moreover, in contrast with earlier designs, tests soon disclosed it could be pulsed up to about 10 kilowatts output, making a new generation of radars possible. The tube (Figure 2) required extensive machining of the copper resonant cavities, for which England was unable to divert its manufacturing capabilities from other wartime demands. A sample was brought to the U.S. in great secrecy in November 1940 to enlist manufacturing assistance. The U. S. Naval Research Lab., Bell Labs., Western Electric, M.I.T. Radiation Lab. and Raytheon Company were principals in this effort, with Raytheon ultimately producing over 70 percent of the magnetrons used by Allied radars in WWII.

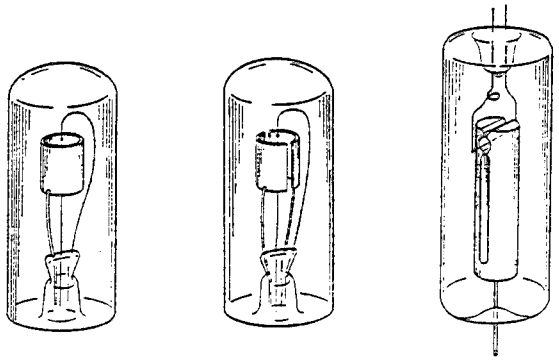


Figure 1. Early Experimental magnetrons
- Hull 1921 cylindrical diode.
- Split anodes; rf circuits added

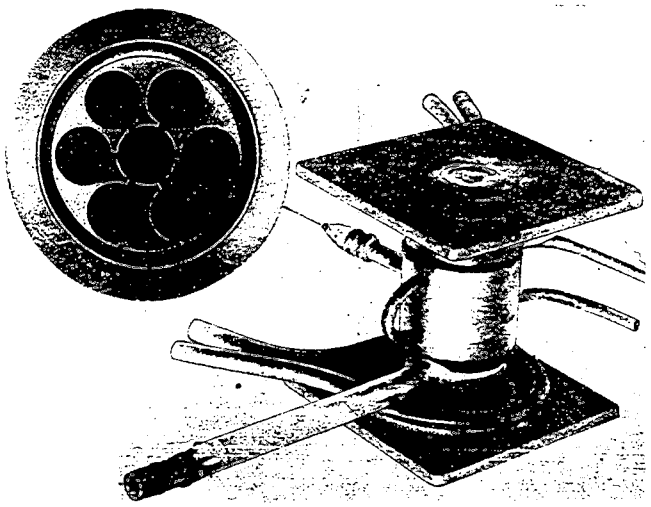


Figure 2. First British"All Metal"
Six Cavity Magnetron
- As tested February 21, 1940.

Innovations and Refinements

Many contributions were made by laboratory and industry scientists to extend magnetron performance, by both theoretical design interpretation and empirical hardware observation [5] [6]. A few highlights representing major improvement areas are mentioned here. As early as mid-1940 it was found that unwanted rf field configurations, or modes, could be suppressed by tying alternate vane tips of the rf system together with wires (called straps). This enhanced operation in the desired "pi mode" (180 degrees phase shift between vane tips), and separated other modes away from it in frequency and operating voltage. Efficiency was quickly improved to about 30 percent in S-band tubes, and the upper current boundary for stable operation was increased. Magnetrons were soon running at 100 kW peak power output.

As tubes were scaled to higher operating frequencies, however, such as X- and Ku-band, the straps became too small and produced large rf losses, reducing efficiency. Another technique, designated the "rising sun" anode, was employed for these higher frequencies. This involved alternating large and small resonant cavities around the anode circuit, rather than having all the same size. Unwanted modes were split into "families" and separated away from the desired pi mode. Columbia Radiation Lab. concentrated on this approach and eventually had tubes capable of 1 megawatt at X-band, and at least 50 kW at Ka-band.

Significant design improvements were also made in many other areas, of course. The early barium and strontium oxide coated cathodes were replaced in some tubes by higher temperature thoria cathodes, able to withstand higher power levels and more severe electronic "back bombardment". Later, in the 1960's, the dispenser cathode was introduced, consisting of a sintered tungsten porous base impregnated with barium aluminate. The barium was slowly released at normal elevated operating temperatures to replenish the emitting surface, prolonging life. This style of cathode has become a standard in various other microwave tubes as well.

Alumina ceramics replaced glass for high voltage input bushings and rf output windows. These provided more rugged structures for better tube reliability in field use, and appeared in production versions starting in the early 1950's. Another important advance was the introduction of "packaged" magnetrons during the early 1940's. The magnetic circuit was generally separate from the tube itself in the original models. By making a permanent magnet that was attached, or integral with the tube, overall weight was appreciably reduced, often by 10 pounds or more.

Frequency tuning was first added to production magnetrons by introducing a movable element in the vane tip region of the resonant cavities, in some cases mounted above or entering between the vane tips, and in others entering between the straps, to alter the capacitance of the resonant circuit. Later, a group of cylindrical pins was employed, entering the outer (inductive) portion of the cavities. This had the advantage of operating in an area of lower rf voltage than the capacitive tuners. It was more suitable for high power tubes for there was less likelihood of rf arcing, though generally requiring a greater tuner stroke for an equivalent tuning range.

Commencing about 1960, rotary tuners were developed to provide high speed frequency agility for some radars. A segmented disc was suspended over the cavities and rotated by magnetic coupling through the vacuum wall. The concept was originated by the Philips company in Europe, and was used in a number of European radars, and in some Japanese systems, but never gained popularity in the U.S. Tuning ranges for all these techniques are typically about 10 percent of the operating frequency.

Voltage tunable magnetrons have been promoted by General Electric Company and Mictron Company in the U.S. By proper selection of the rf circuit and controlling the electronic space charge, including injection of an electron stream from the end space into the interaction region of the tube, tuning over frequency ranges as wide as an octave can be achieved. The "VTM" designs are principally CW versions, and are useful for ECM, signal sources, etc., at power levels ranging from a few watts up to 100 watts.

The contributions made in theoretical analysis of magnetron performance by numerous scientists had a major influence on tube development. Hull [7], Hartree, Reike, and many others provided a foundation for understanding performance characteristics and for extending designs into new areas. The advent of the computer was also important, enabling design equations to be programmed for rapid optimization of new tubes and reducing the number of experimental hardware samples needed to meet new requirements.

Perhaps the greatest breakthrough was the invention of the "coaxial magnetron" by J. Feinstein [8] at Bell Labs. in 1958. Figure 3 shows a 125 kW Ku-band tube of this design, type 7208,

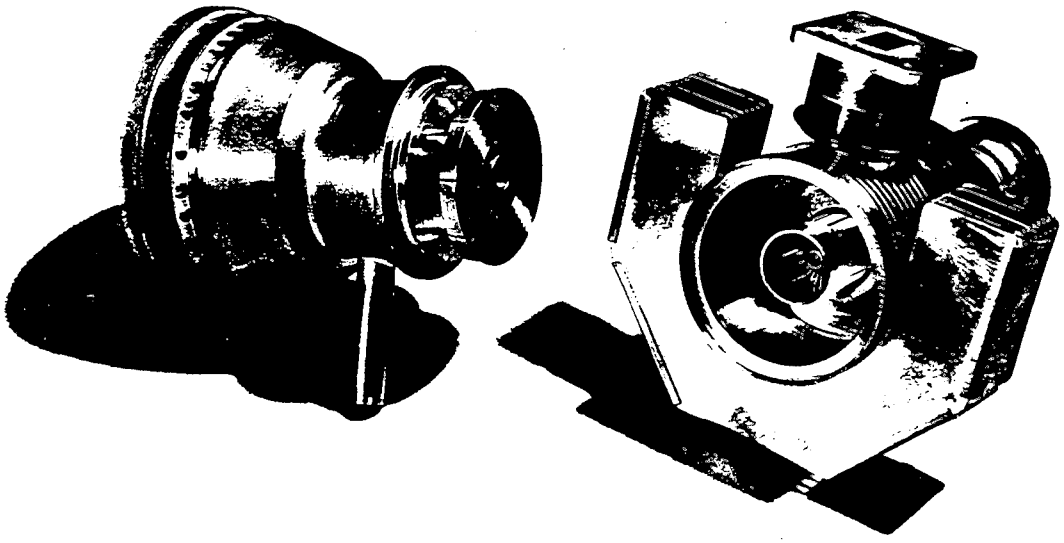


Figure 3. "Coaxial Cavity Magnetron": 125 kW, 15.5 - 17.5 GHz.
- Invented by J. Feinstein, Bell Labs. for improved frequency stability and life.

with a TE011 mode cavity surrounding the vane/cavity structure, coupled to it by slots in the outer wall of alternate cavities. Increased energy storage and stabilization from this added cavity raised overall efficiency, improved frequency stability and rf spectrum quality, and increased tube life. Stable, efficient operation was now possible with resonant circuits having 30 or more vanes. Anode and cathode surface areas could be much larger, reducing their power densities and also the electronic emission demands from the cathode. Frequency tuning is accomplished in this case by varying the height of the TE011 cavity, by moving one end plate up and down. The 7208 design can tune 14.5 to 17.5 GHz. During the 1960's most of the major U.S. manufacturers developed families of coaxial magnetrons, ranging from S-band to Ka-band frequencies. With different styles of tuner actuators applied, such as "voice coil" tuners (introduced by Litton), motor/cam tuners, and the Varian "Accutune" system, frequency agility became possible, and was utlized in many military radars such as the Texas Instruments airborne units.

Conventional type magnetrons remain popular for a number of applications, especially at the lower frequencies, where the increased size and cost of the coaxial cavity tubes becomes prohibitive. Also, at the lower frequencies the size of conventional anodes and cathodes becomes large enough to provide adequate performance and life for many uses (various classes of radars, microwave cooking, etc.). Magnetrons have varied in size from beacon tubes weighing only a few ounces to a production model weighing 220 pounds, delivering 2 megawatts at 420 to 450 MHz for use in radar picket planes.

Other Foreign Magnetron Activities

Japanese scientists were actively studying magnetrons as early as the mid-1920's. By the late 1930's they had built tubes with performance rivaling that of tubes from Western countries. Two post-war papers by Dr. Nakajima of Japan Radio Company [9] [10] offer considerable detail on the history of Japanese magnetron development. Extracts from these papers are presented in Table 2 and Figures 4 and 5. It is stated that a successful "rising sun" magnetron was tested in 1937, though the term was sometimes applied to what we would call a uniform "vane type" resonant structure (see Figure 4) with all cavities the same size. In 1939 a 500 watt CW, 10 cm. tube was demonstrated, actually predating the first practical British tube (Figure 2) by a few months. During the 1941-1942 period, operating models were running at 5 cm. and 2.2 cm. wavelengths. There was even a Super Power Program for high power CW tubes, aimed at disabling the electronic circuits of enemy planes and ships.

Table 2: Japanese Magnetron History
(Per Dr. Nakajima, New Japan Radio Co.)

1927	-	Split anode magnetron - Dr. Okabe, Tohoku Univ.
1932	-	Radar reflection reports spurred magnetron research - Dr. Ito, NTRI.
1937	-	"Mandarin" 8 slot/cavity tube invented - Naval Tech. Research Inst.
1939	-	"Rising sun" 500 W. CW, 10 cm., 8 cavity tube - Japan Radio Company
1941	-	"Rising sun" 7 kW peak, 9.9 cm. 8 cavity tube to Production - JRC
1941	-	"Rising sun" Local oscillator magnetron to Production - JRC

1941 - "Rising sun" 60 kW peak, 5 cm., 10 cavity tube - Japan Radio Company
1942 - 12 Slot/cavity 70 kW. peak, 2.2 cm. tube - Japan Radio Company
1942 - 44 - Super Power Program - 20 KW. CW, 15 cm. developed - JRC
1942 - 44 - Super Power Program - 100 KW. CW., 20 cm. developed - JRC

The diagrams of Figure 4 illustrate some of the types of anode resonant circuits tested by the Japanese in their early magnetron work. They include uniform vane-type systems, hole-and-slot, strapping, and a modified "rising sun" structure (called "Mandarin Orange"). Photographs of the tubes reveal that many were mounted in glass envelopes, as seen in the 2.2 cm. tube of Figure 5. Machining facilities for making all-metal tubes were scarce in Japan, as they were in England in the early 1940's, and the resulting models were not particularly well suited for rugged field use. Moreover, the Japanese military agencies did not fully appreciate the usefulness of radars or magnetrons to power them, according to Dr. Nakajima. Thus, although the early experimental work had advanced quite significantly, the actual field deployment and utilization of military radars by the Japanese lagged behind that of the Allied nations.

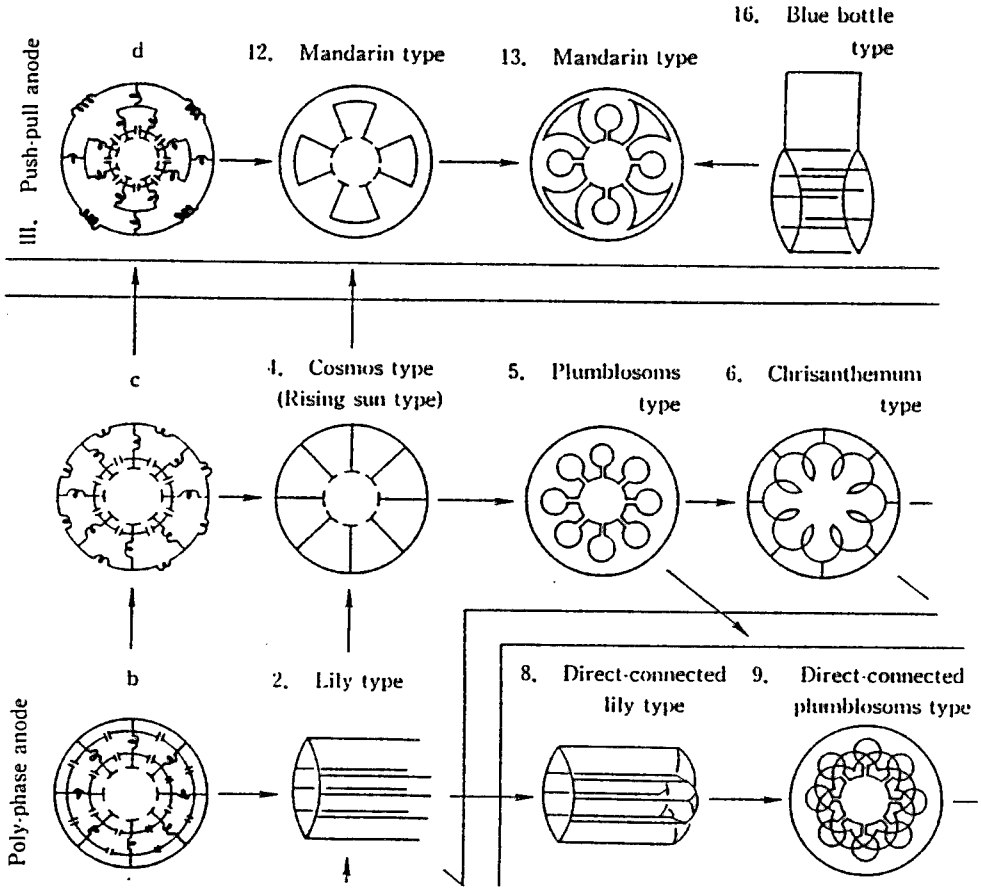


Figure 4. Early Japanese Anode Resonant Systems for Magnetrons

Magnetron research was also being conducted in Russia during the early years, as evidenced by some published papers [11]. During WW II this effort fell behind that of other countries, but recovered in following years to produce some very useful devices. Russia had provided third-world countries with military systems for their self defense during the 1970's. For various

reasons those countries were unable to procure replacements for failed components. U.S. agencies were requested to have U.S. companies manufacture duplicates of the components, including magnetrons, to restore the systems to full use. This activity [12], performed in the early 1980's, afforded an opportunity to evaluate performance of Russian magnetrons. Most were of an older design period, of course. Several C-band 600 kW. tubes, and 80 to 100 kW. X-band tubes were produced, as well as low power data-link versions. Hole-and-slot rising sun designs were commonly employed, with inductive tuning fingers in both the large and small

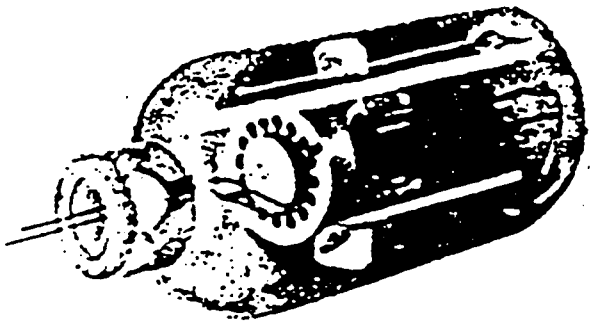


Figure 5. Japanese 16 Vane Magnetron (1941-42); 2.6 cm, 50 kW pk. output.

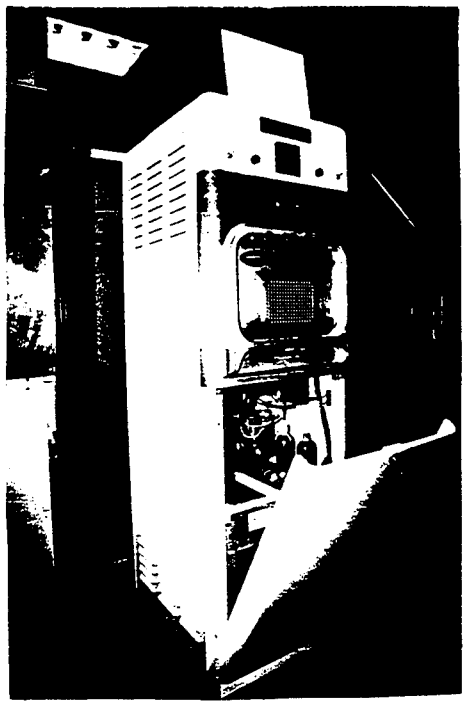


Figure 6. Early (1947) Raytheon Microwave Oven for Restaurants.

cavities. In the lower frequency tubes there were also strapped vane structures bearing a similarity to U.S. C-band designs. The interior workmanship, machining finishes, and parts alignment were generally very good, as was the electrical performance. Less attention was devoted to weight optimization and exterior "customer appeal" than in comparable products of Western countries. Subsequent to the 1950's their design capability caught up with that of the Western countries, so that by the end of the 1960's it might be considered equal in many respects, and in certain areas exceeded that of the West.

Commercial Uses of Magnetrons

Following World War II there was interest in promoting magnetrons for commercial applications. There were, of course, air traffic control radars and small boat radars produced as an obvious outgrowth of the military systems. However, other uses also were found which had not been originally predicted. In the late 1940's Raytheon Company began delivering medical diathermy equipment to hospitals and doctors offices, to feed limited microwave power into

patients muscles and joints for therapeutic purposes. CW rf power of up to 80 watts at 2450 MHz was utilized. However, because of the difficulty of controlling proper use of these units in such diverse installations, they were abandoned in the U.S. as a commercial product. It is interesting to note that the Boston Globe reported in October 1995 that U.S. medical authorities have now approved use of focused rf for treatment of prostate cancer. The procedure has been employed since 1991 in 25 other countries.

Microwave cooking technology is generally considered to have originated in 1945, when Raytheon's Percy Spencer discovered that popcorn held at the output region of an operating magnetron could be quickly cooked. By 1947, the company was producing microwave ovens for sale to restaurants, hotels, and hospitals. The floor model seen in Figure 6 is typical of these ovens - rather large, with glass rectifier tubes and heavy transformers mounted in the base - and quite expensive. Other companies, such as Litton, also entered this market. Raytheon's 1960 acquisition of Amana as a subsidiary was an important influence in rapidly expanding microwave oven use into the ordinary home. Amana had the established distribution, sales and maintenance network, and the commercial product experience to reduce manufacturing costs to make the ovens more widely acceptable by the general public. As the market expanded, ovens were produced (or sub-contracted) by Litton, General Electric, Westinghouse, Tappan, Hotpoint, Sears and other U.S. manufacturers. Japanese and Korean companies entered the market, and ultimately captured the major portion of it with the lower cost mass-produced ovens which most of us have in our homes today.

A present-day cooking magnetron and an earlier Raytheon version are shown in Figure 7. Some were also unpackaged tubes, an electromagnet mounted in the oven furnishing the required magnetic field. The most common rating was 700 watts CW output at 2450 MHz with 60 percent efficiency. Later, several packaged versions were introduced, having small high-energy magnets, air cooling fins, and rf leakage suppression circuits included in the assembly. A maximum manufacturing rate of 2000 tubes per day was reached, but again, severe price competition from Japanese, Korean and other Far Eastern companies, who were delivering tubes at $15 each, forced all U.S. companies out of the business. The annual world market for these magnetrons in 1994 was estimated at approximately 25 million tubes. Most are, of course, built with automation techniques for such a large market. Power ratings for current models range from 400 to 800 watts CW output at 2450 MHz, depending upon oven size, and utilize a design which is based upon refinement of the earlier models.

An important business area has developed in the use of high power magnetrons for industrial heating applications. Both batch-type and conveyor-belt ovens are employed. Typical systems are engaged in treatment of rubber tires, warming frozen food prior to cutting, cooking potato chips and bacon, etc. A popular frequency for this work is 915 MHz, chosen because of favorable rf penetration properties and availability of a commercially designated FCC band. One example of a conveyor oven is seen in Figure 8. The magnetrons are generally rated at power levels of 25, 30, 50 or 75 kW and have been built by many companies over the years (New Japan Radio, Litton, English Electric Valve, Raytheon, RCA and Burle Industries). The DC to rf conversion efficiency of these tubes is truly remarkable. For example, with an input of 12 KV and 2.5 amperes (30 KW in) the output is 25 KW, yielding an efficiency of about 85

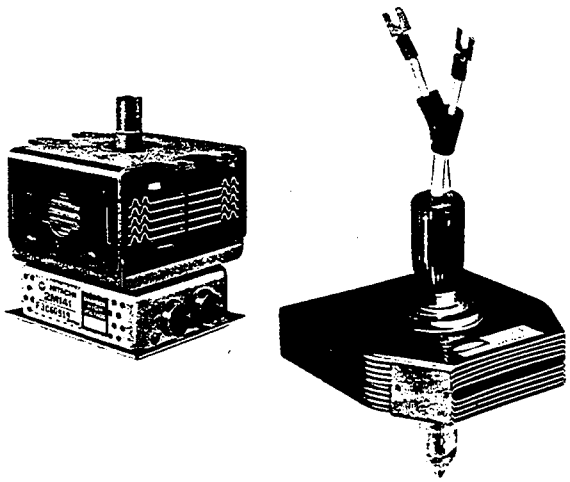


Figure 7. Magnetrons for Microwave ovens.
- Left, typical present design
- Right, earlier Raytheon tube



Figure 8. Conveyor Oven for Industrial Processing
- Uses 30 KW, 915 MHz magnetrons

percent. A significant advantage of high power industrial processing by microwaves is the overall energy efficiency of the installation. Besides the contribution by the high efficiency of the magnetrons, the system only uses power when activated, in contrast to other styles of processing ovens.

Conclusions

Government and military agencies supporting magnetron and other microwave tube work were relatively few in the early days. The U.S. Naval Research Lab., BUSHIPS, U.S. Army Signal Corps- Ft. Monmouth, and Rome Air Development Center became prominent early supporters. Eventually other groups became involved as new applications appeared and responsibilities shifted. At least 12 major U.S companies have manufactured magnetrons, though many abandoned the market due to competition and excess capacity. Several smaller companies have specialized in limited segments of the market, or in salvaging and rebuilding tubes. University laboratories, such as MIT Radiation Laboratory, Columbia Radiation Laboratory, University of Michigan, and many others have contributed greatly to theoretical analysis of the magnetron, and to experimental verification through construction of unique model tubes. There have also been important spin-offs from the magnetron work. The entire crossed field amplifier market was an outgrowth of the magnetron industry. Materials, techniques and facilities were developed which were adaptable to many other products. Radars, industrial heating/cooking, etc., were first made practical or were certainly enhanced by the use of magnetrons.

Thus, we see that a very productive effort has been devoted to exploitation of the magnetron principle in the United States and throughout the world. From a relatively simple concept, devices and systems have evolved which have had a significant impact upon on all our lives.

Traveling wave tubes, klystrons, solid state, and other microwave devices have shown notable capabilities for larger rf bandwidth, better frequency stability, etc., but the magnetron has its place where high efficiency compact size, economical construction and modest degrees of performance sophistication are required. As evidenced by the other papers presented at this conference, there are a number of magnetron studies still in progress, holding promise of further practical uses of this device.

References

[1] "Microwave Magnetrons", M.I.T. Radiation Lab. Series, McGraw-Hill, Vol. 6, Pgs. 1-10.

[2] H.Yagi, Proc. I.R.E., Vol. 16, Pg. 715, (1928).

[3] G.R.Kilgore, Proc. I.R.E., Vol. 24, Pg. 1140, (1928).

[4] Henry A. H. Boot and John T. Randall, "Historical Notes on the Cavity Magnetron", July 1976. IEEE Transactions on Electron Devices, Vol. 23, No. 7,

[5] "Microwave Magnetrons", M.I.T. Radiation Lab. Series, McGraw-Hill, Vol. 6, Parts I-IV.

[6] "Crossed Field Microwave Devices", Academic Press, Vols. I, II, E.Okress, Ed.

[7] A.W. Hull, Physical Review, Vol. 18, Pgs. 31-57, (1921).

[8] J. Feinstein and R.J. Collier, "Crossed Field Microwave Devices", Academic Press, E. Okress, Ed., Vol. II, Chapter 3, Pgs. 123-134.

[9] Dr.-Eng. Shigeru Nakajima, "History of Japanese Radar Development to 1945", London I.E.E. Conference, May 10, 1985.

[10] Dr.-Eng. Shigeru Nakajima, "The Study of Microwave Magnetrons", Japan Radio Co. Publication, April 1947.

[11] N. T. Aleksereff and D.E. Malearoff, Journal Tech. Phys., USSR, Vol. 10, Pg. 1297, (1940).

[12] J. Cosby and R. Edwards, "Foreign Microwave Tubes", Monterey Tube Conference, May 1984.

Low Noise CFA Measurements, Analysis, and Simulation

Steve Hillenberg, Dean Thelen[1], and Alexander MacMullen[2]

Naval Surface Warfare Center, Crane
Crane, IN 47522

[1]Technology Service Corporation
116 W. 6th St., Suite 200
Bloomington, IN 47404

[2]Technology Service Corporation
2950 31st St., Suite 200
Santa Monica, CA 90405

Results are presented for measurements conducted on experimental crossed-field amplifiers (CFAs) developed in the low noise CFA (LNCFA) program. An improvement to the noise measurement technique has been made by using an electronic phase shifter. Frequency swept signal-to-noise ratio (SNR) measurement data has been collected for various cathode positions and cathode oxygen level. S-parameter measurements have been made at various B-fields and with the CFA on and off. Radio frequency (rf) and electronic feedback through the drift space region is discussed. CFA models are introduced and used to analyze data. CFA simulations have been made using the MASK code.

Low Noise CFA Measurements, Analysis, and Simulation

INTRODUCTION

Highly accurate techniques of measuring CFA SNR will be discussed. Introduced will be a recently developed technique that uses an electronic phase shifter, increases SNR measurement capability, and reduces equipment cost.

S-parameter and SNR measurements have been made on CFAs. S-parameter measurements indicate the presence of rf leakage and electronic feedback through the CFA drift space region. SNR studies have been made where cathode position or cathode oxygen level has been varied.

Experimental results are supplemented by simulation results, obtained using the MASK code. Simulations have been made to study the effects of rf drift space feedback and of changing the magnetic field value.

MEASUREMENTS

SNR Measurements: SNR measurements of rf amplifiers have varied from test site to test site even when the same amplifier is measured. These SNR value variations are due to each test system having different distortion levels. An SNR measurement technique and analysis software have been developed[1,2] that minimizes the effect of test system distortions. In contrast to earlier techniques that required manual equipment calibration to eliminate test system distortions, the offset frequency technique discussed here gives SNR values unaffected by these distortions. Both manufacturer and customer can test the amplifier with this technique and have SNR values that typically agree within tenths of dBs.

Figure 1 shows the system diagram used in the offset frequency technique. This technique has been implemented with two experimental setups: (1) using two rf synthesizers and (2) a newer technique that uses an electronic phase shifter and one rf synthesizer. When using two synthesizers, one rf synthesizer generates the signal to the device under test, designated as RF, while the other generates the local oscillator (LO) signal whose frequency is offset from the RF frequency by a small amount (typically 20 Hz). The LO and RF signals enter a vector demodulator (VDM) which outputs low frequency I and Q signals. The I/Q signals are digitized and analyzed by the SNR analysis software. In a typical test, ~100 pulses are digitized with 100 I and Q data samples taken per pulse. The only difference between the newer phase shifter technique and the two-synthesizer technique is that the RF signal is created with a single rf synthesizer and the LO signal is created by phase shifting the same signal. The phase shifter technique has lower equipment costs and increases measurement capability. SNR measurement capability using the phase shifter technique is improved over the two-synthesizer technique. This is due to a lower noise floor that originates from canceling single-source correlated noise through LO and RF paths, which contain uncorrelated noise signals in the two-synthesizer technique.

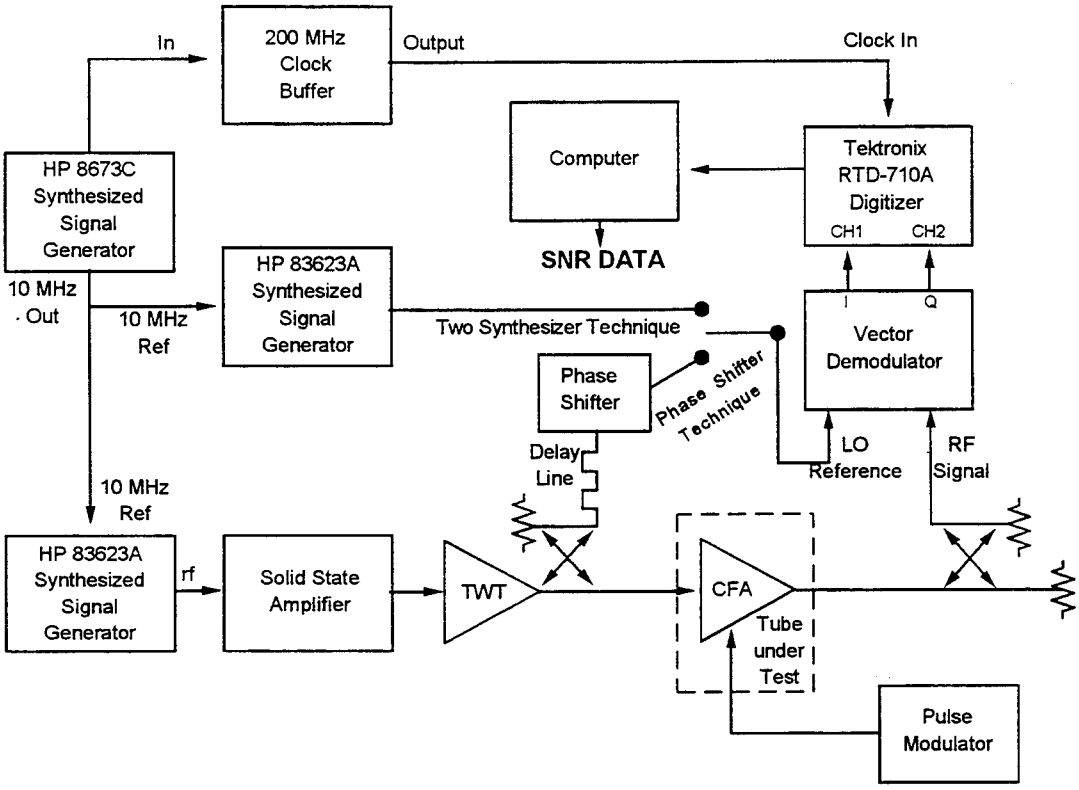


Figure 1. SNR Measurement System Diagram

A mathematical description of the system illustrates test system distortions. A sampled RF signal out of the device under test is given by

$$RF=(A+\Delta A)\cos(\omega t+\Delta\phi) \tag{1}$$

where A is signal amplitude, ΔA, $\Delta\phi$ are the amplitude and phase noises that determine SNR. The local oscillator signal is given by

$$LO=\cos(\omega t+\theta) \tag{2}$$

where θ originates from the offset frequency, numerically equal to the angular offset frequency multiplied by time (typically $\theta=2\pi(20\text{ Hz})t$). For an ideal VDM, the RF and LO signals are converted into I and Q signals given by

$$\begin{aligned} I&=k(A+\Delta A)\cos(\theta-\Delta\phi)\\ Q&=k(A+\Delta A)\sin(\theta-\Delta\phi)\end{aligned} \tag{3}$$

where k is the loss of the VDM.

For an actual VDM, linear and nonlinear I and Q distortions may exist. Figure 2 illustrates the effects of linear distortions, which distort plots of Q vs. I from the circular pattern described in equation (3) to an ellipse. The nonlinear distortions originate largely from the VDM mixers and may be essentially eliminated by using quality, high-level mixers. The remaining linear

distortions cause I and Q to be given by

$$I = k_I(A + \Delta A)\cos(\theta - \Delta\phi) + B_I$$
$$Q = k_Q(A + \Delta A)\sin(\theta + \varepsilon - \Delta\phi) + B_Q \qquad (4)$$

where B_I and B_Q are DC offsets, k_I and k_Q represent different losses in I and Q channels, and a quadrature error ε originating from the VDM hybrid coupler.

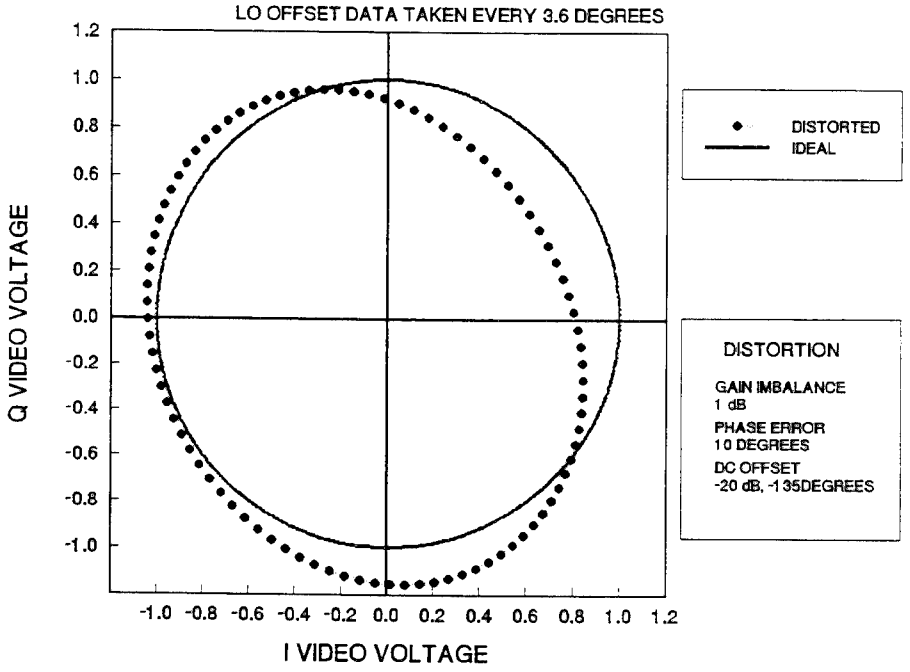


Figure 2. VDM Distortions

The SNR analysis software gives correct SNR values even when VDM distortions are present. The software contains both linear and nonlinear SNR analysis subroutines[1], which not only differ because of the type of data distortions of which they eliminate the effect, but also differ due to the types of algorithms used. The linear analysis subroutine uses statistical SNR calculation methods. The nonlinear analysis subroutine determines linear and nonlinear distortions and uses this information to correct individual data points. The linear and nonlinear subroutines should give nearly identical results, because nonlinearities are eliminated at most frequencies through proper choice of VDM mixer levels and the difference between statistical and data correcting algorithms is small. The two subroutines have been found to give SNR values within 0.01 dB when neglecting nonlinearities.

SNR measurements on the same CFA were made at Crane Division, Naval Surface Warfare Center, located in Crane, IN and Litton Electron Devices in Williamsport, PA. SNR values agreed within ± 0.25 dB at each measured frequency. Previous errors were as much as 4 dB at certain frequencies. This LO offset technique has been used to measure an SFD262 production CFA where the cathode location has been moved. Figure 3 shows the measured SNR values. A value as high as 59 dBc/MHz was found, which is a low noise value for a production CFA. The noise notch at F5.4 is possibly due to an input window resonance.

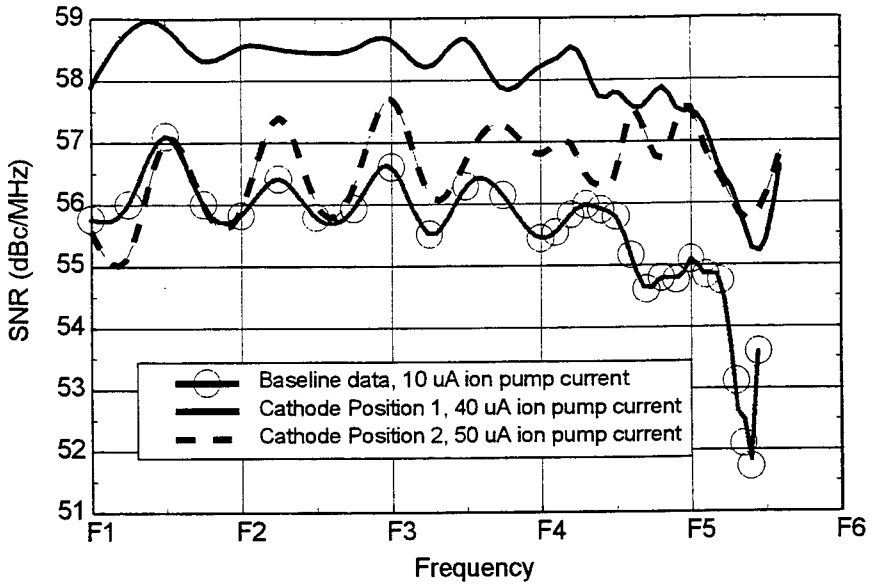


Figure 3. Cathode Position Effects on CFA SNR

A study of CFA oxygen pressure on SNR values has been made using the experimental Communication & Power Industries (CPI) low-noise CFA serial number C326ANR2. Figure 4 shows the SNR data sets collected before and after cathode conditioning. Peak SNR values increase from 62 to 64 dBc/MHz.

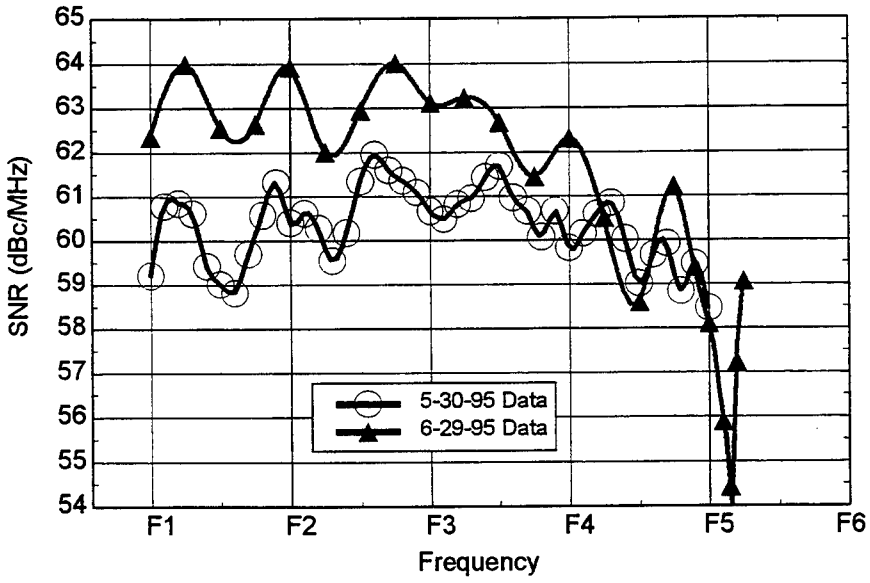


Figure 4. CPI C326ANR2 SNR Data

S-Parameter Measurements: S-parameter data was collected using an HP8510C vector network analyzer. Data values were collected using a linear frequency sweep. Time domain data was obtained from the frequency data using the HP8510C built-in inverse Fourier transform, which involves Kaiser windowing and the chirp-Z transform. Typical CFA operating conditions varied in experimental studies include CFA drive power, magnetic (B-) field, and on/off state.

S-parameter data was collected on an experimental low-noise CPI tube serial number F178AMR2. B-field was varied in these measurements as indicated by the change in cathode

voltage, being proportional to B-field value. Figures 5 and 6 contain S_{21} and S_{11} data sets collected in these measurements. Figure 5 contains $S_{21}(t)$ data where first and third peaks split at 11.8 kV cathode voltage but do not split at lower cathode voltages. Figure 6 contains $S_{11}(t)$ data collected at 9 and 11.8 kV cathode voltages that exhibits the three major time peaks near 2, 17, and 31 nanoseconds. The 10.7 kV $S_{11}(t)$ data contains additional nulls near these time peaks.

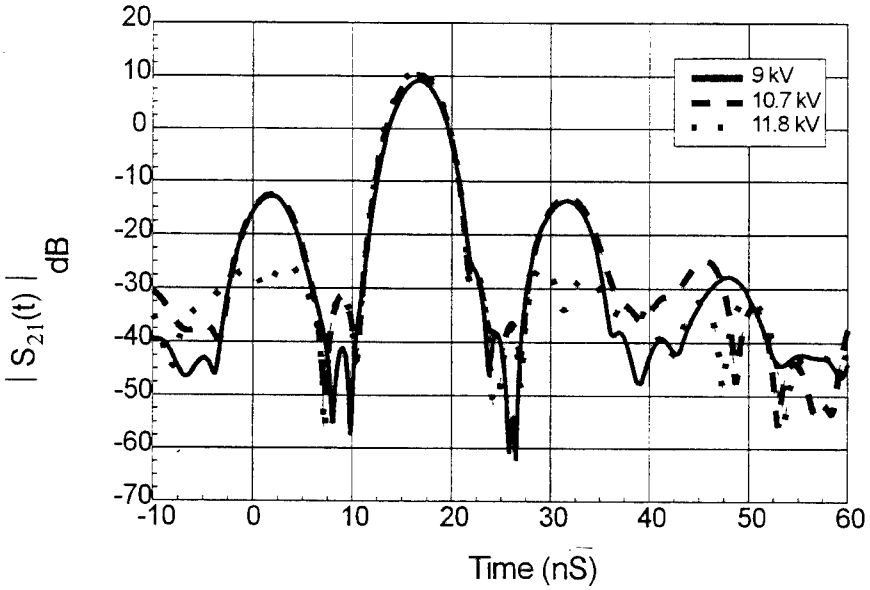


Figure 5. S_{21} data for various B-fields, CPI CFA Serial Number F178AMR2

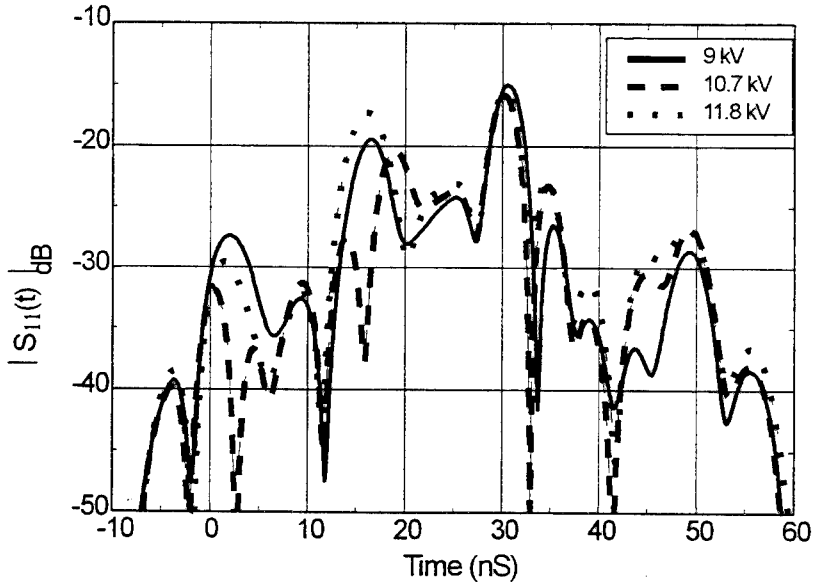


Figure 6. $S_{11}(t)$ data for various B-fields, CPI CFA Serial Number F178AMR2

Data on CFA deviation from linear phase over frequency should be quantitatively analyzed instead of time responses. This is because it can be analyzed without obscuring the data by making a transform from the frequency to time domain. Figure 7 shows the measured CFA deviation from linear phase obtained from $S_{21}(f)$ phase. Phase oscillations arise from rf drift space and electronic feedback components, as discussed later. Phase oscillations decrease as the B-field

(equivalently cathode voltage) is increased.

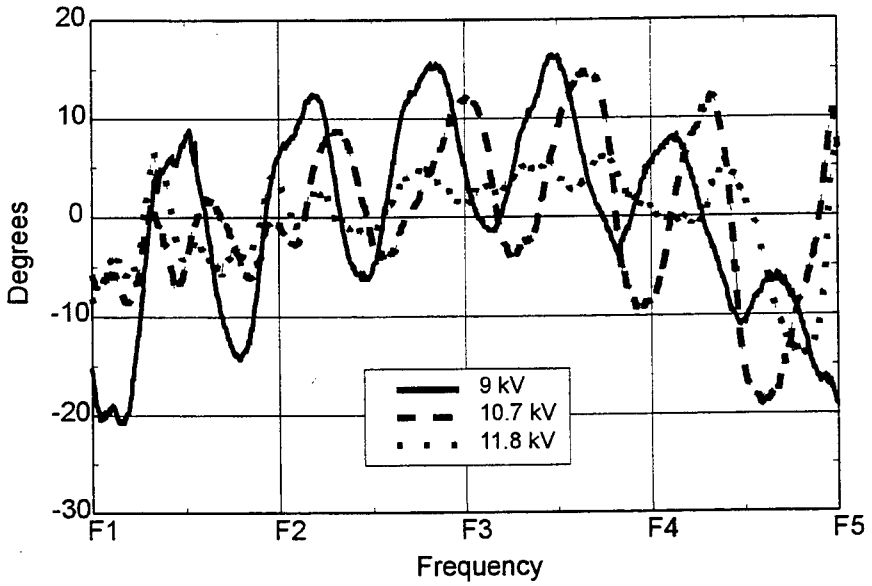


Figure 7. Deviation from linear phase at various B-fields

ANALYSIS

Analyzed in this section are output phase and SNR oscillations over frequency. Rf feedback components are well understood and their contributions to output phase and SNR oscillations can be determined. Electronic feedback components are unknown but their presence can be inferred by the difference between the rf contribution and experimental results.

Figure 8 illustrates how rf feedback is modeled by combining the attenuated output rf signal with the original input signal to arrive at a resultant input signal that depends on the phase difference θ between the two signals. Rf feedback contributions to output phase and SNR oscillations arise from amplitude modulation of the input signal when θ is near 0° and 180° and phase modulation of the input signal when θ is near 90° and 270°.

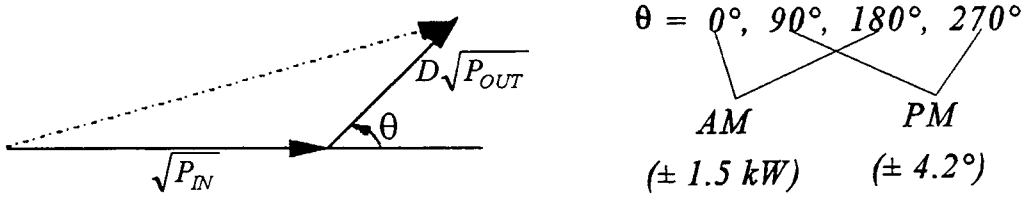


Figure 8. Input signal oscillations

Phase Oscillations: $S_{21}(f)$ phase oscillations are analyzed here by sums of rf and electronic feedback contributions. Figure 9 shows three phase oscillation contributions. The first two contributions originate from the rf drift space leakage contribution, with its amplitude and phase modulation of the input signal. The first contribution is the phase modulation (PM) of the input signal that passes directly to the output phase. The second contribution is the amplitude modulation (AM) of the input signal that changes output phase after an amplitude modulation to

phase modulation (AM-to-PM) conversion. The third contribution is the unknown electronic feedback contribution that we want to determine.

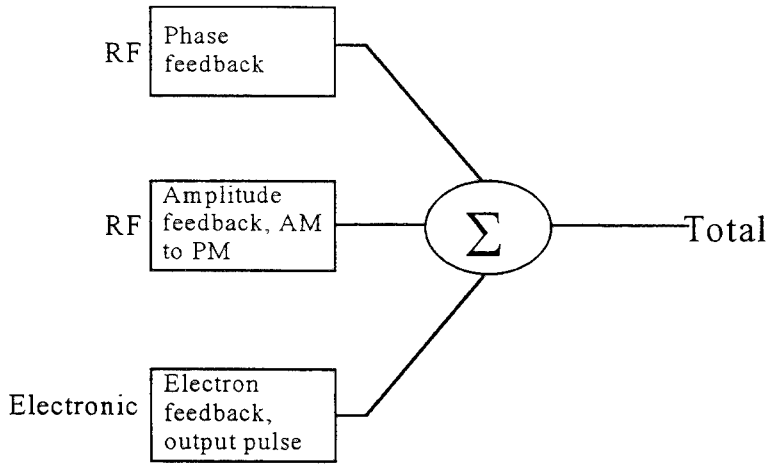


Figure 9. Components of Phase Deviations

Rf feedback contributions to the output phase deviation from linear phase $\Delta\phi_{Out}$ are determined by considering Figure 8. The sinusoidal contribution originating from PM of the input signal is

$$DL\sin\theta \tag{5}$$

while AM of the input signal and subsequent AM to PM conversion leads to the term

$$\left[\frac{\Delta\phi_{Out}}{\Delta P_{In\ dB}}\right] 8.68\,DL\cos\theta \tag{6}$$

where the output phase change with input power $[\Delta\phi_{Out}/\Delta P_{In\ dB}]$ is measured experimentally in units of radians/dB. The total rf contribution to phase oscillations is given by the sum of equations (5) and (6) to be

$$\Delta\phi_{Out} = DL\sqrt{1+b^2}\sin(\theta - \tan^{-1}b) \tag{7}$$

where

$$b = 8.68\left[\frac{\Delta\phi_{Out}}{\Delta P_{In\ dB}}\right] \tag{8}$$

SNR Oscillations: Increasing drive power level improves SNR values. Rf signal feedback through the drift space region amplitude modulates the input signal, changing the effective input power level. Phase modulation of the input signal does not affect SNR values. The rf feedback contribution to SNR oscillations is

$$\Delta SNR = \left[\frac{\Delta SNR}{\Delta P_{In\ dB}}\right]\Delta P_{In\ dB} = \left[\frac{\Delta SNR}{\Delta P_{In\ dB}}\right] 8.68\,DL\cos\theta \tag{9}$$

where the change in SNR with input drive power $[\Delta SNR/\Delta P_{In\ dB}]$ is measured experimentally in units of dB/dB.

Comparisons with experiment: The experimental results for SNR and phase oscillations will now be compared to rf feedback predictions. These results verify the presence of an electronic feedback mechanism.

Rf leakage model predictions of phase and SNR oscillation amplitudes are made by assuming typical model parameter values. Combining these rf leakage predictions with experimental results given in Figures 3 and 7 allows identification of electronic feedback effects. Phase and SNR oscillation amplitudes are determined using equations (7) and (9) by assuming D=-34 dB, L=11.3 dB (DL=4.2°) and obtaining experimental estimates of output phase and SNR sensitivities to input drive power. Output phase sensitivity to input power was measured on the production tube with moved cathode position (Figure 3) to be $[\Delta\phi_{Out}/\Delta P_{In\ dB}]=10°/dB$. Substituting this measured value into equations (7) and (8) yields b=1.5 and 7.6° phase oscillation amplitude due to rf feedback. The production specification value of output phase sensitivity to input power is not allowed to be greater than 3°/dB, corresponding to b=.45 and 4.6° phase oscillation amplitude.

Figure 7 contains phase oscillation data for the experimental CPI CFA S/N F178AMR2. Phase sensitivity to drive power data is not available for this CFA. Figure 7 indicates a phase oscillation amplitude ~10° at 9kV cathode voltage, decreasing to ~2° at 11.8 kV. Electronic feedback must be present to explain the 11.8 kV phase oscillation amplitude, because rf signal feedback alone has a phase oscillation amplitude greater than DL=4.2° that must be canceled by an electronic component to arrive at the ~2° experimental value.

Figure 3 contains SNR data on an AEGIS production CFA with displaced cathode position. Measured SNR sensitivity to drive power was 1.3 dB/dB. Corresponding phase oscillation amplitude predicted with the model is .84 dBc/MHz. Figure 3 experimental results indicate an SNR oscillation amplitude of ~.5dBc/MHz. A small electronic feedback contribution to SNR oscillations may be present to cancel part of the rf feedback contribution, but the deviation of experiment from rf feedback alone is within experimental/prediction uncertainty.

CFA MODEL

Figure 10a shows a representative two-dimensional CFA cross section. Figure 10b contains a pictorial CFA model with passive rf leakage through the drift space region and the reentrant electron flow. Rf drift space leakage flows equally from both output to input and input to output. Electronic feedback through the drift space region only occurs from output to input.

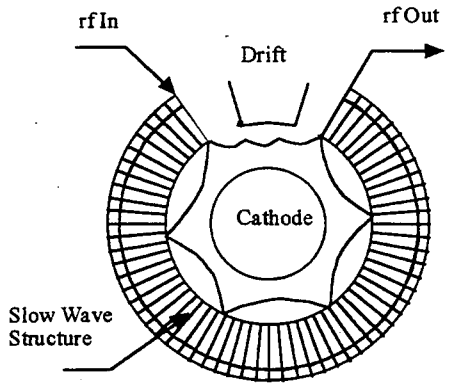


Figure 10a. Two-dimensional CFA Cross Section

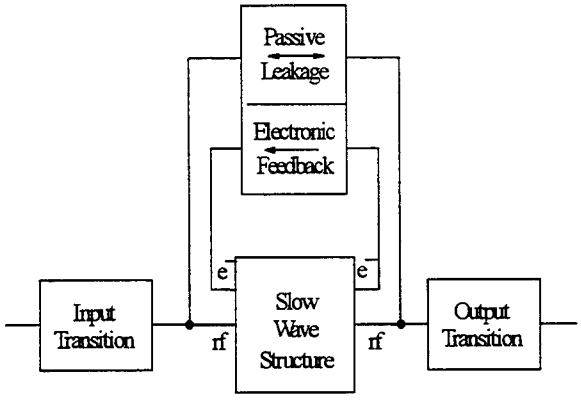


Figure 10b. rf Signal and Electron Flow

Figure 11 contains a CFA signal flow-graph model that includes rf drift space feedback. The flow-graph model neglects electronic feedback and reflections at CFA input and output. CFA slow-wave structure gain/attenuation is denoted by **L** and drift space attenuation is represented by **D**. The S-parameters for this model are simplified by noting that the product of gain and drift space attenuation is much less than one, i.e., $|\mathbf{D}||\mathbf{L}| \ll 1$, and are expressed as

$$S_{21}(\omega) = \frac{D+L}{1-DL-D^2} \approx D+L+DL^2 \qquad S_{11}(\omega) = \frac{DL}{1-DL} \approx DL \tag{10}$$

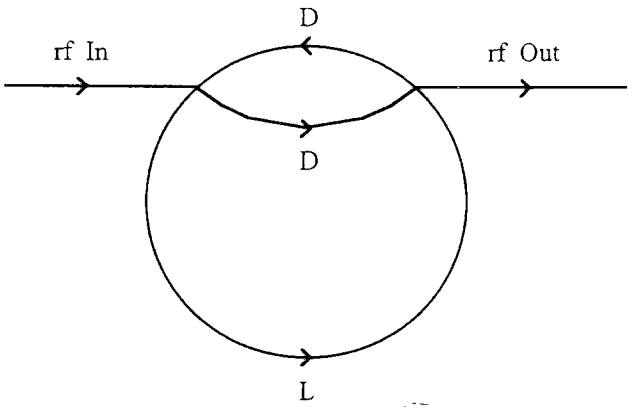


Figure 11. CFA Signal Flow-Graph Model

Expected S-parameter time domain responses for a CFA with rf feedback, neglecting electronic feedback, depends on drive power level and whether the CFA is on or off. The linear regime corresponds to the CFA off and to the CFA on for very low drive power (<1 kW). Figure 12 contains the expected linear responses for S_{21} and S_{11}. The model prediction for $S_{21}(t)$ in the linear regime is three time peaks corresponding to signals that (1) make a quick pass from input to output through the drift space region (**D**), (2) pass through the slow-wave circuit once before exiting (**L**), and (3) pass through the slow-wave circuit, pass through the drift space region, and pass through the slow-wave circuit a second time ($\mathbf{DL^2}$). $S_{11}(t)$ is expected to exhibit three peaks due to (1) input reflections, (2) a signal path through the slow-wave structure and drift space region (**DL**), and (3) output reflections. The saturated regime corresponds to high CFA drive power (>5 kW). Figure 13 contains the expected saturated regime model responses for S_{21} and S_{11}. $S_{21}(t)$ data collected in the saturated regime are expected to contain three peaks, where the first and third peaks are symmetrically placed around the second peak. Symmetrical peaks arise from taking an inverse transform of $S_{21}(\omega)$ frequency data to obtain $S_{21}(t)$ data and are derived in the next paragraph. Saturated regime $S_{11}(t)$ data is expected to contain the same three peaks as in the linear regime, with the second and third peak magnitudes increased due to slow-wave circuit gain. These model predictions are qualitatively consistent with features of the experimental $S_{21}(t)$ and $S_{11}(t)$ data shown in Figures 5 and 6, respectively. However, $S_{21}(t)$ and $S_{11}(t)$ split peaks are not explained by this rf feedback model.

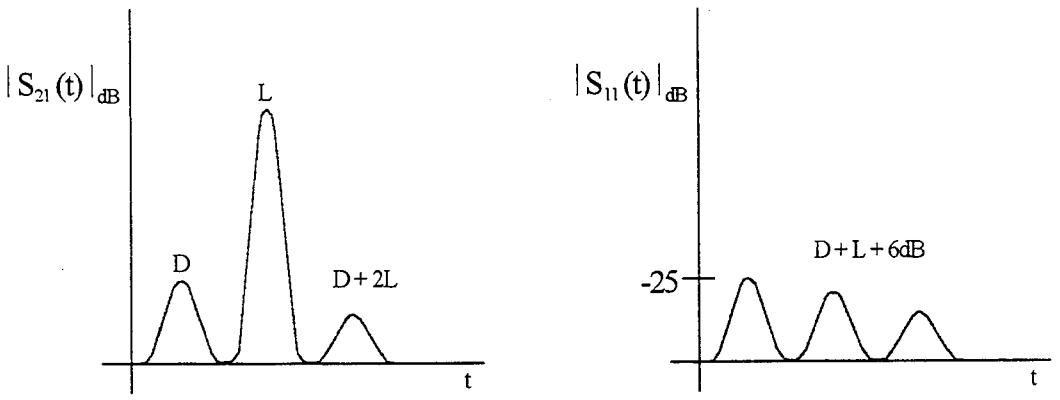


Figure 12. Expected Linear S-parameter Responses with rf Feedback

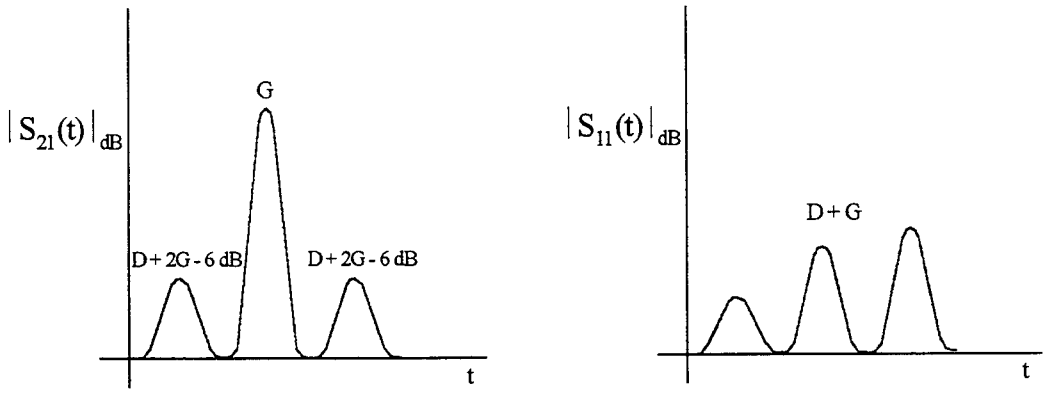


Figure 13. Expected Saturated S-parameter Responses with rf Feedback

The symmetrical peak result obtained from saturated $S_{21}(t)$ model predictions is derived as follows. Defining $L_{Mod}=|\mathbf{L}|$, $D=|\mathbf{D}|$, τ=slow-wave delay, $\Delta\tau$=sum of slow-wave and drift space delays, the frequency data is approximated as

$$S_{21}(\omega) \approx L_{Mod} e^{-j\omega\tau} + DL_{Mod}^2 e^{-j\omega(t+\Delta t)} \quad \textbf{(11)}$$

where the term proportional to D in equation 10 is neglected. Slow-wave gain L_{Mod} is modulated by drift space feedback D to keep constant output power over frequency for a saturated amplifier. L_{Mod} is a function of D expanded in a small parameter DL by

$$L_{Mod}=L(1+\alpha DL) \quad \textbf{(12)}$$

Output power is proportional to $|S_{21}(\omega)|^2$ and is expressed as

$$|S_{21}(\omega)|^2=L^2(1+2\alpha DL+2DL\cos(\omega\Delta\tau)+O((DL)^2)) \quad \textbf{(13)}$$

Achieving constant output power is made by setting $\alpha=-\cos(\omega\Delta\tau)$ so that

$$S_{21}(\omega) \approx -\frac{1}{2}DL^2 e^{-j\omega(\tau-\Delta\tau)} + Le^{-j\omega\tau} + \frac{1}{2}DL^2 e^{-j\omega(\tau+\Delta\tau)} \quad \textbf{(14)}$$

and the time domain symmetrical peaks are expressed by

$$S_{21}(t) = -\frac{1}{2}DL^2\delta(t-(\tau-\Delta\tau)) + L\,\delta(t-\tau) + \frac{1}{2}DL^2\delta(t-(\tau+\Delta\tau)) \quad \textbf{(15)}$$

The previous model did not include electronic feedback effects. The model has been extended to include an electronic feedback contribution to $S_{21}(t)$. Such a contribution would be time delayed (< 1 nanosecond) relative to rf drift space feedback. If perfect time resolution were present, the first and third $S_{21}(t)$ peaks would each be split into two peaks separated by the time delay. Imperfect resolution leads to either single broad peaks or split peaks that are not separated by the time delay value. To illustrate this, we consider two example time delays corresponding to (1) two wavelengths and (2) two and one-half wavelengths at the mid-band frequency. The signals separated by two wavelengths interfere constructively because of a zero degree phase difference. The two and one-half wavelength case corresponds to destructive signal interference, representing a 180° difference. Figure 14 contains the corresponding model $S_{21}(t)$ for both cases. Unsplit broadened first and third peaks are found in the 0° (two wavelengths) case. Split peaks are found in the 180° (two and one half wavelengths) case with nulls located between the peaks. Therefore, the combination of rf and electronic feedback signals causes $S_{21}(t)$ data to contain either split or unsplit peaks, with the presence of split peaks being very sensitive to small delay time changes. These rf and electronic model predictions are consistent with the experimental results shown in Figure 5, where the phase difference changes with cathode voltage.

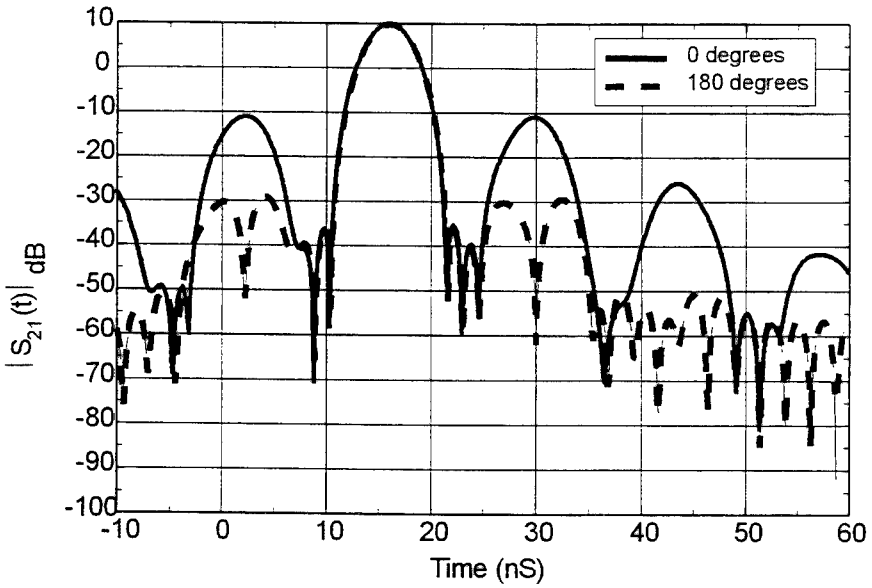


Figure 14. Example model S_{21} calculation including both rf and electronic feedback

MASK CFA SIMULATIONS

We use the MASK simulation code to simulate CFA operation. The current MASK version 5.4.4 simulates an electron reentrant CFA.

MASK Runs: Runs were designed to study the effects of rf signal feedback and B-field values on output power, phase, and SNR values. The modulator was modeled using either the built-in modulator circuit or fixed cathode voltage. B-field values of 2700 and 1800 Gauss were used. Input phase and input power level were varied to simulate rf feedback, as Figure 8 illustrates by varying the rf feedback phase θ.

The input signal is either amplitude or phase modulated as a function of the difference between the fed back output signal and original input signal θ. Experimentally, θ varies nearly linearly with frequency. For these simulations, frequency will be kept fixed and θ will be varied. Original input power value used was 10 kW. Drift space attenuation value was taken to be -34 dB. Gain was taken to be 11.3 dB. The resultant input power then varies ± 1.5kW away from the original input power value. Resultant input phase varies $\pm 4.2°$ away from the original phase (defined as 0°).

The first runs made used the modulator circuit and a B-field of 2700 Gauss. Output files for these runs gave information on the "average voltage applied to simulation." This voltage value was then used in fixed cathode voltage runs that should be more stable. Fixed cathode voltage runs corresponding to 1800 Gauss B-field value were made by reducing the average voltage applied to simulation found in 2700 Gauss runs by a factor of 18/27 to account for the cathode voltage proportionality to B-field.

MASK Results: Figure 15 shows MASK results obtained with fixed cathode voltages for 2700 and 1800 Gauss B-fields. The B-field dependence of the simulation results is consistent with experimental observations. MASK output power results show a decrease from 135 kW to 107 kW when decreasing B-field from 2700 to 1800 Gauss. MASK SNR values increase from approximately 27.5 dB to 31.5 dB as B-field is decreased from 2700 to 1800 Gauss. Experimental CPI low-noise CFAs have lower B-field values to take advantage of this CFA property.

Expected rf feedback oscillations are

$$\begin{aligned} \Delta Power &\propto \cos\theta \\ \Delta SNR &\propto \cos\theta \\ \Delta\phi_{Out} &\propto \sin(\theta - \tan^{-1} b) \end{aligned} \qquad \textbf{(16)}$$

Details of simulation results differ from those expected from equation (16), due to the small rf feedback effects compared with simulation value uncertainty. Simulated SNR values were not always found to increase with increasing drive power (SNR for $\theta = 0°$ should be greater than for $\theta = 180°$) as found experimentally, which may be due to uncertainty of simulated SNR values. Oscillations of output power, output phase, and SNR values are expected to be evident due to changes in the rf signal feedback phase θ. Rf signal contributions to the oscillations are given in equation (16) as a function of θ and are shown in Figure 15.

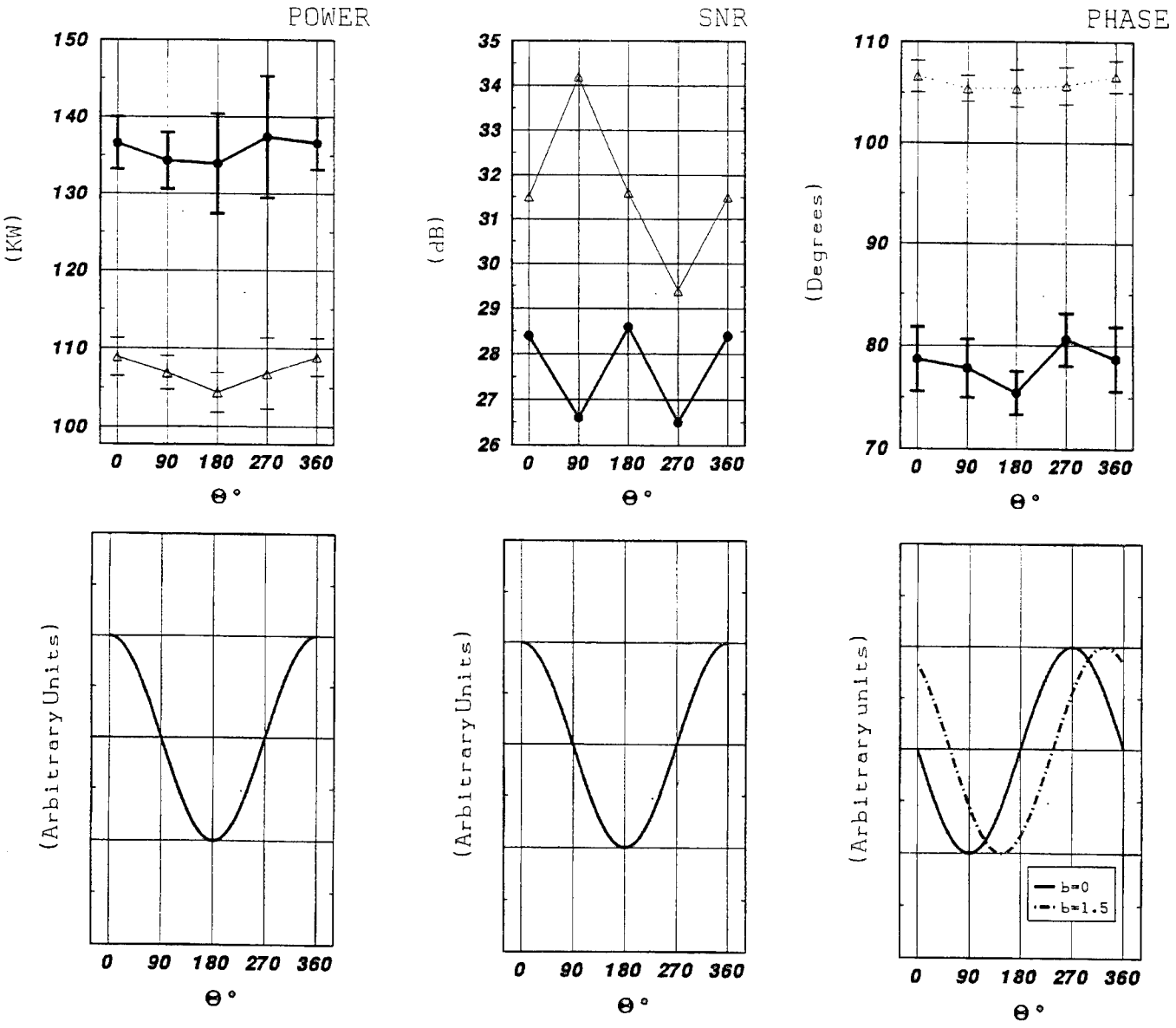


Figure 15. MASK Results and rf Leakage Predictions

SUMMARY

Electronic phase shifter use improves SNR measurements by reducing cost and reducing measurement noise floor.

Interpretation of CFA on $S_{21}(t)$ data is obscured by nonlinear and finite bandwidth effects. Nonlinear behavior causes symmetric time peaks. Finite bandwidth causes resolution problems that cause split peaks or constructive interference affects to appear.

Presence of electronic feedback is shown by S-parameter phase oscillations over frequency and split $S_{21}(t)$ peaks.

MASK studies have been made investigating performance effects of magnetic field changes and rf feedback phenomenon. Magnetic field simulation results agree qualitatively with experiment. Rf feedback simulation results are not conclusive, being limited by simulation uncertainty greater than small rf feedback effects.

REFERENCES

[1] S. Hillenberg, *Installation, Test, & Correlation of Local Oscillator Offset Frequency Technique for High Accuracy MTI IPN Measurements,* Naval Surface Warfare Center Crane Report, 3434 Ser 8065/4017, 22 July 1994.

[2] S. Hillenberg, A. MacMullen, and D. Thelen, *Signal-to-Noise Measurements Using an LO Offset-Frequency Technique,* Federal Lab Test & Measurement Tech Briefs, Supplement to May 1995 NASA Tech Briefs, p. 16a.

LOW-FIELD MAGNETRON STUDY

Thomas E. Ruden
24 Mountfort Road , Newton Highlands, MA 02161
George E. Dombrowski
69 Birchwood Heights Road, Storrs, CT 06268
David Hobbs
145 Washington Street, Belmont, MA 02178
George Boles
Herley-MDI, Inc., 10 Sonar Drive, Woburn, MA 01801

Abstract

A number of papers have recently been written on the performance of the low-field millimeter wave magnetron. In particular, it has been stated that such devices can provide noise characteristics comparable to that of O-type devices. A comparison of experimental data taken on an X-band magnetron, numerical simulation results, and theory provides some understanding of the noise phenomena. The effect of temperature-limited operation of the cathode on noise generation is discussed, and the role of the cathode diameter in obtaining proper operation in the low-field regime is described.

I. Introduction

Millimeter-wave magnetrons normally operate at a relative magnetic scaling value B/Bo of about 2.5. Experimentally, optimum performance occurs with a cathode to anode diameter ratio, σ, adjusted to be about 0.65 . This value will vary with N, the number of anode resonators. To achieve low voltage operation and low weight, reduced B/Bo values of 1.3 or less are employed. This is obtained either by reducing the magnetic flux density B, or increasing Bo the magnetron scaling parameter. Bo can be changed either by adjusting N or σ; the optimum experimental value for σ is approximately 0.22.

Under these low-field conditions, Levin [1] indicates that noise performance of the magnetron is comparable to that of the O-type device. This would imply the noise close to the carrier is as low as -125 dBc/Hz. This is an adequate noise level for doppler radar applications. The low magnetic field design results in a corresponding low voltage, compact, and lightweight magnetron which make the device a candidate for millimeter-wave missile seeker applications. One would expect with injection locking of the magnetron further improvements in the noise level would be achieved in accord with that observed at lower frequencies.

Radar, missile seeker, high frequency particle accelerator at X-Ka band, microwave power transmission, and commercial applications could require substantial average power generation from the crossed-field microwave tube. Conventional millimeter-wave magnetrons are typically narrow pulse width, low duty factor devices. Consideration has recently been given to space har-

monic operation by Yeremka [2], and this approach has resulted in some increase in average power. However, high anode dissipation density will be encountered in devices for the above applications. Devices with large anode area are required to reduce the dissipation density to an acceptable value. Important successes in developing large interaction space crossed-field devices were reported at the 1995 Crossed-Field Device Workshop. The Appendix provides a few comments on large anode area device research carried out in the United States during 1955 to 1965, and briefly describes the substantial progress made in recent years on developing a high average power axial gain Ka-band crossed-field amplifier; an injection locked oscillator version of this device was also demonstrated. The possibility of achieving a low noise, high average power millimeter-wave magnetron has lead to the present study.

To study the low-field operating conditions, measurements have been made on a 16 resonator X-band magnetron. In addition, a magnetron code developed by Dombrowski has been used for numerical simulation of the tube performance [3], and further comparison has been made with experiment using an approximate magnetron analysis by Vaughan [4]. The importance of simulation is evident in that it can treat a wide range of operating parameters while the analysis has limitations in this regard. In both experiment and simulation it is possible to vary the cathode emission and to investigate the effect on noise generation resulting from space-charge instabilities. Levin [1] reports that low noise generation occurs in the low -field regime under conditions of space-charge-limitation of emission from the cathode, and further specifies that the anode current must be limited to a range of 0.4-0.6 times the maximum anode current. Operation is hindered in the low current region by the presence of leakage current, associated oscillation conditions, and more importantly gaussline discontinuities. High values of pushing at high currents, the pushing may not be monotonic, and mode competition is enhanced. It is generally agreed that space-charge-limited operation of the cathode is required to satisfy system requirements of low frequency pushing, stable operation into a variable load mismatch, achieve adequate noise performance which might be degraded by non-uniform emission from the cathode surface, and, most important, the cathode not poison such that reliable, long life is obtained.

It is of interest that experiments by Brown [5] in recent years have shown that very low noise performance can be obtained from the "cooker" magnetron using a tungsten spiral cathode operated in the temperature-limited regime. Various unpublished reports have been made in the past as to low noise magnetron operation using the oxide or B-type cathode when operated temperature-limited, however, it is not clear that such operation was achieved in tubes employed in operating systems.

Numerical studies carried out in the late 1950's and early 1960's by Lehr [6] using the Hartree self-consistent field method with imposed space-charge-limited cathode emission never achieved a stable solution, but stable solutions were achieved under conditions where the cathode field was reduced from the temperature-limited value and approached but did not attain the space-charge-limited condition of zero cathode field . It was conjectured by Lehr that a particular low noise magnetron did in fact operate in a temperature-limited state.

The requirement for small ratio of cathode to anode diameter, σ, to achieve efficient operation at low B/Bo ratio has also been addressed by Yeremka [7]. The predicted value for σ is in accord

with experiment. The ideal Brillouin radius of the space-charge hub has been computed and compared to results from the simulation code for different magnetic fields and values of σ. This comparison has led to some insight into the expansion of the hub; it is found that σ must be reduced when in the low-field regime to ensure that the condition of cutoff is not violated. This analysis also suggests a possible mechanism for the observed low noise in the low-field regime. This mechanism is related to the state of the subsynchronous space charge. Measurement of the noise and voltage-current relationship of the magnetic diode when compared to the performance of operating magnetrons suggest these different devices have similar overall noise characteristics as indicated by Lehr [8].

The crossed-field diode can support single stream space-charge in the hub for the condition of large σ, while both the single stream and double stream configuration can be supported when σ is small. Due to the close proximity of the Hull cutoff voltage and the Hartree voltage when in the low-field regime, the σ value must be small. An analysis by Slater and Allis [9] showed the single stream space-charge-limited hub can support multiple striations or virtual cathodes. These vitual cathodes are a potential source of noise. Lehr [10] suggests that temperature-limited operation of the cathode destroys the conditions for formation of multiple virtual cathodes.

The crossed-field diode analysis work presently being carried out by research teams at the University of Michigan [11a] and the University of California-Berkeley [11b,11c] may further clarify the nature of the diode interaction as it affects magnetron noise processes. Galagan [12] also has published a recent analysis on magnetron diode operating regimes and instabilities.

II. Regimes of Crossed-Field Operation at Millimeter-Waves

Table 1 provides typical tube operating parameters for an early millimeter-wave magnetron [13]. Operation is at a rather high magnetic field level with a corresponding B/Bo value of 2.5. Parameters for more recent lower power tube showing a shift toward operation at a lower magnetic field level are also provided [14].

TABLE I
High-Field Operation of Millimeter-Wave Magnetron

Frequency	90 GHz	94 GHz
Power	20 kW	2.5 kW
Efficiency	15%	8-4%
Voltage	12 kV	6-11 kV
Magnetic Field	25 kG	15 kG*
V/Vo	4	
B/Bo	2.5	1.5*
N	20	
σ	0.65	

* estimated value

Operation at still lower relative magnetic field levels is shown in Table II for an X-band magnetron with B/Bo = 1.3 [15]. This reduced scaling parameter value is approaching that used in the very low-field regime. The measured efficiency is 30%. The design employs a cathode to anode diameter ratio reduced from 0.65 to 0.22.

TABLE II
Low-Field Regime: Experimental X-Band Values

Frequency	9.1 GHz
Power	3 kW
Efficiency	30%
Voltage	5.1 kV
Magnetic Field	1.05 kG
V/Vo	1.6
B/Bo	1.3
N	18
σ	0.22

III. Surface-Wave Magnetron Results

The criteria for obtaining low noise performance in the low-field operating regime have been reviewed by Yeremka [7] as:

1. Anode design must satisfy the condition that

$$k(1 - \sigma) > 2\pi \tag{1}$$

where k is the mode number, and σ is the cathode to anode diameter ratio.

2. Require operation under a high space-charge condition (space-charge-limitation at the cathode) such that single stream flow is developed; electron lifetime is much greater than the cyclotron period.

3. Ratio of magnetic field to critical magnetic field level (B/Bc) be less than 1.15.

4. Operating current must be less than 0.4 - 0.6 times the maximum anode current.

5. The voltage-current relationship as a function of cathode emission density for the low-field magnetron as sketched by Yeremka is shown in Figure 1.

This voltage-current characteristic is typical of lower frequency tubes as it shows an increase in dynamic impedance at reduced cathode current density, Ja < Jb < Jc, and a general transition from space-charge-limited operation to temperature-limited operation of the cathode at the higher current levels. Minimum noise occurs between the points labeled A and B. At low anode current

a transition occurs from the low level buildup oscillations to strong oscillations with apparent suppression of noise mechanisms, and at high current the failure of the cathode to provide adequate emission with associated changes in space-charge behavior both near the cathode and within the spokes results in noise generation.

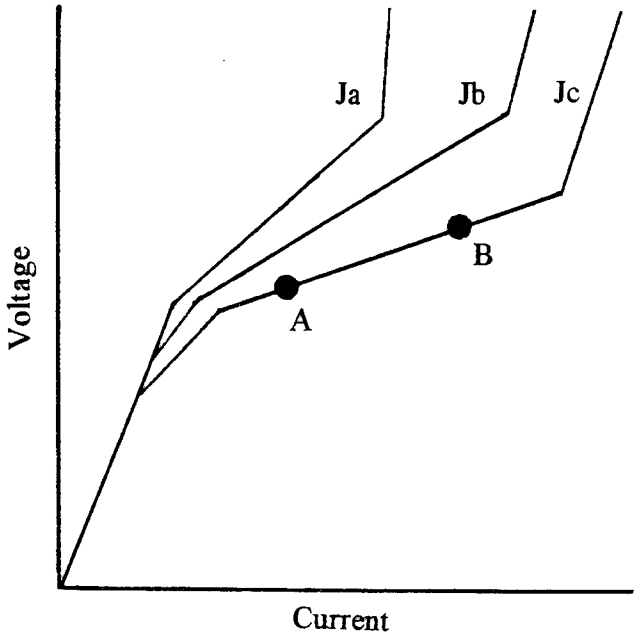


Figure 1. Typical voltage-current curve showing effect of limiting the cathode emission-current density J with Ja < Jb < Jc. Low noise for large emission density is observed between the points A and B.

In this emission-limited regime, noise is enhanced in the magnetron having a solid cathode surface. However, when the electron stream is injected into the interaction space and current limited, as for example in the voltage-tuned magnetron, the result is low noise operation. This result supports the generally accepted concept that a primary noise generating process in the magnetron is related to the space-charge hub surrounding the cathode and specifically related to a transition regime. This observation also supports the concept that a local non-uniformity in cathode emission can lead to noise generation; this can occur at current levels which would normally provide low noise operation.

IV. Experiment Vs. Simulation and Analysis

Table III provides the production performance and operating parameters for a Herley-MDI V1017 X-band magnetron operating in a typical high-field regime with B/Bo = 3.1. The operating current is well below the maximum anode current, and a large diameter cathode is used.

TABLE III
Parameters of V1017 Magnetron

Frequency	9.5 GHz
Power	610 W
Efficiency	17%
Anode Voltage	2.6 kV
Anode Current	1.4 A
Anode Current-Maximum	4.5 A
Magnetic Field	4.5 kG
V/Vo	5.7
B/Bo	3.1
N	16
σ	0.63

Figure 2 shows the computed space-charge distribution for the above operating conditions with the cathode operating space-charge-limited. The spoke is well defined, and the position of the subsynchronous hub is far removed from the anode radius. The average electron angular velocity in the interaction space is synchronous with the traveling rf wave as established by rf circuit fields. The computed electronic efficiency is approximately 50-60%.

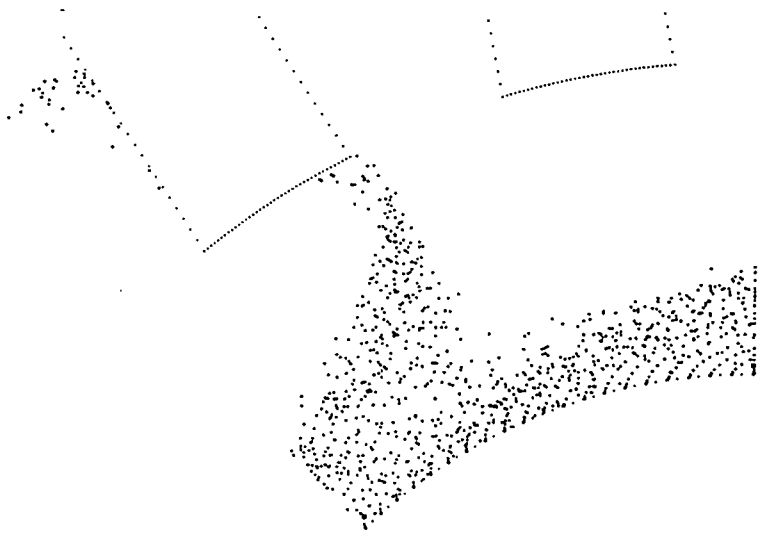


Figure 2. Space-charge spoke and subsynchronous hub; B/Bo = 3.1.

A comparison of experiment, simulation, and theory is shown in Figure 3 for a range of B/Bo values. At B/Bo = 3.1 the maximum current is at greater than 4 amperes, and the optimum performance is at 1.4 amperes which satisfies the general noise criteria as indicated above. Note that good agreement is obtained at this magnetic field level between the measured values, the simulation results, and the Vaughan magnetron theory.

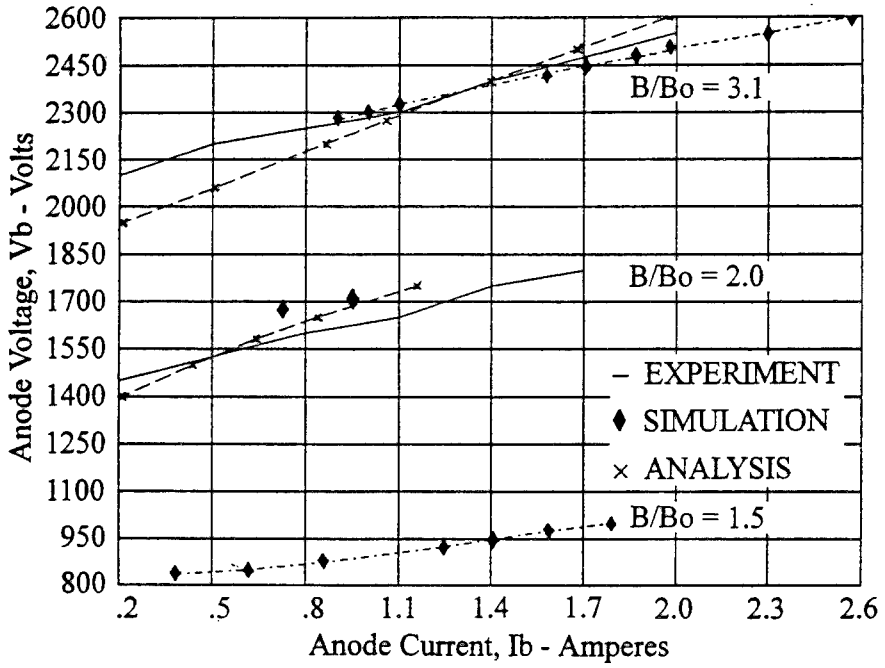


Figure 3. Voltage Vs. current showing comparison of experiment, simulation, and analysis; B/Bo = 3.1, 2.0, 1.5.

The pushing or change in frequency as a function of anode current for a range of heater voltage is shown in Figure 4; data is for B/Bo = 3.1. The pushing is small around the operating point for the condition of space charge limitation of the cathode. At reduced heater voltage the pushing curve exhibits regions of discontinuity, and the tube develops increased noise (modulation of the frequency of tens to a few hundred kilohertz about the carrier) at low and high currents in accord with Figure 1. These regions of discontinuity can be studied with a spectrum analyzer or a microwave interferometer; they appear to occur at essentially the same current levels over a fairly wide range of magnetic field levels. In particular, these regions can be seen at low current corresponding to I/Io = 0.1 where Io is the Allis characteristic current scaling factor. This I/Io value is well below the optimum operating point of the magnetron. Particular design and production processes can cause these regions to occur at higher currents.

These gaussline discontinuities appear to be different from those described in the Workshop paper by Ball, Brady, and Carter [11d] which produce twinning, and appears to be related to endshield design as described by Schumaker [16]. It is believed the discontinuities shown in Figure 4 are related emission processes and endspace design as reported by Ruden [17] which affect the magnetron modulation processes over a wide range of current.

Figure 5 shows the result of a simulation to determine the effect of a large reduction of heater power on the gaussline. The cathode emission transitions to the temperature-limited state at currents above one ampere. Under this condition major discontinuities in the gaussline occur with marked increase in frequency shift with current. This is in accord with the Yeremka analysis [7].

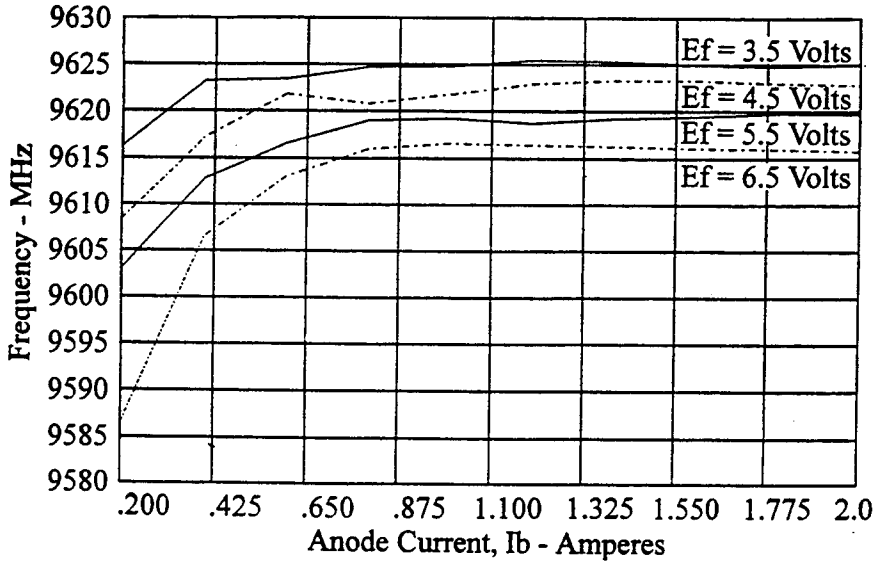


Figure 4. Frequency Vs. anode current. Heater voltage of 3.5 - 6.5 volts.

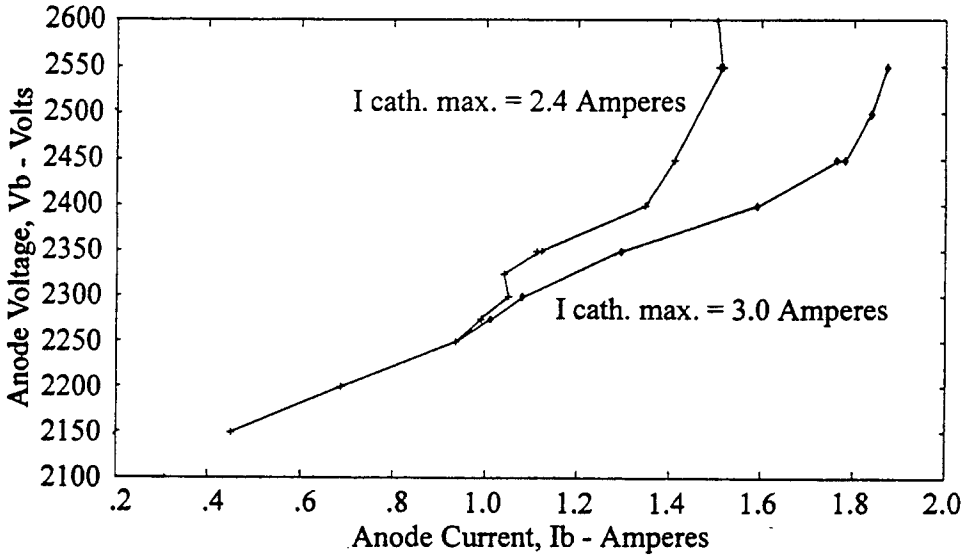


Figure 5. Effect of limitation of cathode emission. Maximum cathode current of 2.4 and 3.0 amperes.

At B/Bo = 2 we see in Figure 2 the general agreement between experiment, simulation, and analysis. However, the tube is starting to frequency modulate severely. At B/Bo = 1.5 the tube will not run stably. The Vaughan analysis fails to provide a self-consistent solution; the simulation does run over a 5/1 range in current, but the electronic efficiency is rapidly dropping from 42% at low currents to 17% at the higher currents. It is believed the efficiency reduction is related to the

location of the Brillouin hub such that electron collection on the anode occurs without conversion of dc potential energy to rf energy.

Figure 6 shows a calculation the Brillouin hub location for B/Bo = 2.85. The edge of the hub is well removed from the anode; at B/Bo = 2 the hub closely approaches the anode at the higher anode voltages. At B/Bo = 1.5 the hub will intersect the anode at the operating voltage thus reducing efficiency. Correction of this effect is to reduce the cathode diameter to provide a σ value of about 0.2 such that the hub is maintained a distance from the anode. Experimentally this reduction in cathode to anode diameter ratio is required to obtain efficient interaction at the low-field levels. A calculation for $\sigma = 0.3$ shows improved confinement of the hub to the cathode region. Results of numerical simulation of the hub radius is also shown in Figure 6. The edge of the hub is seen to be closer to the anode than the ideal Brillouin theory predicts.

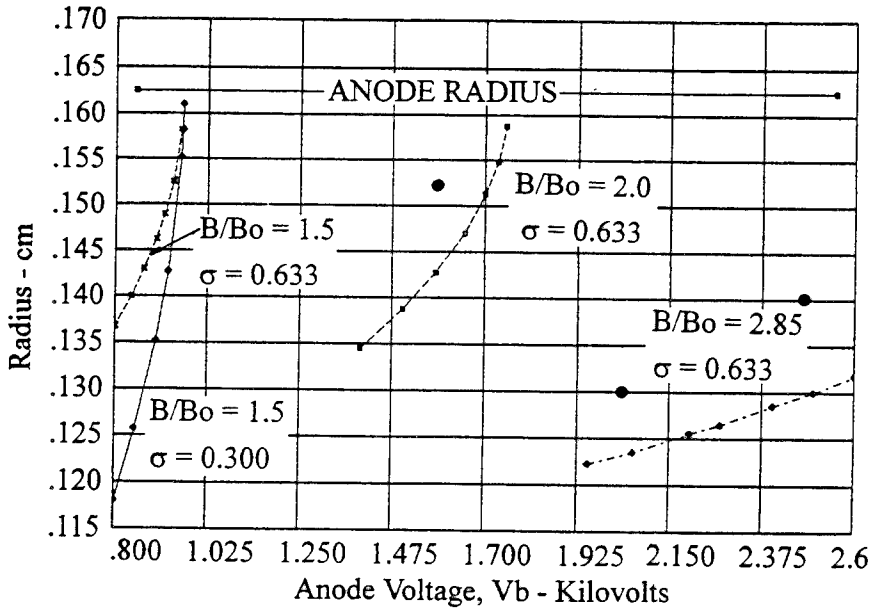


Figure 6. Brillouin hub radius for B/Bo = 2.85, 2.0, 1.5 and $\sigma = 0.633, 0.3$. Simulation results are shown as large dots.

Figure 7 shows the space charge distribution for B/Bo = 1.2. The hub lies close to the anode as expected since the operating point is close to Hull cutoff. The "spoke" is a perturbation of this hub. In contrast to high B/Bo operation where a subsynchronous hub is created, at this low B/Bo value the average angular velocity of all electrons in the interaction space approximates the angular velocity of the rf circuit wave. This implies the entire electron cloud interacts quite strongly with the circuit wave , and thus suggests efficient interaction is possible. The computed electronic efficiency for this simulation is 32%.



Figure 7. Space charge spoke and hub; B/Bo = 1.2.

Appendix

Potential Role for the Low-Field Magnetron

Interest in high power generation at millimeter-wave frequencies from crossed-field devices has been directed toward radar type applications requiring peak power at modest average power levels and short pulse lengths. More recently source requirements for missile seekers in the 35-95 GHz range require modest peak power and high average power. This need can be uniquely satisfied via the phased locked magnetron approach as described by Hobbs [18].

In addition, particle accelerator applications above X-band, and commercial applications that require substantial average or cw power levels suggest that the low-field magnetron concept may be an ideal source to satisfy these possible needs. High power, either peak or average, requires the device to dissipate considerable power. At the high frequencies typical magnetrons have limited anode and cathode area and would operate at dissipation densities well beyond those practical. To address this problem major investigations into very large anode area devices were undertaken in the 1960's, but these programs met with little success. Devices designed to provide axial gain as the Raytheon "Electromagnetic Amplifying Lens" or "EAL", the RCA "Bi-Periodic Magnetron", the GE "Orthotron", and the SFD " Circular Electric Mode Amplifier" ("Pipe") all failed to provide perform probably due to mode competition. Recent advances in mode control in large coaxial interaction structures used in gyrotrons has been reported in a series of papers at an IR and MM Wave Conference [19], and these techniques have direct application to resolving the mode

problems in the large anode crossed-field devices. Some limited success in increasing the power capability and obtaining amplifier gain was achieved by coupling of magnetron structures in tandem by Thal and Lock of GE, Farney and MacDowell of SFD, and by Chandra and Dombrowski at the University of Connecticut.

Fast wave, crossed-field axial gain was first achieved in the U.S. in the late 1980's from a periodic dual slot anode which coupled the interaction space to a TE01 mode coaxial waveguide. This experimental 35 GHz device was originally pulsed at low average power at 50-75 kW at 10-13 dB of gain and 3% bandwidth. Subsequent lower voltage designs achieved gain levels of 8-10 dB, peak power of 15.5 kW at 140 watt average, and 4 kW peak at 200 watts average [20].

Kouznetsov[11e,11f] at this Workshop reported that large area anode structures have been successfully developed in the USSR at lower frequencies. The cw power of the coaxial magnetron was extended to hundreds of kilowatts; this advance came as a result of early studies of cavity modes by Kapitza. It is also known the USSR studied the EAL concept [21]. It is not known if the EAL work had any influence on their large area anode designs. As noted earlier, work has been recently carried out in the USSR on millimeter-wave magnetrons using space harmonic operation of conventional circuits.

The potential of the crossed-field device to provide gigawatt peak and multi-megawatt average or cw power levels was briefly reviewed in a paper by Ruden [22]; the present study of the low-field regime has direct application to achieving this level of performance from low magnetic field, low voltage crossed-field devices.

References

[1] Levin, G. Ya., Semenov, L.A., Usikov, A. Ya., and Belov, Yu. A., "On the Nature of Noise and the Mechanism of Suppressing It in Surface-Wave Magnetrons," Sov. J. of Comm. Tech. and Elect., vol. 37, pp. 128-131,1992.

[2] Yeremka, V.D., Levin, G.A., Terechin, S.N., and Usikov, A. Ya., "Diminutive and Super Diminutive Surface wave Magnetrons of MM Range," International Conference on Millimeter and Submillimeter Waves and Applications, Proc. SPIE 2250, pp. 196-197, 1994.

[3] Dombrowski, G.E., "Simulation of Magnetrons and Crossed-Field Amplifiers," IEEE Trans. Electron Devices, vol. 35, pp. 2060-2067, 1988.

[4] Vaughan, J.R.M., "A Model for Calculation of Magnetron Performance," IEEE Trans. Electron Devices, vol. 20, pp. 818-826, 1976.

[5] Brown, W.C., "The Sophisticated Properties of the Microwave Oven Magnetron", IEEE MTT-S International Microwave Symposium Digest, vol. 3, pp. 871-874, 1989.

[6] Lehr, C.G., Lotus, J.W., Silberman, I., and Gunther, R.C., "Electron Trajectories in a Magnetron," Technical Memorandum T-347, Raytheon Research Division, March 1962.

[7] Yeremka, V. D., Levin, G. Ya., Mospan, L.P., Terekchin, S.N., Usikov, A.Ya., "Russian Surface Millimeter Wave Magnetrons", 16th International Conf. on IR and MM Waves Proc. SPIE 1576, pp. 7-8, 1991.

[8] Lehr, C.G., "The Effect of the Anode-Cathode Diameter Ratio on Magnetron Noise," Raytheon Memo, October 24, 1958.

[9] Slater, J.C., " The Magnetron Oscillator," in Microwave Electronics, Chap. 13, D. Van Nostrand Co., New Jersey, 1950.

[10] Lehr, C. G., "Spectrum Deterioration Caused by Virtual Cathodes in the Subsynchronous Region of a Microwave Magnetron," IEEE Trans. on Electron Devices, pp. 180-182, April 1964.

[11] First International Workshop on Crossed-Field Devices, Ann Arbor, MI, 1995: (a) Paper B4-P5: Christenson, P.J. and Lau, Y.Y., "Electron Sheaths in a Crossed-Field Gap-Equilibrium Solutions and Transition to Turbulence," (b) Paper B4-P5: Verboncoeur, J.P. and Birdsall, C.K., "Rapid Current Transitions in a Crossed-Field Diode at the Hull Cutoff," (c) Paper B4-P1: Cartwright, K., Verboncoeur, J. P., and Birdsall, C.K.,"Transverse Asymmetry in a Crossed-Field Diode," (d) Paper B3-P6: Ball, E.M., Brady, M., and Carter, R.G., "Frequency Twinning in Magnetrons," (e) Paper A4: Kouznetzov, M., "History and Perspective of Crossed-field Devices in Russia," (f) Paper B2-5: Kouznetzov, M., "Applications to Solid Oil Melting,".

[12] Galagan, A.V., Ruzhentsev, I.V., and Shadrin, A.A., "Numerical Modeling of Electron-Wave Interaction in Crossed-Field Systems with Three-Dimensional Effects Taken into account," Sov. J. of Comm. Tech. and Elect., vol. 37, pp. 41-49, 1992.

[13] Bernstein, M.J. and Kroll, N.M., "Pulsed Rising-Sun Magnetrons," in Okress, E., Ed., "Crossed-Field Microwave Devices," vol. 2, pp. 247-252, Academic Press, New York, 1961.

[14] English Electric Valve Catalog.

[15] Robertshaw, R.G. and Willshaw, W.E., "Low-Field Operation of Magnetrons," in Okress, E., Ed., "Crossed-Field Microwave Devices," vol. 2, pp. 315-330, Academic Press, New York, 1961.

[16] Shumacher, C.R., "Spectrum Shape," in Okress, E., Ed., "Crossed-Field Microwave Devices," vol. 2, pp. 457-471, Academic Press, New York, 1961.

[17] Ruden, T.E., "The End-Space as a Source of Noise in the Crossed-Field Device," High Power Microwave Tube Conference, Monterey, CA, May 1992.

[18] Hobbs, D., "X-band Magnetron Missile Seeker Transmitters," U.S. Government-Industry Presentation, Microwave Associates, Inc., Burlington, MA, April 1984.

[19] Conference Digest, Twentieth International Conference on Infrared and Millimeter Waves, Florida, December 1995.

[20] MacMaster, G.H. and Nichols, L.J., "Millimeter-Wave High Gain Crossed-Field Amplifier," Proc. International Electron Devices Meeting , pp. 963-966, 1990.

[21] Volfson, A.O. and Sobolev, G.L., "Analysis of Crossed-Field Traveling-Wave Amplifier," U.S. Army Foreign Science and Technology Center, Translation FSTC-HT-1071, NTIS, AD-735435, 1971.

[22] Ruden, T.E., "The Crossed-Field Device: An RF Source for HPM," Proc. Sixth National Conference on High Power Technology, Lackland AFB, Texas, 1992.

AN ELECTRONICALLY STEERABLE PHASED ARRAY MODULE (ESPAM) USING THE MICROWAVE OVEN MAGNETRON WITH EXTERNAL CIRCUITRY AS A HIGH-GAIN PHASED-LOCKED AMPLIFIER.

William C. Brown
Microwave Power Transmission Systems
6 Perry Lane, Weston MA 02193, (617 893 2315)

ABSTRACT

The common microwave oven magnetron, in combination with external circuitry, has been converted into a phase locked, high-gain amplifier for use in electronically steerable phased arrays for power beaming purposes. The converted device, referred to as an MDA, or magnetron directional amplifier, allows independent control of frequency and amplitude. The MDA is combined with a section of slotted wave guide array to form a module for use in the phased array.

INTRODUCTION AND SUMMARY

A crossed-field device in the form of the common microwave oven magnetron, when fitted with external circuitry to convert it from a simple oscillator to a two terminal phase-locked high gain amplifier, is the critical low cost, low noise, highly efficient device needed for an electronically steerable phased array for power beaming purposes.

The ESPAM or "electronically steerable phased array module" is shown from several views in Figure 1. It consists of a section of slotted waveguide radiator and the microwave generator which is termed the MDA or "magnetron directional amplifier'.

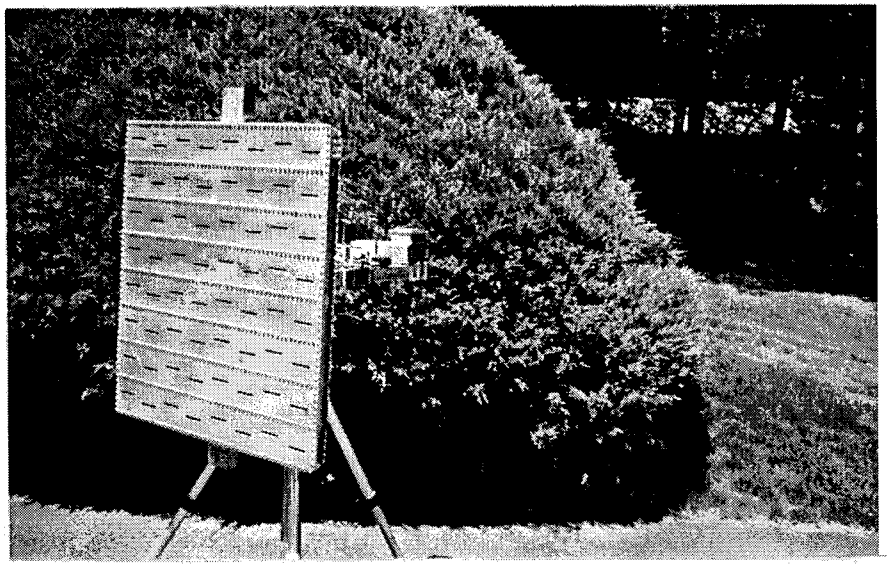
The balance of this paper will address the MDA or magnetron directional amplifier and its properties that are ideally suited for the microwave generator and amplifier in the ESPAMS. In the diagram for the ESPAM shown in Figure 2, the MDA consists of the magnetron, and external accessories that are identified as a ferrite circulator, a phase comparator to measure the relative phase difference between input and output, and a reactance tuner in the output circuit of the magnetron.

How these elements of the MDA function together to produce the phase-locked, high-gain amplifier is explained by the following expression for the phase shift in the output of an oscillator that is locked to an external signal.(1)

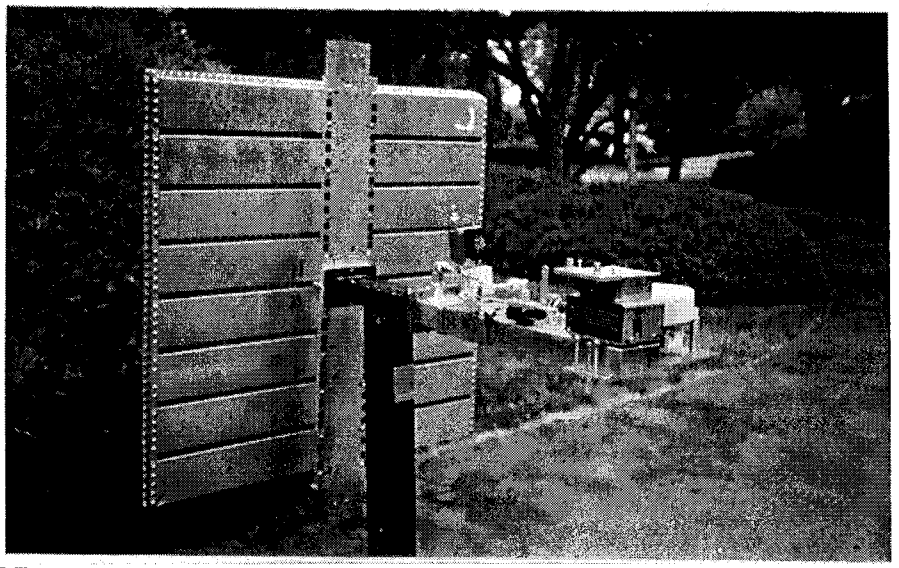
$$\phi = \sin^{-1} \frac{(f - f_o)\, Q_E}{f \sqrt{p_i}/\sqrt{p_o}} \qquad (1)$$

where ϕ = phase shift between input and output of amplifier
f = free running frequency of the magnetron
f_o = frequency of the drive source
p_i = power input from the driver
p_o = power out of the directional amplifier
Q_E = External Q of the magnetron.

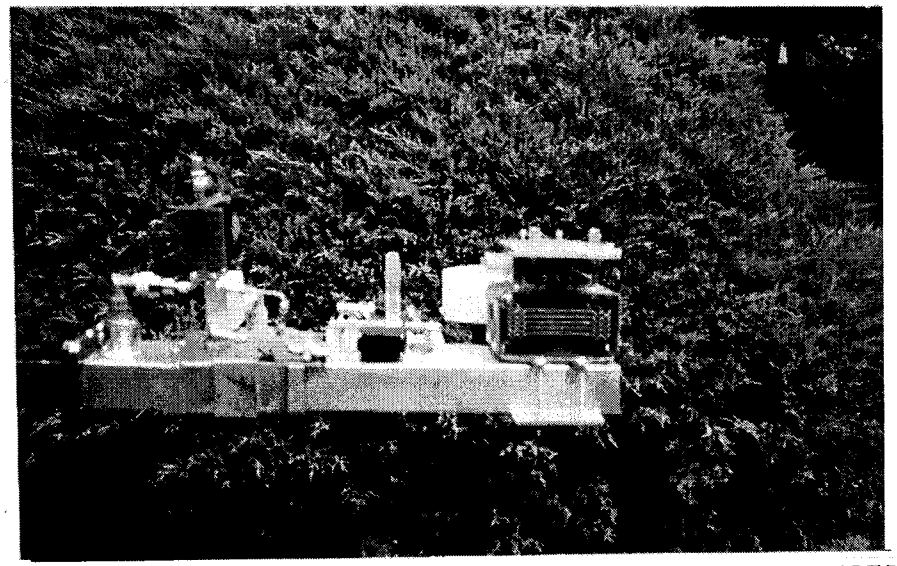
THE ESPAM - ELECTRONICALLY STEERABLE PHASED ARRAY MODULE



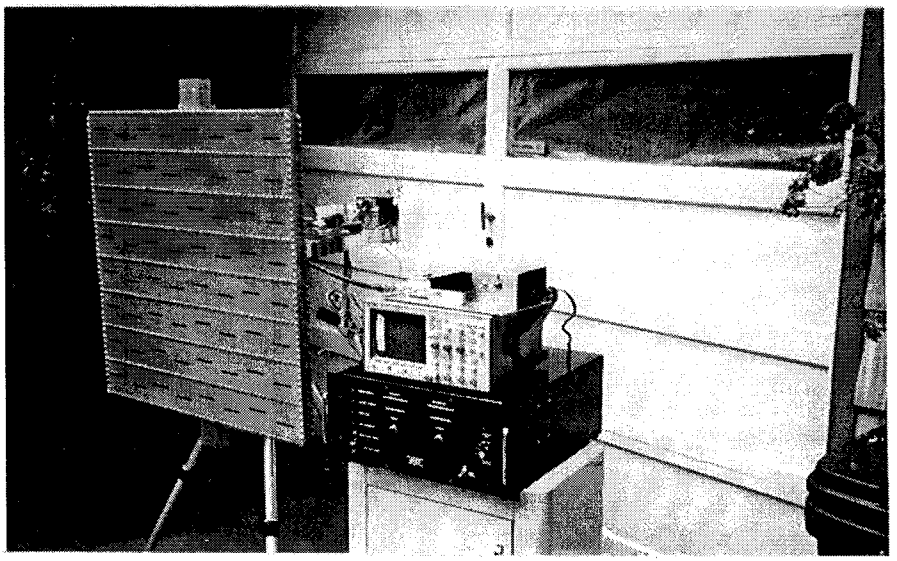
FRONT VIEW SHOWING SLOTTED WAVEGUIDE ARRAY



REAR VIEW SHOWING MAGNETRON DIRECTIONAL AMPLIFIER



NEAR VIEW OF MDA-MAGNETRON DIRECTIONAL AMPLIFIER



ESPAM WITH DC POWER SUPPLY AND INSTRUMENTATION

FIGURE 1

This expression can be identified with the MDA or magnetron directional amplifier where the "input" is at one terminal of the ferrite circulator and the "output" is at the other terminal of the ferrite circulator. Expression (1) clearly shows that the phase shift between that of the drive source and the output of the amplifier is dependent upon the difference in frequency of the drive source and that of the freely running (or unlocked) oscillator, and that the amount of this phase difference is also dependent upon the square root of the ratio of the output power of the amplifier to the power of the drive source. This ratio, of course, is the gain of the device if it is being used as an amplifier.

It is immediately evident from the expression that if the frequency of the oscillator is somehow tuned to the frequency of the drive signal, then the phase shift between input and output can be avoided and also that the ratio of the output power to the power level of the drive source can be increased. Further, if a phase detector is placed between the output of the drive source and the output of the amplifier, any phase difference can be used as an error signal to retune the magnetron to the frequency of the drive source.

Using this signal to retune the magnetron can be accomplished in three basic ways. The first of these is to tune the magnetron internally by altering its internal structure. This would call for the development of a new tube which would be much more expensive and not easily available. The second approach which has been used is to take advantage of the observation that when the current through the magnetron is changed there is a change in the operating frequency. Unfortunately, a change in the current flow into the tube also changes its power output, almost proportionally. The third approch, and the one that has been successfully used only very recently in a development mutually sponsored by the NASA Center for Space Power at Texas A&M and the author, is to change the reactance of the load into which the magnetron operates. (2) This approach allows the amplitude of the output of the device to be independently controlled.

The result of this development is shown graphically in two figures. Figure 3 shows the operating envelope of the tube in response to a change in the drive frequency. It is evident that the amplitude can be varied over a wide range at each operating frequency. The operating frequency can also be varied over a considerable range but it is probable that for power beaming purposes the frequency will preassigned at one frequency.

Figure 4 shows the contrast between the performance of the amplifier with and without the feedback arrangement to tune the frequency of the freely running oscillator to the drive frequency. Without the feedback arrangement, the experimentally measured and theoretically predicted phase shift varies rapidly with the drive frequency and, further, the frequency range is severely restricted. With the feedback arrangement the phase shift is kept within a total swing of about ten degrees over a comparatively wide frequency range.

The value of gain used for obtaining this experimental data was 30 db. However, the gain could be increased to 40 db or more by refinements that would involve (1) a power supply with less ripple current, (2) improvements in the reactance tuner which is a mechanically moveable obstruction in the waveguide.

SCHEMATIC OF THE ESPAM OR ELECTRONICALLY STEERABLE PHASED ARRAY MODULE

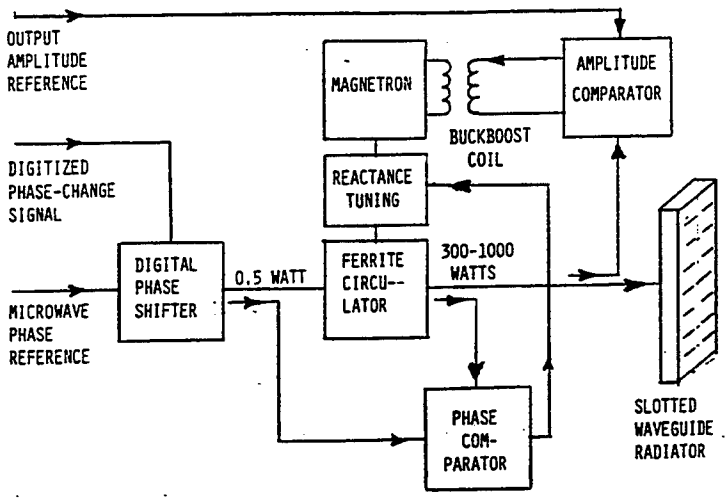


Figure 2. Schematic of the radiation module into which the magnetron directional amplifier is assembled. In the diagram the parts pertaining to the magnetron directional amplifier or MDA are the magnetron with attached buckboost coil, a reactance tuner, the ferrite circulator, the phase comparator and the amplitude comparator.

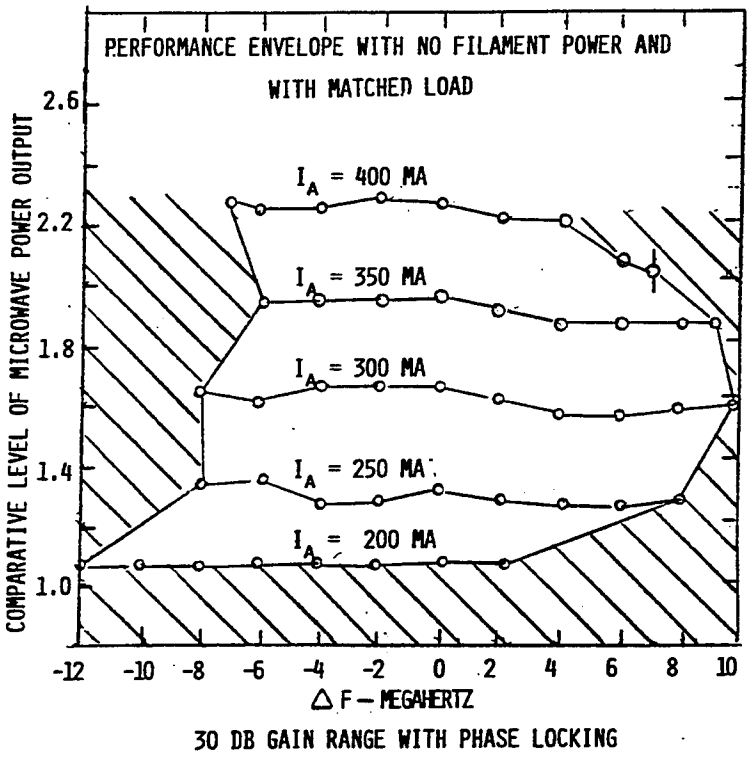


Figure 3 The above performance envelope indicates satisfactory operation over a broad range of power output and operating frequency that are independent of each other. The frequency of operation is controlled by the frequency of the input drive. The reference drive frequency, F = 0, is 2453 MHz. Attention is called to the near constant value of power output for each value of magnetron input current, I_A, over the operating frequency range. Data points were taken at 2 MHz increments. Power output is given in comparative terms but ranges from 400 to 1000 watts. Forbidden regions of operation are cross-hatched. Lower forbidden region is readily accessible by insertion of appropriate value of filament power.

There were some pleasant surprises in this development. One of these was the favorable performance of the magnetron when closely coupled to an external load, as quantified by an external Q of about 50. Such a low external Q, when combined with the internal Q of abut 1000, would indicate a circuit efficiency of about 95%, as compared to the conventional efficiency of about 85% where the external Q is about 150. This improved circuit efficiency shows up as a higher overall operating efficiency as seen in Figure 5. Apparently, the higher coupling of the tube to the external load has not compromised the electronic efficiency of the device.

Another pleasant surprise was the discovery that the small and low cost servo used on radio controlled model airplanes made an ideal arrangement to move the tuner in the waveguide.

AMPLITUDE CONTROL

Another feature of the recent development was the incorporation of an earlier development in which the magnetron could be operated from a common power supply in parallel with other magnetrons and still have the option of independent control over the amplitude of the output. This is accomplished by adding a small buckboost coil to add or subtract t to the magnetic field supplied by permanent magnets attached to the tube. As shown in Figure 2, there is an amplitude comparator in which a small sample of the output is rectified to produce a DC voltage across a fixed resistance. The voltage across this resistance is then compared with a reference voltage and any error signal then used to control the current in the buckboost coil. The reference voltage can be arbitrarily changed or preprogrammed.

The buckboost coil has other valuable uses. One of these is to start or turn off the tube in the presence of an applied voltage from common power supply. Another is to let the cathode warm up in the presence of a common power supply without any current flow from the filament to the magnetron anode.

CLASSES OF THE MAGNETRON DIRECTIONAL AMPLIFIER

There are four classes of the MDA which are referred to in Table I. These four classes are historically related. The first class is the simple frequency locked but not phase locked oscillator. Its unsuitable performance for an electronically steerable phased array that requires phase locked amplifiers is shown in figure 4. A Class 2 MDA is phase locked and uses a change in the magnetron current for phase locking. It does not have independent control over output amplitude. Class 3 is phased locked and uses a change in the reactance of the external load for phase locking. It does have independent frequency and amplitude control. It needs a separate power supply or separate power conditioner if it is powered from a common power supply. Class 4 is the same as class 3 but in addition the magnetron is equipped with a buck boost coil so that it can be used from a common power supply and can be programmed to operate at any chosen power level.

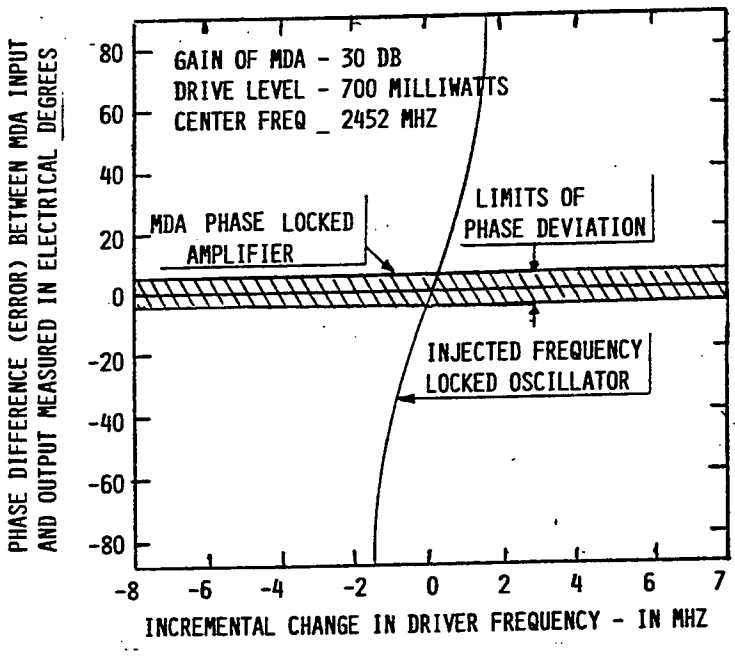


Figure 4. Shown above is a comparison of the phase error performance of the MDA phase locked amplifier and the ordinary frequency locked oscillator. The MDA operated continuously over a 16 MHz frequency band with a phase runout of no more than plus and minus 5 degrees. The injected frequency locked oscillator had a phase shift of 180 degrees over a 3 MHz range of frequency. Not shown is the power output over the frequency range which was constant to within 6%.

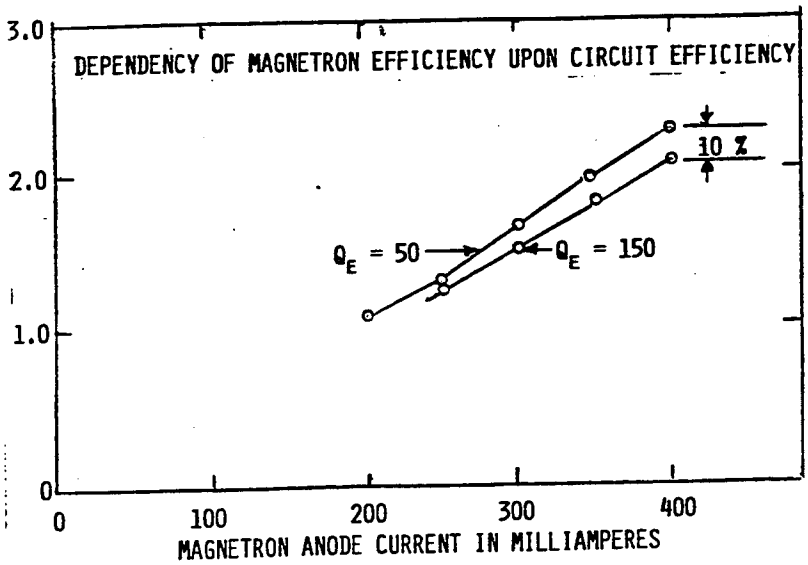


Figure 5. The above data for magnetron operation at very low values of external Q, Q_e, may not have been previously available. Microwave magnetrons are normally operated with Q_e's of 200 to 250. The circuit efficiencies associated with Q_e's of 50, 150, and 250 are, respectively, 96%, 89%, and 79%. If the electronic efficiency is independent of the circuit efficiency, then the overall efficiency is proportional to the circuit efficiency. The above data seems to confirm such a relationship.

TABLE I

Classes of the Magnetron Directional Amplifier

Class	Date of Emergence	Frequency Locked	Phase Locked	Independent Amplitude and Frequency Contr.	Parallel Operation From Common Power Supply
1	1950-1960	Yes	No	No	No
2	Circa 1982	Yes	Yes	No	No
3	1993-1994	Yes	Yes	Yes	No
4	1993-1994	Yes	Yes	Yes	Yes

REFERENCES

(1) E. E. David, "Phasing of RF Signals" in Okress, Crossed Field Microwave Devices, Vol. 2, Academic Press, 1961, pp 375-399e.

(2) W. C. Brown, "Development of Electronically Steerable Phased Array Module (ESPAM) with Magnetron Directional Amplifier (MDA) Power Source", Final Report, November 1995, Texas A&M Research Foundation, Project RF 2500-95, Prime Grant No. NAGW-11194, Subgrant No. L3000060. NASA Center for Space Power at Texas A&M Univ.

ANALYSIS OF MAGNETRON FAILURE MODES VERSUS POWER LEVEL

GEORGE A. SOLOMON

Power Tube Engineering
BURLE INDUSTRIES INC.
Lancaster, Pennsylvania 17601
Phone 717-295-2746
Fax 717-295-6053

ABSTRACT

The analysis of 915 MHz CW magnetrons returned for rebuilding shows that tungsten depletion of the filament is not the main cause of failure. This paper compares the major failure modes versus power levels of 30, 50, 60 and 75 kW. Suggestions are proposed to improve the operating life of the tube. The output spectral purity can be controlled by optimizing the filament power to reduce the noise floor. The filament current can be optimized for an operating point by monitoring the output with a spectrum analyzer and adjusting the filament current for the lowest noise level around the carrier. The magnetrons are less susceptible to anode faults under these conditions.

BACKGROUND

The study consisted of a sample of magnetron returned from 1990 to 1995. The majority of the tubes manufactured in this time frame were 30 and 50 kW magnetrons. Two hundred tubes were evaluated to determine the failure mode. The tubes were tested, the data compared to the pre-ship data, cut and the individual subassemblies are analyzed. The ship date and return date were studied to get a rough order of magnitude of the field life since operating life data is not available from our customers.

FAILURE MODES

The tubes were characterized by seven main failure modes.

1. Broken Dome (BD) -- The ceramic dome covering the output antenna is cracked or broken. The dome can crack from arcs in the waveguide or from RF heating of deposits on the ceramic.

2. Internal Arcing (Int Arc) -- The filament and choke assembly have high energy internal arc marks. The arcing evaporates copper and iron gassing up the tube.

3. Pi-1 Mode (Pi-1) -- The magnetron is a 10 vane(N) strapped resonant system. There are 5 major modes (N/2) which are n=1-5. Pi mode (n=5) is the normal mode of operation is at 915 MHz. The next mode is Pi-1 mode (n=4) is at 1520 MHz. If the tube is operated in this mode,

little energy is transferred to the load and input power is dissipated in the anode. The result is melting of the straps and/or vanes.

4. End of Life Filament (EOL Fil) -- End of Life Filament is characterized by a depletion of tungsten from the helical filament resulting in a necking of the wire until it breaks. This is the most desirable mode of failure for the magnetron. The operating hour data we have for this mode of failure is greater than 20,000 hours.

5. Filament Overheating (Fil OH) -- Filament overheating the result of not decreasing filament power as the output power is increased to compensate for backheating. The result is the thermal stresses damage the filament support structures.

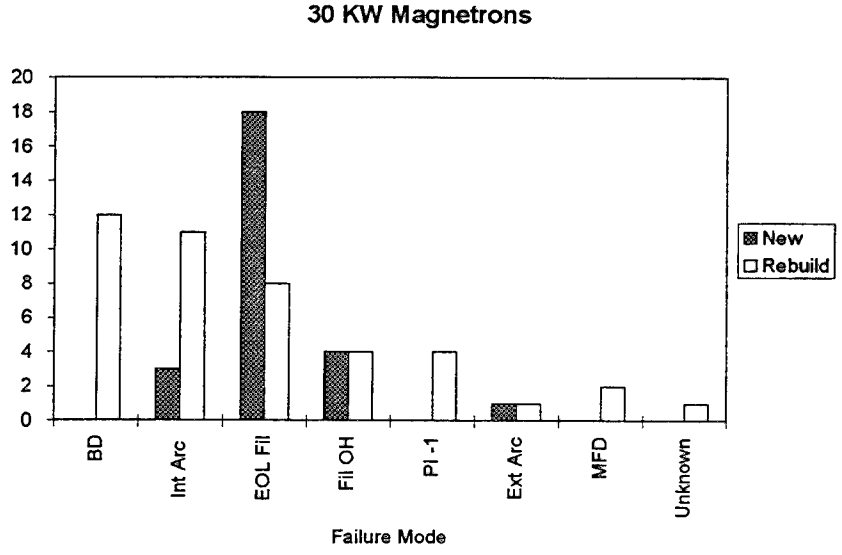
6. External Arcing (Ext Arc) -- External Arcing from the choke to the water pipes. The arcing burns a hole in the ceramic isolation sleeve causing the tube to go to air.

7. Manufacturing Defect (MFD) -- Defect in the tube as a result of the manufacturing process.

8. Failure Mode Cannot be Found (Unknown) -- The failure mode could not be found after testing and analysis.

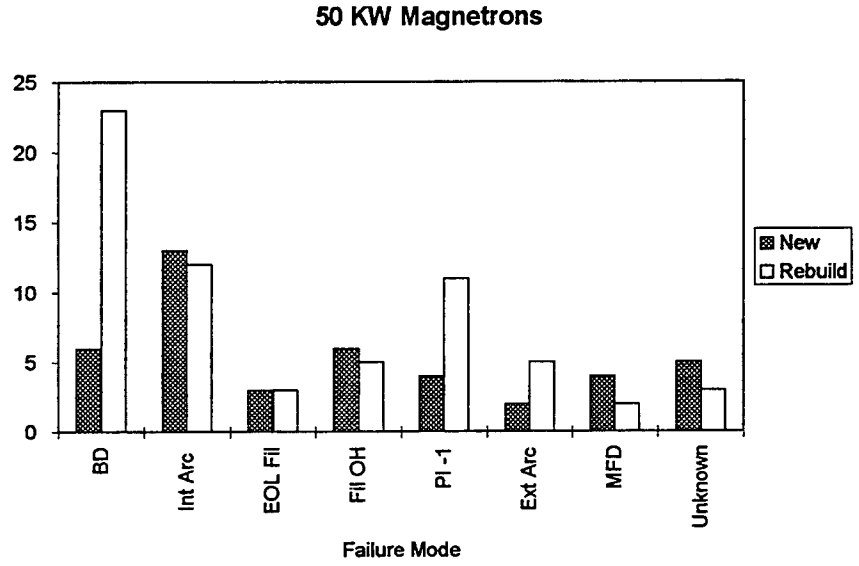
ANALYSIS OF DATA

The 8684, 30 kW tubes are plotted in Graph 1. The new and rebuild tubes are plotted on the same graph. The graph shows the main failure mode for a 30 kW new tube was End of Life Filament (EOL Fil). The average time in the field for the 30 kW new tube was 119 months. The main failure modes for the 30 kW rebuilt tubes were Broken Domes (BD) and Internal Arcing (Int Arc) and then End of Life Filament (EOL Fil). The average time in the field for the 30 kW Rebuilt tube was 47 months.



Graph 1

The S94600E, 50 kW tubes are plotted in Graph 2. The new and rebuild tubes are plotted on the same graph. The graph shows the main failure mode for a 50 kW new tube was Internal Arcing (Int Arc). The average time in the field for the 50 kW new tube was 29 months. The main failure modes for the 50 kW rebuilt tubes were Broken Domes (BD) and Internal Arcing (Int Arc) and Pi-1 Mode (Pi-1). The average time in the field for the 50 kW Rebuilt tube was 21 months.



Graph 2

The first S94604E, 60 kW tubes were manufactured in 1994. No new tubes have been returned for rebuilding. The main failure modes for the 8 - 60 kW rebuilt tubes were split evenly between Internal Arcing (Int Arc) and External Arcing (Ext Arc). The internal arcing damage was considerably greater in the 60 kW with fewer operating hours then in 50 kW magnetrons.

The first S94603E, 75 kW tubes were manufactured in 1992. The 75 kW design was scaled to increase the cathode area and to improve the tubes high voltage hold-off capability. The water cooling was redesigned to allow for the higher dissipation. The first two tubes returned for rebuilding were early life failures due to Pi-1 mode operation. The filament was operated too cold following a curve of constant hot resistance (filament voltage divided by filament current). The failure mode for the last 2 - 75 kW tubes was Internal Arcing (Int Arc).

The operation of the filament was researched on the different power level magnetrons to find the optimum operating point. BURLE, in the past, has recommended that the optimum filament operating point was to maintain a constant hot resistance. The theory was the filament temperature could be related to hot resistance. The filament temperature would increase as the hot resistance decreased. The filament supply power could then be adjusted to compensate for backheating by maintaining a constant filament hot resistance hence a constant filament temperature. This operating point however is not optimum and the filament voltage is difficult to measure floating at 17 kV. The filament current can be optimized for an operating point by monitoring the output with a spectrum analyzer and adjusting the filament current for the lowest noise level around the carrier. If the transmitter does not allow for this level of control, the magnetron filament current should be adjusted to the linear back off curve supplied with the tube.

CONCLUSIONS

The analysis of the returns was completed to find areas to improve the magnetron operating life. There was a significant change in the time between rebuilds when the power was increased from 30 to 50 kW. The data shows the main cause of failure was not tungsten depletion of the cathode when the power level was increased. The operating life of the higher power magnetrons could be significantly improved with the addition of high speed, high voltage protection.

The linear power supply is the main area of focus on solving the internal arcing failure mode. When the magnetron arcs the energy in the supply is dissipated in the magnetron. The arcing evaporates copper and iron gassing up the tube. The tube can be protected with a ignitron high speed protection circuit connected to the output of the supply. The ignitron will dump the stored energy in the supply if the magnetron arcs. The most effective way to keep the magnetron from arcing is to optimize the filament current for the best spectral purity.

The alternative to the linear supply is to use a switching power supply with very low stored energy able to turn the power to the magnetron off in microseconds. The real advantage to this supply is to operate the magnetron in the constant current mode. This mode of operation is the least susceptible to internal arcing and adds a higher degree of control of the operating point of the tube.

The broken dome failures are more prominent in rebuild tubes. The cost of a rebuilt magnetron is approximately half the cost of a new tube, which precludes the replacement of this assembly on all rebuilt magnetrons. The broken domes are analyzed for internal and external deposits. Most broken domes have external deposits from a melted Teflon sleeve or deposits from the cooling air. The sleeve has a tendency to melt at higher powers. Temperature tests were conducted on the dome and seals without the sleeve and with the recommended 25 CFM of air. The air cooling on the dome was adequate and the Teflon sleeve used in AJ2192 transition should be removed.

The current data on the 60 and 75 kW magnetrons are inconclusive at this time. However, the failure modes show the same trends as the 50 kW magnetrons.

REFERENCES

George B. Collins, "Microwave Magnetrons," Radiation Laboratory Series, McGraw-Hill Book Company, INC. 1948.

APPLICATION OF MAGNETRONS WITH MEDICAL LINEAR ACCELERATORS

G. T. Konrad

Siemens Medical Systems, Inc., OCS
4040 Nelson Avenue, Concord, CA 94520

Abstract

Several types of magnetrons have been in use in Siemens radiation therapy equipment for a number of years. More than 700 such machines have been built and the majority are still in service. The most commonly used magnetron in this application is a 2.6 MW unit that powers a side-coupled cavity linac operating in the standing wave mode. Depending on the linac, electron and X-ray energies over the range of 3 to 14 MeV and 3 to 15 MV, respectively, are available from the Siemens machines. The accelerator, RF, and control systems will be described, with emphasis on the magnetron operating requirements. Field experience accumulated over the years will be summarized. It will be shown that magnetron reliability is a key parameter to ensure up-time in a radiation therapy machine.

Introduction

Most radiation therapy machines currently being built make use of a linear accelerator. The latter is driven by a multimegawatt RF system. Many of these RF systems contain a magnetron as the RF power source, although higher energy machines are likely to contain a klystron. The linear accelerator generates an electron beam in the 3 to 15 MeV range in the case of magnetron systems built by Siemens. For tumors near the body surface, the electron beam can be used directly. For more deep-seated tumors, it is usually desirable to use X-rays. These X-rays are produced by letting the electron beam strike a high atomic number target, thus generating a photon beam in the multi-MV range by bremsstrahlung. In Figure 1, a diagram of a radiation therapy setup is shown. Note that the gantry can rotate, thus allowing the patient to be treated from many directions. More modern machines allow the gantry to rotate and the collimation of the X-ray beam to vary under digital computer control during treatment.

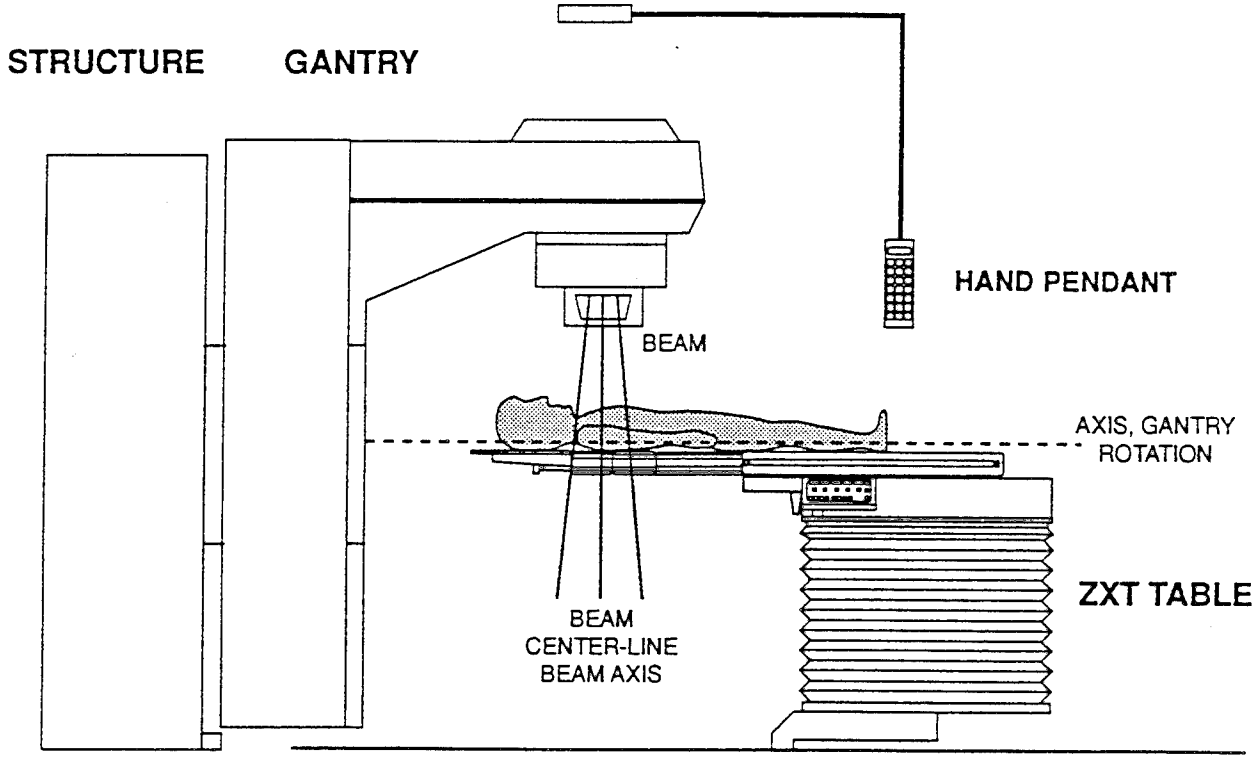


Figure 1. Radiation Therapy Configuration

RF System Description

The heart of the radiaton therapy machine is the linear accelerator. Virtually all manufacturers use a side-coupled cavity structure. This type of structure provides a high accelerating gradient along the axis of the main cavities, and the coupling cavities are offset to the side. Coupling holes are provided to join the cavities electrically. Thus, a very compact accelerating structure results. This is essential in order to have a machine of manageable size. A gridded electron gun is used to inject electrons into the accelerator at the KeV level, and microwave power is used to accelerate the electrons into the MeV range. Pulsed RF power is brought from the magnetron through a rotary joint and a circulator into the accelerating structure. Details of the machine are depicted in Figure 2.

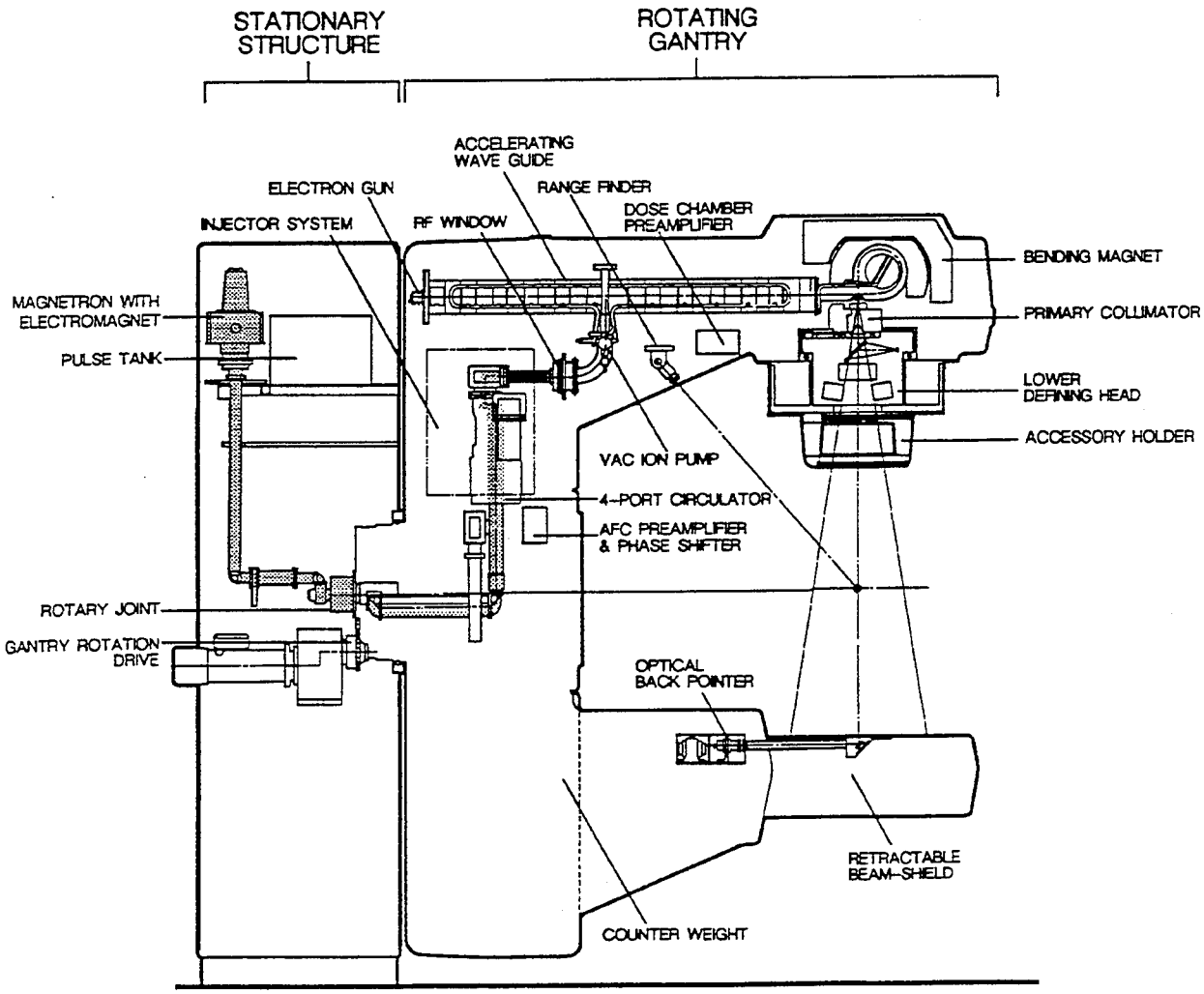


Figure 2. Magnetron Powered Radiation Therapy Machine

Note that the accelerator is arranged in a horizontal position. The patient to be treated is also in a horizontal position. Therefore, the electron beam must be bent through 90° in order to treat the patient. Actually, beam bending occurs through 270°, thus allowing the beam to be focused while being bent. The result is nearly a point source X-ray beam. It is desirable that all components be small and be packaged in a compact manner. On the other hand, it is also necessary that the major components be readily accessible for repair and replacement. A recirculating water cooling system is used to hold the accelerator temperature constant at 40°C ±1°. The magnetron, its electromagnet, the circulator, certain waveguide components, and the bending magnet coils are also cooled by the same system. There are two major control loops in

the radiation therapy machine. One keeps the magnetron tuned to the accelerator resonance frequency, and the other one maintains constant dose rate by varying the pulse repetition frequency of the modulator which drives the magnetron.

Magnetron Requirements and Experience

Siemens uses EEV magnetrons in the radiation therapy machines. Some of the older machines make use of M 5125 tubes, and some recent machines use the MG 5349, a tube with a 3.1 MW peak power rating. The most widely used tube is the M 5193, which is rated at 2.6 MW. Its major operating parameters are listed in Table I. The numbers shown are maximum levels that can be achieved simultaneously with a given tube.

Table I

Magnetron Characteristics in Therapy Application

Operating Frequency	2998	MHz
Frequency Range	9	MHz
Peak Output Power	2.6	MW
Average Output Power	3.1	KW
Average Input Power	6.0	KW
Magnetic Field	1550	Gauss
Operating Voltage	45	KV
Maximum Cathode Current	110	A
Pulse Duration	4.2	microsecond

The majority of machines built by Siemens are dual energy machines. That is to say, the user can obtain two X-ray energies, e.g. 6 and 10 MV, as shown in Table II. The machine can also produce six electron energies, as shown. The magnetron must operate stably over a range of power levels and, therefore, a range of magnetic field settings. The variation in magnetic field is accomplished by the use of an electromagnet. Since a line-type modulator is used in this application, it is desirable to operate along a constant impedance line when covering the energy range shown. Magnetron stability can become an issue at the low energy extreme, and a tradeoff has to be made between tube and modulator performance so as to achieve overall system stability.

Table II

Therapy Machine Operating Levels

Energy	RF Power (MW)	Magnetron Magnetic Field (Gauss)	Magnetron Current (A)
6 MV	2.1	1450	101
10 MV	2.4	1540	109
5 MeV	1.0*	1300 (1130)	50 (76)
6 MeV	1.5	1280	87
8 MeV	1.75	1360	93
10 MeV	2.0	1450	100
12 MeV	2.3	1510	107
14 MeV	2.6	1550	110

*Must trade-off magnetron stability vs modular performance

A unique requirement in this application is that the therapy machine be in standby mode throughout the working day. Actual treatment time with radiation is typically a few minutes. Setup time for a patient is in the order of 10 to 20 minutes resulting in a typical use pattern, as shown in Table III. While the number of high voltage hours accumulated in a year is not very large, the service required from the magnetron is probably more severe than what would be experienced in a scientific accelerator application or in a radar where the on-time would be continuous over long periods of time. Moreover, in the older Siemens machines, the magnetron was mounted in the gantry near the accelerator. Thus, the magnetron position changed during operation. This put mechanical stresses on the cathode support structure and led to shortened life. For this reason, the tube is fixed in the stationary portion of the newer machines. This comes at the expense of increased RF losses and the requirement for a high power rotary joint.

Table III

Typical Magnetron Use

- 2,500 Filament Hours/Year (8+ Hrs/Day, 5 Days/Week)
- 300 High Voltage Hours/Year
- Filament/H.V. Ratio is Approximately 8:1
- Machine Warm-Up Time : 15 minutes
- Mounting Position of Magnetron : Fixed and Vertical (Magnetron Rotates in Older Machines)

A five-year sample of EEV M 5193 magnetron failure modes was taken. Approximately 400 tubes were included in the sample. The results are shown in Table IV. Note that during the sample period, the dominant failure mechanism was tube arcing. It is surmised that the frequent on-off cycling and the relatively lengthy standby periods with no high voltage applied, lead to

gradual gas build-up in the tube. The arc rate then increases over time until the number of treatment interrupts become unacceptable.

Table IV

Magnetron Failure Modes in Siemens Machines

Arcing, Vacuum	54 %
Unstable, Moding	9 %
Low Power	7 %
Tuner Damage	7 %
Other	23 %

An interesting summary of magnetron performance is shown in Table V. This covers a five-year period and pertains to EEV M 5193 magnetrons used in Siemens machines. Note that there is a slight downward trend in the number of magnetron failures. Over the same period of time, approximately 300 more new machines were introduced into the field. This then resulted in the impressive improvement in magnetron life over the period shown. Some of this improvement was due to design changes in the machine and the modulator. On the other hand, a significant portion of the improvements was reliability enhancements introduced by the tube manufacturer. Machine uptime is very important in an oncology department in a hospital. It is determined by many other components besides the magnetron. Between 1993 and 1994, the Siemens machine uptime increased from 96.5% to 97.5%. This one percentage point increase was due to an increase in overall machine MTBF of approximately 30%. It is our goal to reach an uptime of 98 to 99% in the near future, requiring the MTBF to more than double from what it is now.

Table V

Magnetron Failure Rate

Year	No. of Magnetron Failures	Average Tube Life to Failure (Months)
1990	169	20
1991	156	26
1992	168	28
1993	149	37
1994	145	43

Summary and Conclusions

The following statements can be made about the radiation therapy business using linear accelerators:

1. The U.S. market for radiation therapy machines is mature.
2. There is still significant potential for growth in Eastern Europe and the Far East.
3. Cost and reliability for all components, including the RF system, are very important.
4. Magnetron systems have an advantage over klystron systems in terms of tube and modulator cost.
5. Frequencies higher than S-Band, specifically X-Band, are important only when system size overrides other requirements.

The magnetron manufacturer's point of view can be summed up in the following list of future magnetron requirements for radiation therapy applications:

1. Increased tube reliability
2. Lower cost
3. 3.5 MW peak power in S-Band
4. 6 MW peak power in S-Band for klystron replacement
5. 2.5 MW peak power in X-Band for special applications

Observation and Interpretation of Leakage Current in a Nonrelativistic Smooth Bore Magnetron

Jan E. Eninger Bo H. Vanderberg

Department of Industrial Electrotechnology
Royal Institute of Technology
S–100 44 Stockholm, Sweden

Abstract

Measurement and analysis of the characteristics and origin of leakage current in a smooth bore magnetron are presented. The measurements are made in the MX–1 experiment, an inductive storage pulsed power generator with a smooth bore magnetron used as a magnetically insulated opening switch (MINOS). Below cut-off, we find the transmitted current to be lower than predicted by cold-fluid models. This may be explained by the combined effect of secondary electron emission from the anode and oscillatory current transmission. Observed waves are identified as transit time oscillations. Around cut-off, we measure low power broad-band, noisy oscillations which are strongest around cut-off but decrease with increasing magnetic field. Above cut-off, where oscillations are weak, we find the leakage current to be mainly axial and strongly dependent on the shape and position of cathode end barriers. In contrast to a previous study, we cannot identify any oscillation frequencies associated with known instability modes. Thus, the smooth-bore magnetron in the cut-off state is found to be stable on a microsecond time scale, in accordance with theory. For applications to fast high-power switching, these features imply that good pulse control as well as low losses can be achieved.

1 Introduction

The smooth bore magnetron has been proposed as a fast high-power opening switch based on the MINOS (Magnetically INsulated Opening Switch) concept [1]. In this concept, the current transmitted by a cylindrical vacuum diode is controlled by a fast rising pulsed magnetic field. When the applied field is higher than the Hull cut-off value [2], which in the nonrelativistic case is

$$B_c = \frac{1}{d}\sqrt{\frac{2V_d}{\eta}} \tag{1}$$

where d is the anode-cathode gap width, V_d the diode voltage and η the electron charge-to-mass ratio, electrons return to the cathode and the MINOS is opened.

In the open state, although basic theory predicts that current transmission is forbidden, electron flow through the diode is observed in experiments. This leakage current has been attributed to imperfections in the diode geometry leading to electrons propagating axially along magnetic field lines [3, 4]. Leakage current has also been ascribed to instabilities [5] when electrons acquire kinetic energy from electromagnetic waves to cross the diode gap radially.

Table 1 lists instabilities and oscillations which may be present in crossed-field devices below, around and above cut-off. In a crossed field diode without periodic anode structure, such as the smooth bore magnetron, the magnetron instability gives efficient microwave generation only at relativistic voltages; at nonrelativistic voltages as in the present study, the mismatch between electron drift velocity and electromagnetic wave phase velocity strongly reduces the power exchange between space-charge and RF field. The diocotron instability is ruled out due to the stabilizing effect of wall image charge [6]. The growth rate of the resistive wall instability for metallic anodes is of the order of $10^{-5}\omega_c$ [7]; at fields below 1 T, this corresponds to a growth time of microseconds or longer. Thus, for switch applications of the smooth bore magnetron, we conclude that stability can be expected on time scales sufficiently long to ensure good pulse control as well as low losses.

Oscillation/ Instability	Mechanism	Region	Effect	Smooth Bore Magnetron
Radial–Azimuthal				
Transit time[8, 9]	interaction with external circuit or anode-cathode gap	$B \leq B_c$	affects distribution of space-charge, current limitation	transit time $\approx$ 1 ns, Brillouin equilibration time$\approx$ 10 ns
Magnetron [10]	cyclotron resonance with slow wave structure	$B \approx B_c$	microwave emission, radial leakage current	mismatch between wave phase velocity and electron drift velocity
Diocotron [6]	shear – low frequency resonance between free surfaces	$B > B_c$	radial leakage current	conducting wall shorts out field
Resistive Wall [7]	phase shift between electron current and wall image current	$B > B_c$	radial leakage current	slow growth rate–ms time scale
Axial				
Oscillations [11]	thermal velocity, end effects	$B \geq B_c$	noise emission	stable – no feedback
Electron drift [3, 4]	misalignment of electrodes, fields	$B \geq B_c$	axial leakage current	reduced by electron barriers

Table 1: Instabilities which may be present in a crossed-field device, and reasons why the smooth bore magnetron can be expected to operate stably as a fast opening switch.

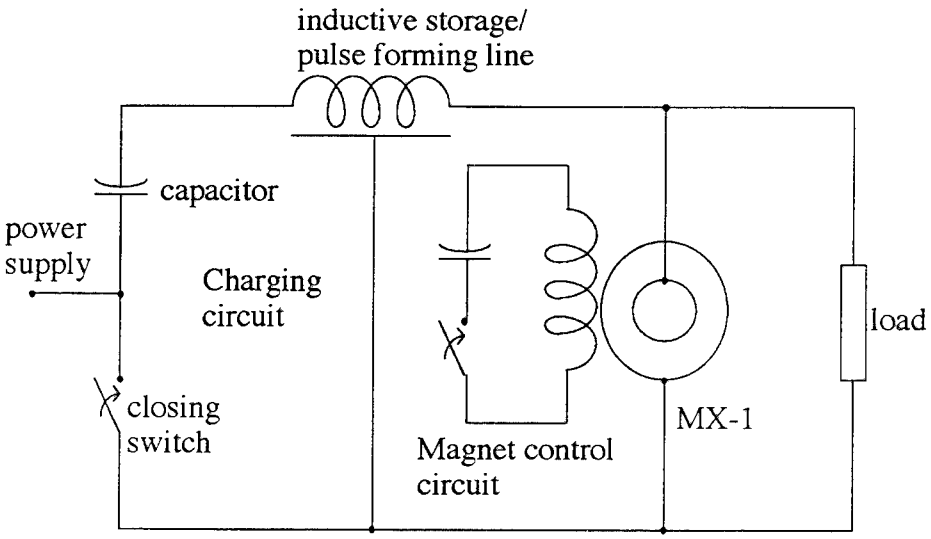


Figure 1: Circuit diagram of the MX-1 experiment, an inductive storage pulsed power generator with a smooth bore magnetron as a magnetically insulated opening switch (MINOS).

We have studied the current characteristics of a cylindrical smooth bore magnetron in the MX–1 experiment [12], where the magnetron is used as a fast opening switch in an inductive storage pulsed power generator (see Fig. 1). Below cut-off, the diode acts as a closed switch with low impedance to charge an inductive storage pulse forming line. With an applied pulsed magnetic field, the magnetron is cut off and the switch is opened, thus transferring the stored energy to a resistive load. For pulsed power applications, the current and voltage below cut-off determine the charging efficiency and the switching speed, while above cut-off, the leakage current is a direct measure of the switching efficiency [13].

In this report, we thus present, and attempt to interpret voltage-current-magnetic field measurements on a nonrelativistic space-charge limited cylindrical crossed field diode. In section 2, the experimental set-up is described. Measurements below, around and above cut-off are presented in section 3, 4 and 5, respectively. Electromagnetic wave measurements are performed to investigate the stability of the magnetically confined electron plasma and possible correlation between waves and diode current. Below cut-off, we find that the current in the smooth bore magnetron is lower than predicted by simple cold-fluid theory. We identify oscillations in the unmagnetized diode as transit time oscillations. Around cut-off, we measure broad-band oscillations, whose amplitude decreases rapidly with increasing magnetic field. In

the highly cut-off magnetron, when oscillations are weak, we find that leakage current is strongly dependent on the shape, size, and position of electron barriers. This suggests that the remaining current is mainly axial.

2 The MX–1 Experiment

The MX–1 experiment consists of a pulsed power generator designed for pulse voltages up to 50 kV, transferred currents up to 2 kA, pulse widths of $1 - 4$ μs and switching times down to 200 ns. The MX–1 switch shown in Fig. 2 is a cylindrical vacuum diode with inner cathode and outer anode. The dispenser type thermionic cathode is operated in a space-charge limited mode. The cathode diameter is 100 mm, the length 125 mm, and diode gap widths of 3 and 10 mm are used. The MINOS is opened when a capacitor is discharged through the magnet coil, so that a uniform magnetic field with strength up to 0.3 T is induced in the diode gap (see Figs. 1 and 2).

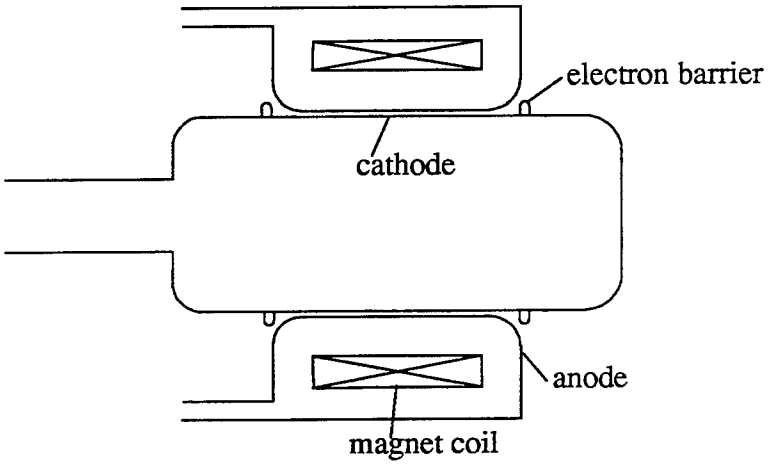


Figure 2: Schematic drawing of the experimental MX–1 switch. The thermionic cathode is a tungsten dispenser cathode. The slotted copper anode can be cooled efficiently to handle switching losses, and concentrates the magnetic flux induced by the magnet coil. At both ends of the diode, electron barriers are installed to reduce open switch leakage currents, analogous to conventional "end caps" in magnetrons.

The diode current and voltage, and the magnet coil current are measured with 1 GHz bandwidth current transformers and a high-voltage probe, and

monitored on 500 MHz bandwidth digital sampling oscilloscopes. Two capacitive probes with insulating ceramic disks inside the anode wall are used to measure electromagnetic waves in the diode gap. The probes are connected to semirigid coaxial cables and their signals are sampled with a digital signal analyzer with a 1 GHz transient, and 20 GHz repetitive bandwidth.

3 Current transmission below cut-off

3.1 Experimental results

3.1.1 I-V-B measurements

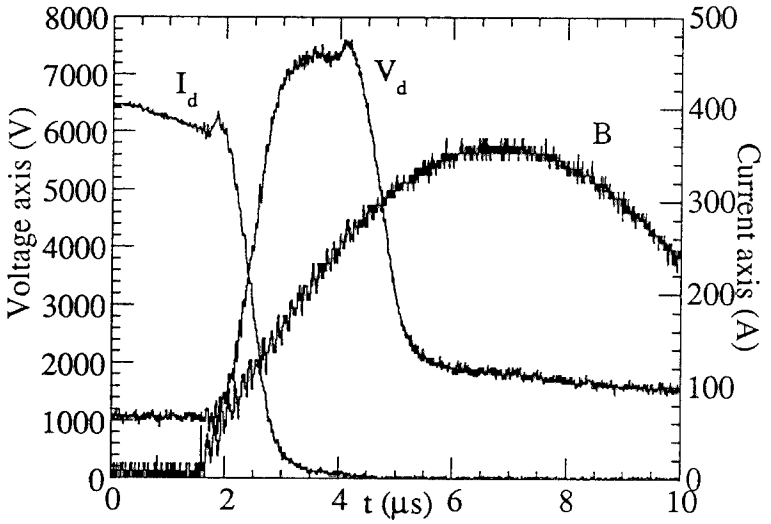


Figure 3: Typical pulsing sequence in the MX-1 experiment. The pulse generator (Fig. 2) capacitor is discharged through the closed MINOS when $B = 0$. When a magnetic field is applied, the MINOS is opened, so that in a transient phase, the switch current is commutated to the resistive load and the switch voltage rises. In this commutation phase, it can be shown that $B \approx B_c$ [12]. When the switch has opened, its voltage V_d has a constant value, and $B > B_c$. Subsequently, the inductive storage line is discharged, and a constant high voltage pulse is generated over the load.

Fig. 3 shows a typical pulsing sequence. The diode voltage V_d, current I_d and magnet coil current I_m ($\sim B$) are monitored when MINOS is closed ($B = 0$) and during the commutation of current from MINOS to the load ($0 < B \leq B_c$). By varying the voltages of the pulse generator charging capacitor and the magnet coil circuit capacitor, both maximum pulse voltage and switching speed can be controlled. The maximum pulse voltage in the present experiment was 45 kV at a diode current of 2 kA. The shortest current fall and voltage rise time in our experiment is 200 ns at the highest $dB/dt = 2.4 \cdot 10^5$ T/s.

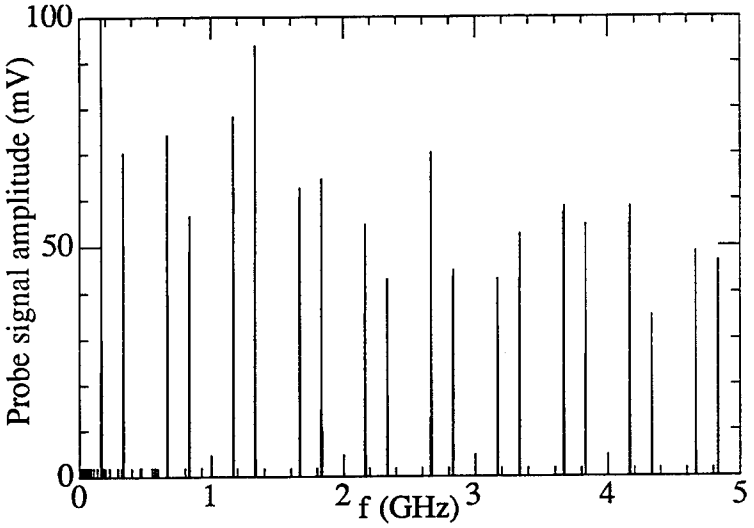


Figure 4: Frequency spectrum of a time window of the sampled probe signal during the charging of the inductive line, with an unmagnetized MINOS. In the time window (width 2 μs), the switch voltage is constant due to the step-increase of the charging current in the pulse forming line.

3.1.2 EM wave measurements

The wall probe signal is sampled in pulsing sequences with pulse voltages $2.5 < V_d < 10$ kV, switching speeds between 200 ns and 2 μs using a 3 mm diode gap. Without applied magnetic field, we observe low frequency signal components (< 100 kHz), as well as high frequency oscillations (> 10 MHz) for voltages between 800 V to 1.5 kV. For these conditions, Fig. 4 shows

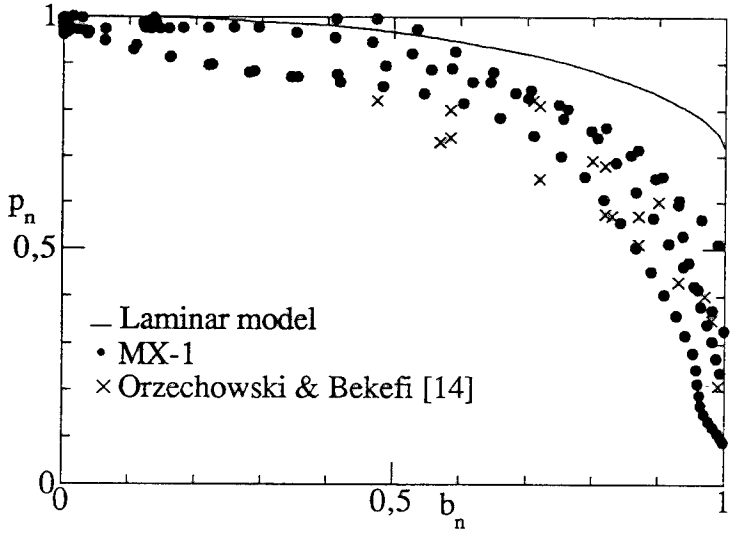


Figure 5: Normalized perveance p_n vs. normalized magnetic field b_n below cut-off. Our experimental results (•) are for switch voltages $2 < V_d < 45$ kV, and voltage rise time > 200 ns. Also shown are the theoretical curve from [14] and results from a 160 kV experiment [15].

the FFT of the probe signal obtained during the charging of the inductive storage when the switch forward voltage drop was constant and $B = 0$.

3.2 Data analysis

For every sample of the digitized V, I_d and I_m, a switch perveance $p_n = I_d/(p_{cl}V_d^{3/2})$ normalized to the Child-Langmuir perveance p_{cl} [16], and normalized magnetic field $b_n = B/B_c$ can be calculated and plotted as in Fig. 5 for voltages $2 < V_d < 45$ kV. In this figure, our measurements are compared with the laminar flow model from [14] and with results from a 160 kV experiment [15]. The measured perveance is generally lower than the theoretically predicted value, and the difference increases with increasing magnetic field. This may be due to the idealizations in conventional cold-fluid models which omit physically important aspects, such initial velocity or electron temperature [8] or space-charge oscillations[17]. We have proposed a current reducing mechanism [18] based on secondary electron emission: with increas-

ing space-charge due to the presence of secondaries emitted from the anode, the electric potential distribution in the gap is depressed so that Hull cut-off may be reached *within* the gap. The combined effect of both secondary electrons depressing the potential, and dynamic transmission may thus explain the observed reduction of current and the simultaneous highly oscillatory current-voltage characteristic seen close to cut-off [19].

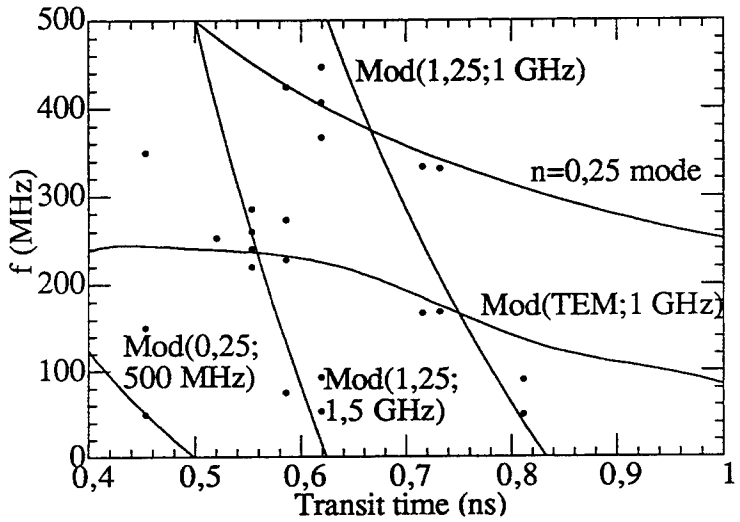


Figure 6: The frequencies measured with $B = 0$ vs. the corresponding Child-Langmuir transit time. The transit time is calculated from the switch voltage, and modulation of structural frequencies by space-charge effects has been taken into account. The indices $mod(n; m)$ correspond to the n^{th} transit time mode [8] modulating a structural mode with frequency m. The TEM mode is taken from [9].

The oscillation frequencies measured in our experiment for $B = 0$ are shown in Fig. 6 vs. the transit time of electrons. While a one-dimensional Child-Langmuir space-charge distribution is stable, the signal impedance of space-charge limited diodes is negative, and can give rise to oscillations if the diode is connected to an external circuit [20, 21]. Oscillations can also occur at fixed diode voltages if the space-charge interacts with the diode gap as a microwave cavity resonator in a "fast" [17] or "slow" mode[22, 9]. In general, we find agreement with this theory, and believe we have identified slow mode transit-time oscillations in the unmagnetized diode.

4 The smooth bore magnetron around cut-off

4.1 Cut-off characteristics

4.1.1 Current-voltage measurements

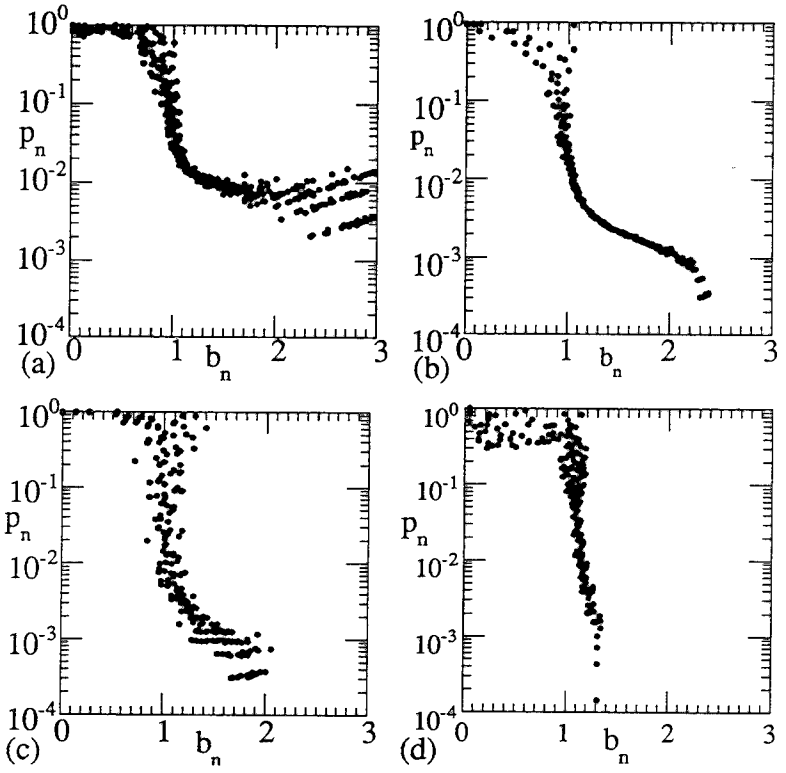


Figure 7: Normalized perveance p_n deduced from experimental data as a function of the normalized magnetic field b_n for different diode gaps and electron barrier configurations. (a) 3 mm gap, no electron barriers (b) 3 mm gap, with barriers (c) 3 mm gap, closely positioned barriers (d) 10 mm gap, with barriers

Fig. 7 shows data of the normalized perveance for different diode cases, each curve deduced from current and voltage samples in a pulsing sequence. We note the reduction of diode perveance by $2-4$ orders of magnitude from closed to open switch when b_n goes from 0.8 to 1.5. The switching time is found to be half the magnetic field rise time, which can be explained by

the diode operation around cut-off where $V_d \propto B^2$. This also verifies that the Brillouin equilibrium is established on a time scale shorter (ns) than the variation of the magnetic field (μs) [23]. Thus, the switching speed is in practice determined by the magnetic field rise time.

We observe that the transition from below to above cut-off is quite smooth and depends only weakly on voltage or gap size. On the other hand, the onset of oscillations in the current signal at $\approx 0.8b_n$ causes an increasing spread in perveance data. These oscillations increase rapidly at $b_n \approx 0.8$, reach a maximum at $B \approx B_c$, and decrease with increasing magnetic field. At higher magnetic fields, where the oscillation amplitude is weak, the increasing spread in perveance in Fig. 7 appears to be related to the decreasing signal-to-noise ratio for small currents.

4.1.2 EM wave measurements

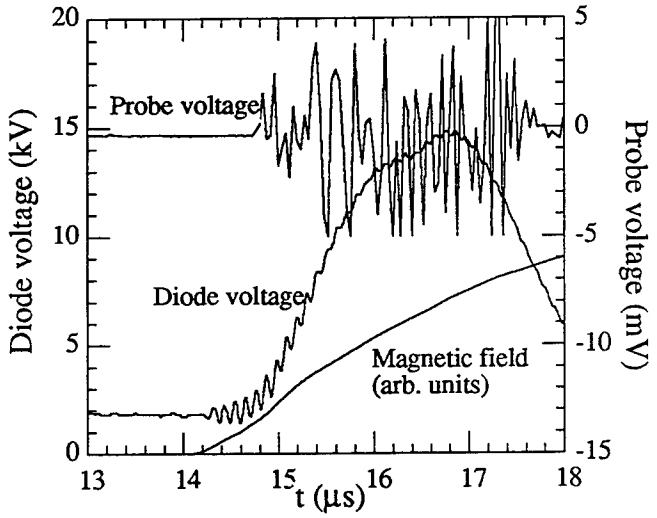


Figure 8: Diode voltage, magnetic field and probe voltage as a function of time in one switching sequence.

To investigate oscillations around cut-off in more detail, we sample the probe signal with high accuracy and sample rate in a small time window when $1 \leq b_n \leq 1.5$. In this procedure, 256 probe signals obtained in a pulsing sequence such as in Fig. 8 were sampled and averaged. The averaged data was then

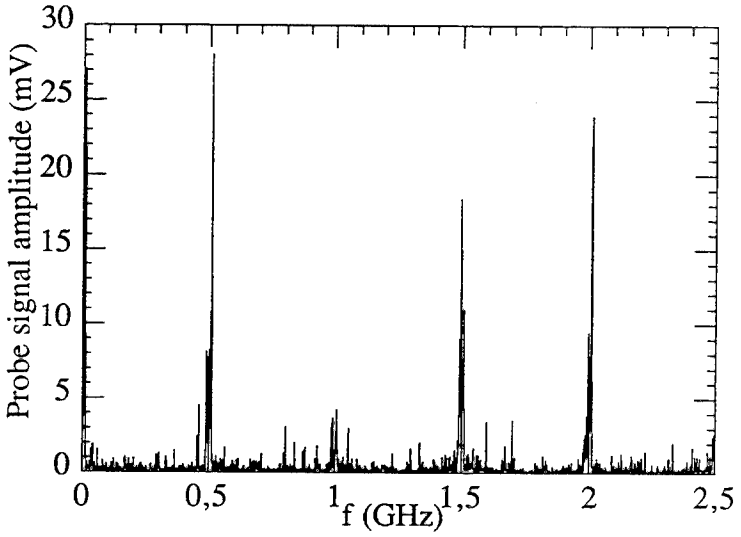


Figure 9: Typical spectrum obtained by applying a FFT to the average of 256 probe signals just past cut-off $1 \leq b_n \leq 1.5$.

processed on a digital computer. Fig. 9 shows a typical FFT of the averaged signals obtained just past cut-off. The measured frequency spectrum contains cavity resonance modes, modulated by noisy oscillations. This modulation appears to be a result of the change of characteristic impedance of the anode-cathode cavity through the presence of time-varying space-charge ("cavity loading"). Much effort was invested in trying to reproduce results from an earlier experiment under similar conditions [5], however, we see no periodic or growing oscillations which can be associated with known instabilities.

4.2 Data analysis

To investigate possible correlation between leakage current and oscillation amplitude, we compare simultaneous diode current and probe signal power in Fig. 10. We note that the onset of current oscillations at $b_n \approx 0.8$ coincides with the appearance of waves in the diode gap, and after cut-off, leakage current and probe signal power decrease together. However, this observation shows no clear correlation between current and electron plasma waves present in the gap, as can be expected, since the amplitude of the electromagnetic waves in the gap is quite weak compared to the kinetic energy of

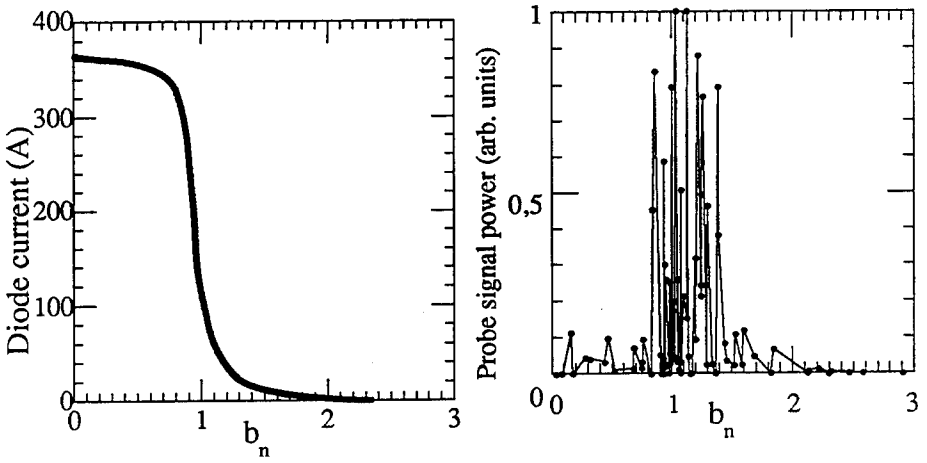


Figure 10: Simultaneously recorded diode current and probe signal power in one switching sequence.

electrons. We can estimate the electromagnetic power radiated by the magnetically confined electron layer from the obtained frequency spectra. The probe signals as functions of time contain circuit, cavity, and electron plasma oscillations. The side-band amplitude in the frequency spectra in Fig. 9, on the other hand, give a more precise measure of the real electron wave amplitude. We can calculate the electromagnetic power of the excited cavity modes in the anode-cathode structure, and calibrate our probe signal with cavity mode oscillations. The sideband amplitude then gives an estimate of the electron wave induced power, which in a typical case ($V_d = 20$ kV, 1 μs rise time) is of the order of a few kW. The total power input at B_c is on the order of several MW, so that the "magnetron efficiency" of our smooth bore magnetron is of the order of 10^{-3}, which as expected is a very low value compared to conventional magnetron oscillators ($> 50\%$).

In summary, our measurements show that in the cut-off region, low power, broad-band oscillations appear. As the magnetic field is increased, the amplitude of these oscillations rapidly decreases simultaneously with the diode current. No distinct wave modes associated with known instabilities have been identified and none are expected on the present time scale.

5 The highly cut-off smooth bore magnetron

5.1 Perveance measurements

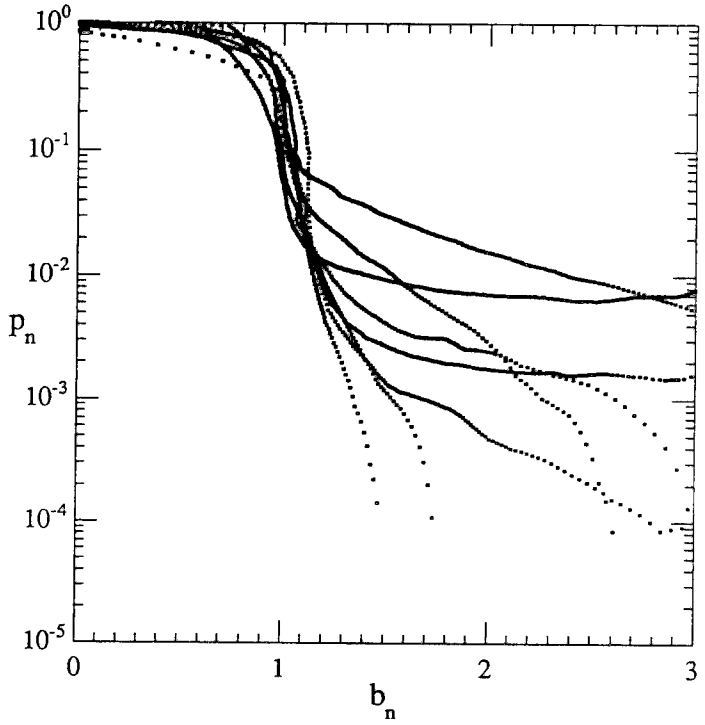


Figure 11: Normalized perveance as a function of the normalized magnetic field for 3 and 10 mm gap widths, and different electron barrier sizes, shapes and positions.

At high magnetic fields, where oscillations are weak, we measure diode current as a function of magnetic field and voltage for two different gap widths (3 and 10 mm), and for different electron barrier positions, sizes and shapes. In Fig. 11, the normalized perveance is calculated from smoothed current and voltage data, and plotted as a function of b_n. The smoothing of sampled data eliminates high frequency noise and high frequency (> 10 MHz) signal components. These high frequency oscillations have a nonlinear voltage dependence and cause a spread of perveance data as in Fig. 7. When the

nonlinear behavior of oscillations is removed, the smoothed perveances overlap for voltages in the range of $2-45$ kV. This confirms that the smoothed p_n is a good parameter for electric circuit characterization of the smooth bore magnetron.

Moreover, the switch perveance in Fig. 11 is only weakly dependent on diode geometry. We find that the perveance without end barriers does not vary when the gap size is varied from 3 to 10 mm. On the other hand, in Fig. 11, we find that the normalized perveance strongly depends on the position of the electron barriers, and that small shift of electron barrier position can result in variations of p_n by an order of magnitude.

5.2 Origin of the leakage current

In an earlier experiment [5], it was assumed that axial leakage current was eliminated after installation of electron barriers, and the remaining radial current in the cut-off magnetron was attributed to a resistive wall type instability. In the present experiment, we have reproduced the leakage current measurements in [5], but find that axial leakage current was not eliminated at the electron barrier position used in [5]. Furthermore, we cannot identify any instability that could account for this current. Although we have no explanation for the different results, the strong reduction of oscillation amplitude with B and the sensitivity of leakage current to electron barrier geometry suggests that leakage current is axial rather than radial.

Simple considerations of electrostatic fields in the magnetron predict that the cylindrical magnetron geometry should confine the electrons axially[10]. However, several mechanisms can lead to axial leakage current, such as emission from the electron barriers, or tilt or misalignment [3]. The barrier temperature in the present experiment is too low to cause thermionic emission. Small changes of the anode position associated with reassembly of the anode-cathode system were found to have no noticeable effects on the leakage perveance. However, distortion of the electric and magnetic field in the diode gap can cause acceleration of electrons along the axial component of the electric field [4]. This "end" effect could partly explain the strong dependence of leakage current on electron barrier position. Moreover, at very close barrier positioning, remaining axial leakage currents may also be caused by transmission of accelerated electrons through the barriers, since the design is not fully opaque.

6 Conclusion

We have presented measurements on the current-voltage characteristics of a crossed-field diode below, around, and above cut-off. We cannot identify oscillations associated with any known instability. This is in contrast to a previous experiment, but agrees with theory on the microsecond time scale used. In the highly cut-off diode, the measured leakage current depends strongly on the electron barrier properties, therefore, we believe the leakage current to be mainly axial.

The feasibility of the MINOS concept for fast high-power switching applications [13] depends critically on (1) stable operation on microsecond time scales, and (2) reduction of leakage current to normalized perveance levels of 10^{-4} or less. For example, open switch losses of 10 % require a leakage perveance $< 10^{-4}$ whereas losses < 1 % require a leakage perveance $< 10^{-5}$ for a typical inductive storage pulse generator. Both stability and low leakage perveance have been demonstrated in the MX-1 experiment. This allows us to project GW peak and MW average power switches at voltages up to ≈ 100 kV with > 80 % efficiency. It should be pointed out that close positioning of electron barriers, leading to low leakage current and thus high switch efficiency, also reduces the voltage stand-off of the switch. Careful design of electron barriers is therefore necessary for making efficient high voltage switches.

7 Acknowledgments

The technical assistance of Mr. Jacques Weinreb and Mr. Rune Landberg is greatly appreciated.

This work was financially supported by Vattenfall AB and by the Faculty of Electrical Engineering and Information Technology of the Royal Institute of Technology.

References

[1] J. E. Eninger. A magnetically insulated opening switch concept. In *Bullet. Am. Phys. Soc.*, page 1342, 1984.

[2] A. W. Hull. The effect of a uniform magnetic field on the motion of electrons between coaxial cylinders. *Phys. Rev.*, 18(13), 1921.

[3] A. F. Harvey. *High Frequency Thermionic Tubes.* Chapman and Hall Ltd., 1943.

[4] J. Golden, T. J. Orzechowski, and G. Bekefi. Magnetic insulation of an intense relativistic electron beam. *J. Appl. Phys*, 45(7), 1974.

[5] R. Kraft and M. W. McGeoch. Experimental study of magnetic insulation. *Phys. Fluids*, 30(4), 1987.

[6] R. H. Levy. Diocotron instability in a cylindrical geometry. *Phys. Fluids*, 8(7), 1965.

[7] D. Chernin. Resistive wall effect on the stability of planar relativistic Brillouin flow. *Phys. Fluids*, 25(8), 1982.

[8] C. K. Birdsall and W. B. Bridges. *Electron Dynamics of Diode Regions.* Academic Press, New York, 1966.

[9] T. M. Antonsen Jr., W. H. Miner, E. Ott, and A. Drobot. Stability of space-charge limited electron flow. *Phys. Fluids*, 27(5), 1984.

[10] O. Buneman. Chapter 5.1.1: The RF theory of crossed-field devices. In E. Okress, editor, *Crossed Field Microwave Devices*, volume 1. Academic Press, 1961.

[11] H. Lee, D. J. Kaup, and G. E. Thomas. Linear stability of Vlasov-Poisson electron plasma in crossed fields. Perturbations propagating parallel to the magnetic field. *J. Plasma Physics (part 3)*, 40, 1988.

[12] B. H. Vanderberg. *Experimental and Analytical Study of a Magnetically Controlled Thermionic Vacuum Switch Concept.* Ph.D. thesis, Royal Institute of Technology, Stockholm, Sweden, 1994.

[13] B. H. Vanderberg and J. E. Eninger. Parametric scaling study of a magnetically insulated thermionic vacuum switch concept. *IEEE Trans. Plasma Sci.*, 24(1), 1996.

[14] Y. Y. Lau, P. J. Christenson, and D. Chernin. Limiting current in a crossed-field gap. *Phys. Fluids B*, 5(12), 1993.

[15] T. J. Orzechowski and G. Bekefi. Current flow in a high-voltage diode subjected to a crossed magnetic field. *Phys. Fluids*, 19(1), 1976.

[16] C. D. Child. Discharge from hot CaO. *Phys. Rev.*, 32:492, 1911.

[17] F. B. Llewellyn and A. E. Bowen. The production of ultra-high frequency oscillations by means of diodes. *Bell Syst. Tech. J.*, 18:280, 1939.

[18] B. H. Vanderberg and J. E. Eninger. Space-charge limited current cut-off in a crossed-field diode. In *IEEE Conf. Rec.-Abstracts 95CH35796*, Madison, Wisconsin, USA, 1995.

[19] B. H. Vanderberg and J. E. Eninger. Current characteristics of a space-charge limited crossed-field diode. Technical Report TRITA-EIE-9406, Department of Industrial Electrotechnology, Royal Institute of Technology, Stockholm, Sweden, 1994.

[20] W. E. Benham. Theory of the internal action of thermionic systems at moderately high frequencies. *Philos. Mag.*, 5:641, 1928.

[21] J. Müller. Experimentelle Untersuchungen über Elektronenschwingungen. *Hochfrequenztechnik und Elektroakustik*, 43(195), 1934.

[22] F. S. Felber and B. A. Spivey. Filamentation of space-charge limited flow. *Phys. Fluids*, 25(7), 1982.

[23] O. Buneman. Chapter 4.2: Symmetrical states and their breakup. In E. Okress, editor, *Crossed Field Microwave Devices*, volume 1. Academic Press, 1961.

INVESTIGATION OF SECONDARY ELECTRON EMISSION FROM CVD DIAMOND FILMS FOR CROSSED-FIELD DEVICES

G.T. Mearini[a†], I.L. Krainsky, J.A. Dayton, Jr.
NASA Lewis Research Center, Cleveland, Ohio 44135

ABSTRACT

Secondary Electron Emission properties of polycrystalline diamond films grown from Chemical Vapor Deposition have been measured. The total secondary yield coefficient (σ) has been observed to be as high as 20 at room temperature and 48 while heating at 700 K in vacuum from as-grown samples. Electron Beam Activated - Alkali Terminated diamond films have shown stable values of σ as high as 60 when coated with CsI and similarly high values with other alkali-halides. Diamond coated with BaF_2 had a stable yield of $\sigma = 6$, but no enhancement of the secondary emission properties were observed with coatings of Ti or Au. Hydrogen has been identified to give rise to this effect in as-grown films. However, electron exposure led to a reduction in σ to values as low as 2. Exposure to a molecular hydrogen environment recovered σ to the original high values after degradation, and enabled stable secondary emission during electron exposure.

INTRODUCTION AND BACKGROUND

Interest in technological applications of diamond has shifted recently from wear resistant coatings to electronics[1,2] due to the Negative Electron Affinity (NEA) of natural diamond[3], coupled with the relative ease of fabrication of conductive diamond films grown by Chemical Vapor Deposition (CVD)[4]. It is also well established that the diamond surface is terminated with hydrogen[5,6], which may give rise to NEA in natural diamond and some well oriented CVD diamond films[7,8]. This present work is a continuation of Secondary Electron Emission (SEE) measurements from diamond on Mo, Si, Ti, AlN, and Pd which began several years ago[9-14] and indicated that diamond may be suitable in many secondary emitter applications due to its high secondary yield (σ).

Devices which utilize secondary emitters include crossed-field devices such as magnetrons, crossed-field amplifiers (CFA), traveling wave tubes (TWT), electron multipliers and photomultiplier tubes (PMT). Such devices are essential in radar, intelligence gathering, space communications, and night vision glasses. Materials used presently in secondary emitter applications may have values of σ as high as 4, but generally fall between 2 and 3[15,16]. A cathode material with significantly higher secondary emission may reduce noise, improve turn-on characteristics and increase stability and efficiency in crossed-field devices.

Hydrogen was identified to be responsible for the high values of σ from as-grown CVD diamond films[9-11]. Total secondary yields as high as 27 from diamond/Mo and as high as 48 from diamond/Pd were measured in vacuum during heating to 700 K[10]. The total secondary yield was observed to degrade as a function of fluence under continuous exposure to an electron beam due to electron induced desorption of hydrogen[9,10]. Subsequent exposure to a molecular hydrogen partial pressure of 1.0×10^{-6} torr for approximately 20 minutes would recover σ to the original values. The total secondary yield from diamond/Mo was stable at $\sigma = 12$ during continuous electron exposure, with a molecular hydrogen partial pressure of 1.0×10^{-6} torr present[9]. The total secondary yield was observed to be stable at $\sigma = 25$ from diamond/Pd during exposure to a continuous beam of electrons at 1 keV while heating at 700 K which produced a hydrogen background pressure of ~1.0×10^{-6} torr[10].

High stable secondary emission ($\sigma = 25 - 45$ @ 1500 eV) in Ultra-High Vacuum (UHV) was achievable by coating CVD diamond with an alkali-halide thin film and activating the surface by electron exposure[12,13]. The activation produced a halogen free surface (as observed with AES) which was terminated by ~ 1 monolayer of the alkali metal, and was reproducible using different alkali-halide overcoatings. These Electron Beam Activated - Alkali Terminated (EBAAT) diamond surfaces showed no degradation of σ after long term electron beam exposure when CsI was used as the overcoating, and promising results with little degradation when NaCl or KCl were used. The EBAAT surface was stable to temperatures in excess of 120° C and when exposed to atmosphere for several months[13].

Emission from EBAAT diamond films has been observed to decrease in the presence of Ar at pressures in excess of 1.0×10^{-7} torr when under exposure to a primary electron beam with current density less than 1 mA/cm^2. The decrease in σ is not permanent, and is probably due to impurity atoms contaminating the EBAAT surface. The effect can be reversed by either an increase in primary current density or a decrease in pressure. However, for this reason the EBAAT diamond is not necessarily as desirable as the hydrogen terminated diamond for specific applications. Also, NEA observations from diamond coated with thin films (submonolayer and monolayer coverages) of Ti and Co[7,17] suggest that these or other materials may produce high stable σ and allow operation at higher temperatures. These considerations were the motivation for this work.

EXPERIMENTAL PROCEDURE

SEE measurements were conducted in a UHV chamber with a base pressure of 1.0×10^{-10} torr. The experimental setup has been described previously[9]. The samples tested were p-type diamond films on Mo and Si substrates, ranging from 1μm to 20μm in thickness, grown by hot filament (HF) and microwave plasma (MP) CVD. Total secondary yield vs. primary beam energy ($E_{primary}$) was measured from all samples, where $E_{primary}$ ranged from 100 eV to 3 keV in 50 eV increments. To investigate the effects of beam exposure on σ, each as-grown sample was

exposed to the electron beam for up to 72 hours at current densities ranging from 50 $\mu A/cm^2$ to 10.0 mA/cm^2. Diamond targets overcoated with various materials were tested for up to seven days under continuous electron beam exposure. The beam diameter ranged from 0.12 to 0.25 mm. The current density was held constant during each experiment and the data were normalized by comparing the fluence dependence of each sample. In all cases the data were collected every 5 seconds while the primary beam energy was held constant in the range 1.0 to 1.5 keV.

Scanning Electron Microscopy (SEM), Raman Scattering Analysis, and Auger Electron Spectroscopy (AES) were used to determine the quality of the diamond targets, and to characterize the affects of heating and hydrogen and oxygen exposure on the diamond samples. AES was used to investigate changes in the shape of the carbon peak from CVD diamond/Si due to ionic bombardment, indicating graphitization of the diamond surface.

BaF_2 coatings, 30 nm thick, were resistively evaporated onto diamond targets in a diffusion pumped high vacuum system with a base pressure of $2X10^{-8}$ torr. Thin coatings of Ti and Au, ranging from < 1 monolayer to 30 nm in thickness, were vacuum deposited from a resistively heated source onto diamond targets in a turbopumped preparation chamber attached to the main UHV test chamber and separated with a gate valve. SEE properties of these samples were measured as described above. Thin CsI coatings were deposited onto representative diamond samples from the depositions used for Ti and Au coatings, and the targets were used as control samples to insure that diamond films from different depositions had similar SEE properties.

EXPERIMENTAL RESULTS

SEE measurements from as-grown samples have been discussed previously[9-11] and some results will be included here for comparison. Figures 1 and 2 show σ vs. $E_{primary}$ and σ vs. fluence data from representative CVD diamond targets, respectively. No differences in the SEE results have been observed to arise from the different deposition techniques (HFCVD and MPCVD). σ_{MAX} from as-grown samples nominally occurred between 1000 and 1500 eV, and ranged from 10 to 20 as is seen in Figure 1. As-grown CVD diamond/Pd had a maximum total yield of ~ 20 at 1400 eV, and a maximum total yield of 48 at 3 keV while heating in vacuum at 700 K[10]. EBAAT diamond/Mo had a maximum total yield of 50 - 60 at 3 keV at room temperature[13, 18].

Figure 2 shows that σ decreased from uncoated targets under electron exposure in vacuum, independent of the hydrogen surface treatment. Stable SEE (σ = 12) was observed from as-grown diamond/Mo in a hydrogen atmosphere of 1.0 X 10^{-6} torr while exposed to a 1 keV electron beam (not shown)[9]. It was noted that at the values of hydrogen partial pressure and current density necessary for stable σ, the hydrogen molecules were impinging on the diamond surface at the same rate as the energetic electrons[9]. Stable $\sigma > 25$ from diamond/Pd was also observed when the sample was heated in vacuum to 700 K (cf. Figure 2) while the target was exposed to a 1 keV electron beam[10]. At this temperature the Pd substrate provided a hydrogen

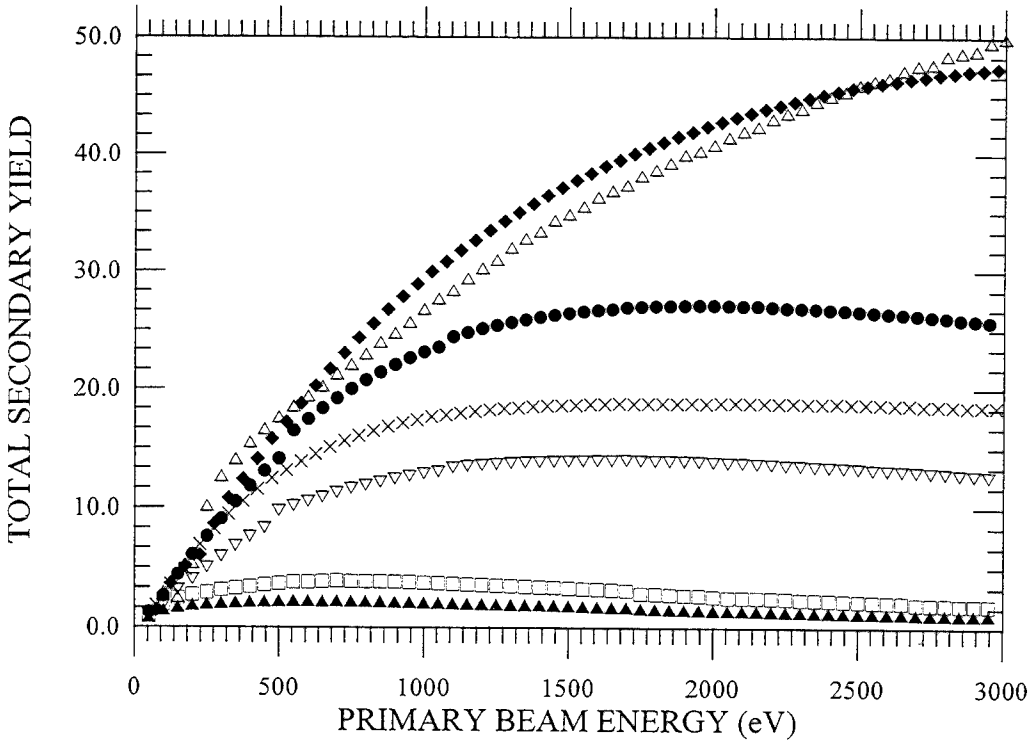


Figure 1. Total Secondary Yield (σ) vs. primary beam energy from CVD diamond: (▽) as-grown on Mo; (×) as-grown on Pd; (●) heating in vacuum to 700 K (Mo); (◆) heating in vacuum to 700 K (Pd); (□) after atomic hydrogen treatment (Mo); (▲) after hydrogen plasma treatment (Mo); (△) EBAAT surface using CsI (Mo).

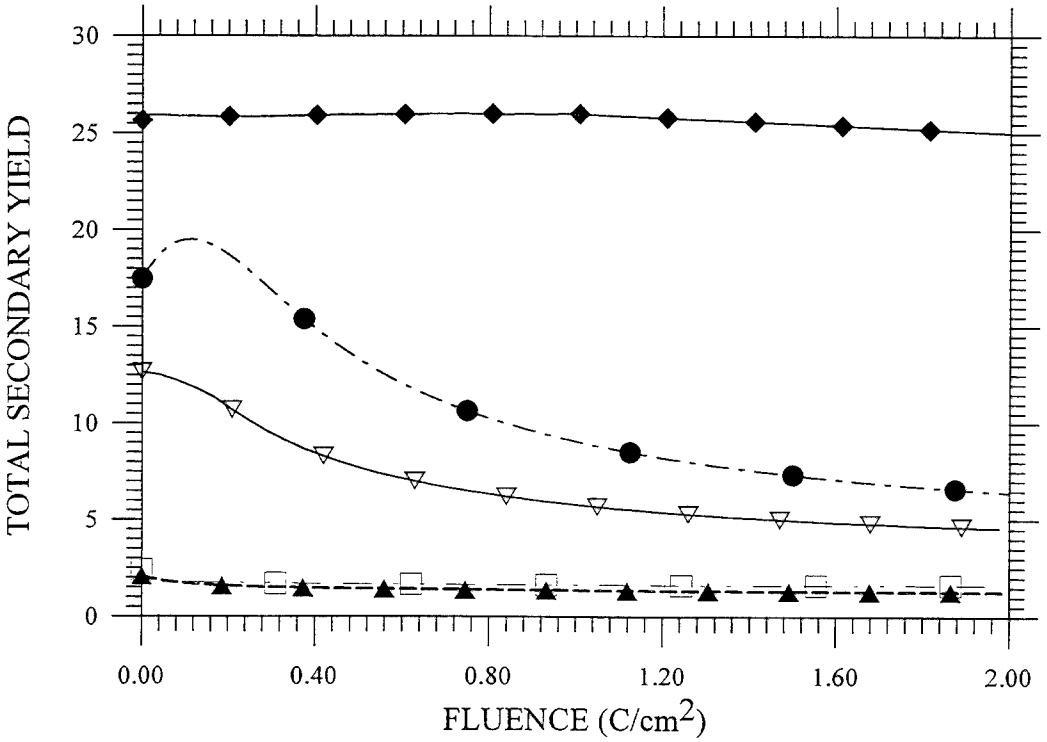


Figure 2. Total Secondary Yield (σ) vs. Fluence from CVD diamond at 1 keV: (▽) as-grown on Mo; (●) heating in vacuum to 700 K (Mo); (◆) heating in vacuum to 700 K (Pd); (□) after atomic hydrogen treatment (Mo); (▲) after hydrogen plasma treatment (Mo)

background pressure of 1.0 X 10^{-6} torr, which was sufficient to replenish the surface hydrogen desorbed by the electron beam. After sufficient heating hydrogen stored in the Pd substrate was depleted and σ decrease with the same behavior seen in the as-grown films (cf. Figure 3). Figure 3 shows that stable SEE (σ = 20-45 @ 1500 eV) was readily observed from alkali-halide coated diamond films in UHV, independent of primary beam current[12,13,18].

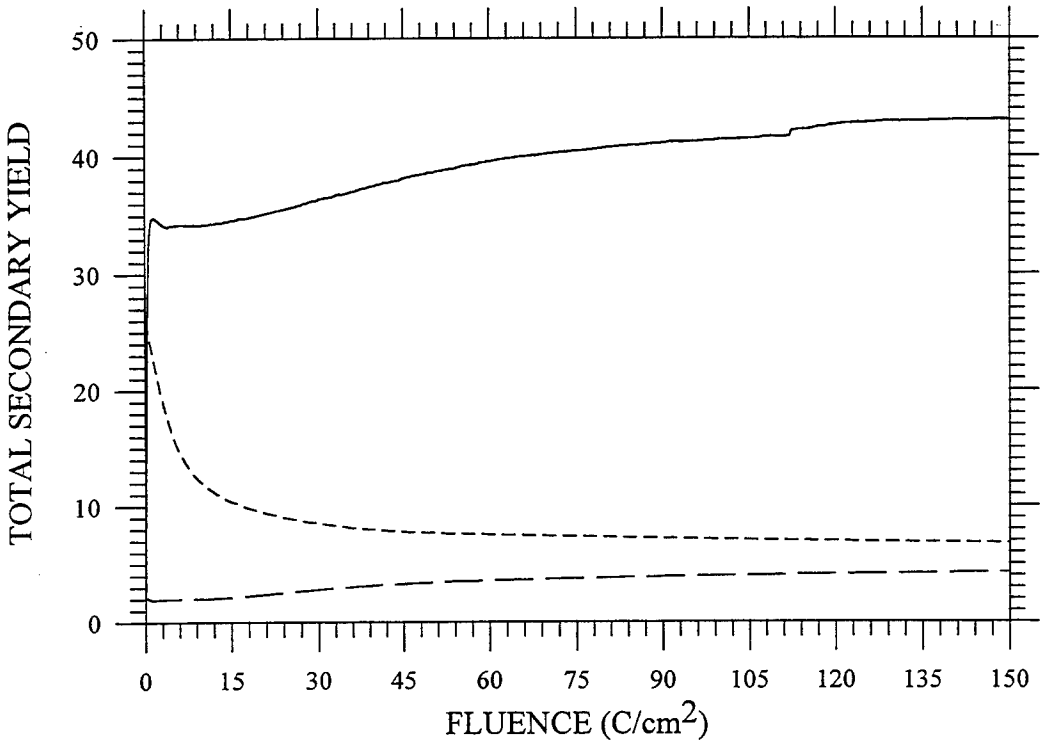


Figure 3. Total Secondary Yield (σ) vs. Fluence at 1.5 keV: (solid line) EBAAT diamond/Si using CsI; (short dashed line) diamond/Pd during heating in vacuum at 700 K; (long dashed line) diamond/Si coated with 30 nm BaF_2.

Barium is well known for lowering the work function of W and Mo, thereby enhancing emission in thermionic cathodes[19-21] To investigate possible enhancement of secondary emission from Ba on CVD diamond, thin BaF_2 films were deposited onto diamond. It was hoped that a monolayer coverage could be produced by electron exposure similar to the EBAAT process, which might lower the work function of the diamond surface. As is seen in Figure 3, σ vs. fluence from BaF_2 coated diamond showed a behavior similar to that of EBAAT samples. However, the maximum value of σ never exceed 6 at 1.5 keV in all samples tested. CsI coated diamond films from the same diamond coated Si wafers used with BaF_2 had values of σ > 30 under the same operating parameters.

The fluence dependence of σ from diamond in vacuum during exposure to electrons, shown in Figure 2, has been observed in all as-grown CVD diamond targets tested, independent of current density or substrate material. It was observed previously that energetic primary electrons induced hydrogen desorption from the diamond surface, which resulted in lower σ(cf. Figure 2).

The carbon Auger peak from an as-grown diamond surface, before and after Ar ion sputtering at 2kV, is shown in Figure 4. Before sputtering the signature diamond Auger peak was observed[22]. After sputtering for 6 minutes the diamond structure was destroyed, as indicated by the graphitic shape of the carbon peak. Ionic bombardment using oxygen at 2kV, and hydrogen to as low as 200 V, produced the same change in the carbon peak from CVD diamond targets. Heating in vacuum led to increased σ in as-grown films (cf. Figure 1), but had no affect on the sputtered surfaces.

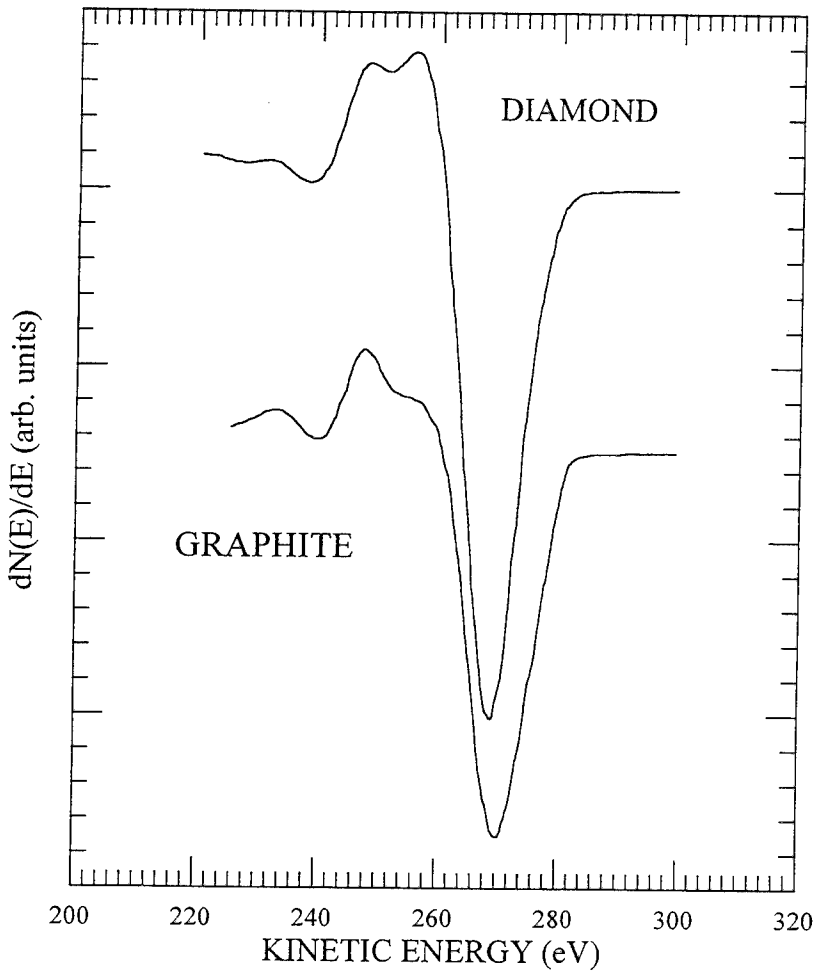


Figure 4. Auger carbon peak from as-grown diamond/Si (top curve) and after Ar ion sputtering at 2kV for 6 minutes (lower curve) indicating a graphitic structure.

Most metals exhibit a maximum value of σ at a primary beam energy between 0.6 and 1 keV[23]. Measurements from as-grown CVD diamond indicate that the maximum value of σ occurs between 1 and 1.5 keV. The total secondary yield vs. $E_{primary}$ curves from EBAAT diamond using CsI and the diamond/Pd during heating shown in Figure 1 are atypical since a maximum value of σ has not been reached at 3 keV. These data suggest that emission is being generated below the surface in these materials, since the deeper penetrating higher energy electrons appear to lead to an increasing number of secondaries. No measurements were made above 3 keV to determine the maximum value of σ from these samples. It is likely that this behavior was not observed in the as-grown films due to the desorption of hydrogen by the

electrons striking the surface before penetrating into the bulk. This, of course, would increase the work function and prevent electrons generated deeper in the diamond from escaping to vacuum.

Secondary electron emission vs. fluence data from EBAAT diamond during heating (T > 150°C) or at elevated pressures (1.0 X 10^{-6} torr Ar, not shown) show the EBAAT surface to be highly sensitive to impurity concentrations and temperature. Multiple Ti and Au depositions were made onto two diamond on Mo films to investigate the possibility of other emission enhancing surface coatings which may have the benefit of withstanding higher temperatures.

The depositions were performed in a preparation chamber without breaking vacuum, and the vacuum during depositions never exceeded 5 X 10^{-7} torr. CsI was deposited in the same way onto a diamond target grown during the same deposition as those used with the metal overlayers to insure that the diamond had potential for high stable SEE. The total secondary yield measured from the CsI coated control sample was stable and exceeded 30 at 1500 eV. Figure 5 shows multiple scans of σ vs. fluence from diamond/Mo coated with Ti, with the overlayer thicknesses starting from < 1 monolayer and increasing in multiple monolayer increments. Measurements from Au coated films indicated the same behavior. The overlayer materials were chosen based on emission enhancing effects reported in the literature. Ti/diamond has been reported as a NEA material[7], and thin Au films have been reported to stabilize field emission from CVD diamond films[24,25]. With each successive deposition the maximum σ was reduced, until the SEE behavior became that of the overlayer material.

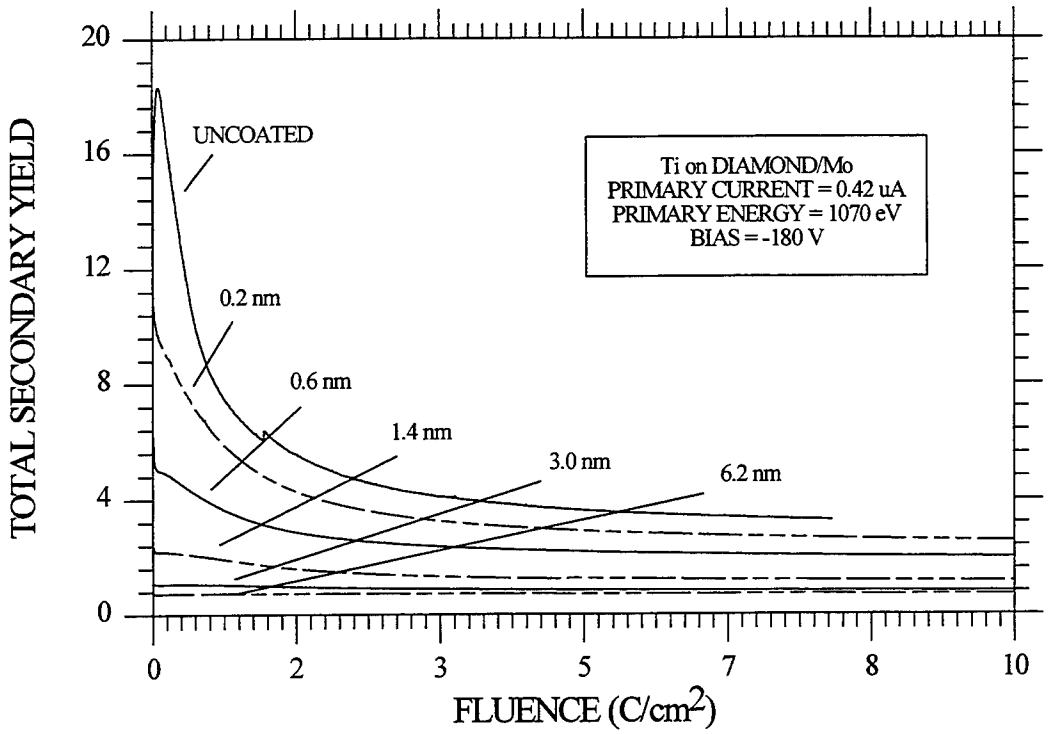


Figure 5. Total Secondary Yield (σ) vs. Fluence from CVD diamond/Mo after successive depositions of Ti.

CONCLUSIONS

High SEE has been observed from CVD diamond films grown on various substrates. In as-grown films the effect is due to surface hydrogen which is unstable under exposure to electrons. Alkali-halide coatings on the diamond films lead to high stable emission in UHV after the surface is activated by electron exposure. No differences in SEE properties have been observed between samples grown by HF or MPCVD. The SEE properties appear to have little or no dependence on the substrate material, except in the case of Pd substrates where heating allows a continuous flow of hydrogen from the Pd onto the diamond surface which stabilizes σ. Thin BaF_2 coatings provided some enhancement in the stability of σ but the maximum yield was considerably lower than EBAAT surfaces or even as-grown films.

The σ vs. $E_{primary}$ data from EBAAT diamond coated with CsI shows higher emission at higher primary energies, indicating that electrons generated deeper within the bulk are drifting to the surface and being emitted into the vacuum. However, the data from as-grown films indicates that the surface properties ultimately determine the SEE properties from CVD diamond.

Although Ti on diamond has been observed to be a NEA material when Ti is $\leq$ 1monolayer thick, no SEE enhancing effect was observed when thin layers were deposited onto diamond. The same results were observed with thin Au films.

High SEE properties of CVD diamond make the material a candidate for crossed-field device applications. More investigation is necessary under harsh environmental conditions like those found in CFD's (i.e. high temperatures, high primary current densities). Graphitization poses a challenging problem since ionic back bombardment of a diamond cathode in CFD's in unavoidable. CsI coatings appear to provide some protection to ion sputtering compared to uncoated films. Other materials which might enhance SEE while protecting the surface are being investigated.

ACKNOWLEDGEMENTS

The authors owe many thanks to D.F. Anderson, and his colleagues at Fermi Lab for providing alkali-halides and "n" invaluable ideas. The authors would also like to thank Louis Maschak and Ben Ebihara at NASA Lewis Research Center, and Robert Kusner and Robert Kunszt at General Vacuum, Inc., for assisting with the experimental setup. Diamond targets were provided by R. Ramesham and M.F. Rose, *Space Power Institute, Auburn University*, Yaxin Wang and John Angus, *Chemical Engineering Department, Case Western Reserve University*, and General Vacuum, Inc. This work was supported by The National Research Council and NASA Lewis Research Center.

REFERENCES

a) National Research Council Fellow
†) Present address: General Vacuum, Inc., P.O. Box 605204, Cleveland, OH 44105

1) M. Geis, Proc. of the IEEE, **79(5)**, (1991) 669.

2) M. Geis and J.C. Angus, Scientific American, Oct., (1992) 84.

3) F.J. Himpsel, J.A. Knapp, J.A. Van Vechten, and D.E. Eastman, Phys. Rev. B, **20(2)**, (1979) 624.

4) J.C. Angus, Y. Wang, and M. Sunkara, Annu. Rev. Mater. Sci., **21**, (1991) 221.

5) B.B. Pate, M.H. Hecht, C. Binns, I. Lindau, and W.E. Spicer, J. Vac. Sci. Technol., **21(2)**, July/Aug., (1982) 364.

6) B.J. Waclawski, D.T. Pierce, N. Swanson, and R.J. Celotta, J. Vac. Sci. Technol., **21(2)**, July/Aug., (1982) 368.

7) J. van der Weide, Z. Zhang, P.K. Baumann, M.G. Wensell, J. Bernholc, and R.J. Nemanich, Phys. Rev. B, **50(8)**, (1994) 5803.

8) I.L. Krainsky, V.M. Asnin, G.T. Mearini, and J.A. Dayton, Jr., to be published.

9) G.T. Mearini, I.L. Krainsky, and J.A. Dayton, Jr., Surf. and Int. Anal., **21(2)**, (1994) 138.

10) G.T. Mearini, I.L. Krainsky, Y.X. Wang, J.A. Dayton, Jr., R. Ramesham, and M.F. Rose, Thin Solid Films, **253**, (1994) 151.

11) T.L. Bekker, J.A. Dayton, Jr., A.S. Gilmour, Jr., I.L. Krainsky, M.F. Rose, R. Rameshan, D. File, and G.T. Mearini, IEEE IEDM Tech. Dig., (1992) 949.

12) G.T. Mearini, I.L. Krainsky, J.A.Dayton, Jr., Yaxin Wang, Christian A. Zorman, J.C. Angus, and R.W. Hoffman, Appl. Phys. Lett., **65(21)**, (1994) 2702.

13) G.T. Mearini, I.L. Krainsky, J.A. Dayton, Jr., Yaxin Wang, Christian A. Zorman, J.C. Angus, R.W. Hoffman, and D.F. Anderson, Appl. Phys. Lett., **66(2)**, (1995) 242.

14) G.T. Mearini, I.L. Krainsky, and J.A. Dayton, Jr., Proc. of the Third Int. Conf. on Appl. of Diam. Films and Rel. Mat., NIST Special Publication 885, (1995) 13.

15) E.A. Kurz, Amer. Lab., March (1979), and references therein.

16) A.S. Gilmour, Jr. *Microwave Tubes*, Artech House, Norwood, MA (1986) 134-137.

17) P.K. Baumann and R.J. Nemanich, Proc. of the Third Int. Conf. on Appl. of Diam. Films and Rel. Mat., NIST Special Publication 885, (1995) 41.

18) I.L. Krainsky, V.M. Asnin, G.T. Mearini and J.A. Dayton, Jr., to be published.

19) A. Lamouri and I.L. Krainsky, Surf. Sci., **278**, (1992) 286.

20) A. Lamouri, I.L. Krainsky and W. Mueller, Surf. and Int. Anal., **21**, (1994) 150.

21) A. Lamouri, W. Mueller and I.L. Krainsky, Phys. Rev. B, **50**, (1994) 4764 .

22) P.G. Lurie and J.M. Wilson, Surf. Sci., **65**, (1977) 476.

23) I.M. Bronshtein, B.S. Fraiman, *Secondary Electron Emission*, Nauka, Moscow (1969).

24) J.D. Shovlin, M.E. Kordesch, Appl. Phys. Lett., **65(7)**, (1994) 863.

25) A. Lamouri, G.T. Mearini, Y.X. Wang and R.E. Kusner, Proc. of the Third Int. Conf. on Appl. of Diam. Films and Rel. Mat., NIST Special Publication 885, (1995) 61.

Secondary Electron Emission Study for Crossed-Field Amplifier Applications

Arnold Shih, Joan Yater, Charles Hor and Richard Abrams
Naval Research Laboratory
Code 6844
Washington D.C. 20375

Abstract

Crossed-field amplifier (CFA) tubes require secondary-electron-emission cathodes with high secondary-electron yield, reliable performance, and long life in the CFA environment. Insulators in general have higher secondary-electron yields than metals and semiconductors. However, means to provide electrical conductivity are necessary to replenish the electrons lost from the secondary-electron-emission process. The results of our recent study involving BeO, MgO/Au cermet and diamond are used to illustrate the methods of providing electrical conductivity, the effect of surface adsorbates on secondary-electron yield, and the effect of electron and ion bombardment on the life of secondary-electron emitters.

I. Introduction

Crossed-field amplifiers (CFA) require secondary-electron emitters with high secondary-electron yield which must be robust in the CFA environment. We will present the results of our recent studies which illustrate some common properties of secondary-electron emitting materials. All of the examples presented here involve insulators. In general, insulators are excellent secondary-electron emitters and metals are poor emitters [1,2]. This fact can be readily explained in terms of the differences in the electronic band structures between metals and insulators. An energetic electron impinging on a sample loses its energy through collisions with surrounding electrons until all its energy is exhausted. In the process, each incident electron generates a copious amount of secondary electrons. The total yield of secondary electrons depends on how efficiently these electrons escape from the sample into the vacuum. The electron-electron collisions are also the major energy-loss mechanism that prevents the escape of secondary electrons. Because of the absence of conduction electrons in insulators, the electrons available for these collisions are the valence electrons. The presence of a forbidden energy band just above the valence band prevents the excitation of valence electrons into that energy. Therefore, a low energy electron moving through the material with an energy less than E_g (the band gap energy) suffers no electron-electron collision and can escape from deep within the material. Thus the total electron yields from insulators are high, and the emitted electrons are dominated by these low-energy electrons. In contrast, large electron densities of states are present in metals just above the Fermi level. An outgoing electron suffers frequent collisions with the high density of conduction electrons and loses energy in the process. When it falls below the vacuum level, it cannot escape. Consequently, metals, in general, have low secondary-electron yields. According to the table compiled by Dekker [1], δ_m (the maximum secondary-electron yield) is much less than 2 for most metals. In contrast, based on the table compiled by Hachenberg and Brauer [2], insulators have δ_m greater than 5, and specifically, MgO single crystals have $\delta_m = 23$.

Electron losses from the secondary-emission process need to be replenished, and electrical conductivity is required to transport the replacement electrons. The results of studies on three different emitting materials are presented below. Each material employs

an entirely different approach in supplying the electrical conductivity. BeO emitters are actually oxidized beryllium; the bulk of the material is metal and only the topmost layer (about 20 Å) is oxidized. The oxide layer is thin and the electrical resistance is small. Another emitter material is MgO/Au cermet, which is a mixture of insulator (MgO) and metal (Au) micro-crystals with particle sizes less than 100 Å in diameter. The MgO/Au cermet that we studied was 75% MgO and 25% Au, and a continuous conducting path is provided through the Au particles. The last example involves diamond. The electrical conductivity in the diamond samples is provided by appropriate impurity doping, which is a widely used method in semiconductor technology.

II. Oxidized Beryllium

Oxidized beryllium (Be) is the material of choice for the CFA cathode hub in the current AEGIS CFA tubes. We found that the secondary emission properties of BeO/Be depend on the oxide thickness, surface roughness, and surface cleanliness, but not on the grain structure of the Be stock. Recently, the Be stock supplied by Brush Wellman Inc. changed in composition from one composed of planar grains to spherical grains because of the latter's desirable mechanical properties. Our comparative study of samples from the two stocks revealed that the oxide layers have comparable thickness and the secondary electron yields are the same within the measurement accuracy.

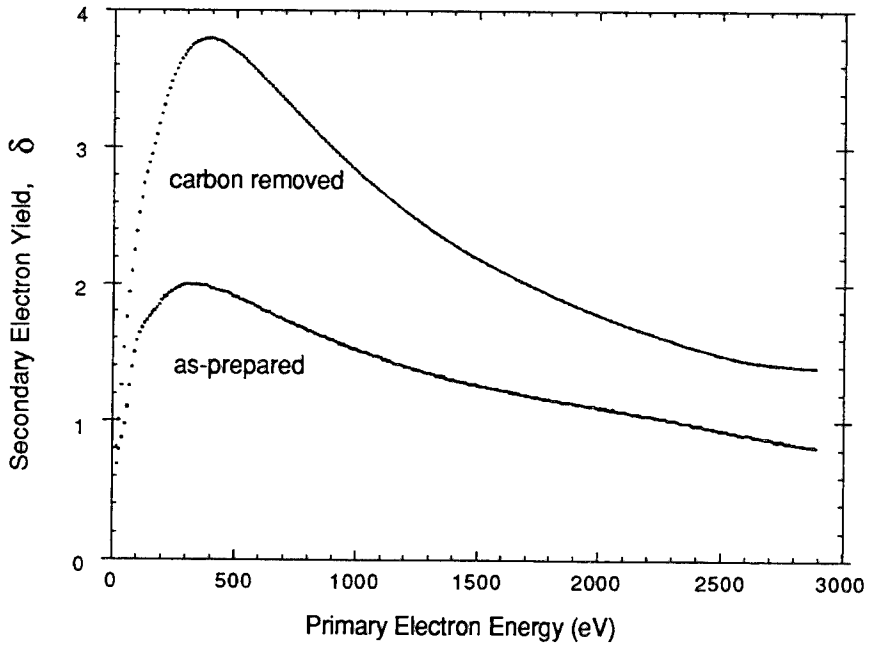


Fig 1. Effect of carbon on the secondary electron yield of an oxidized beryllium sample.

Surface cleanliness has a very strong effect on the secondary-electron yield of the samples. Carbon containing impurities are found to be present on the BeO surfaces, as are commonly found on air-exposed surfaces. The carbon presence significantly suppresses the secondary-electron yield of an oxidized Be sample, as is clearly illustrated in Fig. 1. The as-prepared sample was chemically cleaned and grit-blasted to simulate the surface condition in CFA tubes. A light ion-sputtering removed the surface carbon, and δ_m increased by almost a factor of two. For use in the tube processing, heating is more practical than sputter cleaning. Fig. 2 shows the changes in surface composition and δ_m during a step-wise heating of one hour duration at each temperature. Although the carbon removal was rather slow, a change in the chemical state of carbon was observed from a graphitic type to a carbidic type [3]. Accompanying this change is a rapid rise in δ_m. It is

interesting that the empirically determined tube bake-out procedure is performed at 500-525°C for 6 - 8 hours. This bake-out is just sufficient to convert the graphitic carbon to carbidic carbon. The results here provide the justification for such a high-temperature bake.

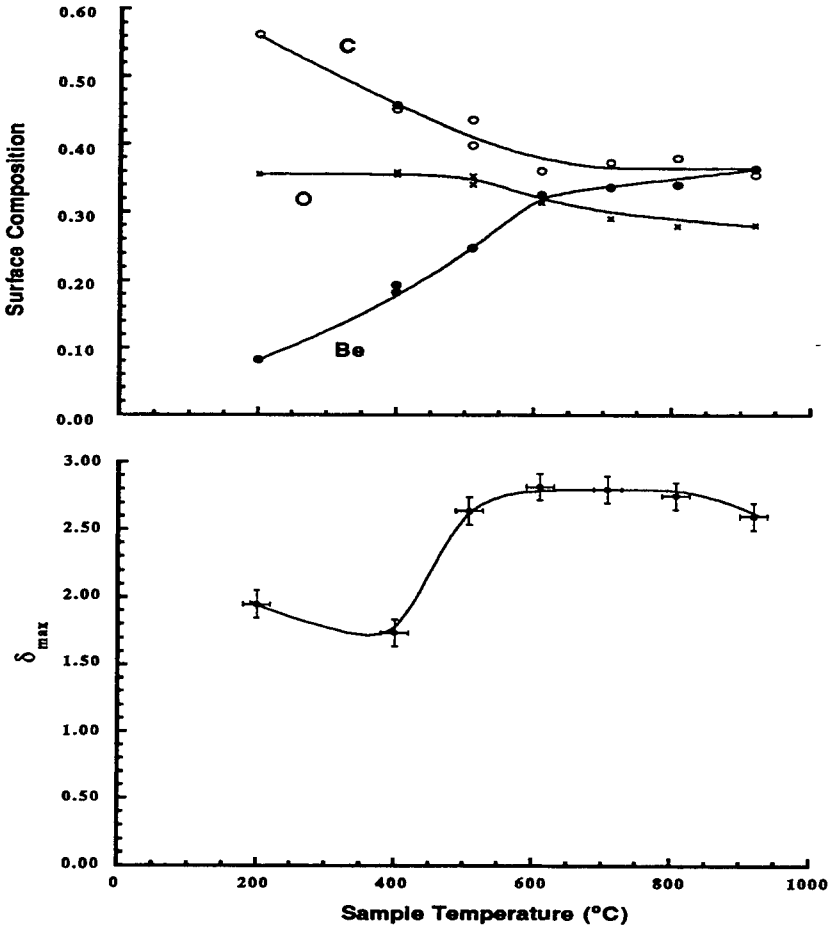


Fig. 2. The changes in surface composition and δ_m as a function of BeO heating.

The oxides present on the oxidized Be surfaces are very thin, and consequently they are removed by electron bombardment and ion sputtering during the initial operation. At this point, an oxygen source (a cuprous oxide appendage) is turned on to re-establish the oxide. This initial burn-in process is labor-intensive and drives up the cost of the tube production. While one possible solution is to use an initially thick oxide coating, the feasibility of this approach needs to be assessed. For example, changes in the secondary-electron yield and film resistivity as a function of oxide thickness need be studied; and the technique required to form thick oxide layers (e.g., plasma discharge method) needs to be established. We are currently pursuing these studies. However, an alternative approach is to find a novel material that will provide long-life operation without relying on an oxygen source. One potential candidate is the cermet-type cathode.

III. MgO/Au cermet

MgO/Au cermet was first suggested by Henrich and Fan [4,5] as an alternative way to achieve high secondary-electron emission and good electrical conductivity. Such

films can have maximum secondary-electron yields of about 8 and can be several thousand angstroms thick to provide long life without an oxygen source. V. Ritz[6] deposited a 4000 Å thick MgO/Au film by sputtering a 75% MgO/25% Au target onto a type 304 stainless steel hub. The cathode hub was installed in a L4707 CFA tube, and a performance test was carried out at Litton Industries in Williamsport by K. Ramacher. The bake-out was carried out at 425°C for 12 hours. The tube started up immediately, and no starting-jitter was observed. The tube was at full operation by the 27th hour and passed all specifications. The noise level was better than that of the average tubes with BeO cathodes. However, the tube showed a linear decline in performance with time and after 560 hours, the tube failed to meet the specifications. A postmortem analysis was carried out and the results were reported earlier [7]. The tube was cut open in an Argon atmosphere, and the cathode hub was transferred to a surface analysis system having AES, δ-measurement and ion-sputtering capabilities. Auger-sputter-profile analyses revealed that only between 5% to 25% of the original cermet film remained on the hub surface. There were visible sharp lines evenly spaced around the circumference. Auger analyses indicated that the sharp lines corresponded to the regions of the exposed stainless-steel substrate where the MgO/Au overlayer was completely removed. An Auger line scan is shown in Fig. 3 where the contour plot of the Fe peak height illustrates the sharpness of the lines and the separation between the lines. The separation between the Fe peaks matches the distance between the vane tips. The anode vanes must have had a focusing effect on the ion beams, which then sputtered the MgO/Au film and created the sharp lines. Our results were unable to determine whether the focusing effect arose from the gaps between the vanes where ions were generated by the multipactor effect (suggested by N. Dionne), or from the electrical field of the leading edges of the vanes (suggested by R. Vaughan). Discolored lines have long been observed on the cathode hubs of CFA tubes after operation. The compositional change from the MgO/Au coating to the substrate on the present cathode hub provides an opportunity to examine the nature of these lines.

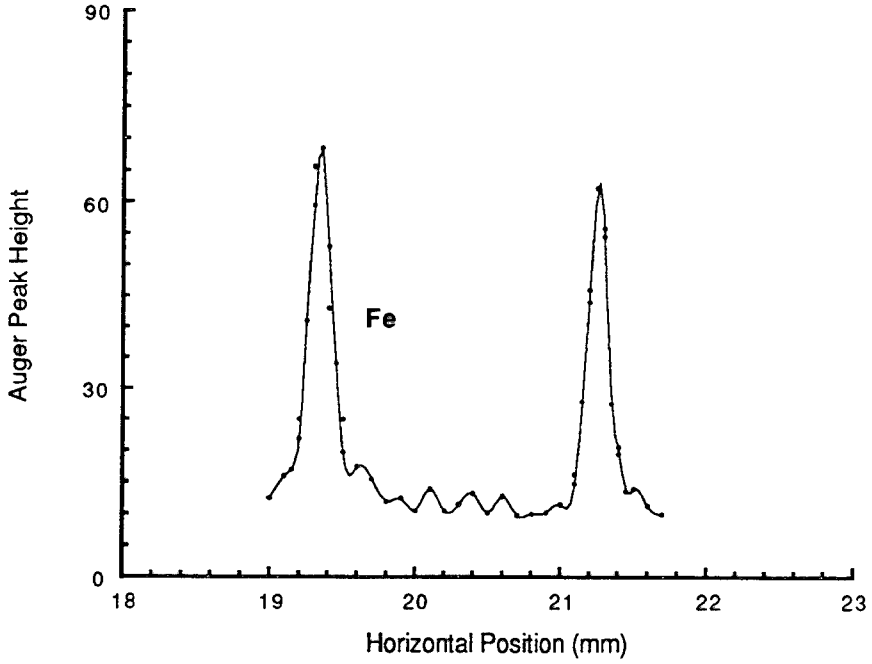


Fig. 3. Fe Auger peak height across two ion-etched lines

Both the electron beam and the ionized gases present in the CFA environment contributed to the general erosion of the MgO/Au film. Assuming the Knotek-Feibelmen

mechanism [8] for the electron-beam dissociation of MgO, we estimated that the electron-beam irradiation was responsible for the removal of 300-800 Å of the film in 560 hours. Using the experimental sputtering rate of a MgO/Au film, we calculated an erosion of 1200-2000 Å. Thus the total erosion due to both mechanisms was 1500-2800 Å, which is fairly close to 3400 Å, the difference between the original film thickness and the remaining film thickness.

The life time of a MgO/Au film can be longer than 560 hours by employing a much thicker coating. It is yet to be determined whether the higher resistivity of such a film will cause an adverse effect in CFA operations. Electron-beam bombardment and ionized-gas impingement are inherent to the CFA tube environment. The reliability and life time of a coated film will depend on the ability of the film to withstand the electron-beam and ionized-gas bombardment.

IV. Diamond

Diamond films can be many microns thick and still be very conductive by means of appropriate doping. The diamond films used in the present study are about 20 μm-hick free-standing films. The secondary-electron yield of diamond has been extensively studied by Mearini et. al. [9,10] and they found an exceedingly high δ_m, (as high as 30-50). For comparison, the oxidized Be cathodes employed in the AEGIS CFA tubes have δ_m = 2.6-2.8. Recently we received a batch of diamond samples from the researchers at Auburn university who had supplied the diamond samples for the Mearini study. In our studies, these samples showed poor secondary-electron yield and poor emission stability, but we are not yet able to identify the reasons for the poor emission. To aid in the development of a more reliable fabrication technique, it is important to understand the factors that govern the high secondary-electron yields of diamond films. In this paper we report on the dependence of the secondary-electron yield on the film conductivity and the type of surface termination.

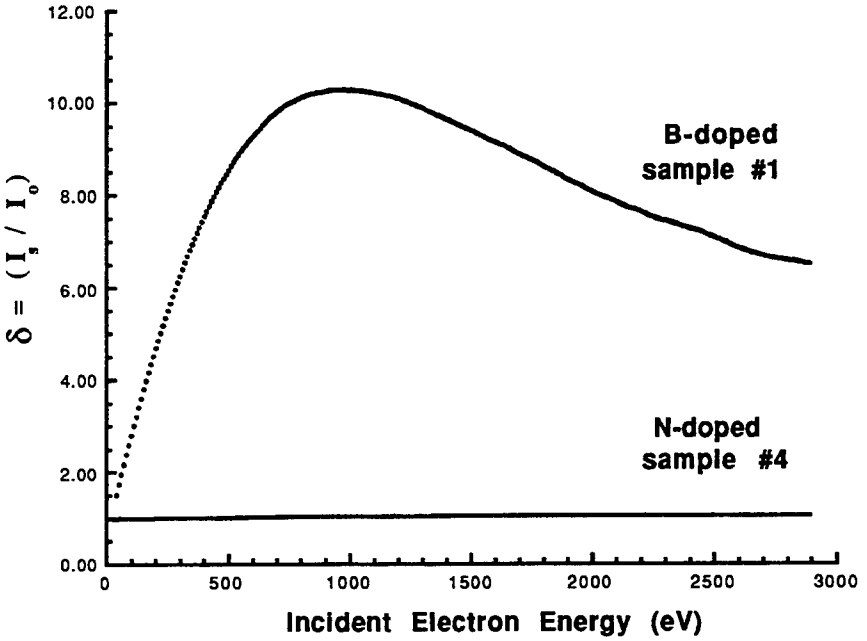


Fig. 4. Secondary-electron-yield curves from a B-doped diamond sample and a N-doped diamond sample.

Diamond samples are commonly doped with nitrogen (N) or boron (B). N creates a deep donor level in diamond, which lies 1.7 eV below the conduction band minimum.

Hence, at room temperature, N-doped diamond is non-conductive. On the other hand, B acceptors have an energy level 0.07 eV above the valence-band maximum, and therefore B-doped diamond is fairly conductive at room temperature. We have studied four diamond samples: samples #1 - #3 are B-doped and sample #4 is N-doped. The N-doped sample showed secondary-electron yields close to 1 for all energies (see Fig. 4), while all B-doped samples showed fairly high yields (see Fig. 5).

Since samples #1, #2, and #4 were prepared with a final hydrogenation step, they have hydrogen-terminated surfaces. Sample #3 was acid cleaned after hydrogenation and thus the surface is oxidized. Fig. 5 compares the secondary-electron-yield curves of the three B-doped samples. The oxidized sample has a δ_m which is more than a factor of two lower than those of the hydrogen-terminated samples. All data in Fig.s 4 and 5 were measured with pulsed incident beam at low current density such that the measured yields would not be changed by the probing electron beam. Although the desorption of hydrocarbons adsorbed on the as-received samples [11] would increase the total yield, the general conclusions of the study are not altered: electrical conductivity is necessary for the secondary-electron-emission process, and hydrogen termination is essential to the high secondary-electron yield of diamond surfaces.

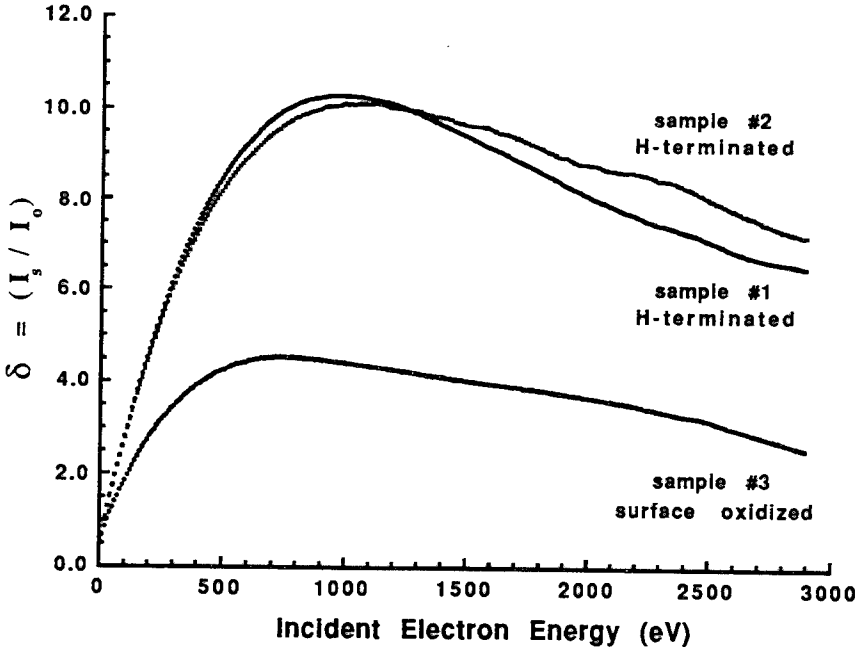


Fig. 5. Secondary-electron-yield curves from samples #1 and #2, which are hydrogen terminated, and sample #3, which is oxidized. All samples are B-doped diamond samples.

We have also studied the energy distribution of the emitted secondary electrons. Fig. 6 compares the energy-distribution curve from a hydrogen-terminated sample with that from the oxidized sample. A sharp peak just above the emission threshold is present in the energy-distribution curves of all hydrogen-terminated samples. Similar sharp peaks were observed in the photo-emission spectra of diamond surfaces. Himpsel et. al. [12] interpreted the feature to be due to "quasi thermalized secondaries in the lowest conduction band". Hydrogen-terminated diamond surfaces are known to have very low electron affinities, and some crystal faces, e.g. (111) and (110), have negative electron affinity. The low or negative electron affinity allows the large density of electrons piled up above the conduction band minimum to escape into the vacuum. The high electron concentration in the narrow low-energy region, within which electrons have a long escape depth, explains the exceedingly high secondary-electron yield observed with diamond.

Furthermore, we observed that the sharp peak became much larger with higher primary energies. At higher incident energy, the primary electrons penetrate deeper into the diamond. Since the secondary electrons travel from deeper within the interior, electron-electron collisions settle more and more electrons near the bottom of the conduction band. Oxidation removes the hydrogen and increases the electron affinity. The higher vacuum barrier prevents the high concentration of low-energy electrons to escape, and the secondary-electron yield drops. Fig. 6 shows clearly that on the oxidized sample the threshold of emission is at a higher energy and the large sharp peak is absent.

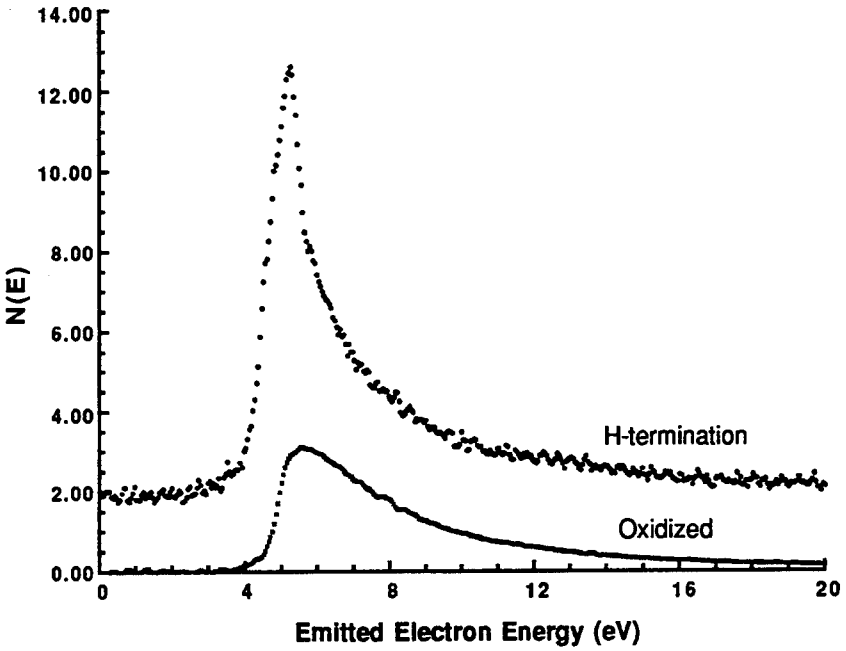


Fig. 6. Energy distribution curves of secondary electrons emitted from samples #1 and #3. The energy of the primary electron beam was 120 eV.

V. Summary

Insulators in general have high secondary-electron yields because the energy-loss mechanism of electron-electron collisions is diminished or unavailable to the low-energy secondary electrons. In order to function as an effective secondary emitter, electrical conductivity is needed to replenish the electrons lost in the secondary-electron-emission process. We have shown in our studies that non-conductive diamond is indeed a very poor secondary-electron emitter.

Surface adsorbates have a strong effect on secondary-electron emission. On BeO surfaces, carbon adsorption severely suppresses the secondary-electron emission. On the other hand, hydrogen adsorption is essential to the high secondary-electron yield of diamond.

Electron and ion bombardment cannot be avoided during operation of CFA tubes. The erosion by electron and ion beams severely limits the useful life of MgO/Au cermet cathodes. The ability to withstand electron and ion bombardment is essential to the reliability and long life of a secondary emitter. This should be an important test in the evaluation of a secondary-electron emitter material.

Acknowledgment

Drs. Pehr Pehrsson and James Butler of the Chemistry Division at NRL are our collaborators in the portion of the work involving diamond. One of the authors (AS)

wishes to acknowledge the helpful discussions with Mr. Richard Thomas. The work presented above is supported in part by NSWC/Crane Division.

References

[1] A. J. Dekker, *Solid State Physics, Advances in Research and Applications*, edited by F. Seitz and D. Turnbull (Academic Press, New York, 1958), Vol. 6, p. 251.
[2] O. Hachenberg and W. Brauer, *Advances in Electronics and Electron Physics*, edited by L. Marton (Academic Press, New York, 1959), p. 413.
[3] A. Shih, J. Yater, C. Hor and R. Abrams, IEEE Trans. Electron Devices **41**(12), 2448 (1994).
[4] V. Henrich and J. Fan, Appl. Phys. Lett. **23**(1), 7 (1973).
[5] V. Henrich and J. Fan, Surf. Sci. **42**, 139 (1974).
[6] V. Ritz, Surf. Interface Anal. **15**, 173 (1990).
[7] V. Ritz, A. Shih and B. Sobocinski, Surf. Interface Anal. **18**, 514 (1992).
[8] M. Knotek and P. Feibelman, Surf. Sci. **90**, 78 (1979).
[9] G. Mearini, I. Krainsky and J. Dayton, Surf. Interface Anal. **21**, 138 (1994).
[10] G. Mearini, L. Krainsky and J. Dayton, Y. Wang, C. Zorman, J. Angus and R. Hoffman, Appl. Phys. Lett. **65**(21), 21 (1994).
[11] B. Thomas, J. Russell, P. Pehrsson and J. Butler, J. Chem. Phys. **100** (11), 8425 (1994).
[12] F. Himpsel, D. Eastman, P. Heimann and J. van der Veen, Phys. Rev. B **24** (12), 7270 (1981).

INVESTIGATIONS OF NOISE MECHANISMS IN A REENTRANT CROSSED-FIELD AMPLIFIER

Robert MacGregor[1], John Z. Ye[1], Chung Chan[1], and Thomas E. Ruden[2]

[1] Plasma Science & Microelectronics Laboratory, Northeastern University, Boston MA

[2] School of Engineering Technology, Northeastern University, Boston MA

ABSTRACT

At Northeastern University, two experimental crossed-field amplifiers at RF frequency have been in operation as test vehicles to study basic and non-linear device physics, noise mechanisms, and examine numerical techniques for computer simulation codes. Our research has taken up a combined approach of *in situ* plasma diagnostics and computer simulations to examine phenomena occurring within the crossed-field gap. The device has been operated in different regimes such as, non-reentrant, fully reentrant, reentrancy controlled, and emitting sole arrangements. Comparison between experimental results and results of the MASK simulation code have been made for various operating parameters under these regimes.

As device gain is a result of well formed electron bunches, or spokes, noise generation can be related to other physical processes such as reentrant electrons, secondary emission, and electron hub instabilities. We have shown that decreasing the amount of reentrant electrons does reduce the noise level, but this may not be a practical solution to the noise problem due to reduced system gain. We are now examining the effects of secondary emission and electron hub characteristics. We have seen electron hub instabilities in the form of discrete frequencies which tune with magnetic field and are presently looking at the effects of RF drive on these oscillations. Examining the wideband frequency spectrum, non-linear effects are present. As the drive power increases, lower frequency components are suppressed and new frequency components are generated closer to the carrier. Higher power operation shows increased modulation close in to the carrier signal as the RF drive increases. Device simulations also show similar results. Results are reported.

I. INTRODUCTION

As the new age of wireless communication becomes more advanced, strict bandwidth management will be of major importance in the development of microwave power sources. Advanced design schemes and techniques for improved device performance and low cost will be necessary for the development of next generation crossed-field devices. Crossed-field devices have been the fundamental source in many applications due to their capability to provide high levels of microwave power. These devices have been in use for more than fifty years and, although advancement in the technology has been evident, larger strides in device improvement are necessary for increased application in industrial and commercial markets.

Microwave tube design involves extensive analysis in various areas of technology. Typical designs are comprised of electrical, mechanical, thermal, and material engineering issues. As a highly creative, multidisciplinary process, tube design often advances the state-of-the-art in physics, engineering, and manufacturing. Although new tube design poses electromagnetic design challenges, the other issues frequently consume equivalent design resources. As next generation designs will incorporate advanced techniques for the overall improvement in device operation, the need for reliable computational tools will become essential. Numerical models for use in the design of microwave tubes are under development and are reaching advanced levels. This necessitates the need for experimental devices with extensive diagnostics. Systems of this type

will be important for the design, development, and verification of algorithms for the simulation of the various design aspects of microwave tubes.

We have designed and constructed crossed-field amplifiers (CFAs) of linear and circular configuration to provide measurements of the interaction region during amplification, verifications of numerical simulation codes, and to study possible noise sources. The CFAs are designed for operation at 100 to 500 MHz, low power, and large in dimension to allow for the insertion of probes for plasma diagnostics. Typically, the CFAs are operated in the injected beam format, but we have incorporated various materials into the circular device to provide for secondary emission operation. We have shown the effective use of our unique *in situ* plasma diagnostic techniques for the measurement of electron density, electron energy, and local RF fields in the interaction region of our previous crossed-field amplifier experiments[1-6]. Our experimental systems will be used extensively to provide information for the verification and advancement of the present computational tools. Comparisons of the measurements with theories and simulations, such as the MASK code[7,8], will provide, not only verifications, but also may give insight into new designs.

The circular format device has been operated in various configurations such as, non-reentrant, fully reentrant, reentrancy controlled, and emitting sole configurations [1]. In this paper we present experimental and computational results of device performance and also examine mechanisms which may lead to noise in the circular CFA.

II. EXPERIMENTAL DEVICE

Crossed-field amplifier devices operate on the principle of energy transfer between electrons and RF electric fields. The energy transfer occurs when $\upsilon_e \approx \upsilon_p$, where υ_e is the electron drift velocity and υ_p is the RF phase velocity as seen by the electrons [5]. The electron drift velocity is controlled by the applied static electric and magnetic fields whereas the RF phase velocity is determined by the anode slow wave structure. The slow wave structure functions to retard an applied RF signal in order to match the circuit phase velocity to the electron drift velocity. Potential energy from the electrons is transferred to the RF field as the electrons bunch and drift toward the anode upon experiencing a favorable RF electric field component, E_{RF}, from the slow wave. As the electrons travel along the circuit, ϕ direction for circular geometry, the RF electric field will oppose the motion of the electrons which will cause the electrons to drift towards the anode (radially outward) with velocity, $\upsilon_r = E_{RF}/B$, hence transferring potential energy to the field while maintaining a constant azimuthal velocity component, υ_ϕ. In this case, gain is observed. The RF electric field can also accelerate the electrons in which case the field transfers energy to the electrons such that the electrons are driven towards the sole electrode. Optimum performance is achieved when the electrons reach the synchronous velocity which is slightly greater than the RF phase velocity, therefore a majority of the electrons will be driven toward the anode.

The design of the circular CFA uses parameters such that diagnostic probes can be placed in the interaction region without disturbing the operation of the device. This leads to a physically large system as described below. The frequency range of 100 MHz - 500 MHz was chosen due to the fact that the wavelength is much larger than the dimensions of the diagnostic probes. This allows for probe measurements with minimum perturbation of the electric field and space charge. Specific details of the design can be seen in [1]. The device structure is shown in **Fig. 1.**

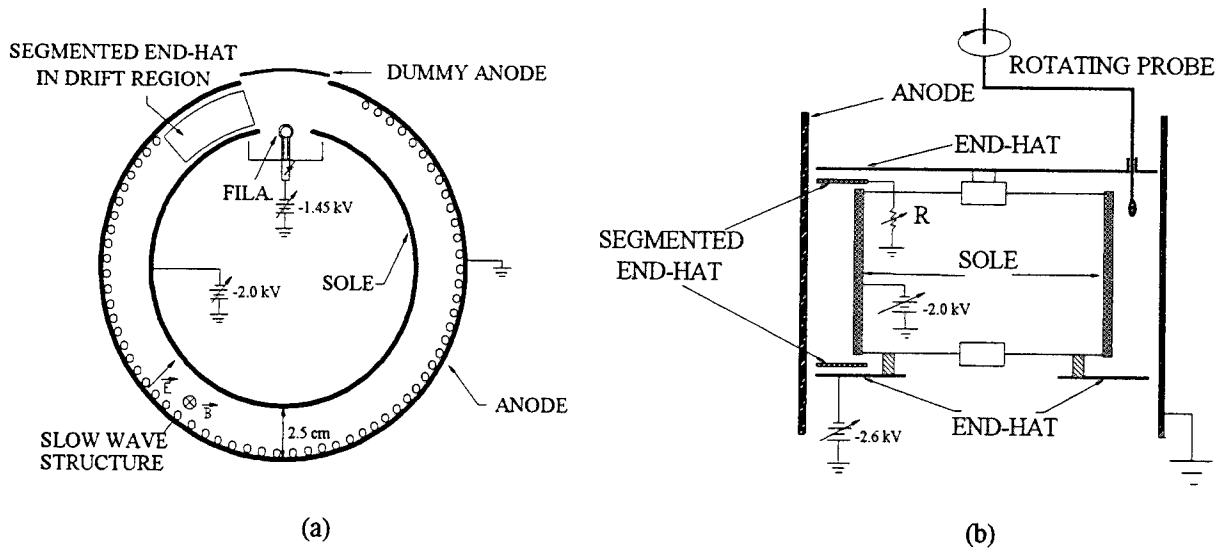


Fig. 1 (a) Configuration (top view) of the circular CFA showing the electron drift region and the segmented end-hats. (b) Configuration (cut-away view) of the circular CFA with segmented end-hats and *in situ* probe.

III. MASK SIMULATION CODE

The MASK code [7,8] is a 2 1/2 dimensional, finite difference, time domain, particle-in-cell simulation code. The code follows three positions and three velocities for each simulation particle and allows for three components of the electric and magnetic fields, but the electric and magnetic fields can only vary in two dimensions, hence 2 1/2 dimensional. Finite differences of various physical quantities are defined on a discrete grid and are used to approximate differential operators. Particle-in-cell computation corresponds to the division of the physical space into cells by a grid. Quantities such as charge density, currents, potentials, and fields are computed only on this simulation grid. Field values are interpolated to the location of the particles, which may be located anywhere within the physical space. MASK can be operated as either an electrostatic code or as a fully electromagnetic code as it advances the full relativistic equations of particle motion, for all particles.

The MASK code has been adapted for crossed-field amplifier simulation by SAIC's Applied Physics Operation. MASK can be used to simulate injected beam devices as well as distributed emission operation. Other capabilities include the representation of forward or backward wave slow wave structures, with or without loss, on the anode and/or cathode, primary and secondary emission, and space charge fields. An extensive diagnostic package is also included with the MASK code. Included are field, particle, emission, and slow wave circuit diagnostics. The MASK CFA simulation cycle can be seen in **Fig. 2.**

III. REENTRANT CONFIGURATION

The reentrant device allows for controllable electron recirculation. We have shown [1] that increasing the number of recirculating electrons increases the noise level in this device (**Fig. 3**). Various experiments and numerical simulations (MASK) to further characterize the Northeastern

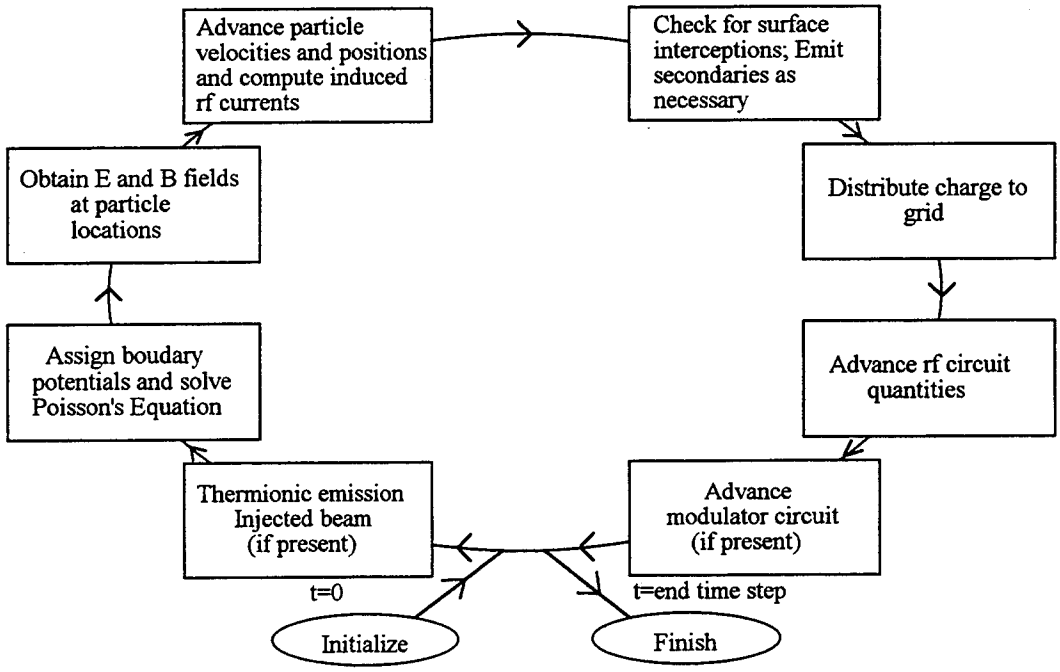


Fig. 2 MASK CFA Simulation cycle.

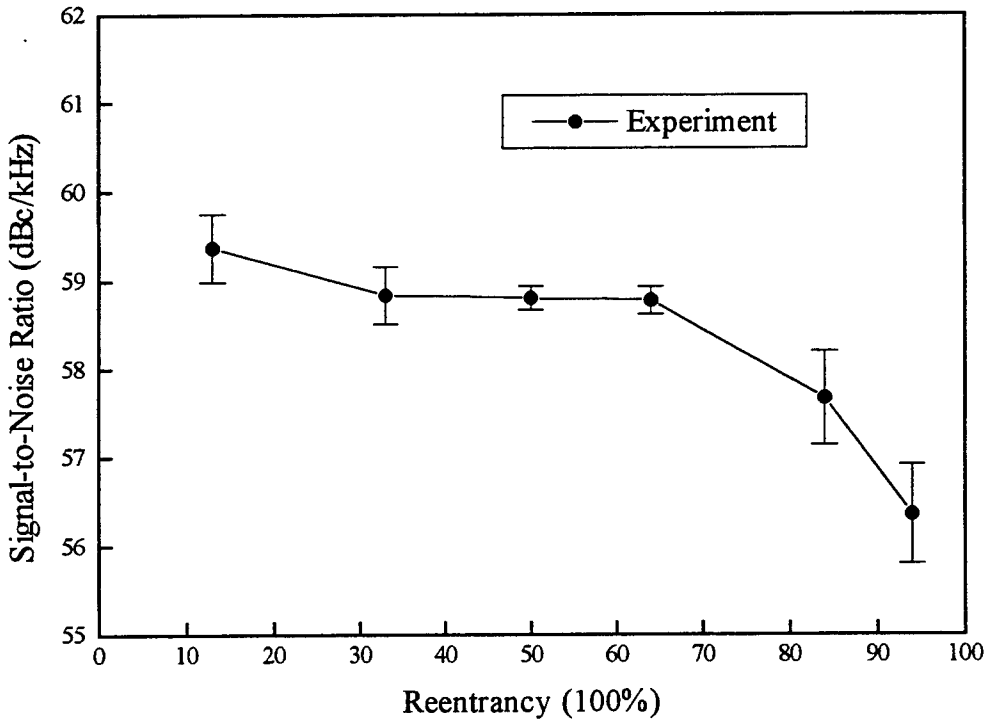


Fig. 3 Experimental narrowband signal-to-noise ratio vs. percent reentrancy.

reentrant CFA have been accomplished. The MASK model of the reentrant device requires the representation of the beam injector as an emitting surface defined on the grid which is assigned a -1.45 kV bias corresponding to the experimental condition. The slow wave structure is also modeled using the observed experimental parameters. Experimentally, we observe a 2 dB circuit loss (insertion loss), this is modeled as a distributed loss in the code. The loss is distributed equally over the 104 circuit sections. We have also examined the effect of secondary emission in the simulation by adjusting the secondary yield coefficient of the sole material. Experimental results for gain vs. sole bias and gain vs. beam current have been compared to simulation results as can be seen in **Fig. 4.** The simulation parameters correspond to the experimental parameters with the exception of the variable secondary yield parameter. As we can see, this curve contains multiple peaks in which MASK has predicted quite well. This is a very important benchmark in the code development. According to a guiding center theory [9,10], the double gain peaks (see **Fig. 4**) which have been observed both through the experiment and in the MASK simulation could be a feedback effect of the recirculating space charge [9,10]. The voltage difference between the peaks of this curve leads to $E \times B$ drift velocities that cause a change in the electron transit time that is equal to one RF period. This result may also be very important in the study of feedback effects on the performance of CFA's [10].

We have examined the effect of secondary emission on system performance using the variable secondary yield parameter in MASK. Simulations have been performed with secondary yields of 0, 1, and 1.5 (**Fig. 4**). We note that the simulation case in which the secondary yield equal to 1 closest matches the experimental data. Experimentally, we do predict a secondary yield of 1 due to the fact that no net sole current is observed. It appears that MASK is quite sensitive to secondary emission from the sole.

For further comparison to the MASK simulation we have examined the wideband noise. This is accomplished by calculating the signal-to-noise ratio by using the statistics of the I (In-phase) and Q (Quadrature) channel signals. We have developed an experimental technique to produce this result. The amplifier output signal is acquired from a Tektronix TDS 520A digitizing oscilloscope through a general purpose interface bus (GPIB) installed in an IBM compatible computer. The signal is then mixed with mathematical cosinusoidal signals which are in phase and 90 degrees out of phase with the input signal. Using an FFT filter, we then filter out the second harmonic, produced by the mixing operation, resulting in the I and Q channel signals. The mean and standard deviation are then calculated for each channel and the signal-to-noise ratio is subsequently defined as

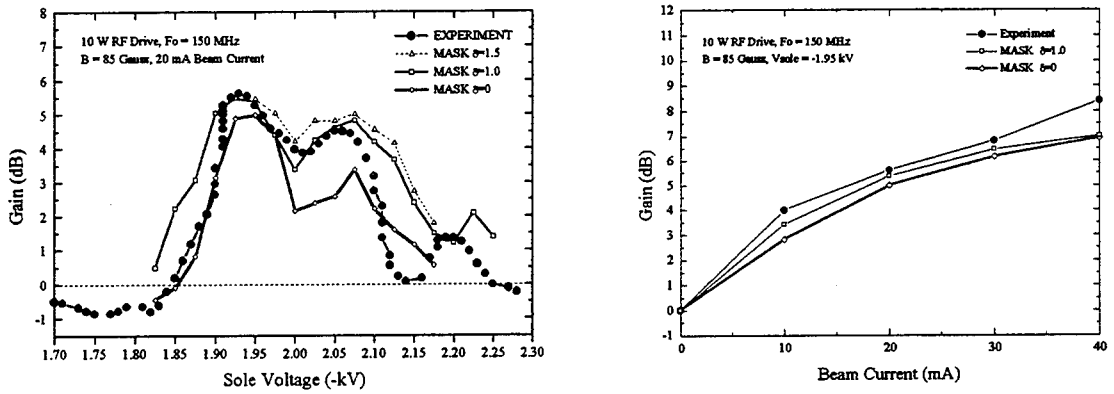
$$\frac{S}{N} = 10\log_{10}\left(1+\frac{\langle I_n\rangle^2+\langle Q_n\rangle^2}{\sigma_I{}^2+\sigma_Q{}^2}\right), \qquad (1)$$

where σ_I and σ_Q are the standard deviations of the I and Q channel signals, respectively, and

$$I_n(t) = 2V_n(t)\cos(\omega t+\phi_0) \text{ and } Q_n(t) = 2V_n(t)\sin(\omega t+\phi_0) \qquad (2)$$

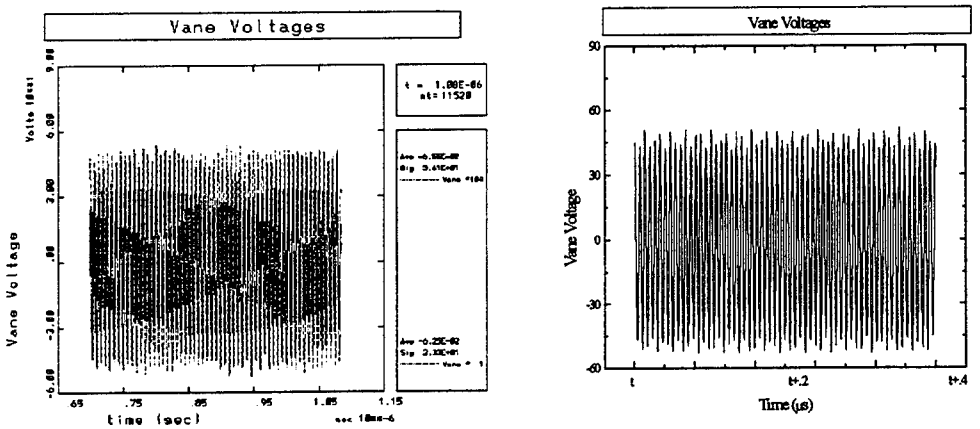
are the in-phase and quadrature components and $V_n(t)$ is the voltage signal on vane #n.

The output signals from the MASK simulation and the experiment are shown in **Fig. 5.** Calculations using eight experimental waveforms for the fully reentrant case show that the device



(a) (b)

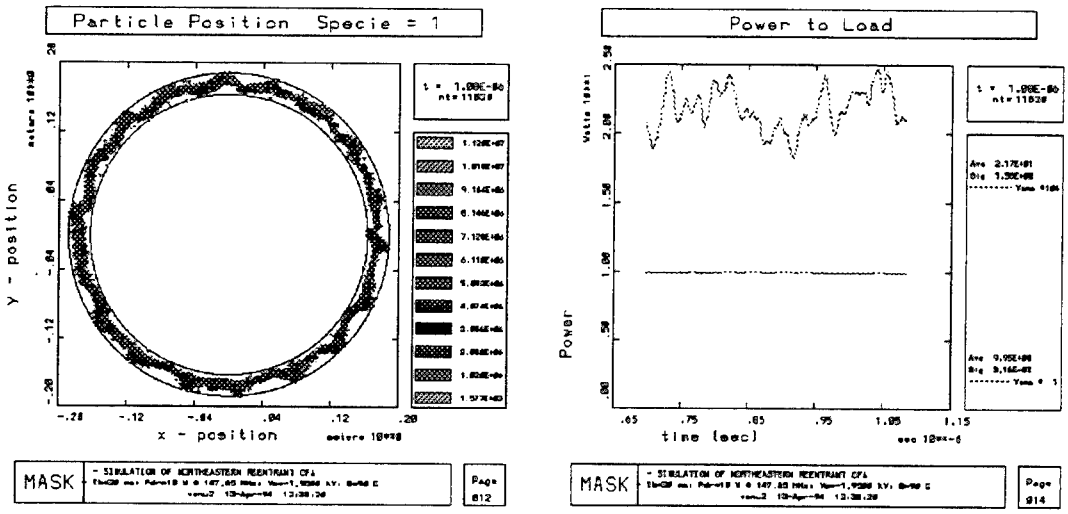
Fig. 4 (a) A comparison of device electronic gain versus sole voltage operating in the fully reentrant configuration. MASK simulations have been performed for three different values of secondary yield. (b) A comparison of device electronic gain versus beam current operating in the fully reentrant configuration. MASK simulations have been performed for two different values of secondary yield.



(a) (b)

Fig. 5 Amplifier output waveforms a) simulation, b) experiment.

signal-to-noise ratio is 25.75 dB ± 1.01 dB as compared the MASK result of 24.25 dB. Diagnostic plots produced by the MASK code can be seen in **Figs. 6**. Figure 6a shows a snapshot of the particle position at t ~ 1.08 μS, the end of the simulation. Figure 6b shows a time history plot of the power delivered to the load. As we can see, this quantity fluctuates over time, this relates to the noise in the device. The time frame here is approximately .5 μS.



(a) (b)

Fig. 6 (a) MASK output. Particle position snapshot. (b) MASK time history plot. This plot represents the power delivered to the load over a time period of approximately .5 microseconds.

IV. EMITTING SOLE CONFIGURATION

A. Device Modification

The key technical issue upon conversion of the reentrant CFA from beam-injection to emitting-sole operation is to develop and maintain an active secondary emitting surface at the sole. We use the original beam-injection mechanism with altered beam optics to provide primary electron bombardment which initiates a chain reaction of secondary emission over the entire sole surface. The RF fringing field further enhances the process leading to a high density electron hub surrounding the sole. For our low power CFA, secondary emitters with relatively high yield and low cross-over energy is necessary.

Experiments have been underway to accomplish emitting sole operation in our circular CFA. Our approach is to incorporate new materials to the CFA sole. The primary beam bombardment is provided by the electron source biased more negatively than the sole electrode, this configuration allows for the adjustment of the primary bombardment energy. The net sole current is monitored as an indication of emitting sole operation. The aluminum and aluminum oxide (grade 6061, part magnesium) sole was used for initial testing, and found to be insufficient to provide enough secondary emission. We then examined the secondary emission properties of pure (grade 1100) aluminum. This material was incorporated into the circular CFA and successfully used to achieve emitting sole operation.

B. Device Operation

Operating parameters under this regime have been increased, as compared with previous experimental configurations [1]. The input RF power is now on the order of hundreds of watts. The electric and magnetic fields have been increased by approximately 50%. The operating sole

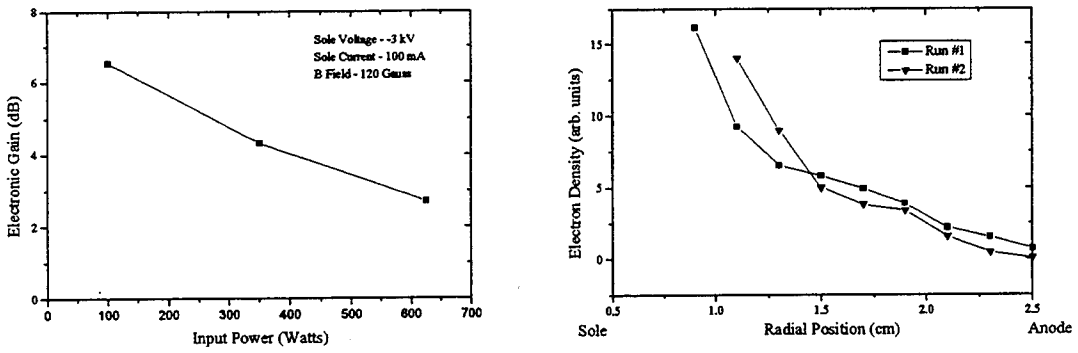
voltage is now -3.0 kV and the magnetic field is 120 Gauss. We are now operating at approximately $\omega_c/2$. We have seen up to 150 mA of emission from the sole.

Basic measurements used to partially characterize the device have been completed. We have examined the electronic gain versus input power. The sole emission current was held constant at 100 mA. The results can be seen in **Fig. 7a**. *In Situ* probe measurements within the interaction region have been used to show the existence of an electron hub. Radial density measurements near the output end of the device clearly show a large increase in electron density close to the sole. Results of these measurements are shown in **Fig. 7b**.

IV. Crossed-Field Noise Mechanisms

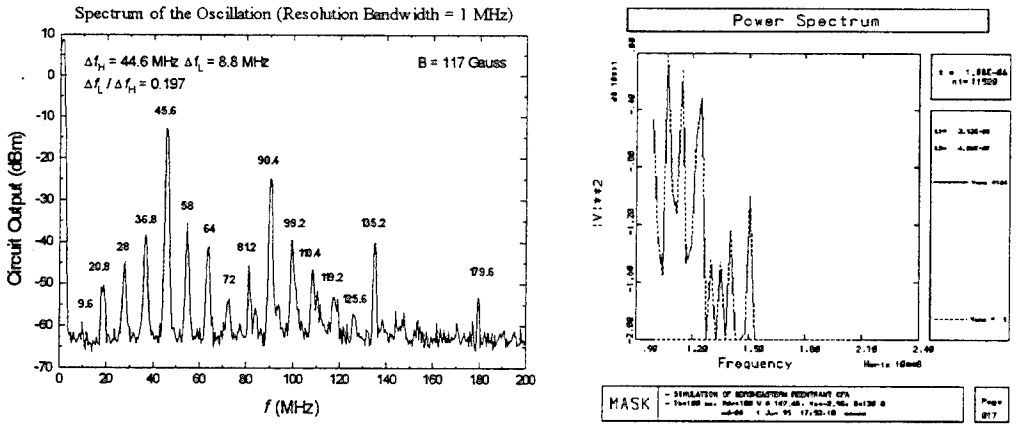
A. Operation without RF Drive

A physical mechanism of the instability associated with a static, reentrant crossed-field electron flow is the self-excitation of azimuthal space charge waves. The wavelength of the eligible oscillations satisfies $K \cdot \lambda_K = L$, where L is the azimuthal length of the cylindrical geometry, and K is the mode number. This relation determines the frequency of the possible oscillations assuming a match between the phase velocity and azimuthal component of the electron velocity, or $v_{ph} = r\,(d\phi/dt)$. As the electron azimuthal velocity varies across the sole-anode interaction space, the resulting oscillation frequencies also vary, i.e. oscillation frequency depends upon the position of the hub electrons which excite the wave [11]. As the magnetic field is increased the secondary hub will be confined closer to the sole surface, and based on Brillouin modeling, the frequency increases as the thickness of the Brillouin hub increases, i.e. as the magnetic field decreases. **Figure 8a** shows the wide band spectrum of our device operating without RF drive. This picture shows numerous oscillations spaced approximately 8 MHz apart, also, higher power oscillations exist and are space approximately 45 MHz apart. Our observation



(a) (b)

Fig.7 (a) Device electronic gain versus input power. (b) Radial electron density measurements taken near output segment of device. This shows the existence of an electron hub as we move to within 1 cm from the sole.



(a) (b)

Fig.8 (a) Experimental output spectrum without RF drive (b) MASK output spectrum without RF drive.

has determined that the high power oscillations are very stable and the intermediate oscillations are unstable, both in terms of amplitude stability. As we operate the device in the emitting sole configuration, both primary electrons (beam injection) and secondary electrons (emission) are present. The stable high power peaks may correspond to space charge waves caused by the primary beam injection, which is a stable, controllable process. Whereas the lower power oscillations (8 MHz spacing) may very well be caused by the secondary electrons which will typically be confined closer to the sole explaining the lower frequency spacing. Also the unstable nature of the oscillations may correspond to an unstable secondary emission process. MASK simulations of this mode of operation also shows similar behavior, i.e. multiple oscillations spaced approximately 7.4 MHz apart (**Fig. 8b**).

B. The Effect of RF Drive

At low RF drive level, the typical effect is a change in the amplitude of the oscillation lines. The amplitude of the high power oscillations ($\Delta f \sim 45$ MHz) is suppressed by about 10 dB; while the lower power oscillations ($\Delta f \sim 8$ MHz) are generally promoted, indicating an increase of sole secondary emission. The low power oscillations are immediately modulated by the carrier frequency, forming distinct side band. As the drive power increases, lower frequency components are suppressed and new frequency components are generated closer to the carrier. Accompanied with the high drive, sole secondary emission also increases significantly. In **Fig. 9** which shows a case of 62 W drive, new fundamental frequencies (e.g., 4 MHz) between the 8 MHz low modes emerge from a broad band spectrum sideband from 80 MHz to 140 MHz. These results set the stage for the examination of the narrow band spectrum and the effect of secondary emission.

C. The Effect of Secondary Emission on Close In Noise

An examination of the narrow band spectrum close to the carrier reveals interesting phenomena. These experiments are designed to look at the noise levels in the output signal of the CFA for various levels of primary and secondary electron current. **Figure 10a** shows the narrow

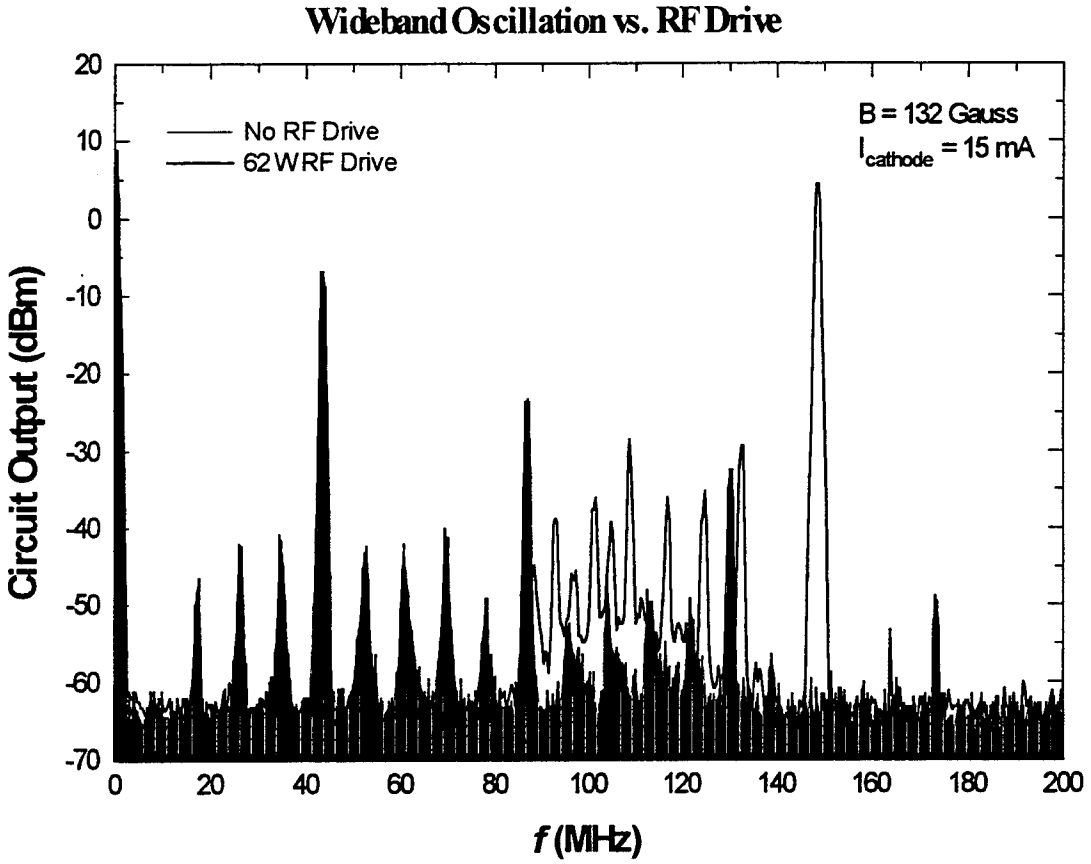


Fig. 9 The effect of 62 watts of RF drive on the out put spectrum.

band spectrum for three operating cases, 1) 200 mA of primary current and 0 mA of secondary current, 2) 175 mA of primary current and 25 mA of secondary current, and 3) 150 mA of primary current and 50 mA of secondary current. As we can see, the noise floor increases drastically with the introduction of secondary emission, also we see distinct sideband structures forming approximately 500 kHz out from the carrier. The sideband structures become very evident as the secondary emission is increased to 50 mA. Due to the frequency offset of the sidebands, this phenomena may be caused by external mechanisms such as power supply resonances. To examine this possibility, a 2 uF capacitor was place in parallel with the CFA to change the loading; the results are shown in **Fig. 10b**. As we can see, the sideband structures have been suppressed, but the noise floor due to the secondary emission is still very evident. Here the noise power is calculated by averaging the spectrum power density across a noise band defined to exclude the carrier signal. We then calculated the signal-to-noise ratio (S/N) using this averaged value as the decibel value below the peak signal per unit frequency (dBc/Hz). **Figure 11** is a plot of the S/N of the circuit output as a function of the net sole emission current and the RF drive level. The range of the calculated S/N is comparable with that of a practical emitting-sole CFA. We see that, at 200 W RF drive, S/N degrades by more than 10 dB as the sole current increases from zero to 25 mA, which indicates that the participation of a small amount of

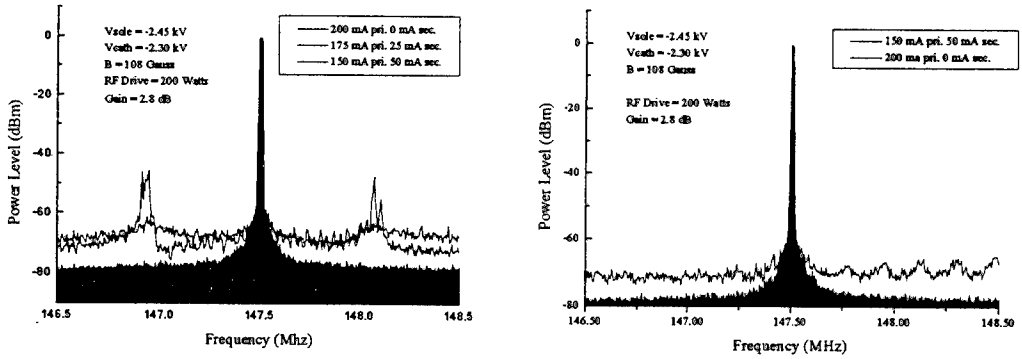


Fig. 10 (a) Output spectrum for three cases, 1) 0 mA secondary electron current (shaded region), 2) 25 mA secondary electron current (sidebands starting to form), and 3) 50 mA secondary electron current (distinct sideband spikes). (b) Output spectrum, with parallel capacitor, for two cases, 1) 0 mA secondary electron current (shaded region), 2) 50 mA secondary electron current (sidebands have been suppressed).

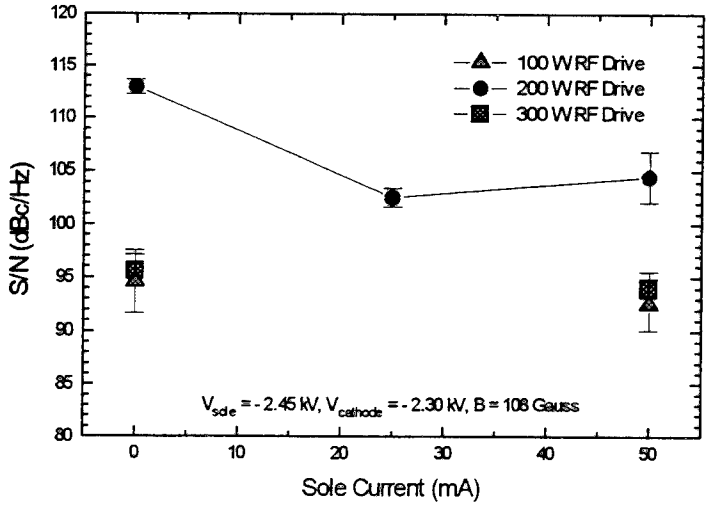


Fig. 11 Calculated signal-to-noise ratio based on the measured spectrum as a function of RF drive level and sole secondary emission.

secondary electrons can introduce a large amount of close-in noise. In the sole current range greater than 25 mA, the S/N deterioration seems to stop. Beyond 50 mA sole current, data is not available at this point as to predict whether there will be a come back for the S/N.

The 200 W drive level in **Fig. 11** is approximately where the reentrant amplifier system has its peak gain. Higher RF drive would result in a decreased gain due to insufficient DC beam power. At 100 W and 300 W drive level, the amplifier is at least 15 dB noisier.

V. CONCLUSIONS

We have developed experimental systems that will provide insight into next generation of designs for microwave tubes, specifically crossed field amplifiers. The experimental crossed field amplifiers have also provided verification of the MASK simulation code. Comparisons of various overall device operating parameters have been made with good agreement.

The emitting sole configuration is very important due to the fact that the operating mode is that of a practical device. We have examined this configuration under various conditions and RF drive levels. Initial evidence that the secondary electron current may generate noise or modulation components close in to the carrier as a function of RF drive exists. Also, evidence of an increased noise floor with the introduction of secondary emission is very prominent. Noise in these devices can also be introduced into by external sources such as power supply interaction. Noise in crossed-field devices is very complex and can be generated by numerous sources. Measurement techniques will be further advanced for more detailed measurements and comparisons of the emitting sole device.

ACKNOWLEDGMENT

The authors would like to thank Dr. D. Chernin for all the support in using the MASK simulation code. The author's would also like to thank Mr. H. McDowell, Mr. A. MacMullen, and Dr. S. Riyopoulos for useful discussions. They also thank Mr. Joe Genevich for his technical support. This work has been supported by the DoD Vacuum Electronics Initiative and managed by the Air Force Office of Scientific Research under Grant # AFOSR-91-0371 and is also supported by the Navy and the NSF under Grant # ECS-9120085.

REFERENCES

[1] R. MacGregor, C. Chan, J. Ye, and T. E. Ruden, "A Circular Crossed-Field Amplifier for In Situ Measurements, Study of Reentrant Beam Effects, and Comparison with Numerical Simulation," *IEEE Trans. Electron Devices*, Vol. 41, No. 8, p. 1456, August, 1994.

[2] J. Ye, C. Chan, R. MacGregor, and T. Ruden, "An Experimental Investigation of the End-Hat Effects in a Crossed-Field Amplifier via 3-D Electron Density Measurements," *IEEE Trans. Electron Devices*, vol. 41, no. 2, pp. 258 - 265, 1994.

[3] J. Browning, C. Chan, J. Ye, T. Ruden, and G. Dombrowski, "Electron Plasma and Wave Measurements in a Crossed-Field Amplifier and Comparison with Numerical Simulations," *IEEE Trans. Electron Devices*, Vol. 39, pp. 2401 - 2407, 1992.

[4] J. Browning, C. Chan, J. Ye, R. MacGregor, and T. Ruden, "Measurements of End-hat Effects in a Crossed-Field Amplifier," *Technical Digest IEDM 92*, pp. 755 - 758.

[5] J. Browning, C. Chan, J. Ye, and T. Ruden, "A Low Frequency Crossed-Field Amplifier for Experimental Investigations of Electron-RF Wave Interactions," *IEEE Trans. Plasma Science*, Vol. 19, p. 598, 1991.

[6] J. Browning, C. Chan, J. Ye, G. Dombrowski, and T. Ruden, "In situ Measurements and Numerical Simulations of Wave-Electron Interactions in a Crossed-Field Amplifier," *Appl. Phys. Lett.*, vol. 59, p. 3384, 1991.

[7] D. Chernin, A. Drobot, G. Hilfer, and S. Riyopoulos, "Computer Studies of Noise Generation in Crossed-Field Amplifiers," *Technical Digest IEDM 91*, p. 593.

[8] D. Chernin, "MASK Code Release Workshop," SAIC, McLean, VA. 1993.

[9] S. Riyopoulos, "Nonlinear Gain Computation for the Sheet Beam Crossed-Field Amplifier," To appear in *IEEE Trans. Plasma Science*, 1994.

[10] S. Riyopoulos, "Feedback Induced Noise In Crossed-Field Devices," *IEEE Trans. Plasma Science*, Vol. 20., p. 360, 1992.

[11] John Z. Ye, "Experimental investigations of electron space charge instabilities and noise mechanisms in a reentrant crossed-field amplifier with distributed cathode emission," Ph. D. Dissertation, Northeastern University, Boston, MA, 1995.

Rep-Rate Operation of a Magnetically Insulated Line Oscillator (MILO)

S.E. Calico and F.J. Agee
PL/WSR
3550 Aberdeen Ave. SE.
Kirtland AFB, NM 87117-5776

M.C. Clark and R.W. Lemke
Sandia National Laboratories
Albuquerque, NM 87185

M.C. Scott
Maxwell Laboratories, Inc.
Albuquerque, NM 87119

ABSTRACT

The Electromagnetic Sources Division of the Advanced Weapons and Survivability Directorate at the Phillips Laboratory is dedicated to the development of HPM sources. This paper will report on the single-shot and rep-rate work done on a magnetically insulated line oscillator (MILO). The MILO is a linear magnetron type device with the bias magnetic field supplied by the current flowing through the tube, hence no externally applied magnetic field is required. This work concentrates on the axial extraction of the microwave power in contrast to most of the previous work which concentrated on the radial extraction of power. Theory has predicted and experiments have shown that a number of parameters, including but not limited to, the boundaries at the ends of the slow wave structure (SWS), the location of the emission region, the method of launching the beam, the anode-cathode gap, and the number of cavities, all have a significant effect on the operation of the tube. A number of tests at diode voltages from 150 kV to over 500 kV have been conducted to gain a better understanding of the mechanisms controlling the operation of the device. Additionally, some preliminary experiments at modest rep-rates have been conducted. To date RF powers over 1 GW for short pulses (<100 ns) have been achieved with the goal of further increasing the output power and increasing the pulsewidth to 100's of nanoseconds. The results of the these experiments and corresponding simulations are reported here.

INTRODUCTION

The MILO is attractive as a source of high power microwaves because it is compact, lightweight, requires no external magnetic field coils and operates at low impedance, typically less than 10 Ω. Operation at low impedance implies that 10's of GW of input power are available at modest pulser voltages (100's of kV). The primary drawback of the MILO is that since the bias

magnetic field is provided by the current flowing through the tube, only approximately 20% of the input power is available to be converted into RF energy.

The feasibility of a MILO as an HPM source has been investigated previously by a number of researchers[1-3] and references therein. These experiments concentrated on radial power extraction out of the cavities because of the inherent nature of the MILO to run very close to a pi mode (no power flow in the axial direction). A few hundred megawatts of power and 10's of Joules were extracted in this fashion. Work on the MILO was reinitiated because simulations with a plasma backfill have shown that the tube operates in a traveling wave mode (not the pi mode) allowing axial extraction and also, it has been predicted that the presence of the plasma backfill enhances the power output. The presence of the plasma neutralizes the space charge of the beam allowing more power to flow in the beam that is interacting with the slow wave structure (SWS), thus generating higher output power.

Experiments to date have studied the vacuum MILO (plasma fill is planned for FY96), and have produced microwave pulses slightly less than 100 ns in duration at powers over 1 GW. It has been found experimentally that the terminations at the ends of the MILO structure and the means of emitting or launching the electron beam into the SWS have dramatic effects on the operation of the tube. By incorporating the appropriate boundaries on the ends of the tube it can be made to operate at diode voltages over 500 kV with output powers of several hundred MW, where without these boundaries the tube never operated over 220 kV and at very low efficiencies, only producing approximately 100 MW of RF power. Through a combination of experiments and computer simulations other modifications were made that further improved the performance so that output powers over 1 GW at diode voltages of 500 kV have been achieved. After a description of the operation of the MILO and the experimental configuration, each of these enhancements to the tube and the performance under rep-rate conditions will be discussed.

MILO OPERATIONAL DESCRIPTION AND EXPERIMENTAL CONFIGURATION

A short description of the operational characteristics of the MILO, using Fig. 1 for reference, will be given. The reader is referred to a previous paper[4] for further details of the operation. A high-voltage pulse is delivered to the tube from the left and the microwaves are extracted from the right. Upon introduction of the high-voltage pulse there is emission along the length of the cathode. The current under the SWS and in the beam dump region is sufficient to cause magnetically insulated flow of the beam, that is, initially before the microwaves are produced the electrons flow parallel to the cathode axis under the SWS. This flow interacts with an electromagnetic wave, whose characteristics are determined by the SWS, and energy is transferred from the electron beam to the electromagnetic wave. The growing electromagnetic wave induces an RF voltage across the extractor gap which produces a TEM wave in the coaxial section around the beam dump. The TEM wave propagates down the short section of coaxial waveguide, is converted into a TM_{01} mode in circular waveguide, which is then radiated from a slant-cut or "Vlasov" antenna.

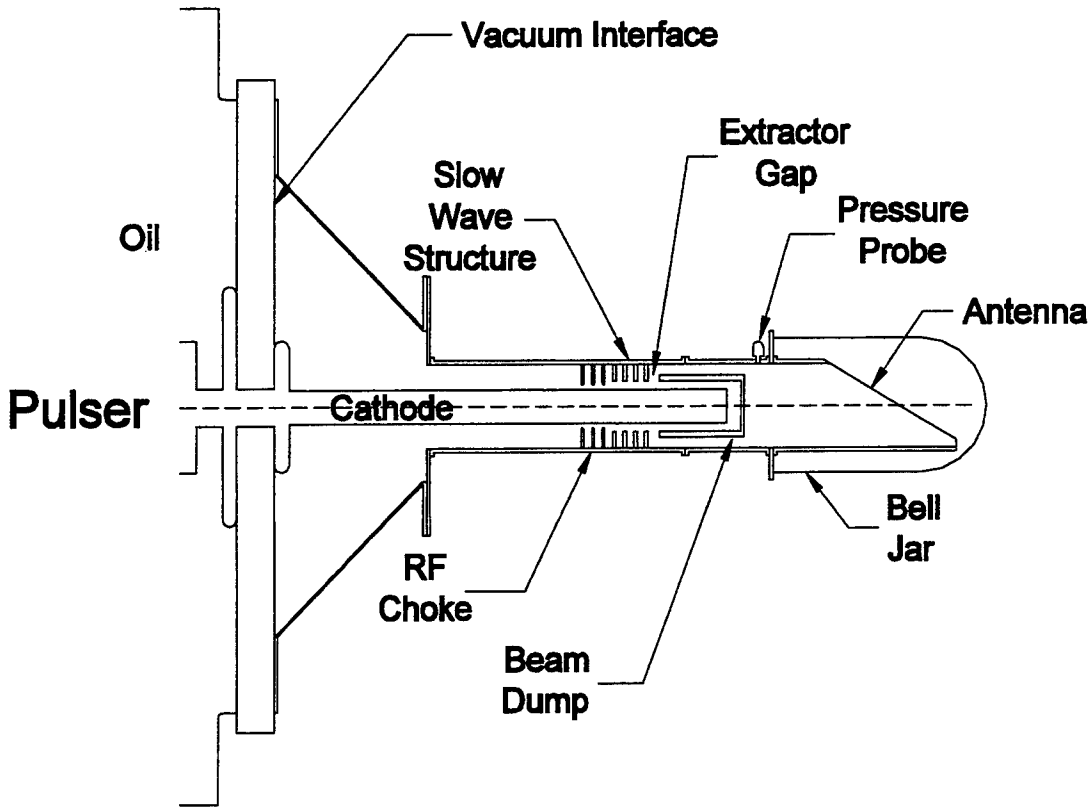


Figure 1. Schematic Diagram of the MILO.

The pulser that delivers the input voltage, depicted to the left in Fig. 1, is the Phillips Laboratory Rep-Rate Pulser[5]. It is a computer controlled, variable voltage (150-500 kV), variable impedance (5, 10, and 20 Ω), rep-rate (a few Hz to 10's of Hz depending on impedance and charge voltage) device. The MILO vacuum chamber is connected to the pulser through an acrylic vacuum interface. All components of the tube are fabricated of aluminum except for the beam dump which has a graphite sleeve on the inside to absorb the energetic electron beam. Velvet is used as the emitting surface and is fixed to the cathode with spray glue. It has been found that the location of this emission surface, or where the emission starts with respect to the beginning of the SWS is critical to the efficient operation of the MILO. The vanes are aluminum annuli with copper fingerstock around the outside circumference. The fingerstock allows adjustment of the vane spacing (SWS period) and the easy insertion and removal of the vanes for vane number variation. The beam dump is supported by two sets of two 6.35 mm diameter conducting rods which also serve as the current return path from the beam dump. The bell jar serves as the vacuum interface on the output end of the tube. Initially a mylar window was located in the circular waveguide section but at high power levels it suffers from electrical breakdown. The actual tube dimensions are: (1) starting from the left, the first three vanes (RF choke), the second three vanes, and the last vane (extractor vane) have inner radii of 7.62 cm, 8.57 cm, and 9.21 cm, respectively and are all 1.27 cm thick, (2) the SWS period (vane separation) is 3.81 cm, (3) the cathode radius is 5.72 cm, (4) the outer wall radius is 14.3 cm, (5) the inner and outer radii of the beam dump are 8.57 cm and 10.48 cm, respectively, and (6) the

cathode length extending into the beam dump is 12.7 cm. A diagram of a MILO simulation is shown in Fig. 2. It should be noted that the diagram is cylindrically symmetric about the z-axis, is not to scale, and only shows the MILO tube and a short section of the beam dump. A voltage pulse is introduced from the left and propagates to the right in Fig. 2. Electrons are emitted from the cathode, interact with the SWS and the RF power is extracted from the coaxial section through a perfectly transmitting boundary to the right. The electron trajectories in Fig. 2 illustrate the π-mode operation of the tube. In the π-mode, the electric fields in adjacent cavities are 180 degrees out of phase, which causes the electrons to be attracted to alternating cavities and repelled elsewhere.

MILO OPTIMIZATION

Experiments were initially performed with a MILO having 9 uniform vanes. During these early tests the importance of the upstream boundary, the RF choke, became apparent. Then, experimentally and through the use of computer simulations the importance of the downstream boundaries, the emission length, the number of cavities, and the dimensions of the extractor vane was investigated. In general the tube was optimized with the particle-in-cell code TWOQUICK[5] and then these modifications were implemented experimentally. This turned out to be a very effective method of optimization because the experimental results were generally in good agreement with the simulation predictions and the amount of hardware that actually had to be fabricated and tested was greatly reduced. Each of the modifications implemented to improve tube performance are discussed below.

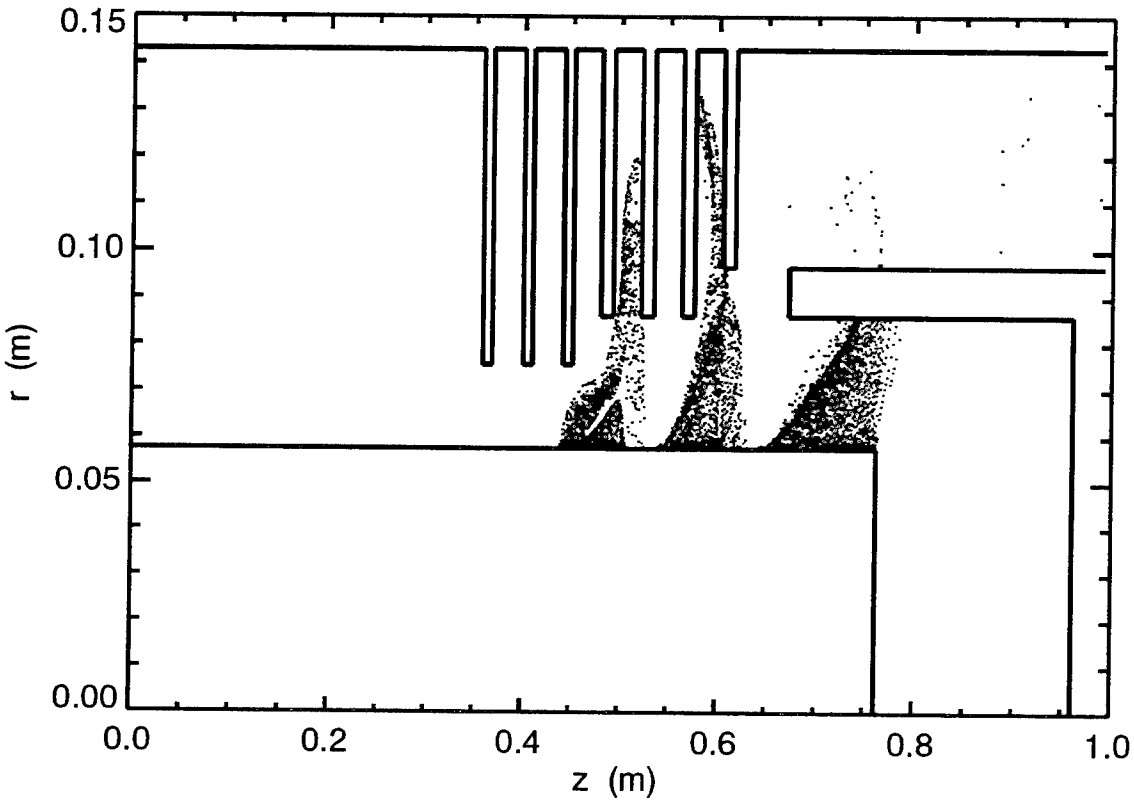


Figure 2. Diagram of the MILO Simulation Illustrating The Pi-mode Operation.

The first three vanes to the left in Figs. 1 and 2 have been designated the RF choke. It has multiple effects on the operation of the MILO tube. The original impetus in the design of the RF choke was to reflect the power escaping upstream, back into the MILO at the correct phase to add constructively within the SWS region. This was accomplished by making the inner radii of the choke vanes smaller than the radii of the primary SWS resulting in the stop band of the RF choke structure overlapping the pass band of the primary SWS. This is a very efficient reflecting boundary. Power reflected back into the tube increases the RF voltage across the downstream vanes, which, in turn, strengthens the coupling to the electron flow. A second effect of the RF choke is in the beam launching at the upstream end of the MILO. Setting the upstream emission limit under the last choke vane (the third vane from the left in Figs. 1 and 2) causes the electron flow in the primary SWS to move closer to the cavity openings where the RF voltage is highest, thus increasing the conversion efficiency. Thirdly a MILO with an RF choke operates at a lower impedance than a MILO without a choke. At lower impedance there is more current in the electron flow under the primary SWS, and hence more power in the electron beam to generate microwaves. Figure 3 shows a comparison of experimental data obtained for configurations with and without the RF choke. The error bars on the graph correspond to shot-to-shot variation in the output power, at a fixed voltage, for a series of shots. The "with choke" data corresponds to the experimental configuration described earlier, and for the "without choke" data the three RF choke vanes were replaced with vanes identical to those in the primary SWS. In both cases the

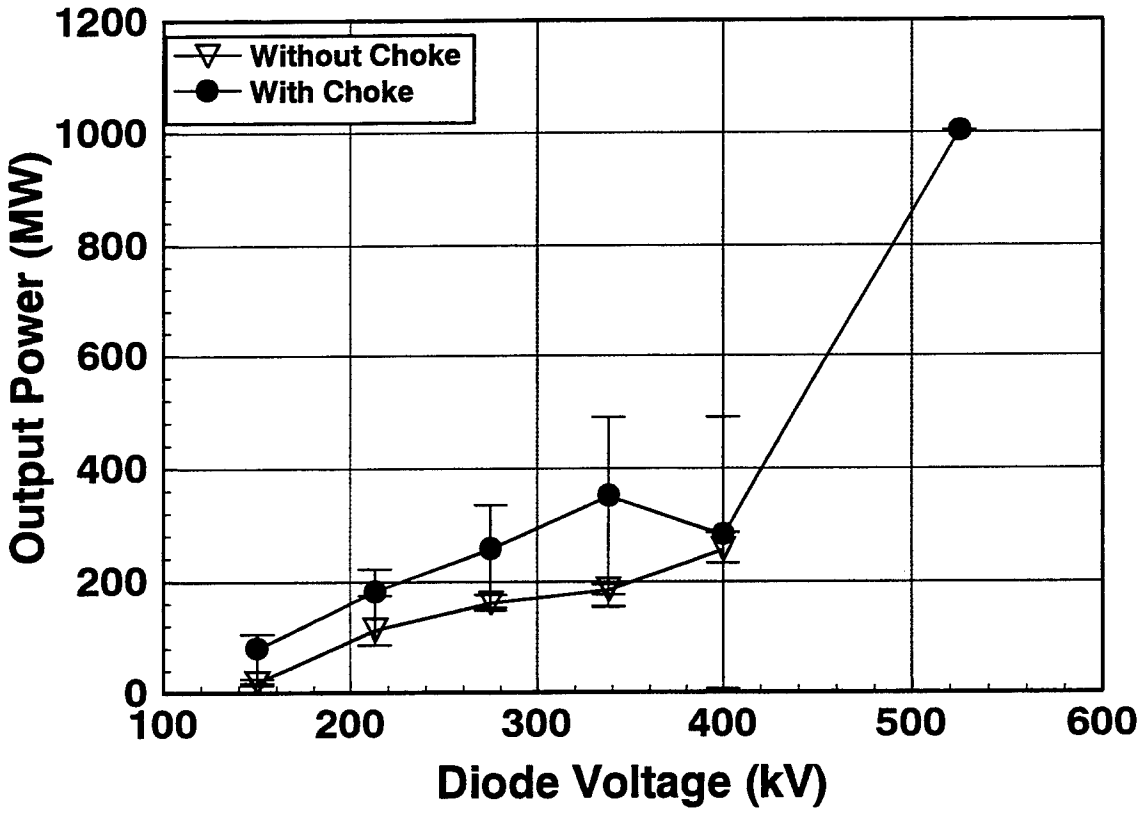


Figure 3. Comparison of the RF Output Power for the Configurations With and Without the RF Choke vs. Diode Voltage.

emission was allowed to start under the third vane. It can be seen that the inclusion of the RF choke essentially doubles the power radiated by the MILO. The anomaly in the data trend for the "with choke" data at diode voltages of 400 kV is a result of an RF breakdown of the antenna and bell jar which reflects power back into the tube and causes it to hop to an asymmetric mode of operation. During a pulse there is an increase in pressure within the tube because of heating of the graphite beam dump or from the velvet cathode. This pressure increase gets worse the higher in voltage the tube is operated, and at high voltage and high power causes the antenna and bell jar to break down. The reflection from the plasma that is formed causes the tube to hop into a non-radiating asymmetric mode. The data point at 525 kV showing an output of approximately 1 GW was obtained from a single shot after the tube was allowed to pump over night. A means of mitigating this breakdown problem is a topic currently under investigation.

The oscillation phase, the phase between voltages in adjacent cavities, of a MILO depends on the number of cavities in the primary SWS. As was discussed in reference to Fig. 2, simulations show that a four cavity MILO oscillates in the π-mode, which is the highest Q (quality factor) spatial harmonic associated with the SWS, and also, the field distribution associated with the π-mode produces the strongest coupling to the electron flow. When a tube is operating in the π-mode there is a 180 degree phase difference between the electric fields in adjacent cavities. A tube with more than four cavities tends to operate in a mode comprised of multiple harmonics, which do not couple to the electron flow as efficiently as the π-mode. A measurement of the phase difference in azimuthal magnetic field in cavities 2 and 3 of the primary SWS was made and found to be 180 degrees as predicted by the simulations. For all configurations tested, which includes MILO's with up to 15 cavities in the primary SWS, the four cavity MILO with the RF choke was found to be most efficient and operationally stable.

Another important parameter affecting the operation of the MILO is the inner radius of the extractor vane (the last vane to the right in Figs. 1 and 2). Simulations show that by adjusting the inner radius of the extractor vane the electromagnetic wave within the SWS is more efficiently coupled out of the SWS. By increasing the inner radius of the extractor vane slightly the voltage induced across the extractor gap is enhanced which more effectively couples to the TEM mode in the coaxial section. If, however the extractor vane inner radius is made to large, not only is the voltage induced across the extractor gap decreased, but also the coupling of the beam to the last cavity is decreased, both of which decrease the output power. Figure 4 shows the experimental data confirming this prediction. Once again, the error bars denote shot-to-shot variation at a fixed operating voltage. For both cases the experimental configuration was the 4 cavity MILO with the RF choke. The only difference was the inner diameter of the extractor vane was 17.14 cm in one case and 18.42 cm in the other. Clearly this parameter effects the output power of the tube and at a diode voltage of 400 kV there is approximately a 50% increase in radiated power.

The final parameter to be discussed is the length of the cathode extending into the beam dump. The distance the cathode extends into the beam dump effects the insulated flow of the electrons under the primary SWS. If the cathode extends into the beam dump too far the flow is overinsulated, pulling the electron flow away from the inner radius of the primary SWS, which weakens the coupling to the electromagnetic wave. If the cathode does not extend far enough into the beam dump the flow is underinsulated and the electrons would just flow out to the vanes,

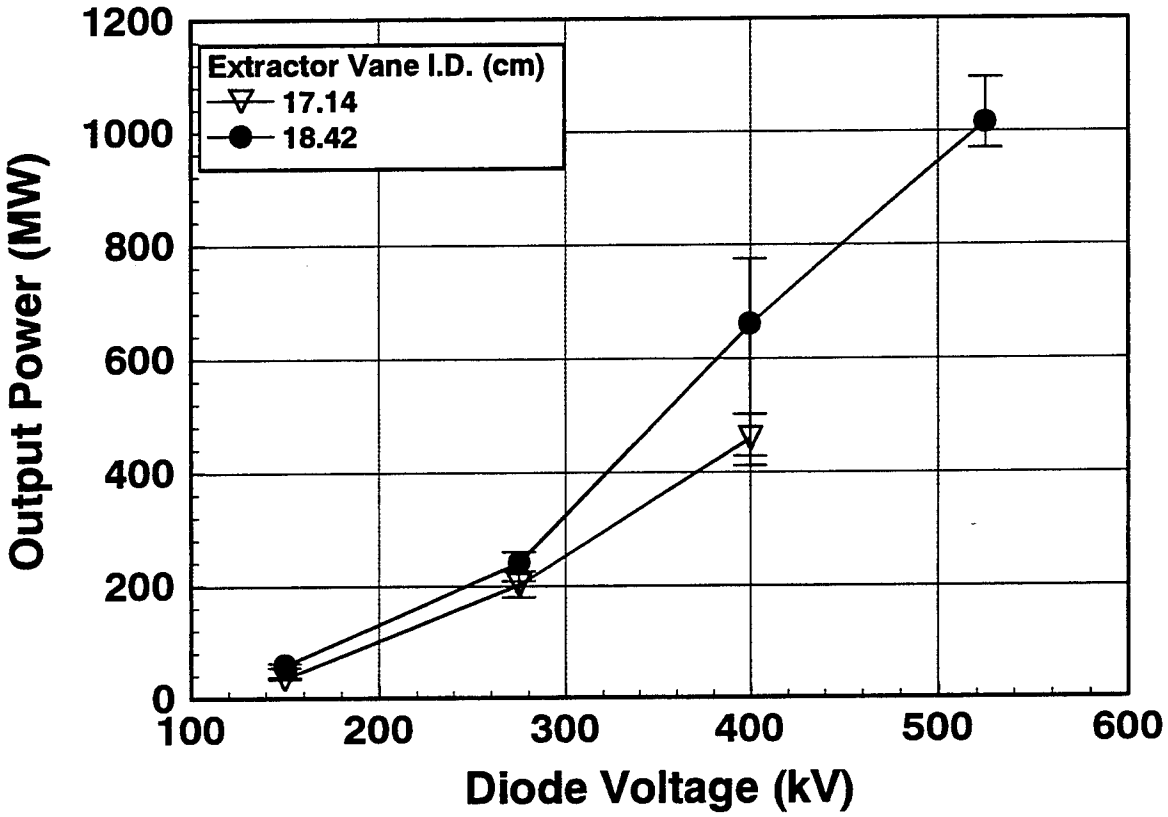


Figure 4. Output Power vs. Diode Voltage for Extractor Vane Inner Diameters of 17.14 cm and 18.42 cm.

initiating an arc. An expression for the length, L, the cathode must extend into the beam dump can be derived by requiring that the current emitted in this length be just equal to the minimum current required to insulate the electron flow under the primary SWS. This relation is given by:

$$L = 1.6 \times \frac{d^2}{r_c \ln\left(\frac{r_a}{r_c}\right)} \frac{\left(\gamma_a + 1\right)^{1/2}}{\left(\gamma_a - 1\right)} \tag{1}$$

where r_a and r_c are the anode and cathode radii, respectively, d is the A-K gap, and γ_a represents the relativistic factor, which is related to the applied voltage, V, by:

$$V = 511\left(\gamma_a - 1\right) \tag{2}$$

which gives the voltage in kV. The effect of changing the length of the extension of the cathode into the beam dump is illustrated by the experimental data shown in Fig. 5. The data designated by the open triangles corresponds to the case where the electron flow under the primary SWS is overinsulated and therefore weakly coupled to the electromagnetic mode. The data designated by the filled triangles corresponds to a cathode length very close to that predicted to be optimum.

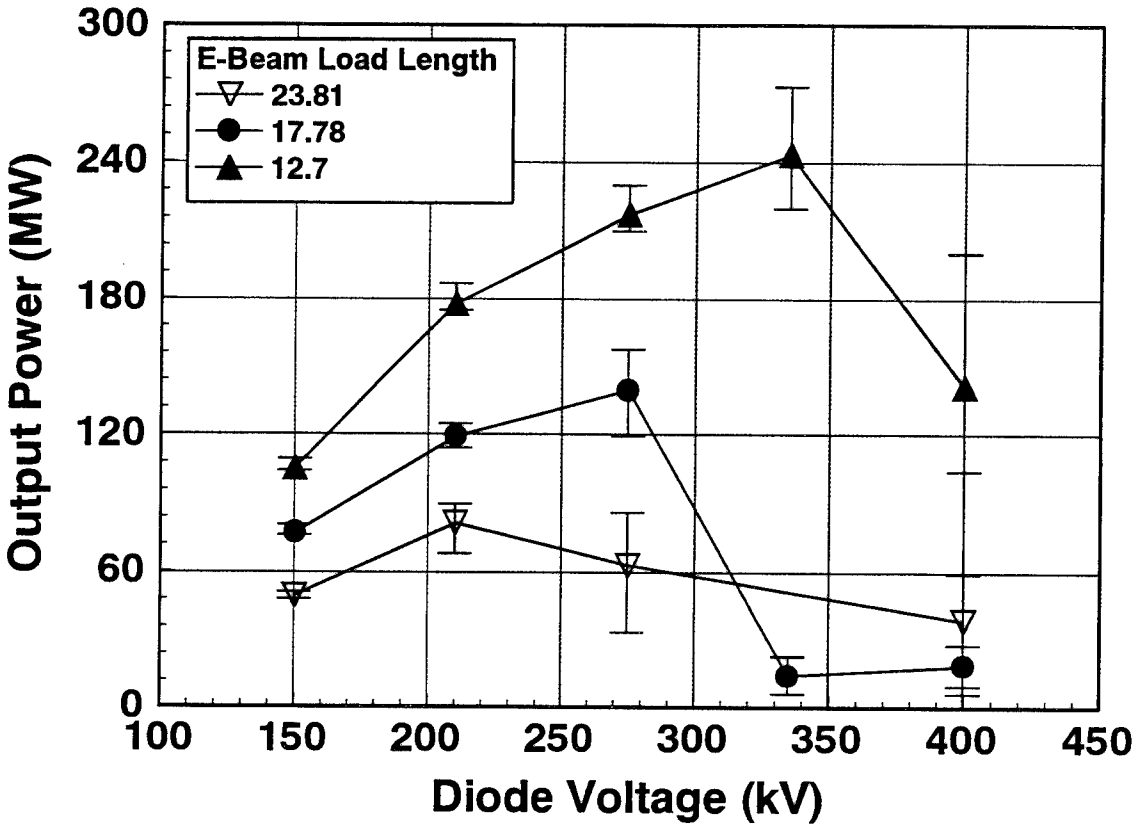


Figure 5. Output Power vs. Diode Voltage for Three Different Cathode Lengths into the Beam Dump Can.

The fall off in RF output power at higher voltage is a consequence of not having an RF choke in the system during these tests. If the RF choke were incorporated into the system the data would have followed the general trend shown in Fig. 4. From Fig. 5 it can be seen that a significant increase in the output power can be gained by having the cathode extend into the beam dump the appropriate distance.

SINGLE-SHOT EXPERIMENTAL DATA

Some of the data taken for a partially optimized MILO will now be given. This MILO is partially optimized in the sense that the beam dump and extractor vanes are the ones described previously in the experimental setup and the cathode extends into the beam dump 23.81 cm. Otherwise there are 4 cavities in the primary SWS, an RF choke upstream, and the 18.42 cm inner diameter extractor vane. For this sequence of shots the radiated power was verified with far-field antenna measurements. Figure 6 shows the diode voltage and current, the radiated power, and the signal from a microwave mixer used to diagnose the RF frequency. The diode voltage is measured with a water resistor voltage divider and the diode current is obtained from a Rogowski coil. Power measurements are made with a high-power directional coupler located in the circular waveguide before the antenna. The mixer signal is a difference frequency obtain by splitting off the directional coupler signal and mixing it with an 1180 MHz signal from a local oscillator in the standard heterodyning technique. This data shows a MILO operating close to 5% efficient,

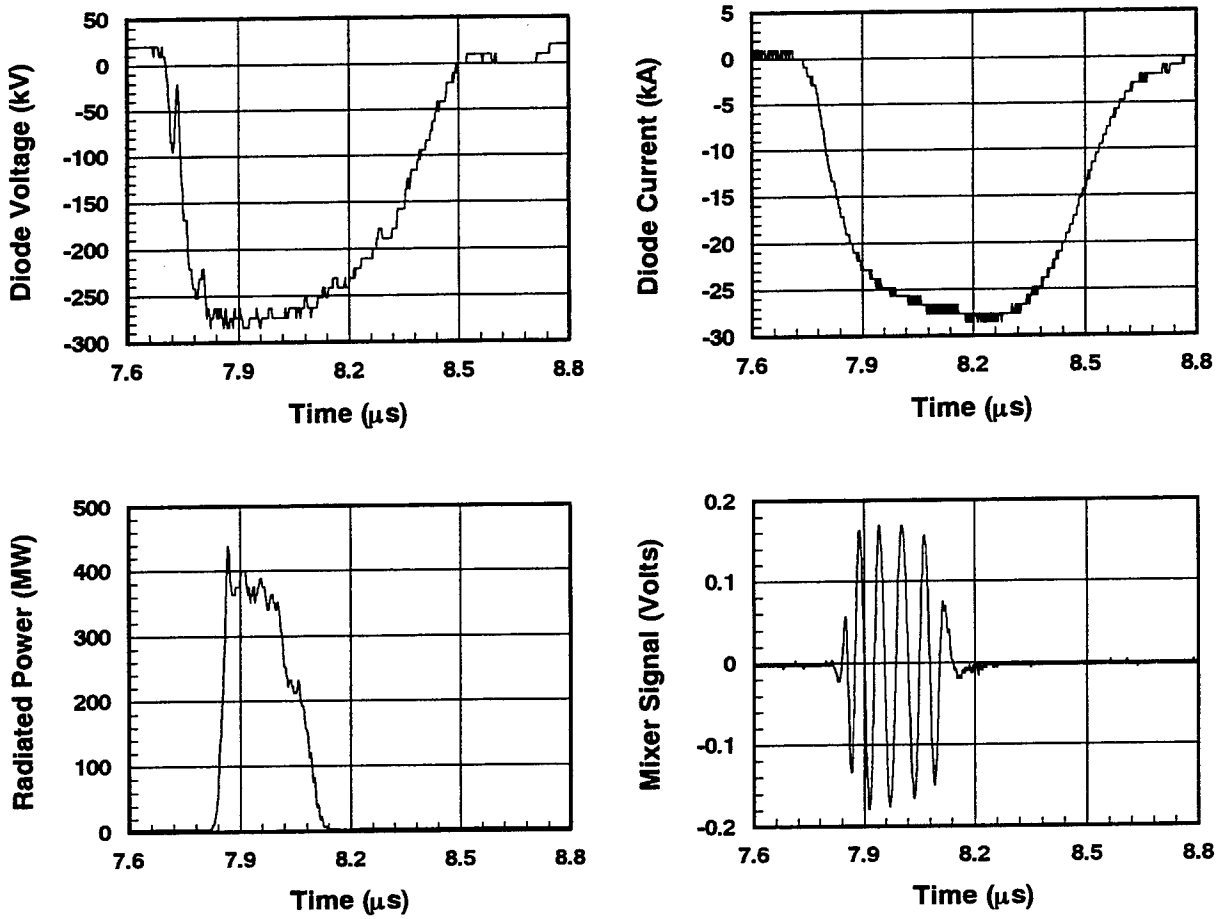


Figure 6. Experimental Waveforms from a Partially Optimized MILO Shot. The Diode Voltage and Current, the Radiated Power, and a Mixer Signal which Measures the Operating Frequency are Shown.

radiating approximately 100 J, and operating at about 1.2 GHz in a stable mode. It is clear from the radiated power graph that the tube is not running for the duration of the voltage pulse, a problem that is exacerbated at higher operating voltages. Figure 7 shows radiated power waveforms at higher operating voltages for the same experimental configuration. This data is for diode voltages of 400 and 525 kV. The pulse shortening observed at high voltages is of primary concern in current experimental endeavors.

Rep-Rate Experimental Data

Since the pulser that drives the MILO in this case has an inherent rep-rate capability, it was decided to try some rep-rate MILO shots. These were preliminary tests and only a short series of experiments was conducted because it was found that due to gas evolution within the system the lucite vacuum interface would get coated with debris, flash over, and cause the pulser to short. The pressure in the tube was monitored using a cold cathode guage located as shown in Fig. 1. The typical starting pressure for the tube was less than 5 μTorr. Other experimental parameters that were monitored were the diode voltage and current and the radiated RF power. Figures 8 and 9 show experimental waveforms from these tests. The operational parameters that

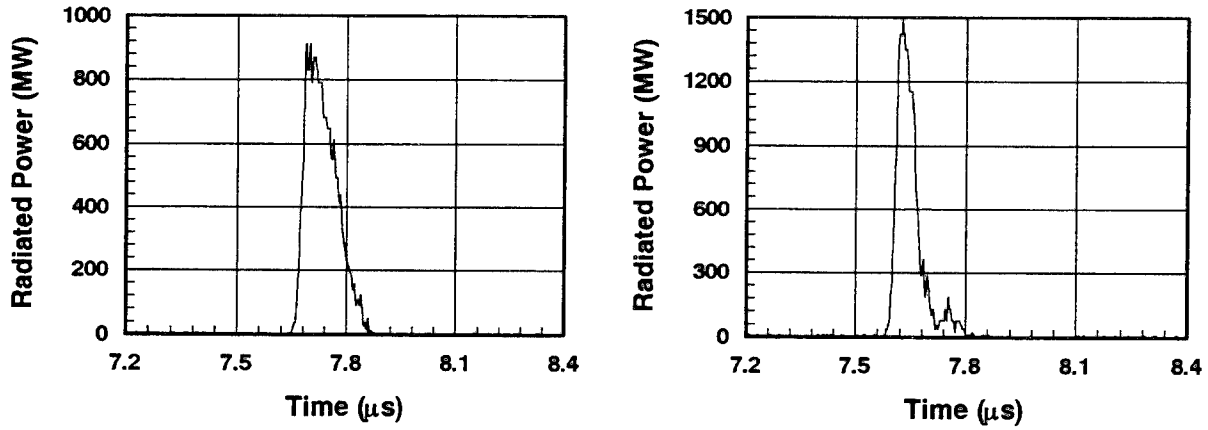


Figure 7. Radiated Power Pulses for the Same Experimental Configuration as Shown in Fig. 6. The Data on the Left is for a Diode Voltage of 400 kV and the Data on the Right Corresponds to a Diode Voltage of 525 kV.

correspond with Fig. 8 are as follows: 5 Hz rep-rate, 300 kV diode voltage, 10 shot burst. For this setup the beam energy and average power were 3.9 kJ/pulse and 19.5 kW respectively. There is no detectable degradation in the diode voltage pulses and the RF power envelope pulses were very reproducible. Referencing the pressure graph of Fig. 8 it can be seen that the pulser did not fire on the second pulse, indicated by the absence of a pressure increase 200 ms after the pressure increase caused be the first pulse. After that the pressure steadily increased with each subsequent pulse to a steady state value of about 2.5 mTorr on the sixth pulse. The data shown in Fig. 9 is for a 10 Hz, 300 kV, 5 shot burst. The beam energy per pulse is still 3.9 kJ but the average power in the beam has doubled to 39 kW. There is severe diode voltage pulse degradation during the burst and the reason this run is only for 5 pulses is because the vacuum interface flashes after the fifth pulse. In this case the pressure in the diode region exceeded 3 mTorr where the diode begins to behave very erratically.

During the course of the experiments in rep-rate mode it was found that for average beam powers below approximately 28 kW there was no diode voltage pulse or RF power pulse degradation, and above this power level is where pulse degradation began. For average beam powers of 28 kW the pressure in the diode region would rise to between 2.5 mTorr and 3 mTorr which is interpreted as the threshold for reliable diode operation. At this time it is unclear as to the source of the pressure increase, but it is postulated that it is the graphite beam dump heating up and outgassing and/or the velvet outgassing during emission. An important observation from these experiments is that in the course of many rep-rate bursts and the associated cycling of the pressure within the vacuum region, the vacuum interface on the pulser gets coated with debris, which causes the interface to flash above voltages of 400 kV. When the interface is free of this coating the machine can be operated at voltages above 500 kV reliably.

CONCLUSIONS

Through a series of optimization steps the operational efficiency of a MILO has been improved from much less than 1% to that approaching 5%. The radiated power has increased from less than 100 MW to over 1 GW. The inclusion of the RF choke in the system provides

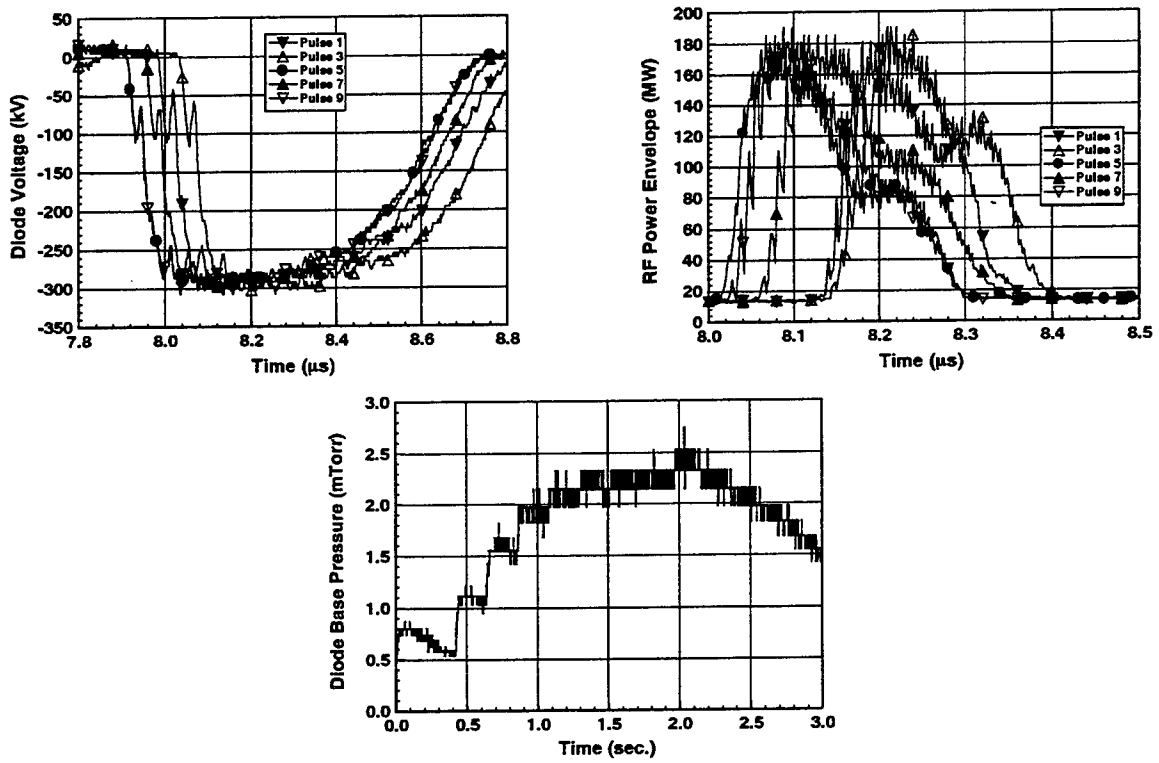


Figure 8. Diode Voltage, RF Power Envelope, and Tube Base Pressure for a 5 Hz, 10 Pulse, 300 kV Burst.

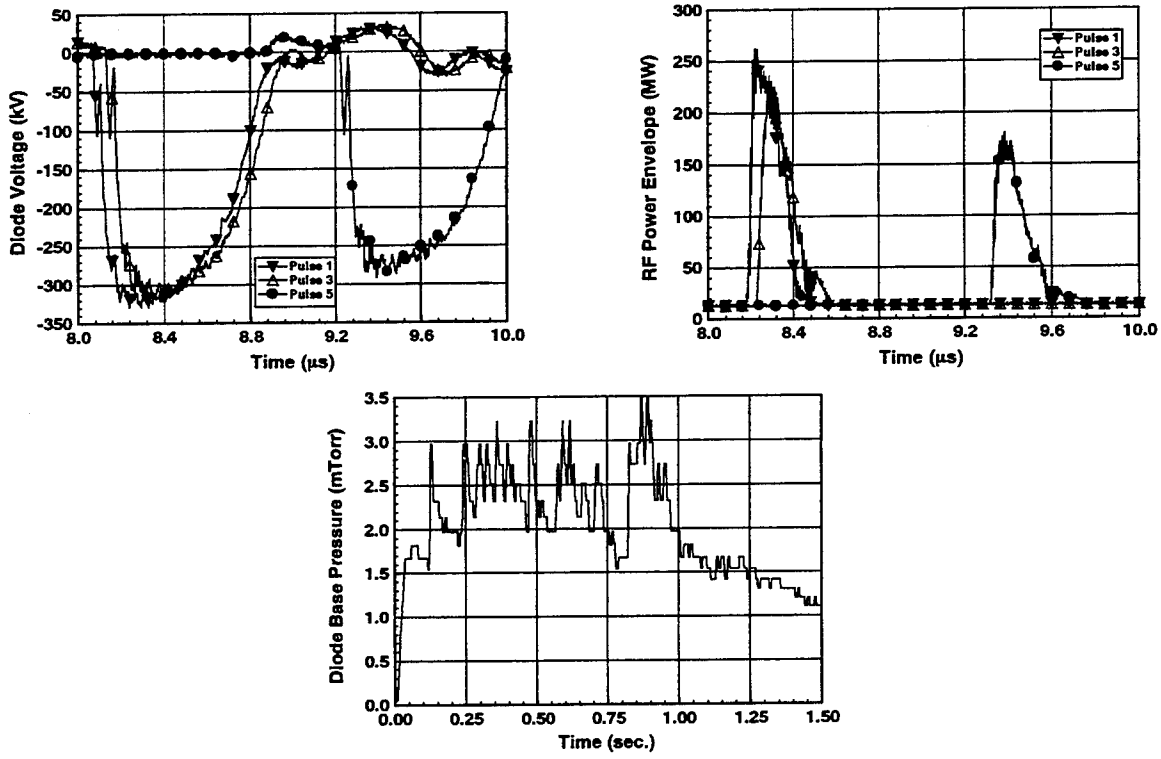


Figure 9. Diode Voltage, RF Power Envelope, and Tube Base Pressure for a 10 Hz, 5 Pulse, 300 kV Burst.

approximately a doubling of the radiated power in comparison to a tube without the RF choke. Additionally the RF choke allows the tube to operate at higher voltages than without the choke. This can be attributed to the choke providing appropriate feedback to the tube, enhanced beam launching on the upstream end of the SWS and the lowering of the tube impedance when the choke is used. A 50% increase in radiated power is realized when the extractor vane radius is optimized because of the enhanced coupling of the electromagnetic wave from the SWS to the TEM mode in the coaxial section. There is a substantial gain, yet to be quantified, in output power when the cathode extension into the beam dump is optimized. Work is focusing on the pulse shortening at high voltage and the RF breakdown of the antenna. The goal is to get a multi-gigawatt HPM source in a compact lightweight package. It has been shown that a laboratory tube can be operated at modest rep-rates. For this particular tube if the beam power is kept below about 28 kW and correspondingly the background pressure is kept below about 2.5 mTorr there is no pulse degradation during a 10 pulse burst. Experiments will be conducted to determine the source of the pressure increase within the tube and steps will be taken to remedy the problem.

ACKNOWLEDGMENTS

The authors would like to thank Mr. David Trujillo of Maxwell Laboratories Inc. and Mr. Bobby Seals of K-Tech for their excellent technical support in this effort.

REFERENCES

1. D.E. Voss, et al., *Experimental Study of a Self-Magnetically Insulated High-Power Microwave Cross-Field Oscillator Device*, AFWL-TR-88-32, Air Force Weapons Laboratory, Kirtland AFB, NM, November 1988.
2. R.W. Lemke and M.C. Clark, *Theory and simulation of high-power microwave generation in a magnetically insulated transmission line oscillator*, J. Appl. Phys., Vol. 62, No. 8, 3436-3440, 15 October 1987.
3. H.A. Davis, R.D. Fulton, and E.G. Sherwood, *Resistively Loaded MILO Experiments*, LA-UR-89-1199, Los Alamos National Laboratory, Los Alamos, NM, March 1989.
4. S.E. Calico, et. al., *Experimental and theoretical investigations of a magnetically insulated line oscillator (MILO)*, Proc. Intense Microwave Pulses III, 50-9, July 1995.
5. S.E. Calico and M.C. Scott, *Performance enhancement of the Phillips Laboratory Rep-Rate Pulser with a triggered output switch*, Conf. Record of the 1994 Twenty-First International Power Modulator Symposium, 56-9, June 1994.
6. D. Seidel and T. Pointon, Sandia National Laboratory, Unpublished.

The Cooker Magnetron as a Standard in Crossed-Field Device Research

John M. Osepchuk, Ph. D.

Full Spectrum Consulting
248 Deacon Haynes Road
Concord, MA 01742
Tel/Fax: 508 287-5849
E-Mail: 75754.3663@COMPUSERVE.COM

ABSTRACT

The surprising world-wide development of the microwave oven in the last fifty years was triggered and enabled by the development of the "cooker magnetron", the design of which is pretty much standardized whoever the manufacturer. It is estimated that the annual production of this device is at least 20,000,000 per year. The OEM price is of the order of $10 per unit in large quantities. This device is used in many commercial and industrial applications and laboratories. It is reliable, reproducible and easily available. It is proposed that research be focused on this device for the purpose of validating theoretical models, i.e. in particular the modern computer codes. The existence of crisp robust phenomena in the cooker tube affords the research community a means of clear unambiguous check points on theory--in particular the existence of three regimes in every tube. High noise at low currents, spurious discrete sideband spurious at moderate currents and low noise at high currents. The boundaries between these regimes are sharp and reflect discontinuous transitions or thresholds, which are clear benchmarks for checking validity of computer models.

A review of the development of the cooker magnetron not only presents a consistent detailed database on these regimes but also some other interesting and important phenomena heretofore known only in the narrow community of cooker tube and microwave oven scientists and engineers. These include:

(a) A preoscillation mode involving secondary electron emission from end shields and axial electron-flow with multipactor-like properties. This is one cause of high-voltage transients.

(b) Anomalous moding caused by the presence of high-amplitude ("violent") spurious VHF signals in the sideband regime and suppressed by appropriate cathode-anode impedance.

(c) "Warm emission" modes involving end cavities, hysteresis in gas discharge modes, and the role of the "adjacent" mode in permitting transient-free cold starts.

History

The rich history of the magnetron, as a microwave power generator has been told by many, including Brown [1]. Of course, for many years its most prominent use was for radar. Spectral purity is more important than efficiency for such an application. Nevertheless, it was recognized [1] that the magnetron enjoyed an inherent basis for high efficiency compared to other types of microwave tubes. Thus it was natural that the magnetron was the tube of choice for the earliest versions of the microwave oven [2]. Some of the peculiarities of the magnetron as developed for the microwave oven led to the name "cooker magnetron" for the variety eventually developed for mass production. Its propensity for high levels of noise and spurious as a concomitant to high efficiency was recognized by microwave-oven engineers [3].

The early cooker magnetrons were bulky and expensive. A substantial copper anode, strapped-vane, was utilized but water cooling was required. Furthermore the magnetic field was provided by a power-consuming and heat-generating solenoid which in some oven designs was placed in series with the tube. The total weight of a tube assembly could be over twenty pounds and replacement costs would be in the hundreds of dollars (1950's). The evolution from this primitive state to the modern cooker magnetron has been described both in the engineering literature [2] and in the trade press [4]. Although originally developed at Raytheon, the modern cooker tube was largely shaped by contributions from New Japan Radio Company [4] and later others. In the process water cooling was replaced by air-cooling fins surrounding the anode block, the cathode became a thoriated tungsten helical filament (carburized) and most importantly the development of new ferrite technology permitted the use of inexpensive permanent magnets (Strontium ferrite). The filter box attached to the cathode lead end of the tube evolved with the use of two feedthrough capacitors (with the order of 1000 pF each) and two ferrite-core choke coils. Note that cooker magnetrons were designed to operate with a half-wave doubler DC power supply so that the anode current waveform is a half-sinusoid-like pulse at the repetition rate of the line frequency (60 or 50 Hz.). This is in contrast to the normal use of a DC power supply in most conventional uses of CW magnetrons in the past--for communications, jamming or industrial heating applications. The nature of the consumer market has to this day dictated the most inexpensive power supply, the half-wave doubler. Modern switched-mode power supplies with filtering is still too expensive for the consumer market.

Other aspects of the cost reduction and manufacturing refinement of the cooker magnetron is described in the literature, e.g. the article by Oguro [5]. He describes the evolution to ferrite magnets and alumina ceramic insulators. Figure 1 shows a photograph of cooker magnetrons of the early eighties. The weight of these tubes is two pounds or less each, and the size less than a 4 inch cube. In large quantities the cost per tube is in the range of $10-15. Typical operation would be at 4.0 kV peak, 1 A peak, 0.3 A average and an efficiency of at least 70% when operating into a matched load. This means an output power in the range of 800 to 900 Watts. Typical filament power for the directly heated cathode used to be in the range of 40 to 50 Watts, but this is more like 30 to 40 Watts in today's cost-reduced versions.

Interaction Space Design

The cross-sectional drawings in Figure 2 depict the main features of the cooker magnetron design and construction. One can see that the output coupling is by means of an "antenna" or probe connected to a single vane just outside of the strap region. This antenna is meant to be the probe coupling to a rectangular waveguide output at an appropriate distance from a waveguide short. The output adjustment is made so as to achieve at least 70% efficiency into a matched load. This roughly means that the tube circuit efficiency is around 90%, with a loaded Q of about 100 and unloaded Q typically around 1000. The cooker magnetron is thus in a heavily-loaded condition and even more so if operating with a mismatched load in the vicinity of the sink region. This condition is, of course, necessary if efficient heating or power conversion is to be achieved. This also means that noise and spurious oscillation phenomena will be magnified.

The remarkable aspect of the cooker magnetron is that despite the fact that there are probably in the order of a hundred different tube types presently under manufacture around the world, particularly in Japan and Korea, the interaction-space design and noise properties do not vary very much among these different types. Furthermore, the cooker magnetron production world-wide is estimated to be well over 20 million per year. Therefore this device appears ideal as a vehicle or test object for a canonical and meaningful test of modern computer models of the magnetron.

The relative invariance of interaction-space parameters among various types of cooker magnetrons is reflected in Table 1. In this table, the classic early design developed by New Japan Radio is represented by the QKH1845, the last tube type (of ceramic construction) manufactured by Raytheon. Like almost all subsequent cooker magnetrons, it was designed to operate at 4 kV and produce at least 700 or 800 Watts. The design magnetic field for that tube was around 1850 Gauss. It was a 12 vane tube and substantially larger and heavier than subsequent cost-reduced versions.

The first phase or family of cost-reduced type in Table 1 is that of the other 12 vane tubes listed which have similar interaction-space dimensions relative to the early or original design (QKH1845) but were cost reduced in terms of less copper in the vanes and anode block, less (thinner) cathode material, shorter magnet gap, fewer cooling fins, etc.

This was followed in the mid-eighties by the appearance of 10 vane tubes, with further cost reductions. In this family the interaction space dimensions are changed by a small amount, especially to smaller anode and cathode diameters and, therefore, a slightly smaller cathode to anode spacing. Presumably little change in magnetic field was then required.

The net result is that interaction space parameters have not varied much in the last thirty years and do not vary much between tube types today. Therefore, the cooker magnetron is a stable test vehicle for the testing of computer codes. We should add that the noise properties of cooker magnetrons also have shown remarkably little change in time or among tube types-at least in the main features which we describe later.

Table 1.
SUMMARY of KEY TUBE DIMENSIONS (inches)

Vane No.	Tube Type	Anode Dia.	Cathode Dia.	Anode Lgth.	Cathode Lgth.	Wire Dia.	No. of Turns
12	QKH1845	0.400	0.200	0.400	> 0.400	---	---
12	2M107A-78H	0.416	0.198	0.396	0.425	0.0245	~ 7
12	2M167	0.435	0.205	0.396	0.440	0.024	~ 6.5
12	2M172J	0.397	0.203	0.395	0.420	0.024	~ 6.5
12	OM75A	0.404	0.197	0.396	0.438	0.025	~ 7
12	"Sanyo"	0.395	0.198	0.357	0.404	---	---
10	2M172AJ(A)	0.357	0.152	0.374	0.413	0.020	~ 8.5
10	2M167A-M10	0.347	0.158	0.394	0.432	0.020	~ 8.5
10	2M107A-304	0.365	0.154	0.386	0.406	0.020	~ 8.5
10	2M204-M3	0.350	0.158	0.397	0.430	0.0195	~ 8.5
10	2M214	0.354	---	---	---	---	---
10	2M229	0.349	---	---	---	---	---

Measurements indicate at least +/- 0.010" scatter in cathode axial position with respect to anode.
Antenna pole in most tubes is "North", except for Panasonic designs.
Toshiba: 2M172J, 2M172AJ(A), 2M229
Hitachi: 2M107A-78H, 2M107A-304, 2M214
Panasonic: 2M167, 2M167A-M10, 2M204
Samsung: OM75A

DC Operation (Conventional) of Magnetrons

The prior conventional operation of CW magnetrons is quite different to the modern operation of the cooker tube. It is important to describe the important differences so that one may more easily relate data and reports on conventional magnetrons to data and reports on the cooker magnetron.

Like almost all tubes in history the conventional magnetron cathode was first preheated (warm-up). Then high voltage was applied usually by manual control. The anode voltage supply was usually well regulated so that steady state operation was at some DC anode current with little ripple. As the anode current was changed by manual control, the cathode or filament heater power would be adjusted as desired to improve stability, decrease noise, etc.

In Figure 3, we depict the type of gauss-lines which were recorded with such static, steady state test conditions. Most CW magnetrons were found to exhibit two states with distinct gauss-lines. The lower-voltage gauss-line was the more easily achieved state marked by high noise and perhaps maximum efficiency. The higher-voltage-line, if achievable, would be found by an appropriate reduction of filament or cathode heater power, perhaps even to zero. The higher

gauss-line would exhibit lower noise and perhaps a bit less efficiency. It would also be more temperamental with regard to long-term stable operation--with the tendencies of jumping to a no emission state or to the higher noise state. To trace the higher gauss-line under DC operation a continuous adjustment of filament heater power was generally necessary. The low-noise gauss-line was indeed the basis for low-noise magnetrons in past military applications, for which successful design and manufacture involved careful selection of materials and certain special types of tube processing.

AC Operation of the Cooker Magnetron

The cooker magnetron operation is greatly different to that of conventional magnetrons. First of all, in most cases there is no cathode preheat (warm-up). Especially for the consumer oven magnetrons are subjected to a cold-start. A half-wave doubler supply (high-voltage transformer in series with a high-voltage capacitor) is applied to the cooker magnetron which is in parallel with the appropriately oriented rectifier diode. At the same time a low-voltage (about 3 volts) filament supply is applied to the cooker magnetron cathode leads, marked F and FA. At time, t = 0, there is no cathode emission and an open-circuit voltage of 7 to 10 kV is applied to the tube depending on the oven design details. During the period of about 2 seconds in which the cathode warms up to near full-emission capability the tube proceeds through various transient states. In the subsequent steady state there is a roughly square anode voltage pulse during a half cycle period at 60 Hz (or 50 Hz) during which a roughly half sinusoid current pulse occurs. Thus the anode current proceeds from zero to a peak of about one Ampere back down to zero during every cycle. On top of this 60 Hz variation is any slow variation or modulation that is caused by oven mode-stirrer changes of tube load or other load changes. Thus in the steady state, the cooker magnetron passes through several distinct regions with consistently different noise properties. These regions are depicted in Figure 4. The low-current or high-noise region is that below I_{a2} in Figure 4. There is the fine point concerning I_{a1} in this Figure that relates to the possibility of secondary phenomena such as discontinuities associated with AM radio noise, etc. We will not explore these secondary matters here. The high-current or low-noise region is that above I_{a3} and below the peak current or the moding current I_{am} (in the case that the desired peak current is above what is available). Note that the potential moding at peak current is due to insufficient cathode emission and is eliminated by increasing cathode heater power. In between I_{a2} and I_{a3} is the region of spurious oscillations associated with discontinuities as depicted. These oscillations may or may nor occur depending upon many parameters including filament power, microwave load (VSWR and phase), cathode impedance at VHF frequencies, etc. When they occur they can be very strong as depicted in the Figure 4.

Without exception to my knowledge, every cooker magnetron in the world exhibits a high noise region and a low-noise region, presuming normal operating conditions--i.e. absence of excessive cathode heating or insufficient anode voltage. Thus there is a discrete and discontinuous change under dynamic AC operation from high noise at low currents to low noise at high currents. This change is always there. The region of change between the two states may be complicated by the existence of the spurious oscillation state, but if not then there is one threshold.

In Figure 5 we depict gauss-line traces with amplified ordinate ($50\,V/div$) so that we can see various details. For example at the lowest filament voltage which is close to the emission-mode condition one can see the turning up of the V-I trace as the peak current almost reaches the emission limit. At higher values of filament voltage there may be regions of discontinuities and associated spurious oscillations as depicted.

Characteristics of Cooker Magnetron Noise

In Figure 6 we show typical noise spectra and three values of anode current corresponding to high noise, spurious oscillation, and low noise. These are taken with a cooker magnetron operating into a matched load on the bench without oven complications and using the appropriate gating devices to sample noise only in a small region of current (small time period, much less than a millisecond).

At an anode current of 0.2A we see broadband random noise on both sides of the fundamental signal at around f_0 = 2.45 GHz. We call this noise sideband noise since it tends to peak up at frequencies like $f_0 \pm \Delta f$. The value of Δf increases with anode current perhaps as the square root of anode current. Associated with these noise sidebands is low-frequency noise that is conducted and radiated from the high-voltage cathode leads. This low-frequency noise will exhibit peaks at Δf, which tends to vary within the range of 150 to 300 MHz typically. This noise and its harmonics (e.g. 300 to 600 MHz) will cause some discernible interference with either VHF or UHF TV or both in the case of a microwave oven. In this case the RFI varies periodically with a period of about a second in synchronism with the mode-stirrer cycle.

At an anode current of 0.5 A we see discrete spurious (sideband) oscillations at $f_0 \pm \Delta f$. These peaks can be quite strong, e.g. only 30 dB or less below the fundamental. The associated low-frequency power at the cathode can be quite high. Values as much as 10 Watts have been measured at the cathode. Clearly the magnetron anode voltage is being modulated strongly at a rate in the VHF range with subsequent AM and FM phenomena across the whole spectrum--i.e. sidebands around the fundamental and all harmonics.

At the peak anode current of 1.0 A we find no measurable noise above the floor of the spectrum analyzer. Clearly we are in the low-noise region at 1.0 A.

These distinct spectra and their respective associated regions of anode current exist in all cooker magnetrons. This picture changes or is modified as we vary parameters like filament voltage, microwave load, cathode impedance, peak voltage etc. but not drastically. One can track the distinct regions quite well. Increased microwave loading (i.e. towards sink) tends to move the regions up in current and decreased loading vice versa. Associated with this is an increase in Δf with lighter load and a decrease in Δf with greater load. In a similar manner increase of filament (heater) power moves the regions to higher current but with little change in Δf. A change in the cathode to anode impedance at VHF frequencies will affect the spurious oscillations strongly and to a lesser extent the noise. One can make the spurious oscillation at Δf lock to a resonant circuit

in the cathode leads. The detailed dependence of the magnetron noise on secondary parameters, including the B-field, has been thoroughly documented [6].

Theoretical Analysis

The magnetron noise properties are not in accordance with any quantified theory but they behave phenomenologically in accordance with the pattern of noise and spurious observed in M-type backward-wave oscillators [7]. In the M-BWO where space charge increases with beam current at fixed voltages and B-field, we find low noise just above the start-current, discrete spurious sidebands above some higher threshold current, and finally a sudden transition to random noise sidebands at a still higher threshold current.

If we remember that the circulating current and not the anode current is a better measure of space charge in the magnetron, then we see an inverted pattern because circulating current is high at low anode current and low at high anode current. The M-BWO phenomena are well explained by theories which describe the competition between the circuit and space-charge forces--both small signal and computer large-signal calculations. The value of Δf for the M-BWO is well described by a formula which takes into account a feedback time for relaxation oscillations--i.e. the time for the beam to pass the length of the circuit plus the time for an RF signal to come back along the circuit at a speed equal to the group velocity of the circuit.

In the case of the cooker magnetron no simple formulas or theories are at hand. Presumably the value of Δf is related to the time for electrons to migrate from "hub" to anode plus some type of circuit voltage decay time. What seems very clear, however, is that a valid computer code for crossed-field interaction should be able to predict the existence of the distinct regions of noise and predict threshold values for the transitions from region to region. Even if these predictions are not accurate they may shed light through parametric studies of what design changes will reduce noise, etc. The application of computer models should be straightforward except for the question of modeling the cathode-anode impedance at VHF frequencies.

It is interesting to note that early computer studies [8] showed signs of strong spurious modulation of anode current--presumably similar to that in the M-BWO where there is almost a 100% modulation of collector current when strong spurious oscillations are present. Unfortunately nobody has pursued computer studies of the magnetron in a thorough fashion to elicit dependence on anode current to the end of delineating noise regions and threshold currents. It should be much easier to apply modern computer codes.

It is apparent that the cooker magnetron probably does not exhibit the ambiguous parameter of an emission that depends on RF field strength through secondary electron emission as in the CFA. This ambiguity confuses the juxtaposition of circuit and space-charge forces. Presumable this is not a major factor in the cooker magnetron. It is admitted, however, that the proper role of secondary electron emission in the cooker magnetron remains to be determined.

Practical Aspects of Cooker Magnetron Noise

The existence of magnetron noise is assuming a very practical aspect. There are over 200 million microwave ovens in the world operating at 2.45 GHz. There also are plans for a wide variety of new "wireless" services to operate with frequency allocations ranging from 1.5 GHz to 3.0 GHz and possibly even higher, especially at 5.8 GHz. There are some serious questions about the potential that some of these systems will encounter unacceptable interference from microwave ovens--i.e. the sideband noise. Thus the characteristics of microwave oven noise are being studied extensively [9] and there are plans for interim and final (tighter) specifications to limit such noise through regulations originating in current activities of the CISPR community within the IEC (International Electrotechnical Commission). Because the noise is predominantly at low anode currents most of the time microwave oven noise shows up as sub-millisecond pulses of noise. Some experts believe modern digital and spread-spectrum communication techniques can live with this. On the other hand, if discrete spurious show up especially at close to peak current the RFI might not be tolerable. The magnitude of the peak noise or spurious in the worst cases is of the order of 100 dB above a pW as measured in a 1 MHz bandwidth or even higher (or similar numbers in units of $\mu V/m$ as measured at 3 meters from the oven). At present some authorities are investigating peak limits near such levels along with limits 30 to 40 dB lower when using narrow video bandwidths (e.g. 100 Hz) to yield "average" measures of the noise.

Cooker magnetron noise, therefore, will attract regulatory pressure in the future at the same time that others, i.e., the DOE in the U.S., are pressuring for higher oven efficiency which is, in principle, associated with higher noise. At the same time there are other magnetron-driven ISM devices that may amplify the concern about noise, e.g. the microwave "sulfur" lamps [10] , that are very efficient light sources that some day may operate for many hours per night illuminating large areas in buildings and parking lots, etc. One can presume that users of magnetrons may be forced to find ways of reducing such noise. Otherwise, competing devices might for the first time in history pose a threat to the magnetron as the power source of choice for ovens and other power applications. In the past year there was the preliminary report [11] of an efficient (67%), low-voltage (600 Volts) multi-beam klystron suitable for microwave oven use. Its developers estimate that in three years problems of cost, size and weight might be resolved. The klystron poses no noise problems and has other advantages. One can expect controversial discussions of competing power sources at meetings such as those of IMPI (the International Microwave Power Institute).

Cold-Start Transients

It has already been pointed out that cooker magnetrons are required to operate under "cold start" conditions. The magnetron thus passes through a rich variety of transient states, some of which under certain conditions can lead to destructive voltage transients. This happens through the $L\,di/dt$ mechanism in the presence of the large inductance of the high-voltage transformer on the microwave oven.

Figure 7 is a trace of an instantaneous $V_a - I_a$ pattern of a cooker magnetron during a phase of normal buildup of anode current before sufficient emission is available to reach the desired peak current (~1 A) without moding. Thus we see a lower gauss-line which is the normal π mode ending with a moding to a higher gauss-line after which the current decreases without incident. The higher gauss-line represents oscillation in an inefficient mode at frequencies around 4.3 GHz. (Some call this the "adjacent" mode. I believe it is not the "adjacent" mode.) If it were not for the clamping action of this higher mode, the higher gauss-line, the ceasing of oscillation at some maximum current in the lower gauss-line would normally cause a high-voltage transient, well over 20 kV, to ensue which will cause great havoc, e.g. destroying rectifier diodes, feedthrough capacitors etc. Nobody has explained it, but the fact is that normally whenever the π mode is in oscillation the higher mode is always ready to oscillate and act as a clamp and protection against voltage transients.

There are, however, other states or modes during the cold start that do not have the accompanying protective presence of the higher mode. The result is the precipitation of voltage transients as shown in Figure 8. In this case at about 1.5 seconds after start one can see voltage transients above the normal peak voltage. (these happen to be small but in some cases the transients exceed 20 kV). These occur just before the beginning of the buildup of thermionic emission from the cathode. At this time one can see an anomalous gauss-line at around 4 kV with a maximum current less than 100 mA, but since there is no clamping mode the cessation of this anomalous mode leads to the observed transient voltage. More detailed studies have linked this anomalous mode to a state of axial space-charge streaming between end-shields as depicted in Figure 9. The buildup of such a state was predicted and observed by Sloan [12] in the early work on cold-cathode magnetrons. It corresponds to a multipactor like instability involving thermo-field emission from the end-shield edges followed by secondary electron emission from the end shields. Early solutions to this problem employed Zirconium or Titanium rings welded to the end shields. The more satisfactory solution and the one now universally employed is the use of "grooves" or channels in the end shields as depicted in Figure 2. An interesting historical note is that this state probably explains early observations of a ring like space-charge state in the magnetron by Reverdin [13]. Note also that this anomalous state is shut off by the presence of the normal space charge. Presumably the increased E-field prevents motion from end shield to end shield. Note also that this axial oscillation state exists only at high magnetic fields. If the B-field in the normal cooker magnetron is lowered by 10 to 20% this phenomenon disappears. This probably explains the sensitivity to phasing of the filament voltage of this phenomenon. Note that the cathode terminals are marked F and FA in order to guide the user in applying the proper phase for minimum voltage transients.

The other less anomalous state which causes voltage transients in microwave ovens is plain voltage breakdown. The typical cooker magnetron exhibits cold emission at anode voltages above 8 kV. These currents are due to field emission and could be the precursor to a voltage breakdown across the cathode to anode gap--at closest approach at the corners of the end shields. Experience indicates that low leakage of less than 0.1 μA at 10 kV is less likely to be a precursor to breakdown than leakage currents of greater than 10 μA which are considered undesirable. Although infrequent such breakdowns do occur and can cause significant voltage transients. An example is shown in Figure 10 where the peak voltage is over 20 kV. This phenomenon not

only explains the occurrence of some diode failures but also an occasional capacitor failure or other damage in a microwave oven.

Anomalous Moding

Anomalous moding is detected in the microwave oven when the moding occurs not at peak current but at a lower current. An example is shown in Figure 11. The countermeasure when encountered in practice is to lower the filament or heater voltage. This is in contradistinction to the case of normal emission-limit moding where the countermeasure is to increase the filament or heater voltage.

The explanation for this anomalous moding is the presence of very strong spurious oscillation. It is estimated that the instantaneous fluctuation of the anode voltage in the presence of "spurious" can be as much as ±200 Volts or more. It is believed that this may be enough to cause the spokes to lose their phase locking and therefore causing the oscillation to cease. An alternative and appealing theory is that the spurious oscillations might pump energy into the 4.3 GHz mode enhancing its competing strength. This theory is discounted in view of the more general conditions under which anomalous moding occurs. The details of the spurious oscillation largely have not been quantified by any theory.

Anomalous Gas Discharges

The last phenomenon we present in this paper is that of anomalous gas discharges. This is occasionally seen in old tubes when subjected to a normal cold leakage test. In such a test the anode voltage is slowly swept upward from 0 to 10 kV and the leakage current recorded. This leakage current is then also monitored on the way down from 10 kV to 0. In Figure 12 at the far right we see the recorded normal leakage currents for a tube. In addition, however, we see the more striking and anomalous currents at lower voltages. On the way up we see substantial currents of mA magnitude at around 1 kV anode voltage. No other currents are observed on the way up except the normal leakage of μA magnitude at 10 kV. Then on the way down, however, large currents, in the mA range, appear at voltages in the range of 7 to 4 kV--in a series of repeated discharges. Then when passing below 4 kV down to 0 kV there are no more discharges. Thus there is a striking hysteresis present. In other studies we have determined that the voltages at which these anomalous discharges occur are the lower (1 kV) and higher (7 kV) boundaries, roughly of gas discharge in the magnetron as predicted by classical theories. It seems, therefore, that when one enters into this region of discharge anomalous discharges occur which then disappear presumably because of the gas-pumping action of a magnetron. Then it is only after one exits from this normal region that gas can build up again in the magnetron. In other words, the discharge appears only when entering into the region of normal discharge but not when exiting. During the discharges at higher voltages microwave signals are generated but their levels have not been quantified. This phenomenon lacks a quantified theory and is of interest as a practical indicator of some types of tube wearout in the field.

Conclusions

We have reviewed several anomalous phenomena in the cooker magnetron. The most prominent and most important of these phenomena is the "anomalous" excess noise which is now classical for crossed-field devices. The key point is that this noise pattern in the cooker magnetron is a well-defined repeatable one with distinct boundaries between high noise and quiet regions. This pattern occurs in the millions of inexpensive cooker magnetrons throughout the world. A critical and unique test for any modern computer code is that it should predict this pattern for the cooker magnetron. If this is successfully done, it will help not only the microwave oven community better control this type of magnetron but valuable insights into the relative roles of emission parameters as well as microwave and cathode circuit parameters would be developed.

References:

1. W. C. Brown, "The History of the Microwave Magnetron and Its Derivatives", IEEE Trans. ED-31, No. 11, pp. 1595-1605, November 1984

2. J. M. Osepchuk, "A History of Microwave Heating Applications", IEEE Trans. MTT-32, No. 9, pp. 1200-1224, Sept. 1984

3. J. M. Osepchuk, "Life Begins at Forty: Microwave Tubes", Microwave Journal 21 [11], pp. 51-54, 56-60 (1978)

4. J. P. Nayak & J. M. Ketteringham, Breakthroughs, Rawson Associates, New York, 1986

5. T. Oguro, "Trends in Magnetrons for Consumer Microwave Ovens", J. Microwave Power 13 [1], pp. 27-36, March 1978

6. J. M. Osepchuk, A Study of Noise in Cooker Magnetrons, Report R-75, Raytheon Research Division; Lexington, MA, 1976

7. J. M. Osepchuk, et al., Reports on Contract No. 39-70-C-2543, Study of Spurious Signal Generation in Microwave Tubes, (1968-1971)

8. S. P. Yu, G. P. Kooyers and O. Buneman, "Time-Dependent Computer Analysis of Electron-Wave Interaction in Crossed Fields", J. Appl. Phys. 36, pp. 2550-2559 (Aug. 1965)

9. P. E. Gawthrop, F. H. Sanders, K. B. Nebbia, and J. J. Sell, Radio Spectrum Measurements of Individual Microwave Ovens, Vols. 1 and 2, NTIA Reports 94-303-1 and -2, Wash. D. C., March 1994

10. C. Supice, "A New Kind of Illumination that Burns Brightly, but Not Out", Washington Post, Science Section, p. A3, October 21, 1991

11. G. J. Kim, et al., "The Development of Multi-Beam Klystron for a Microwave Oven", Proc. 30th Microwave Power Symposium, pp. 73-74, IMPI, Manassas, VA; August 1995

12. Various Reports by Prof. Sloan and students, e.g. M. Chamran, Electron Beam in the Cold Cathode 8732 Magnetron; Univ. of California; Report Series No. 60, Issue No. 453, June 15, 1962; ASTIA Accession Number AD424413

13. D. L. Reverdin, "Electron Optical Exploration of Space-Charge in a Cutoff Magnetron", J. Appl. Phys. 22, p. 257, (1951)

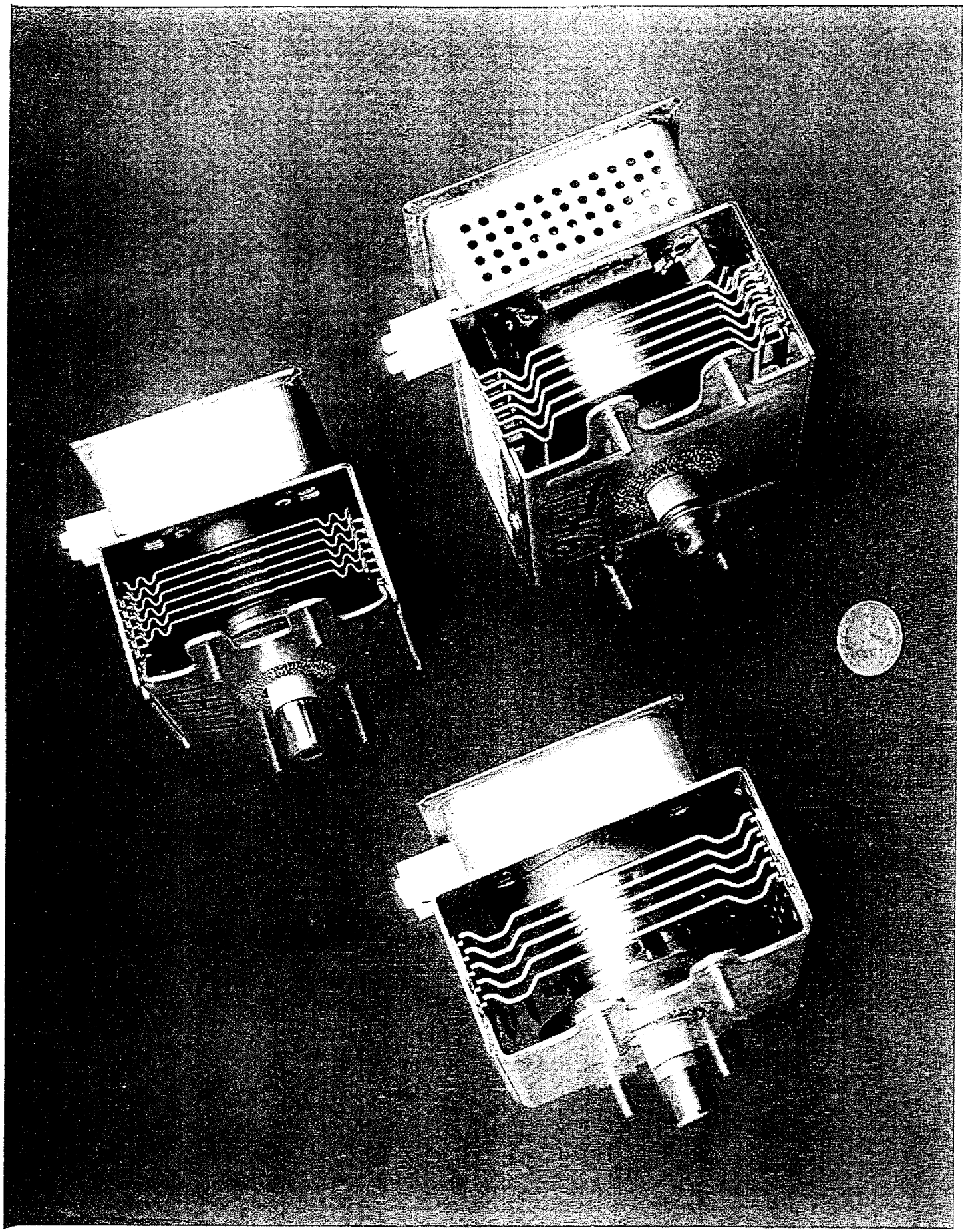


Fig.1 Photograph of modern cooker magnetrons

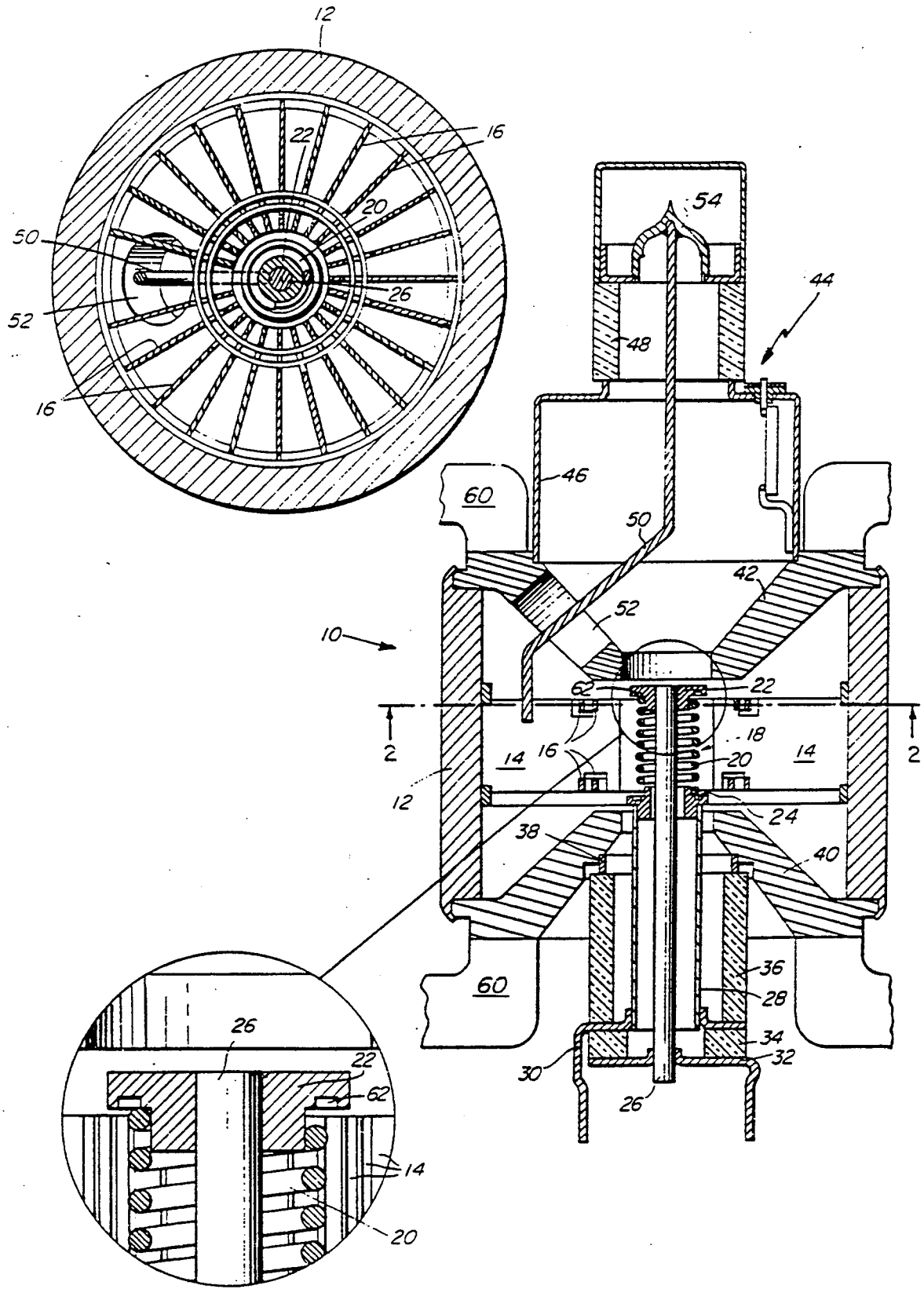


Fig.2 Drawings of typical cooker-magnetron construction

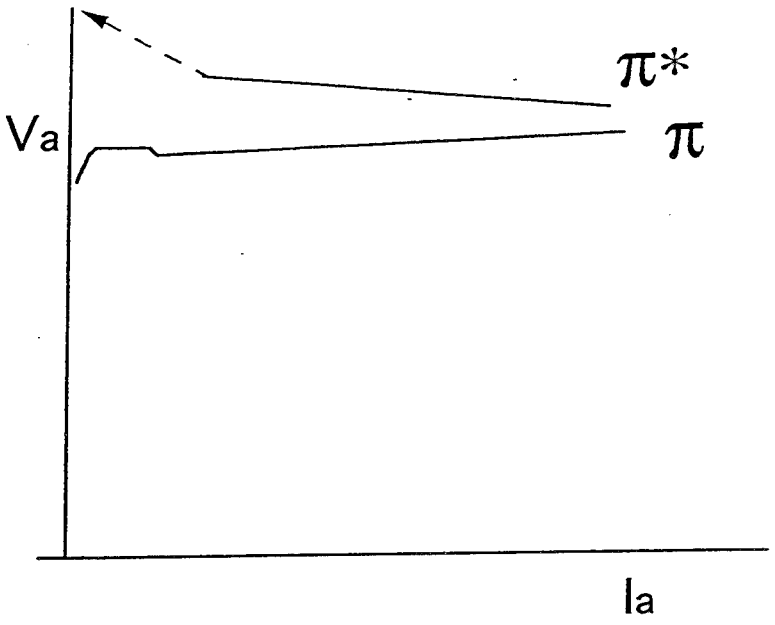


Fig.3 Depiction of low-noise and high-noise gauss-lines (states) in a magnetron when operated with D.C. anode voltage (taken from old data on CW magnetrons)

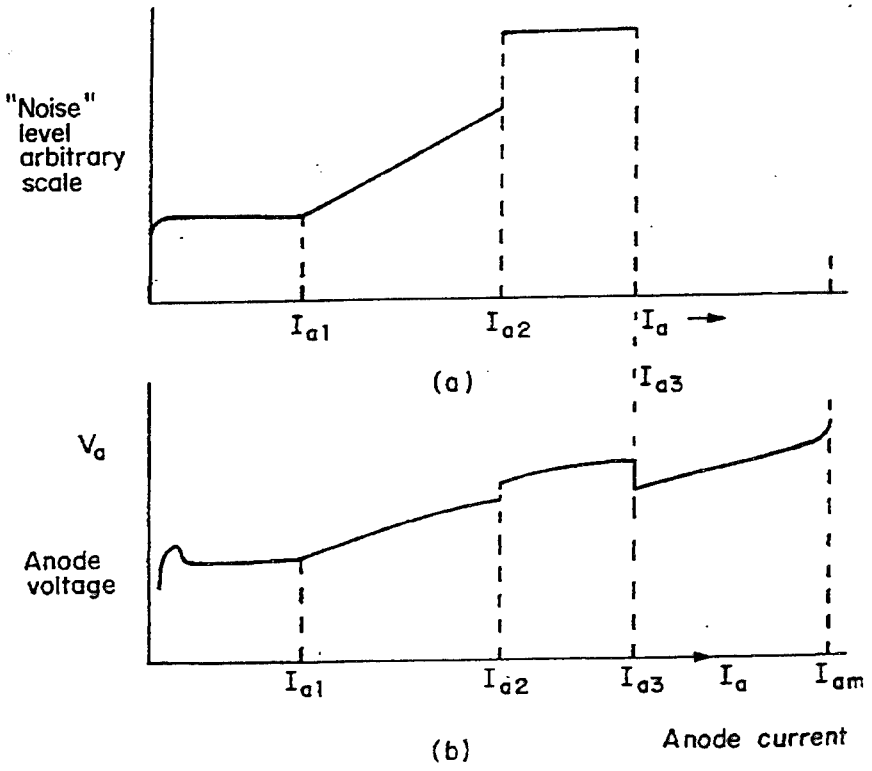


Fig.4 Regions of different noise characteristics during operation of a cooker magnetron with rectified ac voltage

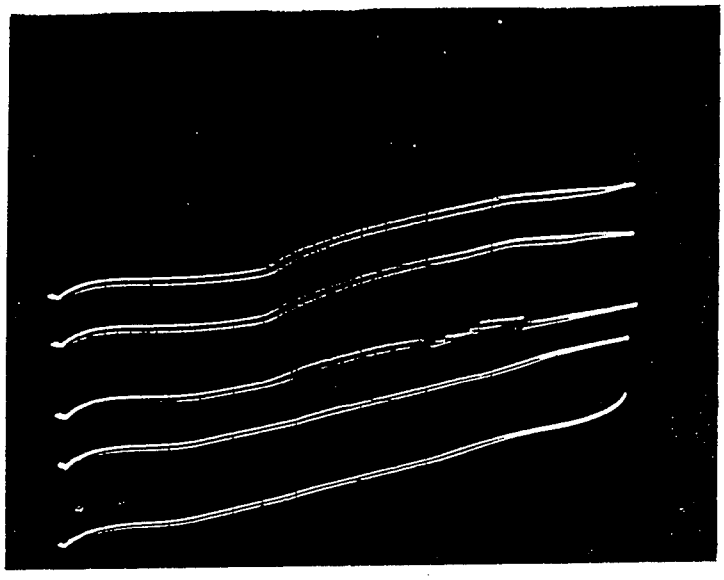
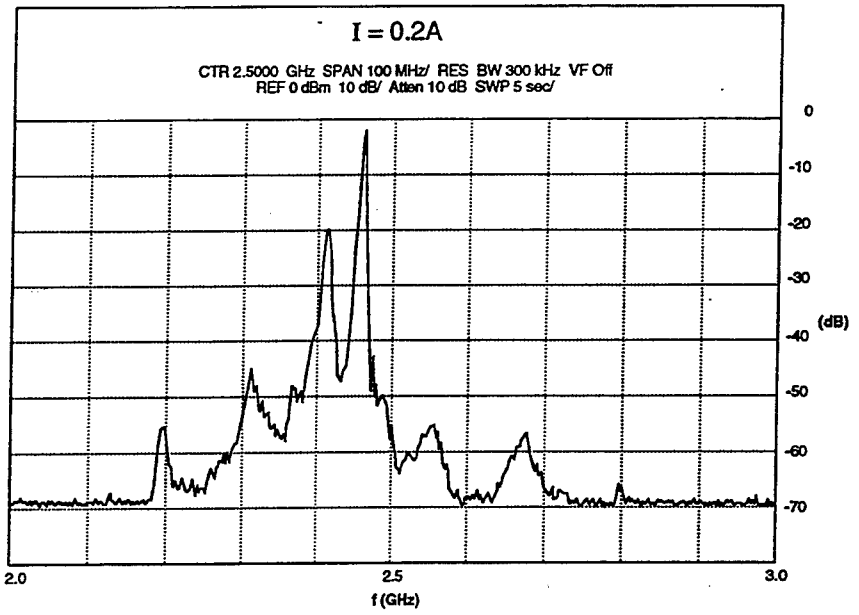
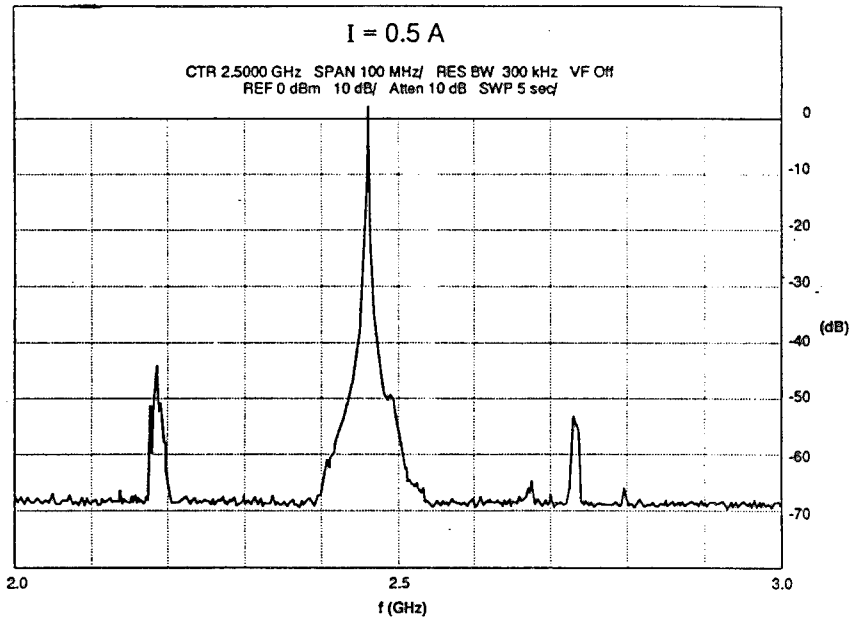


Fig.5 Gauss-line traces (50 V/div; 0.1 A/div.) of a cooker magnetron at varying filament voltages (1.65, 2.0, 2.5 3.0 and 3.5 volts) showing presence of discontinuities associated with spurious oscillations (traces displaced for viewing purposes)

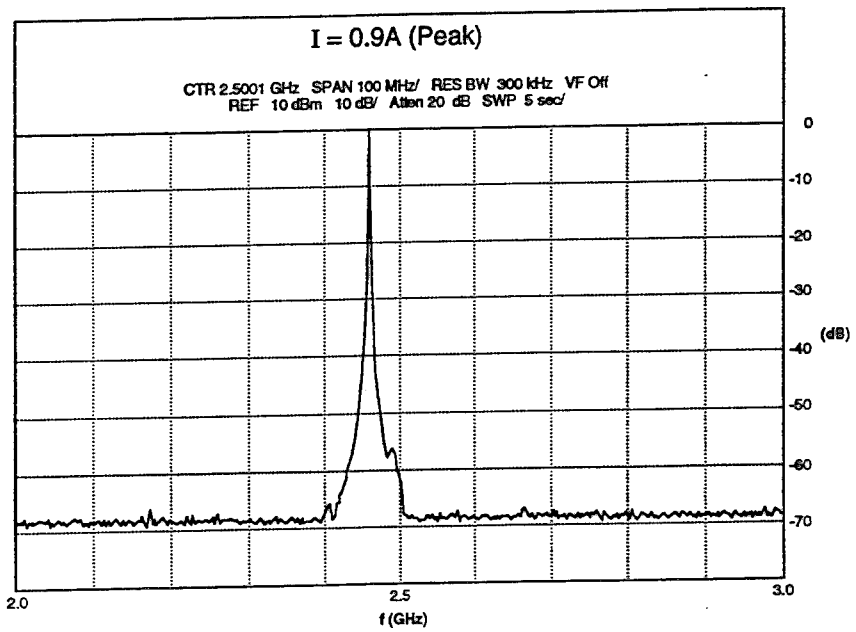


6a

Fig.6 Typical cooker magnetron noise spectra at (a) low currents, (b) moderate currents and (c) high currents



6b



6c

Fig.6 Typical cooker magnetron noise spectra at (a) low currents, (b) moderate currents and (c) high currents

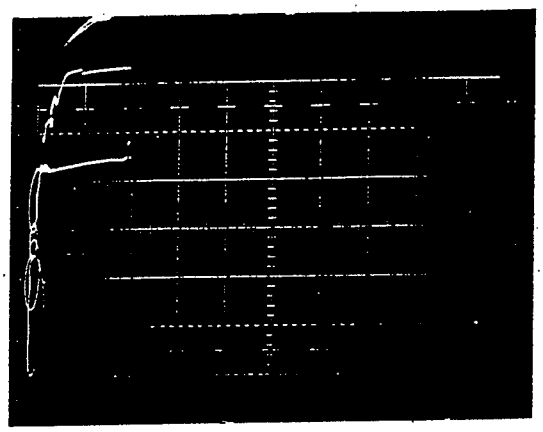


Fig.7 Typical V_a- I_a trace during normal buildup in a cold start of a cooker magnetron

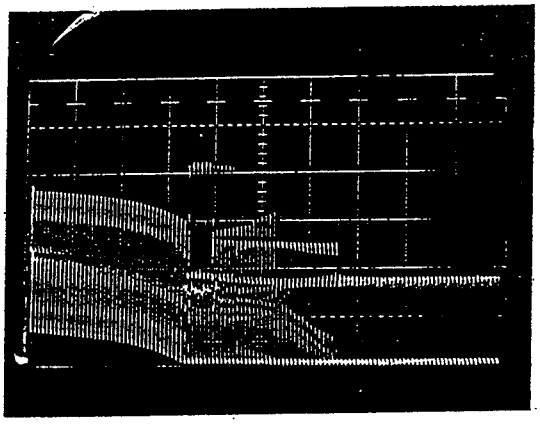


Fig.8 Voltage waveform during cold start of a cooker magnetron. In this case a voltage transient due to end-shield emission is present. (2 kV/div; 0.2 sec/div.)

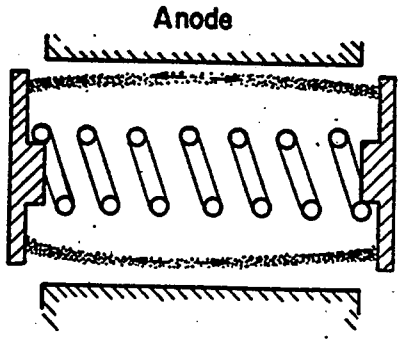


Fig.9 Depiction of the double-stream state that precipitates the "secondary-emission" transient.

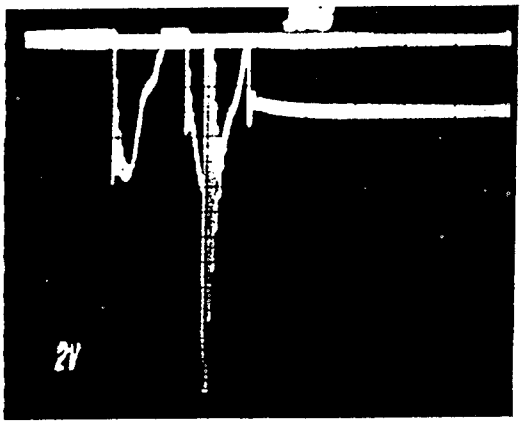


Fig. 10 Voltage waveform during cold start of a cooker magnetron. In this case there is an interelectrode voltage breakdown which causes voltage transients.

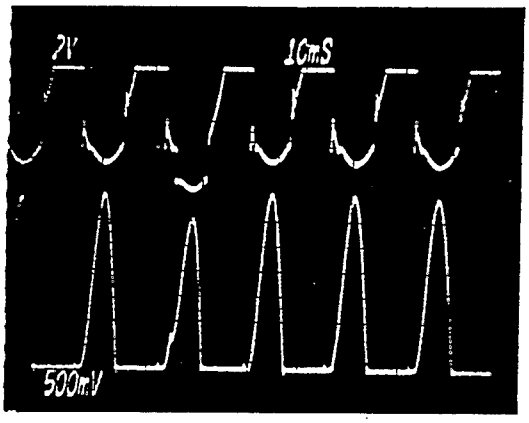


Fig. 11 An example of moding due to spurious oscillation in a cooker magnetron.

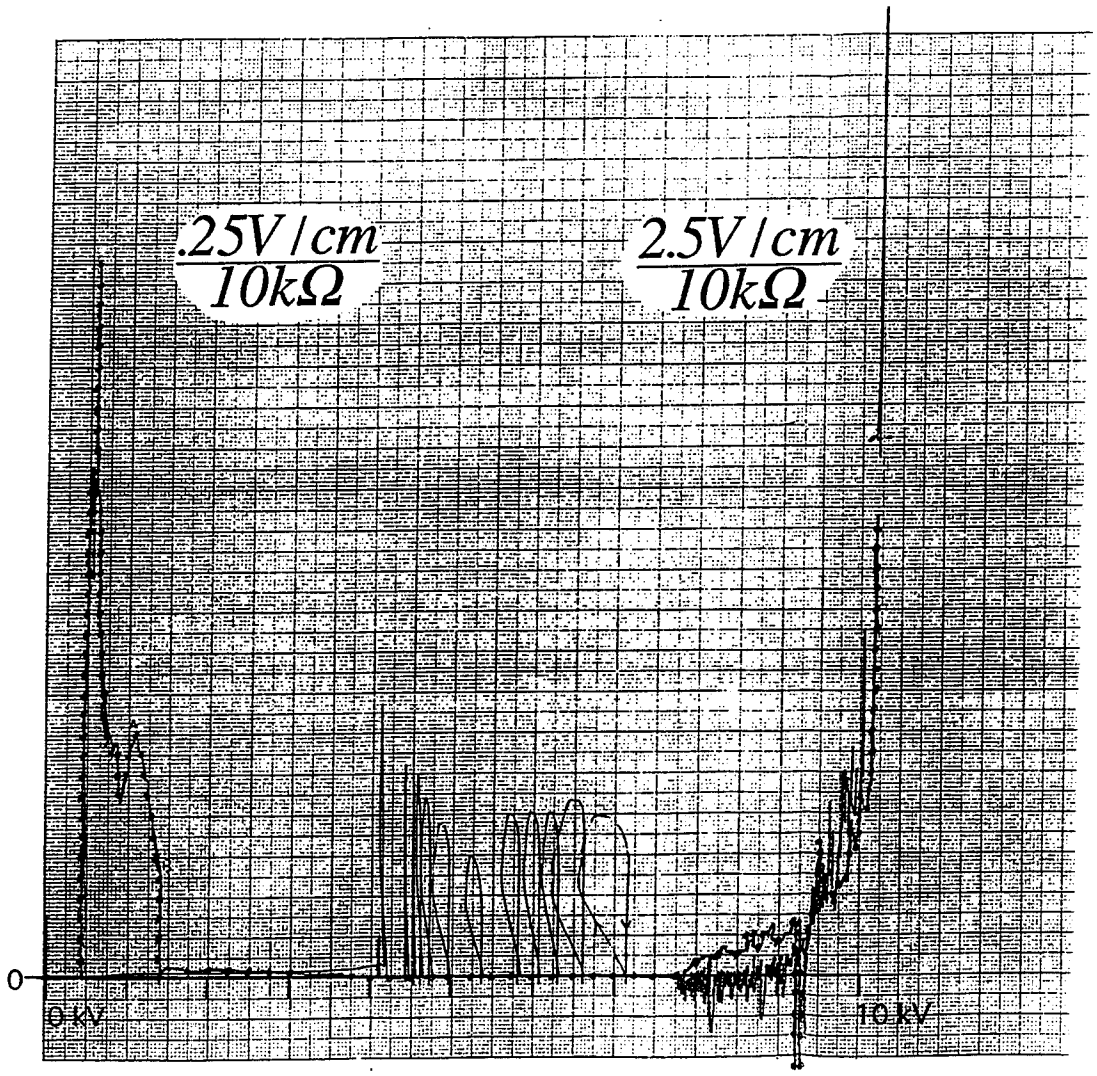


Fig.12 Cold leakage curves; I_a vs. V_a, showing normal pre-breakdown cold (field) emission at high anode voltage (10 kv) and the presence of anomalous gas discharges in the low (~ 1 kv) and high (~4 - 7 kV) voltage regimes. Note the hysteresis effect: the low-voltage discharge (dotted line) is observed only on the upward trace (0 to 10 kV) while the high-voltage discharges (repeated solid lines) occur only during the downward trace (10 to 0 kV). The current scale is 25 μA/div for the discharges and .25 μA/div for the pre-breakdown leakage current at around 10 kV.

THE HIGH SIGNAL TO NOISE RATIO OF THE MICROWAVE OVEN MAGNETRON AND EVIDENCE OF A NEGATIVE FEEDBACK LOOP TO CONTROL IT

William C. Brown
Microwave Power Transmission Systems
6 Perry Lane, Weston MA 02193

ABSTRACT

During the DOE/NASA sponsored study of the Solar Power Satellite, it was discovered that the microwave oven magnetron, operated either as a free-running oscillator or as a locked oscillator with high gain, had an extremely low noise level when it was operated on a well filtered DC power supply and the source of external filament power was removed after starting. Under these operating conditions, and with special noise measuring equipment, the spectral noise density (noise in one hertz of the spectrum) of random noise at frequencies removed by 10 MHz or more from the operating frequency was found to be 176 dbc below the 700 watt output of the magnetron. By externally tuning an auxiliary rf short placed in the magnetron cathode support the rms noise level was reduced 20 db more to a level of 196 dbc. Thus a 10 gigawatt transmitter , if equally performing, would radiate one microwatt of noise power in a 4 kHz bandwidth.

This low level of noise in a companion tube, with an optical window in it to observe the temperature of the carburized thoriated tungsten filamentary cathode, was found to be correlated with temperature limited emission from the cathode. Without any source of external power to heat the cathode after initial startup, its temperature was found to increase and to follow the Richardson-Dushman relationship between temperature and emission, as demands were made upon it to supply more current to the tube. The natural inclination of the tube to run in this quiet mode was confirmed by a novel method of applying a step function of anode voltage to the tube to determine if the cathode were indeed emission limited . If it were, time would be required to heat up the mass of the cathode to the temperature that would be needed to supply the additional current required for steady state operation. This additional heating is accomplished by increased backbombardment of the cathode by electrons returning to the cathode.

An interesting observation is that if the anode current is held constant, and external filament power is injected to heat the cathode, the backbombardment power is reduced by nearly the same amount as the injected external power is increased, to hold the observed filament temperature nearly constant. This implies some kind of negative feedback control to operate at temperature limited emission. Also, at a fixed value of anode current, the cathode temperature is found to be independent of a large change in magnetic field that causes a correspondingly large change in the operating voltage and the power output, and also to be largely independent of a large change in the impedance of the external load.

The material in this paper which has not been previously published expands upon these observations and derives an expression from formal control theory that predicts the time for the filament to heat up to meet the increased emission demands.

INTRODUCTION

In the general activity involving the development of the SPS (Solar Power Satellite) concept the author became involved with an in-depth evaluation of the conventional microwave oven magnetron in terms of both experimentally measured noise and an evaluation of long-life potential[1,2]. During this activity he was amazed to find that the tube, when run with a well-filtered DC power input and with the external source of filament power turned off, controlled its cathode backbombardment mechanism to heat the cathode to an apparent temperature limited emission condition but no further. When moderate amounts of external filament power were applied, with the anode current kept constant, the cathode in a tube with a viewing port was observed to continue to operate at the same temperature while the tube's efficiency increased only slightly. This observation indicated that the tube had adjusted itself to reduce the amount of microwave power that was converted into backbombardment power in a manner analagous to a negative feedback process.

The practical benefits of this self-disciplined behavior were noise-free operation and maximum cathode life, the latter resulting from automatically minimizing the operating temperature of the cathode.

During the investigation it was found that the optically observed increase in the cathode temperature as the magnetron anode current was increased matched very closely that predicted by the Richardson-Dushman equation for temperature limited emission from a carburized thoriated tungsten cathode. This data is shown in Figure 1. However, it is noted that the cathode temperature increased more rapidly with anode current than the Richardson-Dushman relationship predicts if indeed the cathode were always emission limited.

On the other hand, if the anode current were kept constant, the filament temperature was not observed to vary with magnetic field or with external coupling (external Q) over relatively wide excursions of these parameters as shown in Figures 2 and 3. The constancy of cathode temperature with variation of the magnetic field over a wide range was particularly interesting since the DC power input and microwave power output obviously varied with the change in voltage that accompanied the change in magnetic field. These observations were surprising to the author and, I suspect, counter to the prevailing wisdom in the crossed-field community.

It should be noted in Figure 2, however, that when the magnetic field and operating voltage exceed certain values there is a sharp increase in the operating temperature of the cathode. These values of voltage and magnetic field are the same as those for a sudden increase in noise from the magnetron as may be seen in Figure 4-2 of Appendix V.

The carburized thoriated tungsten cathode, central to the theme of this paper, is a relatively unique cathode to be used in a crossed field device. It is essentially a primary emitting cathode. The carburization makes it a very poor secondary emitter. It is also free from chemical breakdown by electron bombardment that seems to be associated with all other cathodes than pure metals. Life in tubes

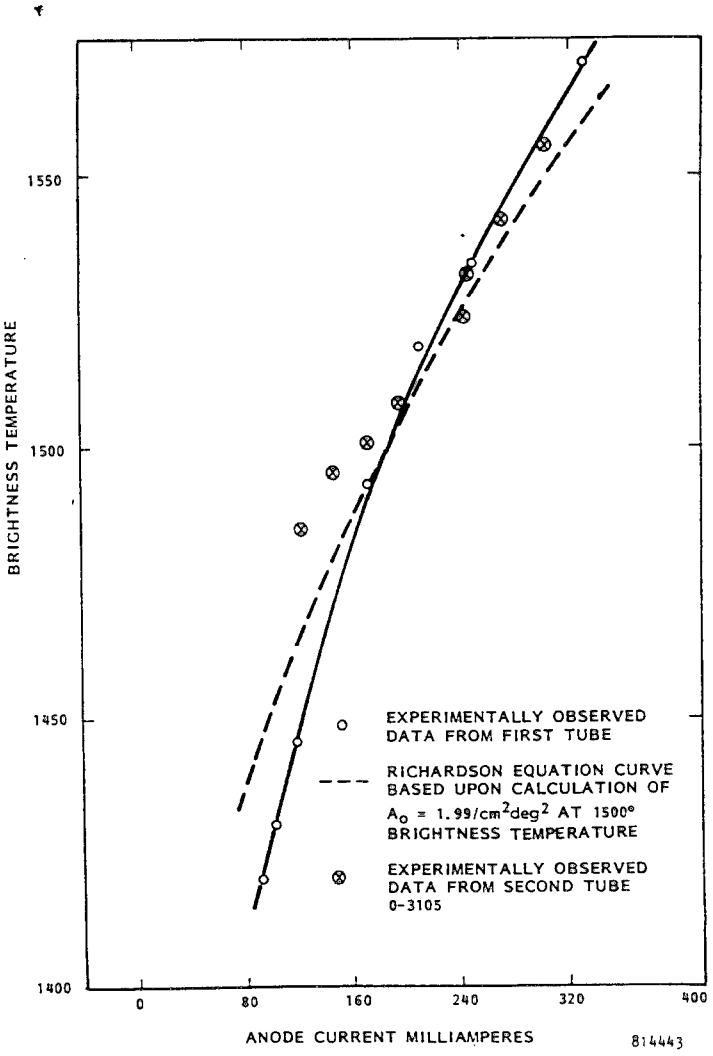


Figure 1. Experimentally Observed and Theoretically Predicted Relstionship Between Cathode Temperature and Anode Current.

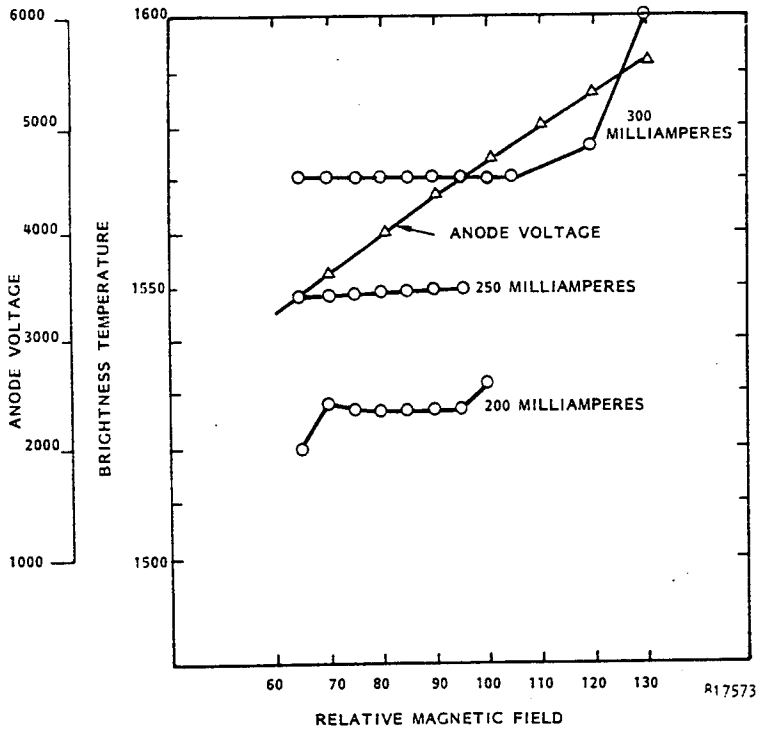


Figure 2. Anode Voltage and Cathode Brightness Temperature as Function of Magnetic Field.

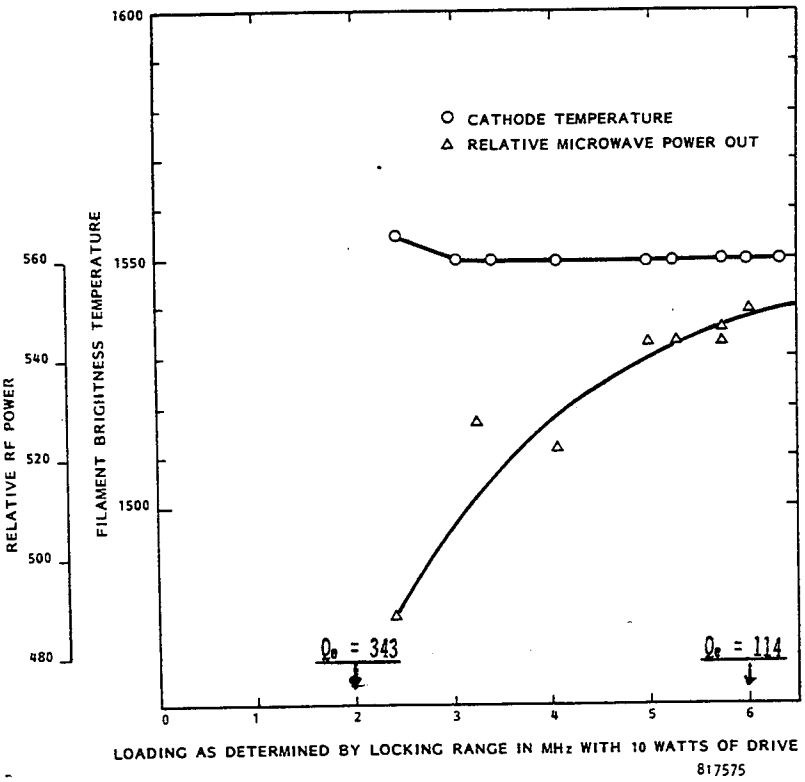


Figure 3. Cathode Brightness Temperature and Power Output as Function of Loading.

with good vacuum is limited only by the slow evaporation of thorium from the surface of the cathode. If the temperature is low and the depth of carburization several mils, life can run into scores of years. The good performance of the cathode in the microwave oven tube where it is routinely insulted, attests to its general ruggedness and reliability. Further, there is a wealth of excellent theoretical and experimental information on the carburized thoriated tungsten cathode, including life test information that confirms theoretical prediction of long life.

The author has sought to both quantify and generalize the observed behavior of the carburized thoriated tungsten cathode in the microwave oven magnetron by characterizing it in terms of feedback control theory. In this treatment, no attempt will be made to examine the physical phenomena within the magnetron. Rather, it will be treated as a black box, and characterized by external observation of its behavior. However, there are some very fundamental issues raised concerning this characterization because the feedback mechanism has such a very high control ratio. One major issue is whether the microwave oven magnetron behaves in the manner that it does because of a chance combination of design parameters. A second issue that is raised is how does the observed behavior scale to other frequencies and power levels. Still another issue is how well do any codes describing the internal behavior of the space charge flow in magnetrons describe the back bombardment behavior.

A very interesting byproduct of this exercise and one which will help introduce the negative feedback characterization of the observed pehnomenon is a pulse technique for measuring excess emission from the cathode. Excess emission is defined as that emission which the cathode could furnish over and above that required to satisfy the anode current operating value.

PULSE TECHNIQUE FOR MEASURING EXCESS EMISSION

The principle of the technique is simple. If the filamentary cathode is operating exactly at the temperature limited emission condition and a sudden increase in anode voltage is applied, there will not be an instant increase in current because the filament cannot emit more current until it is heated up by additional backbombardment. If the filament is operating above the temperature limited condition, there will be an instantaneous increase in current up to the actual temperature limited condition and then a slower increase in anode current as the cathode heats up from additional backbombardment. This behavior is clearly shown in Figures 4 and 5. To interpret the behavior, however, we must refer to Figure 6 which defines the parameters associated with Figures 4 and 5.

In Figure 6, the relationship between the applied potential V to the magnetron and the anode current I is shown. Because of the presence of the magnetic field, current is not drawn until the "Hartree" Voltage V_1 is reached, then, in a CW magnetron, the voltage-current characteristic is nearly flat. For the subsequent analysis, it will be considered flat.

If the power supply is characterized as having an open circuit voltage V_o above that of the V-I characteristic of the magnetron and of being connected to the magnetron through the resistance R, then the steady state current $I_o = V_o/R$ is established as shown in Figure 6. In the experimental work, a voltage regulated power supply was used and a known resistance R was inserted between the power supply and the magnetron.

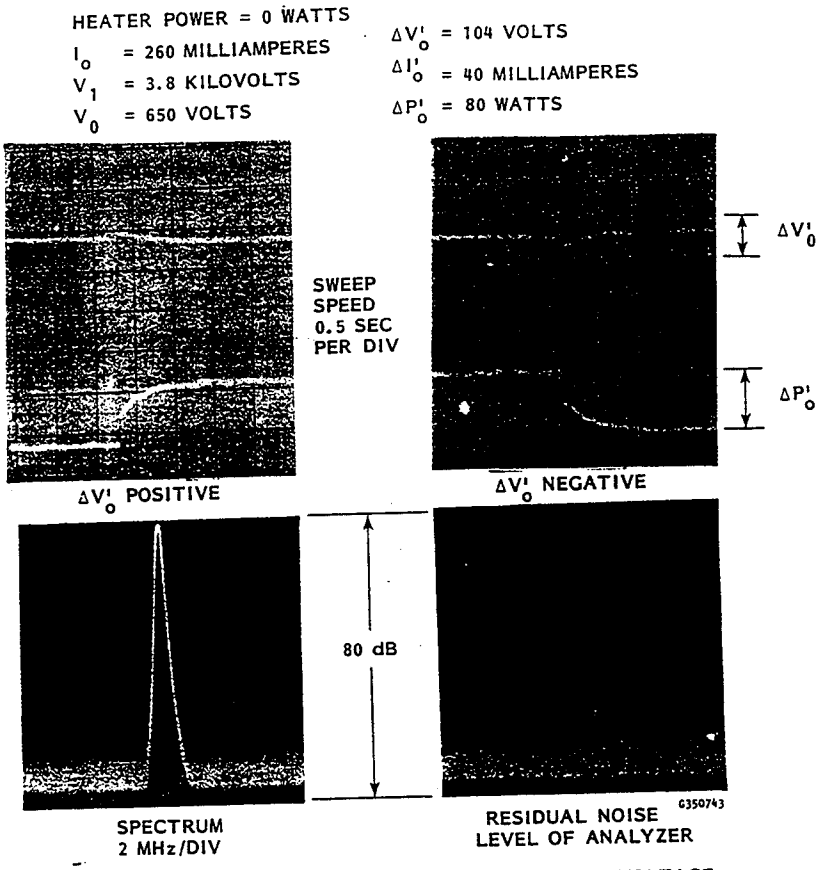


FIG. 4 MICROWAVE OUTPUT RESPONSE TO STEP FUNCTION OF VOLTAGE

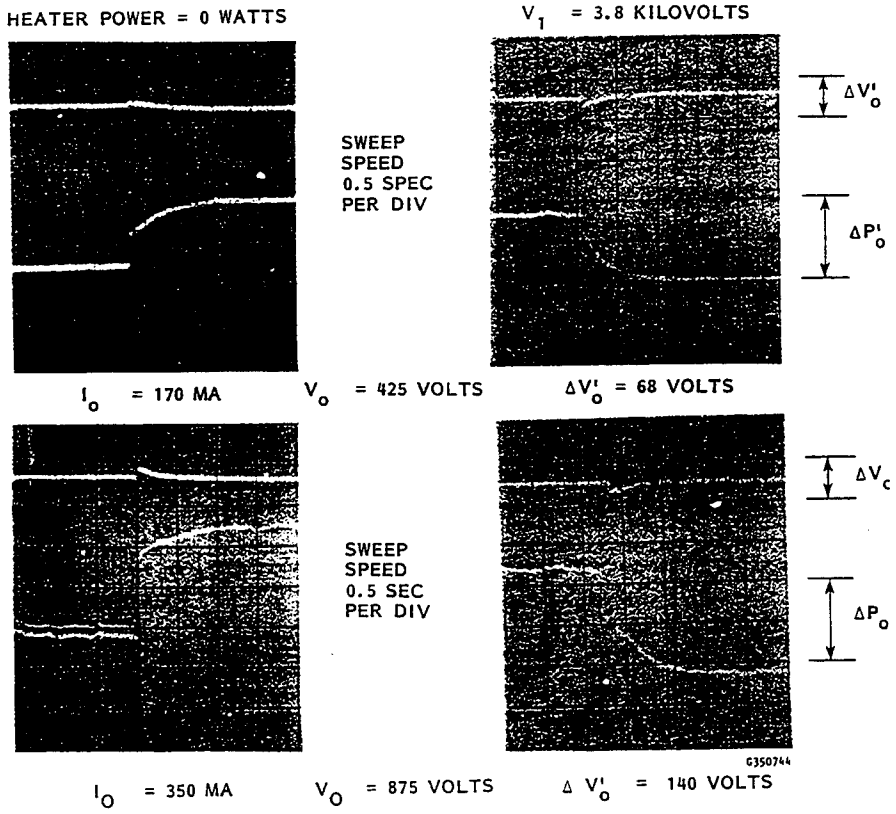


FIG. 5. MICROWAVE OUTPUT RESPONSE TO STEP FUNCTION OF VOLTAGE

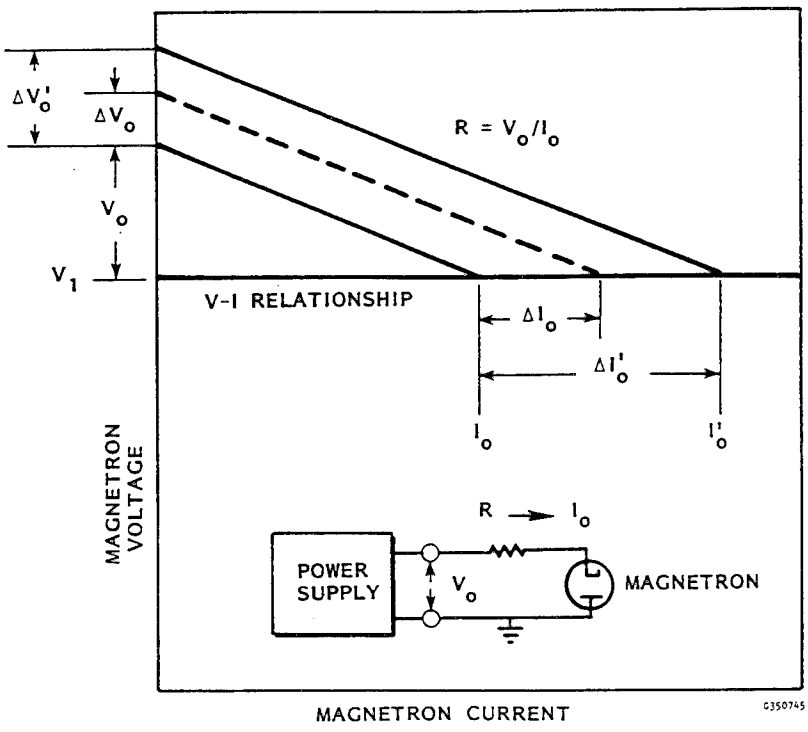


FIG. 6. DEFINITION OF COMPONENTS OF FEEDBACK CONTROL LOOP

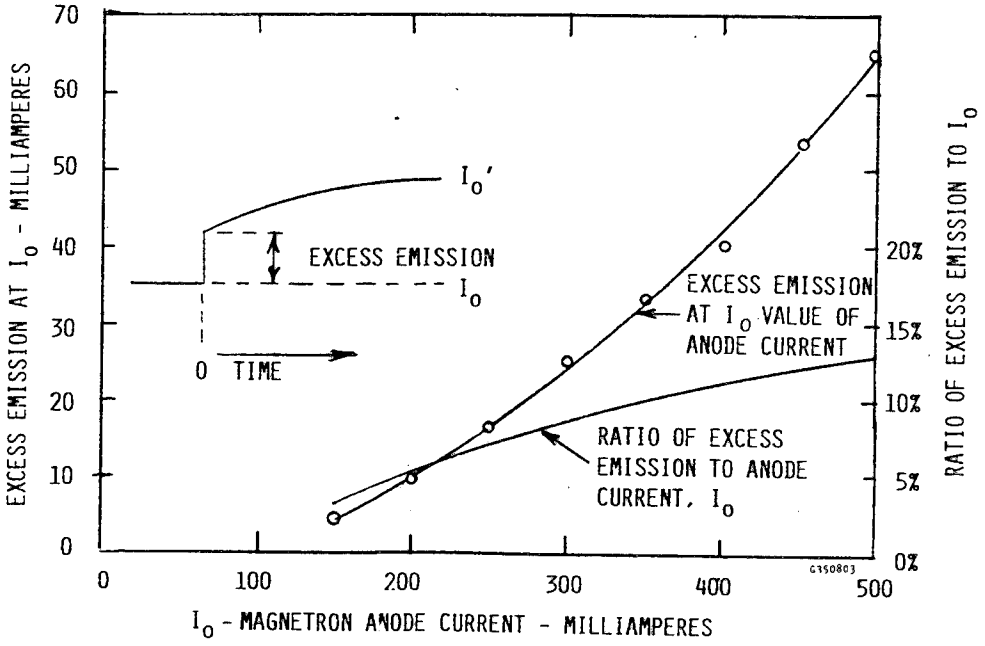


FIG. 7. QUANTIFICATION OF EXCESS EMISSION AS A FUNCTION OF ANODE CURRENT.

Now if V_o is increased by $\Delta V_o'$, a steady state $\Delta I_o' = \Delta V_o'/R$ results. Initially, however, if the current I_o is supplied by a truly emission limited cathode, the cathode has to increase in temperature $\Delta T_o'$ to produce $\Delta I_o'$. This is a time-consuming process that depends upon the increase in backbombardment power and the thermal mass of the cathode. Initially at time t = 0, there is an excess voltage $\Delta V_o'$ at I_o that produces more backbombardment. The conversion factor from excess voltage to watts of backbombardment power is determined experimentally as will be described later.

The backbombardment power, applied to the cathode, heats it at a rate of temperature rise that depends upon the thermal mass of the filament. The emission current increases as the temperature increases, reducing the exessive $\Delta V_o'$ applied to the tube and reducing the backbombardment. The increased emission will be equal to the incremental increase in temperature multiplied by the slope of the Richardson Dushman equation for temperature limited emission. Finally the steady state $\Delta I_o' = \Delta V_o'/R$ is reached.

However, if the cathode is not truly emission limited but is operating at a temperature which will instantaneously supply additional current, previously defined as "excess emission", there will be an instantaneous increase in anode current as shown in Figures 4 and 5. In Figure 6, ΔI_o could represent an instantaneous increase in current from I_o to $I_o + \Delta I_o$ which is the true temperature limited emission of the cathode. Then the excess voltage imposed upon the cathode to create additional backbombardment will be reduced from $\Delta V_o'$ to $\Delta V_o' - \Delta V_o$. The steady state I_o' will then be reached with a time consuming process as before. The value of excess emission is well defined and quantified on the cathode ray presentation as indicated in Figures 4 and 5.

The excess emission for the condition of no external heater power has been examined as a function of anode current, I_o, as shown in Figure 7. The ratio of excess emission to I_o is seen to increase with I_o, indicating that the feedback process is not perfect (infinite gain). The data also suggests that at a value of I_o of around 100 milliamperes the cathode will be emission starved. This indeed is the case and the tube stops oscillating.

QUANTIFYING THE CONTROL LOOP BEHAVIOR

This process may be generalized and quantified by using formal control theory. Figure 8 is the generalized representation for a control mechanism with a feedback loop.

C(t) denotes the output as a function of time, while R(t) indicates the controlling input as a function of time. The ratio of C(t) to R(t) is called the control ratio and it provides both transient and steady state solutions. The control ratio is specified in terms of the other parameters in the diagram as

$$\frac{C(t)}{R(t)} = \frac{G(t)}{1 + G(t)\,H(t)} \qquad (1)$$

Figure 9 converts the generalized form to our specific application. In Figure 6, both Δv_o and ΔI_o are considered as functions of time. The final values after the transient has subsided are labeled $\Delta V_o'$ and $\Delta I_o'$ as seen in Figure 4.

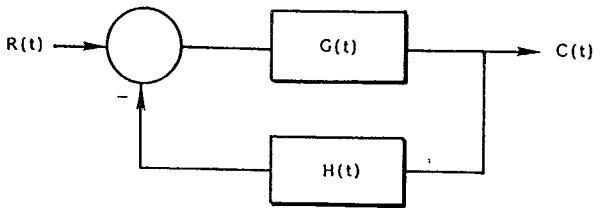


FIGURE 8.

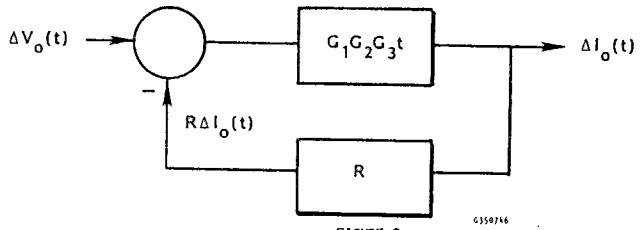


FIGURE 9.

BLOCK DIAGRAM OF BOMBARDMENT CONTROL LOOP

G(t) is defined as the transfer function, that in this instance consists of the product of three constants, $K_1K_2K_3$ and time, t. The constants are defined later.

Having defined G(t) as $K_1K_2K_3t$ and H(t) as R, we may write the control ratio in equation (1) as

$$\frac{\Delta I_o(t)}{\Delta V_o(t)} = \frac{K_1K_2K_3t}{1 + K_1K_2K_3Rt}$$

Converting to the frequency domain by Laplacien transformation, where $t = 1/s$

$$\frac{\Delta I_o(s)}{\Delta V_o(s)} = \frac{K_1K_2K_3}{s + K_1K_2K_3R} = \frac{a}{R}\left(\frac{1}{s+a}\right) \qquad (2)$$

where $a = K_1K_2K_3R$

If $\Delta V_o(s)$ is a step function of voltage $\Delta V_o'$, then

$$\Delta V_o'(s) = \Delta V_o'/s$$

$$\Delta I_o(s) = \frac{\Delta V_o'}{R}\frac{a}{s}\left(\frac{1}{s+a}\right) \qquad (3)$$

Converting back to the time domain, we have

$$\Delta I_o(t) = \frac{\Delta V_o'}{R}\left(1 - e^{-K_1K_2K_3Rt}\right) \qquad (4)$$

From 4 we see that at time 0, $\Delta I_o = 0$ and for $t = \infty$, $\Delta I_o' = \Delta V_o'/R$. The time constant for the simple transient is $K_1K_2K_3R$.

Description and Determination of the Constants K_1, K_2, and K_3.

K_1 is a proportionality constant that converts the excess voltage ($\Delta V_o' - R\ I_o$) in to backbombardment power. K_1 is obtained by observing a tradeoff between external heater power and backbombardment power to keep the filament at the constant temperature required to produce temperature limited emission at I_o. Associated with this tradeoff is a variation in anode voltage which, when calibrated, can be used as a measure of backbombardment power. To make this calibration the anode voltage is noted with no external heater power. Then filament power is added in increments and the reduction in anode voltage for each increment is noted. The relationship is found

to be linear. The ratio of ΔV_o to external filament power is thus established and assumed to be equal to the ratio of ΔV_o to backbombardment power. It follows that:

$$K_1 = \frac{\Delta W}{\Delta V_o}$$ where ΔW is change in external heater (5)

power (watts) and ΔV_o is corresponding change in anode voltage.

K_2 is the ratio of the resulting temperature rise ΔT_o of the carburized thoriated tungsten cathode to each watt of backbombardment power for each second of time.

$$K_2 = 1/4.18\ m_f\ c_f \quad (6)$$

where 4.18 is conversion of calories to watt seconds
m_f is the mass of the filament
c_f is the specific heat of the filament material at temperature T_o.

K_3 is the ratio of the increased emission ΔI_o from the cathode to ΔT_o and is equal to the product of the cathode area and the slope of the Richardson Dushman equation at T_o

$$K_3 = A_f \frac{d}{dT} J$$
$$= A_f\ d/dT\ A_o T^2\ e^{-\theta/kT} \quad (7)$$

This slope may be obtained from the experimental data

where J = Emission current density as given by Richardson Dushman equaiton

A_f = emissive area of cathode in sq. cm.

A_o = Richardson constant, obtained experimentally

T = Temperature in ^oK

θ = work function of emitting material

k = Boltzmann constant = 8.6×10^{-5}

Application of Theory to Microwave Oven Magnetron

It is of interest to apply equation (4) to the microwave oven magnetron with the following values for the parameters:

I_o = 0.185 amperes from reference point on Figure 1

T_o = 1893 ^oK corresponding to 1500°C Brightness temperature at reference point on Figure 1.

A = one square centimeter

A_O = 1.99

m_f = 1 gram

c_f = .03 calories per gram per degree C

θ = work function of carburized thoriated tungsten

= 2.85 volts

from which

K_1 = 0.13 watts per volt

K_2 = 7.97 degrees K per watt second

K_3 = 1.838×10^{-3} Amperes per ^oK

R = 1000 ohms

from which

$a = K_1K_2K_3R = 1.9$

so referring to equation 4, the time constant 1/a is o.53 seconds, which is close to that observed.

REFERENCES

1. W. C. Brown, "Microwave Beamed Power Technology Improvement" Final Report, JPL Contract No. 955104. Raytheon PT-5613 May 15, 1980. Section 5, pp. 1-26.

2. W. C. Brown, "Satellite Power System (SPS) Magnetron Tube Assessment Study" NASA Contractor Final Report 3383 ou Contract NAS8-33157, February 1981.

3. Walter Kohl Handbook of Materials and Techniques for Vacuum Devices. Rheinhold 1967.

Instabilities, Turbulence and Organized Structures in Magnetized Electron Columns

K.S. Fine, C.F. Driscoll, A.C. Cass, T.B. Mitchell,*
and X.-P. Huang

Department of Physics and Institute for Pure and Applied Physical Sciences
University of California at San Diego, La Jolla, CA 92093

Abstract. Magnetically confined electron columns evolve as near-ideal two-dimensional $\mathbf{E} \times \mathbf{B}$ flows, allowing quantitative study of instabilities and turbulence. Experiments are discussed from the regime of linear waves, where the usual step-profile analysis proves inadequate, to the fully nonlinear regime of separate interacting vortices, where we find good agreement with vortex merger simulations. In between these extremes, we find both perspectives are important to understand the observed behavior.

1. INTRODUCTION

Magnetically confined pure electron columns are excellent systems for quantitative observations of 2D vortices, turbulence and self-organization in a cross-field geometry at low energies. Here, we describe several experiments which characterize this process from the seemingly disparate perspectives of near-linear waves and fully nonlinear vortices. Interestingly, a number of similarities are seen.

A "generic" experimental apparatus is shown schematically in Fig. 1. The electrons are contained in a grounded conducting cylinder. A uniform axial magnetic field ($B \lesssim 1$T) provides radial confinement, and negative voltages applied to end cylinders provide confinement at the ends. The apparatus is operated in an inject/manipulate/dump cycle. For injection the leftmost cylinder is briefly grounded, allowing electrons to enter from the negatively biased tungsten filament. Then the confined plasma is sensed and manipulated by antennas on the wall. Finally, after a confinement time which may be as long as hundreds of seconds, the rightmost cylinder is grounded and the z-integrated electron density $n(r, \theta)$ is measured by accelerating the electrons onto a phosphor screen and imaging the resulting light with a CCD camera.

For the experiments discussed here, the electron gyrofrequency is a few GHz, much higher than other frequencies in the system. The gyroradius is the order of a few μm, much smaller

*Present address: Los Alamos National Laboratory, Los Alamos, NM 87545

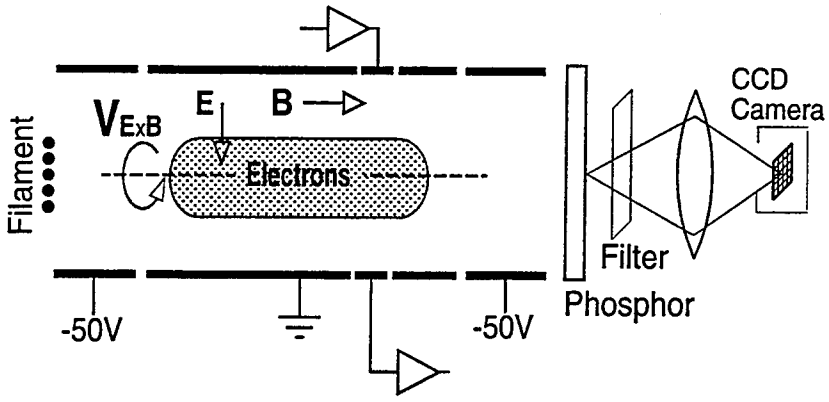


Figure 1. The cylindrical experimental apparatus with phosphor screen/CCD camera diagnostic.

than the diameter of the conducting wall ($2R_w = 7$ cm). In addition, the density is far below the Brillouin limit ($n/n_B \sim .01$), *i.e.* electrons move slowly enough so that electron inertia can be ignored. In this regime the electron motion is well-described by the $\mathbf{E} \times \mathbf{B}$ drift equations. Finally, the axial bounce frequency of an individual electron (~ 1 MHz) is much larger than the drift rotation frequency (10–100 kHz), so the electrons behave as "rods" of charge.

In this approximation, the (r, θ) flow of the electrons is described by the 2D drift-Poisson [1] equations,

$$\frac{\partial n}{\partial t} + \mathbf{v} \cdot \nabla n = 0 \,, \quad \mathbf{v} = -\frac{c}{B} \nabla \phi \times \hat{z} \,,$$
$$\nabla^2 \phi = 4\pi e n \,, \tag{1}$$

where $n(r, \theta)$ is the (z-averaged) electron density, $\mathbf{v}(r, \theta)$ is the $\mathbf{E} \times \mathbf{B}$ drift velocity, and $\phi(r, \theta)$ is the electrostatic potential. The vorticity of the flow, $\zeta \equiv \hat{z} \cdot \nabla \times \mathbf{v} = (4\pi ec/B)n$, is proportional to the electron density, which is directly measured. These equations are isomorphic to the Euler equation [2,3]. A column of electrons in vacuum surrounded by a conductor thus evolves as would a 2D vortex in an incompressible inviscid fluid surrounded by a circular free-slip boundary. Of course, there are also various "viscous" plasma effects [4] on small spatial scales, which are *not* modelled by the Navier-Stokes equation. However, we believe the effects described in this paper do not depend on the details of the fine-scale dissipation.

2. MODES AND INSTABILITIES

We first consider an isolated electron plasma column, *i.e.* an isolated vortex. Asymmetries in the $n(r, \theta)$ profile can be treated as waves on an otherwise circular vortex. Our $n(r, \theta, t)$ data allows us to completely characterize the $k_z = 0$ modes, varying as $\exp(im\theta - i\omega_m t)$. It is well known that hollow density profiles can have diocotron (*i.e.* Kelvin-Helmholtz) instabilities, whereas monotonically-decreasing profiles have only stable

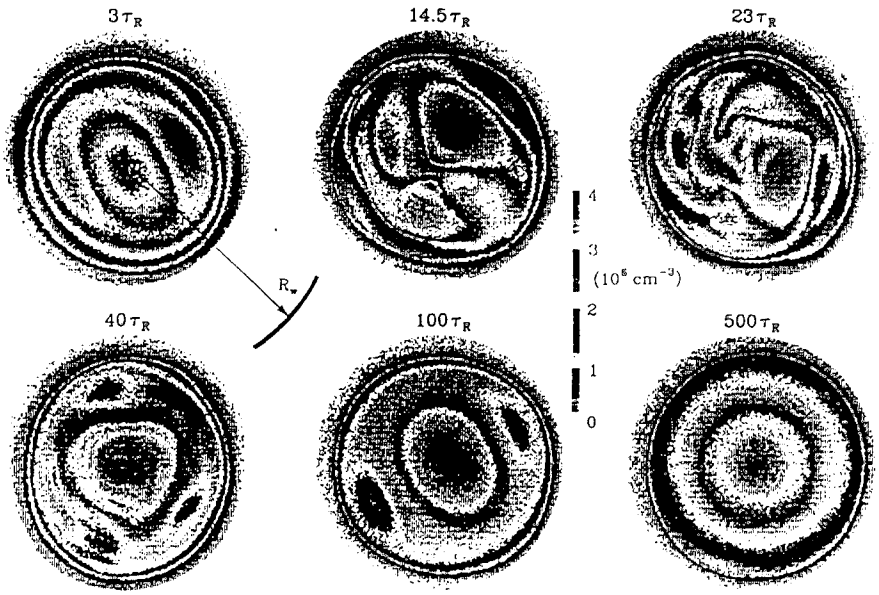


Figure 2. Camera images of electron density (*i.e.* vorticity) showing the evolution of an initially hollow electron column.

or damped modes. More precisely, Rayleigh's inflection-point theorem [5] as extended by Arnold [6] shows that the system is nonlinearly stable if $n(r)$ is monotonically decreasing.

When $n(r)$ and the resulting drift rotation frequency $\omega_E(r)$ are sufficiently non-monotonic, $m \geq 2$ exponential instabilities are predicted by inviscid 2D fluid theory [2]. These $m \geq 2$ shear-flow instabilities are readily observed on hollow beams and trapped electron columns [3,7,8]. Figure 2 shows an $m = 2$ instability leading to turbulence and large-scale transport to a stable, monotonic profile, and will be discussed below.

It is important to emphasize that the stable and unstable diocotron modes are separate and apparently mutually orthogonal, and may co-exist on hollow profiles [3,9]. This distinction is missed by the usual "step-profile" vorticity patch analysis. The step-profile approximation gives modes occurring only in complex conjugate pairs [1]. Experimentally, the stable and unstable modes for $m \geq 2$ have completely different real frequencies, and one mode can be unstable even when the other is not significantly damped. Both the frequencies and growth rates of the $m \geq 2$ modes are reasonably well characterized by computational solution of the eigenvalue equation using the measured density profiles. For short wavelengths (*e.g.* $m \geq 15$), however, experiments have observed stabilization by plasma effects outside 2D fluid theory [8].

For $m = 1$, a strong exponential instability is also observed experimentally [9]. This exponentially growing mode does not exist within 2D fluid theory, although an initial-value analysis demonstrates that perturbations can grow algebraically with time [10]. More recent analyses suggest that finite Larmor radius and finite length effects outside 2D fluid theory can result in exponential growth of $m = 1$ [11,12].

Before leaving the topic of shear instabilities, we note that in annular systems (such

as magnetrons) the shear is strongly affected by the bias on a central conductor, whereas our system has no central conductor. In addition, for the experiments discussed here the plasma edge is typically only about one-half way to the wall, so that image charge effects are relatively small.

3. DIRECT AND BEAT-WAVE DAMPING

Small amplitude surface waves on an isolated, circular, constant-density plasma of radius R_p are all stable, with frequencies $\omega_m = \omega_E\ [m - 1 + (R_p/R_w)^{2m}]$. For this case, the $\mathbf{E} \times \mathbf{B}$ rotation frequency, ω_E, is constant throughout the vortex, and all surface waves have $\omega_m < \omega_E$. For more general density profiles there arises the possibility of a resonant radius r_s where $\omega_m = m\ \omega_E(r_s)$, *i.e.* where the wave moves with the same velocity as the fluid [13]. This "direct" resonance can give rise to inviscid, spatial-Landau damping of the wave [2], *i.e.* symmetrization of the vortex. For even moderate wave amplitudes, this damping is typically nonlinear, and the damping may decrease [14,15] or cease [3] when the resulting "cat's-eye" flows generate fine-scale filaments inside the vortex. For reasonably sharp-edged vorticity profiles, the resonant radii can be completely outside the vortex, in which case no direct resonance damping occurs.

Of perhaps more interest for real plasmas and flows are the large amplitude modes. The Kirchoff ellipse is an exact nonlinear solution [16] for an $m = 2$ distortion of a constant density patch, and nonlinear solutions for $m \geq 3$ have been found numerically and analytically [17]. For large amplitude distortions, $\omega_E(r)$ no longer adequately describes the θ-dependent flow. Figure 3 shows an experimental example of a large amplitude $m = 2$ distortion on a nearly constant density patch. For this case, filaments generated at the resonance "X-points" lie outside the vortex [17,18]. The evolution of this process will be highly nonlinear, and the resonant damping may cease with the formation of these steady-state filamentary structures. This structure is also described as a "tripole," since the "holes" surrounded by the filaments are negative vorticity relative to the center [19]. Furthermore, this state seems to be the "linear wave" analogue of the long-lived "holes" discussed in the next section.

Even when no "direct" resonance occurs, we find [20] that a single, excited wave varying as $\sin(m\theta)$ will decay into a daughter wave varying as $\sin[(m-1)\theta]$, through resonance damping of the nonlinear "beat wave" at frequency $\omega_m - \omega_{m-1}$ [21]. The direct and beat wave damping processes are shown diagrammatically in Fig. 4. When this beat-wave resonant coupling exists, a single surface wave is an unstable equilibrium, and no equilibrium exists with two waves.

This beat-wave damping is seen to give global symmetrization of an asymmetric vortex, while presumably also generating fine-scale resonance filaments within the vortex. For many vortex profiles, this beat wave damping is observed to be the fastest mechanism for symmetrization. Figure 5 shows the measured density (*i.e.* vorticity) distribution before and after beat-wave damping of an $m = 3$ perturbation on an otherwise symmetric column, and shows the daughter growth rates γ_{m-1} for decays of m-number $4 \rightarrow 3$, $3 \rightarrow 2$, and $2 \rightarrow 1$. For $3 \rightarrow 2$, the $m = 3$ pump mode decays rapidly to an $m = 2$ daughter mode plus a diffuse

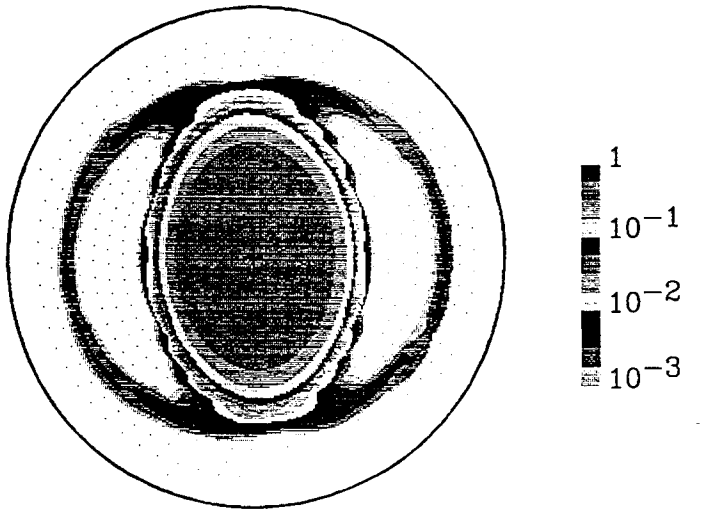


Figure 3. Measured density $n(r, \theta)$ phase coherent with a partially damped $m = 2$ diocotron mode.

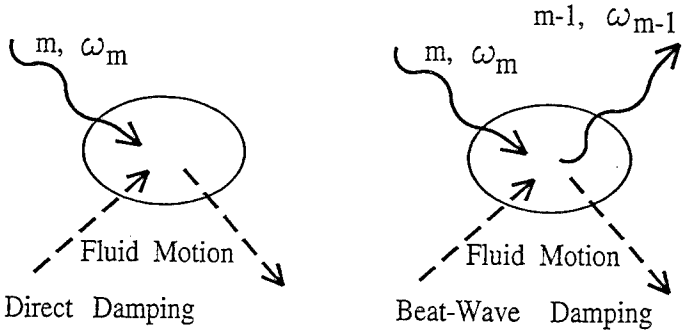


Figure 4. Diagrammatic representation of (a) direct spatial Landau damping and (b) beat-wave damping.

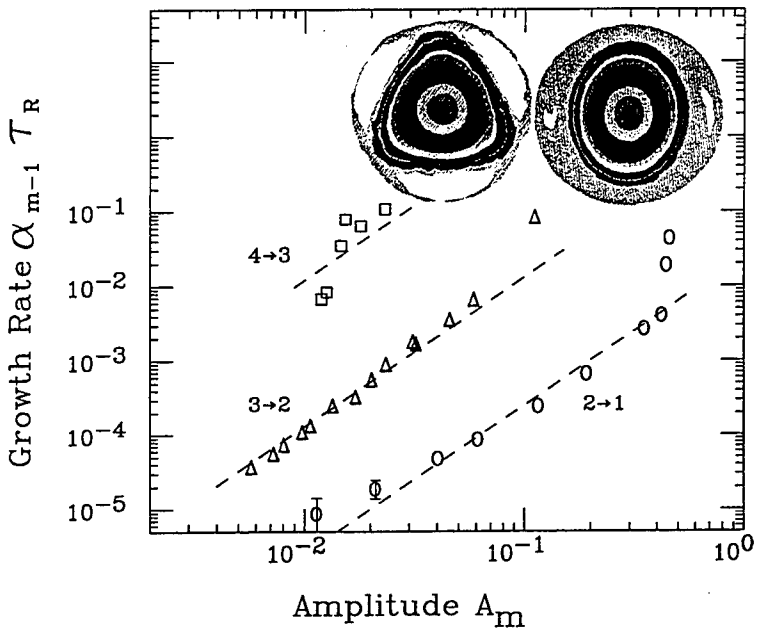


Figure 5. Measured decay instability growth rates $\alpha_{m-1}\tau_R$ versus mode amplitude A_m, for $m = 4$, 3 and 2. Insert shows $n(r, \theta)$ before and after the $3 \rightarrow 2$ instability.

halo, within 10 rotations of the vortex. The resultant $m = 2$ mode is then unstable to decay into an $m = 1$ mode. We note that the initial condition exhibits slight filamentation due to direct resonance damping of the large $m = 3$ mode.

The nonlinear couplings involved in beat-wave damping have been treated in general by Crawford and O'Neil [21], although no quantitative coupling rates Γ_{ij} have yet been calculated. Energy and angular momentum conservation between waves and particles predicts that the coupling between pump mode i and daughter mode j will occur at a radius r_s where

$$\omega_i - \omega_j = \omega_E(r_s^{i \rightarrow j})(i - j) \ . \tag{2}$$

The unstable mode j is predicted to grow as

$$\frac{d}{dt} A_j = (-\alpha_j + \Gamma_{ij} A_i^2) A_j \ , \tag{3}$$

where α_j is the linear damping of mode j and the coupling rates Γ_{ij} are independent of mode amplitude A_i for small A_i. A similar nonlinear coupling to *external* field asymmetry amplitudes A_i gives rise to an "induced scattering instability" which has been previously observed on these electron systems [22].

The predicted dependence on the square of the pump mode amplitude A_i in Eq. (3) agrees with the experimental data of Fig. 5. This allows us to estimate the coupling rates Γ_{ij}: the dashed lines in Fig. 4 give $\Gamma_{21} = 0.025/\tau_R$, $\Gamma_{32} = 1.3/\tau_R$ and $\Gamma_{43} = 120./\tau_R$. These measured rates are about 10 times less than estimated from first order perturbation theory [23]. Presumably, this is because the instability generates filaments (or "cat's eyes") which

then suppress the instability. Fine-scale diffusion or viscosity eventually smoothes out the filaments, allowing the instability to proceed further, and this effect determines the overall rate of evolution. This is similar to the situation with direct damping of large amplitude surface modes, where "bounce" oscillations and less-than-expected damping rates have been observed [15].

Our observations show that surface wave damping from direct and beat-wave resonances should contribute significantly to the relaxation of vortices in inviscid 2D flows. Indeed, the beat wave damping measured here suggests that when there are available longer-wavelength modes, surface waves of finite amplitude will always be damped, and fine-scale filamentation or cats-eyes within or outside the vortex will be generated. One consequence of this beat wave damping is that a long-wavelength mode (such as an $m = 2$ ellipse) would appear to actively damp or suppress shorter wavelength modes such as $m = 3$. These shape distortions are an inherent result of vortex-vortex interactions, including those leading to merger [24] or filamentation [25], so direct damping and beat-wave damping may affect these interaction processes.

Finally, we note that the near-linear perspective of the beat-wave decay instability shows qualitative correspondence with even the highly nonlinear evolution of Fig. 2. For example, the plasma at 40 τ_R has moderate amplitude $m = 3$ components δn_3 and $\delta\phi_3$, and this relaxes to predominantly $m = 2$ components by 100 τ_R. Of course, $\delta n_3(r)$ and $\delta n_2(r)$ do not necessarily correspond to the radial eigenfunctions for linear modes. Both beat-wave damping and vortex merger result in energy flowing to long wavelengths, with concomitant formation of fine scale filamentation.

4. VORTICES STABLE IN SHEAR

From the nonlinear perspective, the rate of relaxation towards symmetry in Fig. 2 is largely determined by the longevity of coherent negative vortices, or "holes" [26] within the larger vortex. These holes are stable for hundreds of bulk rotation times, generally in a preferred configuration of two diametrically opposed holes on a distorted core (a "tripole"). On a longer time scale, these holes creep radially outward and are eventually destroyed. Because of these coherent holes, the observed fluctuation relaxation rate is about 50 times slower than expected from simple, passive-tracer mixing, and the measured fluctuations are strongly skewed from Gaussian.

The longevity of the vorticity holes in the images of Fig. 2 suggests that the holes can be regarded as negative vortices in equilibrium with the background shear flow of the large-scale θ-averaged vorticity distribution $n(r)$. The inviscid equilibria of uniform vorticity patches in an imposed background flow are ellipses, as first derived by Moore and Saffman [27]. In our case, the mean background flow is purely rotational, i.e. $<\mathbf{v}>= \omega_R(r) r\hat{\boldsymbol{\theta}}$, leading to a simple, linear shear in the vicinity of any point. Therefore, the equilibrium depends only on the scaled shear

$$\sigma \equiv r_v \frac{d\omega_R}{dr}|_{r_v} / \Delta\zeta_v \,, \tag{4}$$

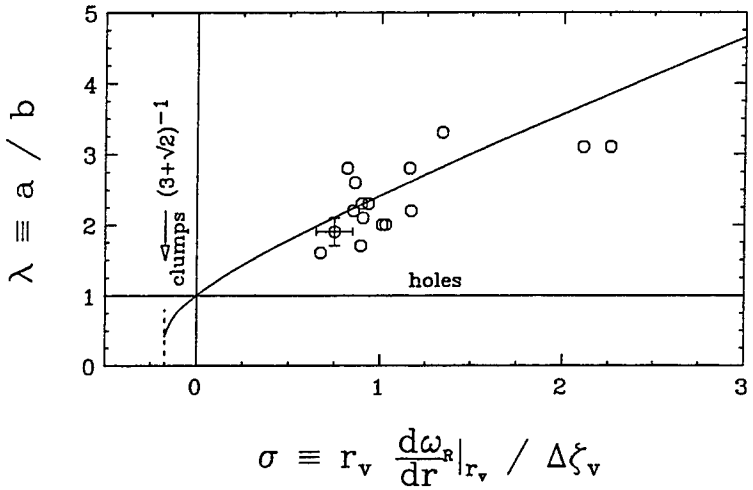


Figure 6. Measured hole aspect ratio λ versus normalized background shear σ and Moore-Saffman model (curve).

where $\Delta\zeta_v$ is the difference between the vorticity at the center of the vortex (at radius r_v) and the background vorticity $< \zeta >$ at r_v. Since the rotational shear considered here is everywhere negative, the equilibria are ellipses oriented along $\hat{\boldsymbol{\theta}}$ (for holes with $\sigma > 0$) or along $\hat{\mathbf{r}}$ (for clumps with $\sigma < 0$).

Figure 6 shows the predicted and measured hole aspect ratios $\lambda \equiv a/b$, where a and b are the elliptical axes along the θ and r directions respectively. Here, λ and σ are measured directly from 16 images such as those shown in Fig. 2 at times $40 \leq t/\tau_R \leq 400$. Reasonable agreement between the measurement and the model is found, validating the applicability of the model to individual holes in this system. The holes are robust because they are prograde with respect to the negative background shear, whereas clumps would be retrograde.

In the model, holes of any depth $\Delta\zeta_h$ can survive in the background flow with negative shear. Of course, a shallow hole would be very elongated, and the local model is no longer valid. In contrast, a clump must have relative vorticity

$$\Delta\zeta_c \geq (3 + 2\sqrt{2})\, r_c \left|\frac{d\omega_R}{dr}\right|_{r_c} \tag{5}$$

to be in equilibrium. Such very intense clumps are not observed for evolutions from initially smooth distributions such as Fig. 2. If we approximate the background as $< \zeta >= \zeta_0[1 - (r/r_0)^2]$, giving $r d\omega_R/dr = -(\zeta_0/2)\,(r/r_0)^2$, then $\Delta\zeta_c$ cannot be large enough to satisfy Eq. (5) provided the clump vorticity is no greater than the central vorticity (*i.e.* $\zeta_c \leq \zeta_0$). However, long-lived clumps *have* been observed in this apparatus during evolutions of highly-filamented, initial conditions with low shear profiles, as we will discuss in the next section [28]. Also, a similar limit to vortex stability has recently been measured in a system with a controlled background shear [29].

After about $40\,\tau_R$, the number of observed holes decreases with time, and the remaining holes tend to organize into symmetric configurations. After $t \simeq 80\,\tau_R$, virtually all the images are in the tripolar configuration of a deformed central core and two elliptical holes

opposite in θ, typified by Fig. 2 at 100 τ_R. The decrease in the number of holes with time is apparently due to mutual advection and merger [30] of the holes. These merger events have been observed in a few camera images, but the shot-to-shot irreproducibility precludes imaging the dynamics of merger. The "tripole" state is stable for hundreds of τ_R because of hole-induced distortion of the background flow not treated in the simple model: the elongated core in Fig. 2 at 100 τ_R maintains the θ-positions of the two holes.

In these evolutions, the quasi-stable tripolar configuration is eventually destroyed by a slow, outward creep of the holes: the holes move from $r_h/R_w \simeq 0.35$ to $r_h/R_w \simeq 0.50$ in about $500\tau_R$. The cause of this outward motion is unknown at present. However, experiments varying L_p and B_z suggest that this outward creep is a 2D $\mathbf{E} \times \mathbf{B}$ drift effect rather than an axial end effect [31,32], and recent theory work suggests the creep arises from the perturbation which the hole induces in the background flow [33]. When the holes approach the edge of the column at $r_h/R_w \simeq 0.57$, they apparently filament in the θ direction and are destroyed.

5. VORTEX CRYSTALS

So far we have discussed experiments where the initial profile is smooth; here we discuss cases where we initially trap a highly-filamented electron density distribution from the spiral electron source [28]. Many individual vortices then form due to local Kelvin-Helmholtz instabilities, and this turbulent state evolves and relaxes by chaotic vortex advection and mergers.

Figure 7 shows the measured vorticity $\zeta(r, \theta, t)$ at five times for two slightly different initial conditions, varied by changing the filament bias voltages. The upper sequence forms ordered patterns of vortices that we call "vortex crystals," whereas the lower sequence relaxes rapidly to a monotonically-decreasing profile. The vortex crystal states consist of 5–11 individual vortices each with vorticity 4–6 times the background vorticity, arranged in a lattice pattern which rotates with the background. In plasma terms, rods of enhanced electron density ($n \sim 7 \times 10^6$ cm^{-3}) are maintaining self-coherence and positions relative to each other for several seconds, while $\mathbf{E} \times \mathbf{B}$ drifting with a diffuse background ($n_B \sim 2 \times 10^6$ cm^{-3}). Vortex crystal states are repeatably observed over a range of filament bias voltages, but the characteristics of the initial $n(r, \theta)$ required for these states are not yet understood.

In both sequences, the unstable filamentary initial condition forms $N_v = 50 - 100$ vortices of roughly equal circulation, after which the number of discrete vortices N_v initially decreases as $N_v \sim t^{-\xi}$, with $\xi \approx 1$. This relaxation is generally consistent with the predictions of the "dynamical scaling" theory of Refs. [34]; the experimentally-observed ξ range from 0.4 to 1.1 as the initial conditions are varied, with 0.8 being commonly observed. Here, the merger, filamentation, and diffusion results in a decrease in the discrete vortex circulation, roughly as $\sum \Gamma_v \sim t^{-\xi/2}$.

In the evolution of the top sequence in Fig. 7, the relaxation is arrested by the "cooling" of the chaotic vortex motions, with formation of vortex crystals by $10\,\tau_R$. When the vortices all have about the same circulation, the patterns are quite regular, as seen at $600\,\tau_R$ in Fig. 7. After about 10^4 τ_R, N_v decreases to 1 as the individual vortices decay away in place. Other

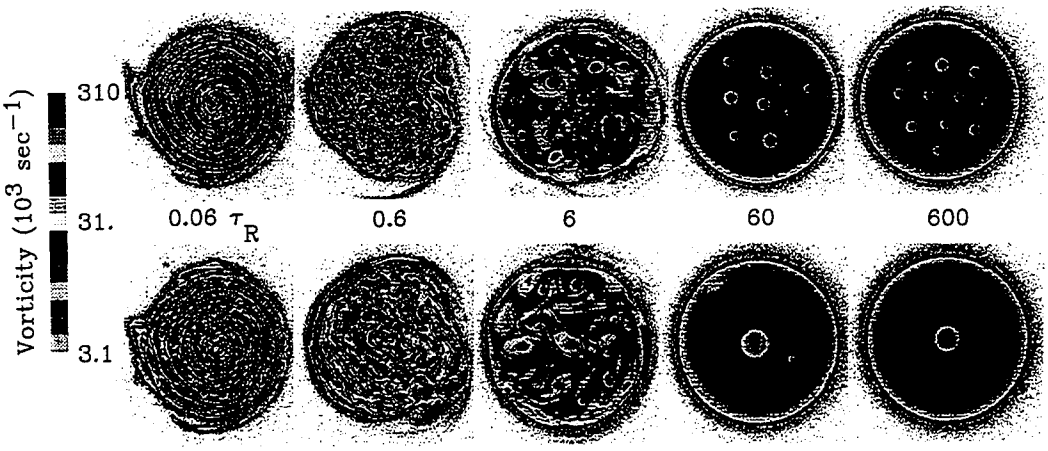


Figure 7. Images of vorticity at five times for two sequences from similar initial conditions. The black arcs indicate the wall radius.

experimental images show that as N_v decreases, the remaining vortices re-adjust to a new rigidly-rotating, symmetrically-spaced pattern.

Reduction of the chaotic advective motions of the individual vortices is required to form the vortex crystal states. This "cooling" is shown in Fig. 8. Here, the average magnitude of the random velocities of the individual vortices, $|\delta V|$, is relative to the rotating frame in which the mean discrete vortex velocity is zero. The velocities are obtained from the potential $\phi(r,\theta)$ calculated from the measured $n(r,\theta)$ and boundary conditions $\phi(R_w,\theta)=0$. The measured $|\delta V|$ decreases a factor of 6 between 2 τ_R and 100 τ_R for the crystals sequence, whereas only slight cooling is seen before $N_v = 1$ (and $|\delta V| = 0$ by definition) for the monotonic sequence. The residual $|\delta V|$ for $t \geq 100\ \tau_R$ may indicate incomplete cooling, measurement noise, or systematic errors such as uncertainty in the position of the trap axis.

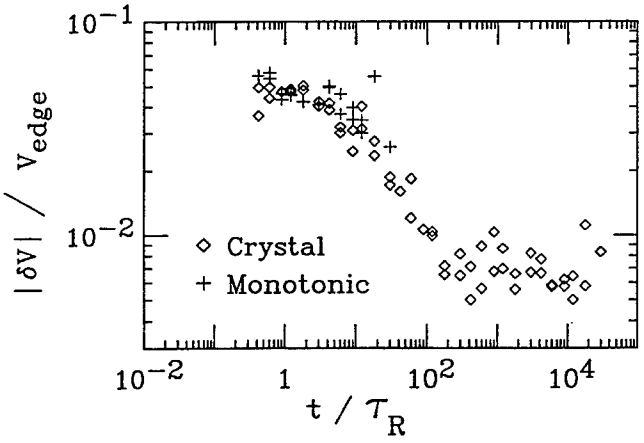


Figure 8. Evolution of the average chaotic velocity $|\delta V|$ of the vortices for the two sequences, normalized by $V_{\rm edge} \equiv 2\pi R_p/\tau_R = 5.5 \times 10^4$ cm/sec.

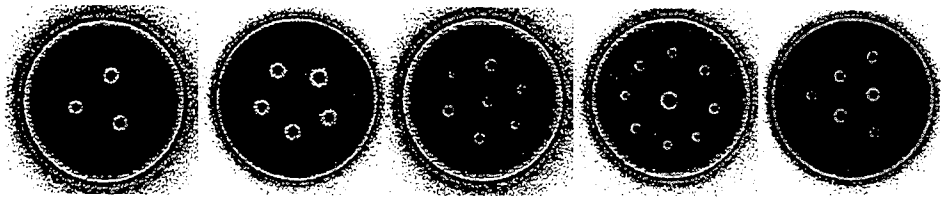


Figure 9. Selection of vortex crystal patterns obtained from initial conditions similar to those of Fig. 7.

We believe this cooling and cessation of relaxation through mergers is a near-inviscid 2D fluid effect, *i.e.* independent of the details of the fine-scale dissipation. However, two essential characteristics of this system are the non-zero total circulation and the boundary of the vorticity patch, effects which may not be present in other systems. It appears that the vortex cooling occurs due to an interaction between the individual vortices and the boundary of the background vorticity [33]. In this theory, the vortices excite surface waves on the background, and these waves are damped by direct or beat-wave spatial Landau damping as discussed previously. For strong interactions and short wavelengths, this corresponds to entrainment and mixing of low vorticity regions from the edge of the column. Some of the experimental images suggest this latter process, which has also been observed in preliminary 2D vortex-in-cell simulations. A similar process may cause negative (relative) vorticity "holes" to become symmetrically situated, as described above.

Figure 9 shows a selection of the symmetric crystal patterns which have been observed. Apparently, there are many different "meta-equilibria" to which the system can evolve under near-inviscid 2D dynamics. Experimentally, these meta-equilibria appear to last "forever" ($\gtrsim$ 1 sec), until plasma diffusive or viscous effects not included in Eqs. (1) act to dissipate the individual vortices.

6. INTERACTION OF ISOLATED VORTICES

The vortex dynamics underlying the turbulent relaxation can also be studied as isolated processes. Straightforward manipulation techniques allow us to form an initial condition consisting of two electron columns of chosen profile and placement. Here, we consider the particular case of two equal columns that are placed symmetrically on either side of the cylindrical axis, separated by a distance $2D$ [35].

The evolution of the two-vortex state depends critically on the separation to diameter ratio, $2D/2R_v$. If $D/R_v = 1.5$, the vortices merge within one orbit, forming filamentary tails. If the same vortices are initially separated by $D/R_v = 1.6$, then their mutual interaction still results in filamentary tail formation, but the vortices orbit around each other for about 100 orbits before merging at the center. If the vortices are separated by $D/R_v = 1.8$, then we observe that they orbit around each other for about 10^4 orbits before merging or degrading.

Figure 10 plots the time to merge, τ_{merge}, versus D/R_v for vortices with radii ranging from $R_v = 0.53$ cm to 1.02 cm. It is particularly striking that τ_{merge} increases by 4 orders of magnitude between $D/R_v = 1.4$ and 1.8. It is also striking that the curves for different R_v

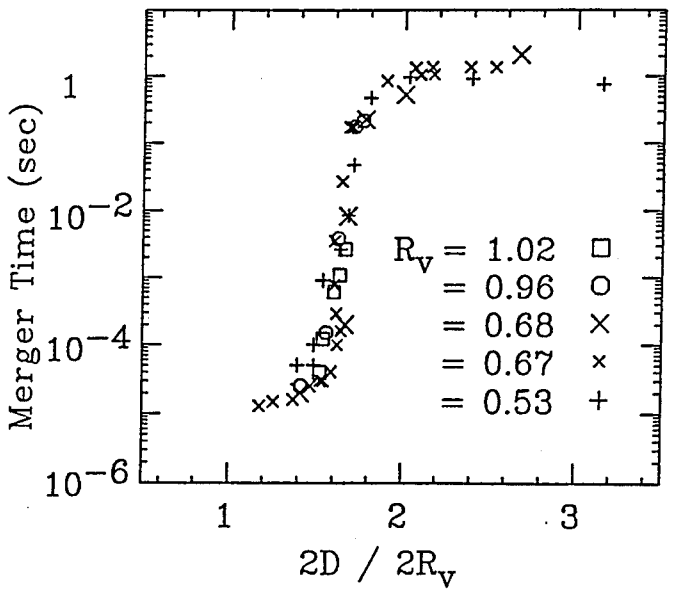


Figure 10. Measured two-vortex merger time as a function of separation 2D normalized to vortex diameter $2R_v$.

overlay one another, indicating that R_v alone determines the length scale. The wall radius R_w does not enter the scaling, because wall interactions are negligible for our ranges of D.

These results are in good agreement with theory and computational results of two-dimensional ideal fluids. Moore and Saffman [36] used an approximate analytical model for elliptical patches of constant vorticity and found no two-vortex solutions for $D/R_v < 1.43$. Numerical solution of an equilibrium equation by Saffman and Szeto [37] predicts a critical separation of $D/R_v = 1.58$. Computer simulations by Rossow [38] based upon collections of 36 point vortices give a critical distance of $D/R_v = 1.7$. Extensive computer simulations by Malendar, Zabusky, and McWilliams [39] also observed merger depending critically on separation distance. These authors have also developed an approximate moment model of the two-vortex interaction.

We have also studied the dynamics of the circular equilibrium orbits of two vortices too far apart to merge [24]. Here, each vortex is moving in the flow field from the other vortex and from the image charges in the wall. A common theory assumption has been that the advection can be well described by treating the spatially extended vortices as (Hamiltonian) point vortices unless they are close enough to merge [40]. This is often called "punctuated Hamiltonian dynamics," *i.e.* integrable motion punctuated by discrete vortex merger events. However, prior experimental studies of vortices in water [41], in electrolyte [42], and in superfluid helium [43] have typically found interactions quite different from that predicted for point vortices, apparently because of viscous and/or boundary effects. Our experiments demonstrate the validity of the Hamiltonian dynamics approximation in most regimes we can access.

In equilibrium, each vortex orbits around the center of the cylinder at constant radius.

We find that some of these equilibria are linearly stable, others are unstable [24]. We have measured both oscillations about stable equilibria and exponential divergence from unstable equilibria. The measured equilibrium positions, orbit frequencies and instability rates are well predicted by treating the spatially-extended vortices as if they were point vortices. This point vortex stability analysis was first done by T.H. Havelock in 1931 [44].

We find that departures from this point vortex approximation occur only when vortices closer than 1.6 times their diameter merge, or when the vortices scrape the cylindrical wall and circulation (charge) is lost. This point vortex approximation neglects the effects of surface wave and shape distortions: the fields outside an extended vortex are the same as the fields outside a point vortex only if the extended vortex is circular. Experimentally, we observe elongations away from circularity of $\lesssim 10\%$ in general, and up to 30% for $r_1 = r_2 \sim 0.23$ (near merger, since $r_p \sim .15$). These time-varying eccentricities have not, however, been observed to cause experimentally noticeable departures from the predictions of the point vortex model. Thus, it is a non-trivial result to find that the overall stability of this obviously non-integrable system is well described by the integrable point-vortex approximation. This is apparently because the internal degrees of freedom associated with $r - \theta$ shape distortions do not significantly couple to the center-of-mass motion.

Thus, our experiments lend support to the turbulence model of isolated vortices moving as point vortices with isolated merger events. However, some vortex dynamics simulations suggest more complicated merger and filamentation events [45], and give different scaling exponents for the turbulent decay.

ACKNOWLEDGMENTS

This research is supported by Office of Naval Research grant N00014-89-J-1714, Department of Energy grant DE-FG03-85ER53199, and National Science Foundation grant PHY94-21318.

REFERENCES

1. R.C. Davidson, *Physics of Nonneutral Plasmas* (Addison-Wesley, New York, 1990), Ch. 5,6.
2. R.J. Briggs, J.D. Daugherty, and R.H. Levy, *Phys. Fluids B* **13**, 421 (1970); R.H. Levy, *Phys. Fluids B* **8**, 1288 (1965).
3. C.F. Driscoll and K.S. Fine, *Phys. Fluids B* **2**, 1359 (1990).
4. C.F. Driscoll, J.H. Malmberg, and K.S. Fine, *Phys. Rev. Lett.* **60**, 1290 (1988).
5. Lord Rayleigh, *Scientific Papers* (Cambridge Univ. Press, Cambridge, 1899), Vol. 1, p. 474.
6. V.I. Arnol'd, *J. Mec.* **5**, 29 (1966).
7. G. Rosenthal, G. DiMonte, and A.Y. Wong, *Phys. Fluids* **30**, 3257 (1987).
8. A.J. Peurrung and J. Fajans, *Phys. Fluids A* **5**, 493 (1993).
9. C.F. Driscoll, *Phys. Rev. Lett.* **64**, 645 (1990).
10. R.A. Smith and M.N. Rosenbluth, *Phys. Rev. Lett.* **64**, 649 (1990).
11. R.A. Smith, *Phys. Fluids B* **4**, 287 (1992).

12. S.N. Rasband, R.L. Spencer, and R.R. Vanfleet, *Phys. Fluids B* **5** 669 (1993); S.N. Rasband, *Bull. Am. Phys. Soc.* **39**, 1549 (1994).
13. W. Kelvin, *Nature* **23**, 45 (1880).
14. J.S. deGrassie and J.H. Malmberg, *Phys. Fluids* **23**, 421 (1980).
15. S. Pillai and R.W. Gould, *Bull. Am. Phys. Soc.* **38**, 1970 (1993).
16. H. Lamb, *Hydrodynamics*, 6th ed, New York: Dover Press, 1932, §158,159.
17. G.S. Deem and N.J. Zabusky, *Phys. Rev. Lett.* **40**, 859 (1978); D.I. Pullin, *Ann. Rev. Fluid Mech.* **24**, 89 (1992).
18. M.V. Melander, J.C. McWilliams, and N.J. Zabusky, *J. Fluid Mech.* **178**, 137 (1987).
19. E.J. Hopfinger and G.J.F. van Heijst, *Ann. Rev. Fl. Mech.* **25**, 241 (1993).
20. T.B. Mitchell and C.F. Driscoll, *Phys. Rev. Lett.* **73**, 2196 (1944); T.B. Mitchell, Ph.D. Thesis, Univ. of Calif., San Diego (1993).
21. J.D. Crawford and T.M. O'Neil, *Phys. Fluids* **30**, 2076 (1987).
22. D.L. Eggleston and J.H. Malmberg, *Phys. Rev. Lett.* **59**, 1675 (1987).
23. W.G. Flynn, Private communication.
24. T.B. Mitchell, C.F. Driscoll, and K.S. Fine, *Phys. Rev. Lett.* **71**, 1371 (1993); K.S. Fine, C.F. Driscoll, J.H. Malmberg, and T.B. Mitchell, *Phys. Rev. Lett.* **67**, 588 (1991).
25. D.G. Dritchell and D.W. Waugh, *Phys. Fluids A* **4**, 1737 (1992).
26. X.-P. Huang, K.S. Fine, and C.F. Driscoll, *Phys. Rev. Lett.* **74**, 4424 (1995).
27. D.W. Moore and P.G. Saffman, *Aircraft Wake Turbulence and its Detection*, (Plenum, New York, 1971), p.339; S. Kida, *J. Phys. Jpn.* **50**, 3517 (1981); D.G. Dritchel, *J. Fluid Mech.* **210**, 223 (1990).
28. K.S. Fine, A.C. Cass, W.G. Flynn, and C.F. Driscoll, *Phys. Rev. Lett.* **75**, 3277 (1995).
29. D.L. Eggleston, *Phys. Plasmas* **1**, 3850 (1994).
30. P.S. Marcus, *Nature* **331**, 693 (1988); P.S. Marcus, *Ann. Rev. Astron. Astrophys.* **31**, 523 (1993).
31. X.-P. Huang, Ph.D. Thesis, Univ. of Calif., San Diego (1993).
32. A.J. Peurrung and J. Fajans, *Phys. Fluids B* **5**, 4295 (1993).
33. D.H.E. Dubin, *Bull. Am. Phys. Soc.* **40**, 1740 (1995).
34. G.F. Carnevale, *et al.*, *Phys. Rev. Lett.* **66**, 2735 (1991); J.B. Weiss and J.C. McWilliams, *Phys. Fluids A* **5**, 608 (1993).
35. K.S. Fine, C.F. Driscoll, J.H. Malmberg, and T.B. Mitchell, *Phys. Rev. Lett.* **67**, 588 (1991).
36. D.W. Moore and P.G. Saffman, *J. Fluid Mech.* **69**, 465 (1975).
37. P.G. Saffman and R. Szeto, *Phys. Fluids* **23**, 2339 (1980).
38. V.J. Rossow, *J. Aircraft* **14**, 283 (1977).
39. M.V. Melander, N.J. Zabusky, and J.C. McWilliams, *J. Fluid Mech.* **195**, 303 (1988).
40. R. Benzi, S. Patarnello, and P. Santangelo, *Europhys. Lett.* **3**, 811 (1987).
41. R.W. Griffiths and E.J. Hopfinger, *J. Fluid Mech.* **178**, 73 (1987).
42. P. Tabeling *et al.*, *Phys. Rev. Lett.* **67**, 3772 (1991).
43. E.J. Yarmchuk and R.E. Packard, *J. Low Temperature Phys.* **46**, 479 (1982).
44. T.H. Havelock, *Phil. Mag. S.7.* **11**, 617 (1931).
45. D.G. Dritschell, *Phys. Fluids A* **5**, 984 (1993).

Probing Space Charge in a Crossed-Field Amplifier

John Z. Ye, Robert MacGregor, Chung Chan

Department of Electrical and Computer Engineering

and

Thomas E. Ruden

School of Engineering Technology

Northeastern University, Boston, MA

Tel. (617) 373-5364 Fax (617) 373-5185

Abstract

The azimuthal space charge instability of the crossed-field electron hub has been proposed as a mechanism to generate close in noise or modulations in crossed-field devices. Experimental observations made on a reentrant format, experimental crossed-field amplifier with distributed cathode emission show discrete frequency oscillations which characterize the reentrant space charge behavior. The experimental evidence such as frequency tuning and distributed sole back bombardment associated with the free-running amplifier identifies an established azimuthal instability which is similar to that observed in a magnetron diode. A transitional process from the discrete frequency oscillations to a continuous type noise spectra can be initiated by a strong RF drive signal, and is enhanced by a larger magnetic field value or an increased secondary electron hub density. A significant degradation of the system signal-to-noise ratio associated with the transition has been found strongly dependent upon the sole secondary emission process.

I. Introduction

Many advantageous qualities are inherent to crossed-field devices: comparatively low voltages, high efficiency and power level across wide bandwidth, small size and weight. Recently however, as O-type devices (e.g., coupled cavity traveling wave tubes) making significant improvement on their reliability and power level, the role of crossed-field devices for radar system applications is now being seriously challenged due to the relatively high noise level of the crossed-field devices. Recent effort aiming at producing a reliable production crossed-field amplifier with comparable noise performance has been accomplished with only limited success. Are crossed-field devices *intrinsically* noisy or are there regimes of quiescent operation?

In magnetrons and crossed-field amplifiers, high gain and low noise operation are a result of well formed spokes. An idealized picture of the space charge can be visualized as a rotating wheel composed of these spokes, having a consistent spatial envelop and a consistent phase relationship with respect to the circuit wave. Each individual electron in the wheel maintains strict synchronism with the favorable phase of the wave field throughout its entire life span. In reality however, deviation from this idealized space charge structure is by no means small. Various physical processes may cause displaced spokes, missing or extra spokes, envelop modulation, phase space spread or deviation of other forms, all of which may result in noise. For instance, electrons from the collapsed spokes in the drift region may reenter the interaction space with the unfavorable phase; electrons accumulated in the end-hat region due to the field non-uniformity along the axial direction may oscillate. In addition, being a function of material characteristics, secondary emission may not provide electrons, consistently, in the desired phase for a quiescent amplification. The unfavorably phased electrons, together with the recirculating electrons, would typically form a high density electron hub around the sole surface. The physical behavior of the hub would have deterministic effect on the quality of the amplified signal.

Early research on the crossed-field hub were made on magnetrons with smooth-bored anode structure, or magnetron diodes, where the static hub behavior was studied as a state of magnetron preoscillation [3]. In addition to exploring the fundamental physical concepts such as Hull cutoff, Brillouin sheath and electron back bombardment, experiments were aimed at understanding basic magnetron starting mechanisms. Evidence shows that the magnetron field configuration may support a space charge cloud oscillating on certain discrete frequencies while being capable of amplifying over a wide band.

Good understanding of the true space charge structure has not been achieved due largely to the fact that it is extremely difficult to measure current, density and velocity distributions in the electron beam of a magnetron or crossed-field amplifier of practical geometry. Evidence has confirmed that, similar to that of a magnetron diode [4], the space charge in a reentrant crossed-field amplifier has the intrinsic character to establish instability as well. Recent computer simulations found that MASK produced noise of a practical amplifier is *not* random [7]. The spectrum consists of a summation of a finite number of *uniformly* spaced frequencies. Previous Russian work [5], [6] on turbulent electron current of a magnetron diode also found the existence of coherent structures in the chaotic space charge. Is noise actually random? This paper attempts to address the noise question by examining the effect of secondary emission and the contribution of reentrant space charge instabilities to noise generation in crossed field devices.

II. Experimental Setup

At Northeastern University, tube research has taken up a combined approach of in situ plasma diagnostics and computer simulations using two frequency scaled CFA's as test vehicles. **Fig. 1** shows a schematic of our reentrant format CFA. A detailed description and system characterization of the experimental setup can be found in [8].

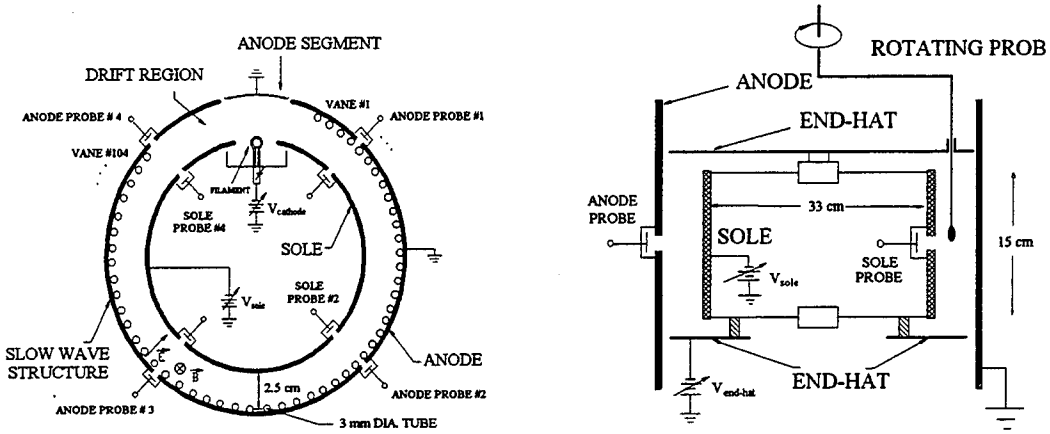


Fig. 1 Configuration of the Northeastern reentrant format CFA with in situ probe installation along the interaction space. Top view (left), and side-view (right.)

The design of the circular CFA uses parameters such that diagnostic probes can be placed in the interaction region without disturbing the operation of the device. This leads to a physically large system. The frequency range of 100 MHz to 200 MHz was chosen due to the fact that the wavelength is much larger than the dimensions of the diagnostic probes. This allows for probe measurements with minimum perturbation of the electric field and space charge. The device was originally designed as an injected beam system in which the cathode, beam optics, and electric and magnetic fields are designed to produce a relatively smooth beam. We have recently incorporated materials which will provide secondary emission from the sole (cathode) to study the space charge instabilities associated with the secondary emission from the sole and the turbulent electron flow.

III. Observation of the Azimuthal Space Charge Instability

A. The Azimuthal Space Charge Wave

A physical mechanism of the instability associated with a static, reentrant crossed-field electron flow is the self-excitation of azimuthal space charge waves. The wavelength of the eligible oscillations satisfies $K \cdot \lambda_K = L$, where L is the azimuthal length of the cylindrical geometry, and K is the mode number. This relation determines the frequency of the possible oscillations assuming a match between the phase velocity and azimuthal component of the electron velocity, or $v_{ph} = r\,(d\phi/dt)$. As the electron azimuthal velocity varies across the sole-anode interaction space, the resulting oscillation frequencies also vary, i.e oscillation frequency depends upon the position of the hub electrons which excite the wave. **Fig. 2** is a plot of the

fundamental oscillation frequency as a function of the applied magnetic field (tuning) based on Brillouin modeling. This frequency increases as the thickness of the Brillouin hub increases.

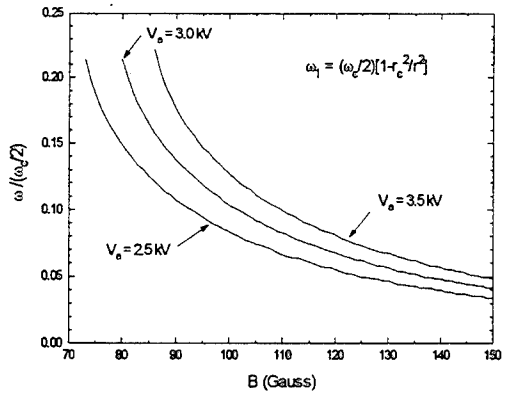


Fig. 2 The fundamental oscillation frequency as a function of the applied magnetic field and anode-sole voltage values.

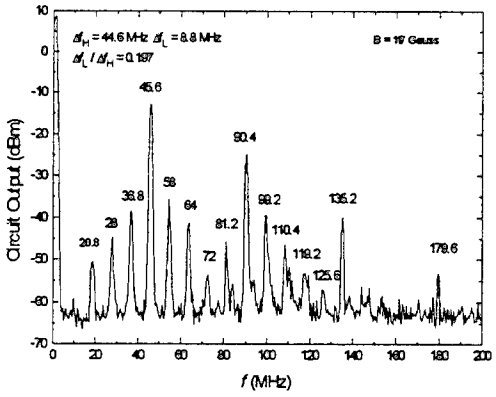


Fig. 3 The spectrum of the circuit output at B = 117 Gauss.

B. Frequency tuning

The variation of the fundamental oscillation frequencies (without RF drive signal) is measured as a function of the device operating conditions. For experimental convenience, we sweep the applied magnetic field B from 117 Gauss to 141 Gauss at a 3-Gauss step while keep other operating parameters constant (sole - 3 kV, cathode - 2.76 kV, endhat -3.9 kV, injected current 15 mA). **Fig. 3** shows an example of circuit output spectrum at B = 117. We use Δf_L and Δf_H to represent the fundamental frequency for the lower modes and the higher modes respectively. The change of the oscillation peak positions is clearly observed as B field varies. **Fig. 4** compares Δf_L and Δf_H with that predicted by MASK code and Brillouin modeling. From **Fig. 4** we see that Δf_L tends to decrease as the applied magnetic field increases. In other words, the spectrum lines tend to cluster together. At high magnetic field regime for the practical devices, Δf_L could even be smaller resulting in continuous type of spectrum. Indeed, the secondary hub surface will be further suppressed by an increased magnetic field, resulting in a reduced fundamental frequency. This variation can be seen in **Fig. 4.**, although the measured fundamental modes are approximately 3 MHz below that predicted based on the laminar flow hub height.

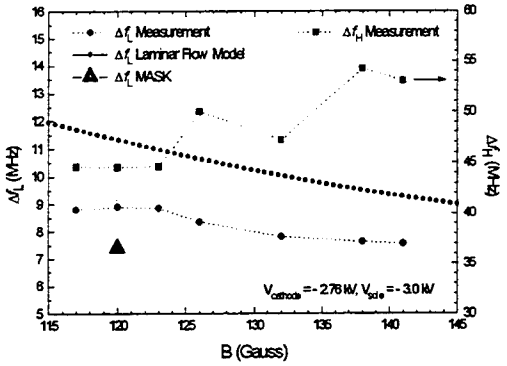


Fig. 4 A comparison with the Brilluoin modeling result and MASK result on the fundamental frequencies.

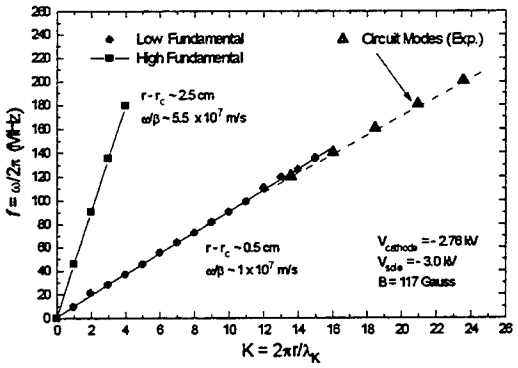


Fig. 5 Dispersion relation of the space charge wave. The circuit modes are obtained from experiment.

C. *The Space Charge Modes*

Since the Brillouin hub would no longer be a valid picture of the space charge condition once the oscillation field has built up, we would like to construct a new one based on the measured data.

Taking for example the case of **Fig. 3**, B = 117 Gauss, we can plot the dispersion relation for both the low and high instability modes as in **Fig. 5.** Both dispersions are linear. With a phase velocity of approximately 1×10^7 m/s, the dispersion for the lower modes overlaps that of the slow wave circuit. The phase velocity of the high modes is about 5 times that of the lower modes. Assuming that electrons start from the cathode at zero initial velocity, the angular velocity

$$v_\phi = r\frac{d\phi}{dt} = \frac{\omega_c}{2} r\left(1-\frac{r_c^2}{r^2}\right) \qquad \text{(III.C.1)}$$

where r_c is the radius of the sole. Using this expression for the azimuthal drift velocity in the circular crossed-field geometry, we then obtain a linear dependency of ω_K to $\frac{d\phi}{dt}$,

$$\omega_K(r) = K\frac{d\phi}{dt} = K\cdot\frac{\omega_c}{2}\left(1-\frac{r_c^2}{r^2}\right) \qquad \text{(III.C.2)}$$

This frequency increases as the thickness of the Brillouin hub, $r = r_h - r_c$, increases. Therefore, we can say that the high modes correspond to the injected beam, and the lower modes correspond to the secondary hub.

Frequency tuning shows that when the magnetic field increases, mode frequencies due to the primary beam satisfy $\Delta f_H = m\cdot\Delta f_L$, where m is an integer and, m = 4, 5, and 6 for the magnetic field value of 117, 126 and 138 Gauss, respectively. As the magnetic field increases,

there are more low modes included between two high modes. However, we have *not* observed a group of high modes with fundamental frequencies which are independent to that of the lower modes. This can be interpreted as the rotating beam electrons attempting to satisfy the azimuthal space charge condition, $K \cdot \lambda_K = L$, as an *entire* space-charge body regardless of their primary or secondary origin. In consequence, the experimental state of a classical Brillouin sheath, if such a state exists during startup, would not be physically observable under a relatively long time scale of the present measurements. The time scale in which these oscillations may establish would then have to be resolved in time-dependent measurements.

Besides the fact that the oscillation frequencies tune with the applied magnetic field, the possibility that the observed oscillations might correspond to any possible RF circuit mismatch is further excluded when repeated observations were made when both the input port and the output port of the RF circuit were terminated with matched load.

IV. Crossed-Field Noise: Secondary Emission and the Effect of RF Drive

A. The Effect of RF Drive

At low RF drive level, the typical effect is a change in the amplitude of the oscillation lines. The amplitude of the high modes ($\Delta f \sim 50$ MHz) is suppressed by about 10 dB; while the lower modes ($\Delta f \sim 8$ MHz) are generally promoted, indicating an increase of sole secondary emission. The low modes are immediately modulated by the carrier frequency, forming distinct side band. As the drive power increases, lower frequency components are suppressed and new frequency components are generated closer to the carrier. Accompanied with the high drive, sole secondary emission also increases significantly. In **Fig. 6** which shows a case of 62 W drive, new fundamental frequencies (e.g., 4 MHz) between the 8 MHz low modes emerge from a broad band spectrum sideband from 80 MHz to 140 MHz. Further increase of the drive level has a tendency to suppress broad band oscillations, and to generate finer structure at a lower magnitude close to the carrier frequency. **Fig. 7** shows an example of the narrow band spectrum at 200 W drive. An increased noise floor is clearly seen as the sole secondary emission increases.

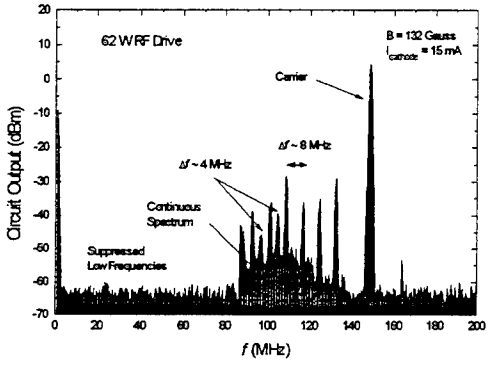


Fig. 6 RF drive effect on the instability.

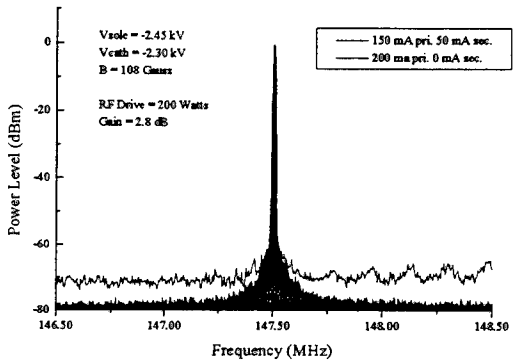


Fig. 7 An example of the narrow band spectrum under high RF drive, 200 W, 0 and 50 mA sole current respectively.

B. The Effect of Secondary Emission on Close In Noise

An examination of the narrow band spectrum close to the carrier reveals interesting variation of the signal-to-noise ratio as a function of RF drive and sole secondary emission current. Here the noise power is calculated by averaging the spectrum power density across a noise band defined to exclude the carrier signal. We then calculated the signal-to-noise ratio (S/N) using this averaged value as the decibel value below the peak signal per unit frequency (dBc/Hz). **Fig. 8** is a plot of the S/N of the circuit output as a function of the net sole emission current and the RF drive level. The range of the calculated S/N is comparable with that of a practical emitting-sole CFA. We see that, at 200 W RF drive, S/N degrades by more than 10 dB as the sole current increases from zero to 25 mA, which indicates that the participation of a small amount of secondary electrons can introduce a large amount of close-in noise. In the sole current range greater than 25 mA, the S/N deterioration seems to stop. Beyond 50 mA sole current, data is not available at this point as to predict whether there will be a come back for the S/N.

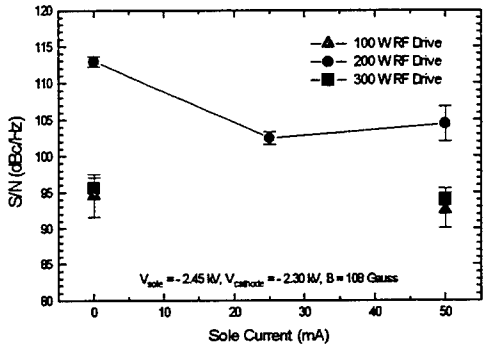


Fig. 8 Calculated signal-to-noise ratio based on the measured spectrum as a function of RF drive level and sole secondary emission.

The 200 W drive level in **Fig. 8** is approximately where the reentrant amplifier system has its peak gain. Higher RF drive would result in a decreased gain due to insufficient DC beam power. At 100 W and 300 W drive level, the amplifier is at least 15 dB noisier.

V. Conclusions

In conclusion, we have proposed the azimuthal space charge instability as a close-in noise mechanism. We found experimental evidence which correlates these instabilities to close-in noise performance at different levels of RF drive and sole secondary emission.

The experimental study of the space charge instability in our reentrant format amplifier shows that, similar to that of a magnetron diode, the space charge in a crossed-field amplifier can develop instability as well. The instability is characterized by discrete frequency oscillations based upon parameter-dependent fundamental frequencies.

We further studied the relationship between the space charge instability and close in noise performance. We have assumed that a *necessary condition* to develop close in noise is the

simultaneous presence of low frequency oscillations with the carrier signal. Our observation shows that a transition process from discrete oscillation frequencies to a continuous noise spectra can be (a) initiated by a strong RF drive signal, (b) enhanced by a larger magnetic field value, (c) by an increased secondary hub density, and (d), by space charge mode intermodulation or a frequency bifurcation mechanism.

In our experiment, contribution to the space charge instability comes from both the primary beam and the secondary electron hub. Secondary electrons kept at low orbit may generate very low frequency modulations under high magnetic field regime. As a result, physical condition close to the sole region may have significant influence on close-in noise. Our experimental data shows a general trend of signal-to-noise ratio (S/N) degradation as secondary electron population increases in the hub. In this sense, our finding suggests that the presence of a low orbit secondary electron hub contribute to close in noise. As such, the future of the cold cathode, crossed-field noise research may take two directions. One is to control this space charge layer, through approaches such as controlling the phase of the sole emission (for example, cathode driven); while the other is obviously to reduce or avoid secondary emission. This latter approach seems to indicate a return to hot cathode tubes.

Acknowledgements

The authors appreciate useful discussions with Mr. H. McDowell, D. Chernin, S. Riyopolous, and S. MacMullen. We also thank Mr. J. Genevich for helping setup the experiment. This work is supported by DoD Vacuum Electronics Initiative under AFOSR grant # 91-0371, and NSF grant # 9120085, NSWC-Crane Division, and NRL.

References

[1] G. Thomas, and J. Deveau, "A new low noise tube: a crossed field amplifier with a 40 dB improvement in noise," *First International Workshop on Crossed-Field Devices*, B1-2, Ann Arbor, MI., August, 1995.

[2] G. Y. Levin, L. A. Semenov, A. Ya. Usikov, and Yu. A. Belov, "On the nature of noise and the mechanism of suppressing it in surface-wave magnetrons," *Sov. J. Comm. and Elect.*, vol. 37, no. 8, p. 128, 1992.

[3] E. Okress, ed., *Crossed-Field Microwave Devices*, vol. I, ch. 4, New York: Academic Press, 1961.

[4] C. B. Bigham, "Dark current and electron energy spread in a magnetron," *J. Microwave Power*, vol. 8, p. 195, 1973.

[5] A. V. Smirnov, and V. G. Usychenko, "Evolution of space charge oscillations in a magnetron diode from startup to chaos," *Sov. J. Comm. and Elect.*, vol. 36, no. 9, p. 132, 1991.

[6] A. V. Smirnov, and V. G. Usychenko, "Coherent structure in the turbulent electron current of a magnetron," *Sov. J. Comm. and Elect.*, vol. 36, no. 9, p. 137, 1991.

[7] Sandy MacMullen, Naval Surface Warfare Center, Crane, IN 47522, private communication.

[8] John Z. Ye, Ph. D. Dissertation, Northeastern University, Boston, MA, 1995.

Frequency Twinning in Magnetrons

E. M. Ball and M. Brady, EEV Ltd., Witham, Essex. U.K

R. G. Carter, Engineering Dept., Lancaster University, Lancs. U.K.

1. Introduction

Twinning is a phenomenon commonly observed in magnetrons. This instability causes the magnetron, under certain operating conditions, to oscillate at two frequencies at once. This is illustrated by figure 1 which shows an example of the frequency spectrum for a low power X-band magnetron whilst the tube is twinning.

The frequency jump, typically between 1 and 6MHz, is relatively small compared to that which is caused by the better known phenomenon of moding. With a gradual increase in anode voltage it occurs as a transition from one twinning mode to the other, one eventually gaining complete dominance. This transition quite often appears to the operator as a frequency jump. Its effect, however, can also be observed on the r.f. and current pulses, as illustrated by figure 2.

The objective of the investigation into twinning was to further the understanding of this phenomenon with the view to reducing the risk of its occurrence.

The investigation was largely experimental. It considered the effect, on twinning, of various operating parameters such as mismatch, heater voltage and magnetic field. It also involved the design, build and test of experimental tubes.

2. Experimental Tubes

Each experimental tube was based upon a standard design but had a single design parameter modified; most involving the cathode. The results from these studies have been summarised and tabulated below.

Modifications		Effect on twinning
Etched cathode	Reduced thermal emission Higher current densities	Twinning worse and induced tripling
Reduction in the % of Barium in the cathode coating	Change in ratio of thermal electrons to secondary electrons	Twinning at higher currents eliminated from the operating region
End hat design	Increased electric field in the end regions Increased current densities	Twinning not improved
Non-circular cathode	Introduced asymmetry to the r.f. fields and emission. May in time promote twinning	Little affect on twinning. However, increased pushing and bandwidth

Table 1. A table summarising the effect of various cathode parameters on twinning

3. Mismatch

A variable load was used in the test set up and calibrated to give a known VSWR and phase. The voltage was set so that the tube under test twinned. For a set VSWR the phase of the load was varied and the operating frequency and spectrum shape recorded. With a VSWR of greater than 2.0 all the tubes tested had a frequency jump of between 50 and 80MHz. Some simple calculations were able to verify that this was not twinning but due to the long line effect.

The points were plotted on a Smith chart as shown in figure 3. The operating points at which the tube twinned have been circled. The chart was found to be divided into two areas. In one region the spectrum was well defined and stable. Whereas in the sink the spectrum was poorly shaped and ragged. Along the dividing line between the two types of spectra was the region of twinning.

Furthermore, it was discovered that the frequency jump of the twin increased on one side of the diagram and decreased on the other. In other words positive and negative susceptance has a converse effect. This can not be explained by considering the pulling figure alone.

4. Magnetic field

The permanent magnets on the low power X-band magnetrons were removed and replaced by a calibrated electromagnet. The magnetic field was varied by 500 Gauss above and below the normal operating value of 4200 Gauss. The upper and lower limits were constrained by moding and spectral break-up.

The pushing curve was plotted for various magnetic fields. An example of the effect of magnetic field on the pushing curve is shown in figure 5. Each twinning mode is represented by a different marker, so that a change in marker denotes a twin. This particular tube twins twice once at a low current around 0.5A and at a higher current of 1.5A. The low current twin is more ragged and continues over a larger voltage range. Notice also that it is not affected by magnetic field to the same extent as the higher current twin.

The higher current twin is moved to a lower current outside the normal operating region with *increased* magnetic field. In Q-band tubes the contrary is true. Twinning is moved to a lower current with *reduced* magnetic field.

5. Summary

The investigation has revealed the existence of more than one type of twinning. One type occurs at lower currents, which in the low power X-band tubes is normally just outside the operating region, and is probably the result of steep pushing gradients. The second type is sensitive to magnetic field and r.f. loading. It would seem, therefore, that there is more than one mechanism causing the phenomenon.

There is evidence to suggest the cathode properties determine whether a tube will twin. The extent to which that tube will twin would seem to be largely determined by operating conditions such as magnetic field, modulator impedance and symmetry.

6. Further work

Work is continuing concerning magnetic field strength and shape. The effects of end hat geometry and pole piece design is being investigated further by computer modelling using OPERA-2d.

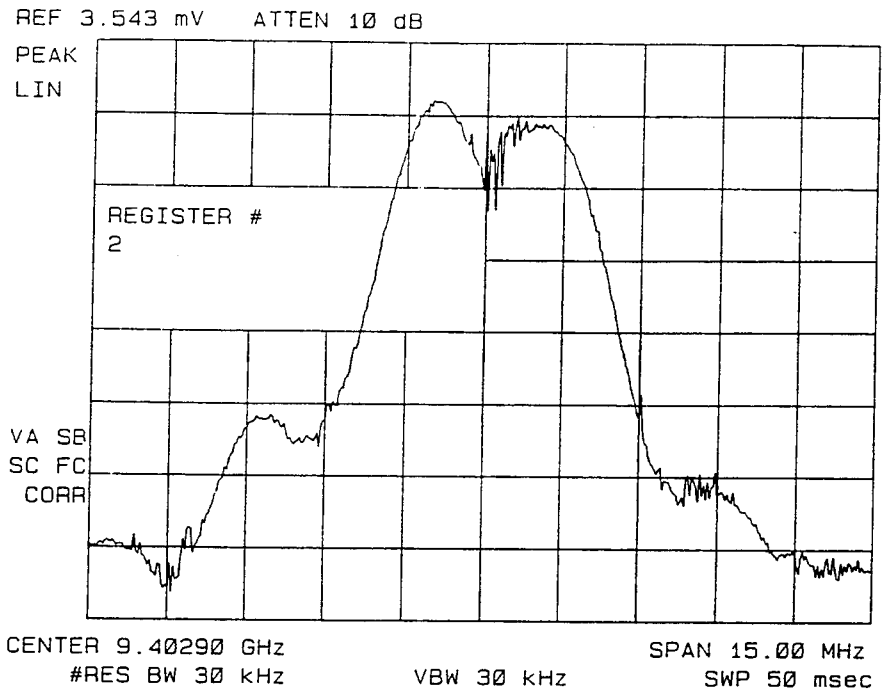


Figure 1. The spectrum of a low power X-band magnetron whilst it is twinning.

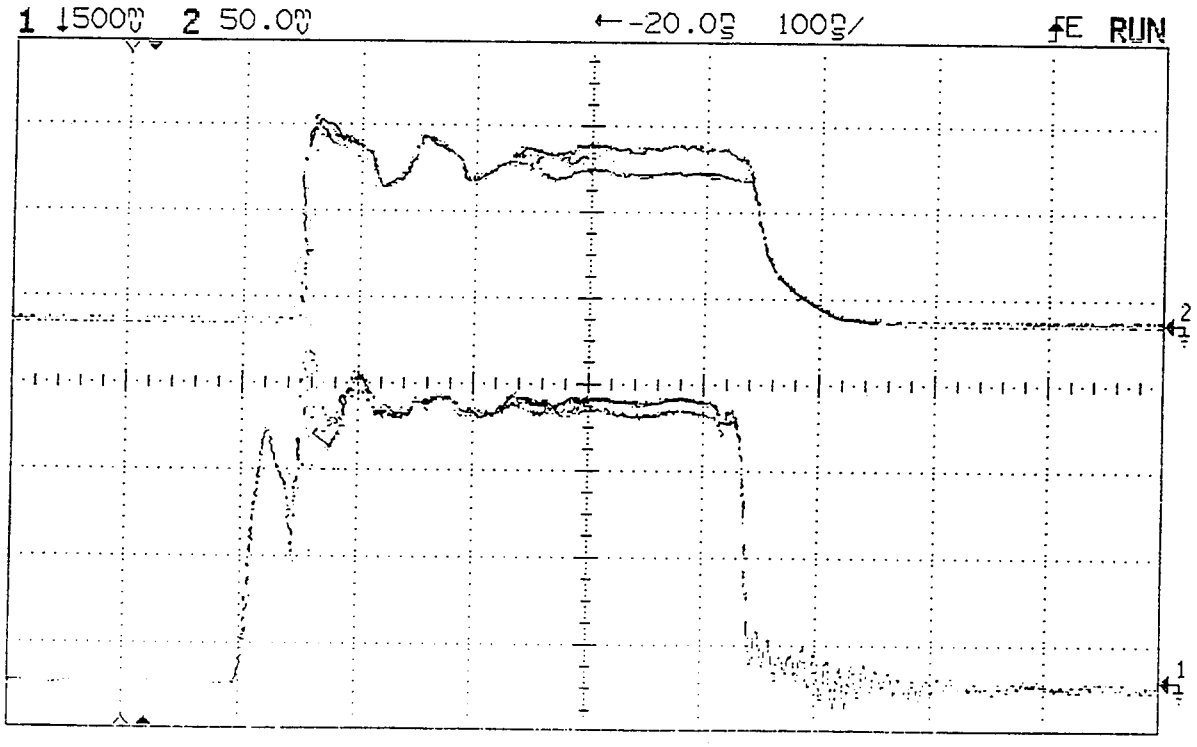


Figure 2. An example of the effect of twinning on the r.f. (top trace) and current pulses

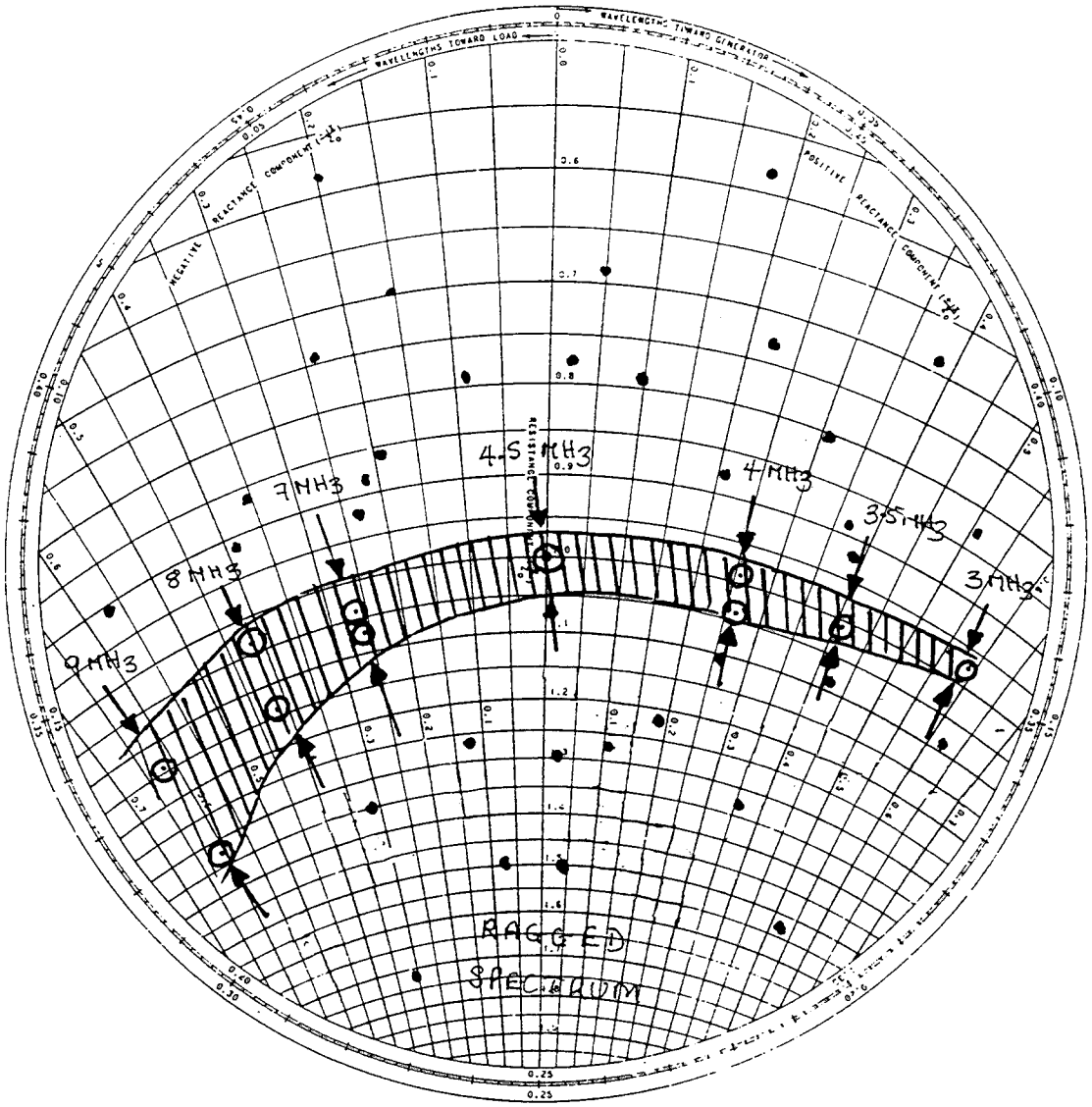


Figure 3. A Smith chart showing the regions in which the tube is twinning. The twinning points have been circled and labelled with the subsequent frequency jump.

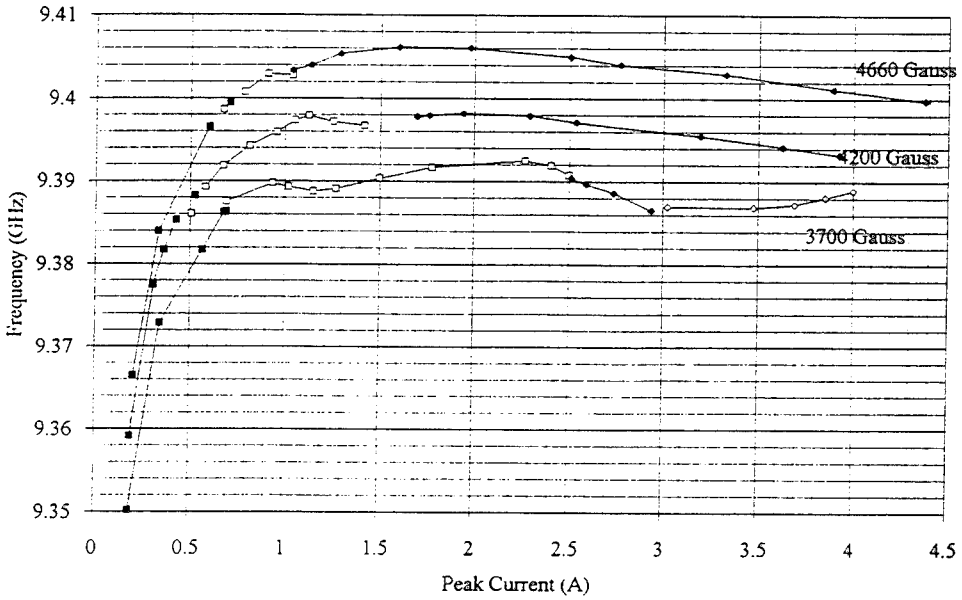


Figure 5. Pushing curves for a low power X-band tube at various magnetic fields

CFA COMPUTER MODELING USING A MOVING WAVELENGTH CODE

Hunter L. McDowell

Communication and Power Industries

Beverly Microwave Division

150 Sohier Road

Beverly, Ma. 01915

ABSTRACT

DECFA is a moving wavelength computer code for modeling crossed field amplifiers (CFAs). It models the interaction between a single traveling wave and the space charge in crossed electric and magnetic fields. Although many assumptions are involved in thus simplifying the CFA model, the code results correlate well with experimental data. through its diagnostics, the code provides a means of studying details of the interaction such as the space charge distribution, electron trajectories, and cathode bombardment conditions. The emission conditions used in the simulations are found to have a major effect on fluctuations of the solution. These results may contribute to the understanding of noise mechanisms in crossed field interaction.

Introduction

DECFA is a moving wavelength simulation code for modeling CFA performance. It is based on the effort of Yu, Kooyers and Buneman in 1965[1]. The present version of DECFA was prepared by CPI (formerly Varian) between 1975 and 1980 under contract to the Naval Ocean Systems Center, San Diego, CA. The model has since been updated, first as part of the Navy's ongoing low noise effort sponsored by the Naval Surface Warfare Center, Crane Division and subsequently under CPI support. Only with the advent of fast computer work stations in the 1990's has it become economical to conduct extended simulation using a code of this nature. DECFA is now considered an intermediate level code. The more advanced MASK code[2] eliminates the restriction to a single moving wavelength, which is the basis of DECFA. DECFA, however, executes faster than MASK and has been found to yield useful simulations of CFA performance. We envision DECFA as being used to evaluate a series of preliminary CFA designs with the more detailed MASK code being used to study the best of these designs on more detail.

A summary of some of the DECFA results was presented at the 1994 Microwave Power Tube Conference[3]. Since that time, the emission algorithm has been modified to place a limit on the emitted current. The maximum emitted current has been made dependent on the amount of charge directly above the cathode. The correlation of the model results with the performance of existing

CFAs has been little affected, but the revisions have modified the nature of internal fluctuations of the model. In particular, the imposition of the current limit has led to the appearance of low fluctuation states at high emission levels. This paper will describe results obtained with this latest version of the DECFA model as applied to a CFA known as the SFD-266 [4] which is currently under development and is intended for use in applications requiring reduced noise.

Description of the DECFA Model

DECFA simulates a single rf wavelength of the crossed-field interaction as shown in Figure 1. The wavelength is advanced along the CFA circuit in small time steps—typically, 1/60th of a cyclotron period. From 1500 to 4000 time steps per transit of the wave around the CFA have been used in the computations discussed in this paper. The interaction wavelength is divided into an array of 96 cells in the direction of propagation and 48 cells in the radical direction. A quasi-static approach is used in which a particle-in-cell Poison solution is executed during each time step. Because the circuit wave velocity is less than 1/5 of light velocity, there is little error in using the quasi-static solutions in place of electromagnetic solutions. Considerable computation time is saved by employing this approach. Periodic boundary conditions are applied to the left and right boundaries of the wavelength in Figure 1. The rf wave amplitude is assumed uniform in the direction of propagation during a single time step but grows in amplitude from time step to time step. Particles crossing a side boundary are reintroduced at the opposite side boundary. The single wavelength and periodic boundary condition assumptions prevent DECFA from including the effects of waves in the space charge having a different wavelength than that of the circuit wave. The DECFA model is two dimensional and thereby employs rods of charge as macroparticles. From 10,000 to 30,000 rods carrying variable amounts of charge are typically employed per wavelength. The anode circuit is represented by a single space harmonic of a

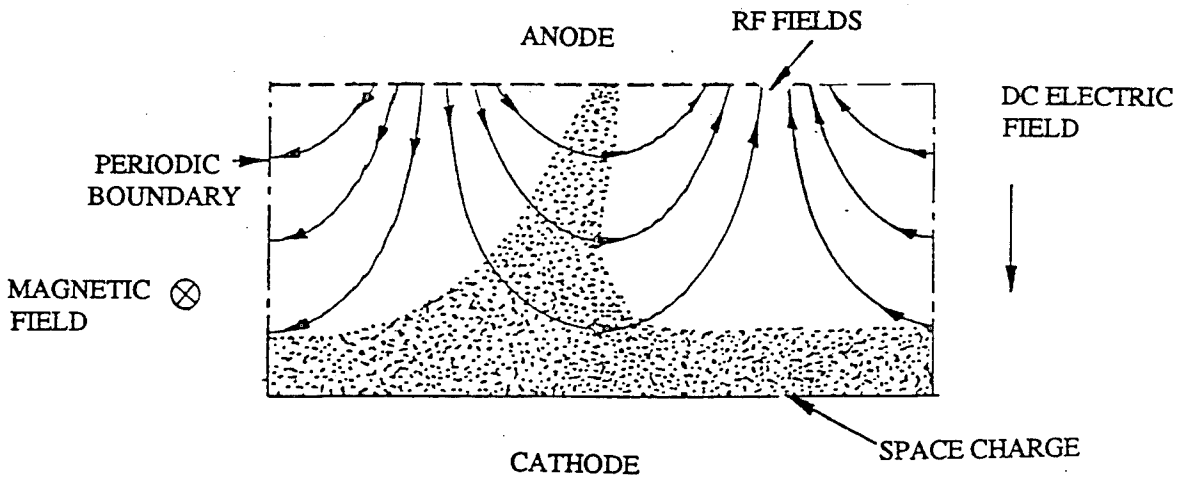


Figure 1. The Interaction Wavelength Followed Through the CFA by DECFA. The center of the favorable phase remains in the center of the box. The phase shift of the wave is represented by shifting the particles relative to the wave.

traveling wave on a smooth anode surface. The details of the collection of particles on the actual CFA vanes is thus not included. The circuit is described by four parameters: frequencty, phase shift per circuit period, interaction impedance, and circuit attenuation. Any difference between group and phase velocity of the wave is not included in the model. The model thus examines the interaction between a traveling wave and the space charge. The DECFA simulation is in linear format with only a simple correction to the magnetic field used to account for curvature. The CFAs studied using DECFA has large numbers of vanes (60) and relatively small curvature so the use of the linear model is not believed to introduce significant error.

On each time step of the simulation, DECFA solves Poisson's equation for the potentials in the moving reference frame. The rods are then advanced in position and the current induced into the anode wave as a result of their motion is computed. The time step is chosen small enough so that the rods move no more than one cell in one time step. Induced current components in-phase and in quadrature with the circuit wave are separately computed and added to the circuit wave to increment its amplitude and shift its phase. If rods strike the anode or cathode, the resulting dissipation is computed. For rods striking the cathode, the secondary emission charge is computed using the incident energy and a table of secondary yield as a function of energy. At present normal incidence is assumed. The computed trajectories arrive within about ± 10 degrees of normal incidence so this assumption is not unreasonable. The secondary charge is accumulated during each time step for each of 96 cells along the cathode. On the subsequent time step any thermionic emission charge is added to the accumulated secondary emission charge and one rod per cell along the cathode is emitted with the accumulated charge for the cell. The charge of the emitted rods thus varies from cell to cell. In the moving reference frame, the one time step delay in emission does not result in phase slippage between the wave and the emission point. The amount of charge emitted is now subjected to a limiting procedure suggested to us by A. Drobot of SAIC. From Gauss' law and the potentials on the first row of the potential array above the cathode, we calculate the amount of charge in each of the cells of the first row required to drive the field at the cathode to zero. The emission is then limited so that the total charge in each cell, both that originally present and that newly emitted, does not exceed this value. The charge is emitted with an initial velocity perpendicular to the cathode corresponding to about 5 volts energy - approximately the correct value for the secondaries but obviously wrong for the thermionic charge. Tests have, however, shown the model results to be insensitive to the initial velocity.

To simulate a reentrant CFA, DECFA uses the procedure shown in Figure 2. A small amount of charge is used to initiate the first pass of the interaction wavelength through the CFA. Charge is allowed to build up as a result of secondary emission multiplication during this first pass. The charge rod file existing at the end of a first pass is fed back to the input to initiate a second pass calculation. This procedure is repeated for 15 to 25 passes. After the second pass, smoothing is initiated by selecting rods from up to four prior passes to make up the rod file for a subsequent pass. The final results of the simulation are obtained by disregarding the initial three passes and averaging the results of the remaining passes.

Cathode voltage		12.5	KV
Cathode current		22.1	Amps
Magnetic field		1560	Gauss
Circuit Synchronous Voltage	Vo	2.22	KV
Characteristic Magnetic Field	Bo	446	Gauss
Characteristic Current	Io	38.0	Amps
Cathode Voltage/Synchrionous Voltage		5.63	
Cathode Current/Characteristic Current		0.58	
Circuit Length - Slow Wave Wavelengths		18.5	
R.F. Interaction Impedance		31.0	Ohms
Vane Tip Gap/Pitch Ratio		0.64	

Table 1. Parameters of the Midband Simulation

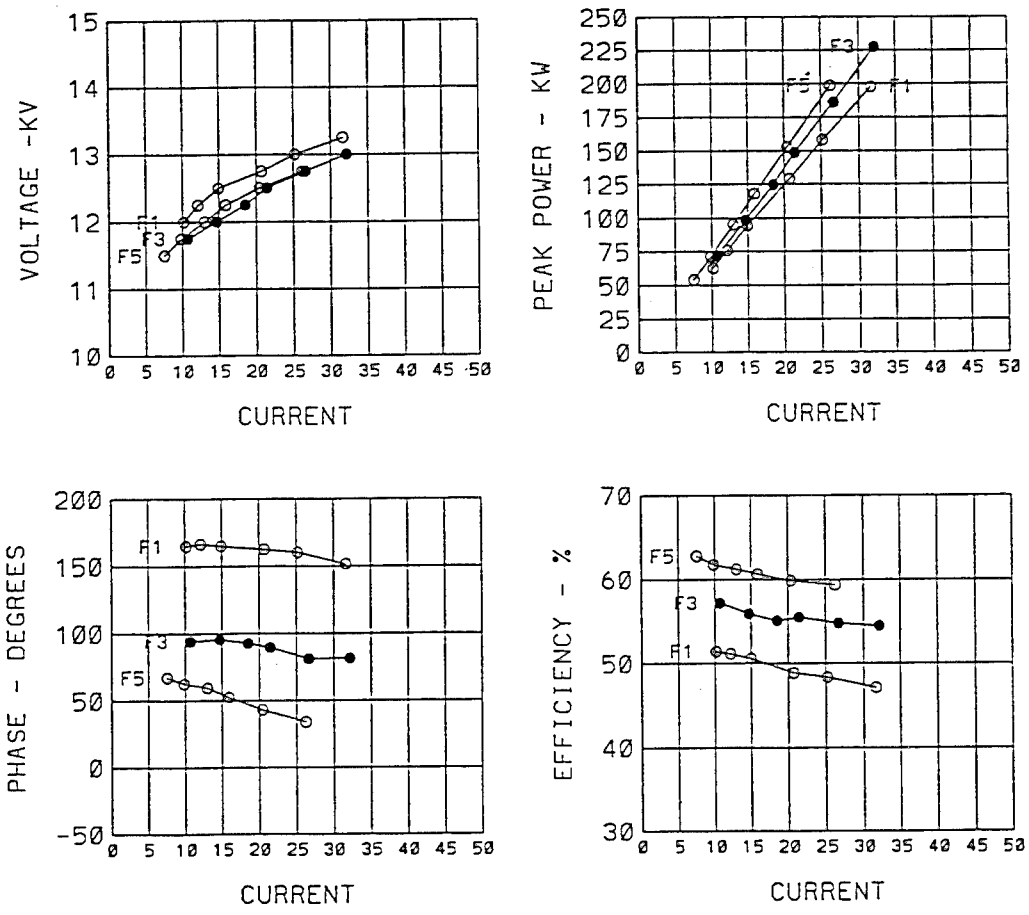


Figure 3. Results of DECFA Simulation of the SFD-266 at Three Frequencies.

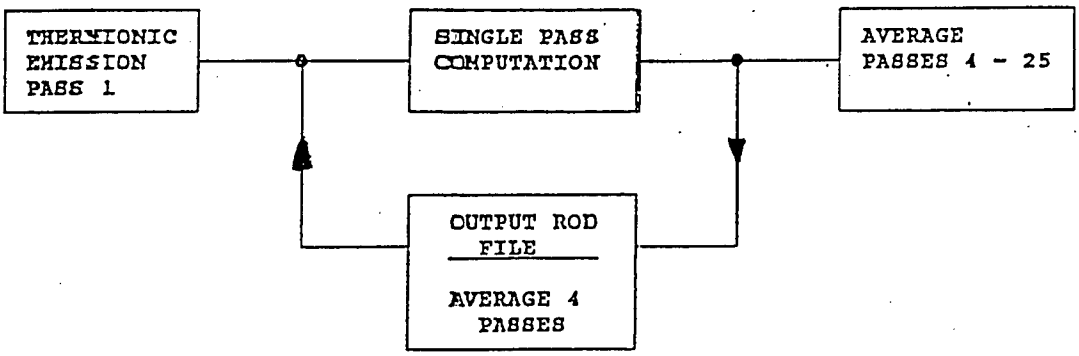


Figure 2. Proceedure for Simulating a Reentrant CFA.

Application of DECFA to the SFD-266 CFA

The SFD-266 CFA is an outgrowth of the earlier SFD-262 CFA which is currently employed in an S-band radar. The correlation of DECFA results with the SFD-262 performance was described in the earlier paper[3]. It was shown that the code results agree with the experimental performance within about 10% and properly describe the effect of pushing the cathode off-center as is done in the actual CFA. The SFD-266 represents an attempt to develop a CFA with reduced noise. The same type of helix coupled anode circuit is employed but the normalized parameters of the interaction space are changed to increase the strength of the rf circuit fields and reduce the space charge density. The resulting design operates at about one-half the magnetic field of the prior SFD-262. The ratio of the operating magnetic field to the cyclotron resonance magnetic field in the SFD-266 is slightly over one. The axial height of the interaction is increased in the SFD-266 so the power generation capability of the SFD-262 is retained. The SFD-266 employs 62 circuit periods wrapped around 310 degrees of the circumference of the anode. The remainder of the anode circumference is a drift region in which charge recirculates from output to input becoming at least partially debunched in the process. As is the case with the SFD-262 CFA, the SFD-266 cathode is a cold beryllium secondary emitter. Table 1 summarizes the principle design parameters of the SFD-266 at midband.

Figure 3 summarizes the results of DECFA simulations of the SFD-266. Results are presented as a function of peak current. The top left graph shows the computed V-I curves at three frequencies covering the operating frequency range. (F1 is the lower limit, F3 is midband and F5 is the upper limit). The lower left graph shows the departure of the phase of the output signal from the phase when the CFA is turned off and the signal transmitted through it. The CFA has about 1 dB loss in this feedthrough mode. The change in phase is the consequence of the rf interaction and represents only a few percent of the rf phase length of the circuit. The slope of these curves is the phase pushing as a function of current. A positive phase shift means the phase length of the CFA has been increased by the interaction. The right hand graphs in Figure 3 show the power and efficiency as a function of current.

Figure 4 shows typical V-I curves measured on the SFD-266. The F3 and F5 V-I curves were essentially identical. A comparison of Figures 3 and 4 shows the experimental and computed V-I curves to have about the same slope and separation. To obtain the desired location of the computed curves along the voltage axis, we used a procedure similar to that used on experimental CFAs. We adjusted the magnetic field to yield the desired current at the desired voltage at frequency F1 and used this field for all the subsequent computations. This procedure left us with a discrepancy in magnetic field - 1560 Gauss for the computations compared to about 1400 Gauss for the experimental CFA. Much of this discrepancy is the result of the smooth anode assumption used in DECFA. The gap between the vanes of the actual CFA lowers the average dc field in the interaction space below that calculated for smooth continuous electrodes. From a study of trajectories using a trajectory tracing code capable of including the actual vane geometry, we find an E/B drift velocity in the middle of the interaction space about 8% lower than that obtained from the voltage and the anode-cathode spacing. This effect explains most of the discrepancy between the experimental magnetic field and that required by DECFA.

The available data on the SFD-266 yields the power only at the operating current of 22 peak amperes. A comparison of the DECFA and experimental results at a single current can be made by comparing efficiencies at the three operating frequencies. Figure 5 shows such a comparison. The computed and measured efficiencies are in close agreement at F1 and F3, but the computed values are too high at F5 - the top of the operating band. Again the probable cause of the discrepancy is the smooth anode assumption made by DECFA. The final interaction as the electrons approach and sometimes penetrate between vanes can be complex. Figure 6 shows the results of tracing trajectories in the actual vane system of the SFD-262 as they approach the vanes. The electrons continue to yield energy to the rf wave as they penetrate between vanes. Secondaries are generated at the vane face and extract energy from the wave. These effects are normally small relative to the total energy exchange and tend to cancel. This is not, however always the case. An experiment with an SFD-262 variant having T shaped tips with a narrow gap

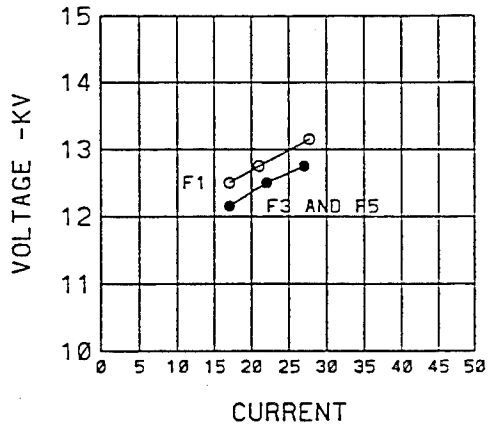


Figure 4. Experimental V-I curve for the SFD-266.

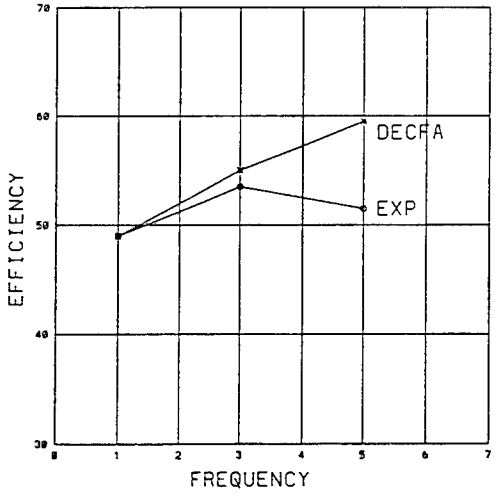


Figure 5. Comparison of computed and measured efficiencies.

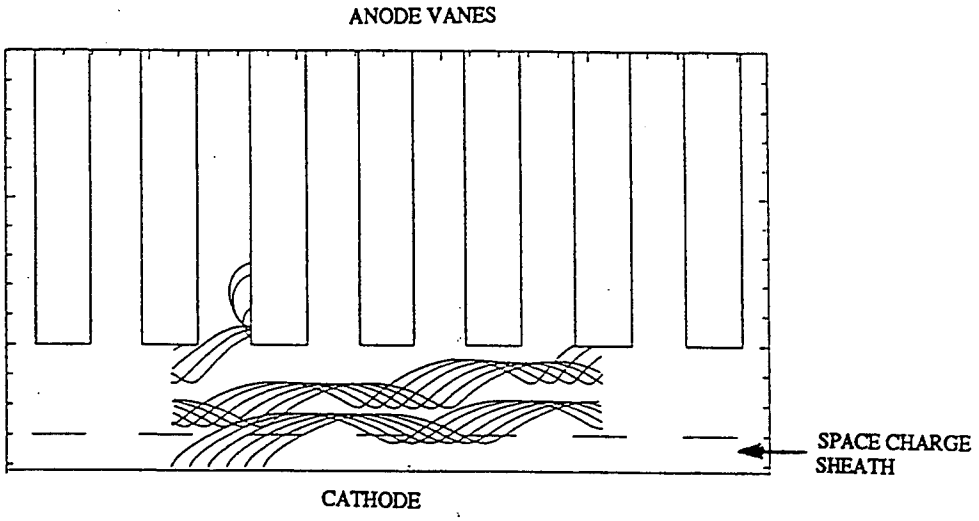


Figure 6. Example of Trajectories Between the Vanes of the SFD-262. At the middle of the sixth vane, the trajectories are set back by four periods and restarted. A space charge sheath is included beneath the dotted line between cathode and anode. Secondary electrons are generated at the vane face, make a single loop and strike the vane in a retarding phase of the rf wave in which no further secondaries may be generated.

between them showed this effect dramatically. Experimentally the efficiency was substantially reduced compared to the standard SFD-262. The trajectory tracing code showed that the electrons were stopped in the narrow gap and accelerated by the wave back to the upstream vane. This resulted in reduced efficiency. The more detailed MASK simulation is needed to study such effects of the vane tip geometry.

DECFA Description of CFA Interaction

DECFA can be used to provide a detailed description of the interaction in the CFA. Such results will be presented on the SFD-266 CFA for a single operating point at midband and at approximately the nominal peak current. Figure 7-9 shows computed quantities as a function of distance from input to output. These results are averaged over the last 22 passes of a 25 pass computation. Figure 7 shows the power on the circuit and the departure of the phase of the circuit wave from the cold circuit value. At the input of the CFA, there is a region in which the space charge becomes bunched. Beyond this initial region power grows approximately linearly as a function of distance. The phase departure from the cold circuit value grows linearly with distance throughout the CFA. Figure 8 shows the dissipation resulting from electron interception on the anode and cathode. The third component of dissipation - the anode circuit loss will be proportional to the power on the circuit shown in Figure 7. From Figure 8 we see that the anode electron dissipation is relatively uniform along the final 2/3 of the circuit length. The rate of current interception is similarly uniform. The cathode dissipation is also uniform and continues into the drift space. The input and output power and the dissipations are given as a percent of the

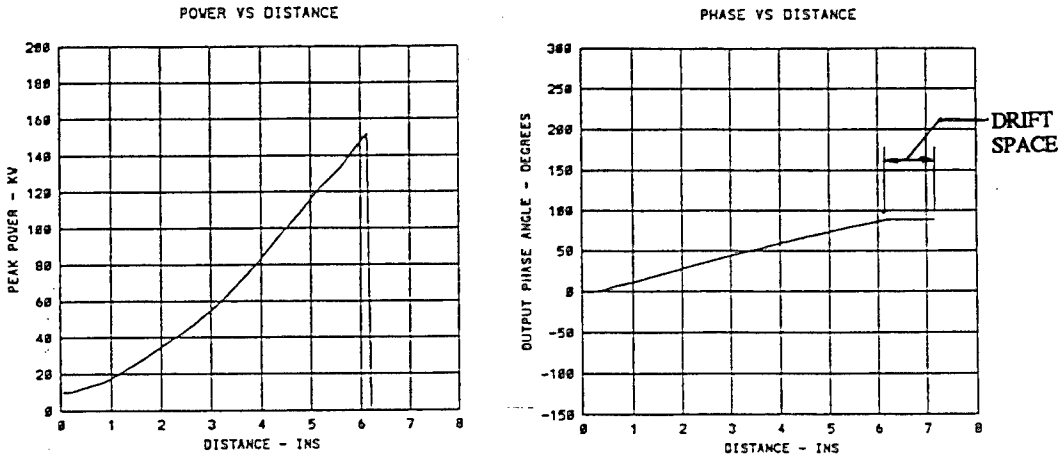


Figure 7. Average Results for 22 Passes of a Midband Simulation. Power and Phase Departure from the Cold Phase as a Function of Distance.

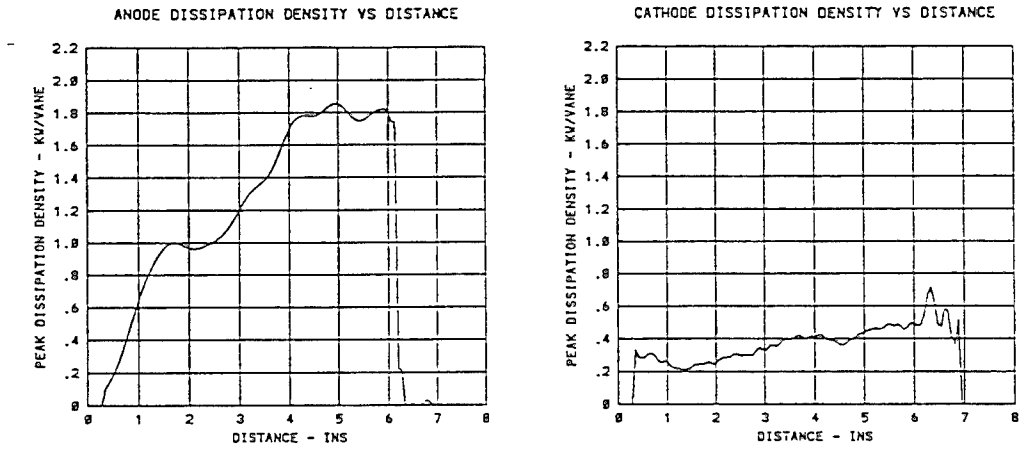


Figure 8. Average Results for 22 Passes of a Midband Simulation. Anode and Cathode Dissipation Density as a Function of Distance.

peak d.c. input power (peak cathode voltage x peak cathode current) in Table 2. The sum of the output power and the three components of dissipation should equal the sum of the d.c. input power and the r.f. input power. The energy balance error of the simulation is about 1% of the d.c. input power.

Figure 9 shows four quantities which provide further detail concerning the simulation. The quantity labeled "angle" shows the phase angle of the current induced in the anode circuit as a consequence of the electron motions relative to that of the anode circuit wave. This angle is a measure of the effective bunch location relative to the rf wave. A positive angle corresponds to a bunch lagging the center of the favorable phase in the rf wavelength. This leads to an increase of the phase length of the CFA - a positive shift in the output phase. The bunch tends to move

Peak Output Power	55.1 %
Anode Dissipation (interception)	27.6 %
Cathode Dissipation	9.9 %
Circuit R.F. Loss	9.9 %
	102.5 %
D.C. Input (voltage x current)	100.0 %
R.F. Input	3.6 %
	103.6 %

Table 2. Powers and Dissipations as a Percentage of the D.C. Input Power for the Midband Simulation.

forward and the induced current angle tends to decrease as the cathode voltage is increased. In the SFD-266 simulations the induced current angle always remains positive (lagging bunch). This contrasts to the situation in the more conventional SFD-262 design in which the angle changes from positive at the low end of the band, to zero at midband and to negative (leading bunch) at the high frequency end of the band. The changes in bunch position and the corresponding changes in the angle of the induced current are responsible for the change of output phase as a function of cathode voltage and frequency which were shown in Figure 7. In the SFD-262 simulations we encountered a maximum current boundary at the high end of the band when the bunch had moved forward to the point where the induced current angle had reached about -50 degrees. At this point the bunch for some of the passes of the interaction wavelength around the CFA began to fall forward out of the favorable phase. The SFD-266 simulation shows that the design is far from such a maximum current boundary.

The charge diagnostic in Figure 9 shows the total charge in the interaction wavelength normalized to 10,000 units to fill the complete wavelength to the Brillouin density. An ideal Brillouin sheath for this case should contain about 2850 charge units. The bombardment energy diagnostic shows the average energy of the electrons incident on the cathode during each time step of the simulation. It is notable that this energy is roughly constant as a function of distance even though the anode wave rf fields are increasing by a factor of 3.9 (15 times increase in power). Much of the energy for the cathode bombardment appears to come from energy exchange within the space charge. Certainly this is the case in the drift space where the anode wave is not present. The cathode field diagnostic shows the field at the cathode averaged over the length of the interaction wavelength and normalized to the space charge free field. (The quantity plotted is actually the potential on the first row of the potential array divided by the cell width and is thus slightly larger than the true field at the cathode.) In a truly space charge limited case the cathode field reported by the simulation should be closer to zero than it is in this simulation. The simulation appears to be slightly charge depleted.

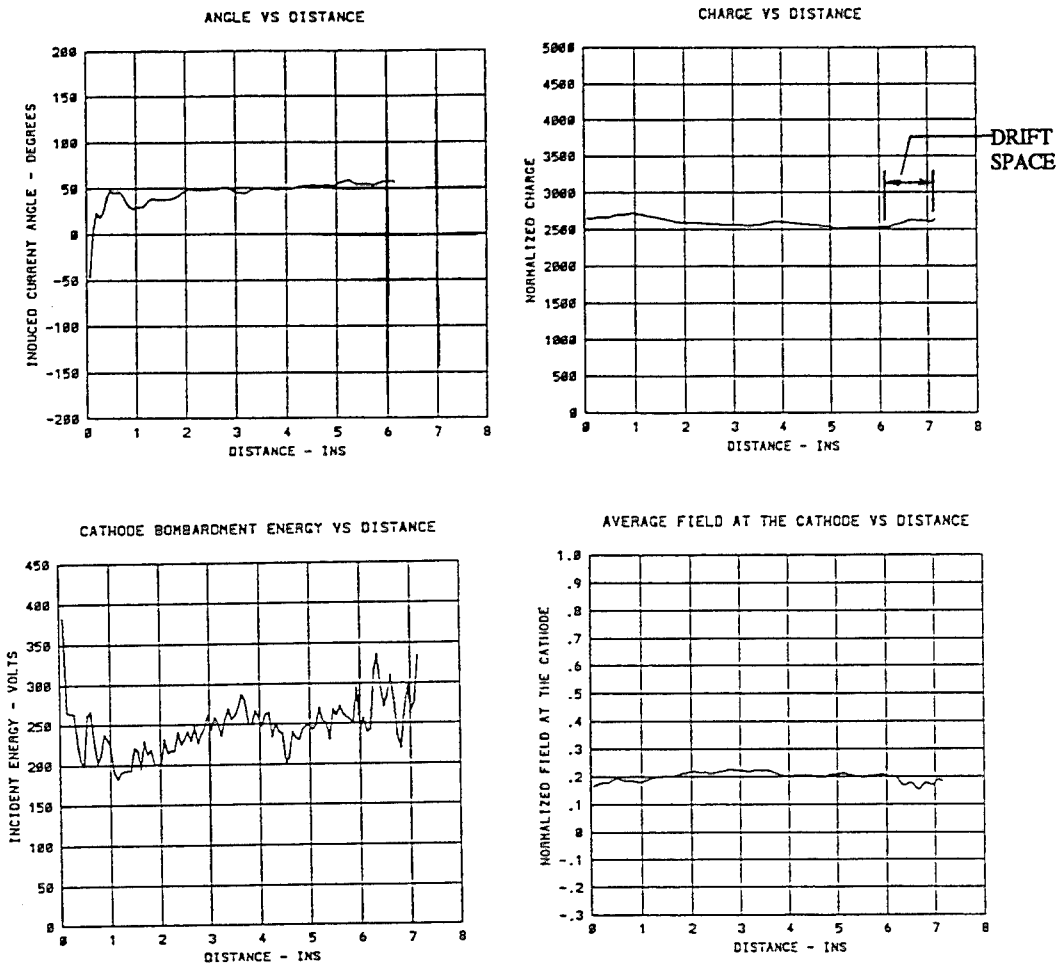


Figure 9. Average Results for 22 Passes of a Midband Simulation. Phase Angle of the Induced Current, Normalized Charge Per Wavelength, Cathode Bombardment Energy Per Electron, and Laboratory Frame Field at the Cathode as a Function of Distance.

The bombardment energy, charge per wavelength and field at the cathode respond together to the emission level of the cathode. The conditions in Figures 9 are obtained when the cathode is capable of supplying nearly all the charge the system can accept before driving the cathode field to zero. Additional emission has little effect on these quantities. Under these conditions the simulation shows the emitted current from the cathode to be about four times the anode current. Three quarters of this current returns to the cathode. When the emission level is not enough to maintain the maximum charge, the charge per wavelength drops, and the field at the cathode and the cathode bombardment energy increase. The increase in cathode bombardment energy is the consequence of the change in trajectory shapes as the space charge is depleted. In the absence of space charge, the trajectories are cycloids. In the presence of the maximum space charge, the dc field in the sheath is reduced and the maximum radial extent of the trajectories is reduced to about half that of a space charge free cycloid. [5]. Depleting the sheath space charge thus increases the radial extent of the trajectories allowing them to interact more strongly with the anode wave and

gain additional energy from it. A beginning of charge depletion at the output in these diagnostics is usually the first indication of cathode emission becoming marginal.

The diagnostics in Figures 7-9 were averages over 22 passes of the interaction wavelength around the CFA. We next consider diagnostics which apply to only a single pass or are "snapshots" of the interaction at a single instant. Figure 10 shows charge profile plots for three successive spokes near the input and near the output of the CFA. These plots are generated at one wavelength intervals as the interaction wavelength passes through the CFA. The plots for successive wavelengths can then be joined to make an approximate representation of successive spokes. The spokes are relatively broad at the input and condense into the familiar spokes in the output region of the CFA. In the SFD-262 simulations, the charge bunches were even broader at the input and there was internal rotation of the charge within the bunch under the influence of the radial space charge forces. The higher rf fields and reduced space charge of the SFD-266 appear to have largely eliminated this internal rotation. The charge profiles illustrate two additional features which relate to the internal fluctuations of the simulations. One is the voids in the space charge above the cathode surface. The other is the "rolls" between spokes which form and move into the base of the spokes. Both of these features drift backwards in the moving reference frame and thus travel at less than the wave velocity in the laboratory frame. Their velocity appears to correspond roughly to the average velocity of the sheath electrons which is in turn about 70% of the r.f. wave velocity.

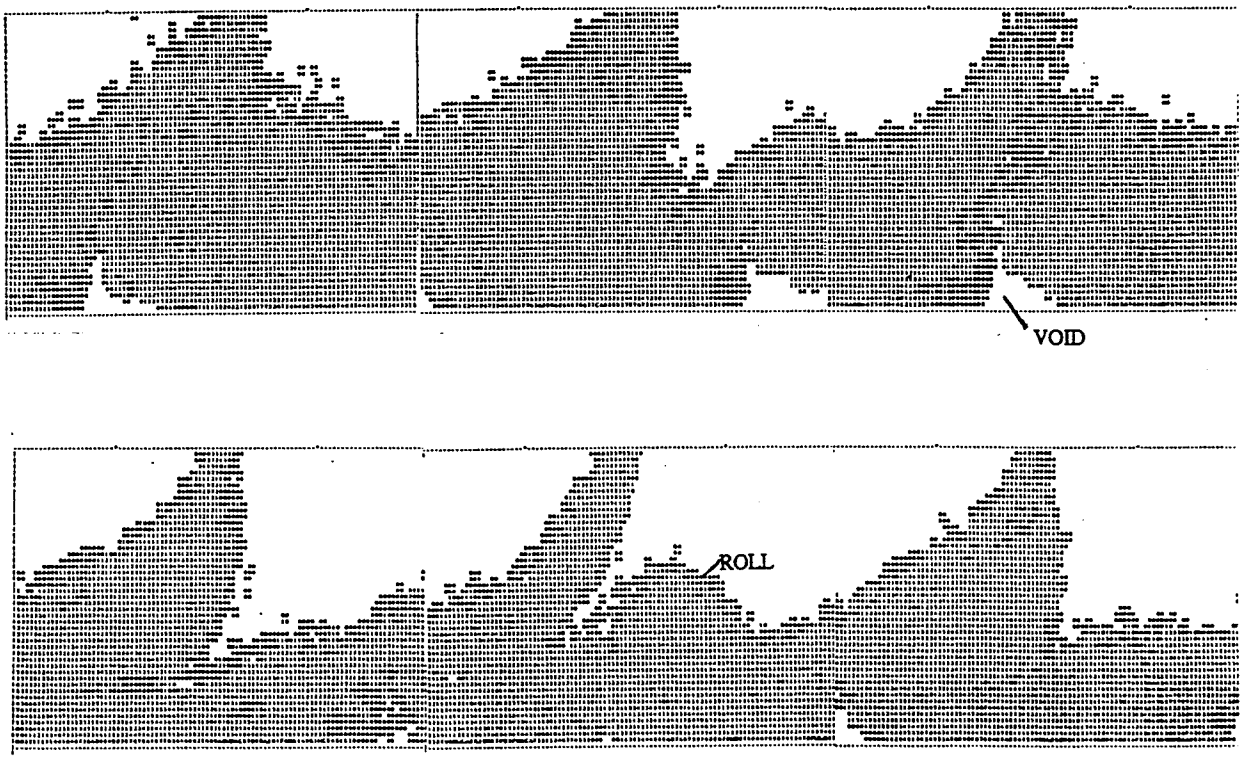


Figure 10. Examples of the Charge Distribution in Three Successive "Spokes" at the Input (top) and the Output (bottom). The voids at the cathode and the "rolls" between spokes drift to the left in the moving reference frame. The spokes are stationary in this frame.

Figure 11 shows two moving reference frame equipotential plots. The dc potential required to make the electron E/B drift velocity equal to the circuit wave velocity has been removed from these plots. This leaves a small residual d.c. field, the r.f. fields and the space charge fields. The guiding center of electron trajectories moves along equipotential lines in the moving reference frame. (The guiding center motion is perpendicular to the electric field and thus parallel to the equipotential.) Arrows in the equipotential plots show the direction of electron circulation in the moving reference frame. These plots were made at the location of the center spoke of each of the two sets in Figure 10. These plots are useful in visualizing the electron motion in the moving frame. The plots show that electrons will move backwards in the moving frame until they reach a region on the left of the plots at the base of the spoke. The equipotentials have a minimum in this region (zero moving frame field) so space charge in this region becomes synchronous with the circuit wave. This is a branching region where trajectories are either drawn into the spokes or continue to drift backwards into the next wavelength to the left. A sequence of these equipotential plots shows the location and shape of these equipotential plots to fluctuate as the wavelength moves through the CFA.

Typical segments of electron trajectories are shown in Figure 12. Timing dots separated by 1/10th of a cyclotron period are superimposed on these trajectories. Two input region and two output region trajectories are shown. For each region we show one trajectory drawn into the spoke and one which does not enter the spoke. When a trajectory exits the left side of the interaction wavelength in these plots, it is reintroduced at the right side. Several general conclusions may be drawn from Figure 7. Conditions in the space charge sheath are far different from those in an ideal Brillouin sheath. The trajectories are not smooth but appear more like the first order trajectories described by Slater [5]. None of the sheath trajectories travel at the circuit wave velocity. Because of the reduction of dc field in the sheath, the trajectories travel on the average at less than the frame velocity, backwards in the moving frame. They tend to reach frame velocity only near the maxima of the trajectories. If sheath trajectories could stay in the system for an appreciable time, they would transform into the smooth trajectories in a Brillouin sheath which represents the lowest energy state. However, in the CFA simulations, individual trajectories remain in the system for only a fraction of a pass of an rf wave around the circuit.

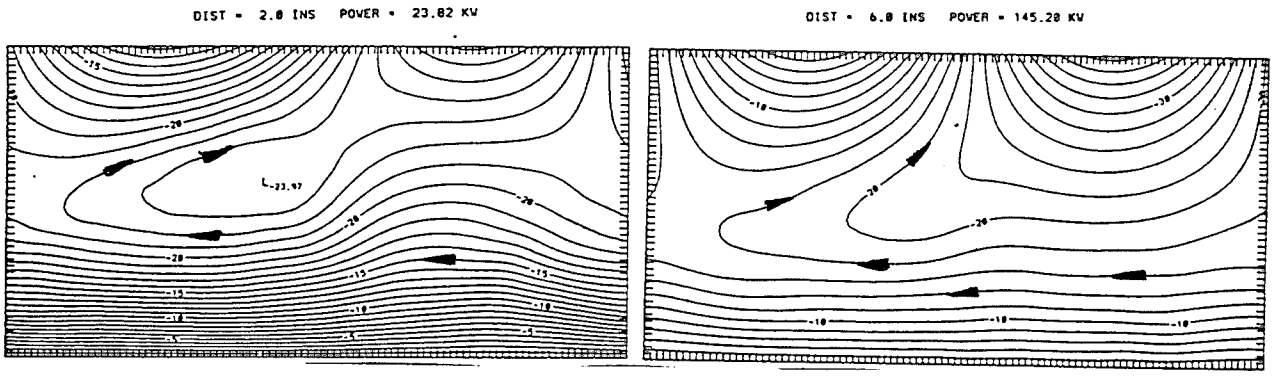


Figure 11. Moving Reference Frame Equipotential Plots Near the Input (left) and the Output (right).

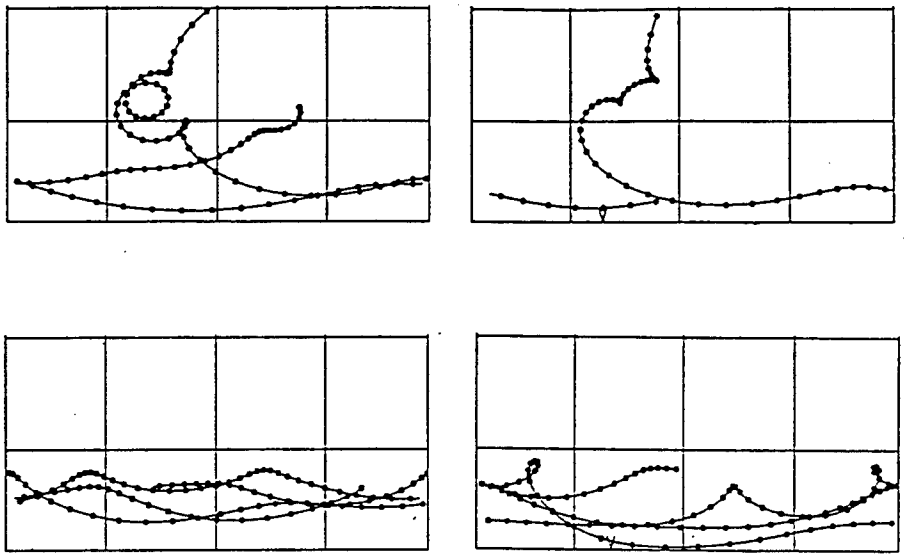


Figure 12. Samples of Trajectories in the Moving Reference Frame at the Input (left) and at the Output(right).

Figure 13 shows four diagnostics averaged over 10 cycloids in the output region of the CFA. The radial space charge distributions is averaged over the complete rf wavelength in the circumferential direction. This diagnostic shows the charge density in the sheath to be about half the Brillouin density but the sheath to be thicker than the ideal Brillouin sheath. The net charge in the wavelength is about the same as in a Brillouin sheath. The remaining diagnostics in Figure 13 relate to the cathode bombardment. They show the energy and angle of incidence distribution of the incident electrons and the distribution of incident current along the cathode within the moving wavelength interaction region. The angle of incidence is seen to remain close to the perpendicular. The relatively uniform incident current distribution along the cathode within the interaction wavelength is the consequence of much of the energy for the cathode bombardment coming from energy exchange within the space charge. A similar set of four diagnostics for the input region of the CFA is almost identical to the output region diagnostics of Figure 13. Again this is suggestive of cathode bombardment being largely the result of energy exchange within the sheath.

Fluctuations of the Solution

The solutions described above fluctuate about a mean. The fluctuations can be devided into pass-to-pass effects and effects within a single pass. Fluctuations of the spoke shape and the equipotential plots have been referred to above and are examples of internal fluctuations. Figure 14 shows the fluctuations in the power and output phase from pass-to-pass of the simulation. The ratio of the rms. power fluctuation to the average value and the rms. phase fluctuation are numerical measures of the degree of fluctuation. These pass-to-pass fluctuations are the consequence of differences in recirculated charge distribution. They have led to the belief that reduction of charge recalculation is a potential means of reducing CFA noise. Figure 15 shows

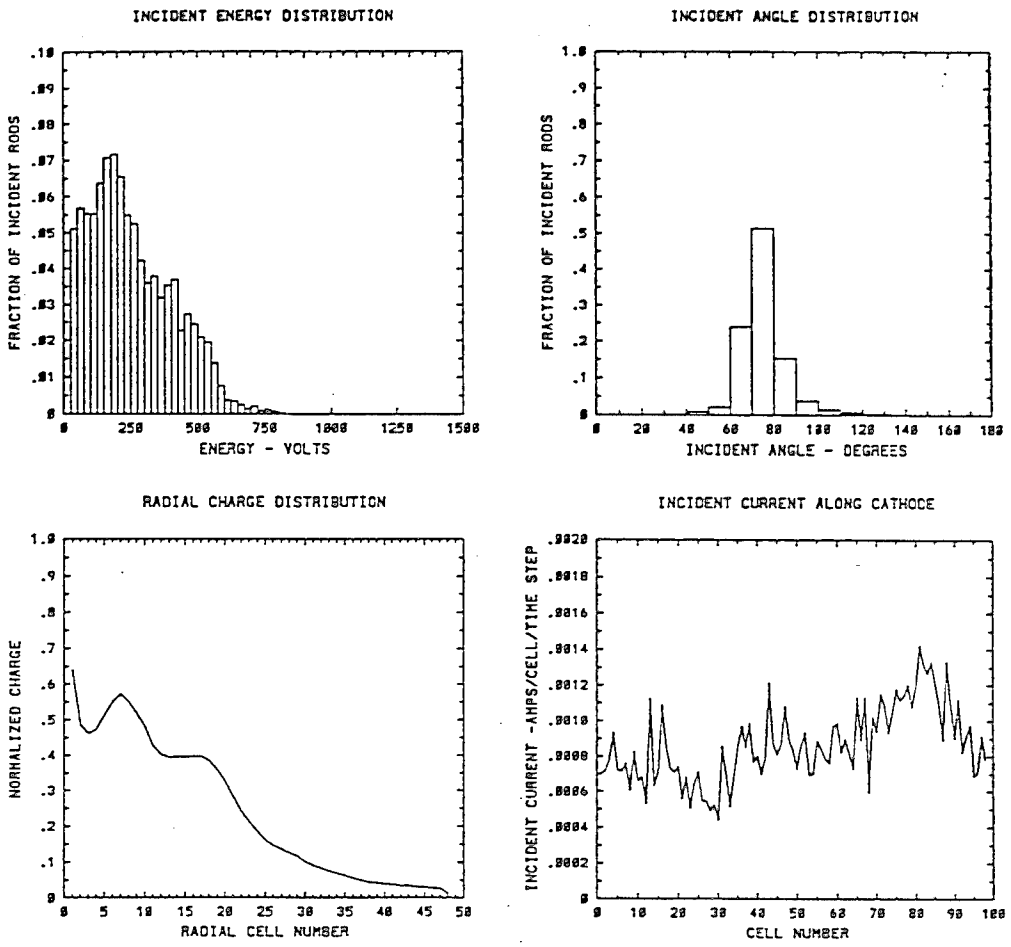


Figure 13. Radial Charge Distribution and Cathode Bombardment Diagnostics near the Output of a Single Pass computation.

another measure of the internal fluctuations - the fluctuations in the field at the cathode. The graph on the left in this figure shows the field at the cathode at a "probe point" at the center of the favorable phase. This field is shown as a function of distance from input to output. This quantity is seen to fluctuate wildly as voids in the space charge pass over the probe location. Examination of the field at different probe points in the moving wavelength shows that the peaks in Figure 14 are moving with a velocity (in the laboratory frame) of about 0.5 the wave velocity. This motion is also illustrated by the graph on the right in Figure 14 which shows snapshots of the field distribution along the cathode in the moving wavelength at intervals separated by four time steps. The maximum of the cathode field is seen to be drifting to the left.

Effect of Emission Conditions on the Fluctuations

The effect of emission condition on the fluctuations of the simulations has been studied in greatest detail for the SFD-266 CFA. Experimentally the noise of the SFD-266 is about 10 dB lower than that of the SFD-262 under the same voltage and current operating conditions. In the simulations,

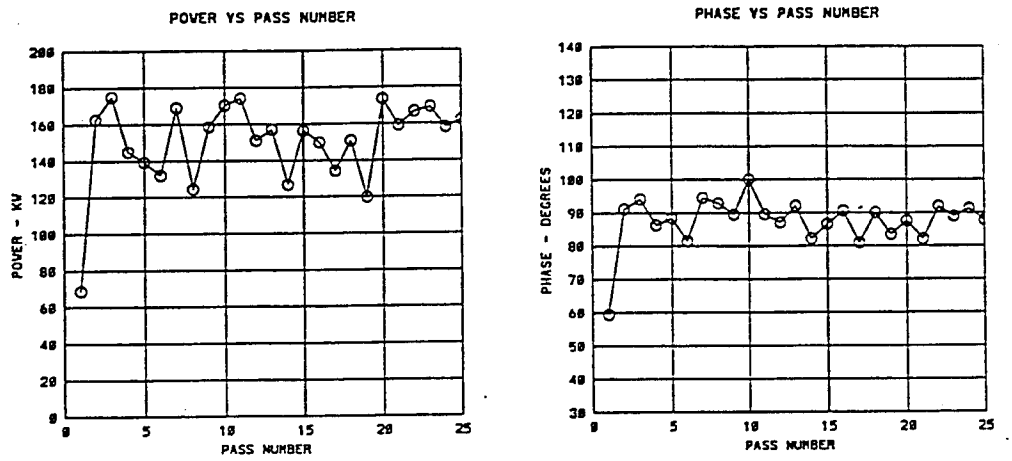


Figure 14. Pass-to-Pass Fluctuations in the Power and Phase for a 25 Pass Midband Simulation.

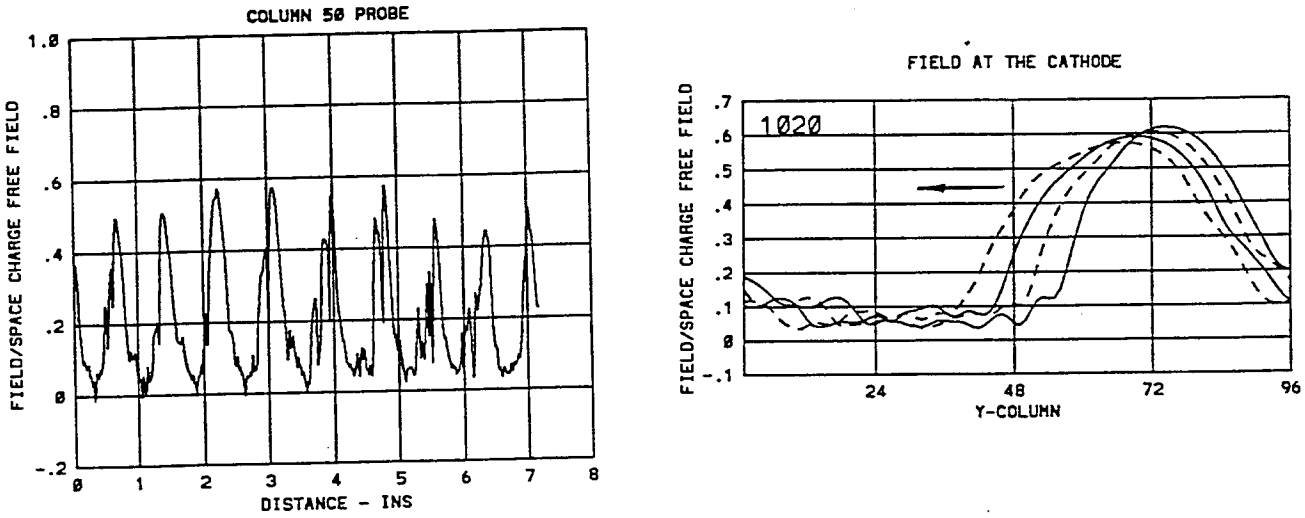


Figure 15. Cathode Field Fluctuations. The graph on the left shows the field at the center of the interaction wavelength as a function of distance from the input to the output. The graph on the right shows the cathode field as a function of distance along the cathode within the interaction wavelength. The field is plotted at timesteps separated by 1/15 of a cyclotron period.

the fluctuations are lower in the SFD-266. The charge profile plots of the SFD-266 appear smoother than those of the SFD-262 and pass-to-pass fluctuations are half to two-thirds of those in the SFD-262.

The effect of emission conditions has been studied in the SFD-266 for thermionic emission alone, secondary emission alone and a combination of thermionic and secondary emission. Figure 16 shows the effect of varying the emission current density when thermionic emission alone is present. This figure contains three columns—one for each of three current densities. The current density, the resulting anode current and efficiency are listed at the top of each column. This is followed by the ratio of the emitted current to anode current and the normalized charge in the interaction wavelength. In the center of each column is a graph showing the field at a probe point on the cathode as a function of distance such as was introduced in the last section. This quantity is a measure of the internal fluctuations within a pass. At the bottom of each column is a listing of the power and phase fluctuations from pass-to-pass.

Figure 16 shows that at low space charge densities the sheath charge is depleted resulting in an increase in the field at the cathode toward the free space value. The fluctuations in cathode field are absent. Efficiency is low because the trajectories are closer to cycloids than to the Slater-like trajectories of the full space charge solution. Pass-to-pass fluctuations are almost completely absent in the low emission density case. At intermediate emission densities, fluctuations in the field at the cathode as well as pass-to-pass fluctuations appear. At even higher emission densities, the field at the cathode is reduced to a low value and the fluctuations in the field again disappear. The magnitude of the pass-to-pass fluctuations is decreased but does not drop to the low value of the low emission case.

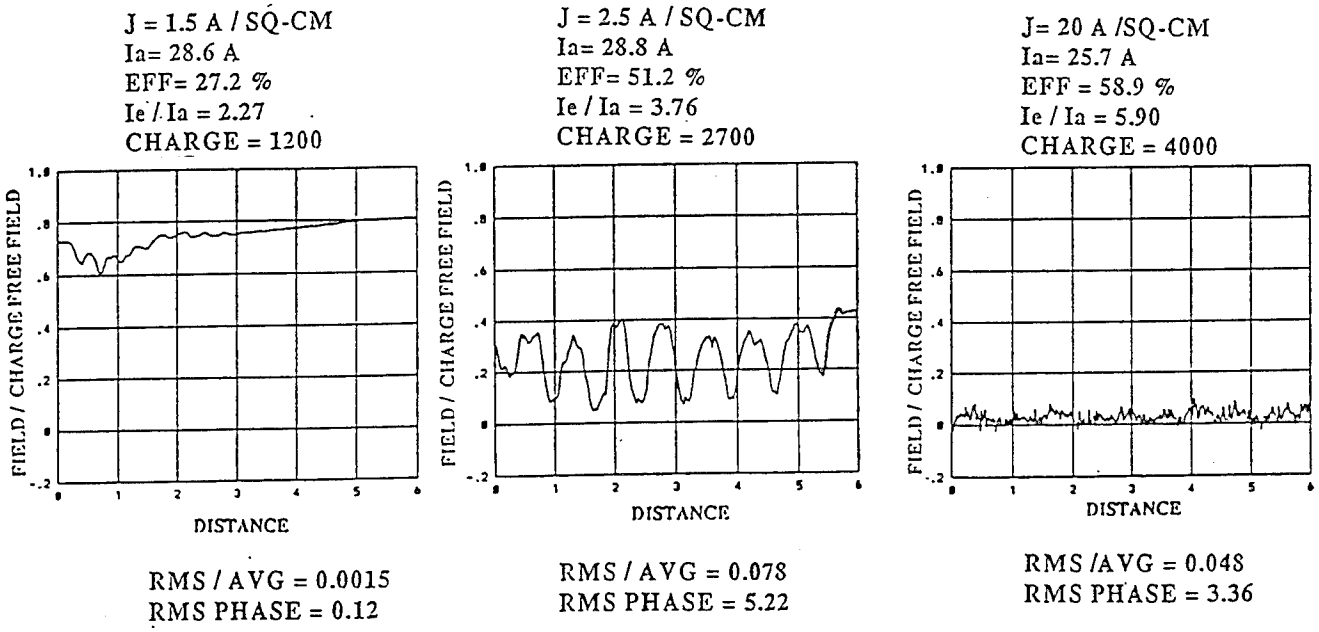


Figure 16. Effect of Thermionic Emission on Fluctuations of the Simulation.

Figure 17 is similar to Figure 16 but applies to secondary emission alone. The maximum secondary yield is listed at the top of each column. This maximum in all cases occurs at an incident energy of 300 volts as is characteristic of a beryllium secondary emitter. The middle column represents the yield of the beryllium secondary emitter currently used in the SFD-262 and SFD-266 CFAs. The lower and higher yield columns were obtained by multiplying the yields by an arbitrary factor at each incident energy. Moving from the center column toward the lower emission, we find the field at the cathode increasing as was the case for thermionic emission. The fluctuations of the field do not, however, disappear. At a very high secondary yield, the field at the cathode again drops to a low value and the fluctuations disappear. As is the case with thermionic emission, the pass-to-pass fluctuations decrease but are not eliminated. The elimination of the cathode field fluctuations as the secondary yield increases occurs in an unexpected manner. At a maximum yield of 10, there is a mixture of passes having high fluctuations as shown in the middle column and passes having low fluctuations as shown in the right column. As the yield increases, the number of low fluctuation passes increases. At a yield of 20, all the passes show low fluctuations.

Figure 18 compares two cases. The left column is the same as the center column of Figure 16 with secondary emission alone. The right-hand column shows the effect of adding 5 amps/cm^2 of thermionic current to the secondary emission. The addition of the thermionic emission causes the cathode field fluctuations to drop to a low value. At the same time the efficiency increases. The increase in efficiency is the consequence of a reduction in cathode dissipation. Charge profile plots generated by the simulation become much more uniform and fluctuations of the equipotential plots are greatly reduced when the thermionic emission is added.

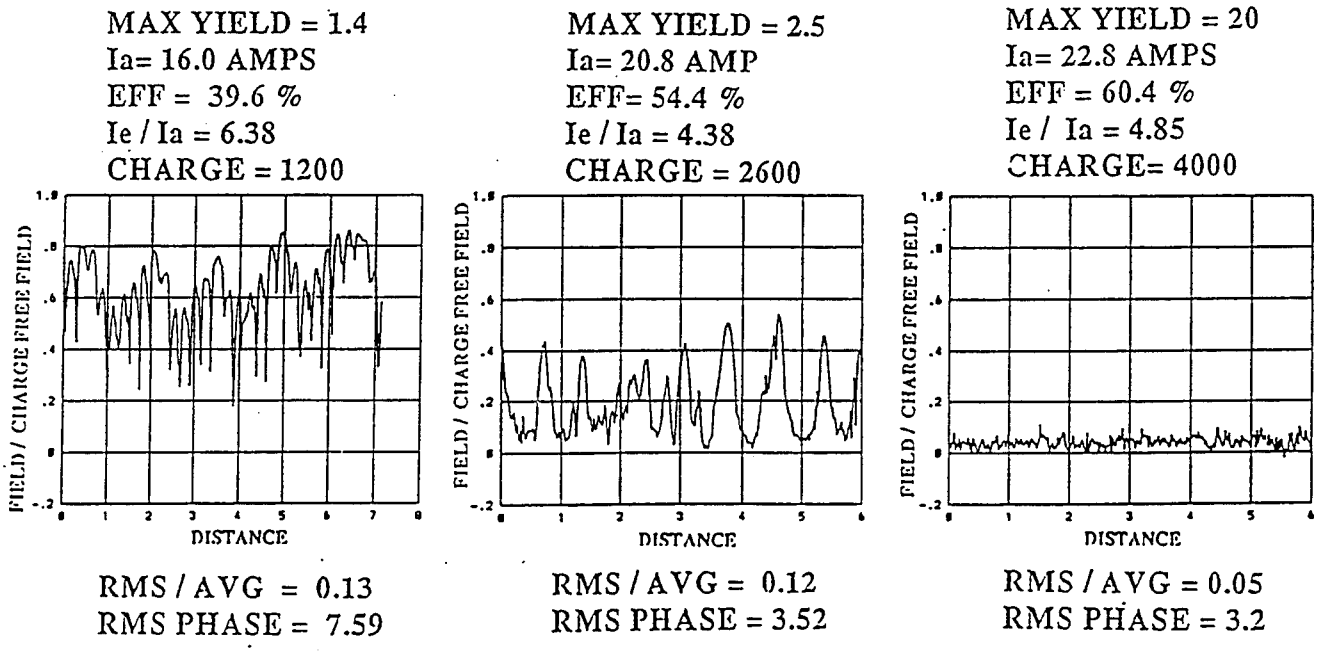


Figure 17. Effect of Secondary Emission on Fluctuations of the Simulation.

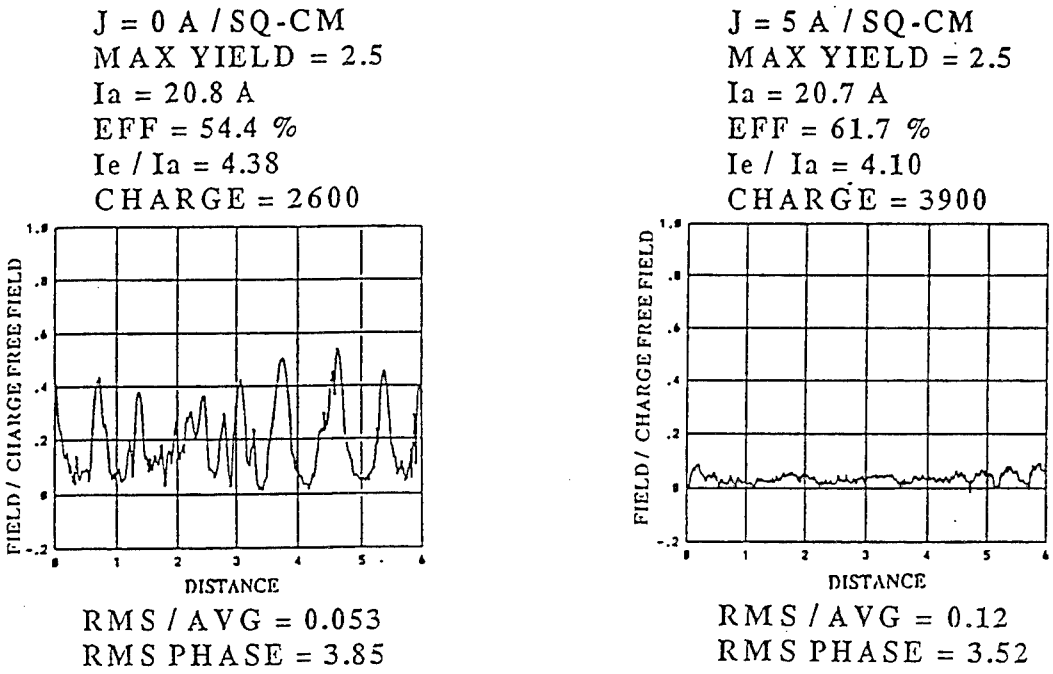


Figure 18 Effect of Adding Thermionic Emission to the Secondary Emission.

Experimental results obtained on an SFD-266 CFA exist corresponding to the two columns of Figure 18. These results were obtained using an SFD-266 CFA employing a dispenser cathode with a heater in place of the usual beryllium secondary emitting cathode. The CFA was operated at low duty so that with the heater off the cathode operated cold and emission was entirely the result of secondary emission. When the heater was turned on and the cathode heated to above 1000°C, there was a mixture of secondary and thermionic emission. The addition of the thermionic emission caused the CFA to transition to a low noise state in which the noise was reduced by about 20 dB. This state suggests a reduction in fluctuation in the space charge. At the same time efficiency increased by about five percentage points—about the amount of the of the increase seen in the simulations.

Conclusions

The moving wavelength DECFA model yields reasonable agreement with the gross CFA performance and provides useful information on how to revise a CFA design to improve performance. Fluctuations of the model appear to represent a crude model of noise mechanisms in the CFA and of the effect of cathode emission on noise. The fluctuations depend critically on the emission algorithim. Low fluctuation states appear at high emission levels when a "Gauss' law" limit is imposed on the emitted current. In the absence of this limit, low fluctuation states are observed at low thermionic emission but not at high emission levels. Further studies with the more complete MASK model [2] is expected to yield improved insight into noise mechanisms.

References

1. S. P. Yu, G. P. Kooyers, and O. Buneman, "Time Dependent Computer Analysis of Electron-Wave Interaction in Crossed Fields," Journal of Applied Physics, Vol 36, No. 8, Page 2550, Aug 1965.

2. H. McDowell, "Computer Modeling of CFAs Using Moving Wavelength and Trajectory Tracing Codes," Vacuum Electronics Annual Review Abstracts, 1994, Palisades Institute For Research Services.

3. D. Chernin, A. Drobot, S. Riyopoulos, and M. Kress, "Computer Model Development for Crossed Field Amplifiers," Vacuum Electronics Annual Review Abstracts, 1994, Palisades Institute For Research Services.

4. G.E. Thomas and J. Deveau, "The SFD-266--A Crossed field Amplifier with a 40 dB Improvement in Noise Performance. Vacuum Electronics Annual Review Abstracts, 1994, Palisades Institute For Research Services.

5. J.C. Slater, "Microwave Electronics," D. VanNostrand, New York, c1950

RECENT ADVANCES IN SIMULATION OF MAGNETRONS AND CROSSED-FIELD AMPLIFIERS

George E. Dombrowski
69 Birchwood Heights Road
Storrs, Connecticut 06268
(860)429-2478

Abstract

Various improvements and enhancements of the author's earlier code (IEEE Transactions on Electron Devices, ED-35, 1988) are presented.

The details of the anode vane geometry are evaluated by application of Hockney's method using Buneman's cyclic reduction. The results of this enhancement show a significant improvement over the previously used solid anode approximation.

The orbit calculation has been reformulated to allow for relativistic mass increase. It has simplicity that makes it equally adapted to ordinary voltage levels.

The previous code requires large storage and computation time for systems with large numbers of rf nodes. Study of the response functions shows that values are important for only a few of these: those for sources close to the test site. Reformulation reduces the data storage and computation time by a considerable fraction. This makes it feasible to handle both the 40-vane and the 104-vane Northeastern University amplifiers.

I. INTRODUCTION

This paper describes three improvements in the author's computer program [1] for the simulation of magnetrons and amplifiers. Some remove limitations on accuracy. Others improve the efficiency of the computer code - a matter of importance for execution on small, 'personal' computers.

II. STATIC FIELD OF THE ANODE VANES

Earlier simulation calculations [2] disclose the substantial interaction between the stream and the space between vanes, yet they ignore the details of the electric field at the vane tips. They use the logarithmic potential of a solid anode. This may be justified for electrons in synchronous circular orbits, as in small-signal conditions. It fails, however, under

the large-signal conditions in the spokes and especially at the terminus of the orbits. Furthermore, vanes of diverse shape have been used in both magnetron and amplifier. The anodes have often been rods rather than vanes. Vane shaping has been shown to improve device performance, likely related to secondary-electron loading [2] and multipactor between anodes [3]. Clearly this aspect must be considered in simulation.

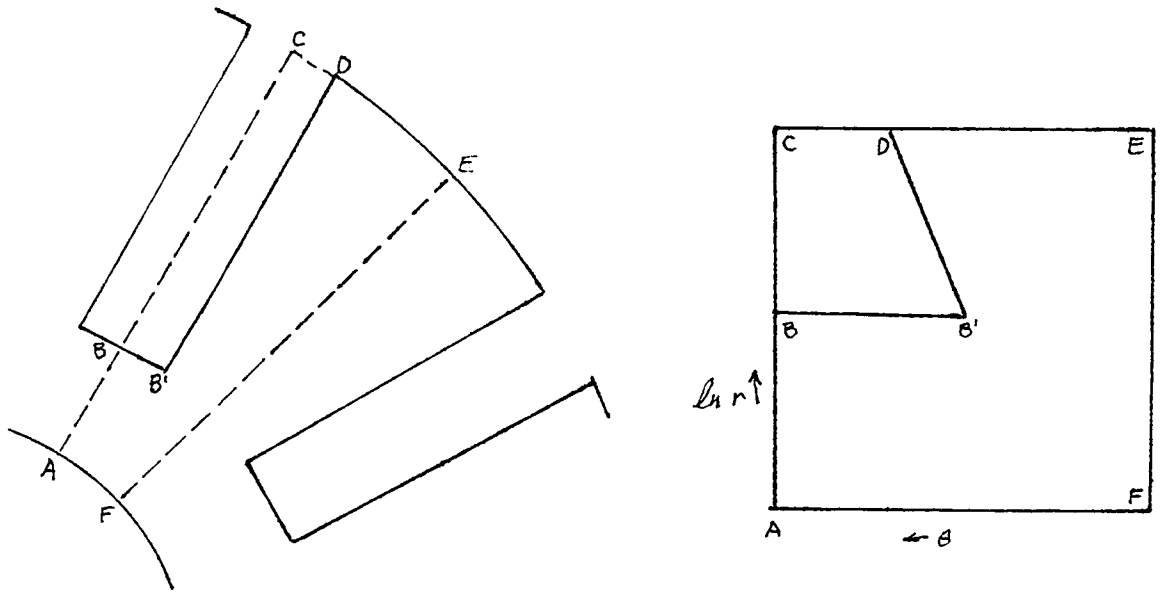


Fig. 1. Vane geometry in real and transformed space.

Buneman's Cyclic Reduction

The cyclic reduction calculation can be used to solve the Laplace or Poisson equation on a binary mesh (having numbers of cells in each direction equal to a power of two). The region must have regular boundaries, as ABCDEFA in Fig. 1. The radial bounds are equipotentials; the azimuthal boundary conditions are Neumann contours ($\partial v/\partial\theta=0$), as apply at AB and EF in view of the mirror symmetry there. It would appear that this method fails to accommodate the vane contour BB'D. Hockney [4], however, devised a method to do so.

The Method of Hockney

Hockney's method may be described by realizing that the mesh charges may be that of free charge - the electrons - and also the surface charges on the vanes. It becomes a task to determine the surface charge distribution that corresponds to the applied anode potential. The method of determining this charge proceeds as follows.

Cyclic reduction is first used to solve the Laplace equation in the regular region with the anode voltage V_b at the outer wall, the cathode potential being zero. The potentials on the M vane contour points form a linear matrix

$$[V] = v_j, \; j=1,M \tag{1}$$

and are in general different from the anode potentials, defining a deficiency

$$[Vx] = V_b - [V] \tag{2}$$

The problem becomes one of determining surface charges to eliminate these differences.

In the next phase a unit charge is placed at one of the vane mesh points (the i-th). Cyclic reduction is executed, resulting in vane mesh point potentials having the nature of reciprocal capacitances that can be designated s_{ij}. This is repeated for all source points i. The complete array $[s_{ij}]$ defines a reciprocal-capacitance matrix, [S]. Its inverse is the capacitance matrix [C] which expresses the coupling between points on the vane contour. It is required that an array $[Q]=[q_i]$ must be such that

$$[Q] \; [S] = [Vx] \tag{3}$$

eliminating the potential deficiency noted above. Eq. 3 has the solution

$$[C] \; [Q] \; [S] = [Q] = [C] \; [Vx] \tag{4}$$

The final step is to assign [Q] to the vane contour and execute the cyclic reduction once more. The resulting potentials are the exact solution of Laplace's equation with the vanes at V_b.

The computational cost of this procedure is the execution of cyclic reduction M+2 times, the inversion of the the M-square matrix [S], and the matrix multiplication to compute [Q]. Fortunately, it needs to be done only once as a preliminary calculation.

During the simulation the static field is computed by interpolation, taking account of the location of the electron with respect to the vanes. This technique provides the static, space-charge-free electric field. It continues to rely on the solid anode model for space-charge field evaluation. The error in so doing is considered small, since the space-charge fields are small in comparison to the vane-tip and rf fields.

The Poisson Equation

As part of the simulation process, the space-charge can be

assigned to the cyclic reduction mesh and the discrepancy matrix [Vx] obtained. The surface charge [Q] is then computed from Eq. 4, the inverted matrix [C] having been saved. A second cyclic reduction with space- and surface charges in place yields the space-charge potential from which the field is evaluated. The computation burden is thus a matrix multiplication and the second cyclic reduction. This part of the procedure is applicable to the simulation of magnetrons in the pi mode. It is not practical for the amplifier, for which the previous technique can reasonably be used. This technique for magnetron simulation has only recently been implemented.

Simulation Results

Simulations were made for the type 4J50 magnetron, with the solid anode and with the detailed vane fields. The results are compared with each other and with measurements made by J. F. Hull [6]. Table 1 shows these results for magnetic field B = 5500 Gauss and with (pulsed) anode voltage V_b = 20.9 kv. This is the nominal operating point. The loaded Q is 280.

Table 1. 4J50 Magnetron: B= 5500 Gauss.

			Simulation		Measurement
			Solid Anode	Vanes	J F Hull
Anode voltage	V_b	kV	20.9	20.9	20.9
Anode current	I_b	a	34.2	24.9	27.5
Load power	P_L	kW	311.	252.	232.
Efficiency	η	%	43.5	48.4	40.4

The solid-anode simulation shows results - anode current and rf power - that are surprisingly greater than the vane-field simulation. These in turn are much closer to the measured result of Hull. Results for higher anode voltage (not shown here) are even more dramatically different. The inference is clearly that the vane fields serve a very useful role.

Further comparison with the simulation and measurement is made in Table 2, in which the slope of the Gauss line is determined.

Table 2. 4J50 Magnetron: Gauss line slope data.

	V_b kV	I_b a	Slope a/kV
Measured [6]:	20.0	0.0	
			12.5
	22.2	27.5	
Simulation:	19.9	14.5	
			10.4
	20.9	24.9	
			13.5
	21.9	38.4	

The slope data are in good agreement here, providing further confidence in the simulation process.

III. RELATIVISTIC ORBIT ALGORITHM

Simulation of the relativistic magnetron [7,8] has called for suitable modification of the orbit calculation. As in the past, rf magnetic fields are assumed to have negligible effects. Also as in the past, the trajectory variables are expressed as power series in 'cyclotron time', $T=\omega_c t$. As may be needed, the orbit during a simulation interval may be subdivided into several smaller intervals in order that $T<<1$ for each. This ensures the convergence of the series.

For each charge in the stream, a radially aligned Cartesian coordinate system is assigned as shown in Fig. 2.

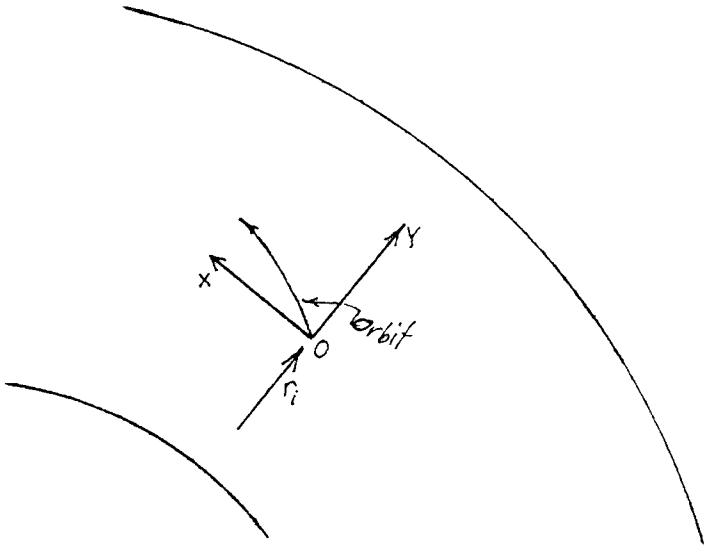


Fig. 2.Coordinates for trajectory calculation

$$UX = a + b\,T + c\,T^2/2 + d\,T^3/6 + \ldots \quad (5)$$
$$X = a\,T + b\,T^2/2 + c\,T^3/6 + \ldots \quad (6)$$
$$UY = m + n\,T + p\,T^2/2 + q\,T^3/6 + \ldots \quad (7)$$
$$Y = m\,T + n\,T^2/2 + p\,T^3/6 + \ldots \quad (8)$$

Also, for relativistic considerations, a power series is introduced for the mass factor

$$\gamma = \gamma_i + b_1\,T + b_2\,T^2/2 + b_3\,T^3/6 + \ldots \quad (9)$$

where γ_i is the initial mass factor determined by initial velocities $a=UX_i$ and $m=UY_i$.

The coefficients in these series are determined by requiring conformity with the motion equations (wherein the primes denote derivatives with respect to T)

$$(\gamma\,UX)' = EX - UY \quad (10)$$
$$(\gamma\,UY)' = EY + UX \quad (11)$$

The polar nature of the field in the magnetron is expressed by rotation of the electric vector as the orbit sweeps through the small angle θ such that $\cos\theta\approx 1$ and $\sin\theta\approx X/r_i$

$$EX = EX_i + EY_i\,X/r_i \quad (12)$$
$$EY = EY_i - EX_i\,X/r_i \quad (13)$$

Eqs. 11 and 12 lead to the energy theorem

$$(\gamma\,m_o\,c^2)' <=> E\cdot U \quad (14)$$

or

$$\gamma - \gamma_i <=> \int E\cdot U\,dT = \int E\cdot dR \quad (15)$$

These energy relations serve to monitor the orbit calculation. In particular the X and Y coordinates are accepted as computed above, and the velocity components are modified to preserve energy balance.

This algorithm performs well for simulation of the MIT A6 relativistic magnetron, for which γ may at times be as high as 3. It is used also for conventional magnetrons; in the 4J50 the relativistic mass increase may be as much as 2 percent.

IV. AMPLIFIER: RESPONSE FUNCTIONS

An essential part of the simulation of the cfa is the determination of the behavior of the rf network. This system consists of a number N of nodes corresponding to the anode vanes. At any discrete time t_i, the state of the network is defined by the set of rf voltages and their time-integrals, $u=\int v\,dt$

$$v_i,\ i = 1,N \quad (16)$$

$$u_i\ ,\ i = 1,N \qquad (17)$$

The state of the rf network at the end of a time interval Δt is determined by the state at its beginning and also depends on the extent of electron stream excitation, as manifested by the electronic currents I_i entering the vanes during the interval

$$I_i\ ,\ i=1,N \qquad (18)$$

There are thus two variables (v and u) to define the state, and three 'stimuli', or sources of network excitation: the initial v's and u's, and the electronic current. For the amplifier, rf input signals must be added.

Simulation calculations rely on a prior computation of network response functions, which are the state variables v and u resulting from independent unit stimuli. Thus,
RV denotes a voltage response, i.e., an rf voltage produced by a stimulus; RU denotes a value of the time-integral u produced by a stimulus. Indices denote the source node and the node where the response appears. Lastly, subscripts are used to denote the type of stimulus producing the response. For example,

$RV_V(i,j)$ is the voltage response to a voltage stimulus at the i-th node. It is observed at the j-th node. By reciprocity, $RV_V(i,j) = RV_V(j,i)$.
$RV_I(i,j)$ is the voltage response seen at node j produced by unit current at node i.

The complexity of these response functions leads to limitations, especially with small computers. First, the one-time calculation of the functions can be tedious. Secondly, their use in the simulation process requires considerable memory storage. Finally, for each stored function there must be at least one multiplication and one addition; this can result in slow calculation. Each of these factors becomes more serious because the time required increases as the square of the number of vanes, N.

Further study of the nature of the response functions discloses what should already be apparent from the nature of the rf network as a ladder. Table 3 lists, for a 40-vane network, a typical response function, viz., $RV_V(12,i)$.

Table 3. Response of a 40-vane network

i	j	$RV_V(12,j)$
12	<6	.0000000000000000
12	6	.0000000000000000
12	7	.0000000000000067
12	8	.0000000000199434
12	9	.0000000371475753
12	10	.0000371133432558
12	11	.0148155093362986
12	12	.9702946803058404
12	13	.0148155093362986
12	14	.0000371133432558
12	15	.0000000371475753
12	16	.0000000000199434
12	17	.0000000000000067
12	>17	.0000000000000000

These and similar data show that for short time steps the slow-wave system responses are negligible outside the range of 5 vanes on either side of the stimuli. They make no contribution to the signals, and simply waste computer time. The computer code has accordingly been revised to eliminate them.

Table 4 presents further insight into the nature of the response functions.

Table 4. Response functions of a 40-vane network

i	$RV_V(i,i)$
1	.71046034646047
2	.97032743738218
3	.97029468032445
4	.97029468030584
5	.97029468030584
6	.97029468030584
.	do
.	do
.	do
35	.97029468030584
36	.97029468030584
37	.97029468030584
38	.97029468032445
39	.97032743738218
40	.71046034646047

These data show that the response functions are principally

identical functions depending on $|i-j|$. Thus the functions $RV_V(i,j)$, $i=1,N$, $j=1,N$ having N^2 values, can be replaced by a simpler function $RV_V(|i-j|)$, $|i-j|= 0,5$ with 6 values.

Exceptions to this rule are apparent at the ends of the rf network, where the response is influenced by connections to source and/or load.

V. Conclusions

Simulation of magnetrons has been improved by accurate calculation of the anode vane fields and also by accounting for relativistic electron dynamics. The effectiveness of the simulation code for amplifiers has been enhanced by use of the response functions of uniform rf networks.

VI. Acknowledgment

The author is pleased to recognize the debt he owes to the University of Michigan - especially to Professor William G. Dow - for his education in physical electronics.

VI. References

1. G. E. Dombrowski, "Simulation of Magnetrons and Crossed-Field Amplifiers," IEEE Trans. Electron Devices, vol. ED-35, p. 2060, 1988.

2. G. E. Dombrowski, "Computer Simulation of Primary and Secondary Anode Loading in Magnetrons," IEEE Trans. Electron Devices, vol. ED-38, p. 2234, 1991.

3. J. R. M. Vaughan, "Observations of Multipactor in Magnetrons," IEEE Trans. Electron Devices, vol. ED-15, p. 883, 1968.

4. O. Buneman, "A Compact Non-iterative Poisson Solver," SUIPR Report No. 294, Stanford University Institute for Plasma Research, 1969.

5. R. W. Hockney, "The Potential Calculation and Some Applications," in *Methods in Computational Physics*, vol. 9, p. 162, (1970); Academic Press, New York

6. J. F. Hull, "Crossed Field Electron Interaction in Space Charge Limited Beams", D.E.E. Dissertation at Polytechnic Institute of Brooklyn, 1958.

7. T. E. Ruden, "Relativistic Magnteron Interaction,"IEEE Conference on Plasma Science, Conf. Rec., (1982)

8. T. E. Ruden and G. E. Dombrowski, "Simulation of High-Power

Relativistic Magnetron Interaction," IEEE Conference on Plasma Science, Conf. Rec., (1991)

Computer Simulations of Low Noise States in a High Power Crossed-Field Amplifier*

David P. Chernin
Science Applications International Corp.
1710 Goodridge Dr. MS 2-5-2
McLean, VA 22102
(703)734-5808

Abstract

A large body of experimental data has been accumulated over the past fifteen years or so on the remarkable ability of both magnetrons and CFA's to operate under certain conditions at noise levels comparable to those achieved in linear beam tubes. The physical origins of these low noise states have been the subjects of considerable speculation, fueled at least in part by results from computer simulation. While computer models have long been able to predict basic operating parameters like gain, efficiency, and peak power dissipation on electrode surfaces with reasonable accuracy, it is only within the past few years that any success could be reported on the simulation of noise. SAIC's MASK code, a $2\frac{1}{2}$-D particle-in-cell code, has been able to compute total, integrated noise power to an accuracy of ± a few dB in a high power CFA, operating with a typical intra-pulse spectral noise density of ~ 47 - 50 dB/MHz. Under conditions that produced low noise (~ 60 - 100 dB/MHz) in laboratory experiments, the MASK code has been, until now, unable to reproduce similar results. The present paper reports the first successful production of a very low noise state in a CFA simulation using the MASK code. The onset of this low noise state is quite sudden, appearing abruptly as the current is raised to a point near which the cathode operates as nearly emission limited. This behavior closely reproduces that seen in an experimentally observed transition between low noise and high noise operation in the SFD-266, a Varian[CPI] low noise CFA. Some comments are made concerning the nature of the noise as observed in the simulation and in the laboratory.

* Work supported by Naval Research Laboratory Contract N00014-92-C-2030

1.0 Introduction

Crossed-field devices, both magnetrons and CFA's, are generally known as noisy devices in comparison to linear beam tubes -- a fact that limits their applicability in many systems, both civilian and military, to which they would otherwise be well suited. While it is often assumed that there is some fundamental feature of the crossed-field interaction that produces excess noise, several experimental developments have shown to the contrary that both magnetrons and CFA's are in fact capable of operating with noise levels comparable to *or better than* linear tubes under certain conditions.

The definitive identification of the sources of noise generation in crossed-field devices nonetheless remains one of the most challenging problems in vacuum electronics and the physical causes of noise have been widely studied and debated for many years[1] A recent Navy funded program designed to identify and reduce the sources of noise in CFA's has produced a large database of information on CFA behavior. Accompanying that program has been an effort to produce computer models of CFA's that can assist in these investigations. Early results from these computer models produced a strong similarity between computed and measured rf output waveforms, as illustrated in Figure 1, which shows a comparison between a measured output waveform from a high power CFA and a simulated output waveform computed by SAIC's MASK particle-in-cell simulation code. These results suggested that the levels of numerical noise and other inherent model limitations might actually be small enough to allow physical sources of noise to be simulated with reasonable accuracy. Still it was thought that the simulation of very low noise operation was out of reach of present codes.

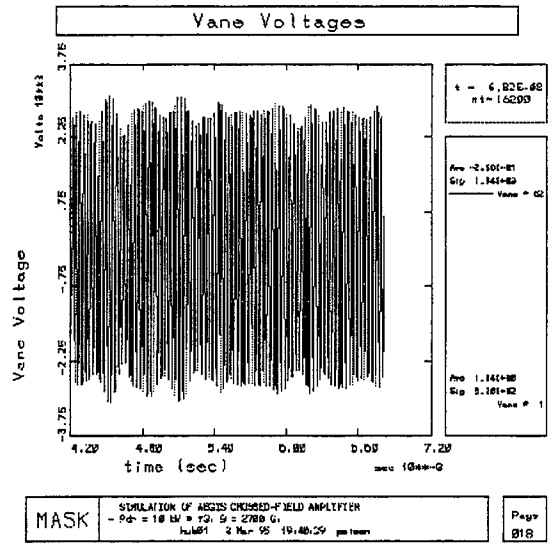


Figure 1a: Typical plot of RF output voltage vs. time for the Aegis SPY-1 CFA, as computed by MASK.

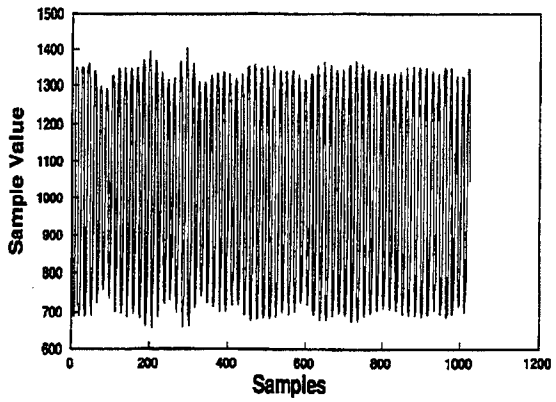


Figure 1b: Oscilloscope trace of RF output voltage vs. time for the Aegis SPY-1 CFA, under the same conditions as those used in the simulation of Figure 1a. [Courtesy Technology Services Corp.]

"Noise", in this paper, will be defined as any departure from a perfectly sinusoidal output signal at the drive frequency, either measured or computed. A signal-to-noise ratio may be defined to quantify such departures and one possible definition, similar to that used in some radar applications, will be given and applied below. One obvious characteristic of such a definition is that it has no way of differentiating between random

sources of noise and, say, a perfectly periodic amplitude or phase modulation, for example. In fact, the quasi-periodic nature of the modulations seen in the waveforms of Figure 1 raise the interesting possibility that at least some part of what is called noise is really the result of a complicated, but deterministic interaction among the circuit, the space charge, and the rate of emission from the cathode. This possibility seems more likely when one considers that, except possibly for roundoff errors, there is nothing random about the computer calculation[2].

Whatever the cause(s) of the waveform modulations in Figure 1, they are observed to persist over large variations of operating parameters and were long thought to be an inescapable feature of the high power CFA's in which they were observed. The initial discovery of low noise states, however, in which the modulations were virtually absent, followed by the results of the simulations described below, shows that the modulations are not fundamental to the crossed-field interaction in the CFA.

It has recently been found that the MASK simulation code is capable of reproducing a transition between high and low noise states observed in the lab and in particular of simulating very low noise states in a CFA in which the waveform modulations are greatly reduced in amplitude. Evidence will be presented to show that the computed noise level in the quiet state is bounded by the numerical discretization noise associated with density fluctuations caused by the use of a finite number of simulation macroparticles.

In the following sections we give a brief review of the experimental data that prompted these simulations, a description of the model of a CFA implemented in the MASK code, and a discussion of the simulation results, including a comparison with experimental observations.

2.0 Experimental Observations

The first demonstration of an abrupt transition between low and high noise operation in a crossed-field device was carried out by W.C. Brown of Raytheon in 1979-1980[3]. He observed that when the heater power in a microwave oven magnetron was removed, the noise power underwent an abrupt transition to values well in excess of -100 dB/MHz, a 5 to 6 order of magnitude reduction in noise from the normal operating value. The transition was accompanied by a small discontinuity in the voltage-current, or gauss line characteristic and by a small change in operating frequency. About 10 years later, during an intensive effort to develop low noise CFA's for the Aegis SPY-1 radar, certain low noise operating points, called 'sweet spots,' were observed at Raytheon, Litton, and Varian in the operation of experimental high power CFA's. These sweet spots corresponded to particular parameter settings and were ephemeral in nature. Still their existence proved that crossed-field amplifiers could operate as very low noise devices. In these experiments as well as those described below, the S/N ratios were computed using a 3-pulse cancellation method and only included noise in a narrow band very close to the carrier.

Varian/Beverly[4] has obtained S/N ratios in the range of 80-90 dB/MHz near the carrier for certain parameter ranges in an S-band tube using a low magnetic field, while maintaining high efficiency[5]. It has proven to be very difficult, however, to find a combination of design values that permits all other tube specifications to be met while maintaining low noise. S/N ratios are observed to depend on operating frequency, cathode current, magnetic field, tube age, and even on the material composition of the anode circuit. The achievements of this work are nonetheless very significant. No one thought as recently as 7 or 8 years ago that high power CFA's could operate at anywhere near these noise levels, nor operate with good (~ 50%) efficiency at low magnetic fields.

One of the most interesting results from the Varian work has been the observation of a transition from high noise to low noise operation as the cathode current was raised, as shown in Figure 2.

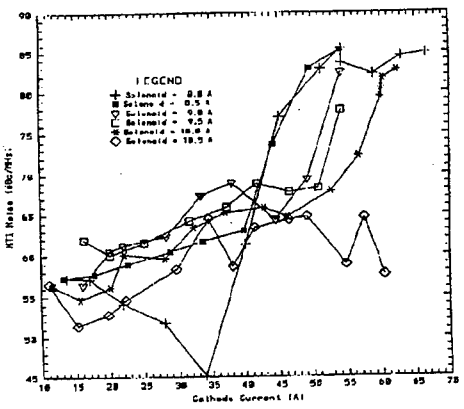


Figure 2: Measured S/N ratios vs. cathode current for the SFD-266 for different magnetic fields. [Courtesy Varian/Beverly]

Though not as sharp as that observed by Bill Brown in the cooker magnetron, the transition still produces jumps in excess of 40 dB/MHz for a small change in current, the exact value of the jump being dependent on the value of the magnetic field. The transition gets less and less pronounced as the magnetic field is increased, as seen in the Figure, and it is nearly washed out altogether at the highest magnetic fields used in the experiment. The clear challenge to computer simulation is to reproduce this behavior and to explain its source. This is what we have set out to do, using the MASK code.

3.0 Computer Model Description

SAIC's MASK code is a particle-in-cell simulation code designed to perform so-called 'full format' simulations of CFA's. This means that the code simultaneously treats the entire interaction and drift spaces, in contrast to moving window codes[6] which are based on the single wavelength/single frequency approximation. MASK is in this sense similar to the first full format crossed-field simulation code, written by George Dombrowski[7]. Full format codes are capable of simultaneously including waves of different wavelengths and frequencies and of tracking their interactions with particles, which themselves interact with each other. They also permit continuous simulation of electronic feedback through a drift space.

Figure 3 shows a schematic drawing of how a CFA is represented in the MASK code.

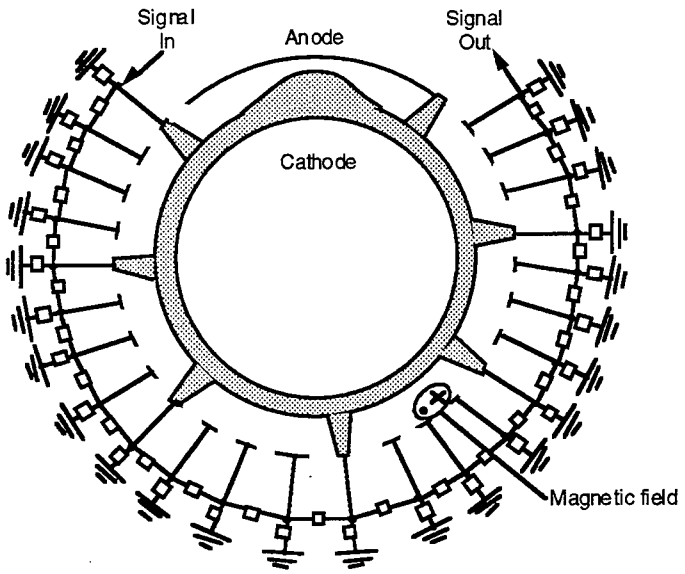


Figure 3: Schematic diagram of MASK CFA model

The anode is usually represented as a smooth surface composed of segments of metal alternating with segments of vacuum, though the vane tip geometry can also be represented if desired. The potentials applied to the metal segments, or vane tips, are controlled by their connections to a lumped element slow wave circuit that is designed to have the same properties (dispersion and energy storage) as the physical slow wave circuit. The potentials in the gaps between the metal segments are assigned values that are interpolated between the values on the adjacent metal segments. When particles move in the interaction space they induce currents in the slow wave circuit that are calculated[8] according to the prescription given originally by Ramo[9].

The cathode in MASK simulations can be defined to be a primary emitter, a secondary emitter, a field emitter, or any combination. Its DC potential can be assigned to be uniform along the cathode surface, or it can be made piecewise constant, or can be dynamically controlled by an external modulator (power supply) circuit model.

There are certain basic assumptions that MASK makes about the kind of CFA simulations of interest. First, the simulations are two-dimensional, by which is meant that no variations of any field are accounted for in the direction of the magnetic field. Second, the simulations are electrostatic, that is, all electric fields are assumed to be derivable from the solution of Poisson's equation for the potential; it follows that the rf magnetic field is neglected. This approximation is a good one when the phase velocity of the rf wave is small compared to the speed of light. Third, the application of the code to a specific CFA requires that the slow wave circuit can be adequately represented over the frequency band of interest by a pi-section, lumped element transmission line of the type first applied to crossed-field tube simulations by Dombrowski[10].

Within these constraints there exists a large number of CFA simulations of importance. In particular, the code has the flexibility to simulate forward or backward wave tubes with either anode or cathode circuits or both, distributed emission tubes with cathodes having different emission properties along different segments, tubes with cathodes having embedded electrodes maintained at a bias with respect to the rest of the cathode (e.g., quench electrodes), and tubes with tapered circuit properties (impedance, phase velocity, ...) and with tapered magnetic fields. The result is a code that is capable of realistic full format, multi-wave CFA simulations under a large variety of operating conditions.

Among the diagnostics produced by the MASK code are plots of various circuit quantities vs. time, snapshots of particle locations, and energy dissipation as a function of location. The code also computes a S/N ratio, defined as

$$S/N = 10 \cdot \log\left(1 + \frac{\langle I \rangle^2 + \langle Q \rangle^2}{\sigma_I^2 + \sigma_Q^2}\right) \qquad (1)$$

where I and Q are the in-phase and quadrature components of the output signal, using the input signal as a reference, σ_I and σ_Q are the standard deviations in the I and Q signals over a user-specified time window, and the angle brackets $\langle\rangle$ denote a time average over the specified time window. It is important that the simulation be run at least one group delay time, allowing time for the energy to travel from input to output; in the simulations reported here, that time is about 50 rf cycles and the time averaging window for I and Q is taken to be the final 50 rf cycles in a simulation of 150 rf cycles duration[11]. Note that no filtering is done to the I and Q channel signals, so that the S/N ratio represents a spectrally integrated value, and that no 3-pulse cancellation is performed. Typical values computed for the S/N ratio using the above formula for a high power S-band tube range between 15-20 dB over a circuit passband of 1200 MHz, corresponding to an average noise power density of about 45 to 50 dB/MHz, which is a typical operating range for these tubes.

4.0 Simulation Results

The transition from high to low noise states at low magnetic fields observed in the SFD-266 has been reproduced in simulations using the MASK code. Figure 4 shows the behavior of the S/N

ratio as computed using Eq.(1) versus the cathode current for an emitted current density of 1.5 A/cm^2 and a magnetic field of 1320 Gauss.

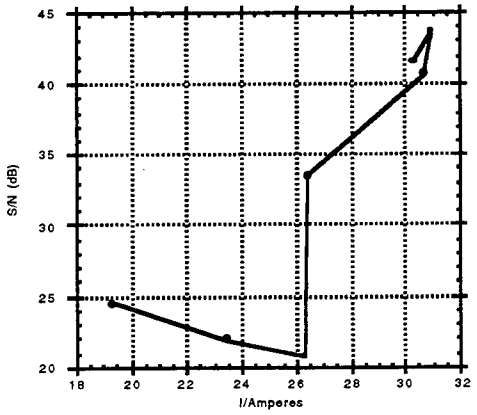


Figure 4: S/N ratio as a function of current for the SFD-266 for B=1320 G, as computed by MASK.

A sharp transition of nearly 15 dB is seen near a current of 26 A. As in the measurements shown in Figure 2, the simulated transition is very abrupt. Further increases in S/N are observed as the current is increased beyond the transition. Figures 5a and 5b show the computed rf output waveforms for cases just below and just above the transition. Note the remarkable reduction of modulation level in the quiet state.

Figures 6a and 6b show snapshots of the charge distributions in the same cases, at the end of the simulations. Though no dramatic differences are evident in the distributions, the spokes are seen to "lean" somewhat more below the transition (higher noise case) than above it. This leaning is due to a shear in the ExB velocity, which in turn is produced by the space charge density within the spoke. The result is a reduced matching of the ExB velocity of the spoke with the phase velocity of the rf wave. This observation is supported by the data on the average normal electric field at the cathode, as a function of location, which is plotted in Figure 7. The additional space charge present near the cathode depresses the electric field more in the noisy state than in the quiet state, which is nearly emission limited. There is, however, almost no difference between the computed values of cathode back-bombardment powers between the two states.

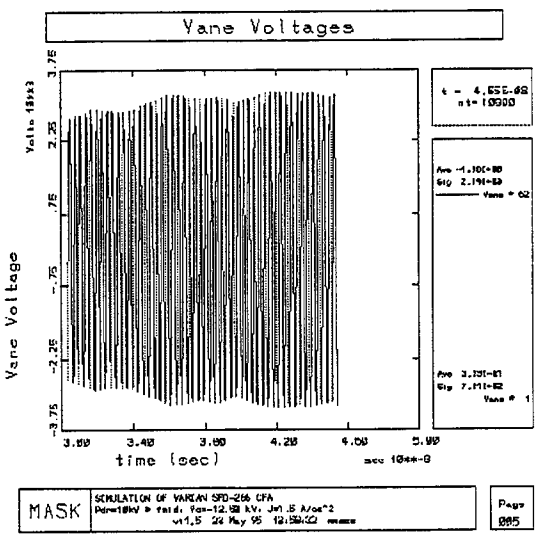


Figure 5a: RF output voltage vs. time for the SFD-266, as computed by MASK. V_C = -12.5 kV

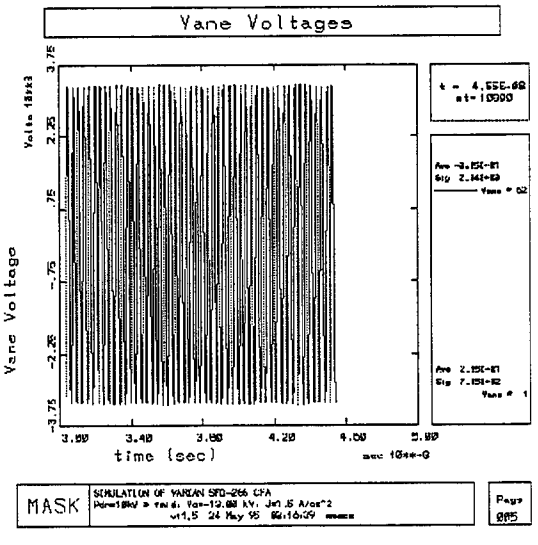


Figure 5b: RF output voltage vs. time for the SFD-266, as computed by MASK. V_C = -13.0 kV.

Figure 8 shows the computed voltage-current characteristic in the vicinity of the transition. The quiet state is seen to occur near the end of the gauss line, as the cathode is being 'starved[12].' In fact, about half of the current emitted from the cathode is reaching the anode at the transition point. This is in contrast to a typical

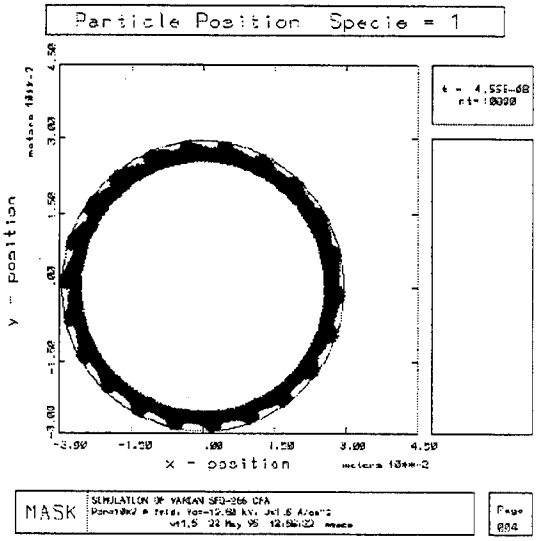


Figure 6a: Snapshot of the steady-state particle distribution for the SFD-266, just below the transition to low noise operation. V_C = -12.5 kV.

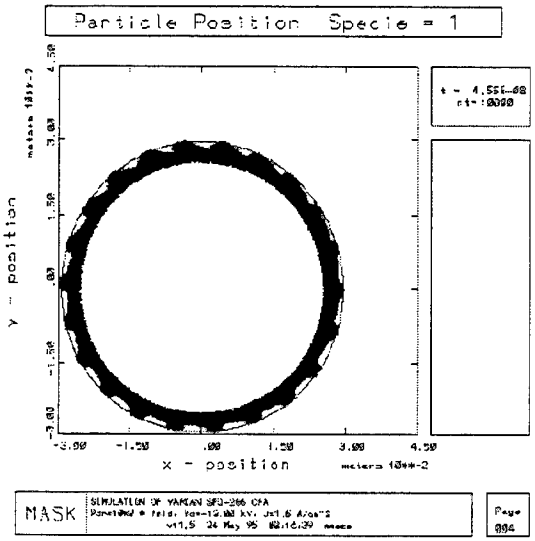


Figure 6b: Snapshot of the steady-state particle distribution for the SFD-266, just above the transition to low noise. V_C = -13.0 kV.

simulation, using a secondary cathode, of the Aegis production CFA in which only about a tenth of the current emitted by the cathode reaches the anode, the remaining 90% being returned to the cathode. In those simulations, which are noisy, the hub density is much larger, as a fraction of the Brillouin density, than that found in our low noise runs. Clearly, the evidence points to operation in the emission limited regime for low noise, as found by Bill Brown in the cooker magnetron. The explanation of the abrupt nature of the transition between high and low noise, however, remains a mystery, as in the magnetron.

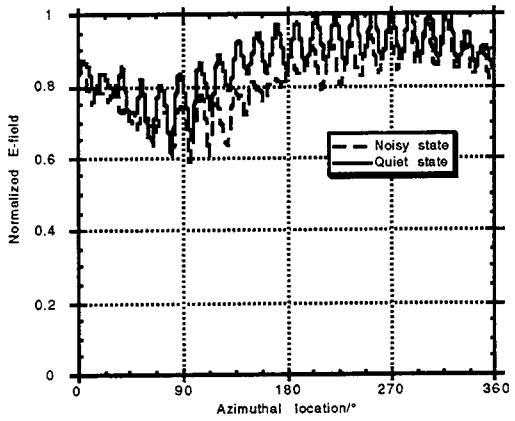


Figure 7: Normal electric field at the cathode surface, for the noisy and quiet states, as computed by MASK. The electric field is normalized to the value in the absence of space charge. The abscissa is an angle measured from the center of the drift space, positive toward the input. The circuit extends from about 25° to 335°.

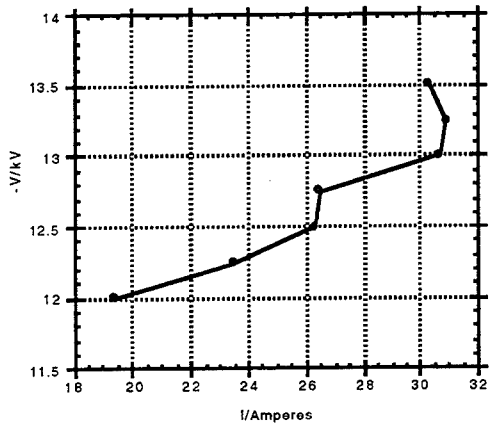


Figure 8: Voltage vs. current for the SFD-266, as computed by MASK. The transition from high to low noise operation occurs at a current of ~26 A.

The simulations shown in Figures 5b and 6b are among the most quiet ever produced by the MASK code; they are at least 20 dB quieter than any other simulations made for the Aegis production tube. The small amount of noise remaining is actually of a numerical nature, rather than being due to a physical process, that is, the value of the computed S/N ratio in the low noise states depends on the precise way in which the physical problem is discretized by the code.

Consider for example Figure 9, which shows a plot of the S/N ratio and the rf output power as functions of the number of simulation macroparticles used in the low noise simulation. Each macroparticle used in a simulation represents many physical electrons. In the simulations shown in Figures 5 and 6, this 'weight' is 3×10^6. If the weight is changed, the code adjusts the number of macroparticles it follows so that the total physical charge in the system is approximately unchanged. In principle, all results for physical quantities should be independent of the macroparticle weight, as long as it is small enough so that a sufficient number of macroparticles is followed to resolve the important physical processes adequately. In Figure 9 the S/N ratio increases roughly linearly with the number of macroparticles, with a best-fit slope of approximately 1/2, while the output power is essentially independent of particle number, as it should be. This result strongly suggests that the simulated noise in the low noise state is due to numerical density fluctuations, the amplitude of which tend to scale as the inverse square root of the number of macroparticles used in the simulation; if the noise were numerical (diode) shot noise, one would expect the slope of the line to be ≈ 1. Quite remarkably, the use of just over 500 particles (~ 30 per wavelength !) is sufficient to compute the output power with reasonable accuracy in this particular case.

In simulations of the noisy state, the computed S/N ratio typically rises slowly up to a point and then fluctuates about an average value as the number of simulation particles is changed, as shown in Figure 10, while the computed rf output power again remains insensitive to the macroparticle count. This result lends support to the view that the fluctuations seen in the noisy state are due to physical phenomena within the tube, and are not numerical artifacts.

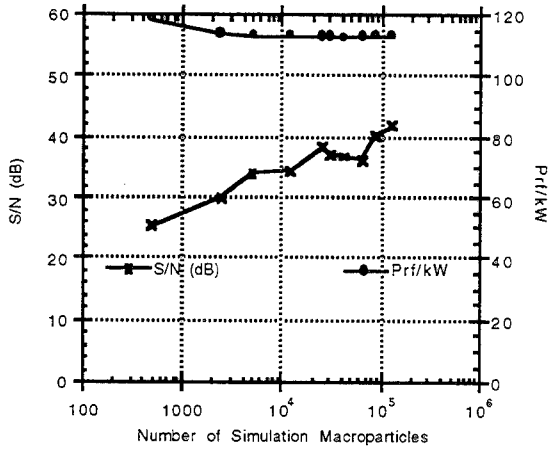


Figure 9: S/N ratio and rf output power as functions of simulation macroparticle count, in the quiet state.

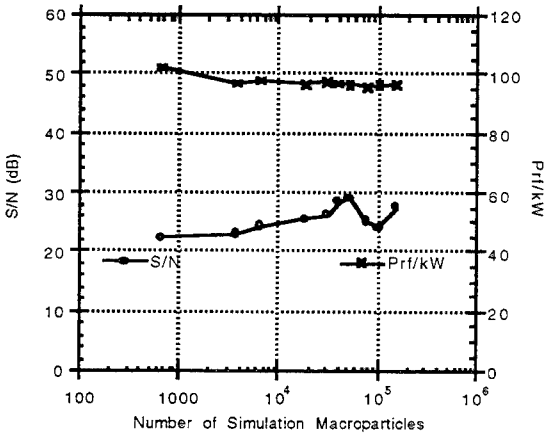


Figure 10: S/N ratio and rf output power as functions of simulation macroparticle count, in the noisy state.

The low noise states illustrated in Figures 5 and 6 used primary emission exclusively. We have so far been unsuccessful in producing similar low noise states with the code using a BeO cathode operated near the end of its V-I characteristic. All other parameter values in the BeO simulations (magnetic field, dimensions, etc.) were identical to those used in the runs using primary emission only. Typically, in the BeO case, the S/N ratio stays largely unchanged as the 'emission limit' is approached and the tube simply goes open circuit as the cathode voltage is raised. The ratio of cathode current to total emitted current approaches a value of about 0.24 at the emission limit, significantly below the value of 0.56 observed in the low noise state of Figures 5b and 6b. One interesting question is, how much secondary emission can be added to low noise simulations using primary emission before the low noise state is spoiled ? The answer to this question is presently under investigation.

5.0 Acknowledgments

I have benefited from countless discussions with G. Farney, YY Lau and S. Riyopoulos. This work was supported by the US Naval Research Laboratory, under contract N00014-92-C-2030.

References

[1]Some references are: *Crossed-Field Microwave Devices*, E. Okress, ed., v.1, chap 4, (1961); J. Arnaud, F. Diamond, and B. Epsztein, "Spurious phenomena in 'M'-type tubes," Proc. 4th International Congress on Microwave Tubes, Scheveningen, Sept. 1962, pp. 133-138; W.C. Brown, "The sophisticated properties of the microwave oven magnetron," 1989 IEEE MTT-S International Symposium, June 1989; O. Doehler and G. Doehler, "Parametric oscillations in high power injected beam crossed-field amplifiers and TWT's," IEEE Trans. on Electr. Dev., ED-26, No. 10, 1602-1608, (19879); K. J. Harker and F.W. Crawford, "Noise in planar crossed-field electron guns - I: theory", and " ...-II: numerical simulations", IEEE Trans Electr. Dev. ED-26, No 10, 1623-1633 and 1634-164 (1979); M.A. Pollack and J.R. Whinnery, "Noise transport in the crossed-field diode," IEEE Trans. Electr. Dev., 81-89 (1964); T Van Duzer and J.R. Whinnery, "Study of noise in crossed-field electron guns, " Proc. International Conference on Microwave Tubes, " Munich, June 1960, pp. 425-429. The present author has a copy of an extensive bibliography, originally compiled by A.S. Gilmour, Jr., which includes several hundred references on noise and other aspects of crossed-field devices. A limited number of requests for copies of the table of contents can be accommodated.

[2]The effects of roundoff errors may be tested by running the simulation on a computer using a different word size. Figure 1b was produced by a simulation run in single precision on a 32-bit word workstation; the result is quantitatively very similar when the simulation is run on a 64-bit word Cray Y-MP. In fact, one other source of randomness is present. Simulations commonly employ so-called random number generators to assign initial conditions to particles emitted from the cathode, in order to simulate a thermal distribution, for example. The code used to produce Figure 1 did use such a random number sequence to launch secondaries from the cathode. Tests have been conducted in which all secondary particles were launched with identical initial conditions. Again, the results are quantitatively very similar to the waveforms of Figure 1.

[3] W.C. Brown, "The sophisticated properties of the microwave oven magnetron," 1989 IEEE MTT-S International Symposium, June 1989. See also, "A Reporting of Personal Observations of Noise in Magnetrons and CFA's," Raytheon Company report PRP-5504, March 1988.

[4]Now Communications and Power Industries/Beverly

[5]Gary E. Thomas and James Deveau, "The SFD-266 CFA -- A Crossed-Field Amplifier with a 40 dB Improvement in Noise Performance," 1994 Microwave Power Tube Conference," Monterey, CA May 1994.

[6]S.P. Yu, G.P. Kooyers, and O. Buneman, "Time-Dependent Computer Analysis of Electron-Wave Interaction in Crossed Fields," J. Appl. Phys. **36** 2550 (1965).

[7]G. Dombrowski, "Simulations of magnetrons and crossed-field amplifiers," IEEE Trans. Electr. Dev. **35** 2060 (1988).

[8]The calculation of induced currents is the single most time consuming part of the simulation, in cases in which a direct solver, like an FFT/tri-diagonal solver, is used to solve Poisson's equation..

[9]See, for example, M. Chodorow and C. Susskind, *Fundamentals of Microwave Electronics*, McGraw-Hill, New York (1964), Appendix 2.

[10]G. Dombrowski, idem.

[11]Using 72 steps per rf period, these simulations consumed about 12 hours of cputime on an HP-9000/755 workstation while following 90 - 100,000 particles.

[12]Operation near the end of the gauss line in a CFA using secondary emission was shown to produce low noise by Bill Smith at Raytheon. These early results were intermittent and difficult to reproduce, however, which is understandable since the emission from a secondary cathode cannot be directly controlled and depends on changeable surface conditions.

Improved Formulas for Magnetron Characteristic Curves

Spilios Riyopoulos

Science Application International Corporation

McLean, VA 22102

Abstract

Improved analytic formulas for the magnetron characteristic curves (V vs. I and P vs. I for fixed B) are derived using the authors guiding center fluid model. It is shown that if the anode voltage V, the Hartree voltage V_H, and the rf voltage V_{rf} satisfy the inequality $|V - V_H| \leq V_{rf}$ then the anode current is directly proportional to the rf voltage. Under these (typical) conditions, explicit expressions for the V-I and P-I relations may be obtained. The new equation for V vs. I, which differs significantly from the classical relation of J. Hull, predicts that current is drawn to the anode for voltages both above and below the Hartree voltage, in direct contradiction with the traditional view of magnetron operation; this result is closely related to the fact that the gain in a crossed-field amplifier is an even function of the difference between the phase velocity of the wave and the drift velocity of the electrons, when space charge effects are small. A new expression is given for the Hartree voltage that includes the effect of the spce charge in the spoke. It is also shown that the best quantitative agreement between the new formula and experimental measurements of magnetron V-I curves is obtained when the hub density is taken to be about 1/2 of Brillouin density.

Magnetrons, the earliest developed sources of high power coherent radiation, have remained the least well understood. The complications in magnetron theory stem from the various time scales involved in the wave-particle interaction, the high space charge, and the fundamentally *two dimensional* nature of the instability: the growth rate is tied to the field gradients (both DC and AC) transverse to the wave propagation direction. Among other differences, magnetrons convert potential energy to radiation, opposed to the rest of the unbound electron devices (traveling wave tubes, cyclotron masers, free electron lasers) which convert kinetic energy. Furthermore, it has been recently demonstrated, that, in the low gain, low space charge regime, the gain curve is *symmetric* relative to frequency detuning from synchronism; most other devices exhibit *antisymmetric* gain vs. detuning.

The first theoretical efforts in parametrizing high power magnetron operation resulted

in the scaling laws[1], introduced by Slater (1943) and documented by Collins (1948). In effect they comprise a set of similarity transformations, aiming at extrapolating the operation parameters for a desired tube from an existing design. The next systematic effort on theoretical modeling was undertaken by J. F. Hull (1958). That model follows the $\mathbf{E} \times \mathbf{B}$ drift motion in the spokes[2,3] and is based on the following assumptions (i) a cathode layer (hub) in Brillouin equilibrium (ii) a hub top that is treated as a perfect conductor forming a "virtual cathode" for the RF cavity modes (iii) a spoke charge treated as a point charge q (iv) a synchronous condition imposed always at the same fixed location ("synchronous base point") in the A-K space.

The magnetron characteristic curves obtained in Refs. 2-3, relating the DC anode current I and the RF power P to the applied DC voltage V at given RF frequency, are of the form

$$I = A\, V\, (V - V_s)^2 \tag{1}$$

$$P = B\, V\, (V - V_s)^2 \left[1 + C\, V^{1/2} (V - V_s)\right] \tag{2}$$

The current I is positive for current reaching the anode. The constants A, B and C depend only on the anode circuit parameters, vane geometry and RF frequency, while V_s is the synchronous (Buneman-Hartree) voltage, inducing $\mathbf{E} \times \mathbf{B}$ velocity at the top of the hub that matches the RF phase velocity. One of the least satisfying features of Eqs. (1)-(2) is that both anode current and RF gain go to zero when the resonance condition $V = V_s$ is met. In addition, the operation voltage V is a double-valued function of the current I according to (1); there exist two, nearly symmetric operation voltages around V_s at the same current I, as shown in Fig. 1. Yet magnetrons, and the related crossed-field amplifiers (CFA's), are known to exhibit stable operation with single valued $V - I$ characteristics well below V_s, which cannot be accounted by (1)-(2). Current cut-off is also observed at voltages above the B-H voltage; Eq. (1) provides no current cut-off on the high voltage side.

New, improved formulas for the magnetron characteristic curves, free of the previous

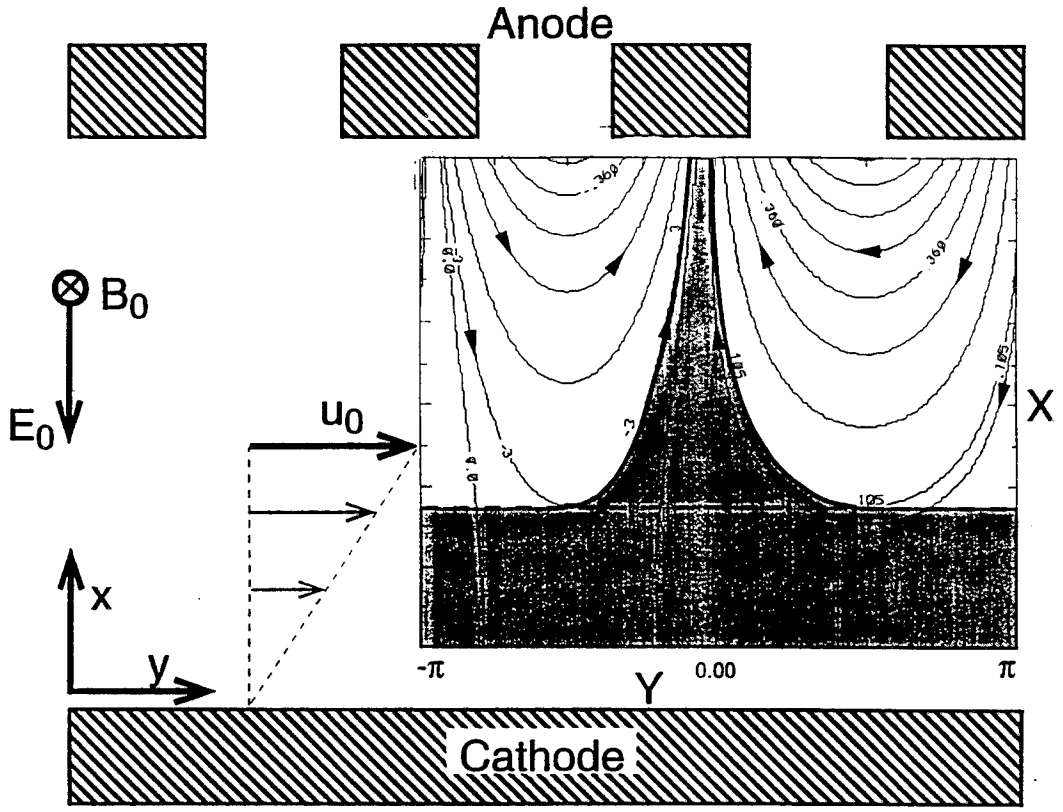


Figure. 1 Schematic illustration of the magnetron interaction space. X and Y are the GC coordinates in the frame moving with the wave phase velocity. The spoke profile shown corresponds to perfect synchronism and neglecting spoke charge fields.

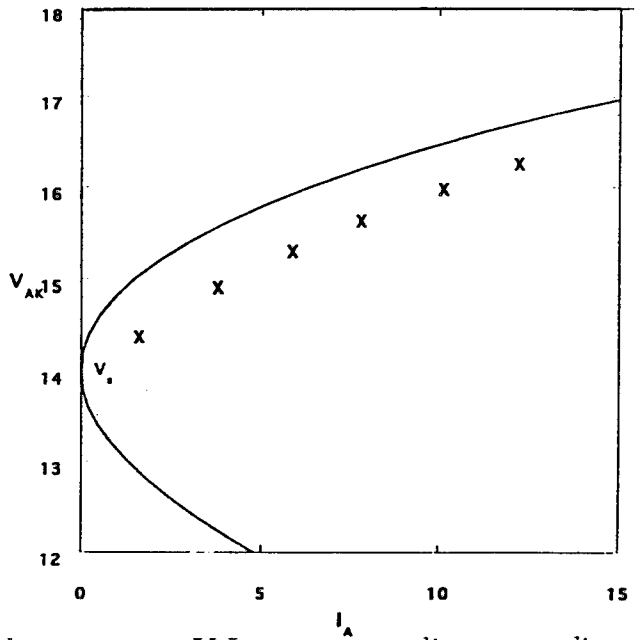


Figure 2 Typical magnetron V-I curve according to earlier results, given by Eq. (1), against experimental operation points (X' s), taken from Ref. 2, Fig 6.44 (Litton 4J52 at $Q_L = 166$).

shortcomings, are derived in the present work by applying a systematic guiding center approach, without making use of the assumptions (i)-(iv) employed in earlier work. Fluid equations following the GC orbits have already been developed and applied[4-5] in the study of CFA's; results[5] from the numerical implementation of the model are in good agreement with the characteristic curves for the SFD 262 tube. For steady-state magnetron operation the equations can actually be solved analytically, taking advantage of the uniformity and periodicity around the tube.

The GC fluid model treats the cathode electron layer (hub) as a "passive" source of the spoke charge. The hub density is prescribed and the hub height is obtained from the density and the A-K voltage subject to zero cathode field (space-charge limited emission). The spoke charge and current are obtained self-consistently from the hub density and the incompressible GC flow. Energy exchange with the cavity modes takes place through the GC motion in the spokes, while cyclotron rotation effects average out. Both DC and AC spoke charge effects are self-consistently included. The synchronous (B-H) voltage V_s is redefined by including the DC component of the spoke potential. The "loaded cavity" mode profiles, including the AC spoke potential, are approximately modeled through an amplitude boost factor Λ and a constant phase shift Ψ, preserving the similarity with the vacuum solutions. All the spoke charge related quantities are obtained by expanding the exact formal solutions in powers of ν/V_1 around the unperturbed (zero space charge) profiles, where $\nu = n_s/n_h$ is the ratio of the effective spoke density to hub density.

At steady-state the current through a spoke is constant and equal to the current drawn at the spoke base. The current is determined by the flow of the GC streamlines, and the spoke topology depends on the departure from synchronism. By exhausting all possible topologies it has been proven[6] that there exists a synchronous operation range around V_s, of width

$$\left|\frac{V}{V_s} - 1\right| \leq \frac{V_1}{V_s}\,\frac{sinh(kD)}{kD}. \tag{3}$$

where D is the A-K gap. In that range the spoke base-width remains constant and equal

to half-wavelength despite the changes in the details of the streamline topology. The spoke current assumes a maximum, saturated value that is simply proportional to the AC amplitude

$$I_s = \frac{V_1}{\mathcal{L}}, \qquad \frac{1}{\mathcal{L}} = 2\,b\,\frac{en_h}{m\Omega}\,\frac{sinh(kd)}{sinh(kD)}, \tag{4}$$

where n_h is the hub charge density and $\Omega = eB_0/m$ is the cyclotron frequency. The constant $\mathcal{L}$ is a "hybrid impedance", connecting DC current to AC amplitude. The extent of the saturation range increases with increasing AC amplitude V_1, as the tolerance to detuning increases with increasing RF bunching action. The power balance equation at steady-state is given by

$$\frac{1}{Q}\,\frac{V_1^2}{2\mathcal{Z}} = Mb\int_d^D dx\int_0^\lambda dy\;\mathbf{J}\cdot\mathbf{E}_1. \tag{5}$$

The left-hand-side is the loss rate for the energy stored in the cavity, Q being the loaded cavity Q, and the total cavity impedance is $\mathcal{Z} = \sqrt{L_c/C_c}/2N$ where $\sqrt{L_c/C_c}$ is the impedance for each of the N anode segments[7]. The power transfer in the right-hand side is the integral over the interaction space where $M = N/2$ is the number of spokes, J the spoke current density, λ is the operation wavelength and b is the axial height of the cavity. Expressing the current $\mathbf{J}$ in terms of the GC velocities in the frame moving at the phase velocity one obtains

$$\frac{1}{Q}\,\frac{V_1^2}{2\mathcal{Z}_i} = I\int_d^D dX\;E(X). \tag{6}$$

Because current conservation through the spoke, $I_x(X) = I_s$ has been factored outside the integral in the rhs of (6), and

$$I = MI_s \tag{7}$$

is the total anode current from M spokes. The efficiency is defined as η = (power into AC) / (supplied DC power). Using $P_{dc} = VI$ where I is the total anode current, and Eq. (6), it follows,

$$\eta = \frac{\int_d^{\hat{D}} dX\;E(X)}{V} \simeq 1 - \frac{\rho + d}{D}. \tag{8}$$

Expression (8) shows that the energy transferred from each electron to the AC field equals the change in the GC potential energy between the top of the hub $X = d$ and the GC location $X = \hat{D} \equiv D - \rho$ when the electron strikes the anode. Higher order efficiency corrections from the kinetic energy of the RF-induced $\mathbf{E} \times \mathbf{B}$ drift are given in Ref. 6.

Combination of the power balance at steady state

$$\frac{1}{Q}\,\frac{V_1^2}{2\mathcal{Z}} = \eta\, V\, I, \tag{9}$$

with the current equations (4) and (7), yields an $I - V$ characteristic of the form

$$I = \frac{V}{R}, \tag{10}$$

where the "radiation resistance" R is given by

$$R = \frac{(\mathcal{L}/M)^2}{2\eta Q \mathcal{Z}}. \tag{11}$$

Notice that R is proportional to the square of the impedance $\mathcal{L}/M$ from M spokes connected in parallel, divided by the interaction impedance $\mathcal{Z}$. Spoke charge effects enter the efficiency η, the B-H voltage and the effective AC field Λ. It turns out that the effective spoke density ν can be computed from the profile of an unperturbed (zero self-field), symmetric spoke in perfect synchronism. The spoke self-field parameters Λ, Ψ and ν are then obtained by expanding the perturbed by the space charge flow around the symmetric spoke profile in powers of ν/V_1. Λ and ν are tabulated as functions of the cyclotron-to-rf frequency Ω/ω and the normalized A-K gap kD in Ref. 6.

Expression (11) is a non-linear Ohm's law because R depends among other factors on the A-K voltage V. In the synchronous range the dependence of R on V is weak, coming from the dependence of the hub-height d on the A-K voltage

$$V = \frac{1}{2\epsilon_o}\, n_h d\, \left(D - \frac{d}{2}\right) + \frac{1}{4\epsilon_o}\, \nu\, n_h\, \bar{w}\, (D-d)^2 \tag{12}$$

and the dependence of η, Λ and ν on the hub height. The synchronous hub height d_s corresponds the phase velocity equal to the $\mathbf{E} \times \mathbf{B}$ velocity at the hub top. From $E(d) =$

$\omega_p^2 d$ where $\omega_p^2 = en_h/\epsilon_o m$ is the hub plasma frequency follows

$$d_s = v_p \frac{\Omega}{\omega_p^2}\left[1 - \frac{\omega}{\Omega\left(kr_c + \Omega\omega/\omega_p^2\right)}\right]. \tag{13}$$

where $\omega = 2\pi f$, f is the π-mode frequency in Hz, and the π-mode wavenumber $k = 2\pi/2a$ with a the vane period. Cylindrical effects are included only in the definition of the d_s through the cathode radius r_c, due to the sensitivity of the resonance condition to detunig. Expansion of (11) around V_H, by expanding $\mathcal{L}$ around the synchronous hub height d_s, results in the new "linearized" characteristics to replace (1)-(2)

$$I = \frac{V}{R_s}\left[1 + \beta\,\frac{V - V_H}{V_H}\right], \tag{14}$$

$$P = \eta_s\,\frac{V_H^2}{R_s}\left[1 + \alpha\,\frac{I - I_s}{I_s}\right], \tag{15}$$

$$P_s = \eta_s V_H I_s = \eta_s R_s I_s^2, \qquad I_s = \frac{V_H}{R_s}$$

where I is in Amperes, V in Volts P in Watts, α, β are dimensionless,

$$\beta = V_H\,\frac{d}{dV}\left(ln\frac{1}{R}\right)_s, \qquad \alpha = I_s\,\frac{d}{dI}\left(lnP\right)_s. \tag{16}$$

(the analytic formulas for (16) are given in Ref. 6) and R_s is given in Ohms

$$R_s = \left(\frac{1}{4\pi\epsilon_o v_p}\right)^2 \frac{2\,\pi^2\Omega^2\omega^2 sinh^2(kD)}{\mathcal{Z}\eta\; Q\;(kb)^2\omega_p^4 M^2\Lambda^2 sinh^2(kd_s)}, \tag{17}.$$

All subscripted quantities $(_s)$ are computed at the B-H voltage V_H, given by

$$V_H = U_o\left[2\,\frac{\Omega}{\omega}\,\left(kD - \frac{kd_s}{2}\right) + \frac{\nu}{2}\,\frac{\omega_p^2}{\omega^2}\,\bar{w}\left(kD - kd_s\right)^2\right], \tag{18}$$

where $v_p = \omega/k$ is the phase velocity and the synchronous kinetic energy U_o is given by $U_o = (m_e v_p^2/2)(6.241418 \times 10^{18}$ Volt/Joule) Neglecting cylindrical effects $kr_c \to \infty$ in d_s, and taking the Brillouin density limit $\omega_p^2 = \Omega^2$ one gets from (18)

$$V_H = U_o\left[\left(2\,\frac{B}{B_o} - 1\right) + \frac{\nu}{2}\,\frac{\Omega^2}{\omega^2}\,\bar{w}\left(kD - 1\right)^2\right], \tag{19}$$

where $B_o \equiv m_e c v_p/eD$ Gauss. The first bracketed term in the rhs is the familiar expression[3] for V_H, while the second carries the spoke charge contribution. The precise value of V_H is

higher than the B-H value based merely on the hub charge. The dynamic impedance is defined by the slope of the V-I curve (14),

$$\mathcal{R} = \frac{dV}{dI} = \frac{R_s}{1+\beta}. \tag{20}$$

The projected lower current cut-off voltage, given by

$$V_c = (1 - 1/\beta)V_H, \tag{21}$$

falls well below the B-H voltage. The above equations hold within the synchronous voltage range characterized by the maximum achievable spoke current at given AC voltage. When operating outside the limits (3) the departure from synchronism restricts the spoke width and limits the current that reaches the anode. The narrowing of the current channel must be taken into account to obtain exact location of the current cut-off votages V_c above and below V_H.

The theoretical results from (14)-(19) are compared with the V-I curves for two tubes, Litton 4J50 at Q=208, Fig. 3a, and Litton 4J52 at Q=282, Fig. 3b. The experimental points, taken respectively from Figs. 6.42 and 6.44 in Ref. 2, are marked by X's. The various solid curves correspond to different hub densities (normalized to the Brillouin density). The theory assumes constant hub density along each characteristic. Though a different density yields the best match for each tube, the optimum densities generally fall between $0.45n_B$ and $0.55n_B$. This is taken to imply that the hub density is not close to the Brillouin density, a frequently made assumption, but in fact quite smaller. The comparison between theory and the experimental P-I curves is given in Figs. 4a, and 4b for the same tubes as in Figs. 3. Again, the experimental points are taken respectively from Figs. 6.27 and 6.28 in Ref. 2. The hub density yielding the best V-I fit also yields the best P-I fit.

The fact that a particular density choice yields good agreement between theoretical predictions and experimental results for various characteristic curves strengthens the validity of the present approach. It is further encouraging that the optimum density choices for two tubes of different designs all fall close to half the (nominal) Brillouin density.

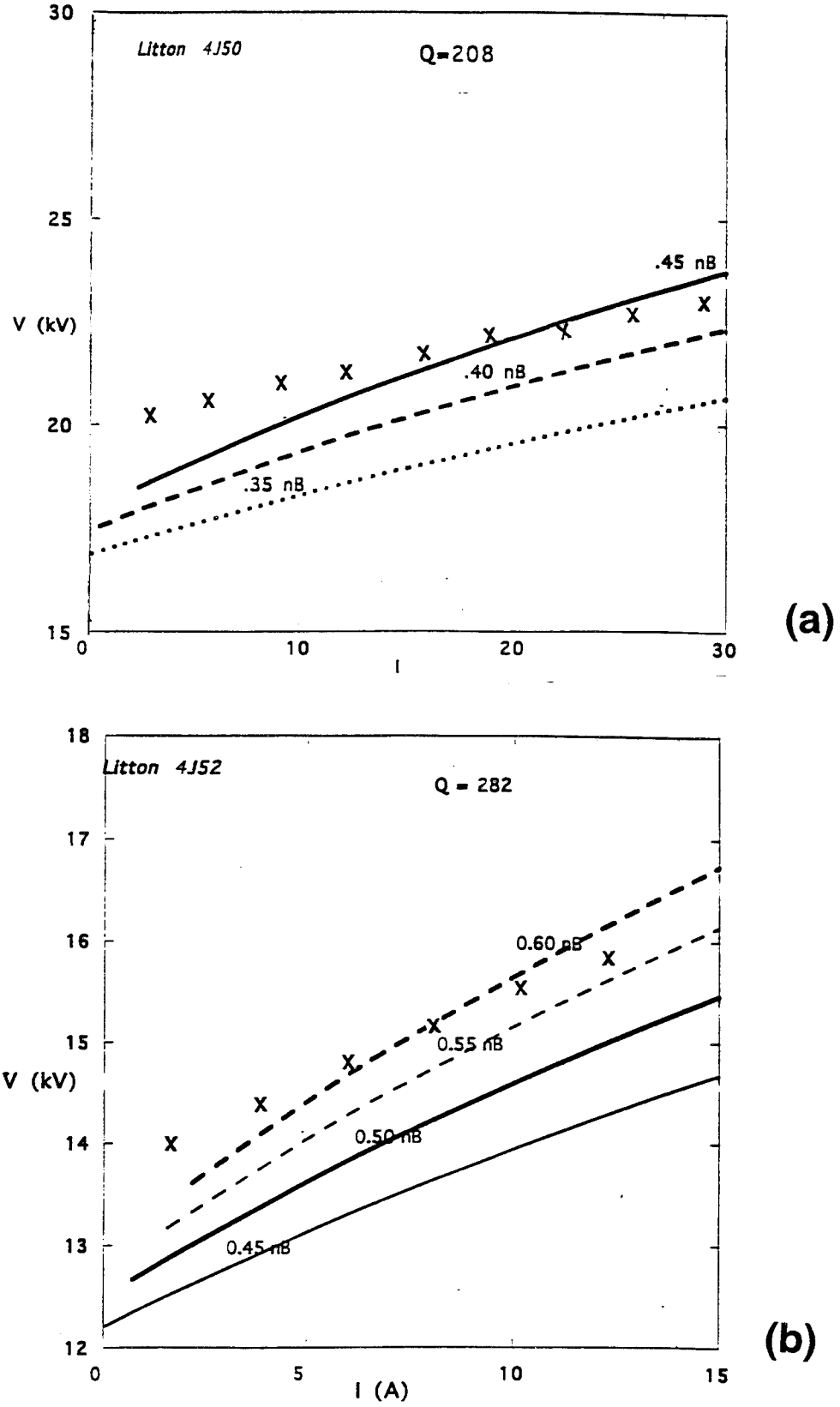


Figure 3 Theoretical V-I curves (solid) vs. experimental data (X's) for (a) Litton 4J50 at Q=208, and (b) Litton 4J52 at Q=282. Different curves in each plot correspont to different choices of the hub density ρ_h/ρ_B, as marked.

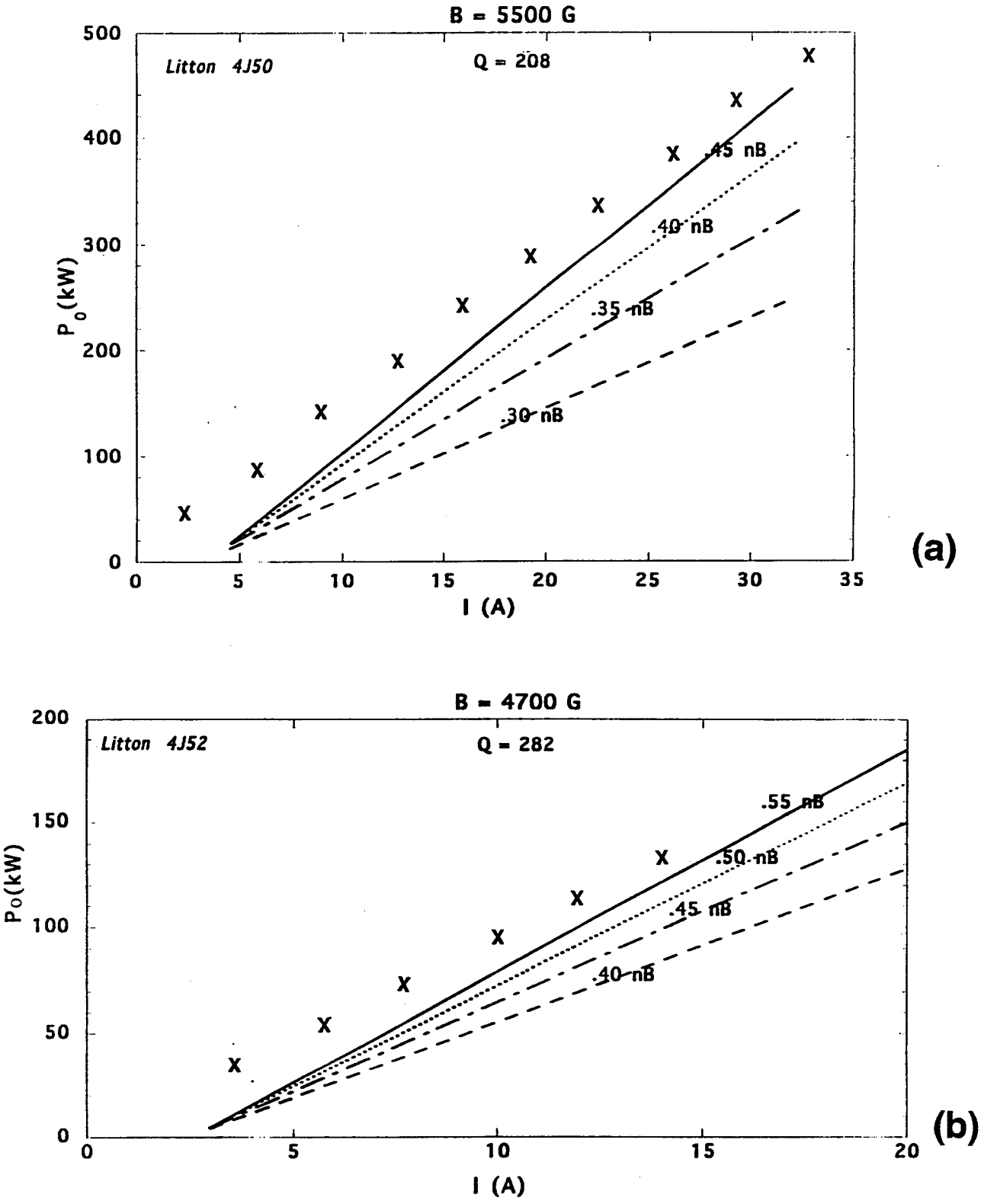


Figure 4 Theoretical P-I curves (solid) vs. experimental data (X's) for (a) Litton 4J50 at Q=208, and (b) Litton 4J52 at Q=282. Different curves in each plot correspont to different choices of the hub density ρ_h/ρ_B, as marked.

A similar average density is found in PIC simulations of high power CFA's, using the code MASK.

Abandoning the Brillouin equilibrium picture for the hub marks a break from the traditional approaches. At high power operation the spoke cannot be considered as a perturbation of a pre-existing Brillouin flow; rather, it is the RF action that determines, to a large extend, the hub density. While the approximation of a uniform density cathode layer is still admissible, the steady-state hub density should be determined by the balance between the current emission from the cathode (secondary or thermionic) and the spoke current drawn at the hub top. For simplicity, the hub is presently treated as a "black box" of prescribed density; the latter is validated by comparison with experiments.

A main result from the GC fluid model is that the operation range for magnetrons (as well as CFA's) is centered around the (B-H) voltage V_H; finite AC power and anode current are drawn at synchronism $V = V_H$. Although zero gain at synchronism applies to other microwave devices (TWT's, FEL's), it has been recently shown experimentally[8-9] and theoretically[10-11] that the low space charge, small signal operation exhibits symmetric gain vs. voltage detuning $V - V_H$, with maximum gain at resonance. The symmetry is broken at high power, high space charge operation, but the fact remains that magnetrons operate well below, as well as above, the Hartree voltage. The range of below-synchronism operation becomes more extended when the spoke charge effects are included in the definition of the Hartree voltage; that pushes V_H to higher values, moving synchronism further up from the low voltage current cut-off point.

Further comparisons with a larger variety of experimental data will determine whether the new equations can become a useful analytic tool, providing zeroth-order scaling laws for magnetron design. The applicability of previously introduced "scaling laws" for magnetron operation is limited between similar tube designs: in essence, one reproduces variations of an existing design. The present approach allows performance evaluation from "scratch", without any reference to existing tube performance.

Acknowledgements

The author wants to thank David Chernin for many useful and stimulating discussions. This work is supported by US NRL contract #N00014-92-C-2030.

REFERENCES

1. A. M. Clogston in "Microwave Magnetrons", edited by G. B. Collins (McGraw-Hill, New York, 1948), pp 401-459.

2. J. F. Hull, Doctoral Dissertation, Dept. of Electrical Engineering, Polytechnic Institute of Brooklyn, 1958.

3. J. F. Hull in "Cross Field Microwave Devices", edited by E. Okress (Academic Press, New York NY, 1961), pp. 496-527.

4. S. Riyopoulos, D. Chernin and A. Drobot, IEEE Trans. Electron Devices **39**, 1529 (1992).

5. S. Riyopoulos, Phys. Rev. **E47**, 2839(1993).

6. S. Riyopoulos, to appear in Physics of Plasmas (1996).

7. In earlier literature, such as Refs. 2-3, the circulating power is expressed using the peak-to-peak AC voltage $V_{pp} = 2V_1$ in the left-hand side of (6). Hence, the circuit impedance $\sqrt{L_c/C_c}$ reported in Refs. 2-3 is four times larger than the impedance defined via the AC amplitude V_1 in (6).

8. J. Browning, C. Chan, J. Z. Ye, and T. E. Ruden, IEEE Trans. Plasma Science **19**, 598 (1991).

9. R. McGregor, C. Chan, J. Z. Ye, and T. E. Ruden, IEEE Trans. Electron Devices **41**, 1456 (1994).

10. S. Riyopoulos, IEEE Transactions on Plasma Science **22**, 626 (1994).

11. S. Riyopoulos, IEEE Journal of Quantum Electronics **31**, 1579 (1995).

Rapid Current Transition in a Crossed-Field Diode †

J. P. Verboncoeur and C. K. Birdsall
Electronics Research Laboratory
University of California, Berkeley, CA 94720
johnv@eecs.berkeley.edu

Abstract

The transmitted current in a crossed-field gap has been characterized analytically by a number of authors. Using a one dimensional PIC simulation, we explore the behavior of the crossed-field diode at $B = B_{Hull}$. For mono-energetic (cold) emission, a rapid reduction of transmitted current is observed when the injected current exceeds the critical current by just 1%. Addition of a small electron temperature normal to the cathode eliminates the transition, even for $kT/V \sim 10^{-5}$ ($V = 10$ kV, gap $= 1$ cm, $B = 337$ G, $J = 1.69$ A/cm^2), while an isotropic velocity distribution accelerates the transition.

†Accepted for publication in *Physics of Plasmas*.

Crossed-field planar and cylindrical electron diodes were first studied analytically and experimentally by Hull over 70 years ago [1]. The noise properties near cutoff have been studied by Pollack [2] and Van Duzer and Whinnery [3]. The Hull cutoff is well known; a summary appears in [4], drawing upon the work of Pollack. See also [5] and the references therein.

Recently, Lau, Christenson, and Chernin revived the study of the smooth-anode crossed-field diode [6]. Their analytic limiting current curve for planar diodes complements some of the older works [2]-[4]. Their limiting current analysis was for cold current injection, with electron velocity $v \rightarrow 0$ at the cathode.

This work is concerned with the critical point in the planar crossed-field diode. The critical point occurs at the Hull cutoff, $B = B_{Hull}$, with the injected current at the limiting (critical) current, $J = J_c$. For an idealized cold cathode, the Hull cutoff can be written

$$B_{Hull} = \frac{m}{ed}\sqrt{2eV/m + u_0^2}, \tag{1}$$

where u_0 is the electron velocity at the cathode, V is the gap voltage and d is the gap width.

At the Hull cutoff, the limiting current is given by $J_c/J_{CL} = 9/4\pi$ [2, 6], where J_{CL} is the Child-Langmuir limiting current for an unmagnetized diode with gap d and applied voltage V :

$$J_{CL} = \frac{4\epsilon_0}{9\sqrt{m/2e}}\frac{(V - V_m)^{3/2}}{(d - x_m)^2}\left(1 + \frac{2.66kT_e}{e(V - V_m)} + ...\right), \tag{2}$$

where kT_e is the electron temperature at the cathode, V_m is the minimum in potential, and x_m is the distance of the minimum measured from the cathode [7].

The behavior of the smooth-electrode crossed-field diode at the critical point has been characterized using PDP1 (Plasma Device Planar 1-dimensional) [8], a one-dimensional electrostatic particle-in-cell (PIC) simulation. During verification of the limiting current described by Lau [6], we discovered that the transmitted current at the critical point was very sensitive to the electron velocity at the cathode. In particular, a strong dependence on electron temperature and isotropy, injection current, and magnetic field was observed.

In this study, the anode voltage is $V = 10$ kV, and the gap width is $d = 1$ cm. The voltage source is an ideal battery of zero impedance connecting the anode to the cathode. The code requires a non-zero initial velocity for the injected electrons in order to avoid a singularity in charge density at the cathode. The initial velocity is $u_0 = 4.2 \cdot 10^5$ m/s, or 1/2 eV, small compared to the anode voltage. The resulting Hull cutoff is $B_{Hull} = 337$ G.

Case A. For injected electron current $J \leq J_c$, the diode is stable and all electrons are transmitted across the gap. Selected results for the critical point are shown by the solid

curves in Fig. 1. The flow is laminar; each electron follows the same trajectory in phase space, and there are no measurable oscillations in the current, potential, or electron density. The transmitted current is equal to the injected current, up to J_c. At the critical point, the potential profile showed the spatial dependence $\Phi(x)/V = (x/d)^{1.47}$. In contrast, the potential profile of an unmagnetized current-limited diode ($J = J_{CL}$) is proportional to $x^{4/3}$.

Case B. Increasing the injected current to 1% above the critical value, the behavior changes dramatically, as shown by the dashed curves in Fig. 1. The temporal development of the current and potential follow that of the Case A until about 33 ns. Note, however, that the space charge in the gap exceeds that of Case A (Fig. 1e). At 33 ns, the current undergoes a rapid transition, dropping to 10% of the critical current. The transition occurs in about τ_{tran} =14 ns, and the transmitted current remains at $J_c/10$. Since $f_c\tau_{tran} = 13.2$, where f_c is the gyrofrequency, the transition is quite rapid. The flow is laminar prior to the transition, and becomes turbulent after (see Fig. 1d; later in time the hole in phase space collapses). The transmitted current and potential exhibit oscillations at the cyclotron frequency during the transition, which die out when the transition is complete. The noise level in the current increases significantly after the the transition (Fig. 1a). The potential profile in this case is proportional to $x^{1.78}$, so substantially more space charge is stored in the gap due to the recirculated electrons.

Case C. At injected currents $1.01J_c < J < J_{CL} = 4\pi J_c/9$, the behavior is similar to Case B. The duration of the transition and magnitude of the final transmitted current are relatively insensitive to the injected current. The onset of the transition occurs between 3.2-5.3 ns for $J \geq 1.1J_c$, compared to 33 ns at $J = 1.01J_c$. At currents above J_{CL}, the post-transition transmitted current declines slightly. The spatial and temporal evolution is similar to Case B shown in Fig. 1.

Case D. Next, the injected electrons were given a small anisotropic temperature, $kT_e =$ 1/10 eV, normal to the cathode, in addition to a $\frac{1}{2}$ eV drift. The perpendicular temperature was zero. Since $kT_e \ll V$, the change in B_{Hull} due to the electron temperature is negligible. This thermal distribution has no effect on Case A, but at $J = 1.01J_c$ (Case B) the transition is does not occur; the diode exhibits stable, laminar behavior. The diode remains in this state indefinitely. Furthermore, the diode is also stable when retaining the anisotropic temperature, but eliminating the $\frac{1}{2}$ volt drift term.

Case E. Finally, an isotropic electron temperature, $kT_e = 1/10$ eV, was applied to the injected electrons for Case B. The combination of the isotropic temperature and the $\frac{1}{2}$ eV drift results in onset of the current transition in about 5 ns. The diode starts to oscillate much like a virtual cathode at about 10 ns, with a temporally decaying amplitude. A hole forms in $x - v_x$ phase space at the onset of the instability, much like Fig. 1d. This hole

translates spatially, gradually collapsing by 100 ns. In the absence of the drift component of the injected electron velocity, the behavior is the same.

For $B < B_{Hull}$ the transition is not observed; instead, perturbing the current above the limiting value produces virtual cathode oscillations (see Birdsall [4]). The oscillations can be damped by a modest electron temperature at the cathode, although a higher temperature is required than for the effect reported here at $B = B_{Hull}$. For $B > B_{Hull}$, no current is transmitted, and no critical current is defined. Perturbing the magnetic field by +1% for Cases A and B results in a turbulent, cutoff flow described by Christenson [9]. The behavior is not affected by the modification of the emitted electron velocity distribution function.

Rapid reduction of transmitted current is observed for a smooth-electrode vacuum crossed-field diode at the Hull cutoff when the injected current exceeds the critical current. The electron velocity distribution at the cathode plays a crucial role in the evolution of the transmitted current. Modifying the injection velocity distribution with a small anisotropic thermal component normal to the cathode eliminates the transition, while a small isotropic thermal component causes more rapid onset of the transition. The post-transition transmitted current is about 10% of the maximum transmitted current at the critical point, nearly independent of the injected current. The fluctuation level in the post-transition current (Fig. 1a) is significantly higher than that in the laminar diode due to the turbulence in phase space (Fig. 1d).

1 Acknowledgments

We are grateful to Y. Y. Lau and P. J. Christenson for generating stimulating discussions and assisting in this work. This research is supported by the Air Force Office of Scientific Research under grant F49620-92-J0487 and by the Office of Naval Research under grant number FD-N00014-90-J-1198.

References

[1] A. W. Hull, *Phys. Rev.***18**, 31 (1921).

[2] M. A. Pollack, Ph.D. thesis, University of California, Berkeley, Series No. 60, Issue No. 485 (1962).

[3] T. Van Duzer and J. R. Whinnery, "Noise in Crossed-Field Electron Beams", in *Crossed-Field Microwave Devices,* edited by E. Okress, (Academic Press, New York 1961).

[4] C. K. Birdsall and W. B. Bridges, *Electron Dynamics of Diode Regions* (Academic Press, New York, 1966).

[5] J. W. Gewartowski and H. A. Watson, *Principles of Electron Tubes* (Van Nostrand, New York, 1965) 431-436.

[6] Y. Y. Lau, P. J. Christenson and D. Chernin, *Phys. Fl.* **5**, 4486 (1993).

[7] I. Langmuir, *Phys. Rev.* **21**, 419 (1923).

[8] PDP1 (Plasma Device Planar 1 dimensional), © 1990-1995 Regents of the University of California. Code and documentation available electronically via http://ptsg.eecs.berkeley.edu.

[9] P. J. Christenson and Y. Y. Lau, *Phys. Plasmas* **1**, 3725 (1994).

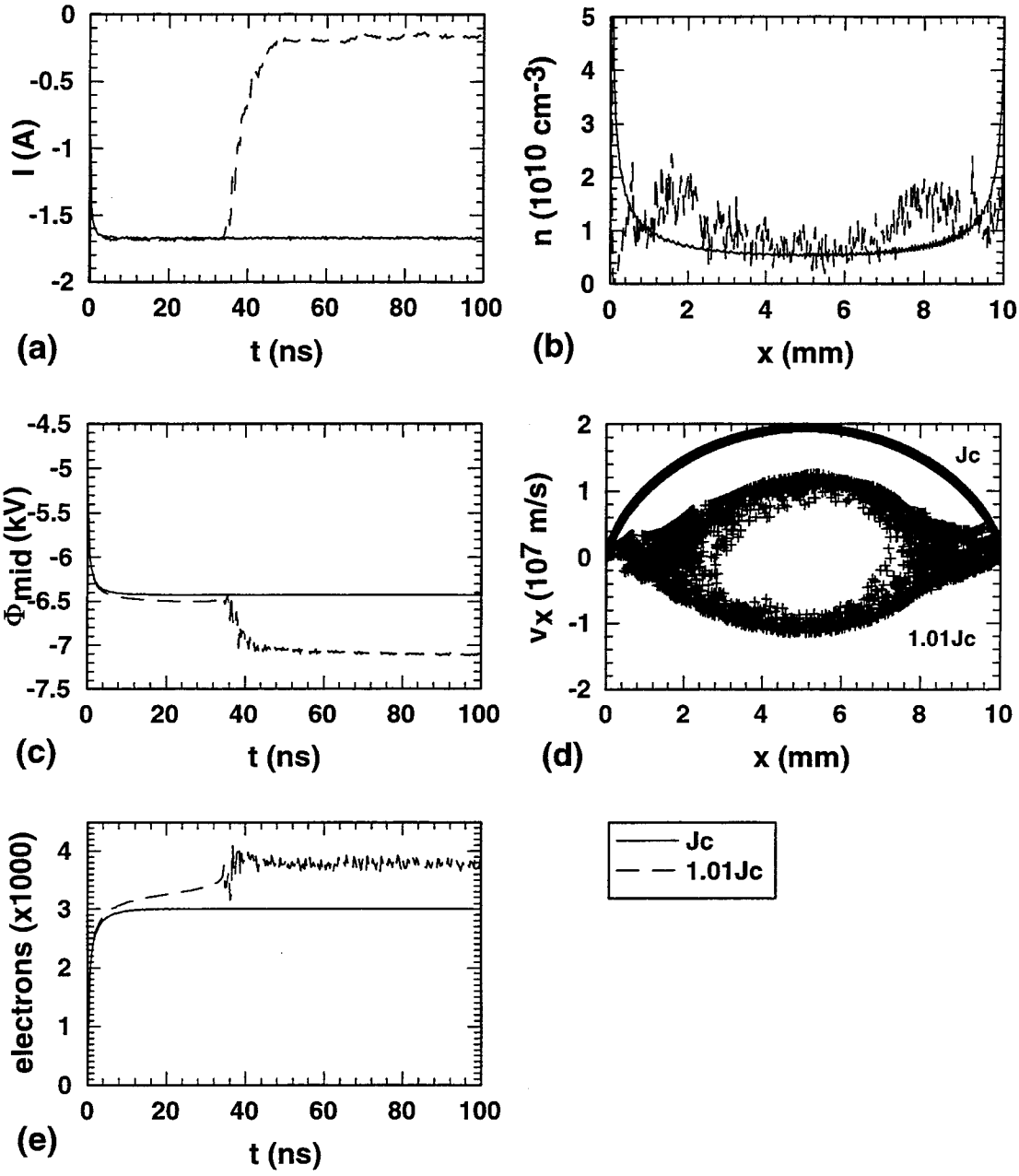


Figure 1: Crossed-field diode for Case A, the critical point (solid curves), and for Case B, at 1% above the critical point in injected current (dashed curves).

Analysis of Multipactor Discharge in an RF Circuit

R. Kishek, Y. Y. Lau, and R. M. Gilgenbach

Department of Nuclear Engineering and Radiological Sciences
University of Michigan
Ann Arbor, MI 48109-2104

Abstract: A simple model is constructed to analyze the temporal evolution of a multipactor discharge in an rf cavity. The multipactor current may, transiently, reach a level comparable to the wall current that is needed to sustain the rf field. It saturates at a much lower level in the steady state, primarily by its loading of the cavity; the image space charge force associated with the multipactor electrons plays a relatively minor role. At saturation, the electron impact energy equals the lowest value that gives unity in the secondary electron yield curve. A new phase focusing mechanism is also discovered, whereby the leading edge of the multipactor discharge grows at the expense of the trailing edge, in spite of the mutual repulsion among the electrons. This phase focusing mechanism may shape the steady state multipactor discharge in the form of a very tight bunch of electrons.

Multipactor is a well known phenomenon of rf breakdown in microwave cavities, windows, satellite rf payloads, and accelerator structures [1-5]. When an AC electric field exists across a gap, an electron from one surface is accelerated toward the other surface, the impact upon which may release more than one electron by secondary emission. It is easy to see that if the electron transit time across the gap equals to half of the rf period, a resonant discharge could result.

The persistence of multipactor discharge requires, at the minimum, stability in the phase of the electron orbit with respect to the rf cycle [1,4]. Vaughan [1] established this phase stability for a multipactor electron that is subject to an rf electric field of constant amplitude. The assumption of a constant-amplitude rf electric field omits the important processes of loading and detuning of the rf cavities as the multipactor current grows. The latter processes may lead to the saturation of the multipactor current. Moreover, as the space charge builds up, Vaughan's σ phase focusing [1] may be destroyed by the mutual electrostatic repulsion among the multipactor electrons. It is conjectured [1] that the multipactor current may saturate when the electrostatic repulsion is about to overcome the phase focusing that is obtained from the consideration of single particle orbit. In this paper, we use a simple model to address these issues, the analysis of which yields interesting information on the multipactor saturation level, the saturation mechanism, the time scale over which multipactor evolves, and possibly the drastic transient growth of multipactor current before the steady state solution is reached. We also find the surprising result that the electrostatic repulsions among the space charges are insufficient to saturate the multipactor. Rather, the repulsions are overcome by a new phase focusing mechanism that makes the leading multipactor electrons grow at the expense of the trailing ones.

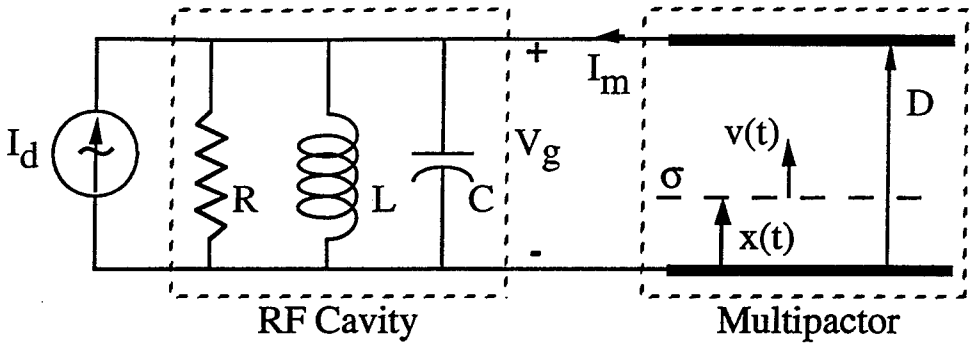


Fig. 1: Model of interaction between rf cavity and multipactor discharge.

For simplicity, we shall use a one dimensional model where the multipactor occurs inside a planar gap [Fig. 1]. The gap separation is D and the gap voltage is $V_g(t)$. We shall first consider a single electron sheet of surface density σ to model the multipactor electrons which move across this gap. Upon impact on a gap surface, a new electron sheet is generated by secondary emission. We assume that the voltage V_g that drives the multipactor is provided by an rf cavity. This cavity is modelled by an RLC circuit [Fig. 1], with a corresponding quality factor Q and characteristic frequency $\omega_o = 1/\sqrt{LC}$. As the multipactor electron sheet moves inside the gap, it induces a wall current, $I_m(t)$, which loads the RLC circuit. Thus, the present model allows for the progressive loading and detuning of the cavity as the multipactor current builds up [Fig. 1]. This loading in turn modifies the electron'σ energy and phase at impact.

Hereafter, we shall use dimensionless quantities with the following normalization scales: D for distance, ω_o for frequency, $1/\omega_o$ for time, $v = \omega_o D$ for velocity, $U = mv^2$ for energy, $V = U/e$ for voltage, $E = V/D$ for electric field, $S = \varepsilon_o E$ for surface charge density, V/Z for current. Here, m is the electron mass, $e = 1.602 \times 10^{-19}$ Coulomb, ε_o is the free space permittivity, and $Z = \sqrt{L/C}$ is the intrinsic impedance of the RLC circuit. The RLC circuit is driven by the normalized ideal current source I_d, and by the multipactor current I_m. Its normalized gap voltage V_g evolves according to the circuit equation [Fig. 1]:

$$\left(\frac{d^2}{dt^2}+\frac{1}{Q}\frac{d}{dt}+1\right)V_g(t)=\frac{d}{dt}[I_{do}\sin(\omega t+\phi)+I_m(t)], \qquad (1)$$

where I_{do} is the amplitude of the driver current of normalized frequency ω, and ϕ is the phase at time $t = 0$. We set $\omega = 1$ in this paper (i.e., resonantly driven).

The normalized multipactor current I_m is given by

$$I_m(t)=-\sigma(t)\frac{dx(t)}{dt}, \qquad (2)$$

where σ is always positive, by convention. Equation (2) accounts for the induced current as a result of the motion of the electron sheet within the gap, $0 < x < 1$. It is this term that is solely responsible for the non-linear beam loading and frequency detuning of the cavity by the multipactor, as readily seen from Eq. (1) and Fig. 1.

During its transit across the gap, the electron sheet is accelerated according to the normalized force law,

$$\frac{d^2x}{dt^2} = V_g + \sigma \bullet (x - \frac{1}{2}), \tag{3}$$

where the first term on the right hand side represents the force due to the gap voltage and the second term the force due to the image charge (of the multipacting electron sheet) on the plates [6].

On impact with a plate at time t_i, the incident electron sheet is removed and a new sheet of surface charge is released by secondary emission. The post-impact surface charge density $\sigma(t_i^+)$ is related to the pre-impact charge density $\sigma(t_i^-)$ by

$$\sigma(t_i^+) = \delta \bullet \sigma(t_i^-), \tag{4}$$

where δ is the coefficient of secondary emission which depends on the electron impact energy, E_i. Here, $E_i = (dx/dt)^2/2$, evaluated at $t = t_i^-$. For simplicity, we adopt Vaughan's empirical formula [7] for δ:

$$\delta = \delta(E_i) \cong \delta_{max}(we^{1-w})^k, \tag{5}$$

In Eq. (5), δ_{max} is the maximum value of δ, $\omega = E_i/E_{max}$, E_{max} being the impact energy which yields δ_{max}, and $k = 0.62$ for $\omega < 1$ and $k = 0.25$ for $\omega > 1$. Equation (5) is ploted in Fig. 2, which shows that $\delta = 1$ at two values of impact energies, E_1 and E_2. The lower energy E_1 is designated as the "first cross-over point". For simplicity, in writing Eq. (5), we have ignored the (small) threshold impact energy that is required for $\delta > 0$.

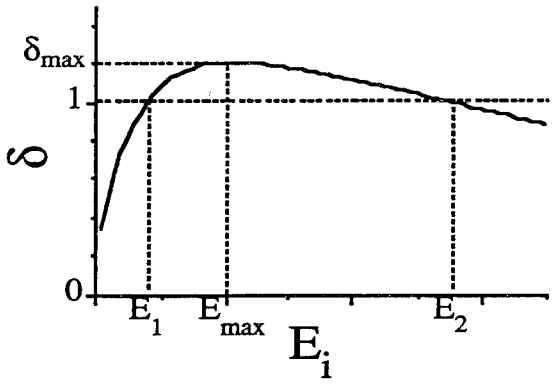


Fig. 2: Secondary electron yield, δ, as a function of impact energy E_i.

To reduce the number of parameters, we assume that the driver current I_d has been turned on for all time so that the cavity is already filled with rf for $t < 0$. The multipactor current is "turned on" at $t = 0$, in the form of an electron sheet with initial surface charge density σ_o that is

released from the plate x = 0, with zero velocity [8]. We assign a sufficiently low value of σ_o to observe the buildup of the multipactor current. The initial phase f [Eq. (1)] at which σ_o is launched is chosen so that this initial electron sheet strikes the other plate in about half an rf cycle. In most cases we run, the precise values of these initial data are not critical. Our simulations thus far have been restricted to two-surface, first-order multipactor [1], i.e, an electron released from one surface always strikes the other surface without momentarily stopping within the gap. The major free parameters are: Q and I_{do}, after having fixed $\delta_{max} = 1.2$, $E_{max} = 0.36$, and $\omega = 1$. [In dimensional units, if the rf cavity has a natural frequency of 1 GHz, and a gap separation of 0.22 cm, over which multipactor occurs, these parameters correspond to an ideal rf driver current exactly at 1 GHz, the first cross-over point $E_1 = 166$ eV, and δ reaches a maximium value of 1.2 when the impact energy is $E_{max} = 400$ eV.]

Shown in Fig. 3a is the multipactor current, monitored at impact, in units of the driver current amplitude I_{do}, for Q = 1, 10, 100, 1000. The very low value of Q, e.g., Q = 1, is included in our study to show the trend of multipactor in a non-resonant structure -- one that is relatively immune to beam loading, such as a window. In all of these runs, we fix the peak rf gap voltage at a value of 0.3 prior to t = 0. The fraction of rf power consumed by the multipactor, $<-V_g I_m>/<V_g I_d>$, is shown in Fig. 3b. Here < > denotes the average over the transit time of an electron. Note that in a high Q cavity, transiently, the multipactor current may reach a level higher than the drive current I_d [Fig. 3a], and at the same time draw much of the power provided by the external source [Fig. 3b]. Alternatively, the rf energy stored in a high Q cavity is capable of driving the multipactor current to a large amplitude when the condition becomes favorable. In this regard, it is interesting to recall the well-known fact [1,2] that multipactor can deposit considerable energy into a tiny spot, and, as a result, causes significant damage to the surface.

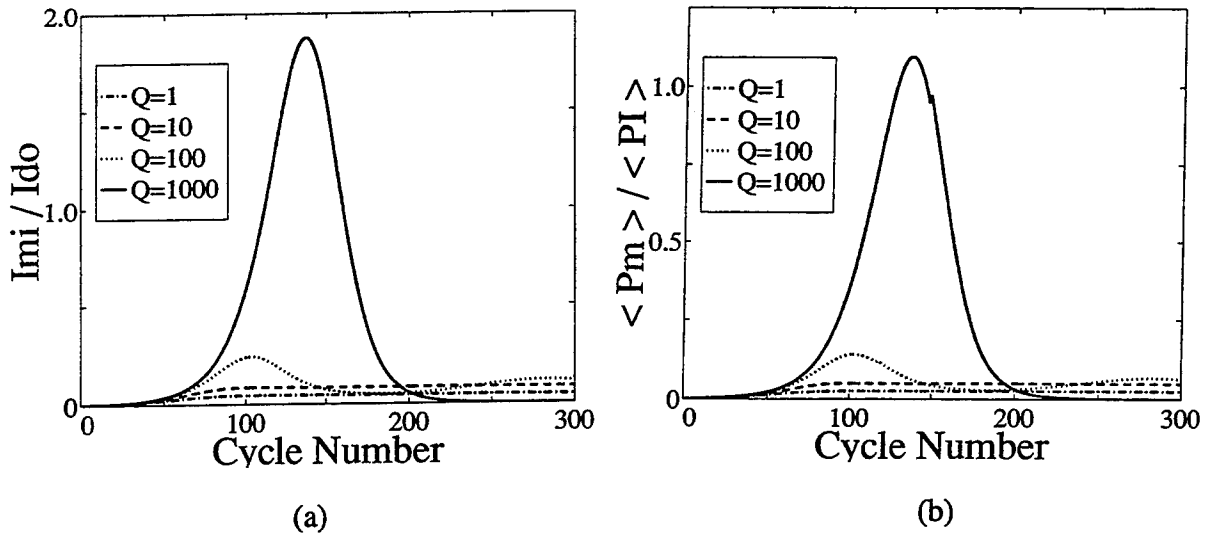


Fig. 3: (a) Transient evolution of multipactor current at impact, in units of the drive current amplitude I_{do}, for various values of quality factor, Q.
(b) Time history of the power consumed by multipactor, in units of the input power, at various values of Q.

The fact that the curves for the multipactor current [Fig. 3a] follow the corresponding ones for power dissipation [Fig. 3b] suggests that a multipactor discharge behaves a lot more resistively than reactively, even during its nonlinear, transient interaction with the rf circuit.

Note, however, that the equivalent resistance is a function of time, since the multipactor current may change over a wide range, as shown in the Q = 1000 case in Fig. 3a, while the gap voltage remains relatively constant during the buildup of the multipactor current [Fig. 4a]. For each curve displayed in Fig. 3, a steady state is indeed reached after a sufficiently long time (longer than that shown in Fig. 3 for the Q =100 and Q = 1000 cases). In these runs, regardless of the values of Q, the steady state multipactor current ranges between 5 to 20 per cent of the driver current. Thus, if 20 watts of rf power would be required to maintain a steady gap voltage on the order of 300 volts, the steady state multipactor would consume about 1-4 watts. However, for a high Q cavity, all 20 watts of the external power may transiently go to the multipactor. If the the spatial extent of the multipactor region is very small, the power density delivered to the gap surface by the multipactor electrons could be very high. [See Ref. 10 below.]

Throughout the transient development of the multipactor, the peak rf gap voltage in each cycle changes relatively little, for either the Q = 1 case or the Q = 1000 case [Fig. 4a]. The secondary emission coefficient δ also stays around unity [Fig. 4b], in fact, in the vicinity of the first cross-over point (E_1) in Fig. 2. A simple physical argument shows that only the first cross-over point E_1 in Fig. 2 gives the stable steady state solution [9]. Our numerical results show that the impact energy indeed approaches E_1 asymptotically in time. We have spot-checked that the steady state values of the gap voltage, of the electron impact phase in the rf cycle, and of the surface charge density, are all in good agreement with those obtained from our analytic formulation [11].

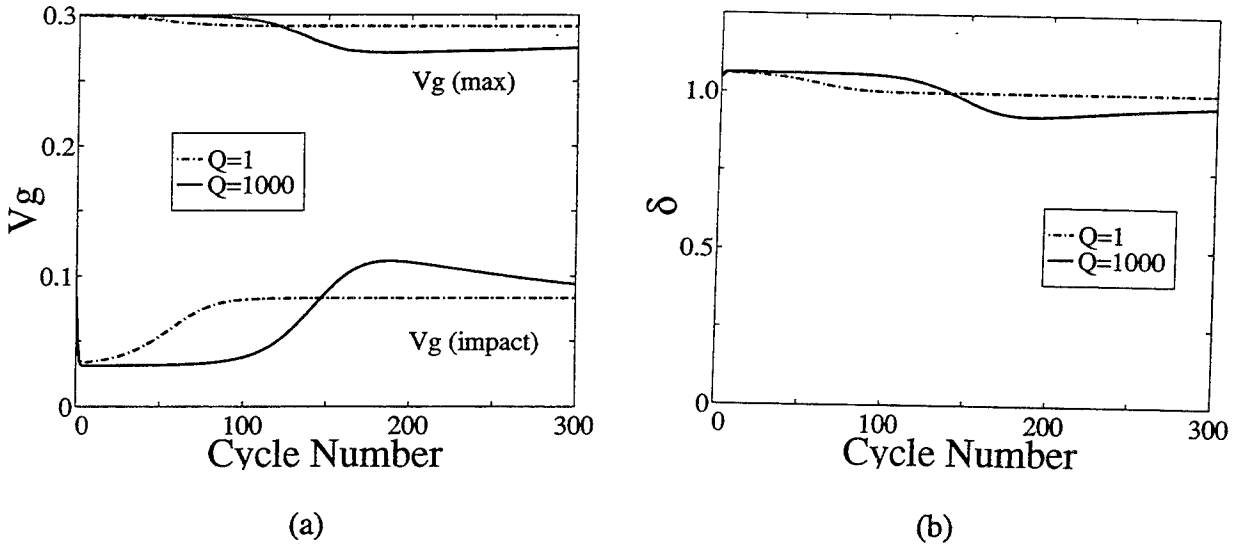


Fig. 4: (a) Evolution of the peak gap voltage, V_g(max), and of the gap voltage at the instant of electron impact, V_g(impact), for Q = 1 and Q = 1000.

(b) Evolution of the secondary electron yield, δ.

In the present formulation, multipactor affects its own evolution in two ways: through its "beam loading" of the cavity [described by I_m in Eq. (1)] and through the image space charge force [described by the last term in Eq. (3)]. It turns out that as long as $Q \gtrsim 10$, the beam loading effect is far more important than the space charge force in determining the saturation level of the multipactor current [10]. The disparity of their relative importance becomes increasingly more pronounced as Q increases, as high Q cavities can be more readily loaded by a multipactor current. This also explains the sensitivity in the high Q cavities, as exhibited in Fig.

3. This figure gives the tantalizing clue that, in reality, the rf energy stored in high Q cavities may relax via a multipactor discharge, albeit transiently in time, and locally in space [10].

The single sheet model [Fig. 1] given above may readily be extended to two electron sheets so as to investigate the effect of mutual interaction among the multipactor electrons [12]. We now consider two electron sheets, of surface density σ_1 and σ_2, located respectively at x_1 and x_2 inside the planar gap [Fig. 1]. Equation (1) remains unchanged. Equation (2) is modified to read $I_m(t) = -\sigma_1 dx_1/dt - \sigma_2 dx_2/dt$. The force law for sheet 1 is modified from Eq. (3) to read $\ddot{x}_1 = V_g(t) + \sigma_1 \bullet (x_1 - 1/2) + \sigma_2 \bullet [h(x_1 - x_2) - (1 - x_2)]$, where the last term, proportional to σ_2, represents the force on sheet 1 due to the presence of sheet 2. It is this term that accounts for the mutual repulsion between the multipactor electrons. In the last equation, $h(\sigma)$ is the unit step function: $h(\sigma) = 0$, $\sigma < 0$; $h(\sigma) = 1$, $\sigma > 0$; $h(\sigma) = 1/2$, $\sigma = 0$. The force law for electron sheet 2 is obtained from that for sheet 1 by interchanging indices 1 and 2. Equations (4), (5) remain unchanged when applied to each sheet.

Figures 5a and 6a exhibit the case where both sheets are launched with the same initial charge density, $\sigma_{o1} = \sigma_{o2}$, with sheet 1 launched slighltly ahead of sheet 2 at time t = 0 (sheet 1 is leading). Figure 5a shows that although both sheets start out with almost the same impact energy and the same secondary electron yield, sheet 2 always has a lower yield (the trailing sheet always has a lower impact energy, hence a lower yield when operating close to E_1). As the charge densities increase, beam loading sets in to reduce the secondary yields of both sheets to near unity (drop in gap voltage leads to lower impact energies). After some time, the repulsion by sheet 1 forces sheet 2 further and further away from the fixed phase, and the secondary yield for sheet 2 decreases below unity [Fig. 5a]. Figure 6a shows that σ_1 increases rapidly, while σ_2 increases at a slower rate, then drops. Eventually, the charge density σ_2 on sheet 2 becomes so low it can be ignored, and the model reduces to the single sheet model of Fig. 1. By the same token, a model consisting of N electron sheets (N large) will have its leading sheets growing faster than the trailing sheets, eventually quenching them one-by-one, until only two sheets, then one, is left [12]. Thus, steady state multipactor, if it exists, may be adequately described by a single sheet model.

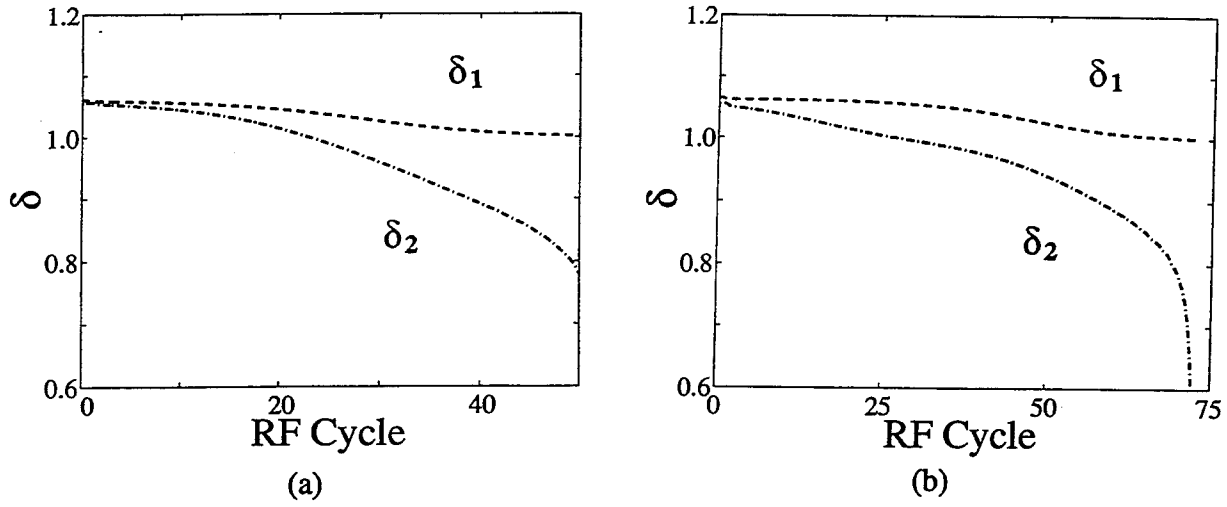


Fig 5: Secondary electron yield (δ_1, δ_2) for sheets 1 and 2 as a function of time: (a) $\sigma_{o2} = \sigma_{o1}$, (b) $\sigma_{o2} = 50\ \sigma_{o1}$.

The above cannibalism mechanism is still operative even if the trailing sheet is initially much stronger than the leading sheet. In Figs. 5b and 6b, the trailing sheet 2 is launched with 50 times the initial charge density of the leading sheet 1. Although the charge density on sheet 2 grows to a relatively high level for some time, sheet 1 dominates in the end. This arises as the yield for sheet 2 is forced to be below unity [Fig. 5b], and σ_2 rapidly diminishes [Fig. 6b]. Hence the above process of cannibalism holds, regardless of initial conditions [13]. These features are also observed for δ_{max} [Fig. 2] as high as 5. Note however that the initial conditions and space charge forces do affect the timing of the multipactor. A slab of a finite width may reach the steady state more rapidly than a single, infinitessimally thin sheet.

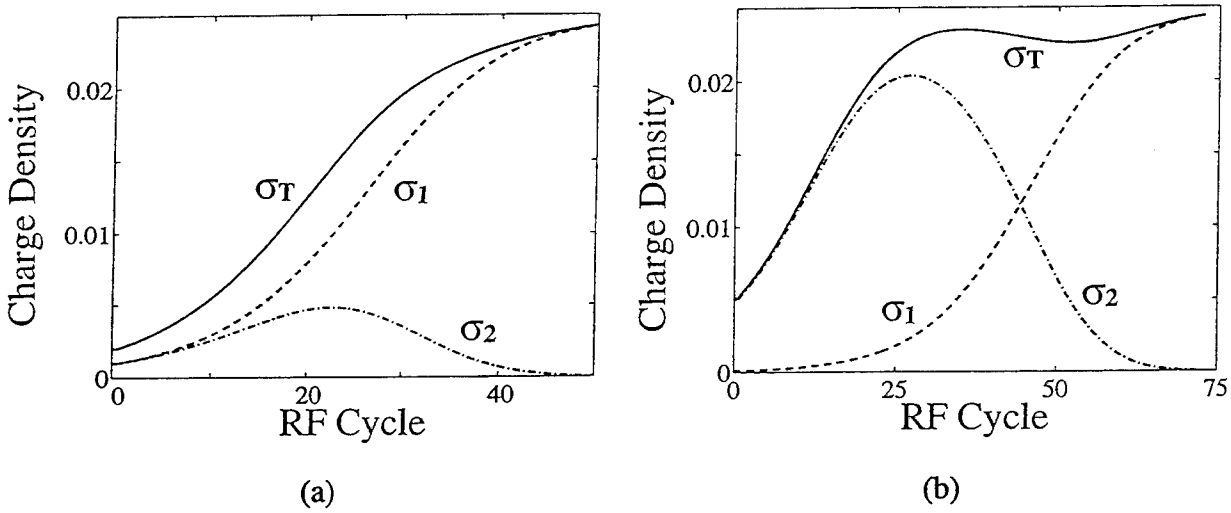


Fig 6: Charge density (σ_1, σ_2) on sheets 1 and 2 and the total charge density $\sigma_T = \sigma_1 + \sigma_2$: (a) $\sigma_{o2} = \sigma_{o1}$, (b) $\sigma_{o2} = 50\ \sigma_{o1}$.

While the above rudimentary analysis provides some quantifications on the temporal evolution of multipactor, we have not really addressed other theoretical issues involving the accessibility of the steady state multipactor solutions and the possible conversions from the first order to higher order multipactors. It must also be remembered that multipactor is known to depend a great deal on the geometry, on the processing and conditioning of the rf structure, on the cleaniness and condition of the surface, on the duration and power level of the rf pulse, and on the external magnetic field, etc. Nevertheless, our simple model does yield the following conclusions: (a) Steady state multipactor discharge occurs when the rf voltage is of the order of the first cross-over energy (E_1, in Fig. 2), confirming the prevailing notion that multipactor is a low to medium voltage phenomenon. (b) There are two phase focusing mechanisms in multipactor - one described in by Vaughan [1] and Riyopoulos et al. [4] and the other one described above. These phase focusing mechanisms may shape the steady state multipactor in the form of a very tight bunch [14]. (c) Multipactor saturates in an rf cavity as a result of loading; the space charge force of the multipacting electrons is insignificant to alter the phase condition or the saturation condition whenever $Q \gtrsim 10$. (δ) The rf energy stored in a high-Q cavity may lead to a large build-up of multipactor current in a transient manner. (e) The peak gap voltage need not be appreciably reduced during the buildup of the multipactor current.

We have benefited from many useful conversations with David Chernin, Spilios Riyopoulos, Perry Wilson, Jake Haimson, and Richard Briggs. This work was supported by NRL/ONR.

References

1. J. R. M. Vaughan, IEEE Trans. **ED-35,** 1172 (1988).
2. A. S. Gilmore, *Microwave Tubes*, (Artech House, Norwood, MA), p. 474 (1986).
3. G. A. Loew and J. W. Wang, SLAC Pub. No. 4647 (1988); A. D. Woode and J. Petit, Microwave Journal, (January, 1992), p. 142.
4. S. Riyopoulos, D. Chernin, and D. Dialetis, Phys. Plasmas **2**, 3194 (1995).
5. R. Kishek and Y. Y. Lau, Phys. Rev. Lett. **75**, 1218 (1995).
6. The force law, Eq. (3), may easily be modified to include a transverse magnetic field. We have extensively studied such cases; the findings will be published elsewhere.
7. J. R. M. Vaughan, IEEE Trans. **ED-36**, 1963 (1989); A. Shih and C. Hor, IEEE Trans. **ED-40**, 824 (1993).
8. It is shown by Riyopoulos et al [Ref. 4] that the inclusion of the initial velocity of the secondary electrons does not qualitatively change their steady state solutions.
9. If the impact energy E_i is greater (less) than the first cross-over point E_1, more (fewer) electrons will be released by secondary emission. As a result, more (less) energy will be drained from the cavity as it accelerates more (fewer) secondary electrons. This leads to a lower (higher) gap voltage which makes E_i closer to E_1 in subsequent cycles. Thus E_1 is a stable steady state solution. A similar argument shows that the second cross-over point, E_2 in Fig. 2, is unstable.
10. Since the space charge effects can be ignored, the analysis given here may actually be applied to a "blob" of multipactor electrons, of total charge $-q_m$, that is *very localized* in space (instead of an electron *sheet* shown in Fig. 1). This is because the induced current I_m is simply $-q_m d(x/D)/dt$ by the Ramo's Theorem [See, e.g., Chapter 1 of C. K. Birdsall and W. B. Bridges, Electron Dynamics of Diode Regions (Academic, New York, 1966)]. Thus, in Eqs. (2) and (4), σ may be taken to represent this localized "blob" of multipactor electrons. In Eq. (3), σ is set to zero when "the space charge effect" is ignored. Equations (1) and (5) are unchanged.
11. R. Kishek, D. Chernin, and Y. Y. Lau, Phys. Plasmas, to be published (1996).
12. R. Kishek and Y. Y. Lau, Phys. Plasmas, in the press (1996).
13. A spread in the emission velocities of the secondary electrons, and the time delays in secondary emission, may weaken (or even destroy in extreme cases) the phase focusing mechanism.
14. The multipactor phenomenon has been proposed as a source for a bunched electron beam by F. M. Mako and W. Peter, Proc. of the 1993 IEEE Part. Acc. Conf., 2702 (1993). The two phase-focusing mechanisms mentioned here indicate that the bunches can be very tight, if the effects discussed in Ref. 13 are unimportant.

Transverse Asymmetry in a Crossed–Field Diode

K. L. Cartwright, J. P. Verboncoeur, V. P. Gopinath and C. K.Birdsall

Electronics Research Laboratory
University of California, Berkeley, CA 94720
e-mail kc@bohm.eecs.berkeley.edu

Abstract

Recent studies of cylindrical crossed-field diodes indicate that the dimension(s) transverse to the gap may play a role in delaying onset of virtual cathode oscillations for currents above the limiting current [2]. Transverse space charge effects in smooth diodes can result in fields which warm the electrons in both the transverse and longitudinal components of velocity. Thermal emission of electrons damps virtual cathode oscillations, as shown by Birdsall [3]. The effects of the transverse dimension are explored using two-dimensional planar PIC codes. The simulations confirm that the transverse direction does delay the onset of virtual cathode oscillations.

1 Introduction

Lau, Christenson and Chernin [1] have re-interpreted the Hull cutoff as the limiting current for a planar crossed–field diode. The cutoff is well known; a summary is given in the text by Birdsall and Bridges [3]. Recently, Verboncoeur and Birdsall [5] performed one-dimensional simulations confirming the Hull cutoff as the limiting stable current for a space-charge limited planar diode, and examined the rapid reduction of transmitted current for injection currents above the current limit at the Hull cutoff. In examining the limiting current in cylindrical diodes of one and two dimensions, Gopinath et al. [2] noted a transverse space charge effect which appeared to damp virtual cathode oscillations for currents in excess of the limiting current.

In this paper, the preceding works are extended to two-dimensions, and the issues of numerical and physical instability are investigated. In particular, we examine the role of the transverse dimension in delaying onset of virtual cathode oscillations. PDP1 and PDP2 were the 1d and 2d PIC (particle in cell) codes used in this study. They are available electronically via the Internet [6].

2 Theory

The critical point occurs at the Hull cutoff, $B = B_{Hull}$, with the injected current at the limiting (critical) current, $J = J_c$. For cold emission the Hull cutoff can be written:

$$B_{Hull} = \frac{m}{ed}\sqrt{\frac{2eV}{m} + u_0^2}, \tag{1}$$

where u_0 is the electron drift velocity at the cathode, V is the gap voltage, d is the gap width, and e and m are the electron charge and mass, respectively.

At the Hull cutoff, the limiting current is given by $J_c/J_{CL} = 9/4\pi$, where J_{CL} is the unmagnetized Child-Langmuir limiting current:

$$J_{CL} = \frac{4\epsilon_0}{9\sqrt{\frac{m}{2e}}}\frac{(V - V_m)^{\frac{3}{2}}}{(d - x_m)^2}\left(1 + \frac{2.66kT_e}{e(V - V_m)} + \ldots\right). \tag{2}$$

Here kT_e is the electron temperature at the cathode, $V_m = mu_0^2/2e$, the initial electron drift energy, and x_m is the position of the minimum in potential. The potential minimum occurs at

$$\frac{x_m}{d} = \left(1 + \left(\frac{V}{V_m} - 1\right)^{\frac{3}{4}}\right)^{-1}. \tag{3}$$

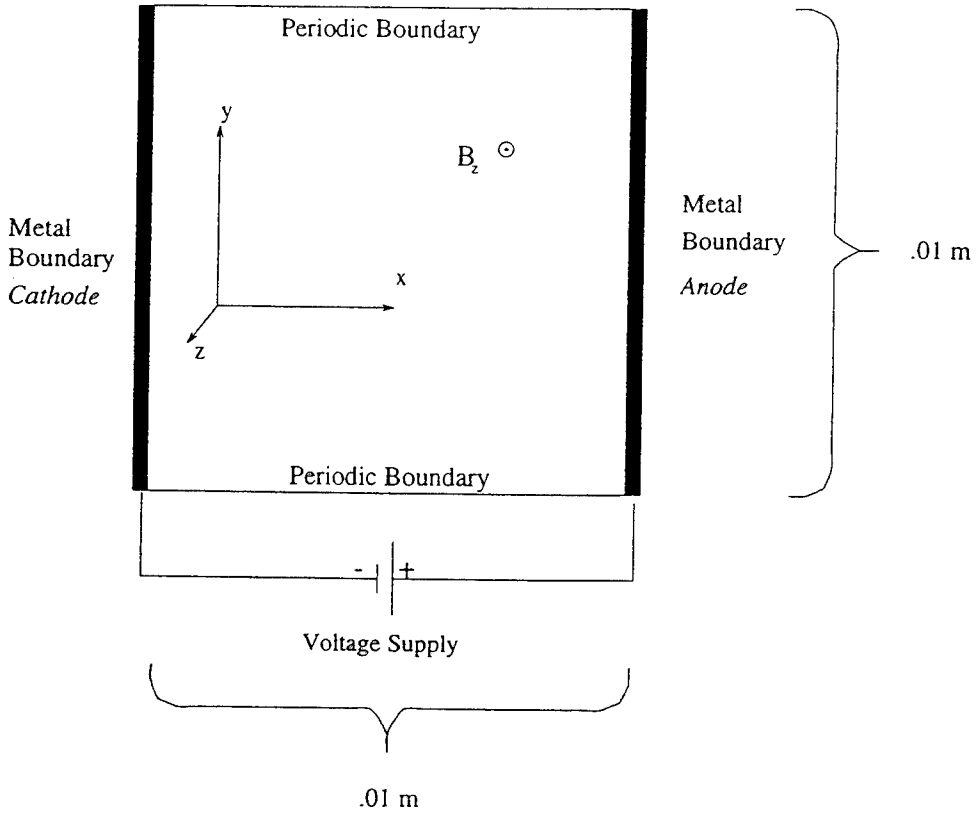


Figure 1: Sketch of 2d Simulation

It should be noted here that the second term in Equation 2 increases J_c for thermal distributions. This allows the diode to be stable at higher currents. For more details see Birdsall[3], Christenson[4], and Verboncoeur[5].

3 Unmagnetized Child – Langmuir Diode and Numerical Noise

The first simulation was done with $B_z = 0$ and $J = J_{CL}/2$. When the particles were injected at random positions in y, significant E_y fields were generated. This caused density fluctuation and heating in v_y. To establish this as a real phenomenon, the number of computer particles used in the simulation was increased, thus decreasing the number of real electrons each one represents. The variance of E_y is plotted as a function of the number of computer particles injected per grid per time step in Figure 2. This shows the variance (noise) of the system proportional $1/\sqrt{N_c}$, where N_c is the number of computer electrons. For a real system with these parameters, 10^6 times as many electrons would be present. Extrapolating the trend shown in Figure 2 to the physical number of electrons in the system,

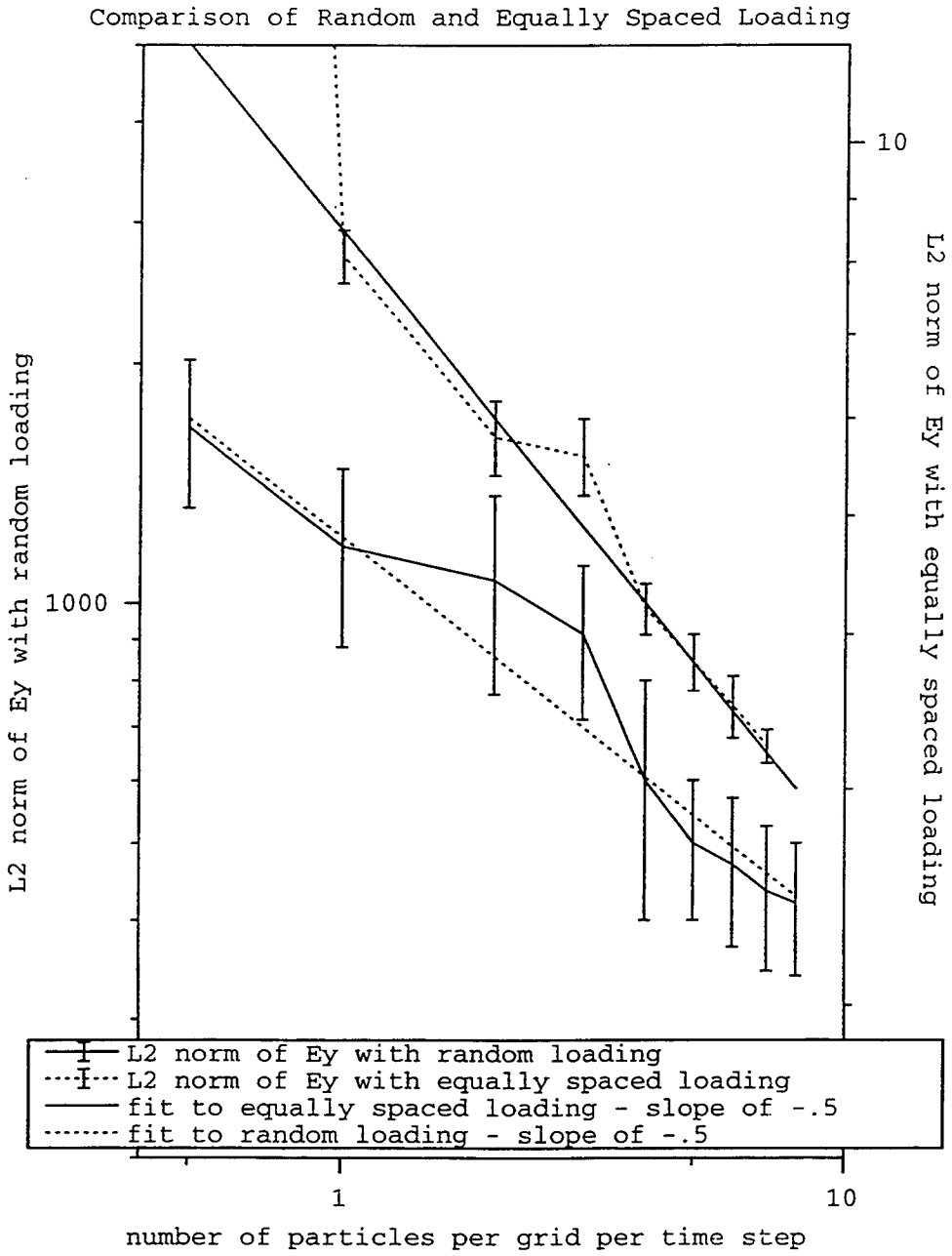


Figure 2: The variance of the E_y is plotted as a function of the number of computer particles injected per grid per time step. The uniform (quiet) load uses the right scale and the random load uses the left scale. The error bars represent the observed maximum and minimum values of the L^2 norm of E_y in time.

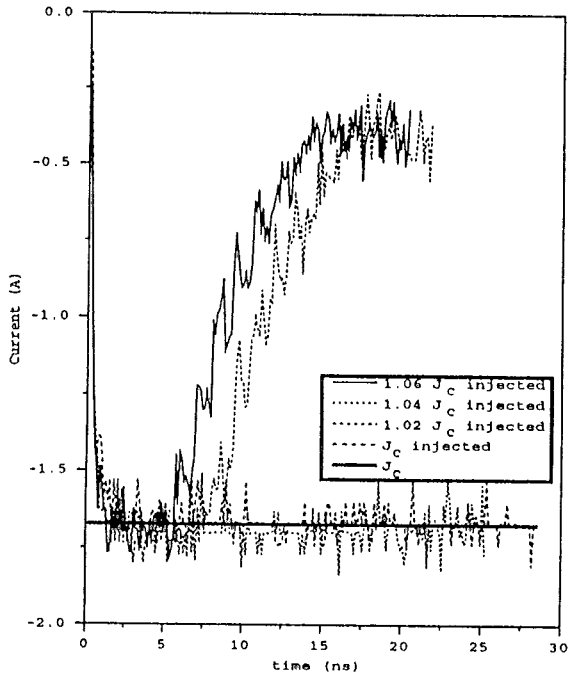


Figure 3: Cold Injection, Current through Hull Diode

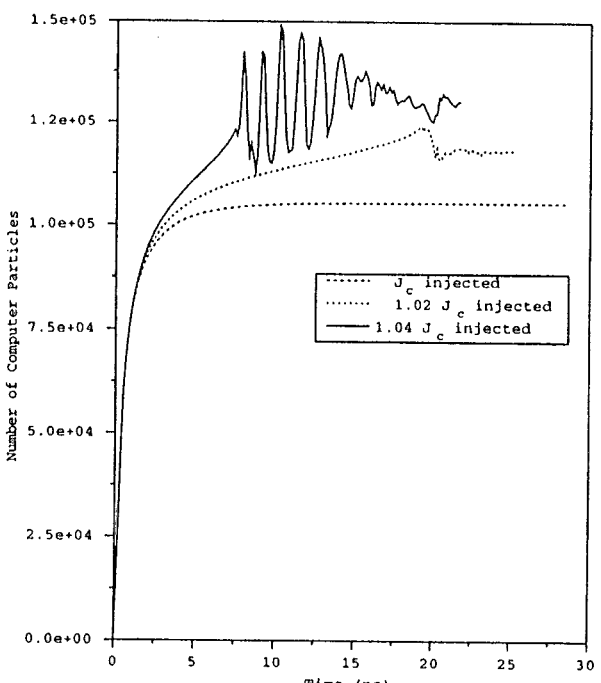


Figure 4: Cold Injection, Number of Computer Particles vs. Time

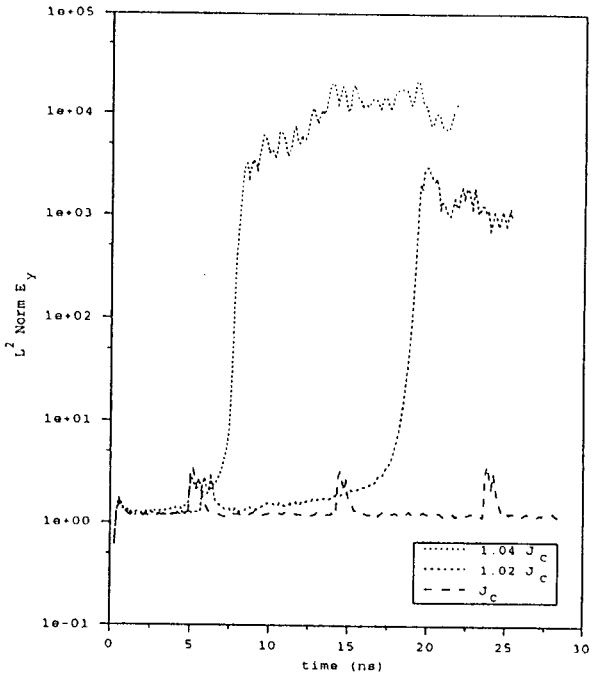


Figure 5: Cold Injection, L^2 Norm of Ey vs Time

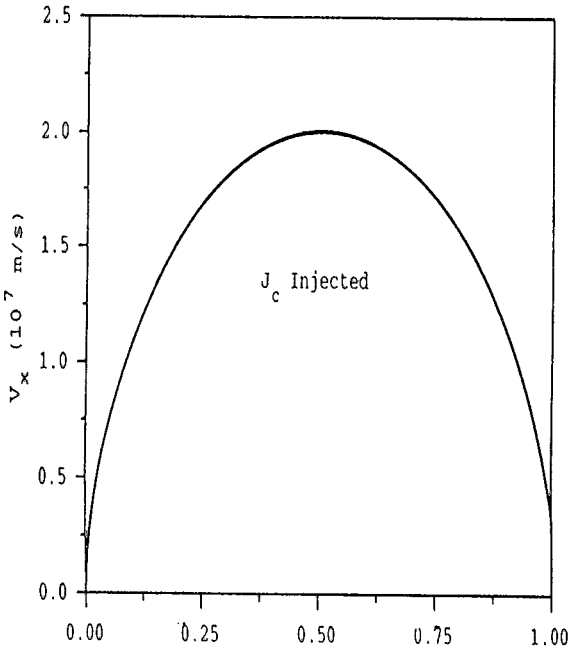


Figure 7: Cold Injection, Electron Phase Space

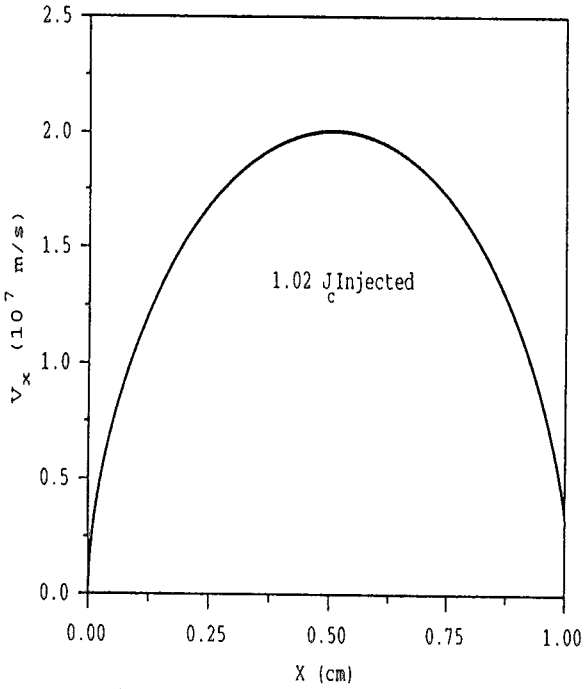


Figure 7: Cold Injection, Electron Phase Space

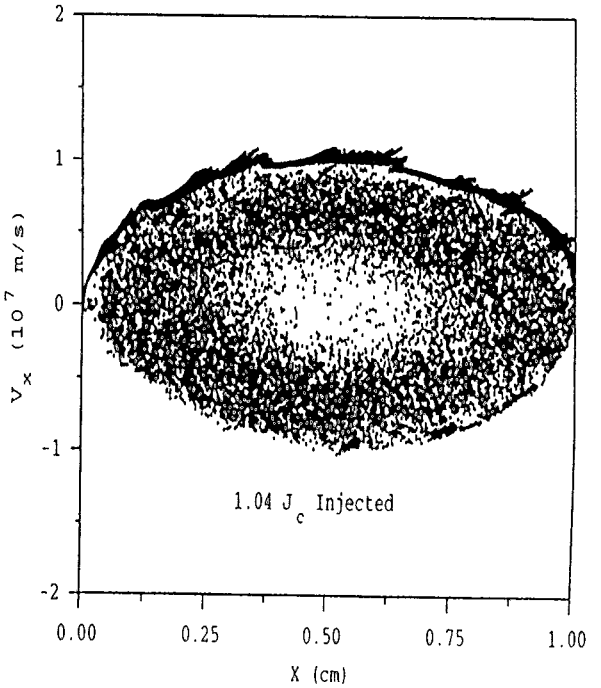


Figure 8: Cold Injection, Electron Phase Space

Physical Parameters	V	10 kV
	u_{0x}	4.2×10^5 m/s
	B_z	.0337 T
	J_c	- 16.9 kA/m^2
	x length	.01 m
	y length	.01 m
Numerical Parameters	Number of grids in x	400
	Number of grids in y	16
	Δt	5×10^{-13} sec

Table 1: Simulation Parameters

one finds the fluctuations in field decrease to a negligible level.

To reduce the noise in the system, particles are injected uniformly across the cathode. This is often referred to as a "quiet" injection. The number of particles injected is an integral multiple of the number of grid cells. The fluctuation level is shown in Figure 2 as a function of the number of particles injected per grid per time step. The quiet load uses the right scale and the random load uses the left scale. This brings the fluctuation down to a level that would be observed if 10^6 times as many electrons were injected randomly along the cathode. Using the quiet load, the E_y fluctuations are reduced and the resulting heating of the electrons is negligible. Thus, the observed transverse effects were numerical artifacts of the statistical nature of the simulation.

4 Critical Current Injection at Hull Field

A static magnetic field is applied perpendicular to the diode gap in the z-direction as shown in Figure 1. The common parameters for these simulations are shown in Table 1. The injection current is varied from J_c to $1.06J_c$.

The 2d results obtained here are compared to the 1d results obtained by Verboncoeur[5]. For an injected current of J_c the results are the same. The current as a function of time (Figure 3) and phase space (Figure 7) are almost identical to the 1d results (Figure 15 and 16). The phase space plot shows that the electrons do not have a turning point, $v_x = 0$, thus the anode current is equal to the injected current. The number of particles as a function of time is steady. The L^2 norm of E_y is also small, reflecting the lack of variation in the y-direction.

When the current is raised 2 percent above the critical current the result does not have a 1d analog. The L^2 norm of E_y, Figure 5, shows variation in the y-direction. However the electron phase space, Figure 7, looks very much like, $J = 1.02J_c$ case. This allows the diode to have a time independent solution with low noise and no oscillations. Thus, this allows

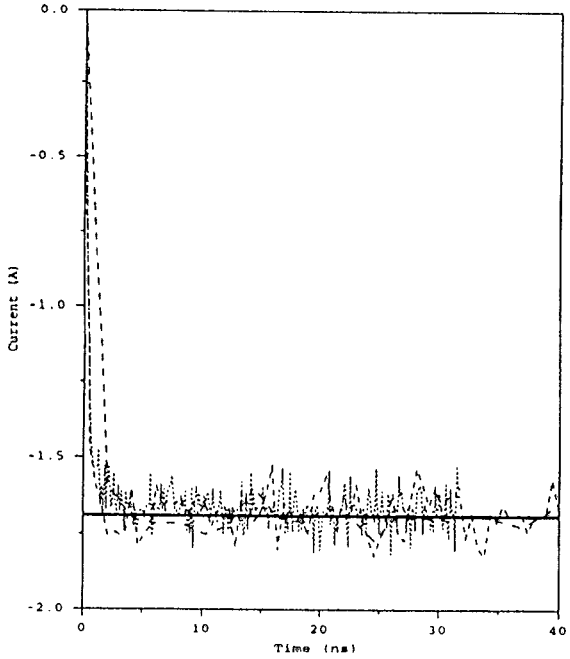


Figure 9: Warm Injection, Current through Hull Diode

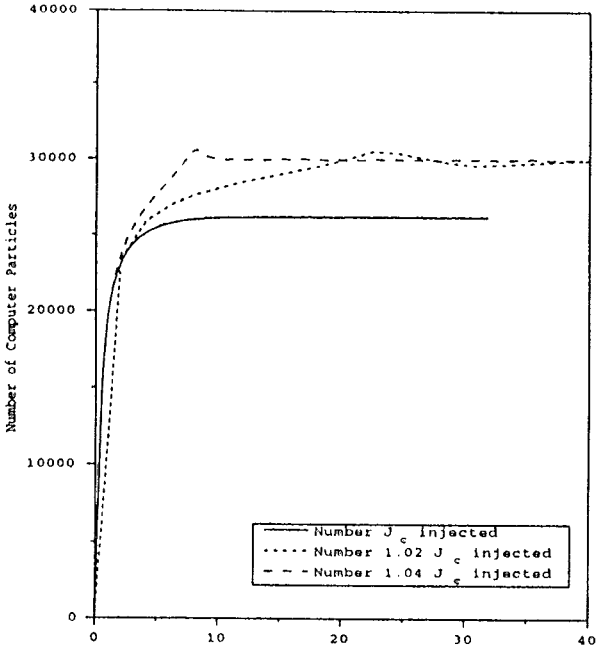


Figure 10: Warm Injection, Number of Computer Particles vs. Time

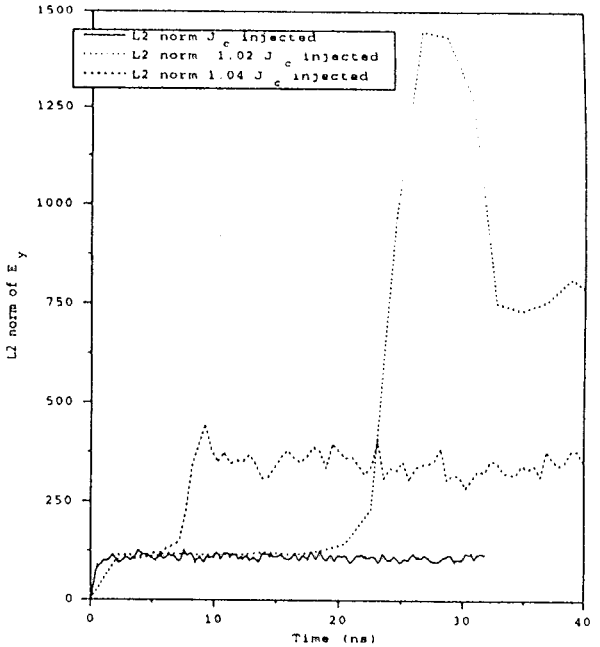


Figure 11: Warm Injection, L^2 Norm of Ey vs Time

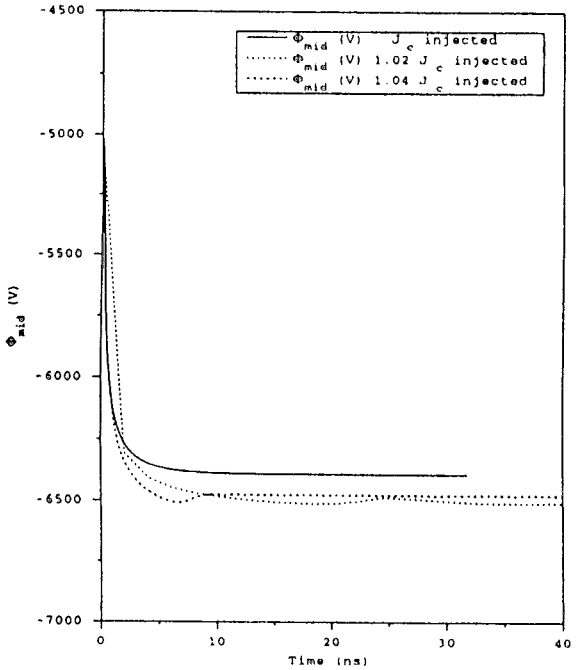


Figure 12: Warm Injection, Center Potential of Diode

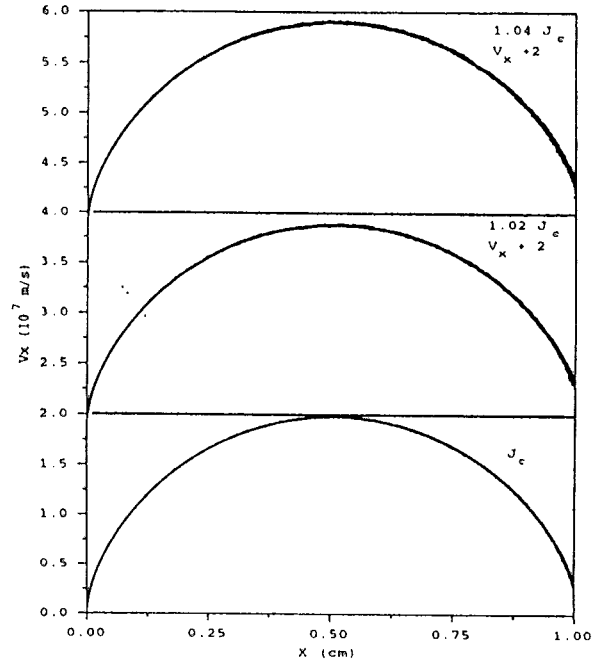


Figure 13: Warm Injection, Electron Phase Space

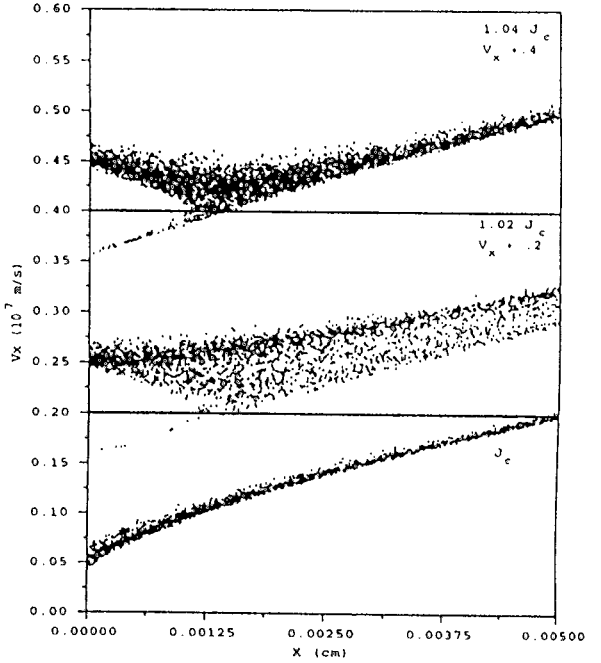


Figure 14: Warm Injection, Close up of Electron Phase Space next to Cathode

the critical (J_c) current to be transmitted. One possible explanation is when the Hull diode undergoes a transition to virtual cathode oscillations, an instability in the y-direction warms the electrons and stabilizes the diode before it becomes turbulent. The transmitted current in this case is the critical current predicted by Equation 2, which is less than the injected current. This indicates formation of a virtual cathode reflecting a portion of the electron population back to the cathode. The electrons reflected must have directed energy normal to the cathode less than the virtual cathode potential, i.e. $mu_x{}^2(x_m)/2 < eV(x_m)$.

Increasing the current by 4 percent above the critical value, J_c, the current ramps up to the critical value as in the first case and remains stable for about 5 ns. During this time, the space charge density in the gap is gradually increasing. The transmitted current then makes a rapid transition to a new mean value that is about 10 percent of the critical current. The current exhibits either a noisy or oscillatory behavior, with fluctuations of a few percent of the mean value. This is also shown in the number of computer particles, Figure 4. The L^2 norm of E_y is small until this transition occurs then it rapidly increases, as shown in Figure 5. The increase of the L^2 norm indicates that the system has some 2d structure. The electron phase space, Figure 8, recorded after the transition to turbulence has taken place shows a complex structure, with electrons traveling in both directions. The void in the center of phase space fills in completely at longer times. Even though this simulation has variation in the y-direction the macroscopic measured current is the same as the 1d simulation that went through a current transition.

5 Thermal Injection

The injected electrons were given a small isotropic temperature, $kT_e = .1$ eV, in addition to a 0.5 eV drift. Since $kT_e \ll V$, the change in B_{Hull} due to the electron temperature is negligible. Equation 2 predicts the addition of a thermal spread to the emitted electrons increases the Child-Langmuir current limit for the diode, with commensurate increase of the critical current at B_{Hull}. However, the 2d diode exhibits stability for injected currents much larger than J_c. This is in contrast to the 1d results [5], which demonstrated stability with anisotropic emission temperature (v_x), but instability for isotropic emission temperature. The thermal stabilization of the unmagnetized diode was described by Birdsall and Bridges [3]. Figures 9 - 14 show the stabilized diode for injected currents of $1.02J_c$ and $1.04J_c$.

Figure 14 shows an enlarged region close to the cathode. It shows the formation of a virtual cathode reflecting a portion of the electron population back to the cathode only transmitting a current equal to critical current, J_c. Injection with thermal electrons does not show a fast transition to a low current state when the injected current is a few percent larger than the critical current.

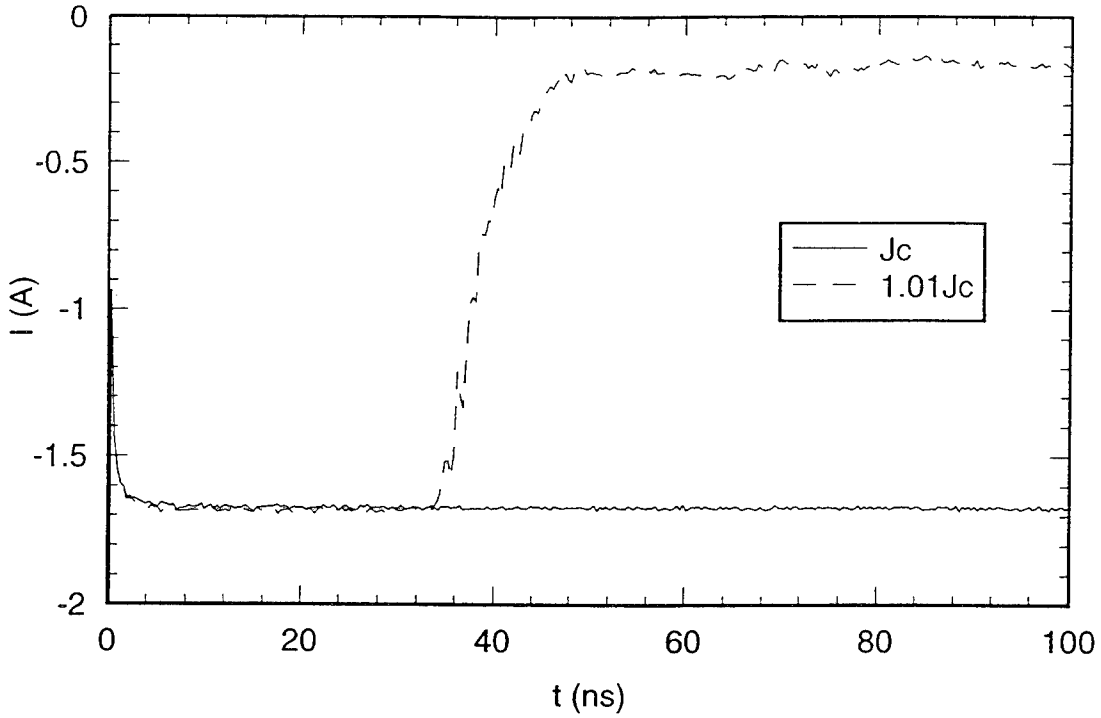


Figure 15: 1d, Current through Hull Diode

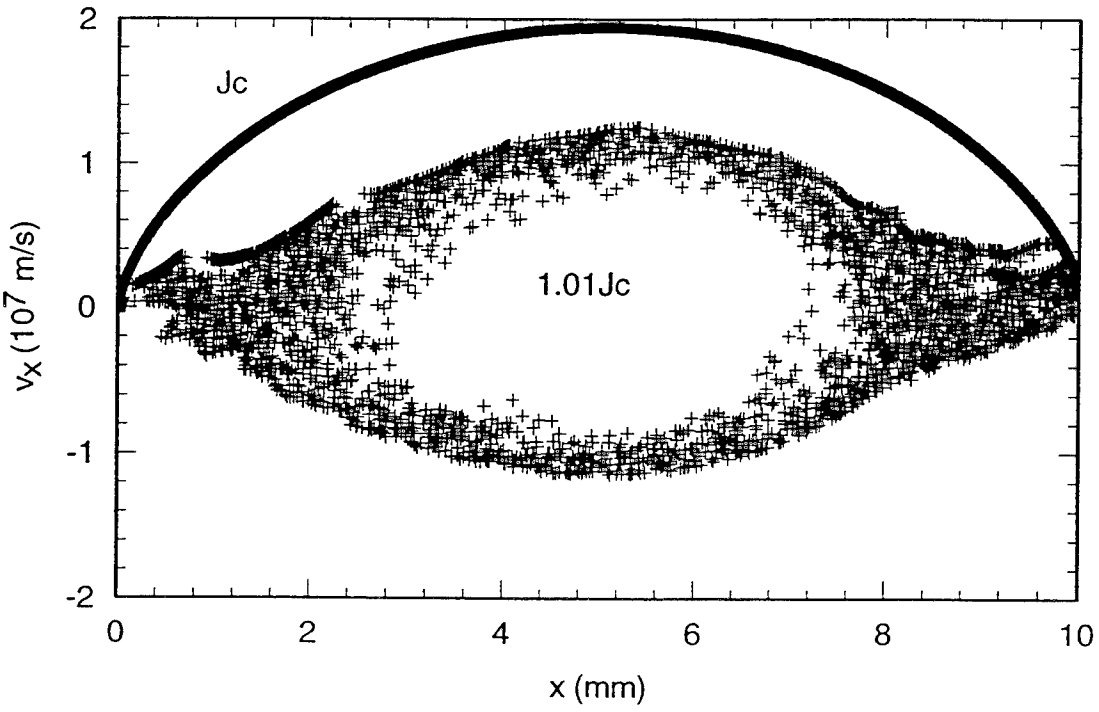


Figure 16: 1d, Electron Phase Space

6 Conclusions

Numerical instabilities must be investigated in order to remove nonphysical noise from the system. In particular, the diode stability is strongly influenced by noise in the injected space charge distribution at the cathode. The numerical transverse injection effect can be reduced to the extrapolated physical level using a reduced noise scheme which injects electrons uniformly spaced along the cathode.

In the absence of the injection noise, an instability occurs above critical current which heats the electrons in the y-direction so that J_c is the current transmitted. In contrast to the one-dimensional analog at $B = B_{Hull}$ and $J = J_c$, the two-dimensional system does not undergo a rapid instability and the associated current transition for $J_c < J < 1.04J_c$; elsewhere, it behaves like the 1d case. The second dimension allows an additional degree of freedom, which allows relaxation of the space charge effects driving the instability in one dimension.

Acknowledgments

The authors wish to acknowledge Y. Y. Lau, P. J. Christenson, and D. Chernin for the stimulating discussions on cross–field devices. This research is supported in part by ONR grant number N00014-90-J-1198 and N00014-94-1-1033, MURI grant F49620-95-1-0253, and AFOSR grant F49620-92-J0487. Travel money for K .L. Cartwright was paid by the First International Crossed–Field Devices Workshop.

References

[1] Y. Y. Lau, P, J. Christenson and D. Chernin, "Limiting Current in a Crossed–Field Gap," *Phys. Fluids* **5**, 4486 (1993).

[2] V. P. Gopinath, J. P. Verboncoeur and C. K. Birdsall, "Simulation of Transmitted Current in a Cylindrical Cross-Field Diode", *Proc. 22nd IEEE Int. Conf. Plasma Sci.*, Madison, WI (June 1995).

[3] C. K. Birdsall and W. B. Bridges, *Electron Dynamics of Diode Regions*, Academic Press (1966).

[4] P. J. Christenson and Y. Y. Lau, "Transition to Turbulence in a Crossed-Field Gap", *Phys. Plasma* **1**, 3725 (1994).

[5] J. P. Verboncoeur and C. K. Birdsall, "Rapid Current Transition in a Crossed-Field Diode", accepted *Phys Plasma*, (1996).

[6] J. P. Verboncoeur, V. Vahedi, M. V. Alves and C. K. Birdsall, PDP1, PDC1, and PDS1: *Plasma Device One-Dimensional Bounded Electrostatic Codes*, Plasma Theory and Simulation Group, University of California, Berkeley (1990). Available via http://ptsg.eecs.berkeley.edu.

Similarity of stability characteristics of planar and coaxial crossed-field diodes

V. P. Gopinath, J. P. Verboncoeur and C. K. Birdsall
EECS Department, University of California
Berkeley, CA 94720

Abstract

Simulations of cylindrical crossed-field diodes for anode/cathode radius ratios of 2 and 5 indicate that the limiting current curve in the region $B < B_H$ in cylindrical diodes follows the planar theory and simulations very closely. Cylindrical diodes also follow planar theory predicting transition to turbulence in the region $B > B_H$. Larger radius ratio (10, 20) diodes show somewhat larger limits. A possible explanation for this behavior is also examined.

1 Background

Limiting currents in planar crossed-field diodes have been studied for over 70 years [1]- [4] for $B < B_{Hull}$. More recently, the transition to turbulence in a cross field gap for $B > B_H$ has been studied by Christenson *et al.* [5]. While the stability characteristics of planar crossed-field diodes has been studied extensively, for both $B < B_{Hull}$ and $B > B_{Hull}$, and for mono-energetic and thermal emissions [5]- [6], corresponding theory for cylindrical systems is somewhat lacking. This study attempts to fill this gap by conducting PIC (particle-in-cell) simulations of cylindrical crossed-field diodes and comparing them to planar theory. This study is particularly significant in mapping the transition to turbulence in the region $B > B_{Hull}$ as an aid in the design and operation of low noise crossed-field devices.

1.1 Space Charge Limited Current in Cylindrical Systems

For zero applied magnetic field, we need to solve the one dimensional Poisson equation in cylindrical coordinates

$$\frac{1}{r}\frac{\partial}{\partial r}(r\frac{\partial V(r)}{\partial r}) = -\frac{\rho(r)}{\epsilon} \tag{1}$$

where $V(r)$ is the local potential and $\rho(r)$ is the local charge density. The kinetic energy gained by a charged particle of mass m, charge e and velocity v, accelerated through a time-independent potential drop V is given by (particle starting at $V = 0 = v$)

$$\frac{1}{2}mv^2 = eV. \tag{2}$$

The current density $J(r)$ inside the system can be written in terms of the charge density and velocity as

$$J(r) = \rho(r)v(r). \tag{3}$$

It should be noted here, that, unlike the planar case, $J(r) = I/(2\pi rl)$, is not a constant across the system. Equation (1) can be rewritten as

$$\frac{d^2}{dr^2}V(r) + \frac{1}{r}\frac{\partial V(r)}{\partial r} = \frac{I}{2\pi rl\epsilon}\sqrt{\frac{m}{2eV(r)}}. \tag{4}$$

Langmuir and Blodgett [8] noticed the similarity between equation (4) and the planar case and found a solution for J_{LB}, the space charge limited current density, as

$$J_{LB} = 2.335 \times 10^{-6}\frac{V_p^{3/2}}{r_c r_a \beta^2}(\frac{\mathrm{A}}{\mathrm{m}^2}) \tag{5}$$

where V_p is the anode potential, r_a is the anode radius and r_c is the cathode radius. The Langmuir-Blodgett factor β^2 varies with r and is tabulated for different radius ratios in [2], [8] and [9]

1.2 Hull Cutoff in Cylindrical Systems

The magnetic field B_H required such that an electron emitted from rest from a cathode will barely graze the anode is given by [2]

$$B_H = \sqrt{\frac{8m}{e}\frac{V_p}{r_a}}\frac{1}{(1-r_c^2/r_a^2)}. \tag{6}$$

This equation reduces to the form given by Hull [1] for the special case where $(r_c^2/r_a^2) \ll 1$.

1.3 Limiting Current Theory for Planar Systems ($B < B_H$)

The critical current density that can be transmitted (J_c) at any value of magnetic field between 0 and B_H, for a planar crossed-field diode has been worked out by Lau *et. al.* [4] and Pollack [7]. The relationship between normalized value of the transmitted current density (J_c/J_{CL}) and the normalized magnetic field (B/B_H) is given by

$$\frac{J_c}{J_{CL}} = \frac{9}{4}\frac{y^2}{(1+y^2)^{3/2}[h(y)]^2}, \tag{7}$$

where

$$y = \frac{B/B_H}{\sqrt{1-(B/B_H)^2}}, \tag{8}$$

and $x = h(y)$ is obtained by inverting the function

$$y = f(x) = \begin{cases} \frac{1}{x^2}(\sin^{-1}(x) - x\sqrt{1-x^2}) & 0 < y < \frac{\pi}{2} \\ \frac{1}{x^2}(\frac{\pi}{2} + \cos^{-1}(x) - x\sqrt{1-x^2}) & \frac{\pi}{2} < y < \infty \end{cases} \tag{9}$$

Equation (9) shows that the value of the normalized limiting current varies continuously from 1, at zero magnetic field to $9/4\pi$ near Hull cutoff, and is the solid line in the region $B < B_{Hull}$ in Figure 1.

1.4 Transition to Turbulence in a Crossed-field Gap ($B > B_H$)

Christenson *et al.* [5] have analyzed the transition to turbulence in a planar crossed-field gap in the region $B > B_H$. The analytical theory predicting the transition for zero emission velocity is given by

$$\frac{J_c}{J_{CL}} = (\frac{9}{8\pi})\,(\frac{B}{B_H})^3\,[1-\sqrt{1-(\frac{B}{B_H})^2}]. \tag{10}$$

Planar simulations conducted by these authors agreed with the theory. Recently, the authors have extended their theory to include non-zero injection velocities [10].

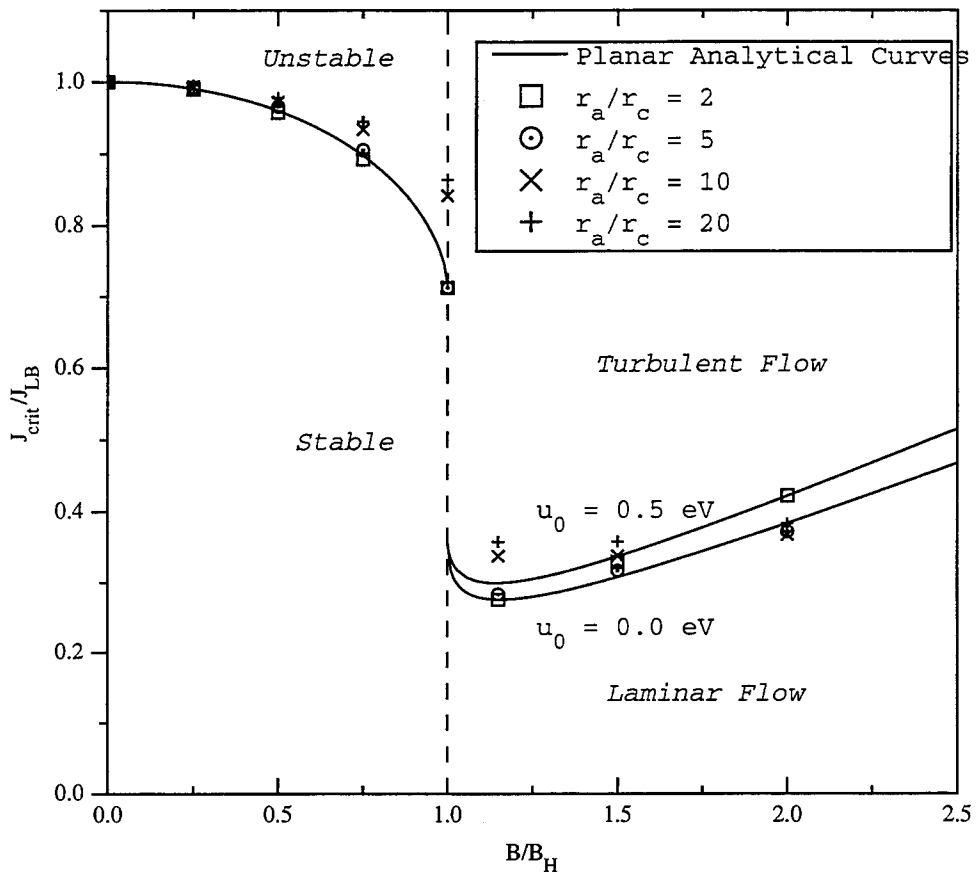


Figure 1: Comparison between critical injected currents found in cylindrical simulations with those from planar theory (normalized to Langmuir-Blodgett and Child's Law Currents, respectively)

2 Discussion of Results

1d3v (r, v_r, v_θ, v_z) PIC simulations in cylindrical coordinates were done using XPDC1 [11]. The cathode cylinder (electron emitter) was the inner conductor and anode cylinder was the outer conductor, held at a positive voltage with respect to the cathode. Runs were conducted for r_a/r_c ratios of 2, 5, 10 and 20 in order to study the behavior in small and large radius ratio regimes. For all these cases, the cathode radius was held at 0.01 m. The cathode was modeled as an electron emitter emitting particles with initial drift energy 0.5 eV, at a given current density. For all these runs, the anode was held at a DC potential of 10^4 V. Theoretical values of J_{LB} and B_H from equations (5) and (6) respectively were used as starting points for the simulations. Numerous runs were conducted to locate accurately the value of the injected current density above which the system exhibited oscillatory/turbulent behavior. The magnitude of this current density for zero magnetic field was considered (and found) to be J_{CL} (planar) and J_{LB} (cylindrical) for the particular radius ratio and was used as the normalizing factor. Similarly, B_H was considered to be the value of the magnetic field above which no laminar flow was present. In all these runs, the simulated values of J_{LB} were within 2% the theoretically calculated values. The simulated value of B_H differed from the theoretical value by less than 0.1%.

The results of simulations for all four radius ratios is given in Figure 1. For r_a/r_c ratios of 2 and 5, J_c/J_{LB} near cutoff ($B = B_H$) was very close to $9/4\pi$ as predicted in the planar model. Therefore, equation (9), represented by the solid line, was numerically calculated, and was used to hunt for the critical current in a manner similar to the search for J_{LB}. For the simulated points, the cylindrical results track the planar theory very closely for r_a/r_c ratios of 2 and 5. However, the transmitted current limit for larger radius ratios increases slightly over the planar theory at higher magnetic fields, transmitting 86% of J_{LB} at B_H as opposed to 71.6% predicted by the planar theory. Equation (10), labeled $u_0 = 0$ on Figure 1, is plotted for the region $B > B_H$. The curve labeled $u_0 = 0.5$ eV was plotted using the data obtained from P. Christenson and Y. Y. Lau [10]. It can be seen the r_a/r_c ratios of 2 and 5 follow the planar theory closely. However the larger radius ratios exhibit a trend away from the planar theory. These simulation results can be used to predict the transition to turbulence in cylindrical crossed-field diodes.

Figure 2 is a representation of a cylindrical and planar cross field diode. It should be noted here that for both these cases, the charge density inside the structure drops from a very large value to a small constant value within a very short distance from the cathode as can be seen in Figure 3 from simulation for $r_a/r_c = 2$. This surface is represented by the dashed line in Figure 2 and is located at a distance δ from the cathode. Since δ is $\ll r_c$, an electron present in this region "perceives" the structure to be planar. Further, from planar theory, it can be shown that an electron emitted from the cathode spends a relatively large amount of time in this region. If τ_δ be the time spent in the high charge density region, τ_T be the transit time across the structure and d be the length of the diode, for the planar case,

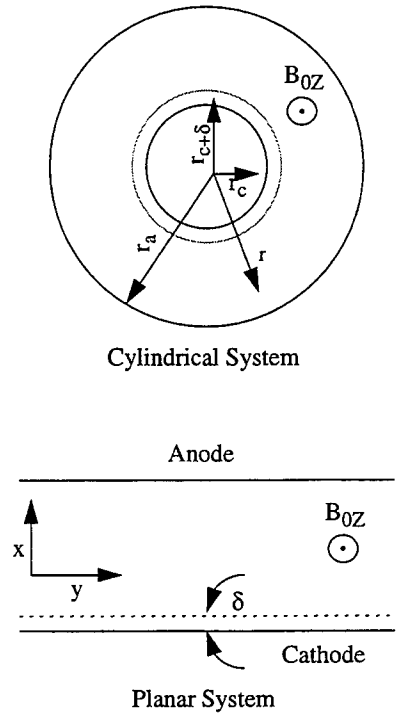


Figure 2: Planar and cylindrical models (δ is a small distance from cathode)

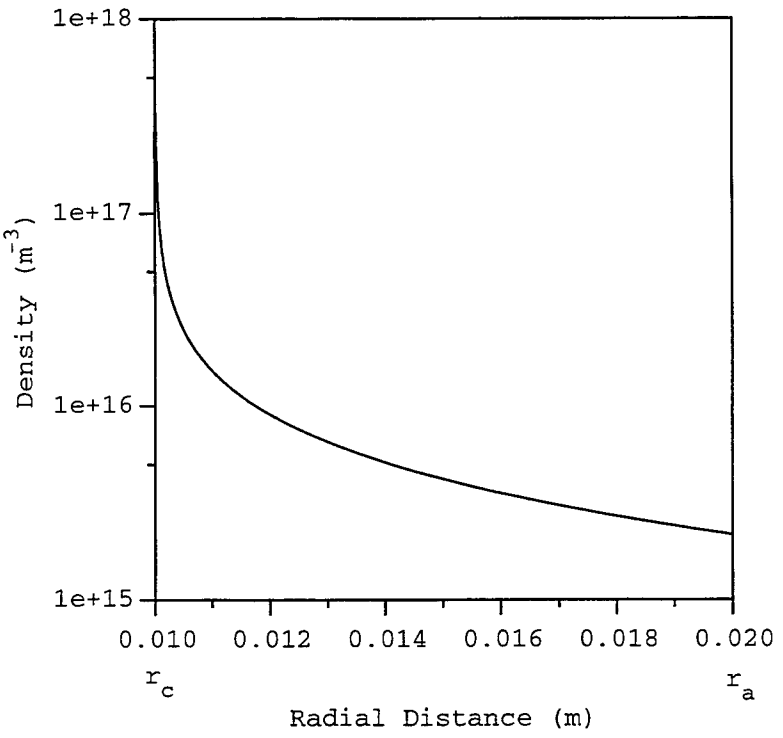


Figure 3: Spatial Variation of Charge Density (Simulation)

it can be shown that since

$$v(x) = \sqrt{\frac{2eV}{m}}(\frac{x}{d})^{\frac{2}{3}} \tag{11}$$

and the time required to traverse a distance y is

$$\tau_y = \int_0^y \frac{dx}{v} \tag{12}$$

that

$$\frac{\tau_\delta}{\tau_T} = (\frac{\delta}{d})^{\frac{1}{3}}. \tag{13}$$

It can be seen here that for $\delta/d = 1/64$, the electron will spend 25% of its lifetime in the small region. Therefore, for systems where δ/d is larger i.e. smaller radius ratios, the cathode region behaves like a region of $r_a/r_c = 1$, i.e. planar.

3 Conclusions

Simulations of transmitted current in cylindrical (coaxial) crossed-field diodes show close agreement with **planar** analytical theory for smaller radius ratios. Further, the transition to turbulence for the region $B > B_H$ was also seen to follow planar analytical theory. These results should be significant in the study of noise in crossed-field devices. We have attempted to explain this behavior by pointing out that the region of maximum significance for transmitted current, in smaller r_a/r_c ratio cylindrical systems, is essentially planar. This effect is further accentuated by the comparatively large amount of time spent by the electrons in this region.

4 Acknowledgments

We thank Y. Y. Lau and Peggy Christenson for the many stimulating discussions on cross-field devices and for providing the data for the analytical curve for 0.5 eV injection velocity. We would also like to acknowledge helpful discussions with D. Chernin, J. Swiegle and B. H. Vanderberg. This work was supported in part by ONR under Contract FD-N00014-90-J-1198 and AFOSR under grant F49620-92-J0487.

References

[1] A. W. Hull, "The Effect of Uniform Magnetic Fields on the Motion of Electrons Between Coaxial Cylinders," *Phys. Rev* 18, 31 (1921).

[2] William G. Dow, *Fundamentals of Engineering Electronics*, John Wiley and Sons, New York, 1937

[3] C. K. Birdsall and W. B. Bridges, *Electron Dynamics of Diode Regions*, Academic Press, (1966).

[4] Y. Y. Lau, P. J. Christenson and D. Chernin, "Limiting Current in an Crossed-Field Gap," *Phys. Fl. I.5* 4486 (1993).

[5] P. J. Christenson and Y. Y. Lau, "Transition to turbulence in a crossed-field gap," *Phys. Plasmas* **1** (12), p. 3725 Dec. 1994.

[6] J. P. Verboncoeur and C. K. Birdsall, "Simulations of Limiting Current in a Crossed-Field Gap, Hull Diode," presented at the IEEE ICOPS, Santa Fe, NM, June 1994.

[7] M. A. Pollack, *Noise Transport in the Crossed-Field Diode*, Ph.D. thesis, University of California, Berkeley, CA, Series No. 60, Issue No. 485 (1962).

[8] I. Langmuir and K. B. Blodgett, "Currents Limited by Space Charge Between Coaxial Cylinders," Phys. Rev., Ser 2. vol 22, pp. 347-357, October 1923

[9] Karl R. Spangenberg, *Vacuum Tubes*, McGraw-Hill, New York, 1948

[10] P. J. Christenson and Y. Y. Lau, "Electron Sheaths in a Crossed- field Gap – Equilibrium Solutions and Transition to turbulence," First International Workshop on Crossed-Field Devices, Ann Arbor, MI, August 1995.

[11] J. P. Verboncoeur, V. Vahedi, M. V. Alves and C. K. Birdsall, *PDP1, PDC1 and PDS1: Plasma Device one-dimensional Bounded Electrostatic Codes,* Plasma Theory and Simulation Group, University of California, Berkeley, CA 94720. Available via *http://ptsg.eecs.berkeley.edu.*

RESONANT DIOCOTRON MODE AND THE EVOLUTION OF THE SHEATH IN A CFA

D.J. Kaup

Institute for Nonlinear Studies and Departments of Physics and Mathematics,
Clarkson University, Potsdam, NY 13699-5815

Gary E. Thomas

Communications & Power Industries, 150 Sohier Road, Beverly, MA 01915

ABSTRACT

We show that the classical Brillouin density profile for a magnetron is nonlinearly unstable when a resonant RF wave is present in the slow–wave structure. The instability arises from a wave–particle resonance, usually called the diocotron resonance. The growth rate of this instability is directly proportional to the density gradient at the edge of the sheath. Thus for the classical Brillouin profile, where the density gradient at the edge of the sheath is taken to be infinite, the growth of the instability is extremely rapid, causing the density profile to become significantly modified within a few cyclotron cycles. This modification occurs as a consequence of the quasilinear diffusion of the unstable mode. The consequences of the quasilinear diffusion on the evolution of the sheath is discussed.

I INTRODUCTION

The modal structure for linearized waves in a magnetron or a crossed–field amplifier (CFA) is very sensitive to the profile of the electron density at the edge of the electron sheath [1]. As is well known, for the classical Brillouin density profile, no propagating diocotron mode can exist. Furthermore, in the parameter regime at which these devices operate ($\omega = kv_d$ where ω is the frequency, k is the wave vector and v_d is the drift velocity at the top of the sheath), such a profile has no unstable modes. However if we replace the Brillouin density profile with a "ramped" density profile (where the discontinuity is replaced by a finite, but large, negative density gradient), then we can show that any mode in the operating regime will become weakly nonlinearly unstable. However these weakly unstable modes, in the presence of the strong density gradient at the edge of the ramped density profile, combine to generate a quasilinear diffusion [2] of order unity. Thus after a time on the order of a few cyclotron periods, the original density profile can become significantly modified.

Many effects that can affect the evolution of the electron sheath. Most recently, there has been studies of space-charge effects [3], limiting currents [4] and turbulent micro–sheaths [5]. These will certainly influence the evolution of the sheath and need to be considered. However, here we shall restrict ourselves to the influences that the RF wave can exert on the evolution of the sheath.

The instability that we find is in agreement with the standard design criteria for CFA's and magnetrons. Current theory [2,6-18] cannot predict with certainty how well a new device will operate. Thus the design and manufacture of magnetrons and

crossed–field devices has remained as a well developed art, simply because the various design rules, and why they work, has not been explained by any theory.

The standard operating procedure in the design of a new device is to use the various design rules to extrapolate into the desired new parameter regime from the known characteristics of current devices, and then build a prototype based on these predictions. The device is tested and then the design is modified, based on the results of the tests. This is continued until one has an operational device.

Numerical simulations [19, 20] have provided insights into the operation of these devices. However they are plagued with an inability to accurately predict what a given device's operating range will be, so much so that prototyping is still required. The obvious conclusion is that either the simulations lack sufficient statistical accuracy or else there are poorly understood physical processes at play, which are not included in the model.

The classical Buneman, Levy and Linson (BLL) theory of such devices [6] is based on a linear instability which, at best, for the operating mode, lies deep inside the electron sheath and does not correspond to the parameter regime used by the design engineers. The predicted instability is indeed there [21], however it seems to have nothing to do with the start–up of a CFA or magnetron. The dominate effect of the instability appears to be to simply diffuse the edge of the sheath, with no growth of the desired mode, which exists in an entirely different region of phase space.

In the next section, we will describe the basic equations that we will use. We take as most fundamental, the design criteria used by the design engineers. This is that CFA and magnetron operation involves a wave–particle resonance, $\omega = kv_d$ where ω is the frequency of the electromagnetic wave, k is the wave vector in the interelectrode spacing between the cathode and anode, and v_d is the electron drift velocity at the top of the electron sheath. We introduce the WKB solution for the linearly perturbed cold–fluid equations and use it to demonstrate the well known fact that the classical Brillouin profile has no resonant diocotron mode. Then in Section 3, we present the WKB solution of the same equations where we replace infinite discontinuity at the edge of the classical Brillouin density profile with a very steep ramp, but which also has a finite gradient. We then show that the ramped profile will cause any RF wave which can satisfy the wave–particle resonant condition for particles along the ramped profile, will become weakly unstable. In Section 4, we then calculate the growth rate for such modes. This result is then used in the next section to calculate the quasilinear diffusion that arises as a result of the presence of such modes. We demonstrate that the combination of the weak instability with a very large negative density gradient generates a quasilinear diffusion at least of the order of unity. As a consequence of this, one concludes that any density profile with a steep density gradient at the edge of the sheath will become rapidly modified in the presence of a resonant RF wave. The implications of this for the future evolution of the sheath is then discussed in the last section.

II BACKGROUND

The geometry and configuration that we shall be using is shown in Fig. 1, which is a diagram of a "planar magnetron". At the bottom is the cathode which is an electron emitting material. It is located in the xz–plane and at $y = 0$. We take the ambient magnetic field to be along the negative z–axis so that the electron drift velocity will be in the positive x–direction. Next to the cathode is the electron sheath which extends out to a distance of b from the cathode. The anode is located at a distance l above the cathode.

The sheath forms adjacent to the cathode. Using the Brillouin sheath as an

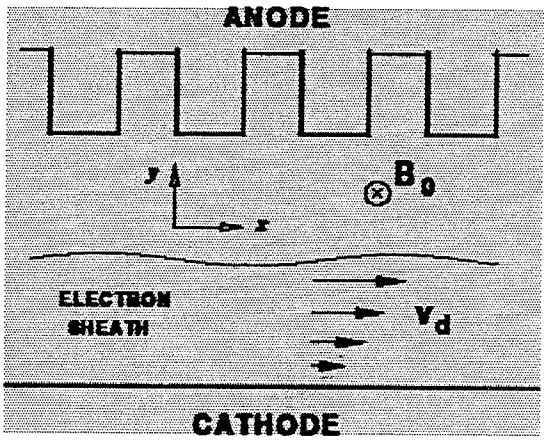


Figure 1: The geometry and configuration of a planar magnetron or CFA. The magnetic field is directed into the paper and the electron drift velocity is to the right. The z-axis is perpendicular to the paper, the x-axis is parallel to the cathode surface and the y-axis is perpendicular to the cathode.

example, it can have a maximum density where the electron plasma frequency, [$\omega_p = (4\pi e^2 n_0/m)^{1/2}$, where $e(m)$ is the electronic charge (mass) and n_0 is the electron number density], would equal the electron cyclotron frequency, Ω, up to a distance, b, with the electron density being zero above this value. The distance b is determined by the applied DC (direct current) voltage. Also, space–charge–limited current condition is assumed to exist at the cathode, which means that the DC electric field at the cathode would vanish. Thus we have an electron density profile in the shape of a box, where between the cathode and the top of the sheath, $\omega_p = \Omega$, and zero above the sheath, up to the anode. This model is an approximation and in actuality, one would expect the real sheath to have a ramped edge instead of an infinite discontinuity at the edge [22].

It is quite straight–forward to work out the basic cold–fluid equations describing this physical system, which are

$$\partial_t n + \vec{\nabla} \cdot (\vec{v}\, n) = 0 \tag{1}$$

$$\partial_t \vec{v} + (\vec{v} \cdot \vec{\nabla})\, \vec{v} - \vec{\nabla}\, \phi + \vec{v} \times \vec{\Omega} = 0 \tag{2}$$

$$\nabla^2 \phi = n \tag{3}$$

In the above equations, we have simplified the quantities by taking n to be the electron plasma frequency squared and ϕ to be (e/m) times the electrostatic potential. We shall use this notation in the remainder of the paper. Also, the velocity vector is in the xy–plane and all quantities are independent of the z coordinate.

From these equations, the basic Brillouin equilibrium solution follows [23]. The sheath thickness is now determined once the DC voltage, V, at the anode is specified. This gives

$$b = l - \sqrt{l^2 - 2V/\Omega^2} \tag{4}$$

The basic design criteria is for the electron drift velocity at the top of the sheath to be equal to the phase velocity of the electrostatic wave. The wave vector, k, is selected by the slow–wave structure. Then requiring these velocities to be equal, one finds

$$b = \omega/(\Omega k) \tag{5}$$

In order to achieve this sheath thickness, one now adjusts the DC operating voltage, using (4).

Next, let us take a small signal to be impressed on this background. Linearizing Eqs. (1)–(3) about this background and taking the perturbed quantities to vary as plane waves, $e^{ikx-\omega t}$, one obtains a set of linear ordinary differential equations. One now has a choice of how to reduce these equations. The most common way [6, 12] is to eliminate the particle density and velocities in favor of the electrostatic potential. However, as we shall see later, the dominate motion of the operating RF mode is one involving particle motions, not variations in the electrostatic potential. Thus it becomes more revealing if one concentrates on the particle velocities instead of the potential. Consequently we take [6, 24]

$$\partial_y p = Au \tag{6a}$$

$$\partial_y u = Bp \tag{6b}$$

where

$$A = \Omega^2 - \omega_e^2 \tag{7}$$

$$B = \frac{k^2}{A} - \frac{k\partial_y n_0}{\Omega\omega_e A} - \frac{2k^2 n_0 \Delta^2}{\Omega^2 A^2} \tag{8}$$

$$\omega_e = \omega - kv_0 \tag{9}$$

$$v_0 = \partial_y \phi_0/\Omega \tag{10}$$

$$\partial_y^2 \phi_0 = n_0\,, \quad \phi_0(0) = 0 = \partial_y \phi_0(0) \tag{11}$$

$$\Delta^2 = \Omega^2 - n_0 \tag{12}$$

$$u = -ikv_{1x} \tag{13}$$

$$p = Av_{1y} \tag{14}$$

In the above, the subscript "0" indicates a background quantity and Eqs. (9) - (11) gives the definitions for a general (non–Brillouin) density profile, n_0, which we shall be needing later. ω_e is the frequency of the RF wave as seen by the moving electron and Δ is the local oscillating frequency for individual particles [25, 22] which vanishes for a Brillouin flow. In (13)-(14), v_{1x} and v_{1y} are the x- and y-components of the perturbed velocity fields. The perturbed electrostatic potential, ϕ_1 and its derivative are obtained from p and u as follows.

$$\phi_1 = \frac{ip\Delta^2}{Ak\Omega} - \frac{iu\omega_e}{k^2} \tag{15}$$

$$\partial_y \phi_1 = \frac{i\Omega}{k} u - \frac{i\omega_e}{A} p \tag{16}$$

The boundary conditions on (6) follow from the boundary conditions on ϕ_1. At the cathode, which is grounded, the perturbed potential must vanish. Thus $\phi_1(y = 0) = 0$. At the anode, one frequently uses the "smooth–bore" approximation. In this

approximation, one assumes that the slow–wave structure appears as a conducting surface to the plasma RF wave. Whence one would take $\phi_1(y = l) = 0$.

Now, the smooth–bore approximation only allows a special class of RF modes, which we shall call "plasma modes". In general, the RF modes in a crossed–field device will fall into two classes: "plasma modes" and "anode modes". By a plasma mode, we mean an RF mode which will be localized in the region of the sheath and which is small in the region near the anode. Under these conditions, the smooth–bore approximation is valid. Such a mode would also dominantly involve particle motion. By an anode mode, we mean those RF modes which can propagate along the slow–wave structure, whose energy is concentrated in the slow–wave structure and whose amplitudes are small in the region of the sheath. It would dominantly involve the electromagnetic field. The slow–wave structure is a wave guide and it is designed to allow an RF wave to propagate along its structure [23].

In actuality, one can use this separation of modes only as long as the dispersion curves (curves of ω vs. k) for the plasma mode(s) and the anode mode(s) are non–resonant (do not cross). When they are resonant and the dispersion curves cross, one has to use coupled–mode theory [26]. But one cannot use coupled–mode theory if there is no plasma mode that resonates with the anode mode. Thus the first problem is to find a resonant plasma mode. For now, we shall use the smooth–bore condition since we first want to study the plasma modes. Later, we will include the anode modes. Thus we take

$$\phi_1(0) = 0 = \phi_1(l) \tag{17}$$

which by (15), determines the ratio of u to p at the cathode and anode.

For the Brillouin case, one can obtain the basic features of the solution by constructing the WKB solution of (6). One has two regions, one is inside the sheath and other is outside the sheath. Outside the sheath, the solution is simply the vacuum solution. Inside the sheath, the quantity A can vary as a function of y. Thus it is possible for A to have a simple zero inside the sheath, which then would give a regular singular point to Eq.(6b). This singular point was thoroughly studied in Ref. [6]. However, it will be important only for high k which is well outside of the standard operating range of such devices. Note that for standard devices, ω is usually less than Ω. Also at the cathode, ω_e initially decreases as y increases when $\omega > 0$. Thus A cannot have a zero until kv_0 becomes at least as large as Ω. But this would then be outside of the known operating parameter region. Thus as long as we limit our attention to the design operating range, then we can ignore the possibility of zeros for A.

The WKB solution of (6) for the physical parameter regime of a Brillouin sheath has been detailed in Ref. [1]. What one finds is that upon using the smooth–bore condition at the anode, there are two sets of eigenfrequencies, and only two, for each value of k. These are given by

$$(\Omega^2 - \omega_{ef}^2)\tanh[k(l-b)] - \omega_{ef}^2\tanh(kb) + \Omega\omega_{ef}\tanh[k(l-b)]\tanh(kb) = 0 \tag{18}$$

where $\omega_{ef} = \omega_e(y = b)$ is the value of ω_e at the top of the sheath. It is a simple matter to solve (18) for ω as a function of k, which will give the possible dispersion curves for these plasma modes. A plot of ω vs. k using scaled variables is shown in Fig. 2 for $b = .3l$, a typical value. Here the x-axis is kl and the y-axis is ω/Ω. The solutions of Eq. (18) are shown in Fig. 2 as solid lines. The middle line, which is dashed and passes through the origin, is the major design criteria, $\omega_{ef} = 0$. One notes that the solutions of (18) are far away from this curve. In other words, there is no plasma mode in the region where these devices operate, when the Brillouin density profile is used.

Now there are density profiles which have plasma modes matching the design criteria. The double–box (DB) density profile [27] has such a mode. The difficulty

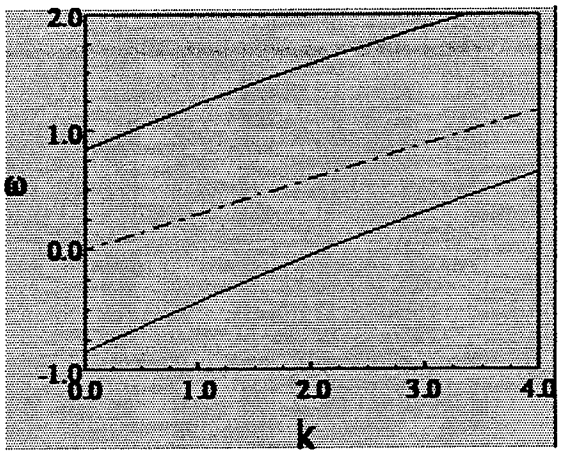


Figure 2: The resonant eigenfrequencies, ω/Ω vs. kl per the BLL theory are shown above as solid lines. The dashed line in the middle is the curve that is used for the design of these devices. Note that the design criteria lies well away from the BLL values.

with the DB model is that there is no explanation as to how it could ever arise. What is the physical process which creates the DB profile? And is this process fast enough to form the DB profile well within one circuit of a crossed–field device? One mechanism by which one could create a DB profile could be a nonlinear diffusion process [2, 24]. However, such a process requires a linear wave which has a nonzero damping (or growth). The standard second–order (quasilinear) diffusion process is given by

$$\partial_t n_0 + C_2 \partial_y n_0 = \partial_y (D \partial_y n_0) \tag{19}$$

where C_2 is a function of time, given by

$$C_2 = \frac{-\int_0^l D \partial_y n_0 dy}{\int_0^l \Delta^2 dy} \tag{20}$$

and D is the quasilinear diffusion coefficient, given by

$$D = \sum_k \frac{2\gamma_k p * p}{\omega_e^* \omega_e A^* A} e^{2\gamma_k t} \tag{21}$$

where p, ω_e and A are as defined before, γ_k is the linear growth (or decay) rate and in general, is a function of k, as is almost all the quantities in (21). As one can see from the structure of D, clearly if the linear mode has a dispersion curve such that ω_e can be very small, then D can become unusually large. However, to contribute to D, this mode cannot be stable. It must be, at least slightly unstable, because if it was perfectly stable, then γ_k would be zero and D would vanish. So, if one is to invoke this mechanism as a possible means for generating a DB profile, then one must first find a linear mode with an instability near $\omega_e = 0$.

A more realistic model, at least for early times, would be to replace the discontinuity with a ramp, as in Fig. 3. In this way, one can more closely model the presence of thermal fluctuations and include the major profile structure found in a Vlasov model [28]. However a pure ramped profile still does not have any plasma modes near

$\omega_e = 0$ [1]. Nevertheless, being a more realistic model in that it has a finite density gradient, it will be of benefit to analyze the result of replacing a discontinuity with a ramp. For a ramp with a very large, negative, density gradient, we find that one can easily obtain an asymptotic series solution in the region of the ramp. The ramped density profile has exactly the same eigenmodes that the Brillouin profile has, not unexpectedly. On the other hand, if ω_e has a zero somewhere along the ramp, then one finds that there is a very distinct and rich structure occurring in the solution. This structure includes logarithmic terms which can introduce imaginary parts into the solution. These imaginary parts will lead to the eigenfrequency becoming complex, and therefore unstable. This entire structure is missed if one assumes a discontinuity at the edge, as in the Brillouin profile, instead of a ramp.

Although the ramped profile has no plasma mode where $\omega_e = 0$ along the ramp, and thus no additional plasma modes beyond those of the Brillouin profile, nevertheless a sharp ramp will very significantly affect any anode modes. Now the effect that such a ramped edge will have on an anode mode is the following. First, the ramped edge will cause almost any anode mode to be slightly unstable. To demonstrate this, first note that slow–wave structures are designed so that in the desired frequency range, the resulting k will also be in the desired range. The desired range comes from the design criteria that ω_e should vanish at or near the edge of the sheath. Although the majority of energy of an anode mode is concentrated inside the slow–wave structure, nevertheless, it must still have a fringing field that exists all the way down to the sheath, and will to some extent, penetrate through the ramp of the sheath and on into the sheath. Because it penetrates into and through the ramp of the sheath, the solution will pick up an imaginary part and the eigenfrequencies will therefore become complex in general. This is a mode which then can drive and initiate the nonlinear diffusion process.

In Section 3, we will obtain the general solution along a density ramp by expanding in inverse powers of the density gradient. Then we match this solution to the interior WKB solutions for u and p and extrapolate to the anode. In Section 4 we will use this solution to determine the damping of an anode mode. In the process, we shall obtain approximate analytical solutions for the growth-rate of this anode mode. From this we can then construct the second–order diffusion coefficient, D, defined above, which is done in Section 5. Numerical and analytical solutions of (19) for short times will then demonstrate that within very short times compared to an RF oscillation, the formation of a DB profile is initiated. Concluding remarks are made in the last section.

III RAMPED DENSITY PROFILE SOLUTION

In this section, we shall briefly discuss the solutions of the linearlized equations when we have a ramped edge on a sheath instead of a discontinuity, as shown in Fig. 3. We take the width of the ramp, ϵ, to be very small in comparison to a wavelength. Thus $\epsilon k << 1$. We also assume that ω_e will have a zero either inside the ramp or very near to it. To analyze this problem, we take the interior to be a Brillouin flow where $n_0 = \Omega^2$, we let b be the value of y at the top of the ramp and introduce the variable z where

$$z = (y - b)/\epsilon \tag{22}$$

so that $z = 0$ is at the top of the ramp and $z = 1$ is at the bottom of the ramp, where the vacuum region starts. Then if v_b is the value of the drift velocity, v_0, at $y = b$, inside the ramp, $0 < z < 1$, the drift velocity is

$$v_0 = v_b + \epsilon\Omega\left(z - \frac{1}{2}z^2\right) \tag{23}$$

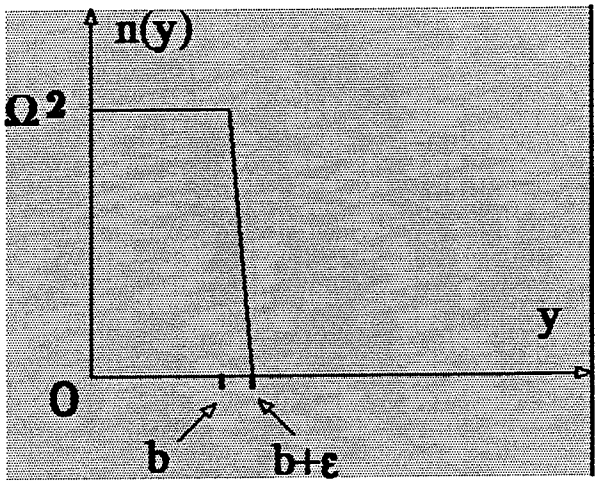


Figure 3: The ramped density profile. The width of the ramp is ϵ and is taken to be very small, but nonzero. This model causes any mode to be slightly damped whenever ω and k are such that ω_e has a zero somewhere along the ramp.

and,

$$\omega_e = \omega_{eb} - k\epsilon\Omega(z - \frac{1}{2}z^2) \tag{24}$$

where

$$\omega_{eb} = \omega - kv_b \tag{25}$$

and is the value of ω_e at the top of the ramp. We assume ω_{eb} to be small and of the order of ϵk. Thus we define a parameter β, of order unity by

$$\omega_{eb} = \epsilon k\Omega\beta \tag{26}$$

From (24) and (26)

$$\omega_e = \epsilon k\Omega(\frac{1}{2}z^2 - z + \beta) \tag{27}$$

If β lies between 0 and 1/2, then ω_e has a zero somewhere along the ramp.

Now, let us turn to Eqs.(6). Since ω_e is of order ϵ, it follows that A, defined by (11), may be taken to be simply Ω^2. Then from the above, Eqs. (6) reduce to

$$\partial_z p = \epsilon\Omega^2 u \tag{28a}$$

$$\partial_z(\epsilon\Omega^2 u) = \frac{p}{\frac{1}{2}z^2 - z + \beta} \tag{28b}$$

upon neglecting terms of order ϵ^2. Equations (28) are nothing more than the Rayleigh equation [29] with a specified flow profile. For the given flow profile, exact solutions exist. One then can construct the solution satisfying the boundary conditions at the cathode, using WKB for the interior solution. The final solution for the vacuum region above the sheath, $y > b + \epsilon$, is [1]

$$\phi_1(y) = \phi_{1f}\cosh[k(y - b - \epsilon)] + \frac{1}{k}(\partial_y\phi_{1f})\sinh[k(y - b - \epsilon)] \tag{29}$$

where the coefficients are

$$\phi_{1f} = \frac{iC_1}{2Rk} \ln\left(\frac{R-1}{R+1}\right) \cosh(kb) \tag{30a}$$

$$\partial_y \phi_{1f} = \frac{-2iC_1}{\epsilon k R^2} \cosh(kb) \tag{30b}$$

and are just the values of the potential and its derivative at the bottom of the ramp. The quantity R is defined by

$$R = (1-2\beta)^{\frac{1}{2}} \tag{31}$$

Clearly, when R is real and < 1, (or β is between 0 and 1/2), the logarithm terms will have branch points somewhere along the ramp. In this case, R (and β) must be shifted off the real axis and take on complex values. By (25) and (26), this then means that the eigenfrequency will become complex. One should also note that when β lies outside of this region, the logarithm terms never have a branch point inside the physical region.

In order to have a resonant, diocotron plasma mode, then it will be necessary for the ramped profile to be modified by some physical process. A mechanism for doing so is considered in the next section where we show that any anode mode with ω_e vanishing along the ramp will be damped, which then will initiate a quasilinear diffusion process, modifying the initial profile.

IV DAMPING OF ANODE MODES

CFA's operate as amplifiers. The presence of an anode wave is necessary for its operation. Also, the initial density profile which is ramped is more realistic than a discontinuity. It also acknowledges the physical fact that density profiles can never be perfectly sharp. As is clear from the previous section, any anode wave injected into a CFA, if its ω and k are such that ω_e will vanish somewhere along the ramp of the density profile, then that anode wave will be damped. We first calculate the expected damping.

In order to do this, one first needs the dispersion relation for the slow–wave structure. Such can be calculated for very simple structures, and examples of such are in standard textbooks [23]. We will use the very simple "comb" model as shown in Fig. 1. We take the width of the vanes to be a, the period from one vane to the next to be L and the depth of the vane to be s. Then it is easy to show that [23]

$$\frac{k\phi_{1a}}{\partial_y \phi_{1a}} = \frac{4\sin^2(\frac{a}{2}k)}{a^2k^3L}(\frac{a\omega}{c})\tan(\frac{sw}{c}) \tag{32}$$

where c is the speed of light. In (32), ϕ_{1a} and $\partial_y\phi_{1a}$ are the values of the potential in the vacuum region and at the tips of the vanes ($y = l$), which is given by (29) for our model. For comparison, we mention that in the absence of a plasma, the slow–wave structure and the vacuum region acts as a wave guide for any RF wave injected into the slow–wave structure. In this case, the vacuum extends down to the cathode and then [23]

$$\left(\frac{k\phi_{1a}}{\partial_y \phi_{1a}}\right)_{ct} = \tanh(kl) \tag{33}$$

where the subscript "ct" indicates the value in the absence of a plasma.

Let us now calculate this ratio for our model of a ramped profile. From (29) we have

$$\left(\frac{k\phi_{1a}}{\partial_y\phi_{1a}}\right)_{\text{ramp}} = \frac{k\phi_{1f} + (\partial_y\phi_{1f})\tanh[k(l-b)]}{k\phi_{1f}\tanh[k(l-b)] + (\partial_y\phi_{1f})} \tag{34}$$

One will observe that due to the relatively larger size of $\partial_y\phi_{1f}$, the real part of (34) is essentially the same as (33), except that l is replaced by $l-b$, the latter being the new depth of the vacuum region. In other words, the plasma appears to be a conducting surface to the anode wave in this approximation.

To calculate the imaginary part of (34), we return to (25) and (26), letting ω have a small imaginary part, γ, of arbitrary sign. Thus β will have both real and imaginary parts also, $\beta = \beta_1 + i\beta_2$, where

$$\gamma = \epsilon k\Omega\beta_2 \tag{35}$$

We will assume β_2 to be small also, namely $|\beta_2| << |\beta|$. From (31), we can calculate the imaginary part of $R = R_1 + iR_2$. We are only interested in the case when $0 < \beta_1 < 1/2$ since this is the only case when there will be a significant imaginary part. It is also the region in which ω_e has a zero along the ramp. Then we have

$$R_1 = (1-2\beta_1)^{\frac{1}{2}},\ R_2 = 2\beta_2/R_1 \tag{36}$$

and it follows that the imaginary part is

$$Im\left(\frac{k\phi_{1a}}{\partial_y\phi_{1a}}\right)_{\text{ramp}} = \frac{\pi k\epsilon R_1 sgn(\gamma)}{4\cosh^2[k(l-b)]} \tag{37}$$

Taking the imaginary part of (32) and equating to (37) gives

$$\beta_2 = \pm\sigma R_1 \tag{38}$$

where β_2 (and also γ) could be of either sign and σ is a characteristic of the slow–wave structure, the tube and the operating point. For our model, it is given by

$$\sigma = \frac{\pi\omega_1}{4\Omega\sinh[2k(l-b)][1 + \dfrac{s\omega_1/c}{\sin(2s\omega_1/c)}]} \tag{39}$$

where ω_1 is the real part of ω. The value of γ follows from (35). Note that it is of order ϵ and therefore small. β_2 is also small due to the *sinh* in the denominator of σ, which is a function of the depth of the vacuum region.

We now have the damping rate for any anode wave satisfying the wave–particle resonance condition at the edge of the sheath. Although this damping is small, the combination of its smallness with the steep ramp will drive a nonlinear diffusion process or order one which will modify the original ramped density profile. We show how this occurs on the next section.

V THE QUASILINEAR DIFFUSION PROCESS

Davidson [2] was the first to recognize the importance of the quasilinear diffusion for nonneutral plasmas. This diffusion process also occurs naturally at second order in a multiple-scale analysis of the cold–fluid equations [24]. The key quantity is the

nonlinear diffusion coefficient, D, given by (21). It has a very simple interpretation if one expresses it in terms of the Lagrangian vertical displacement, ξ_y, defined by

$$\xi_y = i\frac{v_{1y}}{\omega_e} = i\frac{p}{\omega_e A} \tag{40}$$

Thus D is simply

$$D = \sum_k 2\gamma_k |\xi_y|^2 e^{2\gamma_k t} \tag{41}$$

showing that wherever the Lagrangian vertical displacements are large, there will be a large diffusion of the sheath. The largeness of the vertical Lagrangian displacement comes from the resonance condition, ω_e, vanishing along the ramp, where there is also a large density gradient. It is the combination of these two factors, the resonance condition and the steep density gradient, that generates a rapid deterioration of the initial ramped density profile. Another way of looking at this is to realize that when $\omega_e = 0$, then the electron is moving in phase with the electric field. Thus in the rest frame of the moving electron, the electron feels a steady and constant electric field acting on it. Thus it executes a large displacement.

From (29) and (30), we have that the constant, C_1, is given by

$$C_1 = \frac{i\epsilon k R^2 E_{xa}}{2\sinh[k(l-b)]\cosh(kb)} \tag{42}$$

where E_{xa} $(= -ik\phi_{1a})$ is the x-component of the RF electric field at the tips of the vanes. Then from (35), (37), (39), (40) and (42), the value for ξ_y follows.

$$\xi_y = \frac{-E_{xa}}{2\Omega^2 \sinh[k(l-b)]}\left\{\frac{2(1-z)}{(1-z^2-R^2)} - 1 + \frac{}{2R}\ln\left[\frac{(R+z-1)}{(R-z+1)}\cdot\frac{(R+1)}{(R-1)}\right]\right\} \tag{43}$$

Clearly, the first term dominates since it can become singular when R^2 is less than unity.

Lastly, we need to perform the sum over states in (41). We assume that the bandwidth of the input pulse is much wider than that of the resonance, which is the same as taking the limit of ϵ becoming vanishing small. In this limit, one would average over $\gamma|\xi_y|^2$. Taking only the dominate term in (43) and the lowest order in σ, one then finds

$$D = \frac{\epsilon k |E_{xa}|^2 (1-z)^2}{\Omega^3 \sinh^2[k(l-b)]}\cdot \quad \left[\pi - \tan^{-1}\left(2\frac{1-z}{\sigma}\right) + \tan^{-1}\left(z\frac{1-z}{\sigma}\right)\right] \tag{44}$$

This diffusion coefficient is a maximum for z near σ, which is near the top of the ramp for σ small. It is also proportional to ϵ and therefore small. However, the density gradient is of order ϵ^{-1}. Thus this term will contribute a term of order unity to the evolution of the density profile, as one can see from (19). Furthermore, D has a very strong gradient with respect to y due to the tan^{-1} terms. Consequently, the initial evolution of the density profile will be govern by this term. From (19) and the above, we have

$$\begin{aligned} \partial_t n_0 &\sim (\partial_y D)\partial_y n_0 \\ &\sim \frac{\epsilon k |E_{xa}|^2}{\Omega^3 \sinh^2[k(l-b)]}\cdot\frac{\pi}{2\sigma\epsilon}\cdot\frac{\Omega^2}{\epsilon} \end{aligned} \tag{45}$$

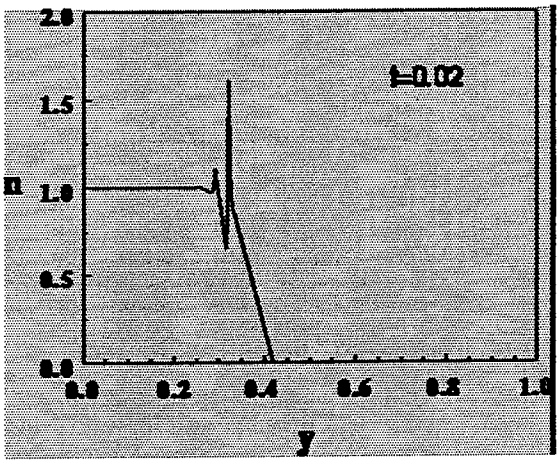


Figure 4: Numerical integration of (27) for typical parameters. Note that the strong, positive, density gradient that forms almost instantaneously.

which has a characteristic response time of

$$\Omega \Delta t \sim \frac{\Omega^4}{k^2 |E_{za}|^2} \sigma(\epsilon k) \sinh^2[k(l-b)] \tag{46}$$

There is a wealth of information compacted into this formula. First, one notes that as ϵ vanishes, the response time goes to zero. Thus a discontinuity in the density ($\epsilon = 0$) would instantaneously be changed, as soon as any resonant input pulse was injected. Second, the response time is inversely proportional to the power of the injected pulse. Therefore, there is a minimum input power required before profile modification can occur. Third, the response time is govern by the slow–wave structure, operating voltage and tube characteristics through the factors of σ and the *sinh* terms. These are all known to affect how a given tube operates.

Numerical integration of (19) for typical values demonstrates the rapid response time. In Fig. 4, we show an initial profile and its modification after a time of $.02/\Omega$. One can clearly see that a spike rapidly develops on the upper part of the ramp of the profile, containing a strong, positive density gradient. This structure would immediately be unstable to the diocotron instability [2] and its future evolution would be for this positive density gradient to degrade into a flat plateau. This is not seen in this numerical integration of (19) since we have not allowed for the diocotron instability to be present in the form of D used, Eq. (44).

There are two approximations used in obtaining the result in Fig. 4 that are, in hindsight, not valid. First, it was assumed that the input pulse was a step–function. In reality, it takes many periods for the input pulse to build up to its maximum amplitude. Second, we have assumed that only the growing mode would be important in the evaluation of the quasilinear diffusion coefficient. In reality, there is always a decaying mode as well and initially, it is usually of comparable amplitude. Thus only after times much larger than $1/\gamma_k$, would the expression (41) become valid. Nevertheless, what Fig. 4 does demonstrate is that strong density gradients are very unstable in the presence of resonant anode modes.

VI CONCLUSIONS

We have shown that there is a very rich structure contained in the edge of the sheath of a magnetron which is missed if one uses the classical Brillouin model. This structure will give rise to a damping of any wave which has a diocotron resonance, $\omega_e = 0$, somewhere along the ramp. We have also obtained an analytical approximation for the growth rate, which shows how the growth rate depends on the slow–wave structure, the tube parameters and the operating point. Then we have applied this result to calculate the quasilinear diffusion coefficient for an input pulse in a CFA, and have shown that the response is an immediate modification of the density profile, generating a very strong positive density gradient, which would then be degraded into a flat plateau by the diocotron instability [2]. Once this occurs, which would be within an RF cycle or so, the profile would become essentially a double–box profile, which then could support a resonant plasma mode [27], undamped. However, this resonant plasma mode would have a dispersion curve that would cross the anode mode at or very near the resonance. Thus these two modes would then linearly couple and one would then have to apply coupled–mode theory [26]. The effect of this is that both modes would then have a complex frequency, with a linear combination of them being the growing mode. Thus both the plasma mode and the anode mode would grow, feeding on the energy stored in the plasma.

What is now clear is that an initial Brillouin density profile will evolve. Clearly, there will be initial transients. But after these decay away, could the system perhaps end up in some stationary state, particularly if the input RF power were to remain constant? If such were to result, then that density profile would have to be a stationary solution of the quasilinear diffusion equation. Such solutions have already been discussed in the literature [24]. Key features of these solutions are: i) these profiles all have finite and nonvanishing, negative density gradients; ii) the density vanishes nowhere; iii) the density gradient is the least wherever the quasilinear diffusion coefficient is a maximum; iv) there exists a nonzero current flow; and v) they therefore are distinctly different from the classical Brillouin density profile. The main difficulty in determining these solutions lies in the consistency requirement. They would have to be determined such that the following conditions were satisfied. First, in the given density profile, which is such a stationary solution, one must find the solutions of the linearly perturbed equations. Then from these solutions, one must construct the quasilinear diffusion coefficient. Next, the integration of the stationary quasilinear diffusion equation, for that obtained quasilinear diffusion coefficient, must return back exactly the same density profile that one started with. At the moment, we do not know if such solutions do exist. However if such profiles could be found, then one would have a means for predicting the current and gain for a particular device.

ACKNOWLEDGMENTS

This research was supported in part by the Air Force Office of Scientific Research, under grant number F49620-93-1-0088 and the Naval Surface Warfare Center, Crane Division.

References

[1] D.J. Kaup and Gary E. Thomas, *Creation of a Resonant Diocotron Mode*, to appear in Phys. of Plasmas.

[2] R. C. Davidson, Phys. Fluids **28**, 1937 (1985);

[3] Y. Y. Lau and D. Chernin, Phys. Fluids B **4**, 3473 (1992).

[4] Y. Y. Lau, P. J. Christenson and D. Cherin, Phys. Fluids B **5**, 4486 (1993).

[5] P. J. Christenson and Y. Y. Lau, Phys. Plasmas **1**, 3725 (1994).

[6] O. Buneman, R. H. Levy, and L.M. Linson, J. Appl. Phys. **37**, 3203 (1966).

[7] R. V. Loveland and E. Ott, Phys. Fluids **17**, 1263 (1974).

[8] J. Swegle and E. Ott, Phys. Fluids **24**, 1821 (1981).

[9] J. Swegle, Phys. Fluids **26**, 1670 (1983).

[10] D. Chernin and Y. Y. Lau, Phys. Fluids **27**, 2319 (1984).

[11] R. C. Davidson, Phys. Fluids **28**, 377 (1985),

[12] T. M. Antonsen, Jr., E. Ott, C. L. Chang, and A. T. Drobot, Phys. Fluids **28**, 2878 (1985).

[13] R. C. Davidson and K. T. Tang, Phys. Fluids **28**, 1169 (1985).

[14] H. S. Uhm, Phys. Fluids B **4**, 740 (1992).

[15] S. Riyopoulos, Phys. Rev. E **47**, 2839 (1993).

[16] S. Riyopoulos, Phys. Fluids B **5**, 4162 (1993).

[17] S. A. Riyopoulos, Phys. Fluids B **3**, 3505 (1991).

[18] S. A. Riyopoulos, D. P. Chernin, and A. T. Drobot, J. Opt. IEEE Transactions on Electron Devices **39**, 1529 (1992).

[19] G. E. Dombrowski, IEEE Trans. Electron Devices **ED-35**, 2060 (1988).

[20] A. Palevski, G. Bekefi, and A. Drobot, J. Appl. Phys. **52**, 4938 (1981).

[21] Mark K. Jablonski [M. Sc. Thesis, MIT (1992)].

[22] D. J. Kaup and G. E. Thomas, Phys. Fluids B **4**, 2640 (1992).

[23] J. C. Slater, *Microwave Electronics* (Van Nostrand, Princeton, NJ, 1959), Chap. 13.

[24] D. J. Kaup and G. E. Thomas, Stud. Appl. Math **81**, 37 (1989); *ibid.* **83**, 271 (E) (1990).

[25] S. A. Prasad, G. J. Morales, and B. D. Fried, Phys. Fluids **30**, 3093 (1987).

[26] Hermann A. Haus and Weiping Huang, Proceedings of the IEEE, **79**, 1509 (1991).

[27] D. J. Kaup and Gary E. Thomas, J. Appl. Phys. **71**, 5752 (1992).

[28] D.J. Kaup, and G. E. Thomas, Phys. Fluids **31** 2362 (1988).

[29] P. G. Drazin and W. H. Reid, *Hydrodynamic Stability*, Ch. 4 [Cambridge University Press, New York, (1981)].

Effect of Random Secondary Emission Velocities in Electron Multipactors

Spilios Riyopoulos, David Chernin and Demos Dialetis
Science Applications International Corporation
McLean, VA 22102

Abstract

Traditionally, the modeling of rf driven electron cascades (multipactors) have been deterministic, employing a given emission velocity for all secondaries. Here we introduce stochastic effects caused by the random emission velocity. By combining the emission related random phase kick with the focusing rf action it is shown that the multipactor phase, though wandering erratically, nevertheless stays in the vicinity of a stable phase-locked multipactor phase; the rms phase deviation from phase locking is directly proportional to the rms fluctuation in the secondary emission. Therefore, for sufficiently small secondary velocities, as in most cases of interest, the modeling of a multipactor with zero emission velocity is sufficient to determine the actual multipactor stability. It follows that multipactor behavior depends on only *two* control parameters, related to the normalized rf and magnetic field strengths.

Multipactor is a resonant discharge produced by an rf field in which an explosive growth (avalanche) in the electron population can occur via secondary emission driven by the rf. Whenever electrons energized by rf waves are driven back into a surface, secondaries are produced. The secondary yield depends on the impact energy and angle, the surface properties and the direction of the rf field at the time of impact. Under certain conditions, the phase of the secondary electrons remains "locked" with the rf field driving the impacts, so that secondaries are produced always at "favorable" phase to continue the process. If more than one electron is emitted for each primary, the electron population can grow sizable enough to dissipate a significant fraction of the rf power inside the cavity before saturation due to space charge effects sets in.

Most of the previous studies[1–4,6] have considered deterministic models with constant

secondary emission velocity. Here we address the question whether phase-locking with the rf can be maintained when random emission effects are included. We proceed in two steps. First the most general results[5] for multipactor in crossed electron and magnetic fields are reviewed. Next the random emission effects are superimposed as a perturbation. In conclusion it is argued that when the emission velocities are small compared to the velocities obtained through the rf acceleration, the multipactor dynamics is sufficiently approximated by a deterministic model with zero emission velocity.

Assuming that all secondaries are emitted with the same initial velocity, the relation between the emission phase ϕ_n and the subsequent impact phase ϕ_{n+1} was found[5] to be

$$F_N(\phi_n,\phi_{n+1}) \equiv \frac{\mathcal{E}}{\Omega^2-1}\left\{sin(\phi_{n+1})-\frac{1}{\Omega}\,cos\phi_n\,sin\big[\Omega(\phi_{n+1}-\phi_n)\big]-sin\phi_n\,cos\big[\Omega(\phi_{n+1}-\phi_n)\big]\right\}$$
$$+\frac{u_y}{\Omega}\,sin\big[\Omega(\phi_{n+1}-\phi_n)\big]-\frac{u_x}{\Omega}\left[1-cos\big[\Omega(\phi_{n+1}-\phi_n)\big]\right\}-d=0, \qquad (1)$$

Relation (1) covers the most general case of either single or two-surface multipactors, where the time between successive impacts is a multiple of the wave period (half-period) for single (two surface) multipactors is

$$\phi_{n+1}-\phi_n=\tau\simeq 2\pi N, \qquad (2)$$

$N = integer, \qquad d=0 \qquad$ for single surface

$N = half-odd, \qquad d=1 \qquad$ for two surface.

(notice that the single surface multipactor is *not* the $d=0$ limit of the two surface case), and the following dimensionless variables are used,

$$\mathcal{E}=\frac{|e|V_{rf}}{m\omega^2D^2}, \qquad \Omega=\frac{\omega_c}{\omega}, \qquad u_i=\frac{v_{oi}}{\omega D}. \qquad (3)$$

ω is the rf frequency, $\omega_c = eB_o/mc$ is the cyclotron frequency, and D, $d=1$ are respectively the actual and the normalized plate separation for two-surface multipactor. The parameter $\mathcal{E}$ may be thought of as a measure of the electric field strength and Ω as a measure of the magnetic field strength; without loss of generality, we will take both $\mathcal{E}$ and Ω to be non-negative. The parameters $u_i,\ i=x,y$ are the normalized initial velocities for the ejected electrons.

Equation (1) may be viewed as an implicit equation for the arrival phase ϕ_{n+1} in terms of the launch phase ϕ_n. The fixed phase(s) correspond to flight time τ exactly equal to $2\pi N$ in (2). The general equation for the fixed point(s) φ follows from (1) letting $\phi_n = \varphi$, $\phi_{n+1} = \varphi + 2\pi N$,

$$\mathcal{F}_N \equiv \frac{\mathcal{E}}{\Omega^2 - 1}\left\{sin(\varphi + 2\pi N) - \frac{1}{\Omega}\, cos\varphi\, sin(2\pi N\Omega) - sin\varphi\, cos(2\pi N\Omega)\right\}. \qquad (4)$$
$$+\frac{u_y}{\Omega}\, sin(2\pi N\Omega) - \frac{u_x}{\Omega}\,[1 - cos(2\pi N\Omega)] - d = 0$$

An electron starting *exactly* on the fixed phase would create an infinite sequence of secondaries. This is not terribly interesting, however, given the vanishing probability of a seed electron at exactly the right phase. The deciding factor is the behavior of electrons in the vicinity of the fixed points. The phase of an electron that for some reason started its journey near a fixed point may either (a) converge to the fixed point as the number of iterations increases or (b) diverge from it. Fixed points with property (a) are *stable* fixed points and can lead to multipactors. Fixed points with the opposite property (b) are *unstable* and lead to truncated cascades. Given the mapping function $F_N(\phi_n, \phi_{n+1})$, the multipactor question boils down to the existence and stability of its fixed points. The fixed points of (1) have been obtained as functions of the control parameters $\mathcal{E}$, Ω and $\mathbf{u}$ by solving (4). Multipactor is possible in the parameter space where (a) fixed points exist and are located in the "favorable phase" region $0 \le \varphi < \pi$, (b) the fixed points are stable,

$$|G| < 1, \qquad where \qquad G \equiv \frac{d\phi_{n+1}}{d\phi_n} = -\left(\frac{\partial F(\phi_n, \phi_{n+1})/\partial\phi_n}{\partial F(\phi_n, \phi_{n+1})/\partial\phi_{n+1}}\right)_{\phi_n=\varphi,\ \phi_{n+1}=\varphi+2\pi N}. \qquad (5)$$

(c) there is no surface impact prior to the resonant time $\tau = 2\pi N$ and (d) the impact energy ε is such that $\delta > 1$, where $\delta(\varepsilon)$ is the secondary yield. An example of multipactor prone area for the case of two-surface, period 3π multipactor (i. e. one impact every one-and-a-half rf period) is shown in Fig. 1. More results on period 2π single-surface and period π two-surface multipactors are found in Ref. 5.

It has been assumed so far that the secondary emission velocity is the same for every impact. In reality the ejection velocity for a secondary is not correlated with the impact

velocity and changes randomly at each step. The relation (1) between launch and arrival phase thus becomes a function of a random variable $\mathbf{u_n}$ depending on the step number n

$$F_N(\phi_n, \phi_{n+1}; \mathbf{u}) \rightarrow \tilde{F}_N(\phi_n, \phi_{n+1}; \mathbf{u_n}), \tag{6}$$

(the dependence on the other control variables is implied). One may now question whether the defocusing effect of random emission velocity completely destroys the phase locking with the rf. The validity of all approaches neglecting random effects depends on how the above issue is settled.

Though a fixed point does not exist when $\mathbf{u_n}$ is randomly distributed we can try to see if the random cascade stays in the neighborhood of a fixed point for an "ideal" case with fixed $\mathbf{u}$. That can happen if the phase locking effect from the rf interaction balances the random phase shifts from the random emission velocity. Let us compare the evolution of two processes with similar initial conditions. The idealized reference case has zero emission velocity at each step. In general this leads to an avalanche characterized by a fixed point φ_o; furthermore the rate of convergence towards φ_o is given by

$$\varphi_{n+1} - \varphi_o \simeq G_o(\varphi_n - \varphi_o), \tag{7}$$

where $\varphi_n = mod(\phi_n,\ 2\pi N)$, $G_o \equiv G(\varphi_o, \Omega,\ \mathcal{E},\ \mathbf{u} = 0)$ and G is given by (5). For the realistic case with random secondary velocity, it is shown that the rate of convergence (or divergence) is governed by

$$\varphi_{n+1} - \varphi_0 \simeq G_o(\varphi_n - \varphi_0) + \nu_n, \tag{8}$$

where the random phase "kick" ν_n is related to the random emission velocity $\mathbf{u_n}$ via

$$\nu_n \simeq -\mathbf{u_n} \cdot \left(\frac{\partial F/\partial \mathbf{u}}{\partial F/\partial \phi_n}\right)_0, \qquad \frac{\partial}{\partial \mathbf{u}} \equiv \hat{\mathbf{x}}\frac{\partial}{\partial u_x} + \hat{\mathbf{y}}\frac{\partial}{\partial u_y}. \tag{9}$$

The subscript (0) denotes the value at $\phi_n = \varphi_0$, $\phi_{n+1} = \varphi_0 + 2\pi N$ and $u = 0$. The linearized relation (8) holds when the emission velocity u_n is much smaller than the velocity obtained from the rf acceleration, which is true in most cases of interest.

To study the dynamics of the stochastic map (8) we iterate once more[7] getting

$$\varphi_{n+2} - \varphi_0 \simeq G_0^2 \ (\varphi_n - \varphi_0) + G_0 \nu_{n+1} + \nu_n. \tag{10}$$

Now set $\Delta\varphi_n \equiv \varphi_{n+1} - \varphi_o$ and let $(d/dn)\Delta\varphi_n \simeq (\Delta\varphi_{n+2} - \Delta\varphi_n)/\Delta n$ where $\Delta n \equiv (n+2) - n = 2$. Assuming that $\Delta\varphi_n$ changes slowly[5], i.e. $|(\Delta\varphi_{n+2} - \Delta\varphi_n)/\Delta\varphi_n| << 1$, then equation (29) is the discretized version of the differential equation

$$\frac{d}{dn}\Delta\varphi = -\frac{1 - |G_0|^2}{2} \ \Delta\varphi + \frac{\nu + G_0\hat{\nu}}{2}, \tag{11}$$

where n is treated as a continuous index according to $f_{n+1} \rightarrow f(n)$ and $\hat{\nu} = \nu(n-1)$. Equation (11) is the well known Langevin equation, describing a Brownian motion in phase $\Delta\phi$ under a friction "force" $-(1/2)(1 - |G_0|^2) \ \Delta\phi$ and a random stirring "force" $(1/2)(\nu + G_0\hat{\nu})$. Its solution depends on the statistical properties of the random variable. It is reasonable to assume that the secondary emission velocities are uncorrelated,

$$< \mathbf{u_n u_m} >=< u^2 > \delta_{n,m}. \tag{12}$$

For an ergodic process, the equivalence between ensemble average and "time" average over dn leads to

$$\int dn \ \nu(n)\nu(m) =< \nu^2 > \delta(n-m), \tag{13}$$

where, according to (28), $< \nu^2 >$ is given by

$$< \nu^2 >= \frac{< \left(\mathbf{u}\cdot\left(\partial F/\partial \mathbf{u}\right)_0\right)^2 >}{\left(\partial F/\partial \phi_n\right)_0^2}. \tag{14}$$

Under the above statistical correlations, traditionally employed in random walk problems, one can show that the phase excursion $\Delta\varphi$, solution of Eq. (11), is bounded when the friction force is restoring, i.e. when $|G_0| < 1$. Furthermore, the long time-average of the phase excursion is given by

$$< \Delta\varphi^2 >\equiv< |\varphi_n - \varphi_0|^2 >= \frac{1 + |G_0|^2}{1 - |G_0|^2} \ < \nu^2 > . \tag{15}$$

thus the multipactor stays nearly phase-locked when the rhs of (15), carrying the rms velocity fluctuations (14), is small.

Equations (11) through (15) lead to the following conclusions. If the secondary emission mean square velocity is sufficiently small, so that $< \Delta\varphi^2 >$ given by (15) is small, a random emission rf-driven cascade is stable whenever the ideal cascade with zero emission velocity is. The impact phase for the random cascade wanders erratically around the fixed point φ_0 of the ideal case; yet the average mean square distance $< |\varphi_n - \varphi_0|^2 >$ remains small and bounded by (8). Around that value of $\varphi_n - \varphi_0$ the focusing action from the rf interaction balances the dispersive effects of the random emission velocity. Given that under normal circumstances the emission energy of a few $eV's$ corresponds to $< u^2 >=< v_o^2/\omega^2 D^2 > \sim 10^{-3}$ for $\omega = 2\pi f$, $f = 1$ GHZ and $D = 1$mm, secondary emission "noise" can destabilize a cascade only (a) when the ideal cascade is near marginal stability, i.e. $|G_0| \simeq 1$, (b) when the fixed phase is a very sensitive function of u, $\partial F/\partial \mathbf{u} >> 1$, and (c) when $\partial F/\partial \phi_n \simeq 0$. Case (b) occurs near the boundary $\mathcal{E} = \mathcal{E}_{min}(\Omega, d, \mathbf{u})$ for the fixed points existence, where a small change in u can significantly alter the fixed point value, or even make a fixed point to disappear.

In conclusion, the existence and stability of a realistic random emission multipactor is covered by the existence and stability criteria for an idealized, zero emission velocity multipactor, provided that the mean secondary velocity is sufficiently small. That has the rather remarkable effect of reducing the number of the independent control parameters for the process. Inspection of the "ideal" Eqs. (1)-(4) reveals that the multipactor parameter space is spanned by *four* control parameters; the six independent quantities of the problem ω, ω_c, V_{rf}, $\mathbf{v}_o$ and D combine into $\Omega \equiv \omega_c/\omega$, $d/\mathcal{E}$ and $\mathbf{u}/\mathcal{E}$. By limiting the cases of interest to $\mathbf{u} = 0$ we are left with only *two* independent parameters: Ω and $\mathcal{E}/d$. The single surface multipactor $d = 0$ depends only on Ω.

Acknowledgments

We wish to acknowledge discussions with Y. Y. Lau and R. Kishek. Work supported by the U. S. Naval Research Laboratory, contract #N00014-92-C-2030.

References

[1] P. T. Farnsworth, "Television by electron image scanning," J. Franklin Institute, vol. 218, pp. 411-444 (1934).

[2] J. R. M. Vaughan, "Multipactor," IEEE Trans. Electron Devices, vol. 35, 1172 (1988).

[3] J. R. M. Vaughan, "Observations of Multipactor in Magnetrons", IEEE Trans. Electron Devices vol. 15, 883 (1968).

[4] H. McDowell, "Multipactor Discharge Across a Magnetic Field", Varian interoffice memo (Varian, Beverly MA) (1976).

[5] Spilios Riyopoulos, David Chernin and Demos Dialetis, "Theory of Electron Multipactor in Crossed-Fields", Physics of Plasmas **2**, 3194 (1995).

[6] R. Kishek and Y. Y. Lau, "Interaction of Multipactor Discharge and RF Circuit", Phys. Rev. Lett **75**, 1218 (1995).

[7] When G is negative the sign of $\Delta\varphi_{n+1} \simeq G\Delta\varphi_n$ alternates from step to step. Hence from $\Delta\varphi_{n+1} - \Delta\varphi_n = (G-1)\Delta\varphi_n$ we have $|(\Delta\varphi_{n+1} - \Delta\varphi_n)/\Delta\varphi_n)| = |G| + 1 > 1$. The map (8) must be iterated twice to ensure small relative changes in $\Delta\varphi$ when $-1 < G < 0$.

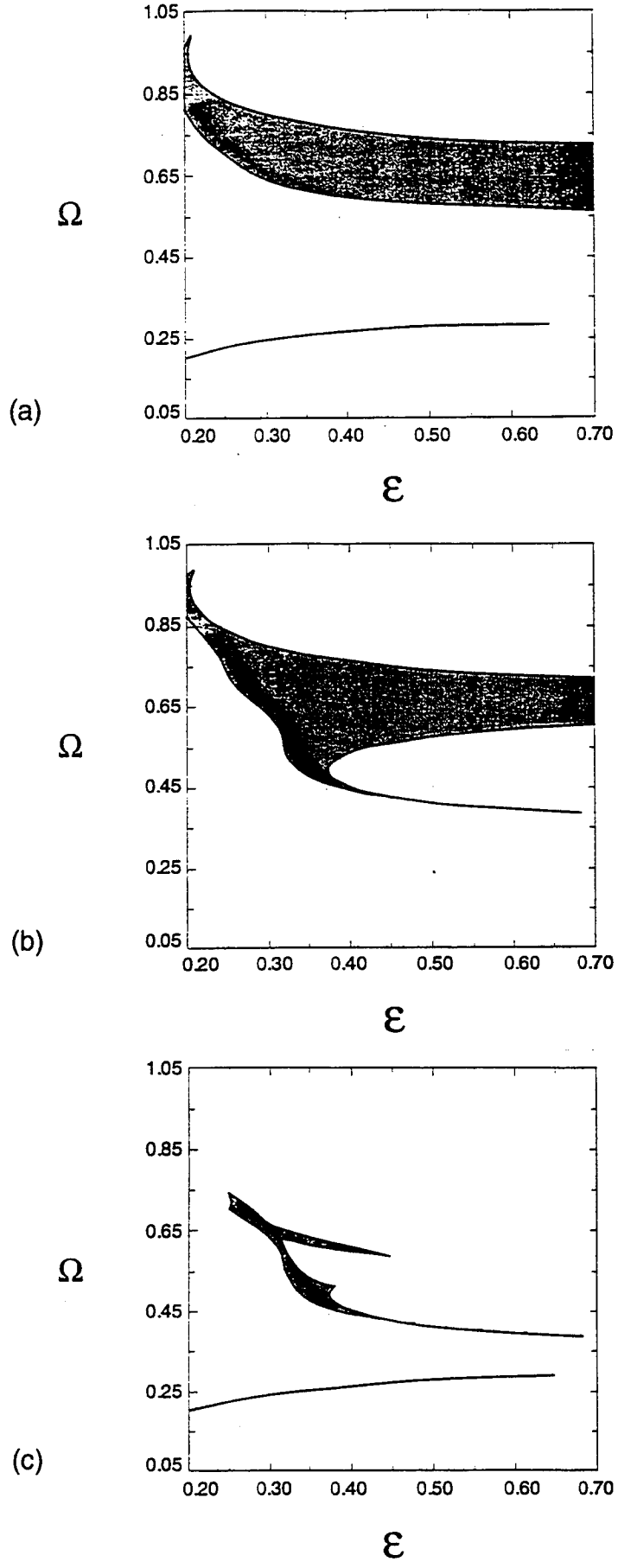


Figure 1. Parameter space for period 3π, two-surface multipactor. Dynamically allowed area (shaded) for (a) first fixed point, (b) second fixed point, (c) combination of dynamical and secondary emission criterion $\delta>1$ for BeO.

Electron Sheaths in a Crossed-Field Gap — Equilibrium Solutions and Transition to Turbulence *

Peggy J. Christenson and Y. Y. Lau

Department of Nuclear Engineering and Radiaological Sciences
University of Michigan,Ann Arbor, Michigan 48109-2104
e-mail: peggyjo@engin.umich.edu, or yylau@engin.umich.edu

Abstract

There is renewed interest in the equilibrium solutions and the transition to turbulence of electron sheaths in a crossed-field gap. Here, an analytic theory is presented which yields the maximum transmittable current across an anode-cathode gap which is embedded in an arbitrary transverse magnetic field (B). The limiting current is found to be relatively insensitive to B for $B < B_H$, where B_H is the Hull cutoff magnetic field required for magnentic insulation. For values of magnetic field above B_H ($B > B_H$), an analytic theory is presented for the critical injected current beyond which a transition from laminar to turbulent behavior occurs within the electron sheath. The analytic theories are found to be in excellent agreement with particle simulations, from which it is apparent that the behavior of the sheaths is quite different, depending on whether $B > B_H$, or $B < B_H$. For example, for many cases above the Hull cutoff, itt is found that there is no electrostatic potential minimum in the equilibrium solution which is a sharp contrast to the regime below the Hull cutoff magnetic field. However, according to the simulations, a potential minimum always appears in front of the cathode whenever the injected current exceeds the critical value. The spatial extent and the frequency of oscillations of this microsheath depends on the injected current, injection energy and magnetic field ($> B_H$). This study seems to have added sustenance to the notion, widely held in the community of ultralow noise crossed-field amplifiers, that a necessary condition for quiescent behavior in a crossed-field gap is that the electron emission be limited.

*Supported by NRL under grant N00014-93-1-G032.

I Introduction

When a sufficiently strong transverse magnetic field B is imposed across an anode-cathode gap, electrons released from the cathode will not be able to reach the anode. Under the steady state condition, that critical magnetic field is the Hull cutoff value which is given by $B_H = \sqrt{(2mV/eD^2) + (mu_0/eD)^2}$, where D is the gap separation, V is the gap voltage, e is the electron charge, and m is the electron mass [1]. The electrons are assumed to be emitted with velocity, u_0, normal to the cathode. It is important to note that B_H is independent of the emitted current density, J.

In this paper, we examine the regime $B > B_H$. Specifically, we present an analytic expression that gives the critical emission current density, J_c, above which steady state solution ceases to exist [6]. We employ a particle-in-cell (PIC) code [2] to examine the dynamical behavior of the gap, both below and above this critical current.

It is anticipated, on physical grounds, that such a critical current exists. If the emission current is vanishingly small, electrons are expected to follow the familiar single particle orbits in the external electric and magnetic fields, which are uniform. A collection of such particles represent a time-independent, laminar solution. If, on the other hand, electrons are released in great quantities, steady state solutions are not expected to exist, as seen from the familiar experiences on the virtual cathode [3]. The latter regime is most easily treated via particle simulations. The transition from laminar to turbulent solutions in a crossed-field gap is the subject of this paper.

This seemingly old problem is of considerable current interest especially in the area of noise analysis in the crossed-field amplifier (CFA). In many CFA's of practical significance, the electrons are released from the cathode (which is part of the interaction region) by secondary emission, and the operating magnetic field is always higher than B_H. Whether it is necessary, and, indeed, how, to control electron emission so as to reduce the amplifier noise has remained a very important consideration [4]. It in part motivates the present study.

II Theory

The above mentioned critical current is most easily established when the electrons are emitted normal to the cathode with a mono-energetic distribution. Consider the emitted current being raised, quasi-statically, from a very low value. All electrons are initially accelerated by the vacuum electric field inside the gap. They all turn back before reaching the anode if $B > B_H$. As the emitted current is raised, the initially accelerating electric field right in front of the cathode is reduced. The steady state solution fails to exist when the emitted current is sufficiently high so as to cause a nonlinear feedback mechanism to grow. If the space charge is too high, then the electrons being emitted from the cathode, which are initially accelerated, will be decelerated much more quickly due to the combined magnetic and electric fields. This causes the space charge in the A-K gap to rise since the magnetic field is actually the main force causing the electrons to return to the cathode. The $\vec{v} \times \vec{B}$ force, however is not strong enough to balance the coulomb force caused by the space charge. The consequences of trying to inject too much current into the gap will be discussed along with the simulation results but they are beyond the scope of the analytical theory. The

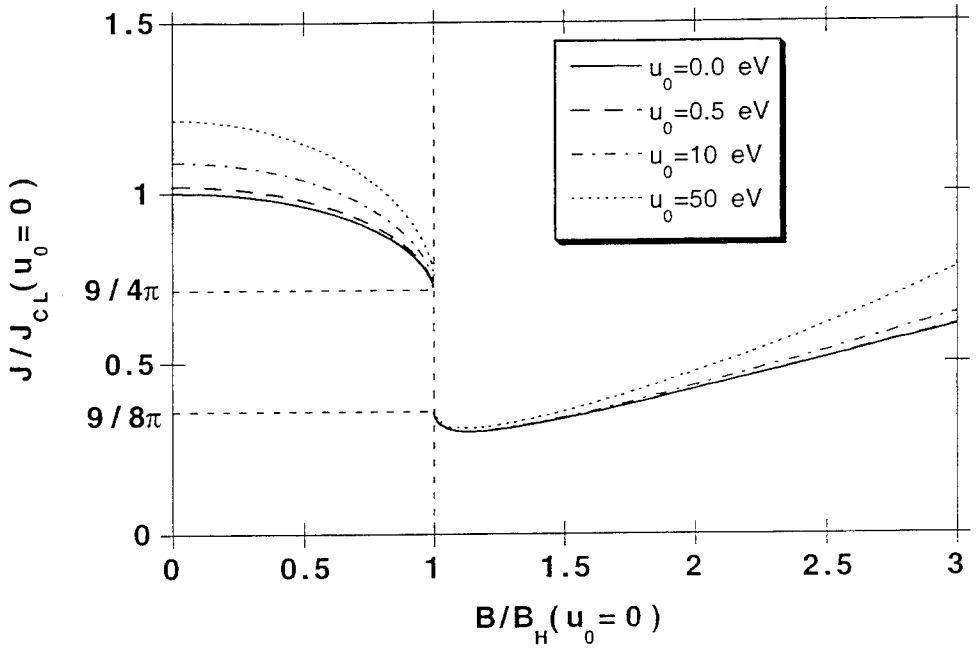


Figure 1: The critical current density (in units of the zero emission velocity Child-Langmuir value) above which steady state solutions cease to exit, as a function of the magnetic field B (in units of the zero emission velocity Hull cutoff value), for various electron emission velocities.

analytic theory is developed for a steady-state system. The critical current density is the maximum injected current density for which a steady-state solution exists.

Consider a time-independent, one-dimensional planar, non-relativistic model. In the Cartesian coordinates, the cathode is located at $x = 0$, and the anode at $x = D$. The anode is held at potential V with respect to the cathode, and an external magnetic field $B\hat{z}$ is applied. Let $\phi(x)$ be the self-consistent electrostatic potential, and $u(x)$ be the (non-negative) velocity component in the x-direction. Using conservation of energy,

$$e\phi(x) = \frac{m}{2}(u^2 + \Omega^2 x^2) - \frac{m}{2}u_0^2, \tag{1}$$

we may write the Poisson equation

$$\frac{d^2\phi}{dx^2} = \frac{en}{\epsilon_0} = \frac{2eJ}{m\epsilon_0} \tag{2}$$

in the Llewellyn form (see e.g., Birdsall and Bridges [3]):

$$u\frac{d}{dx}\left(u\frac{du}{dx}\right) + \Omega^2 u = \frac{2eJ}{m\epsilon_0}, \tag{3}$$

where $\Omega = eB/m$ is the electron cyclotron frequency, and a Lagrangian approach has been used, so $t = \int dx/u$. In Eq. (2), we have used the continuity equation, $nu =$ constant, which also implies that the emitted current density, J, is a constant. The fact that the electron density, n, is due to both the emitted electrons (outgoing from cathode) and the

returning electrons (incoming to the cathode) gives rise to the factor of two in the current density terms of Eqs. (2) and (3).

In terms of non-dimensional variables, $\tilde{x} = x/D$, $\tilde{t} = \Omega t$, $\tilde{J} = eJ/m\epsilon_0\Omega^3 D$, $\tilde{\phi} = e\phi/m\Omega^2 D^2$, $\tilde{V} = eV/m\Omega^2 D^2$, and $\tilde{u} = u/\Omega D$, the differential equation (3) may be integrated to yield the steady-state self-consistent orbit for an electron in a crossed-field gap: $\tilde{u}(\tilde{t}) = 2\tilde{J} + (\tilde{u}_0 - 2\tilde{J})\cos\tilde{t} + \tilde{c}\sin\tilde{t}$, and, $\tilde{x}(\tilde{t}) = 2\tilde{J}\tilde{t} + (\tilde{u}_0 - 2\tilde{J})\sin\tilde{t} + \tilde{c}[1 - \cos\tilde{t}]$. Here, $\tilde{c}$ is a constant of integration, $-\tilde{c}$ is simply the normalized electric field on the cathode surface. Now we may define $\tilde{x}_T$ as the normalized hub height, or maximum excursion of the electrons into the A-K gap, when the critical current is reached. Applying boundary conditions at $\tilde{x} = \tilde{x}_T$ and using conservation of energy and Gauss's law, we express the total potential drop across the gap as the sum of the potential at $\tilde{x} = \tilde{x}_T$, $\tilde{\phi}_T$, and the potential in the vacuum region, $\tilde{x}_T < \tilde{x} < 1$, thus, $\tilde{V} = \tilde{\phi}_T - \tilde{E}_T(1 - \tilde{x}_T)$, where $\tilde{E}_T$ is the normalized electric field at $\tilde{x} = \tilde{x}_T$. This may be written as

$$\begin{aligned}\tilde{V} = \; & \tilde{J}^2\tilde{T}[4\tan(\tilde{T}/2) - 2\tilde{T}] + 2\tilde{J}[\tilde{T} - \tan(\tilde{T}/2) \\ & + \tilde{u}_0(\tilde{T}\cot\tilde{T} - 1)] - \tilde{u}_0\cot\tilde{T}\,.\end{aligned} \tag{4}$$

In order to find the maximum injected current density, $\tilde{J}_c$, for which a steady state solution is possible, we take the derivative of $\tilde{J}$ with respect to $\tilde{T}$ (recall that $\tilde{V}$ is taken as a fixed parameter) and set $d\tilde{J}/d\tilde{T} = 0$. Thus we obtain another equation which is also quadratic in $\tilde{J}$,

$$\begin{aligned}0 = \; & 4\tilde{J}^2\left(\frac{\sin\tilde{T} - \tilde{T}\cos\tilde{T}}{1 + \cos\tilde{T}}\right) + 2\tilde{J}\left[\frac{\cos\tilde{T}}{1 + \cos\tilde{T}}\right. \\ & \left. + \frac{\tilde{u}_0}{\sin^2\tilde{T}}\left(\cos\tilde{T}\sin\tilde{T} - 1\right)\right] + \frac{\tilde{u}_0}{\sin^2\tilde{T}}\,.\end{aligned} \tag{5}$$

These last two equations are to be solved simultaneously for $\tilde{J}$ and $\tilde{T}$ to yield $\tilde{J}_c$ for a given normalized gap voltage, $\tilde{V}$ and electron emission velocity, $\tilde{u}_0$.

The solution of equations (4) and (5), $\tilde{J}_c$, is valid for $B > B_H$. It is shown in Fig. 1 for various values of injection velocity, u_0. The $u_0 = 0$ curve in Fig. 1 is valid for all gap voltages, V, and gap separation, D. The Other curves are obtained for $V = 12$ kV, and $D = 2.16$ mm. For completeness, Fig. 1 also includes the regime $B < B_H$, which was recently reexamined in considerable detail [5,7]. Thus, Fig. 1 provides the critical value of the emitted current, above which time-independent solutions cease to exist, for general values of magnetic field. The discontinuity in J_{CL} at $B = B_H$ reflects a different state of the solutions, a fact observed by Pollack [8], interpreted as the limiting current [5], and reaffirmed by the particle simulations of Verboncoeur and Birdsall [7]. For the case $B > B_H$, it may be shown that as $J \to J_c$, the maximum electron excursion in x, x_T, is simply the Brillouin hub height [3], $D[1 - \sqrt{1 - (B_H/B)^2}\,]$, which is always less than $D(B_H/B)^2$, the latter being the maximum electron excursion when the space charge is negligible.

One interesting result of this study concerns the case of zero emission velocity of the electrons. Below the Hull cufoff, $B < B_H$, the steady state solution which yields the maximum perfectly transmitted current density in the case of $u_0 = 0$ is space-charge-limited, that is, the emitted electrons are initially at rest and non-accelerated. This, of course, implies that the cathode surface electric field, E_c, is zero. One might be tempted to apply the same condition to the case of $u_0 = 0$ for $B > B_H$ as well; however, it is apparent from

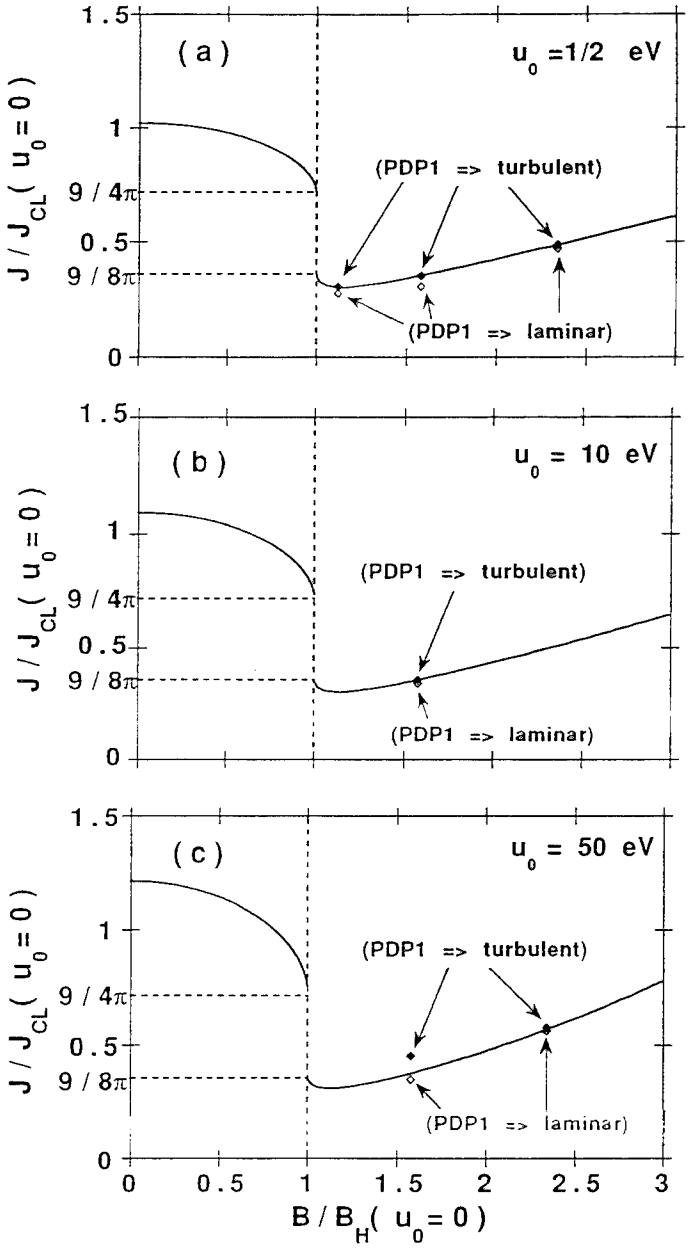


Figure 2: A comparison between the analytic theory (the solid curves) and particle simulation (the open diamonds, which denote quiescent cases, and the solid diamonds, which denote turbulent cases).

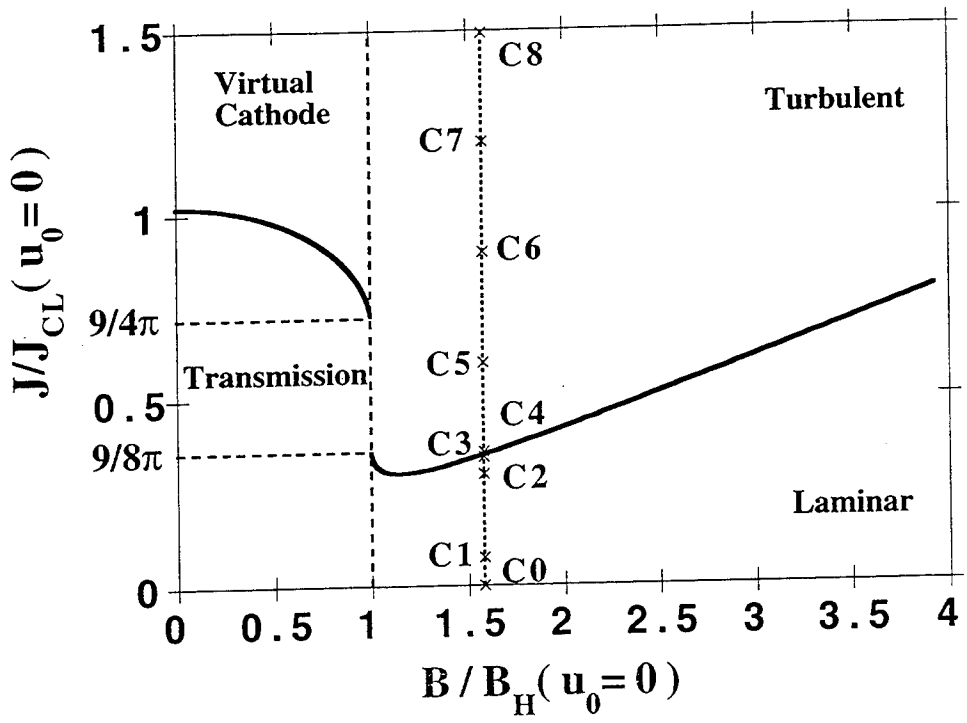


Figure 3: The critical current density (in units of the Child-Langmuir value for $u_0 = 0$) above which steady state solutions cease to exit, as a function of the magnetic field B (in units of the Hull cutoff value with $u_0 = 0$), for electrons emitted with velocity corresponding to 1/2 eV. The points marked C0, C1,...,C8 indicate the cases simulated.

the solution of Eqs. (4) and (5), that this is not necessarily true. Indeed, the maximum emitted steady-state current density for $B > B_H$, and $u_0 = 0$, is not achieved under the space-charge-limited condition. In fact, for most of the parameters used in this study for the particle simulations, the space charge limited regime cannot be reached.

For low emission velocity and an applied magnetic field of less than three times the Hull cutoff value, cathode surface electric field for a non-turbulent electron sheath will always be in the direction such that the electrons are accelerated away from the cathode upon emission. Thus, the crossed field gap cannot tolerate enough space charge (i. e., a large enough electron density) to shield the cathode from the externally applied voltage. This analytic result is verified by particle simulation. The good agreement between particle simulation and analytic theory is seen in Figures 2(a),(b),(c).

III Computer Simulation

We have extensively studied the regime $B > B_H$ using a particle-in- cell (PIC) code, Plasma Device Planar 1-Dimensional (PDP1) [2], especially as the injected current is increased (case C0,...C8 in Figure 3) for a set magnetic field strength. In the simulations, Figs. 4-6, the cathode was held at $V_c = -12000\ V$, while the anode was grounded, thus, $V = 12000$ V, we fixed $D = 0.00216\ m$, and $B = 0.27\ T$, yielding $B_H = 0.171\ T$ and $B/B_H = 1.579$. We assume a cathode area $A = 0.001492\ m^2$, thus, $J_c = 2.1 \times 10^5\ A/m^2$, and $I_c = 313\ A$. The electrons were injected as a cold beam normal to the cathode with, unless otherwise stated,

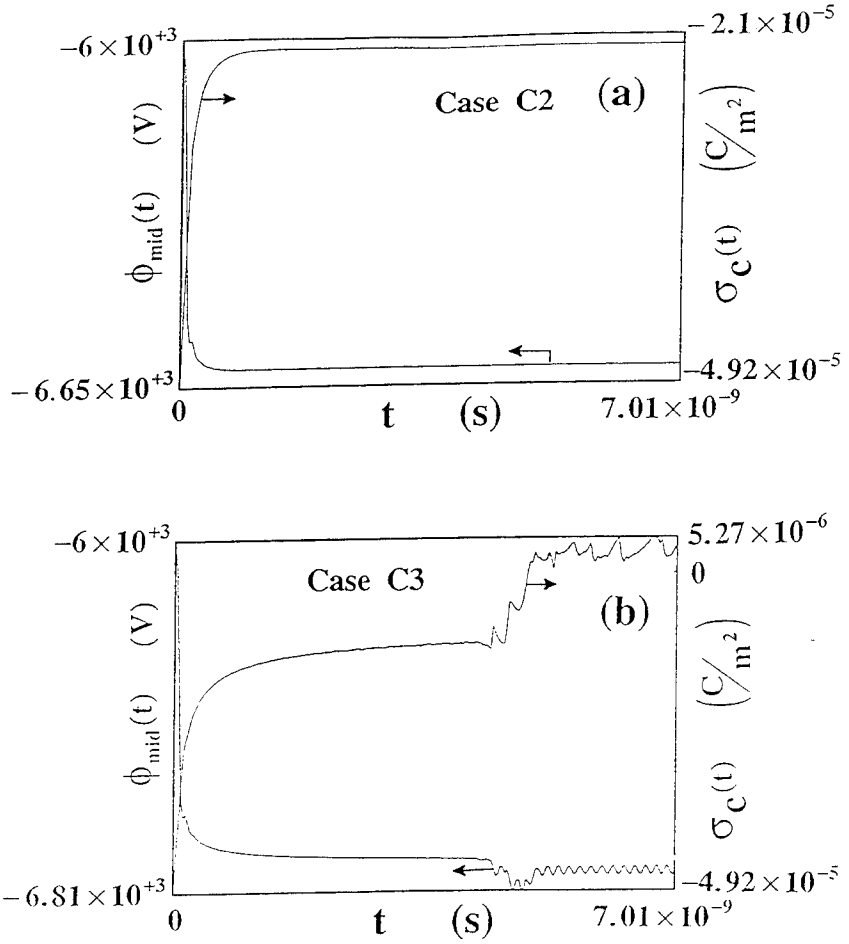


Figure 4: The potential at the midpoint of the crossed-field gap, ϕ_{mid}, and the cathode surface charge density, σ_c, as functions of time, for cases C2 ($I/I_c \approx 0.95$), and C3 ($I/I_c \approx 1.10$).

injection energy of 1/2 eV. (In order to study the effects of injection energy [9], and to better resolve the micro-sheath on the cathode, higher values of 10 eV, 50 eV, and 200 eV were also examined.)

The transition from laminar to turbulent behavior is clearly shown from the simulations just below transition, case C2 ($I = JA = 298$amps), and just above transition, case C3 ($I = JA = 343$amps). For case C2, the potential midway between the anode-cathode gap, $\phi_{\text{mid}}(t)$, and the cathode surface charge density, $\sigma_c(t)$, remain asymptotically constant [Fig. 4(a)], whereas those for case C3 break into oscillations for time $t \geq 4$ ns. The phase-space plot and density profile for case C2 [Figs. 5(a),and 5(b)] are dictated by regular single particle motion. The trajectory of one electron is repeated by all others, and this property is shared by low injection current cases, C0 and C1 in Fig. 3. The corresponding figures for case C3 show turbulent behavior [Fig. 5(c), (d)]. Note from Fig. 4(b) that at the onset of turbulence, $t \approx 4$ ns, the surface charge density on the cathode becomes positive, indicating that a potential minimum exists in front of the cathode. Thus, a micro-sheath is formed for case C3. This characteristic is shared by all cases above transition — C4, C5,...C8 in Fig. 3. Fig. 6 shows the frequencies of oscillation of the micro-sheath on the cathode surface, i.e. the frequencies of oscillation in σ_c, and the frequencies of oscillation of ϕ_{mid}, both as functions of the injected current, I_{inj}, for two values of electron injection energy 1/2 eV and

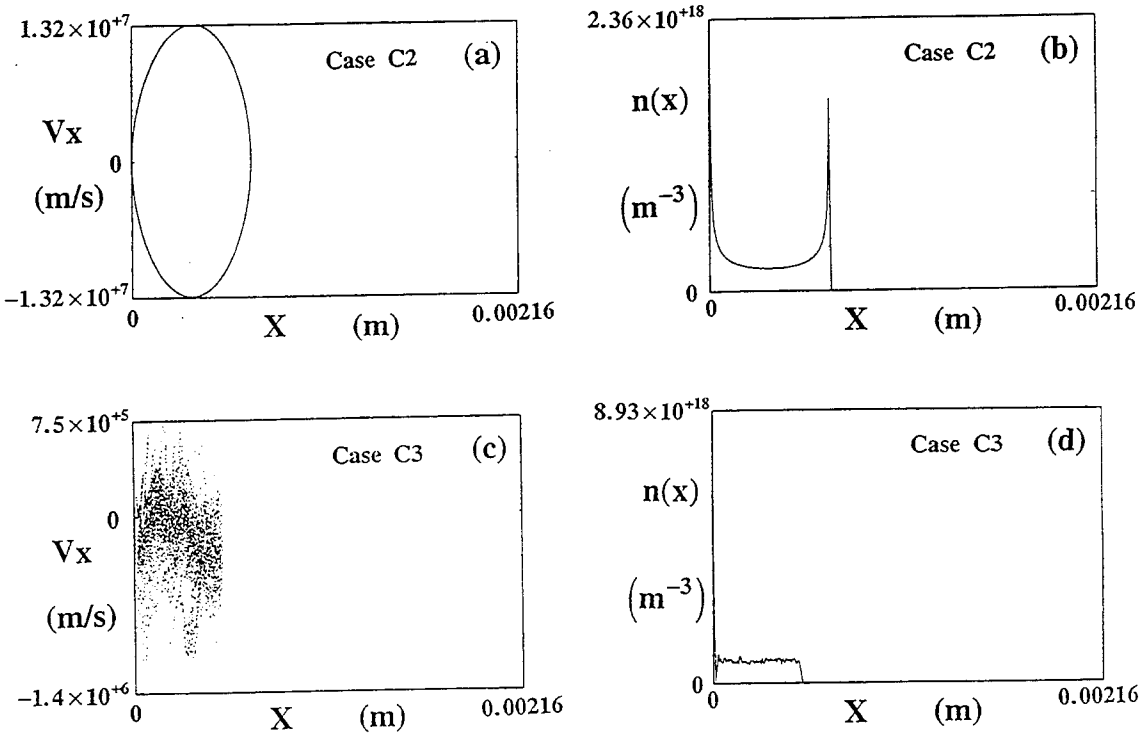


Figure 5: The phase-space plot, and the electron density distribution, $n(x)$, for cases C2 ($I/I_c \approx 0.95$), and C3 ($I/I_c \approx 1.10$).

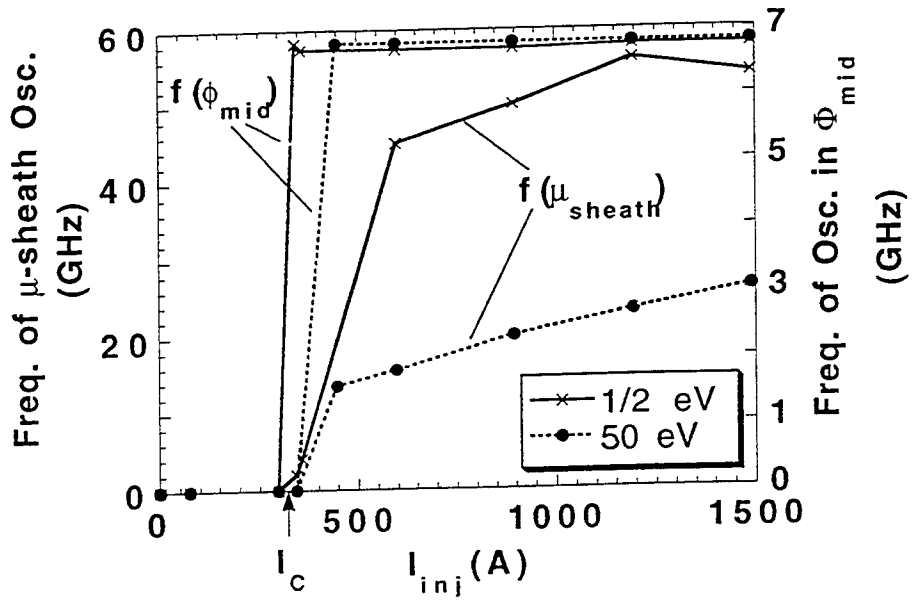


Figure 6: The frequencies of oscillation of the cathode surface charge density, σ_c, (i.e. of the micro-sheath on the cathode surface), and of the mid potential, ϕ_{mid}, as functions of the injected current, $I = I_{\text{inj}}$. Two injection energies (1/2 and 50 eV) are shown.

50 eV. Note from Fig. 6 that transition does occur when $I > I_c$.

The above results, together with our extensive numerical simulations show the following behavior. (1) For $I < I_c$, laminar flows do exist. In fact, the phase space trajectory shown in figure 4(a) is highly regular – the trajectory of one electron is repeated by all others. Its shape is very similar to that of a single electron in the vacuum gap. (2) There is qualitative change when I exceeds I_c by a few percent (the exact amount is not narrowed down in the simulations). The phase space is randomized and the x-component of the particle velocity is substantially reduced as seen in Fig. 5(c). The space charge density within the hub [Fig. 5(d)] is almost flattened, extending from the cathode to roughly the Brillouin height. (3) The surface charge on the cathode [Fig.4(b)] is positive, i.e., a potential minimum is always formed in front of the cathode when turbulent behaviors emerge from the numerical simulation. The depth of this potential minimum is on the order of the injection energy that is given to the electrons in the code. Thus, a micro-sheath is always formed right in front of the cathode for low injection velocity when the injected current exceeds some critical value. (4) This micro-sheath oscillates at a frequency that varies according to the emitted current and to the emission velocity (Fig. 6). (5) No electrons reach the anode in any of our runs for $B = 1.579B_H$. In fact, no electron reach the midpoint, $x = D/2$, in the gap. Because this problem is one dimensional, there is no variation in the fields in any direction parallel to the cathode surface. This means that diocotron or slipping stream instabilities are inherently nonexistent in this study. Thus, these findings do not contradict experimental results such as those discussed in the paper by T. J. Orzechowski and G. Bekefi [10]. (6) The potential at this midpoint oscillates at a frequency that is quite independent of the injected current and initial energy of the electron as can be seen in Fig. 6. Neither the micro-sheath oscillation frequency, nor the oscillation frequency in the mid potential corresponds to the cyclotron frequency, the plasma frequency, nor to the upper hybrid frequency. The physical origin of the oscillations are yet to be explained.

IV Conclusion

In summary, we find that a necessary condition for quiescent behavior in a cross-field gap is that the injection current must be below the analytically obtained critical current, J_c. This current is obtained by simultaneously solving Eqs. (4) and (5) for $B > B_H$, and was confirmed by particle simulation.

Acknowledgements

We are obliged to C. K. Birdsall, J. P. Verboncoeur and V. P. Gopinath for their generous assistance and for their kind interest in this work. We would like to also acknowledge helpful discussions with D. Chernin, N. Dionne, S. Riyopoulos, R. M. Gilgenbach, T. Ruden, and J. Saloom.

References

[1] Hull, A. W., Phys. Rev. **18**,31 (1921).

[2] PDP1(Plasma Device Planar 1 Dimensional), 1990-93 Regents of the University of California, Plasma Theory and Simulation Group, Berkeley, CA. Available from Software Distribution Office of the ILP, 205 Cory Hall, Berkeley, CA 94720, software@eecs.Berkeley.edu.

[3] See, e.g., Birdsall, C. K. and Bridges, W. B., **Electron Dynamics of Diode Regions.** New York, NY: Academic, 1966; Davidson, R. C., **Physics of Non-neutral Plasmas.** Redwood City, CA: Addison-Wesley, 1990; **High Power Microwaves.**, edited by Granatstein, V. L. and Alexeff, I., Norwood, MA: Artech House, 1987.

[4] Chernin, D., Drobot, A. and Kress, M., *Digest of IEEE IEDM* 1993, p. 773.

[5] Lau, Y. Y., Christenson, P. J. and Chernin, D., Phys. Fluids B **5**, 4486 (1993), and references therein.

[6] Christenson, P. J. and Lau, Y. Y., Phys. Plasmas **1**, 3725 (1994).

[7] Verboncoeur, J. P. and Birdsall, C. K., UCB/ERL memorandum **M93/86**, UC-Berkeley, CA (unpublished, 1993); also, *IEEE ICOPS*, June 1994, IEEE Cat. No. 94CH3465-2, p. 226.

[8] Pollack, M. A. and Whinnery, J. R., IEEE Trans. Electron Devices **ED-11**, 81 (1964); Van Duzer, T., IEEE Trans. Electron Devices **ED-8**, 78 (1961); Van Duzer, T., IEEE Trans. Electron Devices **ED-10**, 370 (1963).

[9] Vaughan, J. R. M., IEEE Trans. Electron Devices **ED-36**, 1963 (1989), and Shih, A. and Hor, C., IEEE Trans. Electron Devices, **40**, 824 (1993).

[10] Orzechowski, T. J. and Bekefi, G., Phys. Fluids **22**, 978 (1979).

THE FUTURE OUTLOOK FOR CROSSED-FIELD DEVICES

William C. Brown
Microwave Power Transmission Systems

The term "crossed-field devices" covers a broad category of devices, but I will confine my remarks to the applications and the future of crossed-field microwave tubes.

Crossed-field microwave tubes have already found broad application in radar, in industrial microwave processing and in the home in the form of the ubiquitous microwave oven. More recently they have found application in the generation of plasmas for precision etching and in new highly efficient electric lighting.

The pulsed magnetron was the heart of microwave radar developed during World War II. It was efficient, simple to fabricate, and produced high peak power in tubes designed from 500 MHz to 35 Hz. In the post war period the crossed-field device, in the form of the crossed field amplifier or CFA, found broad application because of its high efficiency and phase linearity over a broad range of frequency. The CFA also eliminated the magnetron deficiency of operating in two distinctive but generally unpredictable modes of operation, one noisy and one relatively noise free.

In industrial microwave processing the magnetron has found wide application because of its high efficiency, relatively low cost, and because it is not required to operate at a carefully controlled frequency. Most of the applications are at a frequency of 915 MHz where there is a magnetron available that has an operational efficiency of close to 90% and a power output ranging from 10 to 50 kilowatts.

As we look toward the longer range future, there is an application which involves a beaming of electric power in the form of microwaves to and from space and within space. One of the applications which is closely associated with a growing need for an environmentally acceptable source of energy is the Solar Power Satellite concept. In this concept energy is captured continuously from the sun in geosynchronous orbit and transported to Earth by means of a microwave beam.

The requirements placed on the microwave generator in one of the radiating modules in the electronically steerable phased array in space are very demanding in terms of low noise, high efficiency, low ratio of mass to power output, high gain, phase locking to the guidance system, and life measured in decades. In addition, the tube must adapt itself to changing output conditions of voltage and current from the photovoltaic solar array, and it must radiate its heat directly into space.

The device that is ideally suited to this application is a magnetron rated at about 4 kilowatts of power output. If the magnetron is 85% to 90% efficient it can radiate the heat generated by the small inefficiency directly into space with a low mass radiating fin composed of pyrolytic graphite whose heat conductivity is three times that of copper, whose density is one third that of copper, and whose radiation coefficient is close to that

of a black body. Further, if it is equipped with a buck boost coil to increase or decrease its magnetic field it can adapt itself to a wide range of operating conditions of the solar photovoltaic array without any need for additional power conditioning. The magnetron in this application is converted into a high gain, phase locked amplifier by operating it with another identical magnetron in a hybrid or magic T arrangement.

The design of the tube for the space application is based upon the design and performance of the ordinary microwave oven magnetron. The ordinary microwave oven magnetron was introduced into the SPS application by a proposed experiment of JPL to use the tube, because of its low cost, in a demonstration of an electronically steerable phased array at the Goldstone facility of JPL. Although this experiment did not materialize, the magnetron was thoroughly studied for the SPS application by a contract from NASA to the Raytheon Company. It was determined during this study that the microwave oven magnetron had a very low noise level and that this desirable state, along with long life, depended upon the preference of the tube to run in a mode associated with a temperature limited emission condition of the cathode.

Although there is ample experimental evidence that the microwave oven tube prefers to operate in this temperature limited emission condition of the cathode under a very wide range of operating conditions, there is no explanation at the present time as to why the tube prefers to operate in this manner. It is therefore desirable to have a theoretical explanation for this behavior, and one that is backed up by computer simulation.

A near term application of the microwave oven magnetron in wireless power transmission is that of supplying power to an aircraft operating at a high altitude for communication and surveillance purposes. For this application in an electronically steerable phased array, the microwave oven magnetron can be used as it is without scaling or modification. This magnetron can also be used without modification for beaming power into space to supply power for the electric propulsion on board inter-orbital space vehicles carrying material from low-Earth orbit to higher orbits, including orbits at geosynchronous distance.

For future effort on crossed field microwave tubes, I believe that the first priority effort should be to find an explanation for the desire of the microwave oven magnetron to operate in a highly desirable mode associated with a temperature limited emission condition of the cathode. An effort to further increase the efficiency of the microwave oven magnetron and related magnetrons and CFAs is also important. To my knowledge, there has never been a concerted program to do this. In my opinion the microwave oven magnetron should be operating at an efficiency of close to 80% rather than at a high of 70%. An effort should be expended in designing it for operation at a higher magnetic field which should provide it with an additional 7 to 10% efficiency. The important need for this is in wireless power transmission applications in the 2.45 Hz frequency region, particularly in space, but a more efficient tube would be useful for the current industrial and home applications of the crossed-field microwave tube.

A Proposed Two-Port, Unidirectional Magnetron Amplifier

George K. Farney
82 Herrick Road
Boxford, Massachusetts 01921
(508) 887-6029
Fax: (508) 887-5843

ABSTRACT

A brief description of contemporary techniques for signal injection into a magnetron is given. A two-port, unidirectional magnetron amplifier with higher gain and wider bandwidth is desirable. The need for special properties for a second port to achieve these goals is explained. An unsuccessful attempt at providing a second port for providing signal injection from a cathode structure is described. A new type of second port to be added to a rising sun anode is described. (U.S. Patent Number 5,084,651) Reasons why it is expected to have directional transmission properties are explained. The new concept has not been fully evaluated at cold test or in an operating tube. Further investigations are required to demonstrate the feasibility of achieving a new type of amplifier with improved properties.

There is continued interest in the use of injection locked magnetrons for generation of coherent microwave power sources. This was illustrated by comments of several of the speakers at this meeting. The basic concept of the injection locked magnetron dates back more than forty years. A single port magnetron is used typically with an attached three or four port microwave circulator. The circulator permits an appropriate input signal to be injected into the magnetron while providing the necessary isolation for the input signal source from the magnetron output power or from any reflected signals from the intended load.

Two approaches to signal injection are used. One is called injection locking, and the other is called injection priming. With injection locking, both the phase and frequency of the magnetron are essentially slaved to the injected signal throughout the magnetron pulse. The input signal can pull the oscillator frequency from its natural, free running frequency by an amount that depends on the external Q_E of the magnetron (hence controlling the attainable bandwidth) and by the magnitude of the input signal level (hence controlling the attainable gain). For injection locking the device operates much like a true amplifier but with limited capabilities. Gain is usually limited to 12-15 dB and bandwidth to 1-2 percent.

For injection priming, a much lower input signal level can be used whose only purpose is to control the starting phase of the magnetron pulse. After the tube is fully operational, the input signal can be removed because it will have no further effect on the magnetron performance. The magnetron will operate at its normal resonant frequency. The priming signal is sometimes more effective if it is actually below the free running frequency of the magnetron by some relatively small amount. However, the effect of the priming signal is to give an oscillator pulse with a much cleaner, pulse-to-pulse spectrum. The spectral quality will depend also upon the stability of the magnetron and upon the pulse modulator used for the tube. Injection priming is a very narrow band effect, but priming gains of 30-40 dB or more have been obtained.

Injection priming of a coaxial magnetron is especially useful to obtain a stable oscillator. The TE_{011} stabilizing cavity of the magnetron leads to a very stable oscillator once it has been fully started. When operated from a reliably stable modulator, successive pulses look very much alike. However, these tubes often exhibit more starting jitter than some conventional magnetrons, but

they are very amenable to injection priming to control leading edge jitter.

This feature was illustrated quite dramatically some years ago. Some interesting experiments were reported in private communications by Tom Schultz of the former Raytheon Microwave Power Tube Division in Waltham, Massachusetts. They had observed in some experiments that the leading edge jitter of a coaxial magnetron could be reduced significantly by irradiating the high voltage bushing of the cathode support using a low level signal from a microwave horn. There were no other physical connections to the tube. This is clearly a form of injection phase priming.

The concept of injection priming of a coaxial magnetron with an attached circulator for a radar transmitter was developed into a marketable system called MAPS (Magnetron Phase Stabilization) by the Varian Beverly Microwave Division. It was deployed in several systems.

Injection priming and narrow band injection locking of magnetrons have found relatively few applications. These vary from phase locked oscillators for linear accelerators to proposed giant phased arrays of magnetrons located on synchronous space satellites. These would be used to convert solar energy into microwave power to be beamed back to the earth's surface as a source of renewable energy. Other applications involve multiple tubes phase locked together for supplying power for industrial microwave heating and/or processing stations. All of these are essentially single frequency applications. But much interest exists in the possible use of injection locked magnetrons with more gain and wider bandwidth for more exotic amplifier operation. There is interest in chains of injection locked magnetron amplifiers to compete with other tube types because of the advantages of lower cost, smaller size, lower weight and lower voltage requirements for operation.

There is a fundamental limitation to the current approach to injection locked magnetrons and circulator concept. Using the same output port for both signal injection and for removing power from the tube does not permit increasing gain and bandwidth simultaneously. To increase bandwidth means reducing the external Q_E to lower the loaded Q_L of the tube. This means that the magnetron resonator system is further overcoupled thereby increasing the mismatch loss for signal injection; i.e., more of the input signal is reflected from the tube output port back into the load. A reduced signal is coupled into the anode for the electron motions within the tube. For a two percent operating bandwidth, the magnetron should have a loaded Q_L of 50 or less. The magnitude of the mismatch loss will depend upon the relative values of the internal Q_O and the external Q_E that lead to a loaded Q_L of 50.

Ideally, the magnetron should have two ports with one optimized (heavily overcoupled) to obtain the necessary output bandwidth and the second optimized (critically coupled or matched) to obtain maximum input power to the tube over the required operating bandwidth. It is not possible to just add another port similar to the normal output port but with different coupling factors. The principal of reciprocity will dictate that power will couple out both ports from the operating pi mode in amounts proportional to the coupling factors. Unidirectional amplification will not be obtained. Alternative configurations are needed. One approach that was investigated was derived from crossed-field amplifier experience.

Cold cathode crossed-field amplifiers have been fabricated with slow wave circuits on the cathode. The intended purpose was to provide increased gain by controlling the formation of electron spokes closer to the space charge source in the circulating hub of electrons. It was also thought that this approach would lead to better noise performance. An input signal was applied to one end of the cathode circuit while the other end of the cathode circuit was terminated in an absorptive load. DC isolation from the cathode voltage was used to protect the input signal source at ground potential. The low power end of the anode circuit was terminated in an absorptive load, and the high power output end of the circuit was connected to the output port of the tube. The electron spokes formed by the cathode circuit induce currents on the anode of the same frequency as the input signal. The cathode driven amplifier concept was investigated at the Raytheon Power Tube Division in Waltham, Massachusetts; at the Varian, Beverly Microwave Division in Beverly, Massachusetts; and at Litton Electron Device Division in Williamsport, Pennsylvania. These investigations occurred primarily in the late 1980's and early 1990's. The attainable gain was improved to 25-30 dB in some cases. There was no reliably significant improvement in noise

performance, and the concept was abandoned in favor of other approaches.

The concept of a circuit on the cathode to yield a two-port device was also applied to a magnetron at Varian BMD. The intent was to use the unidirectional flow of electrons from the cathode to anode to provide the signal isolation between ports. But the problem is more complex in a magnetron than in a CFA. In magnetrons the cathode must be heated to supply both primary and secondary electron emission for start of operation. This makes it very difficult to devise a suitable cathode slow wave circuit that can be heated and will match the anode circuit propagation characteristics. As an alternative, a cathode geometry was used with multiple radial probes extending from the cathode to couple a signal into the interaction space. A dc block was used to isolate the cathode voltage from the input signal source. However, this arrangement was reported to not be very effective in controlling both phase and frequency for signal injection locking. This possibly results from the radial probes not being able to control the space charge in the same way as the cathode circuit in the CFA. Also the reentrant, resonated anode of the magnetron with strong modes may be more dominant in controlling electron motion independent of the cathode than the broad band, matched, anode circuit of the cathode driven CFA. It seems more likely that two suitably isolated ports must be attached directly to the magnetron anode to get proper operation.

An alternative approach using two ports attached to the anode has been proposed by this author, but has not been fully evaluated at cold test or in an operating tube (U.S. Patent Number 5,084,651). The whole concept is involved and only a brief description of the coupling ports configurations will be given here. Hopefully it will encourage others to give some thought to how this problem can be solved.

The proposed approach uses a rising sun anode with a conventional port for the output and a second port with a special input network attached to the magnetron anode. The network is intended to function in one way when coupling a signal into the rising sun anode and function in a different way in response to the magnetron anode while generating pi mode power. This is accomplished using a two conductor input connection with attachments on the anode at positions of equal magnitude and phase when oscillating in the pi mode. The geometry is called a Direction Oriented Coupling (DOC) network. This is to distinguish it from being a nonreciprocal network - which it is not. When an input signal is applied to the anode through the DOC network, the two conductors operate in a plus-minus polarity mode like a coaxial line and drive the reentrant anode as a load composed of two sections in parallel. The manner in which this is proposed to provide a useful control of the circulating electron current flow in the magnetron is beyond the scope of this present discussion which is concerned only with describing the differential operation of the coupling concept. When the anode is generating power in the pi mode, the two wires attached to the anode are driven in the reverse direction by voltages of equal magnitude and phase so that a plus-plus mode excitation is excited. The remainder of the DOC network is configured so that such a mode is prevented from coupling back out to the input signal source. Hence, it is postulated that the second port can be configured to couple a useful input signal into the magnetron anode driving it in a non pi mode configuration while preventing internally generated power in a pi mode on the anode from coupling out in a reverse direction through the same input port. This is not a violation of the principle of reciprocity which applies only to networks with input ports that are capable of only one mode of transmission. Two modes of transmission are involved here.

It is anticipated that the coupling into the rising sun anode for an input signal through the DOC network can be made to present a matched load without reflection. The second, normal output port on the anode can be optimized independently from the first to provide sufficient loading to get whatever bandwidth is desired. Because of the principle of superposition, both the input signal field pattern on the anode and the oscillating pi mode can exist simultaneously. Hence, frequency controlled operation throughout the pulse over some useful bandwidth is anticipated. Higher gain is achieved by the elimination of the mismatch loss.

It is not known whether this new concept will function entirely as postulated. It has not been fully evaluated. Perhaps it won't be entirely successful. But if it doesn't maybe these thoughts will inspire somebody else to think of another way that will lead to an optimized, two-port, unidirectional, magnetron amplifier.

Crossed-Field Research in Universities

Y. Y. Lau
Department of Nuclear Engineering and Radiological Sciences, and
Applied Physics Program
University of Michigan
Ann Arbor, MI 48109-2104

Tel: (313)764-5122 FAX: (313)763-4540 email: yylau@engin.umich.edu

The important functions of a university include generating new knowledge, preserving old knowledge, and helping students learn their own ways of looking into a problem. The natural questions are: How does crossed-field device (CFD) research fit in a university setting and how can such research be coordinated with and have an impact on industrial R&D activities?

First recall that a collection of charged particles in an external magnetic field will invariably experience a crossed electric and magnetic field in some region. Even in the case of a neutral plasma, that region is at the boundary, where the sheath is formed. Yet, in spite of such generality, it has always been a challenge in the academic community to conduct research on electron dynamics in a crossed-field in general and on a specific CFD in particular.

It seems to me that it is relatively easy to generate new knowledge when one works on CFD. The main reason is that the subject matter is rich in unexplained phenomena while the research community is sparsely populated. The subject is known to be difficult [1]. There are lots of things that we do not comprehend even at the fundamental level. For example, though crossed-field devices are generally much noisier than linear beam tubes, the basic mechanisms responsible for noise generation remain obscure, more than 70 years after the invention of the first (Hull) magnetron. Basic research, in which universities excel, may finally provide the clues needed to make real progress in this area.

One relevant and fundamental example is provided by the startling discovery made recently by my student, Peggy Christenson, that cycloidal electron flows in a crossed-field gap are violently unstable when a very small AC voltage is imposed across the gap (which is planar and does not have any circuit element) [2]. This astounding result was discovered after this CFD Workshop was convened. Even more recently, upon the suggestions of Dave Chernin, Christenson found that a small resistive load would destabilize such cycloidal flows even in the absence of an rf signal, and this work is still ongoing [3]. The above-mentioned instabilities, modulational or resistive, are electrostatic and one dimensional -- so they are the most fundamental. They have never been suspected in the past since the more familiar diocotron and magnetron instabilities are necessarily two-dimensional in nature. These recent discoveries are likely to be one of the many reasons behind Pierce's statements on CFD [1],

and we haven't even gone off the ground to venture into the two dimensional analog of these new instabilities.

Another reason that progress can now be made more readily in CFD studies is the availability of a number of very powerful particle codes, as evident from the papers given in this Workshop. This is a distinct, perhaps decisive, advantage we now have which was absent in the late 1950's or 1960's. What is wanting is the dedication of the young generation to learn and to research, with passion. The subject is difficult but it is also fun to work on.

There are obstacles, however. Foremost is the perception and the general lack of interest. The challenge is particularly acute for crossed-field devices. If rf vacuum electronic devices are as "endangered" as the spotted owl, CFD is the most vulnerable among all. For example, the most notable DoD university programs, MURI and ATRI, have only a minimal effort in crossed-field devices. The research activities in these programs have been mainly on linear tubes such as TWT, klystron, free electron laser, gyrotron, cerenkov radiatior, virtual cathode oscillator, and others. Northeastern University (Professor Chung Chan's group) is the only university in the US that has experiments dedicated to CFD noise. Likewise, no national lab or government lab seems to have a significant component in crossed-field research either. Given such a "cultural" bias, it is very difficult to sustain a serious effort in CFD research, or for long. The vicious cycle -- lack of serious interest in CFD erodes support which in turn results in further lack of interest -- must be broken. Given the fact that CFD's are widely used, and that there are many, many good research topics, it is hard for me to accept that CFD works will disappear in a Darwinian fashion. The danger is real, and the precious knowledge base may soon be lost forever.

Another issue is that much of the CFD work is conducted with an interest in national security. In many universities, in particular in their engineering schools, many students who are technically qualified to perform research are foreign students. Already facing many challenges being foreign students, the last thing they or their professors want is to work on a project that provides additional hurdle (real or imagined) just because of their citizenship status.

Finally, I should add that jumping into a subject simply because it is currently fashionable usually is a kiss of death for a researcher. We don't have this problem working on CFD.

[1] J. R. Pierce, 1994, as quoted in Saloom's paper on p. 2 of these Proceedings.
[2] P. J. Christenson and Y. Y. Lau, "A New Modulational Instability in a Crossed-Field Gap", to be presented at the IEEE Int'l Conference on Plasma Sciences, (Boston, MA, June, 1996); submitted to Phys. Rev. Lett.
[3] D. Chernin, P. J. Christenson, and Y. Y. Lau, "A New Resistive Instability in a Crossed-Field Gap", to be presented at the IEEE Int'l Conference on Plasma Sciences, (Boston, MA, June, 1996).

Recommendations and Predictions on the Future of Crossed-Field Devices

John M. Osepchuk, Ph. D.

Full Spectrum Consulting
248 Deacon Haynes Road
Concord, MA 01742
Tel/Fax: 508 287-5849
E-Mail: 75754.3663@COMPUSERVE.COM

Crossed-field devices have enjoyed longevity and growth which has confounded many experts in the past who predicted their demise, especially because of their "excess noise" feature. This ubiquitous phenomenon in akin to that of "multipactor", a wide-spread phenomenon in microwave tubes, though its acknowledgment is avoided in the same fashion that people are averse to admitting the presence of "fleas" in their domiciles [1]. A half-century after the development of the modern magnetron, the crossed-field devices now includes the CFA, a key element in military radar, as well as beacon magnetrons, magnetrons for marine radar, diathermy and most importantly the "cooker magnetron", the heart of the microwave oven.

My recommendations on how to stimulate growth in this field can be characterized in three parts with differing overtones.

Altruistic View

I believe that the cooker magnetron affords modern researchers the ideal vehicle for assessing the validity and usefulness of modern compute codes now being developed for study of crossed-field interaction. The detailed substantiation of my position is in the paper I presented at this Workshop. Here, I'll stress only the key points. The cooker magnetron is now the only entity that resembles a universal standard for crossed-field research. It is inexpensive, stable in design, easily procured world-wide, and exhibits a crisp definitive and reproducible pattern of noise, spurious oscillation and quietness, not observed in any other crossed-field tube.

A computer code, if valid, must be able to predict these features. Beyond that, if the model yields verifiable predictions of the influence of various design parameters, then it will accrue credence as being appropriate for use in the more complicated CFA. The other side of the coin is: Can a computer code be valid if it doesn't predict the crisp features found in the cooker tube?

This exercise, if carried out, will not only help the military but will also help the microwave-oven industry (a "dual use") to find ways of mitigating the excess noise. International groups (e.g. CISPR) are already preparing interim specifications on out-of-band noise with the eventual goal of reducing microwave-oven noise which many fear threatens the many emerging "wireless" technologies which will operate in the 1 to 3 GHz microwave region (e.g. PCS, digital audio, broadcast, etc.).

National View

The ability and facility for large quantity manufacture of high-power efficient crossed-field devices exists only for one application, the cooker magnetron, and only in several Far East countries, principally Japan and Korea. This reality points to a significant void in the national treasures of the U.S. Long-range planners should look for opportunities to establish such a facility in the U.S. with potential applications to future military applications as well as commercial and consumer applications.

Proprietary Advances

I believe that a national goal should be the development of more low-cost magnetrons for different frequencies and different power levels. We have proposed this to NIST without any response or comment. We believe there are proprietary novel advances yet to come which will eventually stimulate economic forces to make available the wider supply of frequencies and powers at low cost.

Predictions

With respect to predictions, my view has been [2] and continues to be that there are many surprises to come. The history of this field exhibits this theme very well [2]--especially the fact that the magnetron survives despite expert predictions of its demise in the 50's and 60's. At a recent conference, one expert predicted that in 10 years the microwave oven will be pretty much the same--with no significant advances. I disagreed. I am not certain of which changes will occur but there will be surprises!

Where? As a possible hint, consider the recent report [3] of the development of a 600 Volt, 67% efficient multi-beam klystron for microwave-oven application. Why was not this breakthrough accomplished in the U.S.? Is the U.S. no longer the leader in tube development, but just users--a "service economy"? Will there be a future in microwave weapons (new pulsed sources), microwave lighting and a host of other promising applications? Will the klystron, TWT or solid-state take over from the maggie because of the noise problem?

Answers to these questions in the next 25 years will be surprising. We in IMPI (e.g. the July '96 Microwave Power Symposium in Boston) will explore some of these questions from the broader view of all types of applications and devices. In future Crossed-Field Device Workshops, I hope we'll see the eventual resolution of the crossed-field noise dilemma--with a definitive recognizable understanding as well as beneficial spinoffs from the new understanding.

References:

1. D. Priest and R. C. Talcott, "On the Heating of Output Windows of Microwave Tubes by Electron Bombardment", Trans. IRE PGED, July, 1961

2. J. M. Osepchuk, "A History of Microwave Heating Applications", IEEE Trans. MTT-32, No. 9, pp. 1200-1224, Sept. 1984

3. G. J. Kim, et al., "The Development of Multi-Beam Klystron for a Microwave Oven", Proc. 30th Microwave Power Symposium, pp. 73-74, IMPI, Manassas, VA; August 1995

List of Authors

Abrams, Richard	125, i
Agee, F. J.	147
Ball, E. M.	212
Birdsall, C. K.	268, 282, 292
Boles, George	66
Brady, M.	212
Brown, William C.	9, 78, 178, 332
Calico, S. E.	147
Carter, R. G.	212
Cartwright, K. L.	282
Cass, A. C.	188
Chan, Chung	133, 202
Chernin, David P.	246, 314, ii
Christenson, Peggy J.	322
Clark, M. C.	147
Dayton, J. A., Jr.	115
Dialetis, Demos	314
Dombrowski, George E.	66, 236
Driscoll, C. F.	188
Edwards, Robert E.	41
Eninger, Jan E.	96
Farney, George K.	334
Fine, K. S.	188
Gilgenbach, R. M.	274
Gopinath, V. P.	282, 292
Hillenberg, Steve	51
Hobbs, David	66
Hor, Charles	125
Huang, X.-P.	188
Kaup, D. J.	300
Kishek, R.	274
Konrad, G. T.	89
Kransky, I. L.	115
Lau, Y. Y.	274, 322, 337, ii
Lemke, R. W.	147
MacGregor, Robert	133, 202
MacMullen, Alexander	51
McDowell, Hunter L.,	217
Mearini, G. T.	115
Mitchell, T. B.	188
Osepchuk, John M.	159, 339
Ruden, Thomas E.	66, 133, 202
Saloom, Joseph A.	1
Scott, M. C.	147
Shih, Arnold	125
Solomon, George A.	85
Riyopoulos, Spilios	256, 314
Thelen, Dean	51
Thomas, Gary E.	300
Vanderberg, Bo H.	96
Verboncoeur, J. P.	268, 282, 292
Vyse, Barry	23
Ye, John Z.	133, 202